Studies on Human Cancer Variant and Mycobacterial Isocitrate Dehydrogenases

A thesis submitted to the Board of the Faculty of Physical Sciences of the University of Oxford in partial fulfilment of the requirements for the degree of Doctor of Philosophy

Raphael Reinbold

Somerville College, Oxford

Michaelmas Term, 2021

Dedicated to my family.

Abstract

Raphael Reinbold *DPhil Thesis*

Somerville College, University of Oxford *Michaelmas Term, 2021*

Studies on Human Cancer Variant and Mycobacterial Isocitrate Dehydrogenases

Mutations in human IDH genes occur in cancer and result in active site IDH variants with a gain-of-function ability to reduce the normal 2-oxoglutarate (2-OG) product of IDH catalysis to 2-hydroxyglutarate (2-HG). As reviewed in Chapter 1, elevated 2-HG levels are proposed to promote tumorigenesis via chromatin remodelling. Efficient IDH1 variant inhibitors bind in an allosteric manner at the dimer-interface and hinder binding of 2-OG and Mg^{2+}. Ivosidenib is an IDH1 variant inhibitor that is approved for acute myeloid leukaemia (AML) treatment; however, acquired second-site S280F mutations to IDH1 render cancer cells resistant to ivosidenib treatment. The research described in this thesis investigated the mechanism of action of the second site IDH1 mutation and how to overcome resistance due to it.

Kinetic analyses show that the IDH1 S280F substitution not only leads to resistance against ivosidenib but results in a higher affinity for 2-OG and Mg^{2+}, and consequently, more efficient turnover of 2-OG to 2-HG. ^{1}H Nuclear magnetic resonance (NMR) studies reveal that IDH1 cancer variants can turn over *D*-isocitrate to 2-HG. The rate of conversion of *D*-isocitrate to 2-HG by S280F substituted variants is more efficient than for IDH1 wildtype or active site variants without the S280F substitution. Mechanistic studies on IDH1 variants provide insights into the influence of various R132 substitutions and the role of the dimer-interface in IDH1 catalysis.

In addition to resistance enabled by more efficient 2-HG production, ivosidenib binding is hindered by the loss of a hydrogen bond to S280, steric hindrance due to the S280F substitution, formation of a new hydrophobic pocket at the dimer-interface, and higher enzymatic affinity for 2-OG and Mg^{2+}. Certain IDH1 variant inhibitors were shown to retain activity against isolated IDH1 R132C S280F and R132H S280F, some with high potency. Non-denaturing mass spectrometry (MS) reveals that inhibitors retaining activity bind with a stoichiometry of two inhibitors per IDH1 variant dimer, in contrast to ivosidenib, which binds with a stoichiometry of one inhibitor per dimer. Several inhibitors reduce 2-HG levels in cell lines overexpressing IDH1 R132C S280F or R132H S280F. Some of these inhibitors are in phase 2 clinical studies (FT-2102, DS-1001B) indicating that S280F-mediated ivosidenib resistance can be overcome by using alternative inhibitors.

Targeting metabolism has also been of long-standing interest in the antibacterial field, including for *Mycobacterium tuberculosis* (*Mtb*) and *Mycobacterium smegmatis* (*Msm*). After establishing production strategies and an activity assay for *Mtb* IDH1/IDH2 and *Msm* IDH, kinetic studies support the proposal that *Mtb* IDH2 is likely the essential IDH isoform for oxidative decarboxylation of isocitrate in *Mtb* metabolism. *Mtb* IDH2 activity is enhanced by several reactive carbonyl group containing metabolites. Most *Hs* IDH1 cancer variant inhibitors are not active against *Mtb* IDH1/IDH2 and *Msm* IDH but some exhibit weak activity.

The overall results provide mechanistic insights into resistance to *Hs* IDH1 variant inhibitors and show how this can be overcome. The studies suggest that targeting IDH may be a viable strategy for mycobacterial treatment.

Table of Contents

Acknowledgements

I should like to thank Prof Chris Schofield for having me in his group and for letting me work on this exciting interdisciplinary project with a strong connection to clinical applications. His enthusiasm and incredible knowledge were always encouraging throughout the journey of my DPhil. His deep scientific understanding and creativity are amazing to experience, and it was a pleasure to work with him. Special thanks to my day-to-day postdoc supervisor Dr Martine Abboud, who conceptualised the projects discussed in this thesis, and supported me in the process of applying for this DPhil position. Her advice, support and guidance throughout my DPhil are appreciated a lot. She not only taught me lots of scientific skills and knowledge, but also many transferrable skills. I would also like to thank Dr Patrick Rabe for all his advice, guidance and supervision with the crystallographic studies conducted in this thesis. I have learned a lot and the success of the crystallography in this thesis would not have been possible without him. Many thanks to Dr Adam Hardy for managing and running our lab. Thanks to Dr Victor Mikhailov for help with non-denaturing MS studies. Thanks to Maximillian Staudt for being a great visiting student on the IDH project.

I would also like to extend my thanks to Dr Luiz de Carvalho and Dr Acely Garza-Garcia for their supervision at the Francis Crick Institute and Dr Rob Young and Dr Jo Redmond for supervision at GSK. Thanks to Prof Akane Kawamura for supervision in my rotation project on LSD1, for being a co-supervisor for my DPhil, and for managing and founding the GSK-Crick Chemical Biology CDT, a great programme with world-leading institutions, together with Nina Stamps. I would also like to thank the BBSRC, GSK, and the Francis-Crick Institute for funding.

From the Schofield group, I would like to thank Tobias John for lots of fruitful discussions, help in the lab and being a tolerable Swabian. Special shoutout to the “Entrepreneurs on tour” and fellow gardeners Klemensas Simelis and Tim Suits for some great teamwork and harvests. Shoutout to the other boys Dr Roman Belle, Dr Jos Kamps, Siegfried Thun-Hohenstein (my successor on the IDH project), Jame(s) Linyard, and Freddie Foster. Thanks to Tika Malla and Xiao Liu for being great friends and bay neighbours. I would also like to thank Dr Lennart Brewitz and Dr Karina Calvopina for proofreading my thesis in addition to the people already mentioned.

Special mention to my flatmates in Casa Amor for most of my time in Oxford, Adam Thomas and Joel Kosmin. After long days in the lab, it has always been great to come home, hang out in the lounge and chat about the most random things (and share the occasional Dominos or Papa John's £100 order ("it would be stupid not to order Pizza for £100 to get 50% off"). I would also like to thank the extended members of Casa Amor, Dr Connor Scott and Jonathan Sheridan for many fun evenings and nights out. You all have been very important for my life in Oxford.

For my very enjoyable Oxford DPhil experience, Somerville College and especially the MCR was crucial. It has been great for balancing all the academic work, having fun experiences and events, and for enabling me to meet great people from all over the world. Special mention to Karolina Weglinska, who has been close to me from the beginning ("2018-Raph"), when we shared great moments over "Love Island" and GTC ball. I really enjoyed our time over the following years when we had fun social-sec parties, nights out (careful with the lime) and summer days in port meadow, and, more recently, some very good chat. I am very happy that we have met, and I am very much looking forward to the holiday(s) together celebrating finishing this DPhil thesis.

I would also like to thank the other members of "JAE": Bahar Kashef (I especially loved our foraging walks), Ashrakat Elshehawy (co-host of Rashbash 2021), and Gaurav Dubey. We ran Somerville MCR during the Covid-19 pandemic, and I am very happy that we became friends for life in the process. I will always remember our Cotswolds trip ("My pants!!!"), our trip to Beachy Head, and I guess we are at a point now where we can laugh about Valentines-gate. Special mention also to Vicky Lee for sharing the social-sec experience, lots of Love Island and fun nights out; and Oana Gurau for sharing my love for port meadow. Thanks to Dominic Gerhartz for the occasional Shisha evenings. I would also like to thank many other unnamed friends and colleagues who have contributed to my doctoral studies and my life in Oxford.

Finally, the biggest thanks goes to my family: my parents Brigitte and Fred, and my sister Annalena. It cannot be appreciated enough how much support I have received all my life. This support and continuous encouragement have enabled me to pursue my education, which in the end made it possible for me to do very exciting research at the University of Oxford and compose this DPhil thesis. I could have not done that without you.

Abbreviations

2-HG	2-hydroxyglutarate
2-OG	2-oxoglutarate
AML	acute myeloid leukaemia
c	concentration
CD	circular dichroism
CV	column volume
DNA	deoxyribonucleic acid
dNTP	deoxynucleoside triphosphate
DpnI	type II restriction enzyme
DSC	differential scanning calorimetry
DSF	differential scanning flourimetry
FDA	Food and Drug Administration
h	hour
HEPES	4-(2-hydroxyethyl)-1-piperazine ethanesulfonic acid
HIF	hypoxia-inducible factor
Hs	*Homo sapiens*
IC_{50}	half maximal inhibitory concentration
ICL	isocitrate lyase
IDH	isocitrate dehydrogenase
IPTG	isopropyl β-D-1-thiogalactopyranoside
ITC	isothermal titration calorimetry
kBp	kilobasepairs
k_{cat}	turnover rate
K_D	dissociation constant
KDM	histone demethylases
K_M	Michaelis-Menten constant
LB	lysogeny broth
min	minutes
MS	mass spectrometry
Msm	*Mycobacterium smegmatis*
Mtb	*Mycobacterium tuberculosis*
$NADP^+$/NADPH	nicotinamide adenine dinucleotide phosphate
NMR	nuclear magnetic resonance spectroscopy
NOG	N-oxalylglycine
OD_{600}	optical density at a wavelength of 600 nm
PEP	phosphoenolpyruvate
pH	potentia Hydrogenii
PHD	prolyl hydroxylase domain
PMSF	phenylmethylsulfonylfluorid
RMSD	root-mean-square deviation
SDM	site-directed mutagenesis
SDS PAGE	sodium dodecyl sulfate polyacrylamide gel electrophoresis

sec	seconds
SEC-MALS	size exclusion chromatography coupled to multi angle light scattering
SOC	SOB (Super Optimal Broth) with 20 mM glucose
TCA	tricarboxylic acid
TCEP	tris(2-carboxyethyl)phosphine
TET	ten-eleven translocation
T_m	melting temperature
Tris	tris(hydroxymethyl)aminomethane
wt	wildtype

Declaration of Authorship

This report, and the work of which it is a record, were carried out by myself unless otherwise acknowledged.

Electrochemical experiments: Ryan Herold, University of Oxford (Chapter 2, 4). Non-denaturing MS/MS: Dr Victor Mikhailov (Chapter 2). DSC and SEC-MALS analyses: Dr David Staunton, University of Oxford (Chapter 2,4,5). Crystallography: Building of a starting model of the crystal structure of R132C S280F complexed with DS-1001B was conducted by Dr Ian Clifton (Chapter 3). Cell work and metabolomic analyses: Dr Chiara Bardella and Dr Alina Finch (University of Birmingham), Ingvild Hvinden (University of Oxford) (Chapter 3). Protein Production: *Hs* IDH1 wt (Chapter 4) and *Msm* IDH (Chapter 5) were produced by Dr Martine Abboud, University of Oxford.

Several analyses in Chapter 5: Conducted by Maximillian Staudt, a visiting student from the University of Freiburg, who I supervised:

- Kinetic analysis of 2-HG production catalysed by *Mtb* IDH.
- Screening for metabolic cross-regulation of *Mtb* IDH1 and *Mtb* IDH2.
- CD and T_m analyses of *Mtb* IDH2 in the presence of several metabolites.
- Screening for alternative substrates of *Mtb* IDH1.
- Activity screening of various divalent metal ions with *Mtb* IDH1 and *Mtb* IDH2.
- Inhibitor screening for *Mtb* IDH1 and *Mtb* IDH2.

Chapter 1

Introduction

Contents

1 Introduction

1.1 Role of Metabolites in Cancer

The first report of changes in metabolism in cancer patients extends to Otto Warburg in 1930.[1, 2, 3] In this report, Warburg described how cancer cells change their energy metabolism by limiting it largely to glycolysis rather than mitochondrial oxidative phosphorylation. Glycolysis is less efficient in producing ATP than oxidative phosphorylation, and consequently, glucose uptake is upregulated in many tumour tissues, in part by upregulating glucose transporters like GLUT1.[1] This knowledge has been exploited to visualise tumours using positron emission tomography (PET)[4]; ^{18}F-fluorodeoxyglucose is injected into the bloodstream and its increased uptake into tumour cells can be visualised by the emission of a positron.[4] While metabolic alterations were not originally defined as one of the six core hallmarks of cancer as described by Hanahan and Weinberg[5], changes in cellular energy metabolism were subsequently added as one of two emerging hallmarks of cancer.[1]

Since the first reports by Warburg et al., the study of metabolic changes in cancer metabolism had not been a priority until the early 2000s, [6] when it was found to be a widespread phenomenon in cancer cells. This work was facilitated by advances in mass spectrometry (metabolomics) and cancer genome sequencing efforts.[6] More recently, dysregulation of metabolism has been linked to mutations in several enzymes involved in the tricarboxylic acid (TCA) cycle and related cellular biochemistry.

Succinate dehydrogenase (SDH) is a TCA cycle enzyme that catalyses the conversion of succinate to fumarate (**Figure 1.1**). Germline loss-of-function mutations in the genes encoding SDH have been reported in several cancer types including paragangliomas and renal carcinomas[7]; the mutations were found to correlate with an accumulation of succinate in cells.[7]

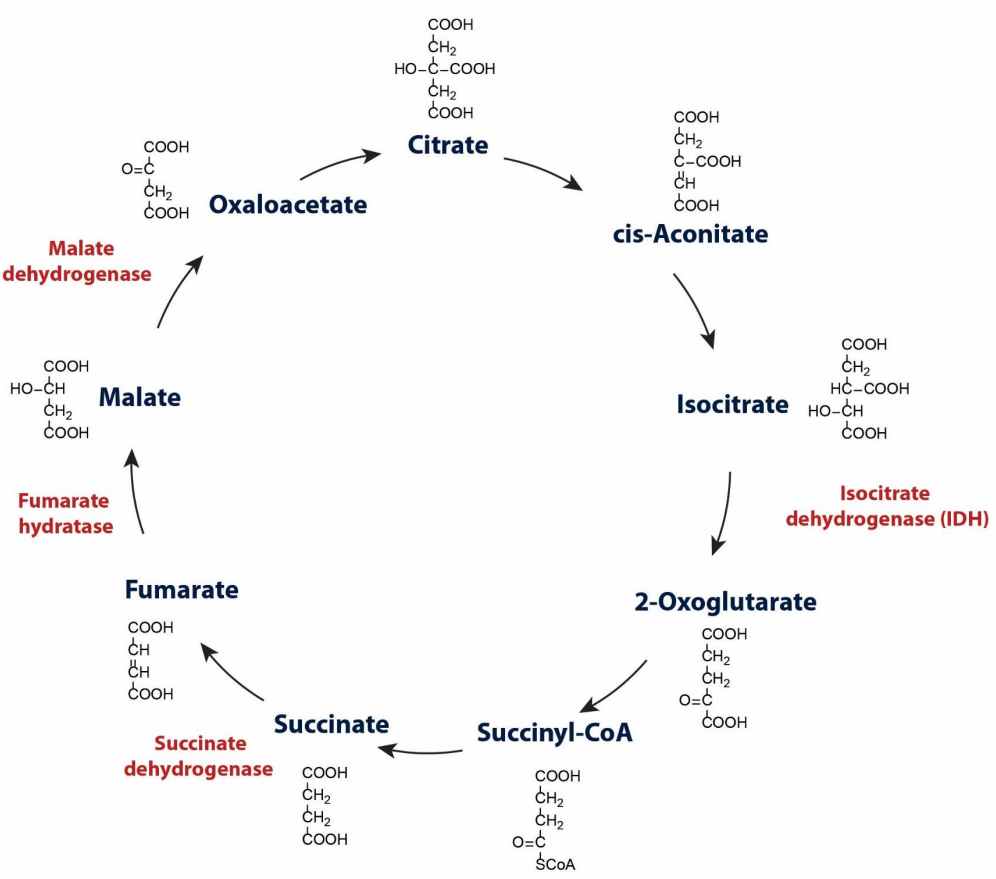

***Figure 1.1** | Tricarboxylic acid (TCA) cycle in humans. The enzymes for which mutations are reported in cancer are shown in red.*

Fumarate hydratase (FH) converts fumarate to malate in the TCA cycle (**Figure 1.1**). Heterozygous germline loss-of-function mutations to FH, which are then followed by a loss of heterozygosity, are found in renal cell cancer or paraganglioma[6]; deletions of FH have also been reported in neuroblastomas.[6] These FH mutations correlate with the accumulation of fumarate in cells.[7]

Malate dehydrogenase 2 (MDH2) catalyses the conversion of malate to oxaloacetate in the TCA cycle (**Figure 1.1**). Germline mutations are found in MDH2 in paraganglioma.[8] However, no accumulation of malate has been recorded inside the cell.[8]

Isocitrate dehydrogenase (IDH) catalyses the oxidative decarboxylation of isocitrate to 2-oxoglutarate (2-OG) (**Figure 1.1**). Mutations in the genes encoding for isocitrate dehydrogenase (IDH) 1 and 2 are the best-studied and most abundant mutations of genes encoding for metabolic enzymes in cancer.[9] Like the mutations in the genes for SDH, FH, and MDH2, IDH mutations were originally classified as loss-of-function mutations. In contrast to the germline mutations in SDH, FH, and MDH2, mutations in the genes encoding for IDH1

and IDH2 are somatic.[10] In 2009, Dang et al. [11] showed that mutations in genes encoding for IDH1 and IDH2 do not result in a loss of function; instead they confer a gain of function in which the IDH variants have an increased ability to effectively reduce the normal 2-oxoglutarate (2-OG) product of IDH catalysis to (*R)*-2-hydroxyglutarate (2-HG, note that hereafter 2-HG refers to (*R)*-2-HG; **Figure 1.2**). Consequently, 2-HG levels are substantially elevated (up to mM levels) inside cells.[11]

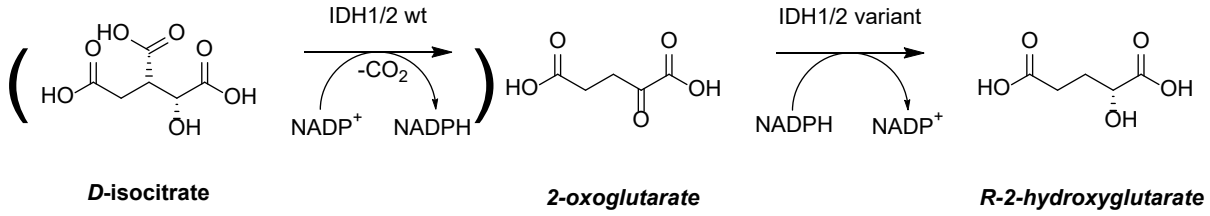

***Figure 1.2** | IDH1/2 variants gain the ability to catalyse the reduction of 2-oxoglutarate to 2-hydroxyglutarate.*

1.2 Role of *Hs* IDH

In humans, there are three isoforms of IDH.[12] While IDH1 is present in the cytosol and peroxisomes, IDH2 and IDH3 are localised to the mitochondrial matrix.[13] IDH3 is a heterotetramer, and responsible for catalysing the oxidative decarboxylation of *D*-isocitrate to 2-OG and CO_2 in the TCA cycle irreversibly (**Figure 1.3**).[13]

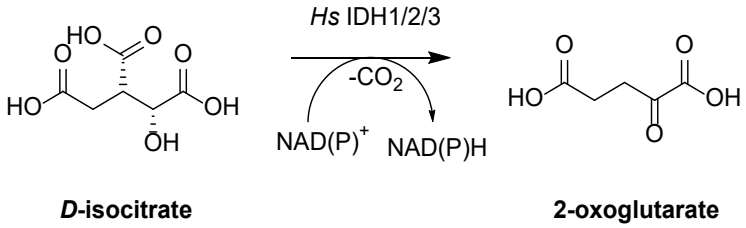

***Figure 1.3** | Oxidative decarboxylation of isocitrate to 2-OG under concomitant reduction of $NADP^+$ to NADPH for IDH1/2 and NAD^+ to NADH for IDH3.*

IDH3 is composed of 2 α-subunits, 1 ß-subunit, and 1 γ-subunit. One α-subunit forms a heterodimer with a ß-subunit (**Figure 1.4**, B); the other α-subunit forms a heterodimer with the γ-subunit.[14] The apparent heterotetramer is a result of the association of the two heterodimers via their CLIP-associated protein (CLASP) domains (**Figure 1.4**, A).[14] CLASP domains are commonly observed in IDHs and consist of two two-stranded antiparallel ß-sheets. The CLASP domain is important for the formation of the IDH3 quaternary structure.[14]

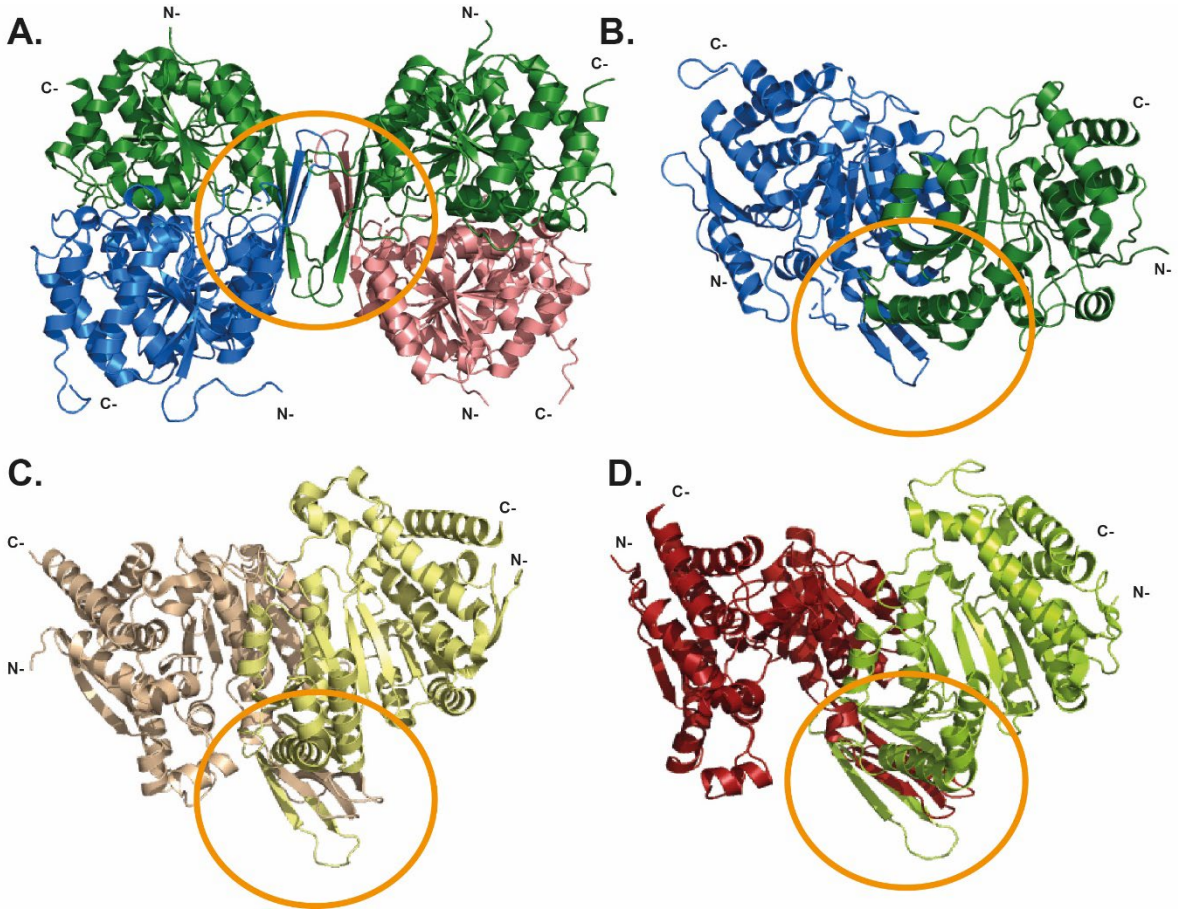

***Figure 1.4** | Views from crystal structures of Hs IDHs. **A.** View from a crystal structure of IDH3 (7CE3[14]). There are 4 chains in the asymmetric unit. One-subunit (green) forms a heterodimer with the ß-subunit (blue) (see **B.**). The other α-subunit forms a heterodimer with the γ-subunit. Both heterodimers associate to a heterotetramer via their CLASP domains. **C.** View from a crystal structure of IDH1 (1T0L[15]). Chain A: wheat, chain B: yellow. **D.** View from a crystal structure of IDH2 R140Q (5SVO[16]; note that there is no reported crystal structure of Hs IDH2 wt). Chain A: red, chain B: limon.*

IDH3 utilises NAD^+ and catalyses the irreversible conversion of isocitrate to 2-OG (**Figure 1.3**).[17] IDH3 is phylogenetically distinct from IDH1 and IDH2, which share 70% sequence identity.[12] IDH1 and IDH2 are homodimeric (**Figure 1.4**, C/D) and utilise $NADP^+$ for the conversion of isocitrate to 2-OG (**Figure 1.3**). The major physiological role of IDH1 is to provide NADPH[17], which is important for the cell to ensure redox balance and also can be used in fatty acid biosynthesis. Similarly, the primary role of IDH2 is to provide NADPH which plays an important role in protecting mitochondria from oxidative damage.[12] In a state of hypoxia, both IDH1 and IDH2 can catalyse their reverse reaction, i.e. use 2-OG (derived from glutamate) and CO_2 to make isocitrate. Isocitrate can then be converted to citrate, which is converted to oxaloacetate and acetyl-CoA by ATP citrate lyase.[18] Acetyl-CoA can be utilised for fatty acid biosynthesis.[18]

All 3 human IDHs are dehydrogenases and hence, belong to the superfamily of oxidoreductase enzymes (EC1) which catalyse the oxidation of one substrate (electron donor) with the

concomitant reduction of another substrate (electron acceptor)[19]. Oxidoreductases are one of the most widespread classes of enzymes and use a variety of different redox cofactors. IDHs utilise the dinucleotides NAD^+/$NADP^+$ for electron transfer.[12]

IDH1, IDH2 and IDH3 have a typical Rossmann fold, which is a key motif in NAD(P)-dependent oxidoreductases because of its involvement in dinucleotide binding.[19] The Rossmann fold is conserved over a wide range of oxidoreductases and contains an α-helix and two parallel ß-strands.[19] There is a glycine-rich loop between one α-helix and a ß-strand which is important for the binding of the pyrophosphate group.[19] Usually the cofactor binding domains exhibit two Rossman-folds: while one interacts with the nicotinamide ring of NAD^+/$NADP^+$, the other one interacts with the adenine ring.[19]

Mutations in IDH1 and IDH2 are found in cancer, but there are very few reports of cancer-associated mutations in IDH3.[13] Consequently, the following sections (1.3-1.5) focus on the roles of IDH1 and IDH2 in cancer.

1.3 *Hs* IDH1 and IDH2 Mutations in Cancer

IDH1 mutations were first observed in secondary glioblastoma multiforme (GBM) and grade 2/3 gliomas, and were mostly found to encode for an IDH1 R132H variant.[20] Shortly after, IDH1 and IDH2 mutations were identified in acute myeloid leukaemia (AML) patient samples.[21, 22] All mutations in IDH1 and IDH2 genes linked to cancer are heterozygous and mutations discussed in this section lead to an increase in the ability of the enzyme to catalyse the reduction of 2-OG to 2-HG.

Since these initial reports, mutations in genes encoding for IDH1 or IDH2 have been identified in various types of cancer. Most abundantly, IDH mutations are found in grade 2/3 gliomas (> 70 %) and in secondary glioblastomas (55-88%).[18] Mutations are also present in AML (15-30%)[18], chondrosarcomas (50%)[23], and other cancers. IDH1 mutations (mostly at R132) are generally more common than IDH2 mutations,[12] but their distribution varies depending on the cancer type, e.g. IDH2 mutations are more commonly found in AML than IDH1 mutations.[24]

IDH2 mutations are located in the codons encoding for R172 (homologous to IDH1 R132) or R140; both R172 and R140 are involved in isocitrate binding in the IDH2 active site.[22] IDH2 mutations in gliomas are rare, and if identified, mostly result in R172K substitutions.[22] The most common (and to date exclusive) mutation in AML is the IDH2 R140Q variant, although other substitutions are also observed, including R140W/L and R172K/M/Q/G.[22]

In gliomas (grade 2/3, and secondary GBM), the most commonly observed substitution is IDH1 R132H (85%). Additionally, other substitutions at the R132 residue are found; including R132C and R132S, but also, with very low incidence, R132L/G/V.[22] Very rarely, IDH1 R100Q variants (homologous to IDH2 R140Q) are observed. [22] It has been reported that the catalytic turnover of a recombinantly produced IDH1 R100Q variant is not efficient, possibly the reason behind its low incidence. [25] As outlined above, the distribution of specific IDH1 variants is dependent on the tumour type.[24] While IDH1 mutations in gliomas mainly lead to an IDH1 R132H variant, the overall distribution of IDH1 R132H in AML is similar to that of R132C. Interestingly, IDH1 R132C is the most common IDH variant in chondrosarcomas.[26, 22]

1.4 Physiological Relevance of *Hs* IDH Mutations

In 2009, Dang et al. showed that mutations in genes encoding for IDH1 and IDH2 are not, as was previously reported, loss-of-function mutations, but confer a gain-of-function which results in the new ability of IDH1 and IDH2 variants to catalyse the neomorphic reduction of 2-OG to 2-HG.[11] 2-HG has been branded an oncometabolite[27] and is one of the most used/validated small molecule biomarkers for cancer. 2-HG is a biomarker used for therapy control in AML by measuring blood plasma-2-HG-levels[28] and can be used for intraoperative diagnosis of the mutation status of gliomas using Raman spectroscopy.[29] Since 2016, the IDH mutation status has become a leading diagnostic criterium for the CNS tumour classification by the World Health Organisation (WHO).[18]

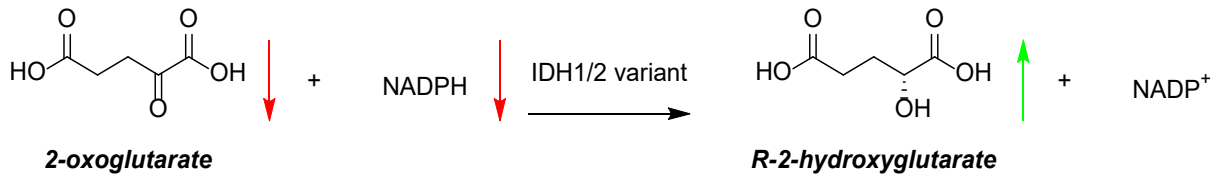

***Figure 1.5** | IDH1/2 variants catalyse the reduction of 2-OG to 2-HG, which could result in a reduction in 2-OG and NADPH levels, and an increase in 2-HG levels.*

In principle, an IDH1 gain-of-function reaction could result in at least 3 direct effects (**Figure 1.5**):

- The depletion of 2-OG, which renders it not available as a substrate for 2-OG dependent enzymes.
- The increased consumption of NADPH, which is an essential reducing agent for the cell and important for controlling oxidative stress.
- The formation of 2-HG in high levels, which, due to its similarity to 2-OG, could inhibit 2-OG-dependent enzymes.

These three hypotheses are discussed with regards to their potential roles in cancer involvement.

(i) 2-OG is turned over to 2-HG which potentially limits its availability as a substrate for 2-OG dependent enzymes. It was proposed that 2-OG oxygenases including prolyl hydroxylase domain (PHD) 2, which hydroxylates hypoxia-inducible factor (HIF)α, histone demethylases (KDMs), which are involved in histone demethylation, and ten-eleven translocation enzymes (TETs), which are involved in DNA oxidation, could be affected by reduced availability of 2-OG. However, in general, no or little difference in cellular 2-OG levels has been observed in cells harbouring IDH1 or IDH2 variants [30]. There is a continuous source of 2-OG in the cell, which might compensate for consumption by IDH variants, including via glutamate metabolism. [30] Consistent with this proposal, in gliomas bearing an R132H mutant, increased expression of glutamate dehydrogenase (GLUD) 1 and GLUD2 has been reported which catalyse the turnover of glutamate to 2-OG.[18]

(ii) NADPH is oxidised to $NADP^+$ in the gain-of-function reaction catalysed by IDH1 variants. NADPH is an essential reducing agent for the cell, protecting it from oxidative damage. NADPH is also important for fatty acid biosynthesis[31] and glutathione (GSH) production. Glutathione is a tripeptide that scavenges free radicals and is an efficient antioxidant.[32] The oxidised form of GSH, glutathione disulphide (GSSG), can be regenerated to GSH in NADPH-dependent processes.[33] IDH1 and IDH2 are important producers of NADPH in the cell (IDH1 in the cytosol and peroxisomes, IDH2 in mitochondria). Bleeker et al. have reported that IDH1 produces 65% of the total NADPH in glioblastoma tissue.[34] When glioblastoma tissue harbouring an IDH variant (IDH1 R132H) was investigated, the NADPH

production capacity was decreased by ~40%. This substantial decrease in NADPH levels is likely not only because of the inability of IDH wt to sufficiently produce NADPH, but also the IDH1 variant catalysed NADPH consumption via the gain-of-function reduction of 2-OG to 2-HG.

(iii) Physiologically, 2-HG is endogenously present only at low levels as it is quickly metabolised into 2-OG via D-2HG dehydrogenase (D2HGDH).[12] IDH variants catalyse the reduction of 2-OG to 2-HG, and as a result, when IDH1 or IDH2 mutations occur, 2-HG levels are elevated by >100-fold. In this scenario, the 2-HG metabolising enzyme D2HGDH may be overloaded, resulting in 2-HG levels of 5-35 μmol per gram of tumour (5-35 mM, if the tissue density is ~ 1 g/mL)[35]. D2HGDH is located inside the mitochondria; spatial separation may thus, especially in the case of IDH1 variants, which produce 2-HG in the cytosol, contribute to the low clearance of 2-HG. [12]

When the gain-of-function reaction of IDH1 variants was discovered[11], three major cellular effects were proposed to be involved in cancer progression: 2-OG consumption, NADPH depletion, and the build-up of 2-HG. The combined reports suggest that potentially lowered 2-OG levels are unlikely to be involved in cancer progression. Depletion of NADPH leads to an increased sensitivity to reactive oxygen species and further metabolic changes (e.g. fatty acid biosynthesis), which likely plays a role in tumour progression in cancer cells bearing IDH variants. The highly elevated 2-HG levels may result in inhibition of several 2-OG-dependent enzymes, which is discussed in the following Section (1.5).

1.5 Physiological Effects of the Inhibition of 2-OG Dependent Enzymes

Inhibition of 2-OG dependent oxygenases by high levels of succinate has been reported as a result of SDH loss-of-function mutations[7,36]; and similarly, this inhibition has been proposed for high levels of fumarate as a result of FH loss-of-function mutations.[6] Furthermore, 2-HG has been shown to inhibit several 2-OG-dependent enzymes. The effects of this are discussed below.

2-OG dependent oxygenases play an important role in the chronic hypoxia response, the inhibition of which has been suggested to be involved in tumorigenesis. PHD2 is a 2-OG and oxygen-dependent oxygenase that hydroxylates HIFα under normoxic conditions. This leads to ubiquitination of hydroxylated HIFα by an E3 ubiquitin ligase, of which the von Hippel-Lindau (VHL) protein is a substrate recognition protein, causing subsequent HIFα degradation

by proteasomes. When O_2 availability is limited, PHD2 catalysed hydroxylation of HIFα is inefficient. HIFα is stabilised and migrates to the nucleus where it dimerises with HIFß to form α,β-heterodimeric HIF. HIF can then bind to the HIF-response element in DNA promoter regions, which leads to transcriptional activation of a myriad of genes ameliorating the effects of hypoxia.

Inhibition of PHD2 by succinate and fumarate is reported to result in stabilisation of HIF even if oxygen is present.[7] It should be noted, however, that fumarate, and , in particular, succinate are weak PHD2 inhibitors.[7] Thus, it is possible that the elevation of HIFα in SDH/FH mutant cell lines may not be due to PHD inhibition. The "pseudohypoxia" could lead to the activation of the chronic hypoxia response and downstream effects like angiogenesis, which may aid tumour growth, and the upregulation of glycolysis and glucose uptake. [37] Hence, the HIFα genes are often viewed as oncogenes.[12]

It was also proposed that 2-HG might inhibit PHD2 creating pseudohypoxia. However, like succinate, 2-HG is a weak inhibitor of PHD2 (IC_{50} = 7.3 mM[27]). Some studies even report 2-HG as an agonist of PHD2[38], but this is likely a result of non-enzymatic conversion of 2-HG.[39] Furthermore, studies on the influence of 2-HG on HIF activity in gliomas harbouring an IDH variant are contradictory and show either no change, upregulation, or downregulation of HIF.[12] Although HIFα is often viewed as an oncogene (and this is almost certainly the case in kidney tumours[40]), there is evidence that HIFα is a tumour suppressor in some tumour types such as glioma[41] and leukaemia[42]. In summary, there is mixed evidence of the involvement of PHD inhibition and HIF-related effects in tumorigenesis of IDH1 variant tumours.

2-OG-dependent oxygenases are also involved in the regulation of histone and DNA methylation. TET oxygenases catalyse the demethylation of 5-methyl-cytosine and KDMs catalyse demethylations of methylated lysine residues on specific histone regions. TETs and KDMs are both involved in transcriptional regulation by directing the methylation status of DNA and histones.

High 2-HG levels are reported to inhibit several 2-OG-dependent enzymes, including the KDMs (e.g. IC_{50} (KDM4A) = 24 μM[27]) and TETs (IC_{50} (TET2) = 5.3 mM[43]). Inhibition of these enzymes leads to hypermethylation of DNA and histones and, consequently, has been proposed to block cellular differentiation resulting in tumour growth.[12] Hypermethylation of DNA and histones is observed in gliomas and AML. Consequently, inhibition of TET and

KDMs by 2-HG might be involved in tumorigenesis as a result of the gain-of-function mutation.[12]

The PHDs, TETs, and KDMs are proposed to be involved in tumorigenesis linked to the gain-of-function mutation in IDH via their inhibition by 2-HG.[12] While inhibition of KDMs and TETs by 2-HG may cause a hypermethylated state observed in gliomas and AML and hence, lead to a block in cellular differentiation, the role and influence of 2-HG on PHDs and the HIF system is less clear.

1.6 Structure and Mechanism of Action of *Hs* IDH1 wt

Due to the higher incidence of IDH1 variants in cancer compared to IDH2 variants, the focus in the following sections is on IDH1 wt and its variants.[22]

1.6.1 Structure of *Hs* IDH1 wt

Hs IDH1 consists of three major domains: a large domain (residues 1-103 and 286-414; this domain also includes a typical Rossman fold involved in dinucleotide binding), a small domain (residues 104-136 and 186-285; this forms an α/ß sandwich structure), and a CLASP domain (two two-stranded antiparallel ß-sheets). The CLASP domain is important for dimer-formation (**Figure 1.6**, A; note that the active form of IDH1 is the dimer).[15] The CLASP domain interlocks the two monomers together to form the two active sites.[15] The formation of the dimer is also facilitated by interactions between the α9 and α10 helices from the small domain of each monomer, which build the dimer-interface (**Figure 1.6**, A). The active site cleft is located between the large and the small domain (**Figure 1.6**, A).[15]

IDH1 has been shown to manifest at least two stable conformations, an open inactive conformation with NADPH bound, and a closed active conformation with NADPH, isocitrate, and metal ion bound.[15] A presumed third stable conformation, labelled semi-open, is proposed to be an intermediate stage between the closed and open conformations.[15]

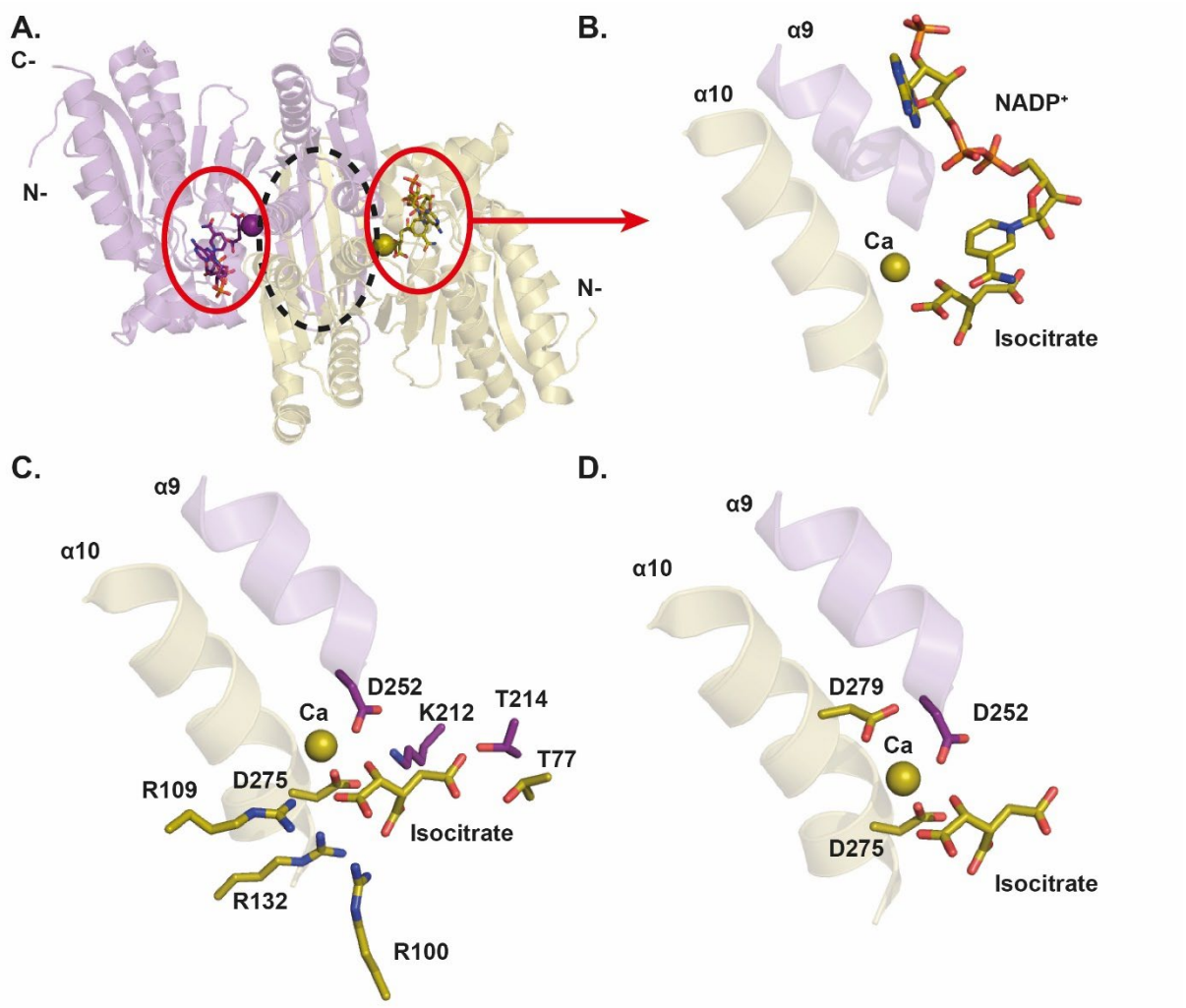

Figure 1.6 *| Crystal structure of IDH1 wt (1T0L[15]).* ***A.*** *View from a crystal structure of IDH1 wt complexed with isocitrate, calcium, and NADP+. The homodimer is formed by chain A (purple) and chain B (olive). Dimer-interface: black, dashed circle. Active sites: red circle.* ***B.*** *Magnified section of the active site with α9 helix (chain A, purple) and the α10 helix (chain B, olive).* ***C.*** *Active site with the residues involved in isocitrate binding.* ***D.*** *Active site view showing the residues involved in metal binding.*

In the active IDH1 conformation, the two active sites of the IDH1 homodimer are composed of residues from both monomers (**Figure 1.6**, A).[15] Eight residues are directly involved in isocitrate and metal binding: 5 from one monomer and 3 from the other (**Figure 1.6**, B/C).[15] While the divalent metal cation utilised by IDH1 is Mg^{2+}, Ca^{2+} is usually used for crystallisation. Ca^{2+} is an inactive divalent cation that helps enable IDH to crystallise in the closed active conformation without enabling turnover, which would result in dynamic changes to the active site and, potentially, the change to an open inactive conformation. The metal ion is bound by three aspartates: D-252 from chain A (α9 helix), and D-275 and D-279 (both α10 helix) from chain B (**Figure 1.6**, D). The metal ion coordinates to isocitrate via its hydroxyl group and the α-carboxylate. Isocitrate is further bound by T77, R100, R109, R132, and D275 from Chain B, and K212, T214, and D252 from Chain A (**Figure 1.6**, C).[44] $NADP^+$ is mainly

bound by residues from the large domain and binding is similar in the open and closed conformation with the exception of D-279, whereby, in the absence of isocitrate, D-279 mimics the substrate and hydrophobically interacts with the nicotinamide ring.[15]

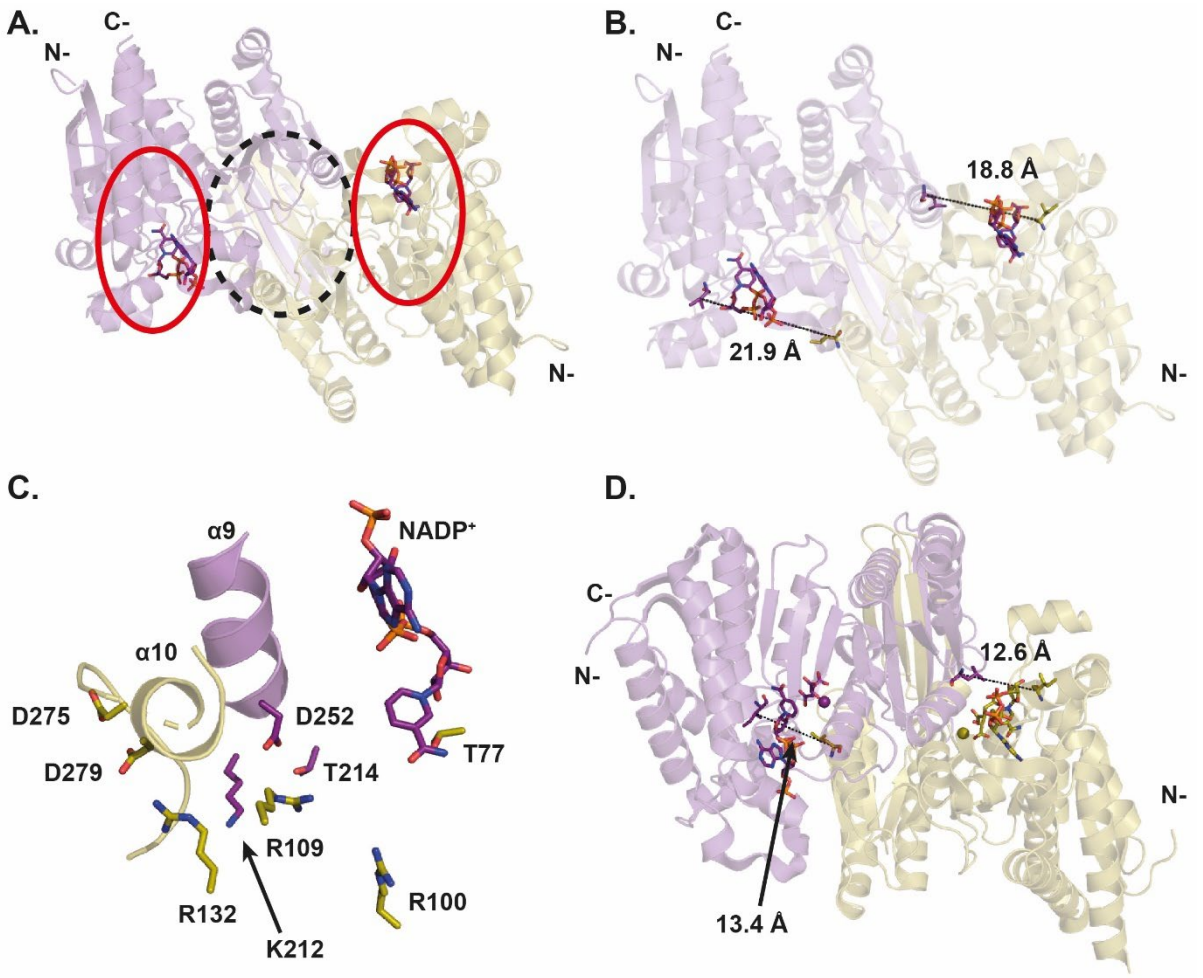

***Figure 1.7** | Crystal structure views of IDH1 wt in the open and closed conformation. **A.** View from a crystal structure of IDH1 wt complexed with NADP⁺ in the open conformation. The homodimer is formed by chain A (purple) and chain B (olive). Dimer-interface: black, dashed circle. Active sites: red circle. **B.** The distance of the active site cleft as measured between C-α of I76 (chain A) and L250 (chain B) is 21.9 Å and of the active site cleft between I76 (chain B) and L250 (chain A) is 18.8 Å. **C.** Magnified section of the active site with α9 (chain A, purple) and α10 (chain B, olive). The residues which are involved in isocitrate and metal binding in the open conformation are shown as sticks. Compared to the closed conformation (**Figure 1.6**, C), many residues are shifted. **D.** View from a crystal structure of IDH1 wt complexed with calcium, isocitrate and NADP⁺ in the closed conformation. The homodimer is formed by chain A (purple) and chain B (olive). The distance of the active site cleft as measured between C-α of I76 (chain A) and L250 (chain B) is 13.4 Å and of the active site cleft between I76 (chain B) and L250 (chain A) is 12.6 Å.*

In the open inactive IDH1 conformation, there are several structural differences compared to the closed active conformation. Firstly, the width of the active site cleft in the open conformation, as measured by the C-α distance between residue I76 from chain A and L250 from chain B, is ~21.2 Å[15] (and 18.8 Å between chain A, L250 and chain B, I76) which reflects "opening" of the active site and hence, an inactive state of IDH1 (**Figure 1.7**, B).[45] In the closed conformation, the two active site clefts have a width of 12.6 Å (between C-α of chain A, I76 and chain B, L250) and 13.4 Å (between C-α of chain A, L250 and chain B, I76) (**Figure 1.7**,

D).[15] Furthermore, the α10 helix partly unwinds to a more loop-like conformation and is less well resolved suggesting higher flexibility (**Figure 1.7**, A/C). [15] The higher flexibility is likely because D275 and D279, which are involved in metal and isocitrate binding, are both located on α10. In the open conformation, the three isocitrate binding residues D252, K212, and T214 from chain A are distant from the active site (**Figure 1.7**, C). The binding of isocitrate and a divalent metal ion recruit these residues back to the active site, enabling a conformational switch to the closed active conformation. This proposal is in accord with a report demonstrating that *D*-isocitrate and Mg^{2+} binding to IDH1 wt (copurified with two NADPH molecules) results in a conformational change from the open inactive to the closed active conformation.[44] Preincubation with isocitrate and Mg^{2+} before the induction of turnover by the addition of $NADP^+$ eliminates the lag phase observed at early reaction timepoints. This lag phase occurs when the reaction is first initiated by the addition of isocitrate and Mg^{2+} and can be attributed to a change from the open to the closed conformation.[44]

1.6.2 Catalytic Mechanism of *Hs* IDH1 wt

The consensus mechanism for the oxidative decarboxylation of isocitrate to 2-OG catalysed by IDH is as follows. The first step is initiated by the hydroxyl group at C2 being deprotonated by a base (Lys-212) which itself has likely been deprotonated by an aspartate (likely Asp-279[46]) (**Figure 1.8**, A). Next, a hydride from C2 of isocitrate is transferred to $NADP^+$, reducing it to NADPH (**Figure 1.8**, A). The enzyme-bound intermediate of this step is oxalosuccinate, a ß-keto-carboxylic acid, which can form a 6-membered transition state enabling efficient decarboxylation (**Figure 1.8**, B). CO_2 is then cleaved from C3 and results in the generation of a decarboxylated enolate (**Figure 1.8**, C). Finally, the enolate species is protonated at the C3 carbon by Tyr-139 to form 2-OG (**Figure 1.8**, D).[46,44,47]

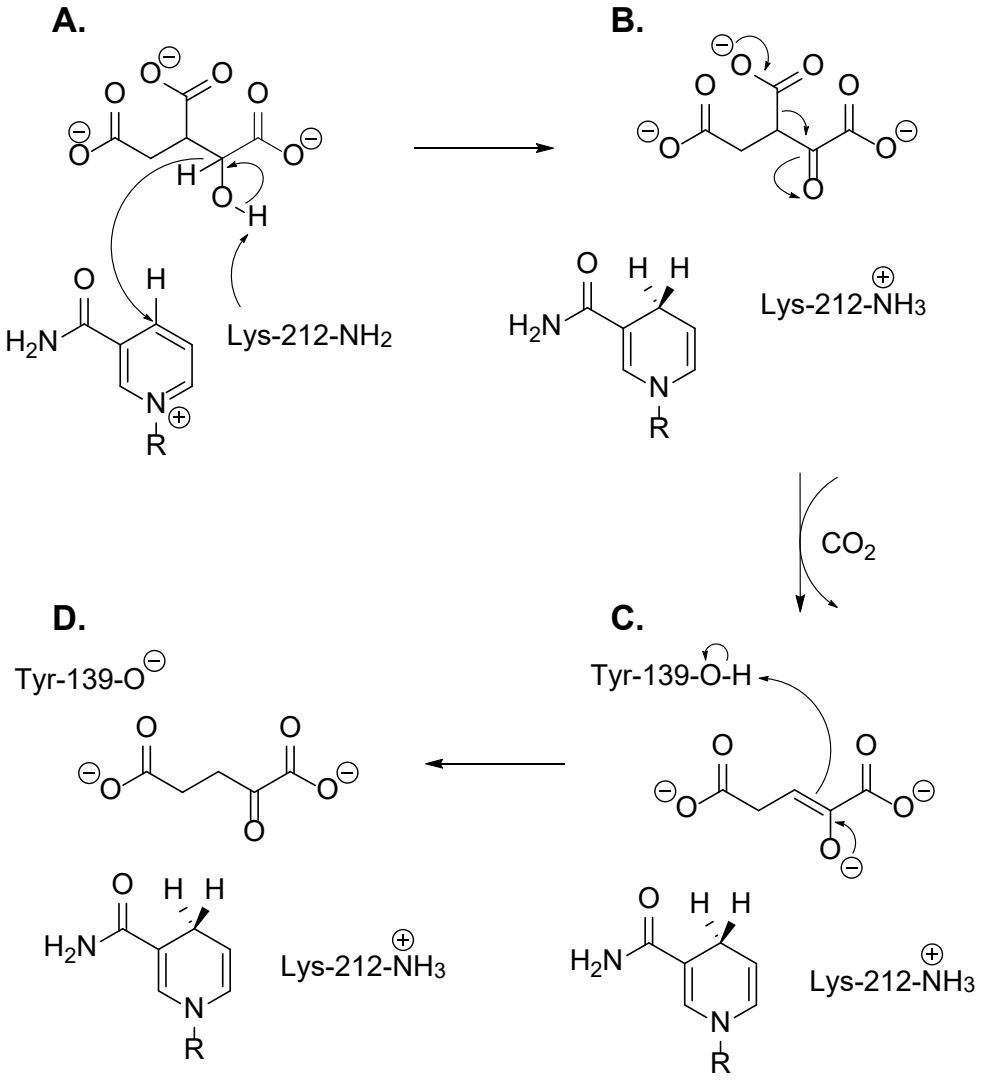

Figure 1.8 *| Mechanism of oxidative decarboxylation of isocitrate to 2-OG as catalysed by IDH. Isocitrate (**A**) is oxidated to oxalosuccinate (**B**). After decarboxylation, an enolate species (**C**) remains which is protonated to give 2-OG (**D**).*

Although crystal structures of IDH1 have been determined, the conformational changes and exact processes during catalysis are not fully understood. Another complicating factor in the IDH1 mechanism is the apparent half-site reactivity observed by Roman et al.[44] Attempts to remove copurified NADPH by prolonged incubation with isocitrate and magnesium led to release of exactly half the bound NADPH suggesting apparent half-site reactivity in the active state, where one subunit retains NADPH at all times. This proposal was supported by NADPH absorbance assays and crystallographic studies.[44] Recent work by Liu et al. has shown that the binding of substrate and metal to IDH1 are not separate, but that isocitrate and magnesium form a complex which binds tightly to IDH1 wt.[48] In IDH1 variants, 2-OG and magnesium bind separately and more weakly. This difference likely enables inhibitor specificity for IDH1 variants (see Section 1.7). In summary, the exact catalytic mechanism and dynamics of IDH1 are complicated and further investigations are needed, e.g. using time-resolved crystallography.

1.6.3 Effects of IDH1 R132 Variations on Enzyme Structure and Mechanism

Mutations in the gene encoding for IDH1 R132 were first reported as loss-of-function mutations because no turnover of isocitrate was observed using NADPH-based assays.[49] It was reported that the IDH1 variation results in a decrease in affinity for isocitrate.[49] However, Dang et al. showed that IDH variants gain the neomorphic ability to catalyse the reduction of 2-OG to the oncometabolite 2-HG. Recent work by Liu et al. has also shown that IDH1 variant homodimers can turn over isocitrate to 2-HG, which cannot be observed by NADPH absorbance assays (the reaction is redox neutral, i.e. overall $NADP^+$ does not change).[48] The overall crystal structures of IDH1 R132H and IDH1 wt overlay well (**Figure 1.9**, A). $NADP^+$/NADPH and calcium are bound similarly, but isocitrate and 2-OG differ in their binding in the active site (**Figure 1.9**, B).

R132 is one of the 8 IDH1 residues which are involved in isocitrate binding.[15] In IDH1 wt, R132 binds the C3 carboxylate of isocitrate (**Figure 1.6**, C). It is proposed that when R132 is substituted with shorter residues, like histidine or cysteine, the side chain is more distant from isocitrate and cannot interact as well with the C3 carboxylate (**Figure 1.9**, C). It is suggested that generally, the loss of the arginine is responsible for the enzymatic gain-of-function[50], various R132 substitutions with different amino acids lead to a similar effect, i.e. the ability of the IDH1 variant to catalyse the reduction of 2-OG to 2-HG. The metal binding aspartates in R132H are slightly altered in conformation compared to IDH1 wt (**Figure 1.9**, D). As R132 is not involved in substrate binding in the IDH1 R132H variant, the Y139 residue is shifted compared to IDH1 wt and is involved in 2-OG binding (**Figure 1.9**, E). IDH1 wt is able to catalyse the reductive carboxylation of 2-OG to isocitrate.[18] R132 is involved in the binding of CO_2 which can react with C3 of 2-OG.[50] Hence, IDH1 has the intrinsic ability to reduce 2-OG, however, without the R132 residue to bind CO_2 and to place it in close proximity to the 2-OG core, reduction of 2-OG leads to the production of 2-HG.

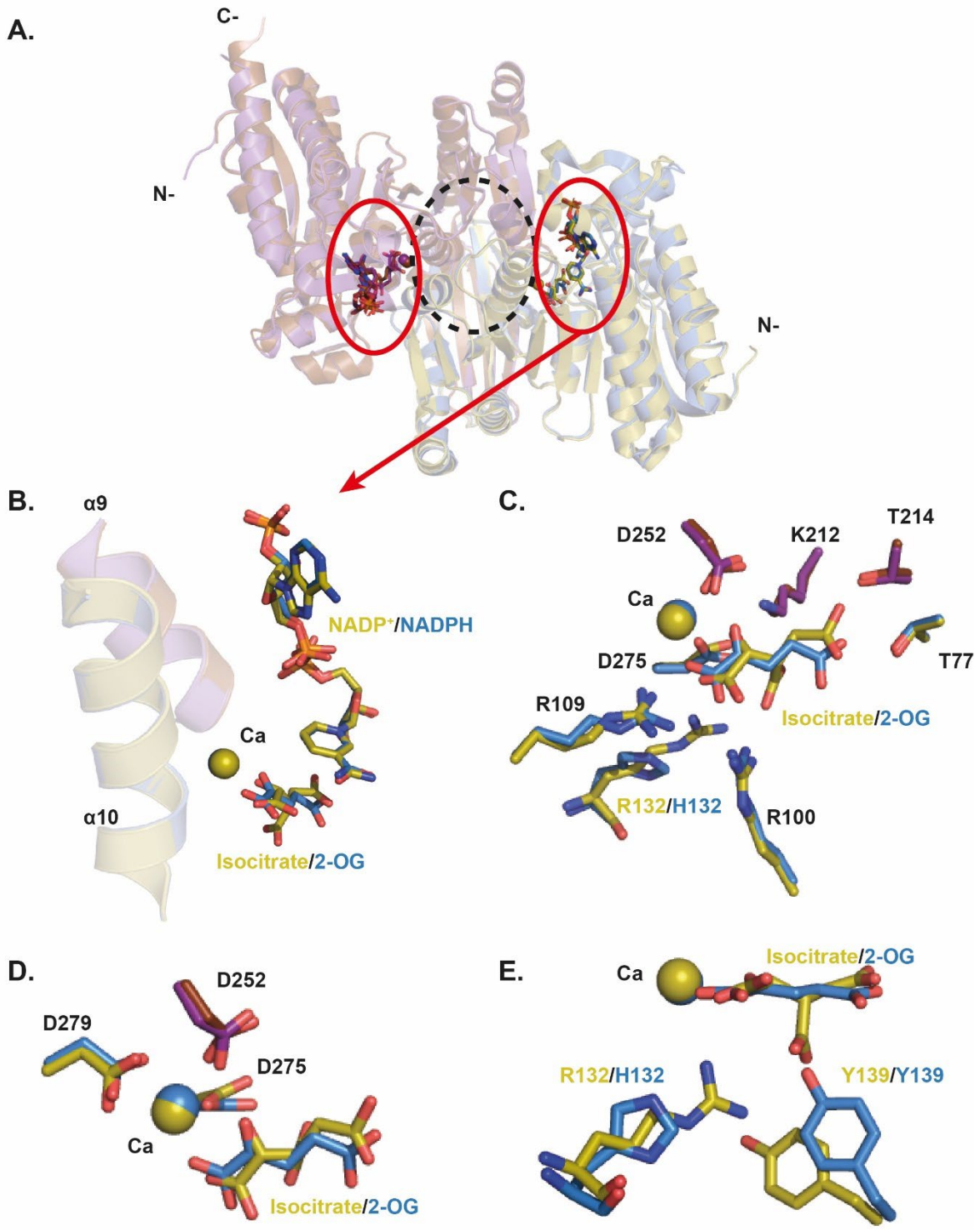

Figure 1.9 | *Views from a crystal structure of IDH1 wt overlaid with one from IDH1 R132H (RMSD: 0.37 Å).* ***A.*** *Ribbon view from a crystal structure of Hs IDH1 wt (chain A: purple, chain B: olive; PDB: 1T0L[15]) superimposed with a view from a structure of IDH1 R132H (chain A: brown, chain B: blue; PDB: 4KZO[51]). IDH1 wt is complexed with calcium, isocitrate, and NADP+. IDH1 R132H is complexed with calcium, 2-OG, and NADPH. Red circles: active sites. Black, dashed circle: dimer-interface.* ***B.*** *Overlay of the active site, and the a9 and a10 helices.* ***C.*** *Overlay of the active site with residues involved in isocitrate and 2-OG binding.* ***D.*** *Overlay of the active site with residues involved in metal binding.* ***E.*** *Overlay of the active site highlighting the loss of the interaction of R132 with the C3 carboxylate of isocitrate due to the R132H variation. Y139 is shifted in the structure of IDH1 R132H and is now involved in 2-OG binding.*

While all known substitutions in IDH1 R132 cancer variants result in an increased capacity to catalyse the reduction of 2-OG to 2-HG, there are differences in cellular 2-HG levels. Pusch et al.[52] reported differing levels in glioma tissues depending on the IDH1 variation. Gliomas harbouring an R132H mutation had lower 2-HG levels than tumours with the R132C variation. The highest 2-HG levels were found in R132S/R132L/R132G. The amount of 2-HG observed in cells inversely correlated with the incidence of the specific mutations, i.e. the most abundant IDH1 variant, R132H, exhibited the lowest 2-HG levels while rarer mutations like R132S exhibited high 2-HG levels. There are few studies comparing the kinetic abilities of various recombinant IDH1 variants. However, Pusch et al. reported that recombinantly produced IDH1 R132H exhibits the highest K_M for 2-OG, while K_M values of other IDH1 variants like R132C were lower. This study on the influences of various R132 substitutions on the reactivity of IDH1 R132 variants was expanded by Matteo et al.[25] who investigated clinically observed IDH1 R132 variants and artificial R132 variations to gain a better understanding of the influence of size and hydrophobicity of the R132 substituent on enzyme kinetics. The authors report that small and hydrophobic substituents at R132 drive the gain-of-function, while larger and more polar residues at R132 favour the turnover of isocitrate to 2-OG (i.e. the wildtype reaction). At ambient temperature, IDH1 R132C displays a higher catalytic efficiency than R132H for the reduction of 2-OG in accordance with the observation of higher 2-HG levels in cells bearing IDH1 R132C compared to IDH1 R132H.[52]

1.7 Exploiting *Hs* IDH Variants for Therapeutic Benefit

Since the initial reports that IDH variants confer a gain-of-function mutation, studies have been conducted to target the IDH1 variant selectively over IDH1 wt. Developing IDH1 variant-specific treatments can be very advantageous compared to many common cancer therapies, as this allows targeted therapy and exhibits substantially lower side effects. Studies on this type of personalised cancer therapy have yielded IDH1 variant-specific vaccines (Section 1.7.1) and small molecule inhibitors (Section 1.7.2).

1.7.1 Peptide Vaccines to Treat Gliomas Bearing IDH1 R132H

IDH1 R132H is presented by the major histocompatibility complex (MHC) proteins on the cancer cell surface[53] and is a tumour-specific neoantigen.[54] Based on this information, peptide-based vaccines against IDH1 R132H bearing gliomas have been developed.[54] Several peptides were studied in mouse models and a 15-mer was found to induce the strongest immune response out of the peptides tested, which was primarily mediated by $CD4^+$ cells.[54] The immune

response triggered by the peptide vaccines could discriminate between R132H tumour cells and IDH1 wt. In mouse models, the peptide vaccines inhibited tumour growth and, in some cases, even led to the eradication of the tumour. [54]

Based on these preclinical results, a human phase 1 clinical trial in which glioma patients were treated with a vaccination scheme (8 vaccinations of 23 weeks) in addition to standard glioma therapy, was conducted. There were no reports of adverse events and 93% of the patients developed an immune response.[55] The 3-year survival rate was 84% and it was demonstrated that immune cells had infiltrated the tumour tissue. After obtaining encouraging data from these phase 1 clinical studies, a further phase 1 study is planned with the addition of a checkpoint inhibitor, which is supposed to increase the immune response to the peptide vaccine. Furthermore, a phase 2 clinical trial on a larger patient cohort will be conducted.[55]

1.7.2 Small Molecules Inhibitors of IDH Variants

While results on peptide vaccines are promising, most drug discovery projects have focused on the development of small molecule IDH1 variant inhibitors. Interestingly, most, but not all, potent IDH1 variant inhibitors bind in an allosteric manner at the dimer-interface (**Figure 1.10**) and have few apparent structural similarities with each other. The inhibitors lock the enzyme in the open-inactive conformation, blocking the switch to its closed-active confirmation.[56] For some inhibitors it is reported that they are competitive with 2-OG or Mg^{2+} binding.[48]

Until recently, it has not been fully understood how the allosteric inhibitors are selective for the IDH variant over IDH wt. At least for IDH1, recent studies by Liu et al. have elucidated the likely reason for inhibitor selectivity. In this study, the authors found that IDH1 wt binds isocitrate and Mg^{2+} as a complex, and binds this complex tightly, while the binding of 2-OG and Mg^{2+} to IDH1 variants is independent and weaker.[48] IDH1 variant inhibitors compete with Mg^{2+} and successfully outcompete Mg^{2+} binding to IDH1 variants, due to its lower affinity, while the metal-substrate complex binds more efficiently to IDH1 wt and as a result, is not outcompeted proficiently.[48]

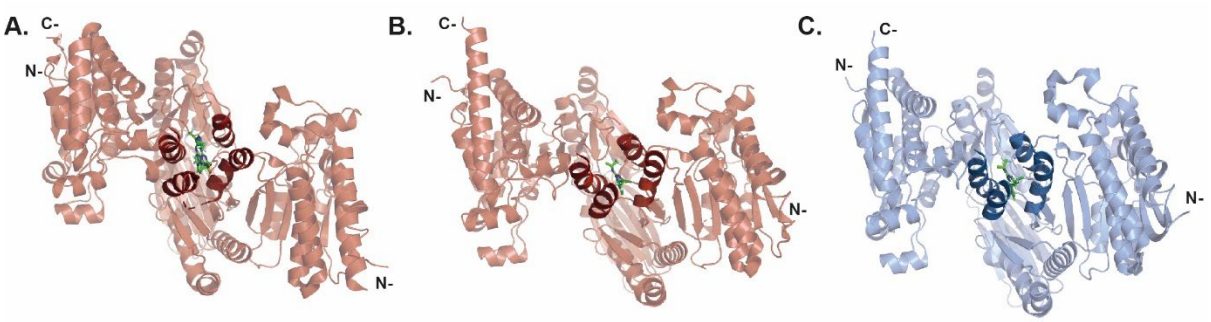

Figure 1.10 *| Crystal structures with AG-221 and AG-881.* ***A.*** *Ribbon view from the crystal structure of IDH2 R140Q complexed with AG-221 (green; PDB: 5I96[57]).* ***B.*** *Ribbon view from the crystal structure of IDH2 R140Q complexed with AG-881 (green; PDB: 6ADI[58]).* ***C.*** *Ribbon view from the crystal structure of IDH1 R132H complexed with AG-881 (green; PDB: 6ADG[58]).*

All reported selective inhibitors of IDH2 variants (AGI-6780, AG-221) have been developed by Agios Pharmaceuticals (**Figure 1.11**/**1.10**). In 2017, enasidenib was approved by the Food and Drug Administration (FDA) for the treatment of relapsed or refractory acute myeloid leukaemia (AML). Agios Pharmaceuticals have also developed a dual IDH1 and IDH2 inhibitor, vorasidenib (AG-881). This is the only example of a class 3 inhibitor according to the definition by Lin et al.[59], i.e. it is an allosteric inhibitor for both, mutant IDH1 and IDH2 (**Figure 1.10**, B/C). Most of the inhibitors published are classified as IDH1 or IDH2 variant allosteric inhibitors (Class 2) and bind non-covalently to IDH1, with the exception of LY3410738, which binds covalently in an allosteric manner. The allosteric class 2 inhibitors are discussed in the next section alongside the class 3 inhibitor AG-881. Class 1 inhibitors constitute inhibitors of IDH1 binding to the active site for which three examples (SYC-435[60], 2-thiohydantoin series[61], HMS-101[62]) have been reported. Class 1 IDH1 inhibitors are generally in early development stages and are discussed at the end of this section.

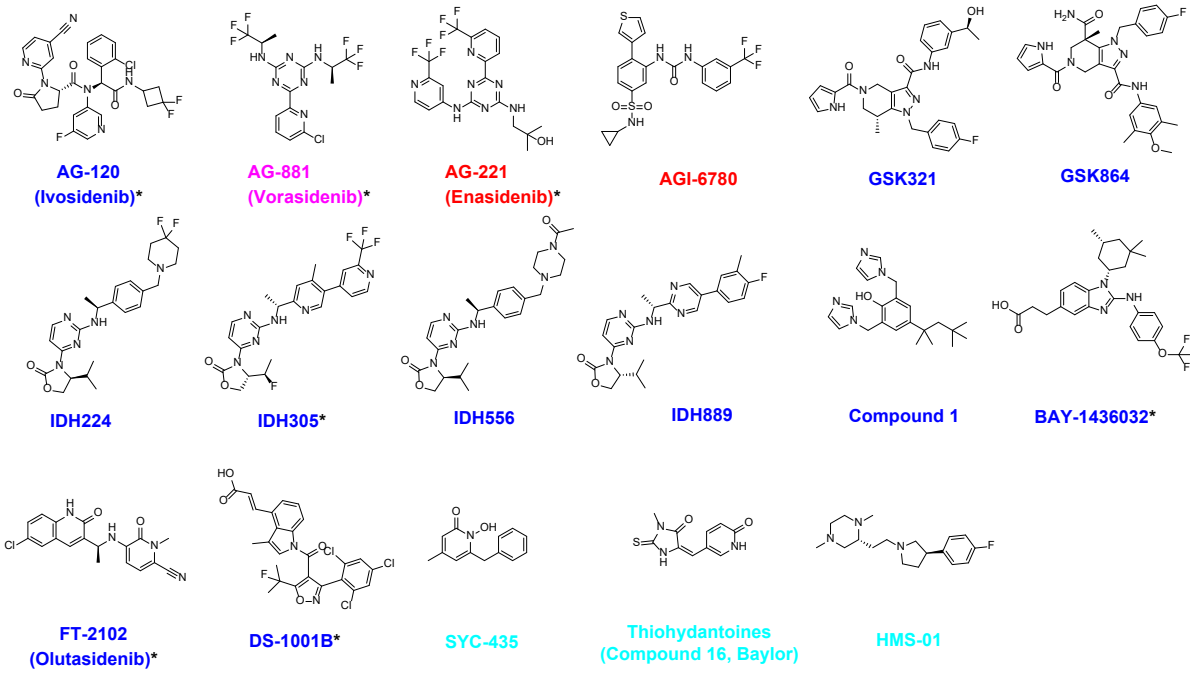

Figure 1.11 *| IDH1 mutant inhibitor structures. Allosteric IDH1 variant inhibitors (blue), the allosteric IDH1 and IDH2 variant inhibitor AG-881 (pink), Allosteric IDH2 variant inhibitors (red), and IDH1 variant active-site inhibitors (light blue). Inhibitors that are FDA-approved or are investigated in clinical trials are indicated with an asterisk.*

(i) The first, and to date only, FDA-approved IDH1 variant inhibitor is ivosidenib (AG-120, **Figure 1.11**), a class 2 allosteric inhibitor that gained approval in 2018 for the treatment of relapsed or refractory AML where an IDH1 mutation has been confirmed. Ivosidenib, developed by Agios Pharmaceuticals, is based on AGI-5198, which exhibited a high potency but poor metabolic stability.[63] Optimisation of AGI-5198 led to AGI-14100, which exhibited better metabolic stability but was a CYP3A4 inducer.[63] AGI-14100 was subsequently optimised to ivosidenib, which is potent and has an acceptable pharmacodynamic and pharmacokinetic profile.[63] In clinical studies, ivosidenib demonstrated a good safety profile and efficacy, which led to FDA approval.[64] Interestingly, there is no crystal structure of ivosidenib bound to an IDH1 variant, but the ivosidenib binding site is assumed to be at the dimer-interface in a similar manner to what has been shown for the ivosidenib-analogue AGI-5198 by crystallographic studies.[63] Ivosidenib inhibits R132H (IC_{50} = 12 nM) and R132C (IC_{50} = 13 nM) but also other IDH1 R132 variants with similar potency.[63] Ivosidenib does not inhibit IDH2 wt but, surprisingly, inhibits IDH1 wt with an IC_{50} = 71 nM (1 h incubation), and with a longer incubation (16 h), it inhibits IDH1 wt with an IC_{50} = 24 nM. Ivosidenib is being investigated in phase 2 clinical trials for the treatment of gliomas,[65] although, it appears ivosidenib is a substrate of p-glycoprotein (PGP) which potentially limits drug uptake through the blood-brain barrier (BBB).[66]

(ii) AG-881 (**Figure 1.11**/**1.10**) inhibits the activity of IDH1 R132H (IC_{50} = 31.9 nM) and IDH2 R140Q (IC_{50} = 31.7 nM) with similar potency. However, there is a time-dependency of the inhibitory activity of AG-881 for IDH2 R140Q - the potency increases over 15 hours to a final value of IC_{50} = 31.7 nM, which is not the case for IDH1 R132H.[56] The authors propose that this is the result of a more rigid coverage of the inhibitor binding-pocket in IDH2 compared to IDH1. W124 and M259 cover the binding pocket in IDH1 and the homologous residues W164 and L298 cover the binding pocket in IDH2. The side chain of IDH2 L298 is likely more rigid than the side chain of methionine (IDH1 M259). Therefore, the entry into the binding pocket of IDH1 may be more straightforward because it exhibits a higher degree of flexibility.

AG-881 locks IDH1 in the open inactive conformation and binds with a stoichiometry of one inhibitor per dimer. In the AG-881-bound crystal structures there is a movement of the α10 helix of 1.5 Å (in IDH1) or 1.8 Å (in IDH2), respectively, while there are no major changes in the rest of the proteins (C-α RMSD of open-inactive AG-881/NADPH/IDH form vs. the closed-active NADPH/Ca^{2+}/2-OG/IDH form < 1 Å). AG-881 has been studied in multiple clinical studies for AML treatment.[67] One other focus of clinical studies is the treatment of gliomas for which no IDH variant inhibitors are approved. AG-881 is reported to penetrate the blood-brain barrier,[56] which is unlikely for ivosidenib (which has been approved for the treatment of AML) for the reasons outlined above. Consequently, AG-881 is in clinical trials for the treatment of patients with residual or recurrent grade 2 glioma for which a phase 3 study is awaiting results[68], and hence, AG-881 is considered the inhibitor closest to regulatory approval.

(iii) GSK was one of the first companies to disclose their inhibitor series developed for the treatment of hematologic malignancies with an IDH1 mutation. A broad screening identified tetrahydropyrazolopyridine compounds which were optimised to the initial lead compound GSK321[69] (**Figure 1.11**/**1.12,** A). This compound inhibits recombinant IDH1 R132H (IC_{50} = 4.6 nM), R132C (IC_{50} = 3.8 nM), and R132G (IC_{50} = 2.9 nM) with high potency. It does not exhibit large selectivity over IDH1 wt (IC_{50} = 46 nM) and does not inhibit IDH2. GSK321 exhibits good cellular potency in HT1080 fibrosarcoma cells (EC_{50} = 85 nM).[69] Chemoproteomic analysis revealed high selectivity for IDH1 in cell lysates. An inhibitor-bound crystal structure of IDH1 R132H shows that GSK321 locks the enzyme in an open-inactive confirmation and binds with a stoichiometry of two inhibitors per dimer.[69]A structural analogue (GSK849), which was used because the high potency of GSK321 would interfere with the assay at low enzyme concentrations, has been shown to inhibit IDH1 R132H

competitively with 2-OG. Treatment of mutant AML cells with GSK321 led to cellular differentiation and decreased intracellular 2-HG. Optimisation of GSK321 yielded an inhibitor with improved pharmacokinetic properties but lower potency (GSK864, **Figure 1.11**).[69] This compound was investigated in xenograft mouse models showing a decrease of 2-HG levels, but further optimisation of GSK864 is likely required for clinical use.[69]

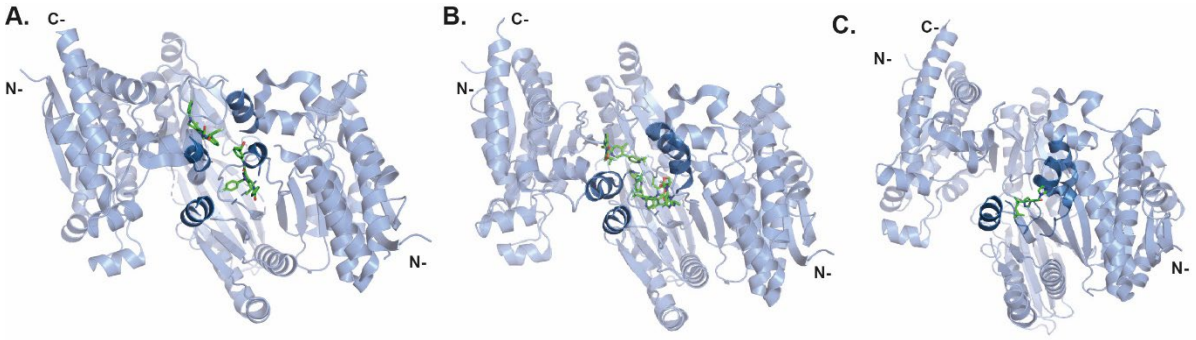

***Figure 1.12** | Crystal structures of IDH1 R132H co-crystallised with GSK321, IDH305, or Compound1 (Sanofi). **A.** Ribbon view from the crystal structure of IDH1 R132H complexed with GSK321 (green; PDB: 5DE1[69]) Note that two inhibitor molecules are bound at the dimer-interface. **B.** Ribbon view from the crystal structure of IDH1 132H complexed with IDH305 (green; PDB: 6B0Z[70]). Note that two inhibitor molecules are bound at the dimer-interface. **C.** Ribbon view from the crystal structure of IDH1 R132H complexed with Compound1, Sanofi (green; PDB: 4UMX[71]).*

(iv) Novartis identified a 4-isopropyl-3-(2-((1-phenylethyl)amino)pyrimidin-4-yl)oxazolidin-2-one in a high-throughput screen and further optimised it to yield the inhibitor IDH889 (**Figure 1.11**).[72] This inhibitor exhibits a good potency against IDH1 R132H (IC_{50} = 20 nM) and is able to penetrate the blood-brain barrier.[72] Further optimisation (improvement of potency, decrease of metabolic clearance, and plasma-protein binding) yielded the clinical candidate IDH305 (**Figure 1.11**/**1.12**, B).[73] IDH305 inhibits IDH1 R132H (IC_{50} = 27 nM) and R132C (IC_{50} = 28 nM) with high-potency and exhibits good selectivity over IDH1 wt (IC_{50} = 6.1 µM).[73] IDH305 is also efficient in reducing 2-HG levels in cell lines and xenograft tumour models in mice, and is selective for IDH1 variants over IDH2.[73] Furthermore, IDH305 exhibits a good pharmacokinetic profile. Crystallographic studies with IDH1 R132H demonstrated that IDH305 binds allosterically at the dimer-interface with a stoichiometry of three inhibitors per dimer and stabilises the open-inactive confirmation of IDH1.[73] Most clinical trials investigating IDH305 have been halted due to safety concerns (e.g. NCT02977689[74]) but a trial investigating IDH305 in "Advanced Malignancies" is still active.[75] Further inhibitors from Novartis were also disclosed (IDH224 (IC_{50} = 16.6 nM, **Figure 1.11**), IDH530 (IC_{50} = 8.4 nM), and IDH556 ($IC_{50} \leq$ 72 nM, **Figure 1.11**)) and were reported to exhibit good potency for IDH1 R132H in a Novartis patent.[76] These inhibitors were further investigated by Urban et al. showing good selectivity and reasonable cellular activity.[77]

(v) Sanofi has identified a potent bis imidazole inhibitor against IDH1 R132H as a result of high-throughput screening (IC_{50} = 13 nM), compound 1 (**Figure 1.11**/**1.12**, C)[78]. It was reported that compound 1 is selective for IDH1 R132H and R132C over IDH1 wt and IDH2. Crystallographic studies demonstrated that compound 1 binds allosterically to the dimer-interface with a stoichiometry of one inhibitor molecule per IDH1 dimer. Compound 1 is not competitive with 2-OG or NADPH, but with Mg^{2+}, which is likely due to the involvement of D279 in inhibitor binding (D279 is one of three aspartates (together with D275 and D252) involved in the coordination of the metal ion, Section 1.5).[78] Furthermore, the structure of the α10 helix is altered in the compound-bound crystal structure compared to the unbound form showing D275 not pointing towards the active site anymore. It was reported by Dang et al. that IDH1 wt has a 300-fold higher affinity (as judged by K_M; for the turnover of isocitrate to 2-OG) for Mg^{2+} than IDH1 R132H (as judged by K_M; for the turnover of 2-OG to 2-HG).[35] Deng et al. proposed that this difference is the reason for inhibitor selectivity of compound 1 (Sanofi) to IDH1 R132H over IDH1 wt as IDH1 R132H is more susceptible to interference with Mg^{2+} binding by the inhibitor when taking the cellular Mg^{2+} levels of 10^{-3} or 10^{-4} M into account.[78] Urban et al. could not reproduce the IC_{50} value for compound 1 in their investigations and reported an $IC_{50} > 13$ μM.[77]

(vi) A compound developed by Bayer, BAY-1436032 (**Figure 1.11**/**1.13**, A), was shown to inhibit IDH1 R132 variants displaying an IC_{50} of 15 nM for the five most common IDH1 variants (R132H, R132C, R132G, R132S, R132L).[79] BAY-1436032 is selective for IDH1 variants as data showed very weak activity against IDH1 wt (IC_{50} = 20 μM) and IDH2 wt ($IC_{50} > 100$ μM). BAY-1436032 binds at the dimer-interface and is competitive with respect to 2-OG levels.[79] A crystal structure of a structural analogue (a crystal structure of BAY-1436032 is not available) demonstrates binding with a stoichiometry of one inhibitor molecule per dimer and shows the residue S280 on the α10 helix to be crucial for inhibitor binding via a hydrogen bond with the benzimidazole nitrogen.[79] Interestingly, R132H is also involved in the binding of the BAY-1436032 analogue (via a salt bridge between the histidine and the carboxylate of the BAY-1436032 analogue) which is not observed for any other allosteric inhibitor. Treatment with BAY-1436032 decreased 2-HG levels in cell lines, and BAY-1436032 was shown to penetrate the murine blood-brain barrier.[79] BAY-1436032 induced differentiation in glioma cell lines and treatment with BAY-1436032 conferred a survival benefit in intracranial glioma xenograft models.[79] A low toxicity and favourable pharmacokinetic properties in preclinical testing[79], led to BAY-1436032 progressing to human

clinical trials. A phase 1 study for AML treatment[80] has been completed, and another phase 1 study for the treatment of solid tumours[81] is ongoing.

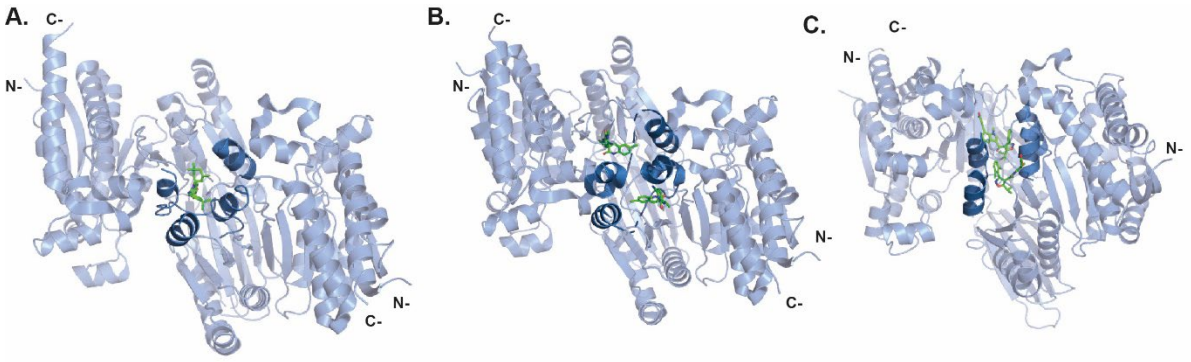

Figure 1.13 *| Crystal structures of IDH1 R132 variants with BAY-1436032, FT-2102, and DS-1001B.* ***A.*** *Ribbon view from the crystal structure of IDH1 132H complexed with BAY-1436032 (green; PDB: 5LGE[79]).* ***B.*** *Ribbon view from the crystal structure of IDH1 R132H complexed with FT-2102 (green; PDB: 6U4J[82]). Note that two inhibitor molecules are bound at the dimer-interface.* ***C.*** *Ribbon view from the crystal structure of IDH1 R132C complexed with the DS-1001B analogue compound A (green; PDB: 6IO0[83]). Note that two inhibitor molecules are bound at the dimer-interface.*

(vii) Forma Therapeutics has identified and optimised a quinolone based IDH1 variant inhibitor via high throughput screening.[84] Optimisation of potency, solubility, pharmacodynamic and pharmacokinetic properties led to FT-2102 (**Figure 1.11**/**1.13**, B). FT-2102 is a potent inhibitor of IDH1 R132H (IC_{50} = 21 nM) and a moderate inhibitor of IDH1 R132C (IC_{50} = 114 nM), while it exhibits no activity against IDH1 wt and IDH2 R172K or R140Q (IC_{50} > 20 μM). FT-2102 was shown to allosterically bind at the dimer-interface with a stoichiometry of two molecules per IDH1 dimer.[84] FT-2102 inhibited 2-HG production in cell lines overexpressing several IDH1 variants (R132H, R132C, R132G, R132L).[84] Good pharmacokinetic properties were demonstrated in mouse studies including the penetration of the blood-brain barrier. As a result of these findings, FT-2102 has progressed to human clinical trials for the treatment of advanced solid tumours or gliomas in combination or as a single treatment (phase 1 and phase 2).[85] FT-2102 is also under investigation for the treatment of AML (phase 2, paused because of Covid-19 pandemic) in combination with ASTX727[86] and another clinical trial to test FT-2102 as a single agent or in other combination regimens (phase 1 and 2) is currently recruiting participants.[87]

(viii) DS-1001B (**Figure 1.11**/**1.13**, C) was developed by Daiichi Sankyo and potently inhibits 2-HG production in chondrosarcoma cell lines harbouring IDH1 R132C or R132G variants with EC_{50} values of 83.9 nM and 45.5 nM, respectively.[88] Inhibition is impaired by high concentrations of 2-OG or Mg^{2+}, but varied NADPH levels did not influence potency.[89] DS-1001B does not affect IDH2 mutant cell lines.[88] DS-1001B impaired growth in

chondrosarcoma cell lines bearing IDH1 R132H and R132C but did not impair growth when no IDH1 R132 variant was present. DS-1001B has also been shown to impair tumour growth in a mouse xenograft tumour model (tumour harbouring IDH1 R132G implanted subcutaneously).[88] DS-1001B also promotes normal chondrocyte differentiation of IDH1 R132C harbouring chondrosarcoma cell lines *in vitro,* making it a promising compound to further investigate for the treatment of chondrosarcoma, for which available treatment options are limited.[88] It was also shown that DS-1001B can reduce 2-HG levels in glioma cell lines harbouring an IDH1 R132H mutation and in cell lines transfected with IDH1 R132C. DS-1001B can cross the BBB; and it was shown to impair tumour growth in an intracranial mouse xenograft model suggesting it may be a promising inhibitor for the treatment of gliomas, in line with results showing DS-1001B can promote glial differentiation.[89]

A crystal structure of an analogue of DS-1001B (Compound A) complexed to IDH1 R132C shows the binding of two inhibitor molecules at the IDH1 R132H dimer-interface and stabilisation of the protein in the open inactive form.[89] Compound A binding influences the arrangement of the metal coordinating aspartate residues (Asp-275, Asp-279, Asp-252). This results in interference with metal cation binding and, consequently, also with 2-OG binding, for which the divalent metal cation is required.[89] DS-1001B is currently investigated in clinical phase 2 studies for the treatment of gliomas with an IDH1 variant.[90,91,92]

(ix) A first in class covalent IDH1 variant inhibitor was developed by Elli Lilly: LY3410738 covalently binds to Cys-269, which is located on the loop connecting the α9 and α10 helix at the dimer-interface (**Figure 1.14**).[93] In patient-derived AML cells bearing an IDH1 mutation, LY3410738 induces cellular differentiation more potently than the FDA-approved IDH1 variant inhibitor ivosidenib.[93] Its prolonged activity *in vivo* is likely a result of covalent binding suppressing 2-HG levels even after clearance of the compound.[93] LY3410738 can cross the blood-brain barrier and reduce 2-HG levels potently in glioma and AML models.[93] There is no inhibition or binding data available for LY3410738, and the structure has not been disclosed. However, LY3410738 is now being investigated in clinical phase 1 trials for the treatment of solid tumours such as gliomas and chondrosarcomas, but also AML.[94,95,96]

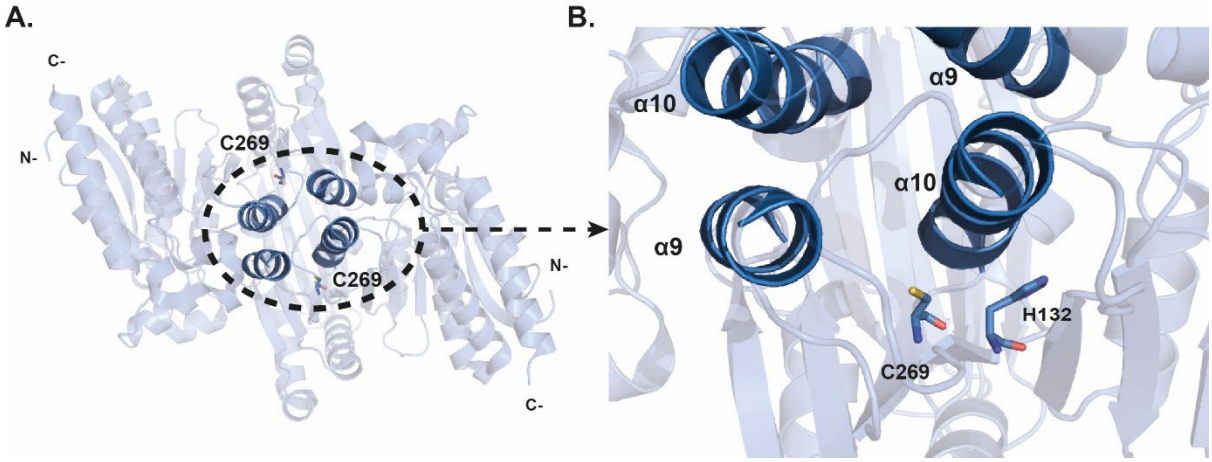

Figure 1.14 *| Crystal structure of IDH1 R132H highlighting the C269 residue.* ***A.*** *Ribbon view from the crystal structure of IDH1 132H complexed with AG-881 (AG-881 not shown, PDB: 6ADG[58]). Black circle: dimer-interface. C269 is shown as sticks and located on the loop connecting the α9 and α10 helices at the dimer-interface.* ***B.*** *Magnified section showing C269 and H132 as sticks. They are on neighbouring loops and spatially close.*

(x) Inhibitors published by Baylor College of Medicine are examples of non-allosteric class 1 IDH variant inhibitors, i.e. they bind to the active site.[97] The first active site inhibitors were a series of 1-hydroxypyridin-2-one compounds with K_i values in the nanomolar range. The optimised lead compound, SYC-435 (**Figure 1.11**/**1.15**, A), inhibits IDH1 R132H (K_i = 170 nM) and R132C (K_i = 120 nM) with 60-fold selectivity over IDH1 wt.[97] SYC-435 also exhibits activity in HT1080 fibrosarcoma cells (EC_{50} = 2.4 μM).[97] Crystallographic studies revealed that SYC-435 binds in the active site and stabilises IDH1 R132H in the open-inactive conformation.[97] SYC-435 blocks the conformational switch to the closed active confirmation and interferes with 2-OG binding. Further optimisation yielded compounds with slightly improved activity and the potential to cross the blood-brain barrier.[98]

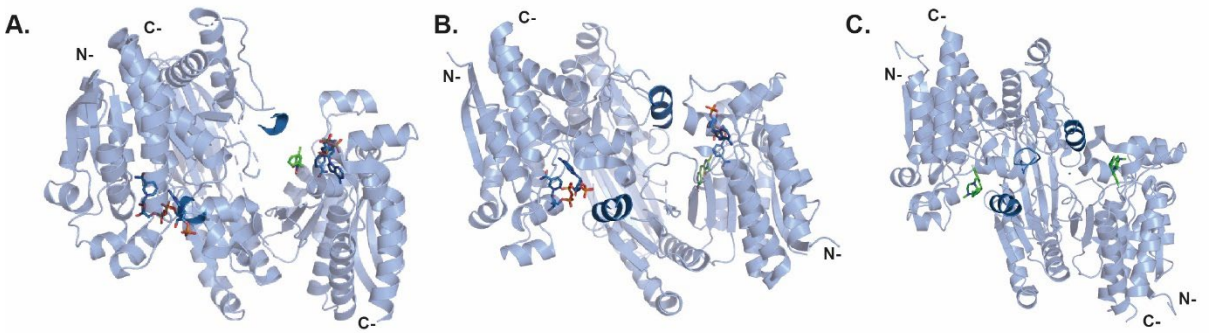

Figure 1.15 *| Crystal structures of IDH1 R132H with non-allosteric inhibitors.* ***A.*** *Ribbon view from the crystal structure of IDH1 132H complexed with SYC-435 (green; PDB: 4I3L[97]). Note that SYC-435 binds in the active site.* ***B.*** *Ribbon view from the crystal structure of IDH1 R132H complexed with a 2-thiohydantoin compound (green; PDB: 4XRX[99]). Note that the 2-thiohydantoin compound binds in the active site.* ***C.*** *Ribbon view from the crystal structure of IDH1 R132H complexed with HMS-01 (green; PDB: 6Q6F[62]). Note that HMS-01 binds in the active site.*

(xi) Another series of class 1 IDH inhibitors, also developed by Baylor College of Medicine[99], are based on a high throughput screening hit of 2-thiohydantoin, which was optimised to yield

compound 16 (**Figure 1.11**/**1.15**, B), which inhibits IDH1 R132H with a K_i of 750 nM and R132C with a K_i of 1.2 μM, but is not sufficiently selective over IDH1 wt (K_i = 8.8 μM).[99] An analogue, compound 18, is potent against R132H (K_i = 420 nM), is less potent against R132C (K_i = 2.3 μM), and inhibits IDH1 wt with a K_i of 10.3 μM.[99] Similarly to SYC-435, both 2-thiohydantoin based compounds bind in the active site as demonstrated by crystallographic studies.[99] Compound 18 binds competitively with 2-OG. Both 2-thiohydantoin compounds can decrease 2-HG levels in the human fibrosarcoma cell line HT1080.[61]

(xii) Another active site inhibitor for IDH1 variants (class 1) has been discovered by computational screening, i.e. HMS-01 (**Figure 1.11**/**1.15**, C).[62] Recombinant IDH1 R132H and R132C are reported to show IC_{50}s of 4 μM and 5 μM with a 20-fold selectivity over IDH1 wt. In primary AML cells, the EC_{50} values for HMS-01 are 0.7 μM (IDH1 R132C) or 0.8 μM (IDH1 R132H), respectively.[62] HMS-01 is bioavailable in mouse models and is reported to prolong the survival of transgenic mice transduced with IDH1 R132C.[100] A crystal structure of IDH1 R132H complexed with HMS-01 revealed that one inhibitor binds to each active site of the IDH1 dimer in close proximity to the NADPH binding site. HMS-01 induces differentiation in primary IDH1 variant cell lines and mice transduced with IDH1 R132C.[62] However, due to its low selectivity over IDH1 wt, there might be substantial side effects.[62]

All three examples of class 1 inhibitor series binding at the active site are in early development stages. These inhibitors need further optimisation, but they provide proof-of-concept that developing IDH1 variant selective active-site inhibitors is possible.

1.8 Acquired Resistance Against *Hs* IDH1 Mutant Inhibitors

Shortly after the FDA approval of the IDH2 variant inhibitor enasidenib (2017), and the IDH1 mutant inhibitor ivosidenib (2018), reports emerged of resistance acquired during treatment with one of these inhibitors. In some cases, isoform switching from an IDH1 variant to an IDH2 variant and *vice versa* was observed in patients treated with IDH variant inhibitors.[101] Three patients with an IDH1 R132C mutation were treated with ivosidenib. Initially, they responded well but then relapsed, indicated by an increase in plasma 2-HG. In two cases, a newly acquired IDH2 R140Q mutation was discovered, in another case, the patient acquired IDH2 R172V.[101] One patient with an IDH2 R140Q mutation acquired an IDH1 R132C mutation during treatment with enasidenib.[101] Isoform switching is, hence, a resistance mechanism to IDH1 variant or IDH2 variant inhibitors.

Furthermore, resistance has been reported due to dimer-interface substitutions acquired under treatment with enasidenib or ivosidenib.[28] AML patients bearing an IDH2 R140Q variant and who were treated with enasidenib, were found to undergo relapse as indicated by increasing plasma 2-HG levels.[28] The relapse was linked to the occurrence of trans-allelic mutants, e.g. the IDH2 R140Q variant together with the acquired variants IDH2 Q316E or IDH2 I319M are produced (without IDH2 wt) (**Figure 1.16**, A).[28] In an AML patient with an IDH1 R132C variation, who was treated with ivosidenib, a relapse indicated by increasing plasma 2-HG levels, was linked to an acquired S280F substitution (**Figure 1.16**, A) at the dimer-interface (note IDH1 S280F is homologous to IDH2 I319). In the case of IDH1, second site mutations have been observed in the same allele, e.g. to give R132C S280F (homodimeric) variants (note there is also the possibility of heterodimer formation with IDH1 wt).[28] Since then, further acquired IDH1 R132C S280F variants following treatment with ivosidenib have been reported.[102, 103]

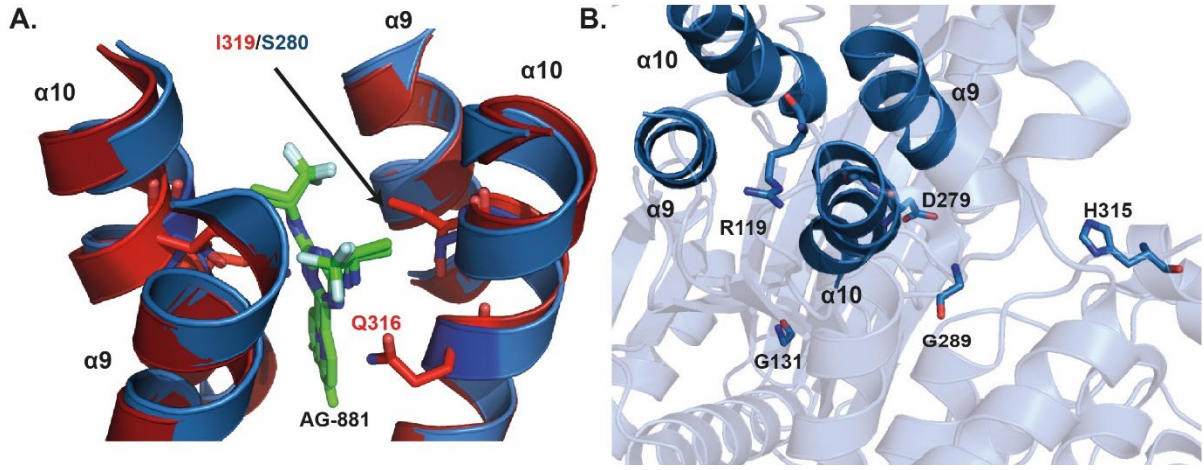

***Figure 1.16** | Acquired second-site resistance in IDH1 R132 variants and IDH2 R140Q. **A.** Views from a crystal structure of IDH1 R132H (blue, PDB ID: 6ADG[104]) complexed with AG-881 (green) superimposed with IDH2 R140Q (red, 6ADI[104]) complexed with AG-881 (inhibitor not shown). IDH1 S280 on the α10 helix and its homologous IDH2 residues I319 are shown as sticks as well as IDH2 Q316. **B.** Magnified section of IDH1 R132H showing residues for which second-site resistance mutations were reported.*

Three more cases of IDH1 R132C S280F were reported by Choe et al. [102] In other patients, the acquired mutations R119P, G131A, G289D, and H315D were each identified once, and a further three patients with an acquired D279N variant linked to inhibitor resistance were reported (**Figure 1.16**, B).[102] Oltvai et al. identified another case of IDH1 R132C S280F and there are two cases of IDH1 S280F variations listed in the gnomAD database without further clinical information.[103] While ivosidenib potently inhibits IDH1 R132C (IC_{50} = 19 nM) in their experimental setting, Choe et al. showed that a recombinantly produced R132C S280F variant is not inhibited at 100 µM ivosidenib.[102] The authors also modelled the ivosidenib analogue

AGI-14686 into a crystal structure of IDH1 R132H (5L57).[105] Then the S280F substitution was modelled; the results suggest that ivosidenib resistance may be due to a steric clash of ivosidenib with the bulky phenylalanine side chain of S280F. Oltvai et al. used the crystal structure of R132H complexed with AG-881 (6ADG[58]) to model ivosidenib binding. The results suggest that ivosidenib can form a hydrogen bond with S280, but that the S280F substitution leads to the loss of the hydrogen bond with ivosidenib, which, in combination with the bulkiness of F280, is likely a reason for ivosidenib resistance. Modelling by Oltvai et al. using a crystal structure of IDH1 R132H complexed with AG-881 shows that the S280F substitution likely interferes with binding of AG-881 due to a steric clash.[103] AG-881 is considered closest to clinical approval in the pipeline (it is currently in phase 3 clinical trials[68]). The likely resistance of R132C S280F to AG-881, in addition to ivosidenib resistance, highlights the urgent need to understand S280F mediated drug resistance in R132C and to investigate alternatives to overcome drug resistance.

Although there are emerging resistance mechanisms, IDH1 variant inhibitors are breakthrough treatments as they show cancer metabolism can be modulated for therapeutic benefit.[106] Their development supports the addition of metabolic alterations to the list of hallmarks of cancer and is an important proof-of-concept for targeting cancer metabolism.[1] Targeting metabolism has also been of long-standing interest in the antibacterial field, including for *Mycobacterium tuberculosis* (*Mtb*). However, this has not been pursued – in part, probably because of apparent structural similarities of IDHs as revealed by crystallographic studies, which could suggest selective inhibitors over *Hs* IDH1 wt would not be possible.

1.9 Role of Mycobacteria in Public Health

In 2015, the World Health Organization (WHO) declared tuberculosis the leading infectious disease killer, surpassing HIV/AIDS. In 2020, 1.3 million people (plus 210,000 coinfected with HIV)[107] died from tuberculosis (TB). A quarter of the world's population is estimated to be infected with TB[107], which is caused by *Mtb*, a pathogen insensitive to most commonly used antibiotics. *Mtb* infects macrophages and persists inside the phagosome, where it switches to a latent phase of infection and thus, avoids clearance by the immune system.[108]

The first-line treatment of TB is a combination of the four drugs isoniazid, rifampicin, ethambutol, and pyrazinamide.[109] The long-term strict treatment regimen and toxic nature of the drugs pose challenges for patients.[109] The first-line therapy lasts for at least six months (a combination of all four drugs for 2 months, then 4 months of rifampicin and isoniazid[109]) and

must be extended when the *Mtb* is resistant. If necessary, second-line drugs can be used, but with the disadvantage of less optimal regimens (treatment of up to 24 months, and increased toxicity). The emergence of *Mtb* resistant strains is making current treatments ineffective - in 2016, 490,000 cases of multidrug-resistant TB (resistance to the two most effective first-line drugs isoniazid and rifampicin) were reported.[107] Amongst other features, the metabolic flexibility of *Mtb* and its ability to persist in a highly antibiotic-resistant dormant state inside macrophages are characteristics of its success as an infectious agent.[108] A better understanding of the molecular and cellular mechanisms of mycobacteria that promote survival is essential for the rational development of novel TB therapeutics. Moreover, other mycobacteria such as *Mycobacterium smegmatis* (*Msm*) are becoming increasingly problematic for immunocompromised patients because they are naturally resistant to commonly used antibiotics.[110] Hence, novel validated targets for effective treatment of pathogenic mycobacteria are needed urgently.

1.10 Isocitrate Metabolism in Mycobacteria

Metabolism in many bacteria has the feature of being able not only to process isocitrate via the TCA cycle but also via an alternative pathway, called the glyoxylate shunt.[111] The glyoxylate shunt is not found in mammals[112], but is essential in bacteria to enable growth using substrates like fatty acids or acetate as the sole carbon source.[111] The metabolic flexibility imparted by the glyoxylate shunt allows bacteria to adapt to varying growth conditions and utilise different nutrients.[111] The glyoxylate shunt bypasses decarboxylation of isocitrate to 2-OG by IDH and, sequentially, another decarboxylation of succinyl-CoA to succinate catalysed by succinyl-CoA-synthetase (**Figure 1.17**), and thus, prevents the loss of two carbon atoms as CO_2.[111] The glyoxylate shunt is not used exclusively but in combination with the TCA cycle and consequently, the enzymes involved in both processes need to be regulated.[111]

Isocitrate in *Mtb* and *Msm* can be metabolised via the TCA cycle or glyoxylate shunt as in other bacteria.[113] The metabolic flexibility enabled by this branch point allows *Mtb* to adapt to growth conditions within macrophages, where the main carbon sources are fatty acids, and is shown to be essential for persistence of *Mtb* inside macrophages.[114] Isocitrate lyase (ICL), the first enzyme of the glyoxylate shunt, catalyses the conversion of isocitrate to glyoxylate and succinate. ICL is upregulated in *Mtb* in certain non-replicating states and an *icl* knockout has been shown to significantly attenuate persistence and virulence[115]. The glyoxylate shunt and the regulation of flux through it are important for *Mtb* to thrive inside the host and finding

inhibitors of IDH and/or ICL may pave the way to new treatment strategies. A detailed understanding of the bifurcating point between the TCA cycle and the glyoxylate shunt is required for validating isocitrate metabolising enzymes as drug targets.

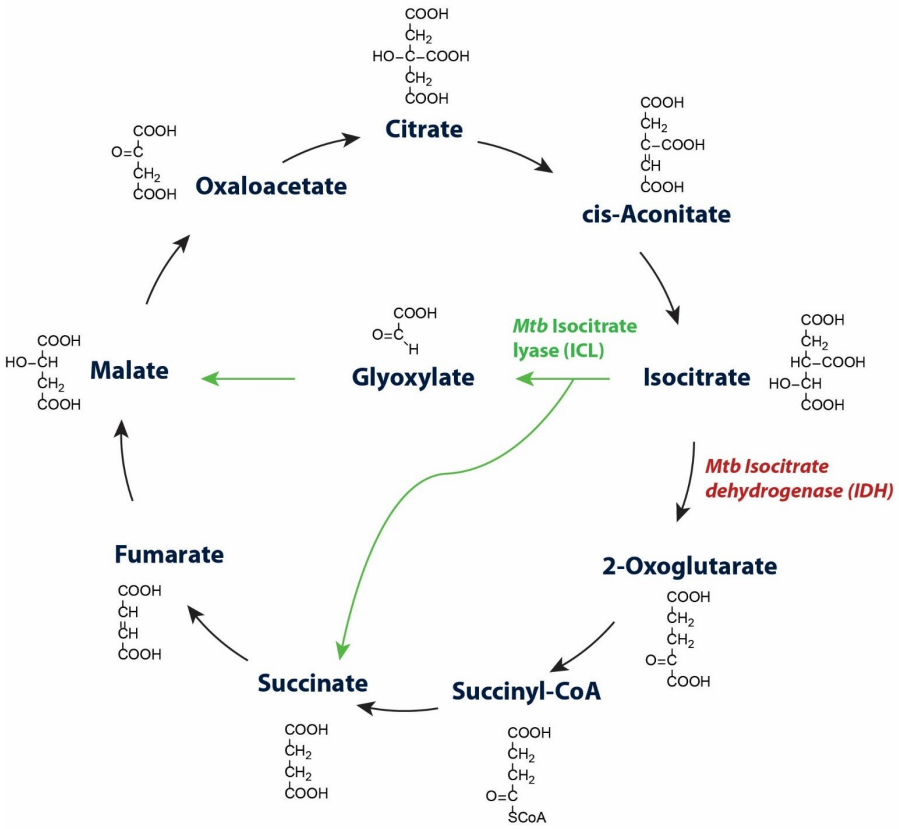

***Figure 1.17** | Tricarboxylic acid (TCA) cycle with glyoxylate shunt. Highlighted are the first enzymes in each pathway: isocitrate lyase (ICL, green) catalyses the conversion of isocitrate to glyoxylate in the first step of the glyoxylate shunt, isocitrate dehydrogenase (IDH, red) catalyses the conversion of isocitrate to α-ketoglutarate in the TCA cycle.*

1.11 Isoforms of IDH in Mycobacteria

Mtb and *Msm* both have two ICL isoforms.[116,117] While *Mtb* produces two IDHs (*Mtb* IDH1 and IDH2), *Msm* only produces one IDH isoform, which is homologous to *Mtb* IDH2.[113]

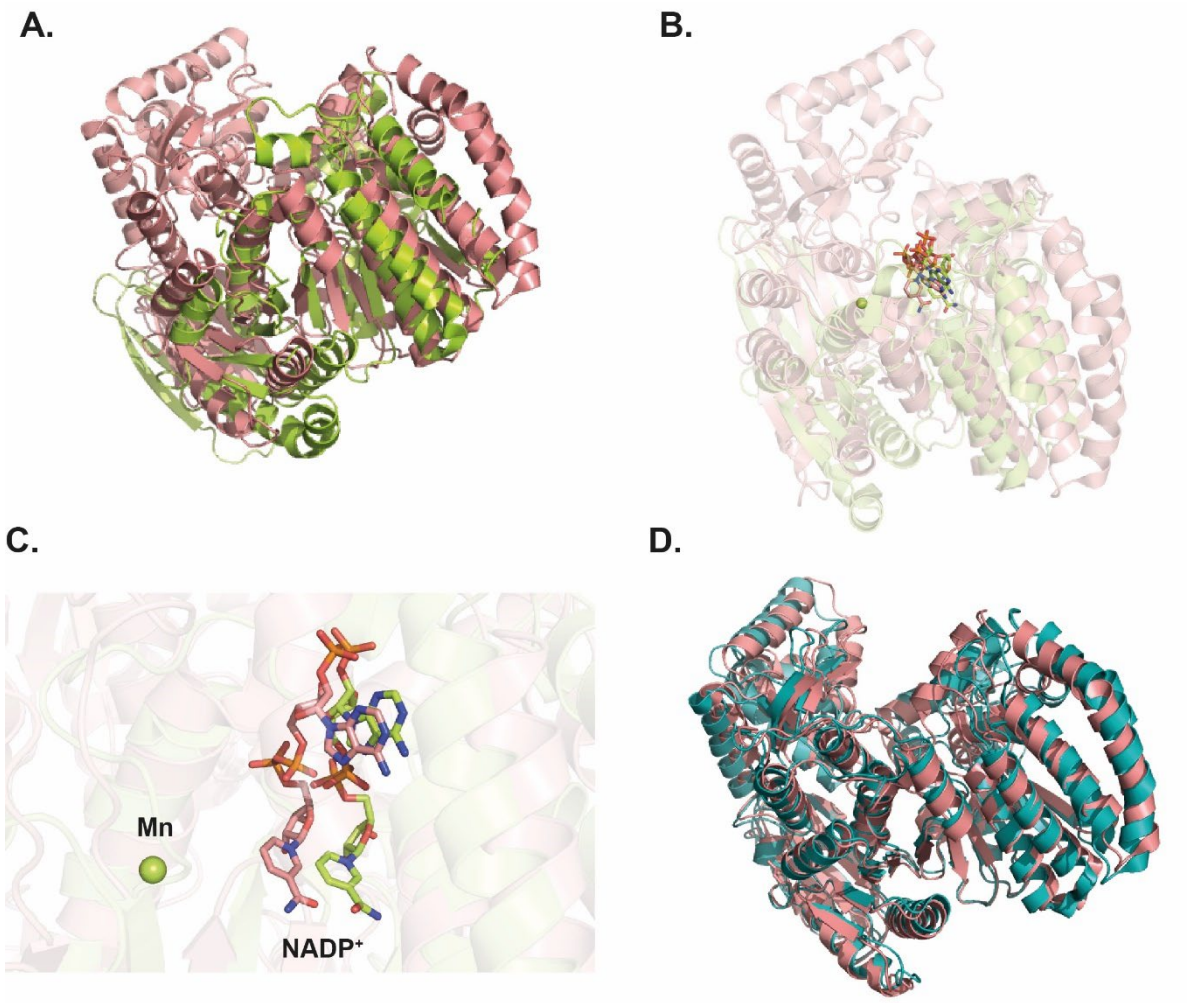

Figure 1.18 | *Crystal structure overlays of mycobacterial IDHs.* ***A.*** *Ribbon view from a crystal structure of Mtb IDH1 (chain A: lime; PDB: 4HCX[47]) superimposed with a view from a structure of Mtb IDH2 (chain A: salmon; PDB: 5KVU; RMSD: 5.92 Å). Mtb IDH1 is complexed with manganese and NADP⁺. Mtb IDH2 is complexed with NADP⁺.* ***B.*** *Substrates in the active sites are shown as sticks.* ***C.*** *Magnified section of the active site.* ***D.*** *Ribbon view from a crystal structure of Msm IDH (chain A: teak; PDB: 4ZDA) superimposed with a view from a structure of Mtb IDH2 (chain A: salmon; PDB: 5KVU; RMSD: 1.90 Å).*

Although both *Mtb* IDH enzymes belong to the isocitrate/isopropylmalate dehydrogenase-like superfamily, IDH2 is significantly larger (82.6 kDa) than IDH1 (45.5 kDa).[118] IDH2 is a member of the structural IDH-family (PF03971) for which sequence analyses show a full prokaryotic phylogeny consistent with it being homologous to *Msm* IDH. On the other hand, IDH1 is a member of the structural Iso_dh-family (PF00180), a family distributed widely including *Escherichia coli (E. coli)* IDH and both, *Hs* IDH1 and IDH2. [118] *Mtb* IDH1 only shares 14 % sequence identity with *Mtb* IDH2,[118] which is reflected in the difference in the crystal structures manifest when the monomers are overlaid (**Figure 1.18**, A). However, some common secondary structure elements in the crystal structures of *Mtb* IDH1 and *Mtb* IDH2 overlay well. For both *Mtb* IDH1 and *Mtb* IDH2, the active site is in a similar location (**Figure**

1.18, B) and $NADP^+$ is bound in the same conformation (**Figure 1.18**, C). *Mtb* IDH2 overlays well with homologous *Msm* IDH (**Figure 1.18**, D).

Mtb IDH1 is phylogenetically closer to *Hs* IDH1 (70% identity) than to *Mtb* IDH2 (14% identity). The homodimeric crystal structures of *Mtb* IDH1 and *Hs* IDH1 overlay well (**Figure 1.19**, A/B). However, the conformations of the $NADP^+$ molecules do not overlay well but are bound in a similar conformation (**Figure 1.19**, C; note that other than *Hs* IDH1, *Mtb* IDH1 was co-crystallised without isocitrate). The *Mtb* IDH1 R135 residue is at a similar location to *Hs* IDH1 R132 (**Figure 1.19**, D).

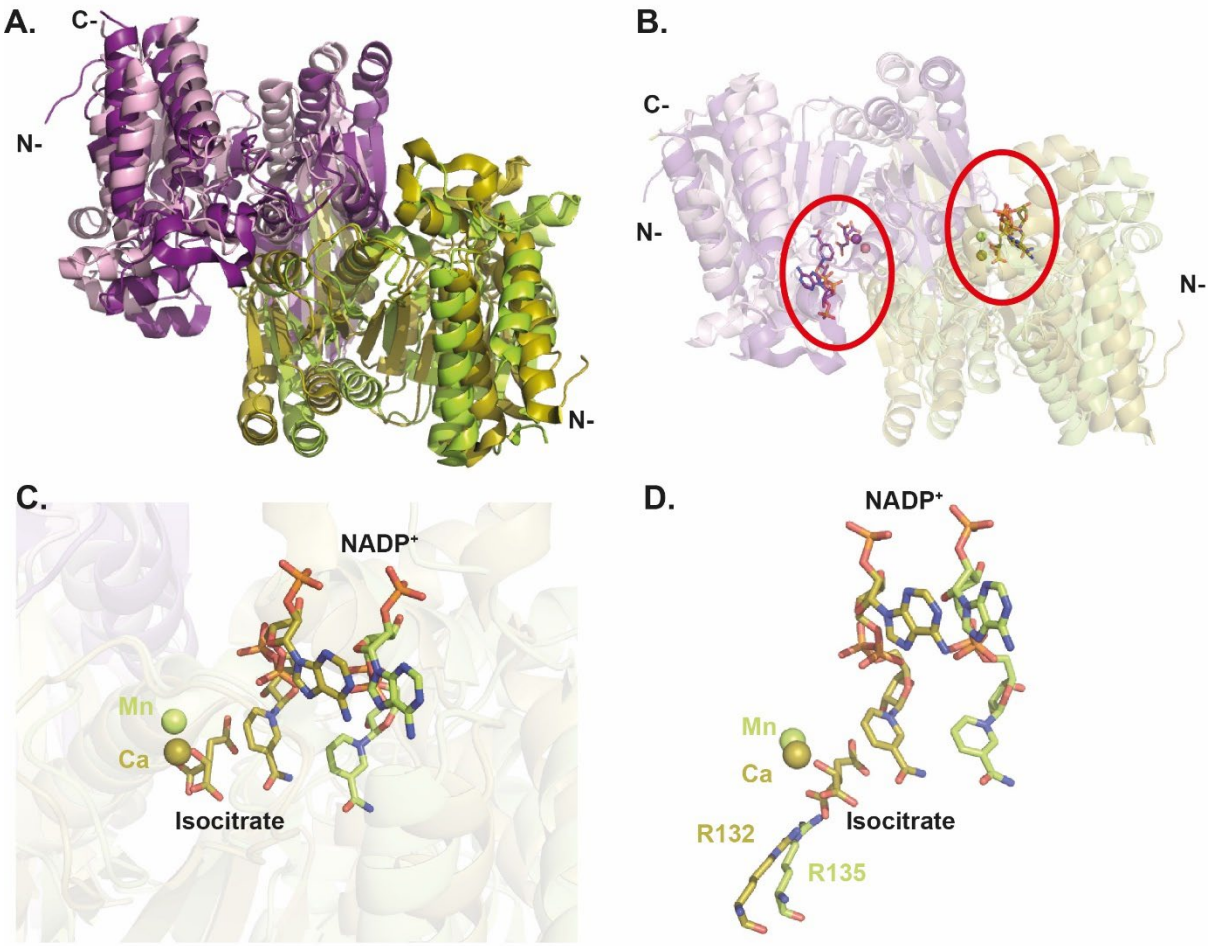

***Figure 1.19** | Crystal structure overlay of Mtb IDH1 and Hs IDH1. **A.** Ribbon view from a crystal structure of Mtb IDH1 (chain A: light pink, chain B: lime; PDB: 4HCX[47]) superimposed with a view from a structure of Hs IDH1 wt (chain A: purple, chain B: olive; PDB: 1T0L[15]). Mtb IDH1 is complexed with manganese and $NADP^+$. Hs IDH1 wt is complexed with calcium, isocitrate, and $NADP^+$. **B.** The substrates are shown in sticks. Red circles: Active sites. **C.** Magnified section of the active site with calcium/manganese, isocitrate, and $NADP^+$. **D.** Magnified section of the active site highlighting Hs IDH1 R132 and Mtb IDH1 R135.*

Initial studies on recombinant *Mtb* IDH1 and *Mtb* IDH2 were conducted by Banerjee et al.[119] Both *Mtb* IDH1 and *Mtb* IDH2 catalyse turnover of isocitrate using $NADP^+$, and not NAD^+.[118] According to these studies, *Mtb* IDH1 can utilise Mg^{2+} and Zn^{2+} as the catalytic metal ion,

while *Mtb* IDH2 can only utilise Mg^{2+}. No activity was observed with Mn^{2+} or Ca^{2+}. The affinity for isocitrate is higher for *Mtb* IDH1 but the affinity for $NADP^+$ is higher for *Mtb* IDH2 (as judged by K_M).[118] *Mtb* IDH2 catalyses turnover of isocitrate to 2-OG more efficiently. *Mtb* IDH1 retains more of its activity at lower pHs than *Mtb* IDH2 and shows higher stability at higher pHs.[118] Hence, Banerjee et al. have proposed that although *Mtb* IDH1 exhibits a lower catalytic efficiency than *Mtb* IDH2, it is more robust.[118] The absence of NaCl does not affect the activity of *Mtb* IDH1 but it does decrease the activity of *Mtb* IDH2.[118] *Mtb* IDH1 is present as a dimer or tetramer in solution but the active form is the dimer.[118] *Mtb* IDH2 can be present as a dimer, trimer, or tetramer depending on the salt concentration.[118]

Quartararo *et al*. have subsequently reported more detailed studies on *Mtb* IDH1.[47] In their studies, *Mtb* IDH1 was shown to utilise Mg^{2+}, but that its activity is 12% higher with Mn^{2+}. Based on mechanistic analyses, Quartararo *et al*. suggested that *Mtb* IDH1 forms a ternary complex with $NADP^+$ and isocitrate (coordinated by Mn^{2+}) with binding occurring in a random order. After the turnover is completed, the co-product CO_2 is released first, then 2-OG followed by NADPH. [47] The crystal structure of *Mtb* IDH1 displays a dimer with a Rossman-fold essential for dinucleotide binding. Each monomer has two ß-hairpins, which form two antiparallel ß-sheets with the other monomer (CLASP domain). Similarly to *Hs* IDH1, Asp-282, Asp-278, and Asp-255 (homologous to *Hs* IDH1 Asp-279, Asp-275, Asp-252) are involved in the coordination of the metal ion (Mn^{2+}). *Mtb* IDH1 and *Hs* IDH1 show a high degree of structural similarity (**Figure 1.19**, A). *Mtb* IDH1 R135H is homologous to *Hs* IDH1 R132; R132 substitutions are found in cancer and confer a gain of function effect making the enzyme an efficient producer of the oncometabolite 2-HG (Section 1.3).[35] Quartararo *et al*. reported that *Mtb* IDH1 wt can produce 2-HG[120], but the role of 2-HG in *Mtb* physiology and/or pathogenesis is undefined.

While initial studies on *Mtb* IDH1 and *Mtb* IDH2 are reported, and inhibitors of metabolic enzymes (e.g. IDHs) are validated in human use for treatment of AML (see Section 1.6), work on *Mtb* IDH inhibitors has not progressed, likely in part because of the perception that it is not possible to obtain selectivity for mycobacterial IDHs over human IDHs.

1.12 Regulation of Mycobacterial IDHs

Investigations on the regulation of isocitrate metabolism, and hence ICL and IDH, are crucial to understand the interplay of the glyoxylate shunt and the TCA cycle, and consequently, are relevant in attempts to disrupt isocitrate metabolism with IDH or ICL inhibitors.

The regulation of the glyoxylate shunt in *E.coli* (one IDH and one ICL isoform) is reported to be linked to the phosphorylation of IDH by the AceK phosphatase kinase. [121] Phosphorylation results in inactivation of *E. coli* IDH[121]; however, *E. coli* IDH is structurally distinct from *Mtb* IDH1 and *Mtb* IDH2, neither of both contain a site susceptible for potential regulation by phosphorylation in *Mtb* IDH1/IDH2.[113] There is also no *Mtb* analogue of AceK.[113] Hence, regulation of *Mtb* IDHs by phosphorylation is perhaps unlikely. Similarly, no potential phosphorylation sites have been identified in *Msm* IDH, which make a phosphorylation-based regulation mechanism unlikely.[113]

Pseudomonas aeruginosa contains two isocitrate dehydrogenases, IDH and ICD, and one ICL. AceK is involved in the regulation of ICD activity.[122] Its kinase activity (i.e. inhibiting ICD by phosphorylation) is stimulated by high levels of acetyl-CoA, whereas its phosphatase activity is stimulated by high levels of oxaloacetate.[122] Regulation of IDH is achieved via the availability of certain precursors - a high abundance of glyoxylate, oxaloacetate and pyruvate activates IDH while it inhibits ICL at the same time. [122]

Murima et al. have reported metabolic cross-enhancement of *Msm* IDH and *Mtb* IDH2 as part of a regulatory mechanism.[113] High levels of glyoxylate, produced as the first metabolite of the glyoxylate shunt, stimulate the enzymatic activity of *Msm* IDH and *Mtb* IDH2.[113] Glyoxylate binds with high affinity to *Msm* IDH (shown by isothermal titration calorimetry (ITC) studies) and docking studies suggest that glyoxylate could bind close to the active site of *Msm* IDH.[113] It is proposed that the metabolic cross-enhancement of *Msm* IDH/*Mtb* IDH2 by the product of the first step of the glyoxylate shunt, glyoxylate, may serve as a feedback mechanism ensuring balance of the isocitrate fluxes.

1.13 Aims and Objectives of the Work Described in this Thesis

The work described in this thesis comprised biochemical, biophysical, inhibition, and cellular studies on *Hs* IDH variants aimed at investigating the mechanism of resistance to ivosidenib and initial studies on IDHs from mycobacteria as potential drug targets.

The work on human IDH1 drug resistance involved:

- Biochemical and biophysical characterisation of ivosidenib-resistant *Hs* IDH1 R132C S280F and R132H S280F variants.
- Investigations on the mechanism of resistance to ivosidenib due to the second-site substitution S280F.
- Inhibition studies to find alternative inhibitors of *Hs* IDH1 R132C S280F and *Hs* IDH1 R132H S280F to overcome S280F mediated drug-resistance.
- Crystallographic studies on *Hs* IDH1 R132C S280F to investigate the structural basis of resistance.
- Investigations on the influence of various R132 variations on IDH1 activity.
- Studies on the role of the IDH1 dimer-interface in catalysis.

The work on mycobacterial IDHs comprised the following:

- Establishing mycobacterial IDH protein production and activity assay procedures.
- Biochemical and biophysical characterisation of *Mtb* IDH1 and IDH2, and *Msm* IDH.
- Investigations on the regulation of IDHs in mycobacteria.
- Investigation of an alternative role of *Mtb* IDH1 in *Mtb* metabolism
- Preliminary inhibition studies on *Mtb* IDH1 and IDH2, and *Msm* IDH.

Chapter 2

Biochemical and Biophysical Characterisation of Ivosidenib-Resistant IDH1 Cancer Variants

Contents

2 Biochemical and Biophysical Characterisation of Ivosidenib-Resistant *Hs* IDH1 Cancer Variants

2.1 Introduction

Ivosidenib was developed by Agios Pharmaceticals[63] and is the first and, to date, the only FDA approved IDH1 variant inhibitor.[64] Ivosidenib is approved for treatment of refractory or relapsed acute myeloid leukaemia (AML) for which an IDH1 variant has been shown to be present. [64] Shortly after the FDA approval for ivosidenib in 2018, drug resistance to it was reported with a relapse in AML patients, correlating with increases in plasma 2-HG levels.[123] The resistance was linked with the occurrence of a second acquired variation in the IDH1 R132C variant, i.e. substitution of Ser-280 to Phe-280 at the IDH1 dimer-interface (due to a an 839C > T mutation in the gene encoding for IDH1[123]). This mutation was not observed before treatment with ivosidenib and has been branded a "2-HG restoring mutation".[102]

Agios Pharmaceuticals has developed an IDH2 mutant inhibitor; enasidenib (AG-221)[124], which gained FDA approval in 2017.[125] However, resistance to enasidenib due to second-site dimer-interface variations emerged shortly after its clinical introduction (in patients bearing the IDH2 R140Q variant).[123] Interestingly, an enasidenib resistance enabling substitution was observed at residue IDH2 I319 at the dimer-interface. Thus, in this patient IDH2 R140Q and IDH2 I319M heterodimers are probably present (Section 1.8). Notably, IDH2 I319 is homologous to IDH1 S280 (**Figure 2.1**). Additionally, an acquired IDH2 Q316E variant (**Figure 2.1**) was discovered in another patient observed to manifest enasidenib resistance to the inhibition of the IDH2 R140Q variant.[28]

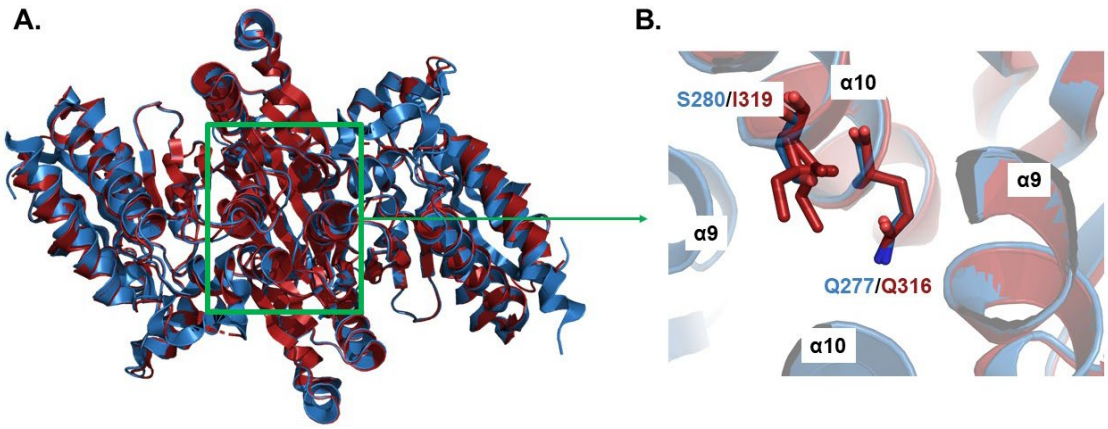

***Figure 2.1** | Overlay of IDH1 R132H and IDH2 R140Q. **A.** View from a crystal structure of IDH1 R132H (blue, PDB ID: 4KZO[126]) superimposed with IDH2 R140Q (red, PDB ID: 5I95[124])The dimer interface is highlighted in green. **B.** The α-helices 9 and 10 are in the centre of the dimer interface. IDH1 S280 is homologous to IDH2 I319. IDH1 Q277 is homologous to IDH2 Q316.*

Since the first report of acquired resistance to an IDH1 variant inhibitor treatment by Intlekofer et al.[28], more cases of ivosidenib drug-resistance linked to the S280F substitution have been discovered.; to date, five cases of R132C S280F have been clearly linked to ivosidenib drug resistance.[28, 102, 103] Due to the limited time ivosidenib has been used in clinical practise, it is likely that the incidence of drug resistance will increase. Furthermore, an R132H S280F IDH1 variant could emerge due to high incidence of the R132H variant in IDH1 cancer variants (Section 1.4).

The work described in this chapter set out to investigate the ivosidenib-resistant variant IDH1 R132C S280F, as well as IDH1 R132C, IDH1 R132C S280A, IDH1 R132H, and IDH1 R132H S280F using kinetic, biophysical, and structural studies. Note that in the subsequent chapter all variants referred to are IDH1 based, except where stated.

2.2 Recombinant Production of IDH1 Variants

Initially, work to prepare recombinant forms of human R132C, R132C S280F, R132C S280A, R132H, and R132H S280F was carried out. A pET22b plasmid containing an open reading frame (ORF) encoding for R132H with a C-terminal His-tag was kindly provided by Dr Martine Abboud. Primers were designed to alter the ORF to encode for R132C, R132C S280F, R132C S280A, and R132H S280F. Forward and reverse primers were designed completely overlapping or according to the protocols of Zheng et al.[127] (Section 2.9.1). After site-directed mutagenesis (SDM) according to Section 2.12.1, the plasmids were transformed into BL21(DE3)pLysS *E. coli* cells and the protein expressed according to standard conditions (Section 2.12.1). Protein purification was conducted according to standard procedures (Section 2.12.1). In brief, the pellet was lysed and purified by nickel-affinity chromatography (5 mL fractions) and size-exclusion chromatography (10 mL fractions) (see Section 2.12.1). Fractions containing purified R132C, R132C S280F, R132C S280A, R132H, or R132H S280F were pooled and concentrated. The proteins were stored in gel filtration buffer (Section 7.1.12). Lower molecular weight protein bands in SDS PAGE gel analysis (**Figure 2.3**-**Figure 2.7**) possibly correspond to degradation products. Protein-observed LC/MS analyses of all IDH1 variants purified identified the right protein mass with an N-terminal methionine loss (**Table 2.1**).

2.2.1 Sequence Alignment

Mutations encoding for R132C, R132C S280F, R132C S280A, and R132H S280F were introduced into the ORF of IDH1 by SDM. The sequences were confirmed by Sanger Sequencing and alignment using MAFFT[128] (**Figure 2.2**).

Figure 2.2 | Protein sequence alignments IDH1 variants*. The red box highlights variations in residue 132. The green box highlights variations in residue 280. The alignment was carried out using MAFFT[128]. The purple box highlights part of the L1 loop. The blue boxes highlight the α9 and α10 helix.*

All IDH1 variants were produced in BL21(DE3)pLysS *E. coli* cells and purified as described in Section 7.1.12. Yields are presented in amount of protein (mg) per litre of 2TY medium (L).

2.2.2 Protein Production of R132H

After cell lysis, purification by nickel-affinity chromatography and size exclusion chromatography (**Figure 2.3**) yielded 34.7 mg/L of R132H, which was aliquoted at a concentration of 27.4 mg/mL (573.8 µM).

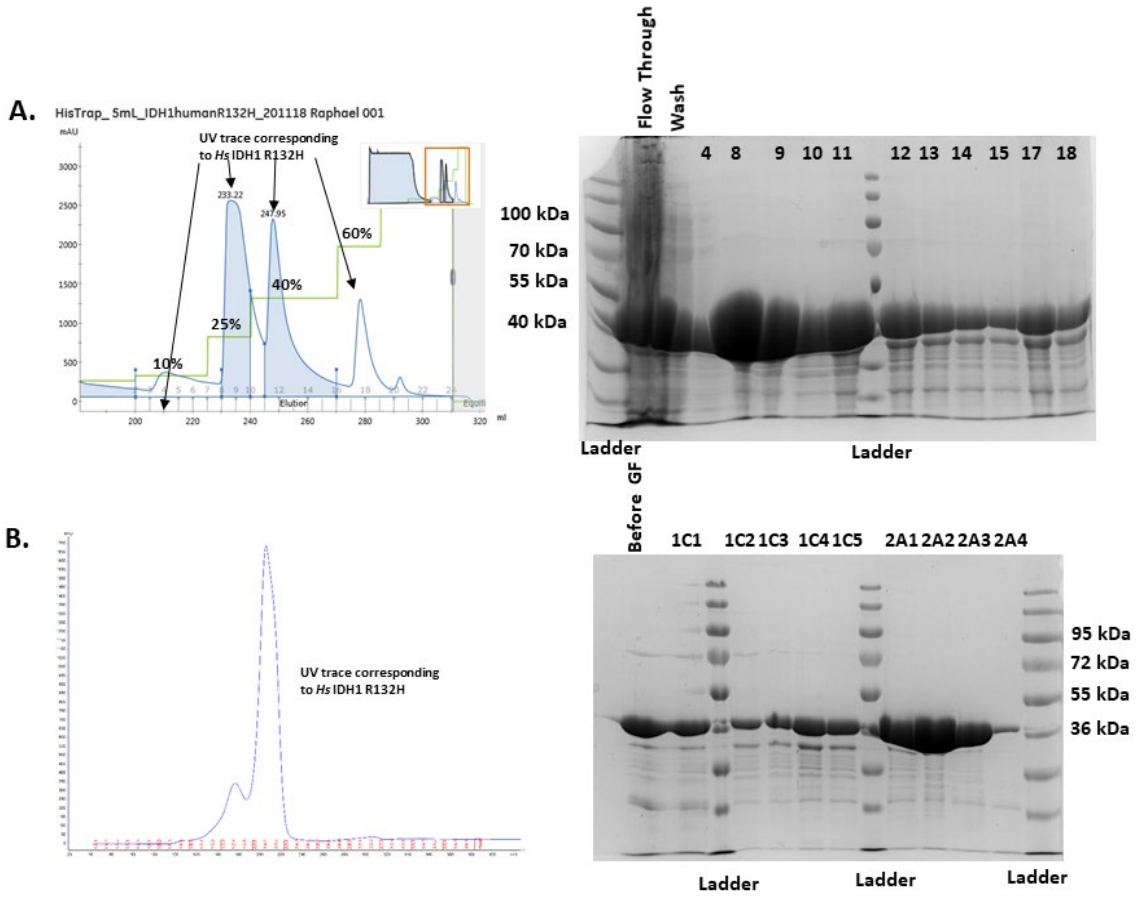

Figure 2.3 *| R132H purification. The chromatograms of each purification technique are shown on the left and the corresponding SDS-PAGE gels of the fractions on the right.* ***A****. Nickel-affinity chromatography using imidazole step gradient elution (percentages of elution buffer are shown on the chromatogram); see Section 2.12.1 for details.* ***B.*** *Size-exclusion chromatography using isocratic elution.*

2.2.3 Protein Production of R132H S280F

After cell lysis, purification by nickel-affinity chromatography and size exclusion chromatography (**Figure 2.4**) yielded 167.3 mg/L of R132H S280F, which was aliquoted at a concentration of 29.7 mg/mL (622.5 µM).

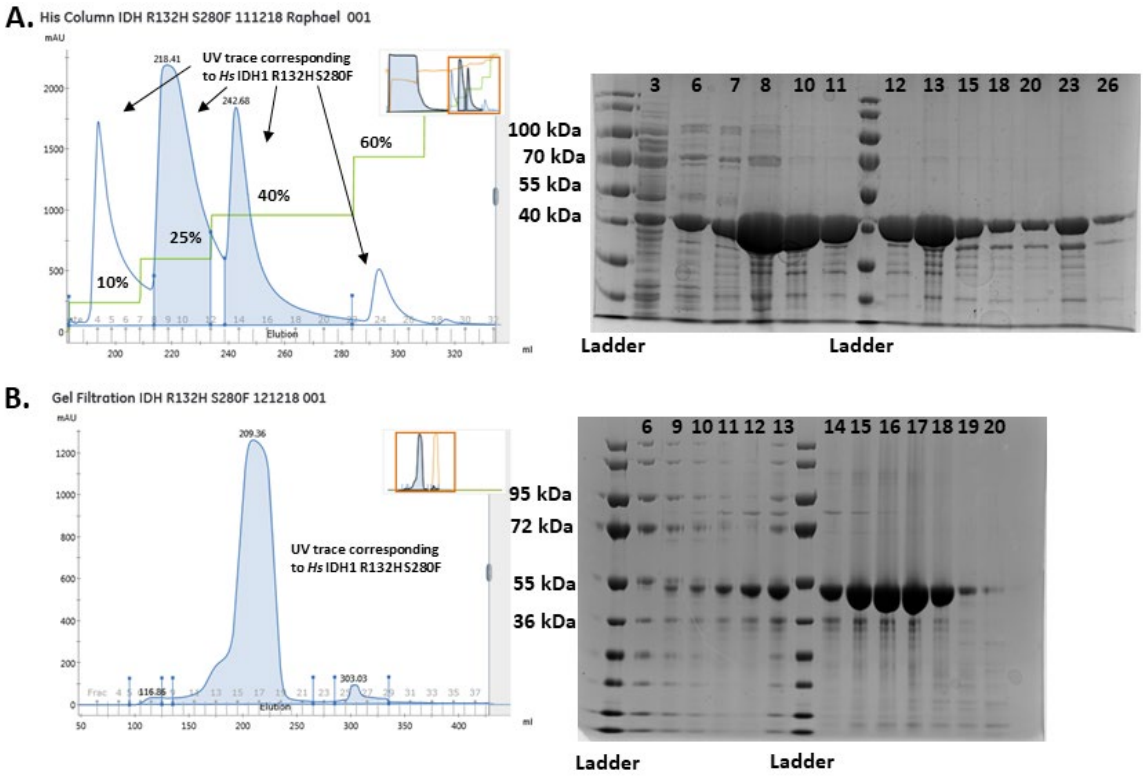

Figure 2.4 *| R132H S280F purification. The chromatograms of each purification technique are shown on the left and the corresponding SDS-PAGE gels of the fractions on the right.* ***A.*** *Nickel-affinity chromatography using imidazole step gradient elution (percentages of elution buffer are shown on the chromatogram); see Section 2.12.1 for details.* ***B.*** *Size-exclusion chromatography using isocratic elution.*

2.2.4 Protein Production of R132C

After cell lysis, purification by nickel-affinity chromatography and size exclusion chromatography (**Figure 2.5**) yielded 29.8 mg/L of R132C, which was aliquoted at a concentration of 25.4 mg/mL (532.7 µM).

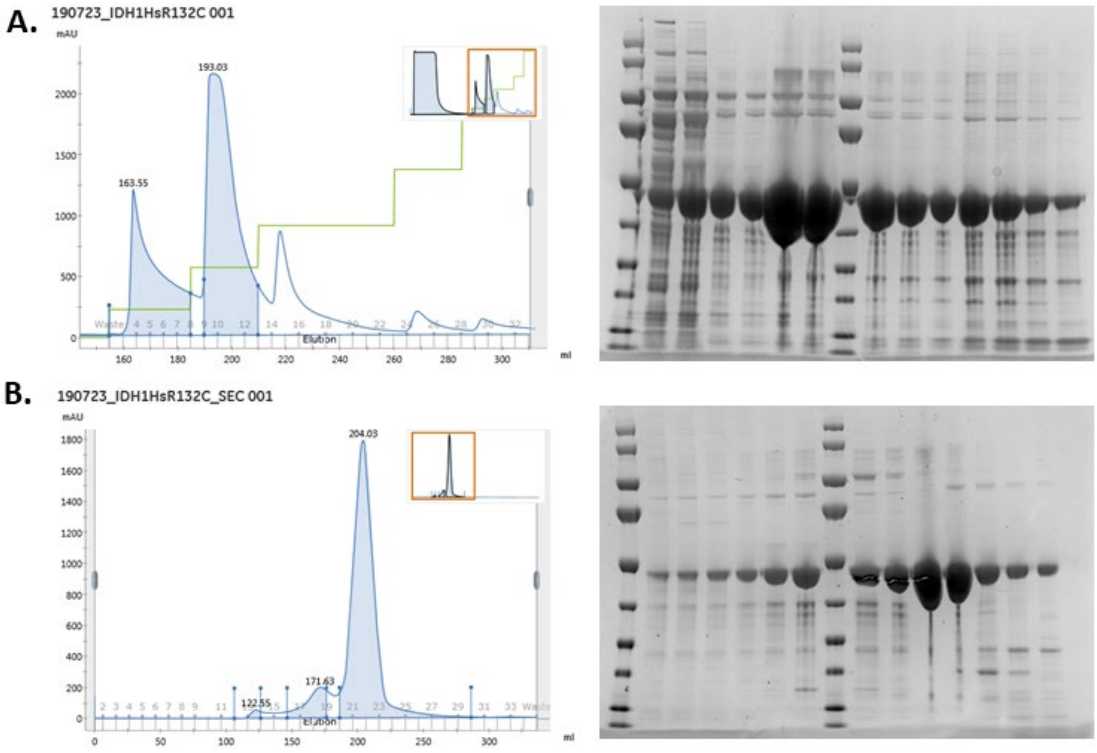

Figure 2.5 *| R132C purification. The chromatograms of each purification technique are shown on the left and the corresponding SDS-PAGE gels of the fractions on the right.* ***A.*** *Nickel-affinity chromatography using imidazole step gradient elution (percentages of elution buffer are shown on the chromatogram); see Section 2.12.1 for details.* ***B.*** *Size-exclusion chromatography using isocratic elution.*

2.2.5 Protein Production of R132C S280F

After cell lysis, purification by nickel-affinity chromatography and size exclusion chromatography (**Figure 2.6**) yielded 42.4 mg/L of R132C S280F, which was aliquoted at a concentration of 23.8 mg/mL (498.0 µM).

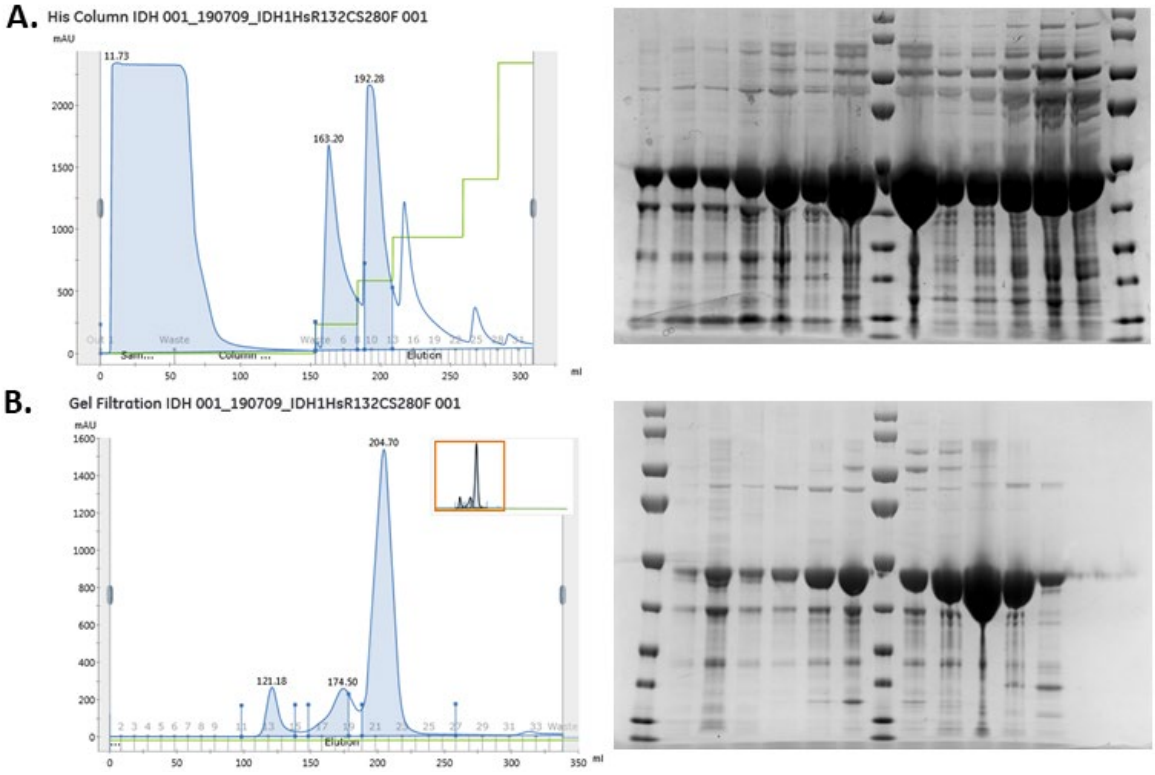

Figure 2.6 *| R132C S280F purification. The chromatograms of each purification technique are shown on the left and the corresponding SDS-PAGE gels of the fractions on the right.* ***A.*** *Nickel-affinity chromatography using imidazole step gradient elution (percentages of elution buffer are shown on the chromatogram); see Section 2.12.1 for details.* ***B.*** *Size-exclusion chromatography using isocratic elution.*

2.2.6 Protein Production of R132C S280A

After cell lysis, purification by nickel-affinity chromatography and size exclusion chromatography (**Figure 2.7**) yielded 8.4 mg/L of R132C S280A, which was aliquoted at a concentration of 15.4 mg/mL (322.6 µM).

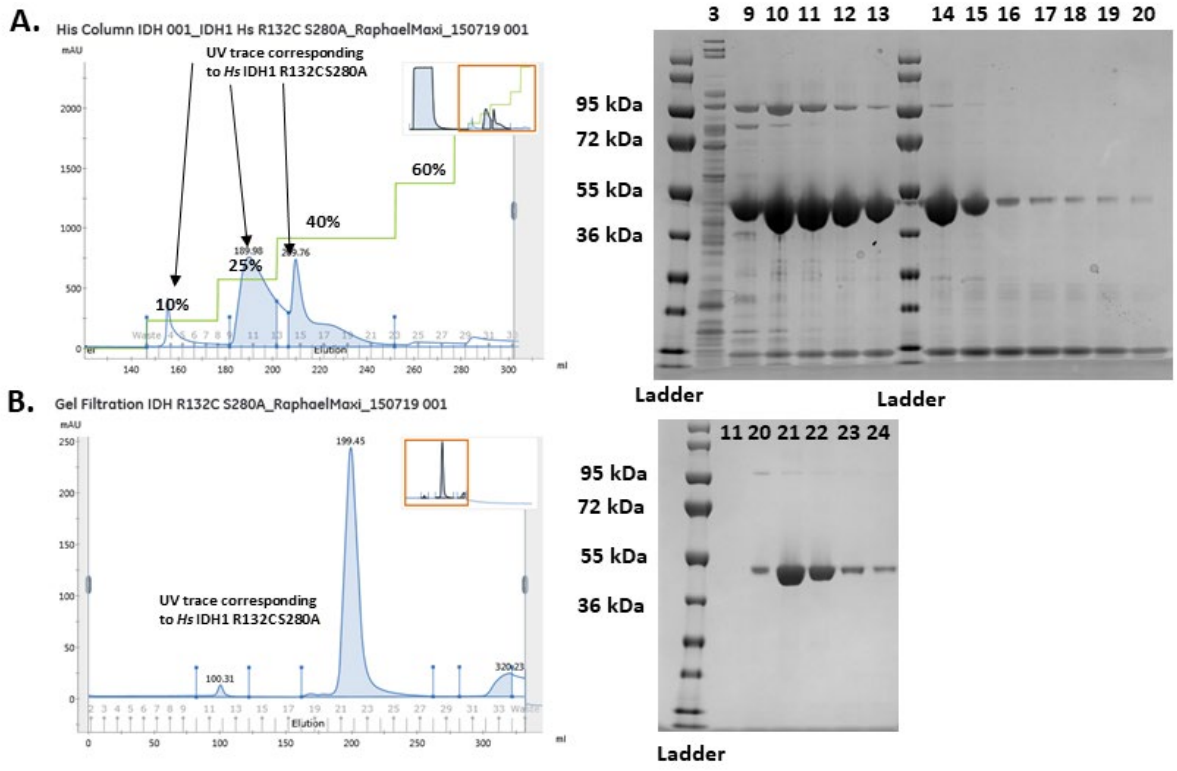

***Figure 2.7** | IDH1 R132C S280A purification. The chromatograms of each purification technique are shown on the left and the corresponding SDS-PAGE gels of the fractions on the right. **A.** Nickel-affinity chromatography using imidazole step gradient elution (percentages of elution buffer are shown on the chromatogram); see Section 2.12.1 for details. **B.** Size-exclusion chromatography using isocratic elution.*

2.2.7 Analysis of Recombinant IDH1 Variants by LC/MS

To confirm isolation of the target proteins, their masses were investigated (additionally to SDS PAGE analyses in Section 2.2.2-2.2.6) using LC/MS. The masses of all IDH1 variants were shown with loss of the N-terminal methionine (**Table 2.1**) which is commonly observed in C-terminally tagged proteins expressed in *E. coli*.[129]

Table 2.1 | *Analyses of proteins by LC/MS confirms their masses with a loss of N-terminal methionine (-131 Da[130]).*

Protein	Mw (calculated)	Mw (observed)	Difference in Mw
R132H	47705.4	47574.4	-131.0
R132H S280F	47765.5	47632.5	-133.0
R132C	47671.4	47539.4	-132.0
R132C S280F	47731.5	47599.7	-131.8
R132C S280A	47655.4	47524.2	-131.2

2.3 Biochemical Characterisation

2.3.1 Activity Assays Using NADPH Absorbance Monitoring

Initially, the kinetic parameters of the R132C, R132C S280F, R132H, and R132H S280F variants were determined using a reported NADPH absorbance assay, which monitors NADPH levels by its specific absorbance at 340 nm.[48]

Previously, several assays have been reported to monitor IDH1 (variant) activity. While some methods observed the product 2-HG by mass spectrometry[50] (end-point assay), spectroscopic monitoring of the depletion of NADPH (**Figure 2.8**) is the preferred method for kinetic characterisation as this allows continuous measurement of changes in NADPH levels in a high throughput format (96 well). ^{1}H NMR can also be used to measure IDH turnover continuously but in a lower throughput manner.

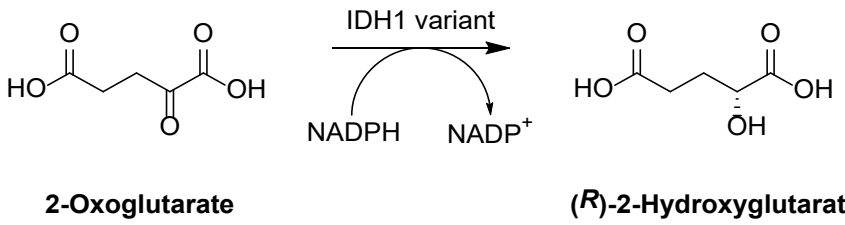

Figure 2.8 **|** *Reduction of 2-oxoglutarate to R-2-hydroxyglutarate and concomitant oxidation of NADPH to NADP^{+}.*

To monitor NADPH, several reports have employed a diaphorase- resazurin-coupled assay in which the fluorescence of the reduced product resorufin is monitored.[50,126,66] While this is an indirect assay using NADPH as a reducing agent, other publications on IDH catalysis have reported direct observation of NADPH by either monitoring its fluorescence[35] or absorbance[35,126,131].

The kinetic analyses of IDH1 variants in this thesis were based on NADPH absorbance measurements according to published procedures. [48] While $NADP^+$ does not absorb light with a wavelength of 340 nm, NADPH displays an absorbance maximum at 340 nm. Therefore, NADPH absorbance can be used to monitor the reduction of 2-OG to 2-HG and the concomitant oxidation of NADPH (**Figure 2.8**), which results in a decrease in absorbance at 340 nm (**Figure 2.9**).

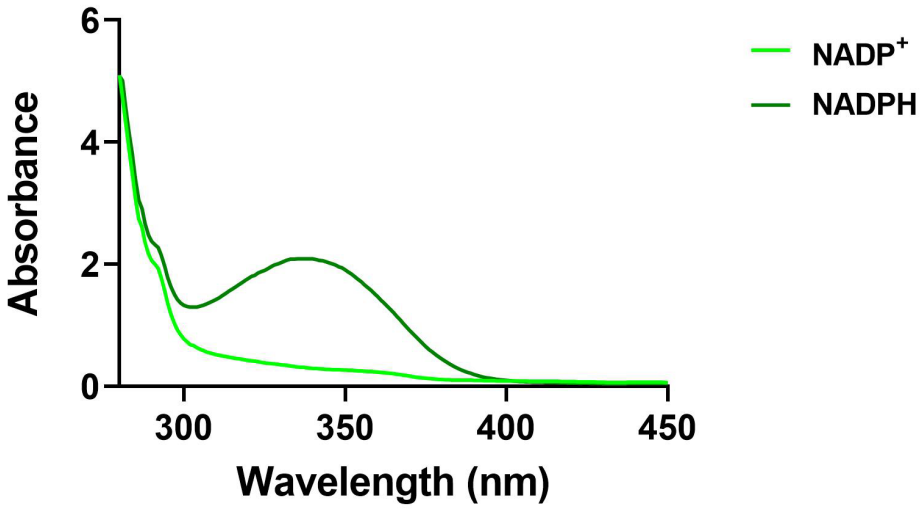

Figure 2.9 *| Absorbance spectra of $NADP^+$ (500 µM) and NADPH (500 µM). NADPH displays an absorbance maximum at 340 nm which is not observed for $NADP^+$.*

2.3.2 Determination of Michaelis-Menten Parameters

Analysis of Michaelis-Menten parameters is used to determine and compare kinetic parameters of enzymatic turnover catalysed by different IDH1 variants.[11,25] Michaelis-Menten parameters were analysed by saturating all substrates/co-factors (based on concentrations reported for R132H[48]) but one, which is the substrate/co-factor of which Michaelis Menten parameters are determined (varying concentrations). The initial rate was measured and used for analysis (note measuring the initial rate prevents potential interference by product inhibition).[132]

The substrate/co-factor of interest was added in varying concentrations; the initial rate was determined and plotted as a function of the substrate/co-factor concentration. In Michaelis-Menten conditions, with a sufficiently high substrate/co-factor concentration (2-OG: 1.5 mM; NADPH: 300 µM, $MgCl_2$: 10 mM), the resulting hyperbolic curve approaches a maximum, which represents the maximal turnover rate V_{max} (**Figure 2.10**).[132] The substrate/co-factor concentration when V_{max} is half, is defined as the Michaelis-Menten constant K_M.[132] The lower the K_M, the lower is the substrate/co-factor concentration needed to achieve half the turnover rate of V_{max}.

The non-linear curve fit function of GraphPad prism was used to determine hyperbolic curves (**Figure 2.10**) and to determine Michaelis-Menten parameters of the variants (see Section 2.12.2).

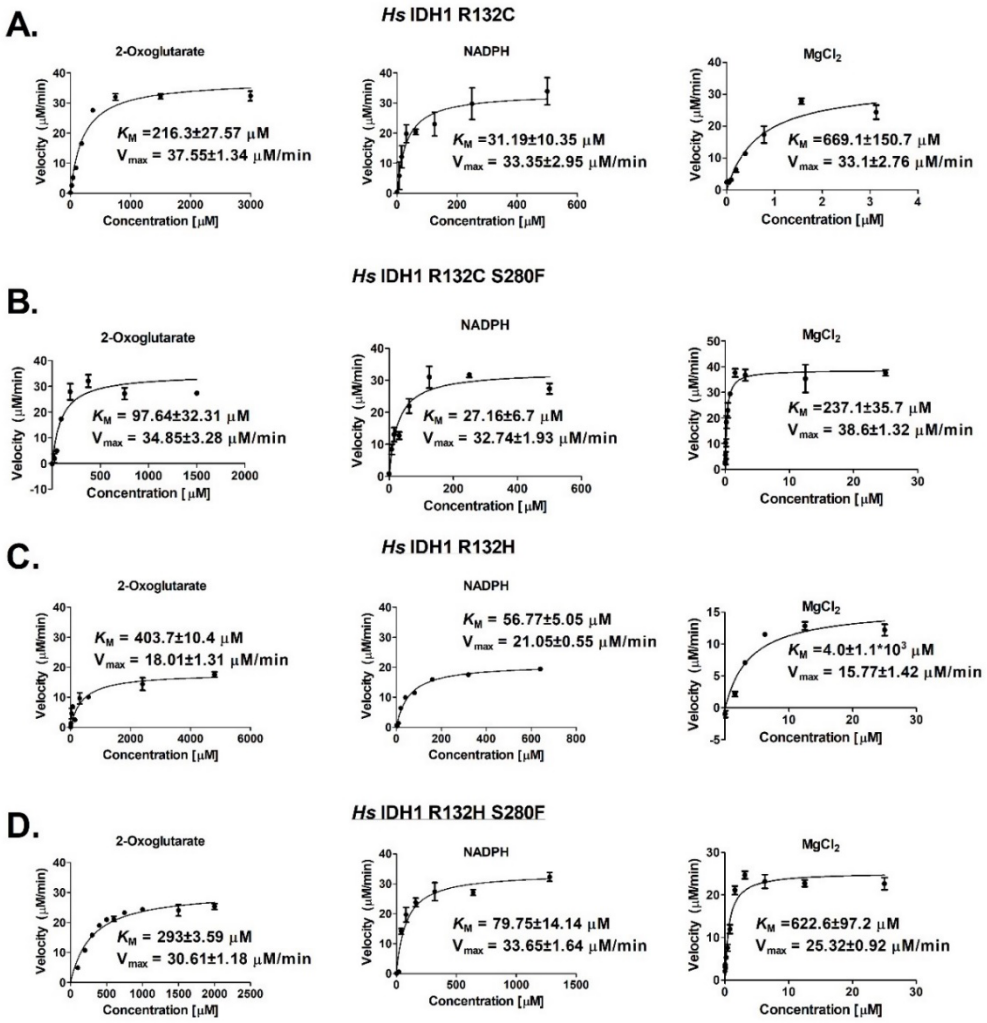

***Figure 2.10** | Kinetic studies on IDH1 variants. Michaelis-Menten analyses of R132C (**A**), R132C S280F (**B**), R132H (**C**), and R132H S280F (**D**). Nonlinear regression curve fits are shown. Errors: standard errors of the mean (n =3). Conditions: 100 mM Tris, 0.2 mM DTT, 0.005 % Tween 20, and 0.1 mg/mL BSA (pH 8.0). Enzyme: 400 nM.*

2.3.3 Comparison of Michaelis-Menten Parameters

To compare the kinetic parameters of R132C, R132C S280F, R132H, and R132H S280F for the reduction of 2-OG to 2-HG, k_{cat}, i.e. the number of substrate molecules an enzyme can turn over in saturated conditions, was measured.[132] The k_{cat} is calculated by dividing V_{max} by the enzyme concentration and indicates maximal rate of turnover. A measure of catalytic efficiency under conditions of non-saturating substrate is given by k_{cat}/K_M. **Table 2.2** compares the kinetic parameters obtained for 2-OG for IDH1 variants.

***Table 2.2** | Kinetic parameters of R132C, R132C S280F, R132H, and R132H S280F (400 nM) for 2-OG from nonlinear regression curve fits with the standard error of the mean (n =3). $MgCl_2$: 10 mM, NADPH: 0.3 mM.*

IDH1 variant	2-Oxoglutarate		
	K_M (µM)	k_{cat} (s^{-1})	k_{cat}/K_M ($s^{-1}\times\mu M^{-1}$) ($\times10^{-3}$)
R132C	216.3±27.57	1.56±0.06	7.2
R132C S280F	97.6±14.4	1.45±0.21	14.9
R132H	403.7±10.4	0.75±0.05	1.9
R132H S280F	293±3.59	1.28±0.05	4.4

Of the tested IDH1 variants, R132H exhibited the highest K_M for 2-OG and the lowest catalytic efficiency as judged by k_{cat}/K_M (**Table 2.2**), which is consistent with previous reports for the turnover of 2-OG to 2-HG by R132H.[133] Compared to R132H, R132C exhibited a lower K_M and a 5-fold higher catalytic efficiency (**Table 2.2**) consistent with literature reports.[133] For the reduction of 2-OG to 2-HG catalysed by R132C S280F and R132H S280F, there was a decrease in the K_M value and consequently an increase in the catalytic efficiency (2-fold) compared to R132C and R132H (**Table 2.2**).

***Table 2.3** | Kinetic parameters of R132C, R132C S280F, R132H, and R132H S280F (400 nM) for NADPH from nonlinear regression curve fits with the standard error of the mean (n =3). 2-OG: 1.5 mM, $MgCl_2$: 10 mM.*

IDH1 variant	NADPH		
	K_M (µM)	k_{cat} (s^{-1})	k_{cat}/K_M ($s^{-1}\times\mu M^{-1}$) ($\times10^{-3}$)
R132C	31.19±10.35	1.39±0.12	44.6
R132C S280F	27.2±6.7	1.36±0.08	50.2
R132H	56.77±5.05	0.88±0.02	15.4
R132H S280F	79.75±14.14	1.4±0.07	17.6

The catalytic efficiencies (k_{cat}/K_M) for the co-substrate NADPH were similar for the R132C and R132C S280F variants (**Table 2.3**). k_{cat}/K_M is 3-fold higher than for R132H and R132H S280F which exhibited similar k_{cat}/K_M values amongst themselves (**Table 2.3**).

***Table 2.4** | Kinetic parameters of R132C, R132C S280F, R132H, and R132H S280F (400 nM) for $MgCl_2$ from nonlinear regression curve fits with the standard error of the mean (n =3). 2-OG: 1.5 mM, NADPH: 0.3 mM.*

IDH1 variant	**$MgCl_2$**		
	K_M (μM)	**k_{cat} (s^{-1})**	**k_{cat}/K_M ($s^{-1}\times\mu M^{-1}$) ($\times10^{-3}$)**
R132C	669.1±151.1	1.38±0.12	2.1
R132C S280F	237.1±35.7	1.61±0.05	6.8
R132H	$(4.0\pm0.7)\times10^3$	0.71±0.04	0.2
R132H S280F	622.6±97.2	1.06±0.04	1.7

IDH1 uses a divalent magnesium (or manganese) ion for catalysis, which is essential for 2-OG binding and hence, enzymatic activity.[48] Consistent with literature reports[48], R132H exhibited the highest K_M for magnesium compared to R132C, R132C S280F, and R132H S280F (**Table 2.4**). R132C S280F and R132H S280F exhibited a decreased K_M for magnesium compared to R132C or R132H, respectively. The decreased K_M of the R132H S280F resulted in an 8.5-fold increase in k_{cat}/K_M compared to R132H (**Table 2.4**). The decreased K_M value for R132C S280F led to a 3-fold increase in catalytic efficiency (k_{cat}/K_M) compared to R132C (**Table 2.4**). R132C exhibited a ~10-fold lower k_{cat}/K_M than R132H.

The S280F substitution not only leads to ivosidenib resistance in patients[28], but also alters the parameters for 2-OG and $MgCl_2$. R132C S280F and R132H S280F might have a higher affinity for 2-OG and $MgCl_2$ (as judged by K_M), and consequently, an increased catalytic efficiency (k_{cat}/K_M). These changes might relate to the involvement of the α10 helix in metal binding and IDH1 catalysis (Section 1.6). Furthermore, R132C exhibits lower K_M values for 2-OG, NADPH, and $MgCl_2$ compared to R132H and consequently, manifests an elevated k_{cat}/K_M. This observation is consistent with previous reports showing R132C to be more efficient in catalysing the reduction of 2-OG to 2-HG than R132H.[25] The Michaelis-Menten parameters for NADPH are seemingly not influenced by the S280F substitution (R132C S280F vs R132C, R132H S280F vs R132H). The effects of the S280F substitution on the kinetic parameters for 2-OG and magnesium, but not for NADPH, were followed up by binding studies using DSF and X-ray crystallography studies (as described in Section 2.9/2.10).

2.4 Time-Course Studies by ^{1}H Nuclear Magnetic Resonance (NMR) Analyses

Direct observation of substrates by ^{1}H NMR resonances is a powerful approach to monitor the turnovers catalysed by IDH1 variants.[48] ^{1}H NMR time course studies complement the kinetic analyses by the NADPH absorbance assay as not only the change of cofactor NADPH, but also the reduction of 2-OG to 2-HG can be observed directly. Furthermore, ^{1}H NMR enables the studies of a potential turnover of isocitrate to 2-HG. The turnover of isocitrate to 2-HG was reported by an MS-based assay for an wt/R132H heterodimer[50] and, very recently, in a R132H homodimer using ^{1}H NMR.[48]

2.4.1 Time-Course Studies of Reduction of 2-OG to 2-HG Using ^{1}H NMR

The time-dependent changes of 2-OG/2-HG and NADPH/NADP^{+} in the presence of 500 nM IDH1 variant were monitored by ^{1}H NMR (700 MHz). Initially, signals between δ_H 1.5-3.0 ppm corresponding to 2-OG and 2-HG were assigned, to be able to use the changes in the integrals of the resonances to calculate the concentration of each substrate/product (**Figure 2.11**).

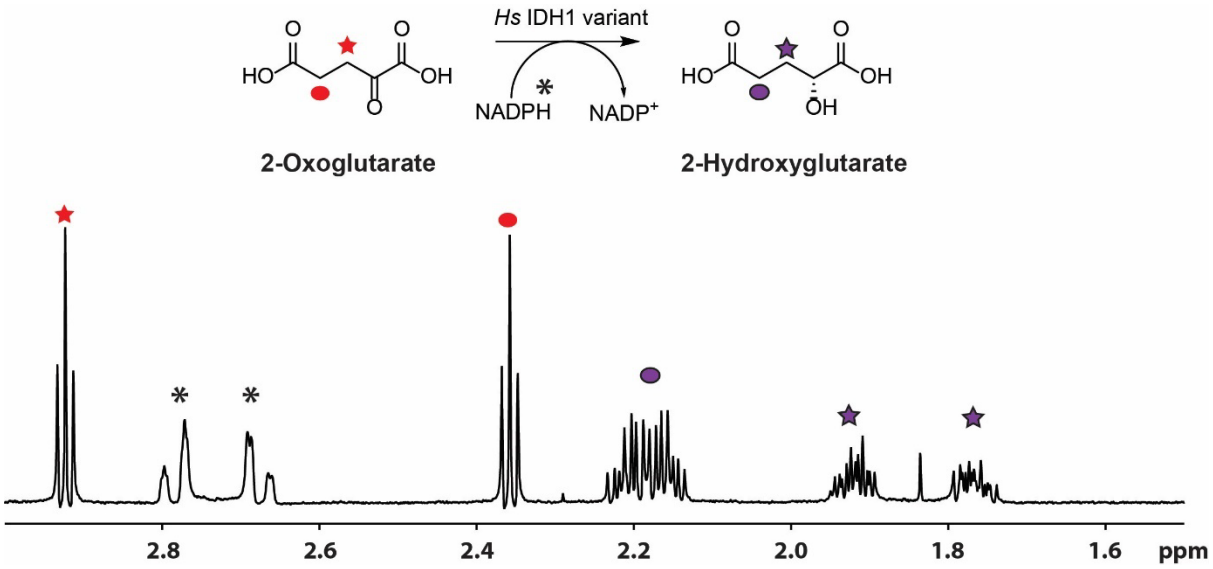

Figure 2.11 *| IDH1 variant catalysed reduction of 2-OG to 2-HG and extract of ^{1}H (700 MHz) spectrum showing corresponding signals. Conditions: 500 nM enzyme, 10 mM $MgCl_2$, 1.5 mM 2-OG, 1.5 mM NADPH; in 50 mM d_{11}-Tris (90:10 H_2O:D_2O; pH 7.5).*

Integration of the resonance of the triplet at δ_H 2.36 ppm corresponding to the two protons attached to the C-atom in α-position to the carboxylate of 2-OG was selected to monitor changes in the 2-OG concentration (**Figure 2.11**). Integration of the resonance of the multiplet at δ_H 1.77 ppm corresponding to one proton attached to the C-atom in α-position to the hydroxyl group was selected to monitor 2-HG concentration (**Figure 2.11**). The two resonances at

δ_H 2.68 ppm and δ_H 2.78 ppm correspond to NADPH; however, NADPH/$NADP^+$ signals in the aromatic region were used for time-course analyses (see below, **Figure 2.12**).

The singlet at δ_H 8.42 ppm corresponding to the proton at the adenine ring highlighted with an asterisk (dark green, **Figure 2.12**) was used to calculate the concentration of NADPH while the singlet at δ_H 8.36 ppm corresponding to the proton of the adenine ring highlighted with an asterisk (light green, **Figure 2.12**) was used for calculation of the $NADP^+$ concentration.

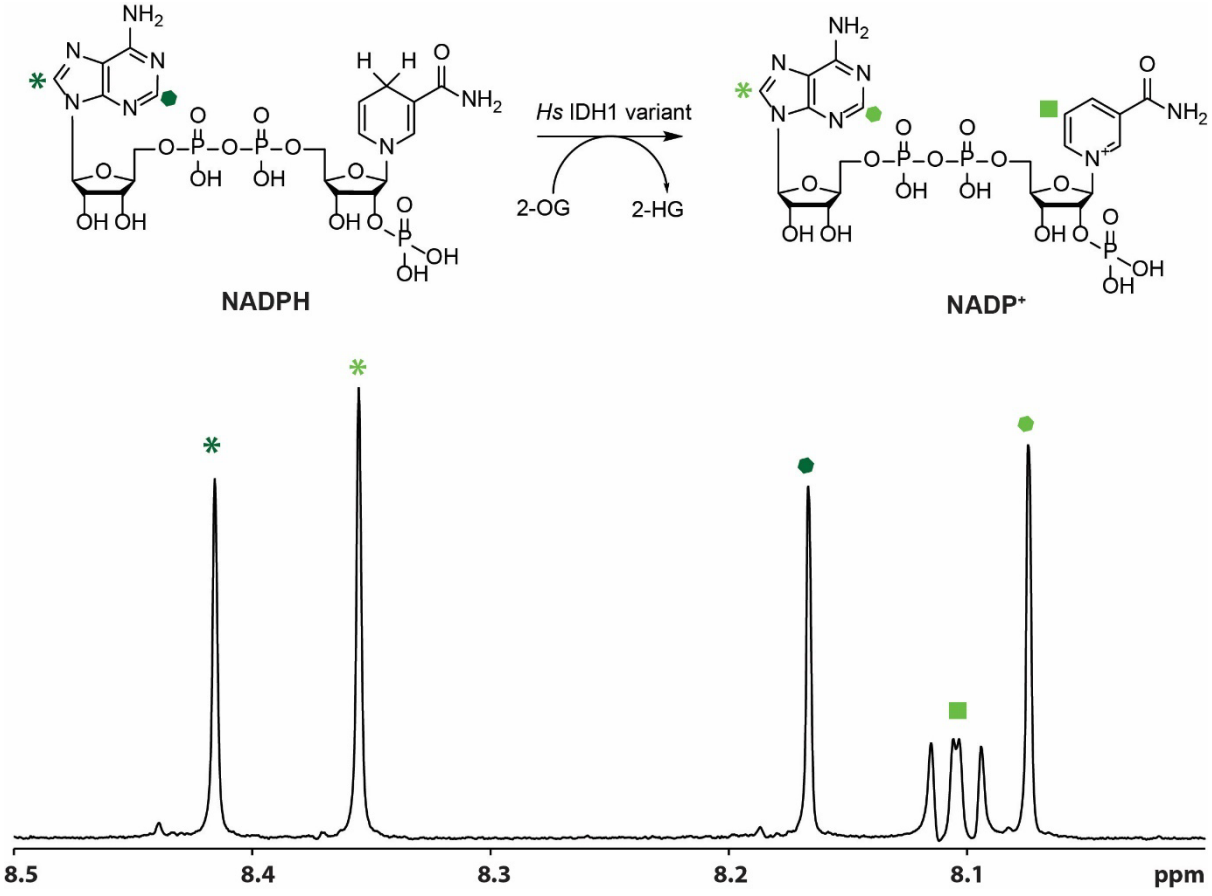

Figure 2.12 *| IDH1 variant catalysed oxidation of NADPH to $NADP^+$ and extract of ^1H (700 MHz) spectrum showing corresponding signals. Conditions: 500 nM enzyme, 10 mM $MgCl_2$, 1.5 mM 2-OG, 1.5 mM NADPH; in 50 mM d_{11}-Tris (90:10 H_2O:D_2O; pH 7.5).*

The starting concentration of 2-OG in the ^1H NMR monitored reaction was 1.5 mM. Turnover of 2-OG to 2-HG was observed by ^1H NMR; no evidence for other 2-OG derived products was observed. Therefore, the total combined concentration of 2-OG and 2-HG should be 1.5 mM at all times. The ratio of the integrals of the ^1H resonance at δ_H 2.36 ppm corresponding to 2-OG (normalised to one proton), and the ^1H resonance at δ_H 1.77 ppm corresponding to 2-HG was used to calculate the fraction of 1.5 mM corresponding to 2-OG or 2-HG, respectively. The initial concentration of NADPH in the incubation was 1.5 mM. Oxidation of NADPH to $NADP^+$ was observed by ^1H NMR; no other NADPH derived products were observed.

Therefore, the combined concentration of NADPH and $NADP^+$ was 1.5 mM at all times. The ratio of the integrals of the ^1H resonance at δ_H 8.42 ppm corresponding to NADPH, and the ^1H resonance at δ_H 8.36 ppm corresponding to $NADP^+$ was used to calculate the fraction of 1.5 mM corresponding to NADPH or $NADP^+$, respectively. ^1H NMR time courses (500 nM protein) were monitored for 1 h (**Figure 2.13**).

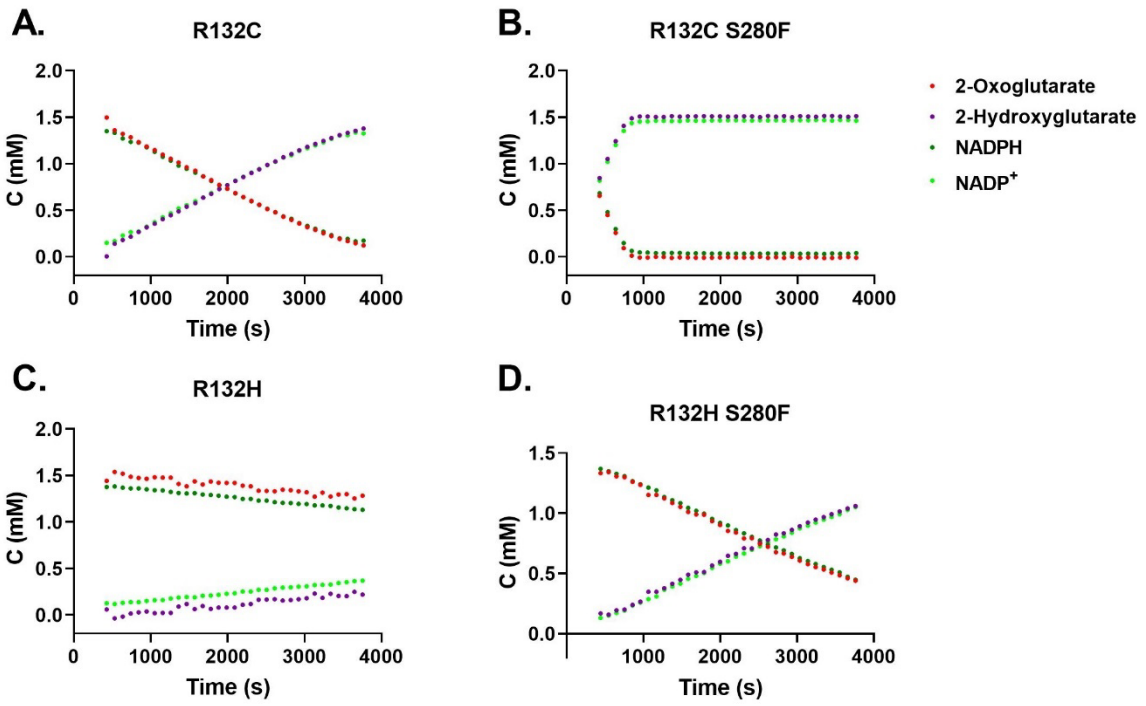

***Figure 2.13** | Turnover of 2-OG to 2-HG and concomitant reduction of NADPH to $NADP^+$ catalysed by Hs IDH1 variants as observed by ^1H NMR (700 MHz). Conditions: 500 nM enzyme, 10 mM $MgCl_2$, 1.5 mM 2-OG, 1.5 mM NADPH.*

R132C, R132C S280F, R132H, and R132H S280F all catalysed the reduction of 2-OG to 2-HG with concomitant oxidation of NADPH to $NADP^+$ (Figure 2.12). These observations supported the findings of Section 2.3, in which the activity of the IDH1 variants was shown by monitoring the changes in the NADPH absorbance. The formation of 2-HG was supported by spiking the product of the enzymatic assay with 5 mM 2-HG (Figure 2.13) or an overlay with a reference spectrum of 2-HG (5 mM in 50 mM d_{11}-Tris (90:10 H_2O:D_2O; pH 7.5).

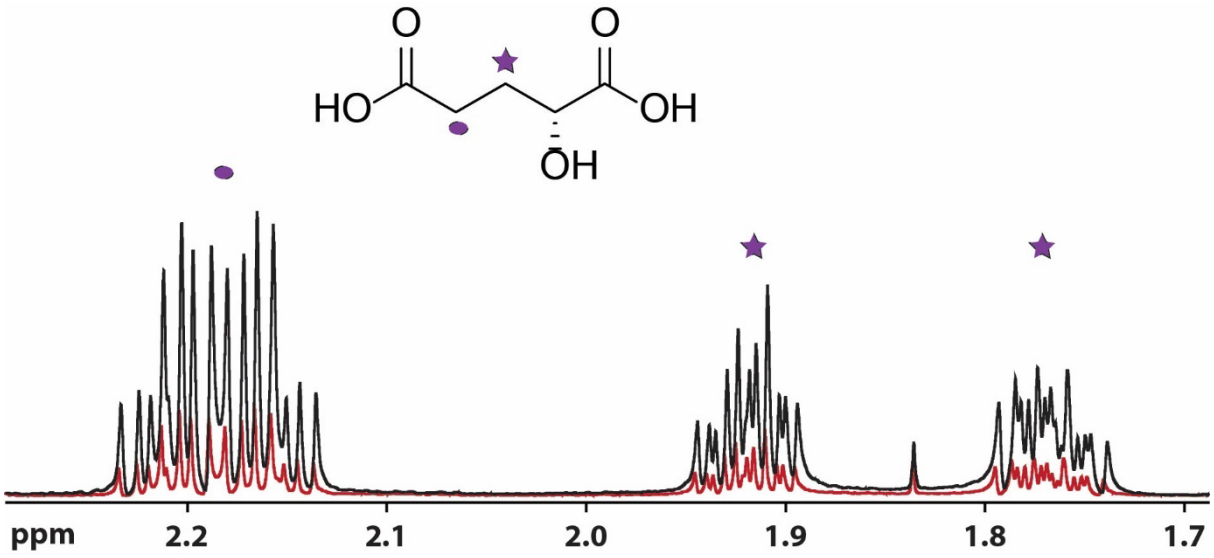

Figure 2.14 *| Confirmation of 2-HG formation in the reduction of 2-OG to 2-HG catalysed by R132C, R132C S280F, R132H, and R132H S280F as observed by ^{1}H NMR (700 MHz). 2-HG formation was supported by spiking the time-course sample (red) with 5 mM 2-HG (black) or an overlay with a reference spectrum of 2-HG. Conditions: 500 nM enzyme, 10 mM $MgCl_2$, 1.5 mM 2-OG, 1.5 mM NADPH. Buffer: 50 mM d_{11}-Tris (90:10 H_2O:D_2O); pH 7.5.*

R132C, R132C S280F, R132H, and R132H S280F displayed apparent differences in reaction efficiency for the reduction of 2-OG to 2-HG. The 2-HG levels were observed to increase as the reaction proceeded (**Figure 2.15**, A). The initial 20 minutes of the turnover of 2-OG to 2-HG as catalysed by R132C, R132C S280F, R132H, and R132H S280F were monitored in triplicates and the 2-HG levels after 12 minutes compared with each other (**Figure 2.15**, B).

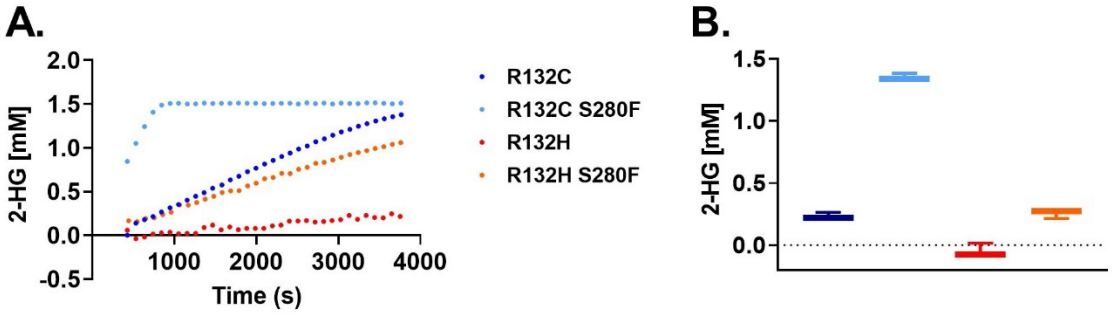

Figure 2.15 *| Turnover of 2-OG to 2-HG catalysed by R132C, R132C S280F, R132H, or R132H S280F as observed by ^{1}H NMR (700 MHz).* ***A.*** *2-HG formation from 2-OG as catalysed by R132C, R132C S280F, R132H, or R132H S280F.* ***B.*** *Comparison of 2-HG levels after 12 minutes of reaction (error bars represent standard errors of the mean, n =3). Conditions: See Figure 2.11 legend.*

For the reduction of 2-OG to 2-HG as catalysed by R132C S280F or R132H S280F, higher 2-HG levels compared to R132C or R132H were observed after 12 minutes. The most efficient IDH1 variant in catalysing production of 2-HG in ^{1}H NMR time-courses was R132C S280F, while R132C and R132H S280F produced 2-HG at a similar rate.

In accord with results obtained by the NADPH absorbance assay, R132C S280F is most efficient of the variants tested in reducing 2-OG to 2-HG as observed by ^{1}H NMR time course analyses, while R132H was the least efficient variant tested. The catalytic efficiencies for the formation of 2-HG obtained in Section 2.3 (2-fold increase of k_{cat}/K_M for 2-OG of R132C S280F or R132H S280F compared to R132C or R132H, respectively) are consistent with ^{1}H NMR time courses. R132C and R132H S280F display a similar efficiency in ^{1}H NMR time courses. In kinetic studies by NADPH absorbance, the k_{cat} for R132C is slightly higher than for R132H S280F but in a similar range, suggesting that both R132C and R132H S280F have a similar efficiency to catalyse the reduction of 2-OG to 2-HG.

The combined results of kinetic studies by the NADPH absorbance assay (Section 2.3) and ^{1}H NMR time-courses for the reduction of 2-OG to 2-HG, confirm that the S280F substitution results in an elevated reaction efficiency (R132C S280F > R132C >R132H S280F > R132H > IDH1 wt (Section 4.4)).

2.4.2 Formation of 2-HG from Isocitrate

In general, the IDH1 variants are reported to lack the ability to turnover isocitrate (Section 1.1).[35] However, formation of 2-HG from isocitrate was reported by Pietrak et al.[50] as catalysed by IDH1 wt/R132H heterodimer using MS analyses, and recently, for the first time in an R132H homodimer, by Liu et al. using ^{1}H NMR.[48] To investigate the turnover of isocitrate by R132C, R132C S280F, R132H, and R132H S280F, ^{1}H NMR was employed. Note that hereafter isocitrate refers to *DL*-isocitrate, unless otherwise stated.

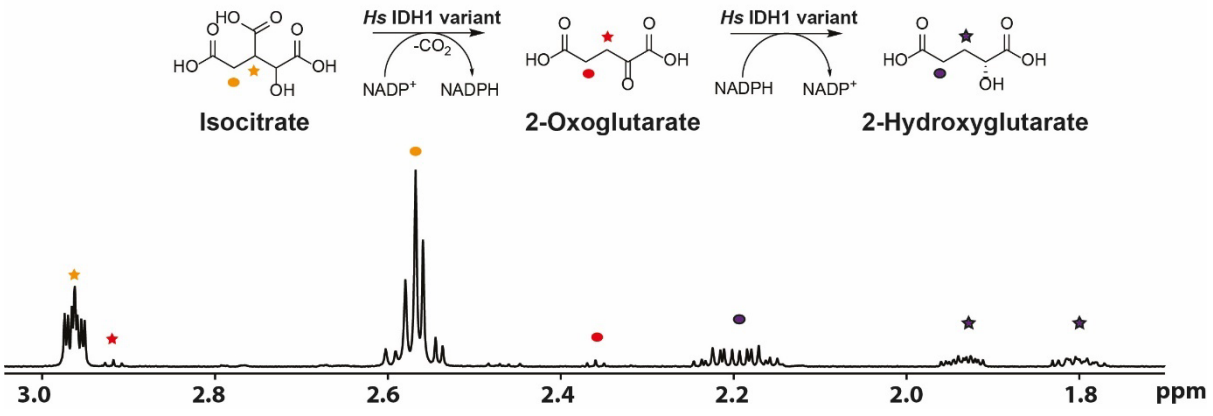

Figure 2.16 | *IDH1 variant catalysed turnover of isocitrate to 2-OG then 2-HG and extract of ^{1}H spectrum showing corresponding signals. Conditions: 750 nM enzyme, 10 mM $MgCl_2$, 3 mM DL-ICT, 1.5 mM $NADP^+$.*

Changes in $NADP^+$ and NADPH were monitored by methods described in Section 2.4.1. Changes in isocitrate, 2-OG and 2-HG concentrations were monitored by ^{1}H NMR according

to **Figure 2.16**. No other products were observed. Integration of the multiplet corresponding to two isocitrate protons at δ_H 2.52 ppm was used to monitor its turnover while 2-OG and 2-HG were monitored as described in Section 2.4.1.

Based on ^{1}H NMR resonances described in the previous paragraph, the time-dependent changes in the concentrations of isocitrate, 2-OG, 2-HG, $NADP^+$, and NADPH were calculated. The starting concentration of isocitrate in the incubation was 3 mM and its depletion was coupled to changes in 2-OG and 2-HG signals. No isocitrate derived products other than 2-OG and 2-HG were observed. Therefore, the combined concentration of isocitrate, 2-OG and 2-HG should be 3 mM at all times. The initial concentration of $NADP^+$ was 1.5 mM and its turnover is coupled to changes in NADPH. Therefore, the combined concentration of NADPH and $NADP^+$ should be 1.5 mM at all times. The time-courses of the turnover of isocitrate to 2-HG as catalysed by R132C, R132C S280F, R132H, and R132H S280F (750 nM protein) were monitored for 2 h (**Figure 2.17**).

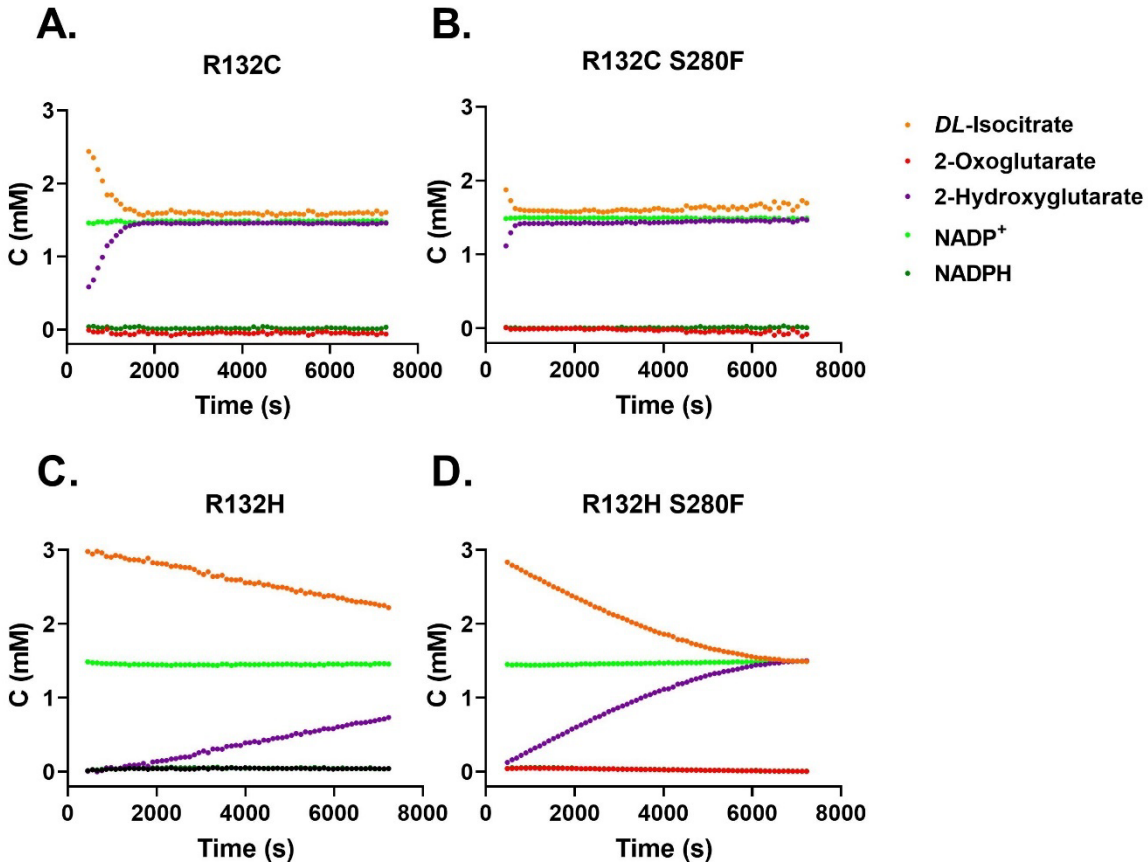

***Figure 2.17** | Turnover of isocitrate to 2-HG catalysed by R132C, R132C S280F, R132H, and R132H S280F variants monitored by ^{1}H NMR (700 MHz). Conditions: 750 nM enzyme, 10 mM $MgCl_2$, 3 mM DL-isocitrate, 1.5 mM $NADP^+$.*

Turnover of isocitrate to 2-HG was observed to be catalysed by R132C, R132C S280F, R132H, and R132H S280F. Only minor changes of 2-OG concentrations were observed while there were substantial differences in the rate of formation of 2-HG between the IDH1 variants tested. The formation of 2-HG (**Figure 2.18**, A) and the concentration of 2-HG after 9 minutes (measured in triplicates) was used for comparison (**Figure 2.18**, B).

Figure 2.18 *| Formation of 2-HG from DL-isocitrate as catalysed by R132C, R132C S280F, R132H, and R132H S280F variants monitored by ^{1}H NMR (700 MHz).* ***A.*** *2-HG formation from isocitrate catalysed by IDH1 variants as measured by NMR.* ***B.*** *Comparison of 2-HG levels after 9 minutes (standard errors of the mean, n =3).*

While there was no turnover of isocitrate to 2-HG observed after 9 minutes as catalysed by R132H (**Figure 2.18**), R132C-catalysed turnover of isocitrate to 2-HG was more efficient. R132C S280F and R132H S280F catalysed the turnover of isocitrate to 2-HG more efficiently than R132C or R132H, respectively (Figure 2.17). However, R132C and R132H S280F catalysed the reduction of 2-OG at a similar rate (**Figure 2.15**), the turnover of isocitrate to 2-HG as catalysed by R132C displayed a substantially elevated rate compared to R132H S280F suggesting that R132C variants are generally more efficient in catalysing turnover of isocitrate to 2-HG than R132H variants. The highest rate for formation of 2-HG from isocitrate was observed for R132C S280F (**Figure 2.18**, A/B). Similarly, R132C S280F was most efficient in catalysing the reduction of 2-OG to 2-HG (Section 2.4.1) compared to the other IDH1 variants tested.

For all IDH1 variants investigated, very low levels of NADPH were observed at early time points, and this appears to be consumed rapidly. As only very low levels of 2-OG were observed it is likely that 2-OG is an intermediate, which mostly remains bound to the protein and is converted to 2-HG efficiently (Section 2.3, 2.4.1), making the oxidation of isocitrate the rate-limiting step (note that when 2-OG (like other small molecules) is bound to a protein it cannot be observed due to the slow tumbling in solution of protein-substrate complexes).[134]

Consequently, the turnover of isocitrate to give 2-HG is redox-neutral. This is likely the reason most reports found R132H and R132C variants to be catalytically inactive for isocitrate turnover because no turnover could be observed in standard NADPH absorbance assays.[48]

The studies described in this section highlight the power of ^{1}H NMR studies to enable direct observation of all substrates involved in IDH1 catalysis and turnover to complement findings by assays solely based on NADPH co-substrate observation. It was found that R132C, R132C S280F, R132H, and R132H S280F can catalyse turnover of isocitrate to 2-HG, which cannot be observed using an NADPH absorbance assay alone. This observation opens new avenues to investigate how IDH1 variants catalyse reactions in a physiological setting, what their physiological relevance is, and how residue substitutions influence reactions mechanics, e.g. R132H vs R132C, or S280F substitutions. Further studies and comments on these observations are in Chapter 4.

2.4.3 Comparison of *DL*-Isocitrate (Racemic) and *D*-Isocitrate

IDH1 wt utilises *D*-isocitrate to produce 2-OG via oxidative decarboxylation. However, *DL*-isocitrate is usually used in assays with isolated IDH1 variants due to its lower price. Only half of the *DL*-isocitrate is turned over by R132C, R132C S280F, R132H, and R132H S280F (**Figure 2.16**) suggesting preference for one isomer. To investigate whether R132C, R132C S280F, R132H, and R132H S280F utilise *D*-isocitrate as a substrate to make 2-HG, ^{1}H NMR time-course analysis were conducted.

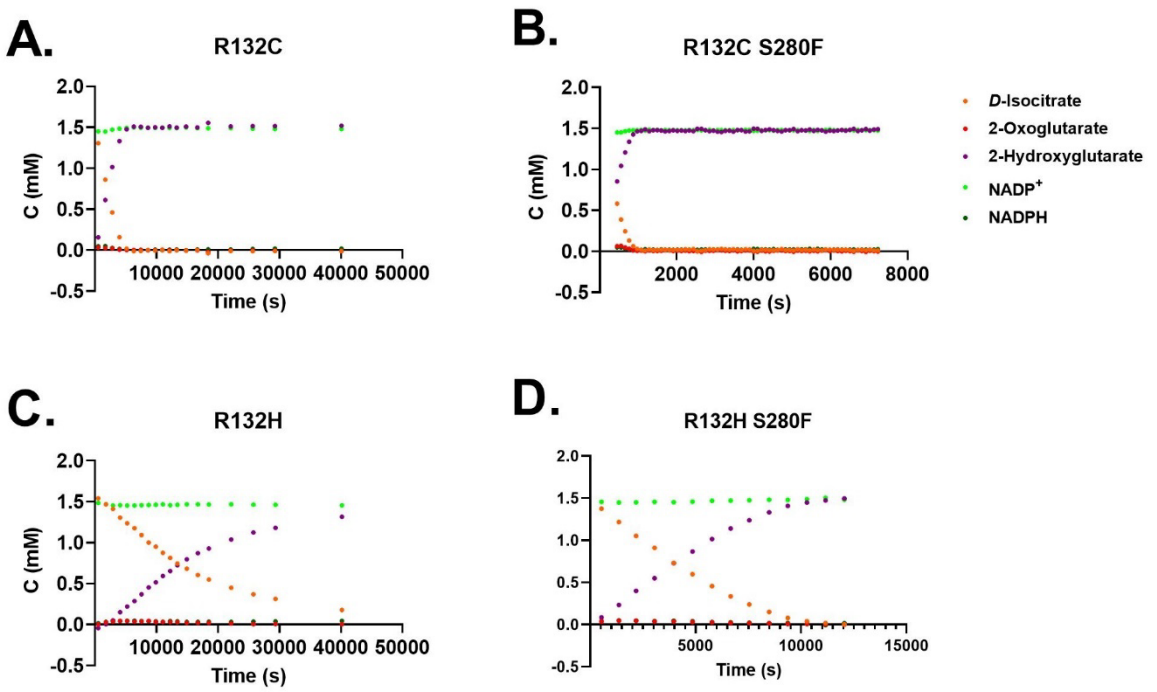

Figure 2.19 *| ^{1}H NMR (700 MHz) analyses of the turnover of D-Isocitrate to 2-HG as catalysed by R132C (**A**), R132C S280F (**B**), R132H (**C**), or R132H S280F (**D**) confirm D-isocitrate as the substrate. Conditions: 750 nM protein, 10 mM $MgCl_2$, 1.5 mM D-isocitrate, and 1.5 mM $NADP^+$ was used 50 mM d_{11}-Tris buffer (90:10 H_2O:D_2O; pH 7.5).*

After pilot studies using *D*-isocitrate mono potassium salt suggested that *DL*-isocitrate turnover is substantially more efficient than *D*-isocitrate, the pH of *D*-isocitrate in NMR buffer (50 mM d_{11}-Tris) was measured. Although Tris buffer was used, the pH was 5 when *D*-isocitrate mono potassium salt was dissolved (10 mM). Therefore, the pH of the *D*-isocitrate stock was adjusted using NaOH before the measurements. As previously observed (**Figure 2.17**), no changes in $NADP^+$/NADPH levels and only marginal changes of 2-OG levels were observed by ^{1}H NMR. *D*-isocitrate was fully turned over to 2-HG confirming that *D*-isocitrate was utilised by the IDH1 variants tested for this reaction (**Figure 2.19**). Turnover occurred at a similar rate as when *DL*-isocitrate was used (**Figure 2.17**, **Figure 2.19**). In summary, ^{1}H NMR studies confirm *D*-isocitrate is utilised by R132C, R132C S280F, R132H, R132H S280F and turned over to 2-HG.

2.5 Studies on IDH1 Variants Using the Electrochemical Leaf Platform

In ^{1}H NMR studies on the turnover of isocitrate to 2-HG, 2-OG seems to be only present in low levels suggesting oxidative decarboxylation of isocitrate is rate-limiting in the conversion of isocitrate to 2-HG (**Figure 2.20**).

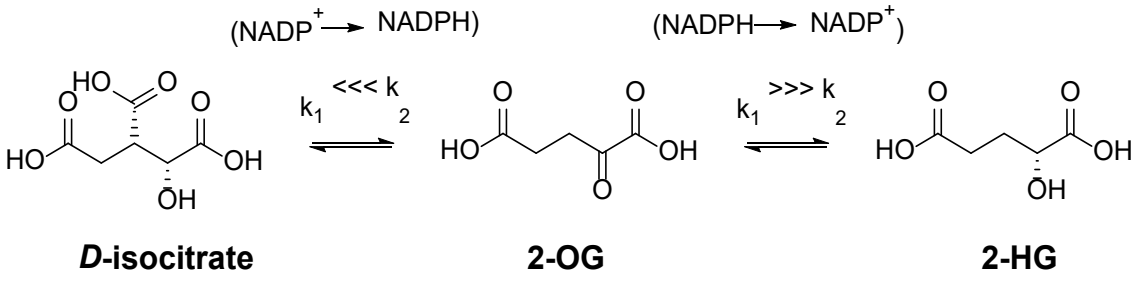

Figure 2.20 *| Scheme showing the turnover of isocitrate to 2-OG and 2-HG. The oxidation of isocitrate is the rate-limiting step.*

2-OG produced from isocitrate by the first part of the reaction (oxidation of isocitrate) is rapidly turned over to 2-HG (**Figure 2.20**). Concomitantly, $NADP^+$ is turned over to NADPH in the first part of the reaction and then quickly consumed to reform $NADP^+$ (**Figure 2.20**). The competing processes of oxidation of isocitrate and reduction of 2-OG makes it impossible to study the initial oxidation of isocitrate by NADPH absorbance or ^{1}H NMR assays, which is illustrated by an NADPH absorbance time-course at high IDH1 variant concentrations (2.5 µM, **Figure 2.21**).

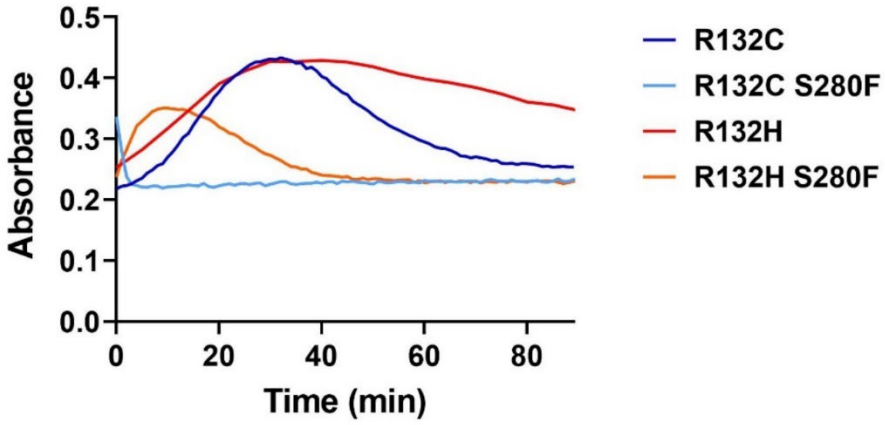

Figure 2.21 *| Time-course analyses of the turnover of isocitrate to 2-HG as catalysed by R132C, R132C S280F, R132H, or R132H S280F as measured by NADPH absorption. IDH1 variants (2.5 µM) were incubated with 10 mM $MgCl_2$, and the reaction was initiated by addition of DL-isocitrate and $NADP^+$. The turnover was measured by absorption at 340 nm.*

Under these conditions, the first part of the reaction in which NADPH was produced led to an increase in absorption. When NADPH was consumed again (by conversion of 2-OG to 2-HG), the absorption decreased back to baseline levels. The competing processes could be observed more clearly with the absorbance assay than by ^{1}H NMR assays suggesting there was an influence of the different conditions used, i.e. either by enzyme concentration, or different buffer compositions and pHs (kinetic assay buffer: 100 mM Tris, 10 mM $MgCl_2$, 0.2 mM DTT,

0.005 % Tween 20, and 0.1 mg/mL BSA, pH 8.0; NMR assay buffer: 50 mM Tris-d_{11}, 100 mM NaCl, 10 mM $MgCl_2$, and 10 % D_2O, pH 7.5).

To enable investigation of the oxidation of isocitrate to 2-OG uncoupled from subsequent reduction of 2-OG to 2-HG, an electrochemical assay was developed.[135] Method development and validation was carried out by Ryan Herold in the group of Fraser Armstrong (University of Oxford) according to Section 7.2.3.[135] The subsequent data in this section (2.5) were produced by Ryan Herold.

The electrochemical method utilises the Leaf platform which enables the user to control previously non-electroactive NADP(H) dependent enzymes like IDH1 by voltammetry.[135] The instrument set up is composed of an electrode (indium tin oxide) in which nanopores are loaded with an enzyme cascade consisting of electroactive FNR (Ferredoxin -$NADP^+$ reductase) and the electro-inactive NADPH dehydrogenase IDH1. In this nanopore, NADP(H) can be recycled with high efficiency rendering IDH1 electroactive via its dependency on the highly localized NADPH recycling. The activity of the electrochemical cascade can be controlled by varying the potential of the electrode and can be read out as the current directly on the screen (Voltammetry).[135]

Using the voltametric approach, it is possible to uncouple the isocitrate oxidation from 2-OG reduction in IDH1 variants by forcing the reaction to remain on the NADPH stage (controlled by potential applied), which allows the study of the oxidative decarboxylation of isocitrate to 2-OG in isolation (**Figure 2.22**).

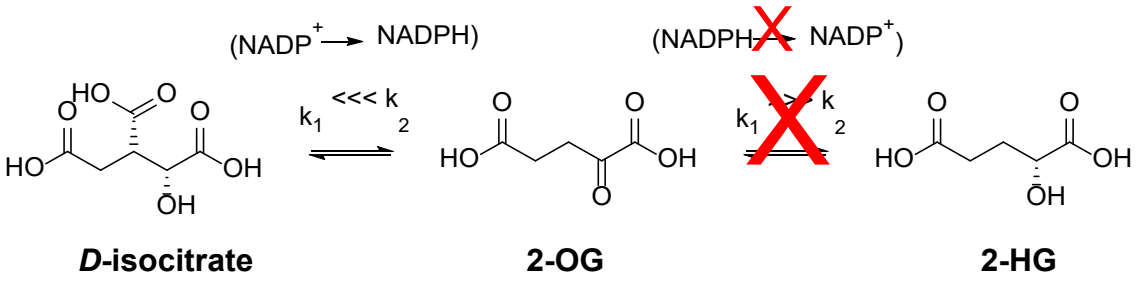

***Figure 2.22** | Scheme showing the turnover of isocitrate to 2-OG and 2-HG. The reduction of 2-OG to 2-HG is halted by the voltage applied.*

R132C, R132C S280F, R132H, and R132H S280F catalysed the oxidation of isocitrate to 2-OG with lower efficiency than the subsequent reduction of 2-OG confirming a preference of the tested IDH1 variants for the reduction of 2-OG (**Figure 2.23**). The relative efficiency of R132C for the decarboxylation of isocitrate compared to the 2-OG reduction rate was highest

of the variants (39%) while for all other variants the relative efficiency was around 20 % (R132C S280F: 18%; R132H: 18%; R132H S280F: 22%). R132C and R132C S280F catalysed the oxidative decarboxylation of isocitrate to 2-OG with similar efficiency suggesting that the efficiency of this reaction step is directed by the R132C variation. R132C variants retained more of the native IDH1 capability of oxidising isocitrate compared to R132H consistent with ^{1}H NMR time courses showing substantially elevated rates for the turnover of isocitrate to 2-HG by R132C and R132C S280F compared to R132H and R132H S280F. The overall turnover of isocitrate to 2-HG (Section 2.4) was more efficient in catalysis by R132C S280F compared to R132C because the rate of R132C S280F catalyse reduction of 2-OG to 2-HG was doubled (2-OG to 2-HG). These results suggest that R132C S280F could be (relatively) highly efficient in producing 2-HG from either isocitrate or 2-OG inside the cell. Compared to R132H, R132H S280F displayed a 2-fold increased efficiency for both isocitrate oxidation to 2-OG and the subsequent 2-OG reduction to 2-HG.

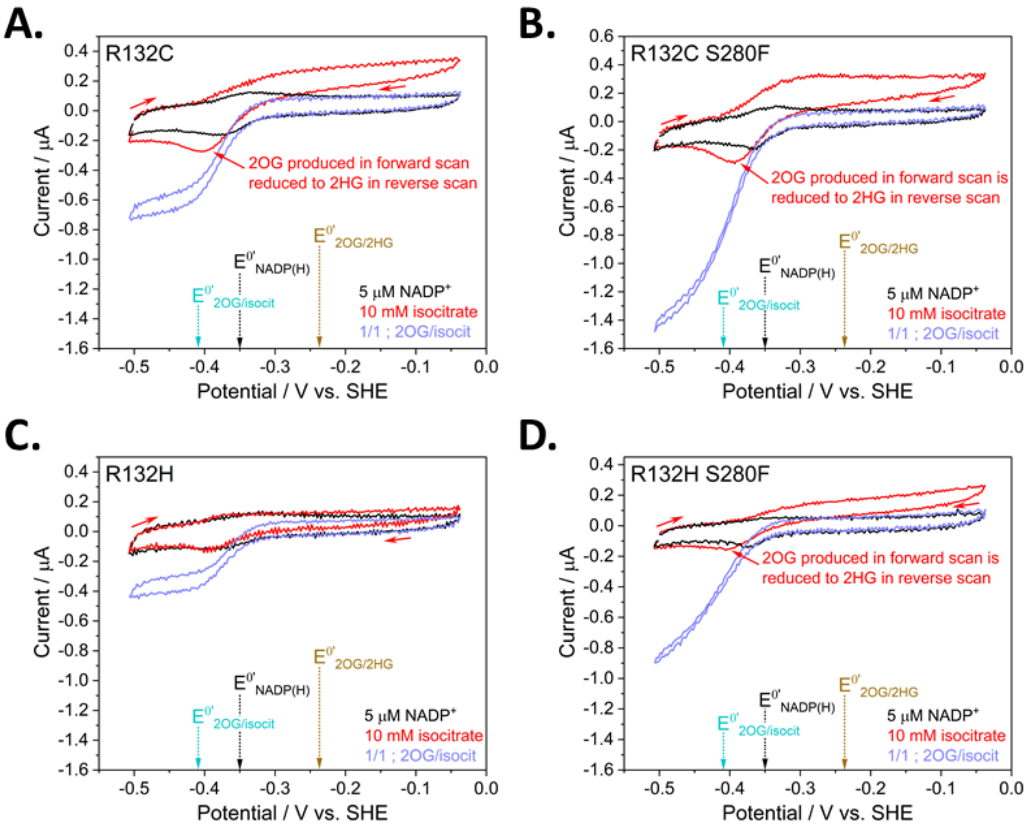

Figure 2.23 | *Stationary cyclic voltammetry measuring the ability IDH1 variants to catalyze the oxidation of DL-isocitrate and reduction of 2-oxoglutarate. Conditions (all voltammograms): stationary (FNR+E2)@ITO/PGE electrode (E2 represents a generic homodimeric IDH1 enzyme), electrode area 0.03 cm^2, scan rate 1 mV/s, temperature 25°C, volume 4 mL, pH 8 (20 mM each: MES, TAPS, CHES), 10 mM $MgCl_2$, 5 µM $NADP^+$. Purple traces (1/1; 2-OG/DL-isocitrate) contained 10 mM 2-OG + 10 mM DL-isocitrate. Enzyme loading ratios (molar): FNR/IDH1; 1/2.5. E0'NADP(H), E0'2-OG/isocitrate, and E0'2-OG/2-HG denote formal potentials for the $NADP^+$/NADPH, 2-OG/DL-isocitrate, and 2-OG/2-HG couples, respectively (see Herold et al.[135] for further information).*

In summary, using the electrochemical Leaf platform, it was shown that the oxidation step (isocitrate to 2-OG) is substantially influenced by the R132 variation. While R132C and R132C S280F catalyse this step with a similar efficiency, R132H and R132H S280F exhibit a lower efficiency than R132C and R132C S280F.

2.6 Kinetic Analysis of R132C S280A

Based on modelling studies[136,137], it was proposed that clinical resistance to ivosidenib might be mediated by hindrance to inhibitor binding because of the substitution with the sterically demanding phenylalanine (S280F), and additionally, that ivosidenib might lose a hydrogen bond to S280.[137] To investigate if resistance is solely mediated by steric hindrance or if other factors are relevant including the potential loss of a hydrogen bond to S280 (as suggested by Oltvai et al. [137], Section 1.8), R132C/S280A was produced (rational discussed in more depth in Section 3.3).

To confirm that the S280A variation does not substantially change enzymatic properties of R132C, kinetic studies on the reduction of 2-OG to 2-HG using an NADPH absorbance assay and ^{1}H NMR time course analyses were conducted. Michaelis-Menten parameters were measured as described in Section 2.3 (**Figure 2.24**).

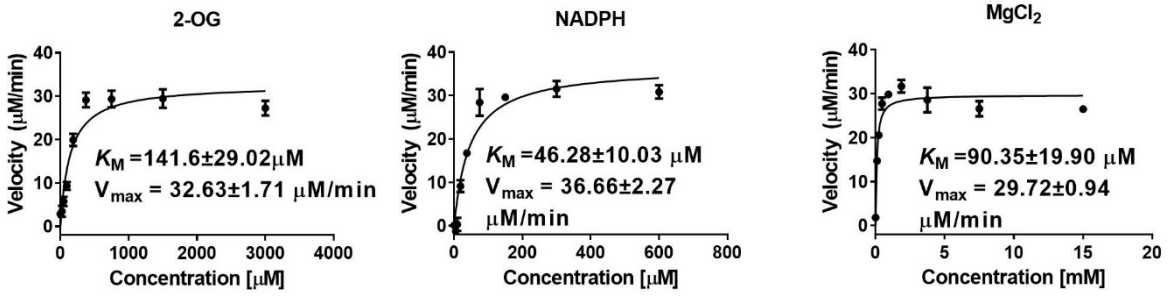

***Figure 2.24** | Determination of Michaelis-Menten parameters. 400 nM protein was used. The NADPH absorbance assay for the determination of 2-OG parameters was saturated with 300 μM NADPH. The assay for the determination of NADPH parameters was saturated at 1.5 mM 2-OG.*

Based on the parameters acquired from non-linear regression, k_{cat} and k_{cat}/K_M were calculated (**Table 2.5**).

Table 2.5 *| Michaelis-Menten parameters of R132C S280A. Saturation concentrations: 2-OG: 1.5 mM, NADPH: 0.3 mM, $MgCl_2$: 10 mM.*

	K_M (µM)	k_{cat} (s^{-1})	k_{cat}/K_M ($s^{-1}\times\mu M^{-1}$) ($\times10^{-3}$)
2-OG	141.6±29.0	1.36±0.07	9.6
NADPH	46.3±10.0	1.53±0.09	33.0
$MgCl_2$	90.4±19.9	1.24±0.04	13.7

R132C S280A was active in reducing 2-OG to 2-HG. The k_{cat} was similar to k_{cat} of the reduction of 2-OG to 2-HG catalysed by R132C or R132C S280F (1.36 s^{-1} vs 1.56 s^{-1} for R132C as determined for the 2-OG dataset, **Table 2.2**). The K_M and the catalytic efficiency (k_{cat}/K_M) for 2-OG as catalysed by R132C S280A ($K_{M(2\text{-}OG)}$ = 141.6 µM, $k_{cat}/K_{M(2\text{-}OG)}$ = 9.6 $s^{-1}.\mu M^{-1}$ $\times10^{-3}$) were in between these parameters for R132C ($K_{M(2\text{-}OG)}$ = 216.3 µM, $k_{cat}/K_{M(2\text{-}OG)}$ = 7.2 $s^{-1}.\mu M^{-1}$ $\times10^{-3}$) and R132C S280F ($K_{M(2\text{-}OG)}$ = 97.6 µM, $k_{cat}/K_{M(2\text{-}OG)}$ = 14.9 $s^{-1}.\mu M^{-1}$ $\times10^{-3}$). The K_M value of R132C S280A for NADPH was about 1.5-fold elevated compared to R132C and R132C S280F. R132C S280A exhibited a lower K_M value for Mg^{2+} and an increased catalytic efficiency as indicated by k_{cat}/K_M ($K_{M(2\text{-}OG)}$ = 90.4 µM, $k_{cat}/K_{M(2\text{-}OG)}$ = 13.7 $s^{-1}.\mu M^{-1}$ $\times10^{-3}$) compared to R132C ($K_{M(2\text{-}OG)}$ = 216.3 µM, $k_{cat}/K_{M(2\text{-}OG)}$ = 7.2 $s^{-1}.\mu M^{-1}$ $\times10^{-3}$) and R132C S280F ($K_{M(2\text{-}OG)}$ = 97.6 µM, $k_{cat}/K_{M(2\text{-}OG)}$ = 14.9 $s^{-1}.\mu M^{-1}$ $\times10^{-3}$).

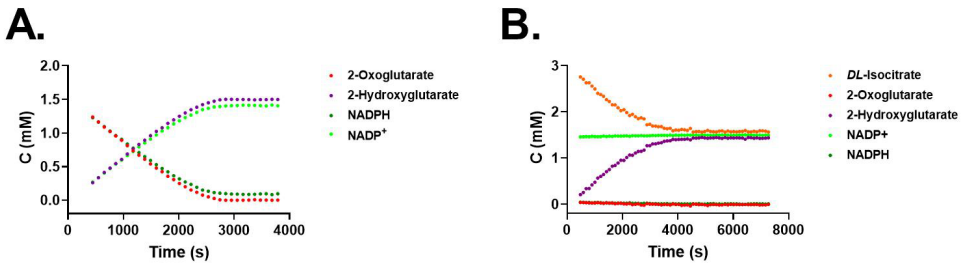

Figure 2.25 *| Turnovers catalysed by R132C S280A as monitored by ^1H NMR (700 MHz).* ***A.*** *Reduction of 2-OG to 2-HG. Conditions: see Figure 2.13 legend.* ***B.*** *Turnover of isocitrate to 2-HG. Conditions: see Figure 2.17 legend.*

^1H NMR time course analysis showed efficient turnover of 2-OG to 2-HG catalysed by R132C S280A (**Figure 2.25**, A). The reaction rate of the reduction of 2-OG to 2-HG catalysed by R132C S280A, as judged by product comparison after 12 minutes, was in between the reaction rate catalysed by R132C and R132C S280F (**Figure 2.26**, A/B) which is consistent with results from kinetic analysis using the NADPH absorbance assay (**Table 2.5**).

***Figure 2.26** | Comparison of turnover of 2-OG to 2-HG catalysed by R132C S280A as monitored by ^{1}H NMR (700 MHz) with R132C and R132C S280F. **A.** 2-HG formation from 2-OG catalysed by IDH1 R132C S280A as measured by ^{1}H NMR. **B.** Comparison of 2-HG levels formed from reduction of 2-OG as catalysed by R132C, R132C S280F, or R132C S280A (t= 12 min). Errors: standard error of the mean, n = 3.*

To investigate whether R132C S280A can, like R132C and R132C S280F, catalyse the turnover of *DL*-isocitrate to 2-HG, ^{1}H NMR time course analyses were employed. R132C S280A could catalyse the turnover of *DL*-isocitrate to 2-HG efficiently (**Figure 2.25**, B). As previously observed for the turnover of *DL*-isocitrate to 2-HG by R132C and R132C S280F, 2-OG, NADPH and $NADP^{+}$ concentrations only changed marginally.

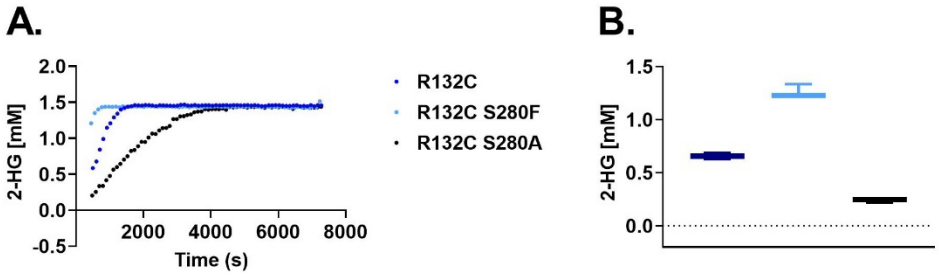

***Figure 2.27** | Comparison of turnover of DL-isocitrate to 2-HG catalysed by R132C S280A (black) as monitored by ^{1}H NMR (700 MHz) with R132C (dark blue) and R132C S280F (light blue). **A.** 2-HG formation from DL-isocitrate catalysed by IDH1 R132C S280A as measured by ^{1}H NMR. **B.** Comparison of 2-HG levels formed from reduction of 2-OG (**A**) as catalysed by R132C, R132C S280F, or R132C S280A (t = 9 min). Errors: standard error of the mean, n =3.*

The reaction rate of the formation of 2-HG from *DL*-isocitrate as catalysed by R132C S280A was slower than in the reactions catalysed by R132C or R132C S280F (**Figure 2.27**, A). The 2-HG product levels after 9 minutes were 3-fold lower than in the reaction catalysed by R132C and 7-fold lower than in the reaction catalysed by R132C S280F (**Figure 2.27**, B).

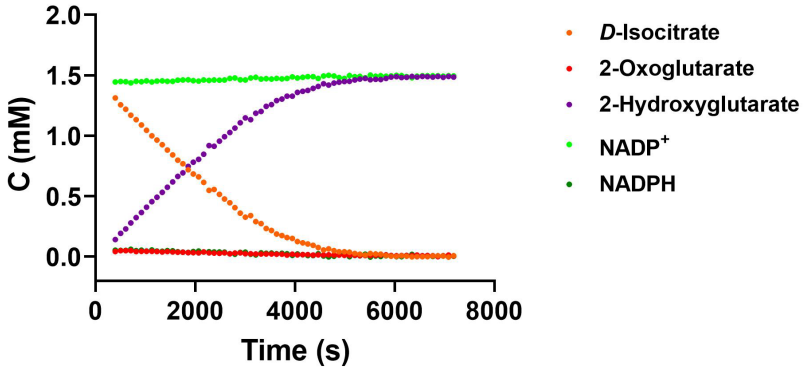

***Figure 2.28** | 2-HG formation from D-isocitrate catalysed by IDH1 R132C S280A as measured by ^{1}H NMR.*

It was previously shown that R132C and R132C S280F use *D*-isocitrate for turnover to 2-HG. To confirm utilisation of *D*-isocitrate by R132C S280A, ^{1}H NMR was employed (**Figure 2.27**). 2-HG was formed by R132C S280A at a similar rate as in time-course analyses with *DL*-isocitrate (**Figure 2.25**) confirming utilisation of *D*-isocitrate for the turnover to 2-HG.

Although there are differences in turnover rate and kinetic parameters in reactions catalysed by R132C S280A compared to R132C and R132C S280F, it is similar enough to allow usage for inhibition studies in Section 3.3 and thus, to investigate the molecular basis why the acquired S280F substitution in an R132C results in resistance to treatment with ivosidenib.

2.7 Biophysical Characterisation

Biophysical studies were carried out to investigate the influence of different R132 and S280 variations on IDH1 structure and stability. Therefore, following techniques were used: (i) the secondary structures were analysed by circular dichroism (CD); (ii) thermal stabilities were studied using CD, differential scanning calorimetry (DSC), and differential scanning fluorimetry (DSF); (iii) the oligomerisation states were determined by non-denaturing gel analyses, size exclusion chromatography multi angle light scattering (SEC-MALS), and non-denaturing MS analyses (Section 2.8).

2.7.1 Circular Dichroism Studies

CD utilises the interaction of circular polarised light with chiral molecules to obtain structural information. [138] It can be used to analyse the secondary structure content of proteins as secondary structural features like α-helices, β-sheets, unfolded regions, or disulphide bonds, interact differently with circular polarised light resulting in specific differences in the CD

spectra.[138] CD can also be used to compare the influence of protein variations on the secondary structure by comparing the CD spectra of the protein variants.[138]

R132C, R132C S280F, R132C S280A, R132H, and R132H S280F were buffer exchanged into sodium phosphate buffer (10 mM, pH 8.0) and diluted to a concentration of 0.2 mg/mL. The spectra were averaged (measurement in triplicates), smoothed and normalised to the protein concentration using GraphPad Prism (**Figure 2.29**).

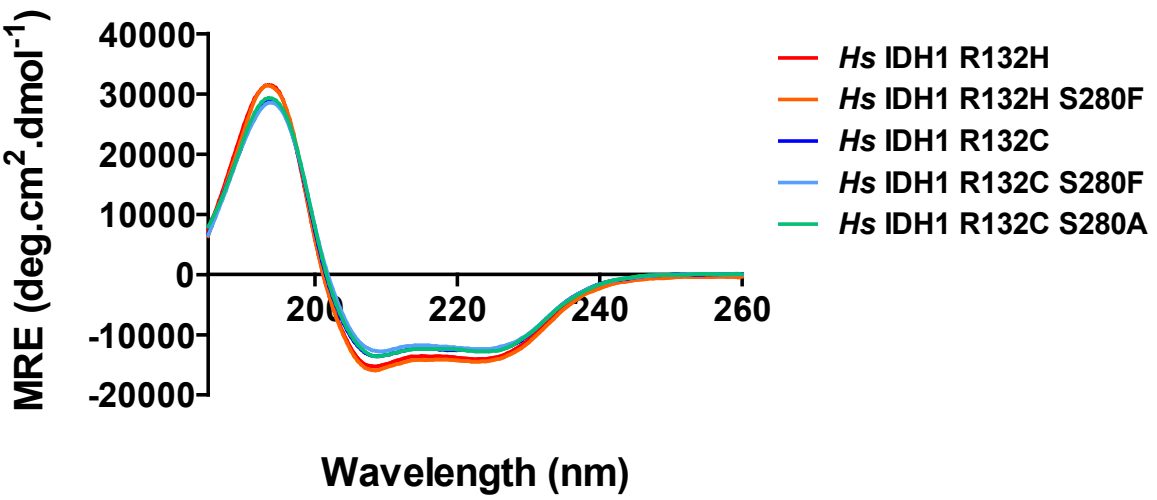

Figure 2.29 | *Circular Dichroism spectra of R132C, R132C S280F, R132C S280A, R132H, and R132H S280F. Conditions: protein (0.2 mg/mL in sodium phosphate (10 mM, pH 8.0) buffer.*

The spectra of all IDH1 variants tested aligned well suggesting well-structured proteins with a high degree of overall structural similarity. Two minima at 208.5 nm and 224 nm are typical for proteins with α-helices present (literature: 208 nm and 222 nm).[138] The maximum at 194 nm can be indicative of α-helices (literature: 193 nm) and β-sheets (literature: 195 nm).[138] These results are in accord with crystallographic data[11] showing IDH1 as a well-structured protein with α-helices and β-sheets. There were no major differences between the IDH1 variants tested suggesting there is no substantial influence of the S280F substitution on the secondary structure. Minor differences in intensities are likely due to minor differences in sample concentration.

2.7.2 Analyses of Melting Temperature (T_m)

The melting temperatures (T_ms) of R132C, R132C S280F, R132C S280A, R132H, and R132H S280F were studied to investigate if the S280F substitution influences the thermal stability. The techniques used in the following section can indicate the unfolding event of a protein either by the change of a secondary structure signal (CD), the difference in heat input into a sample

compared with a reference cell (DSC) or binding of a fluorescent dye to the unfolded protein (DSF).

2.7.2.1 Analysis by CD

For CD studies, the wavelength of the spectrometer was fixed to 215 nm, a wavelength between the two minima corresponding to α-helices.[138] The temperature was gradually increased (1°C/min) and the change in CD signal corresponding to the unfolding of the protein observed (**Figure 2.30**).

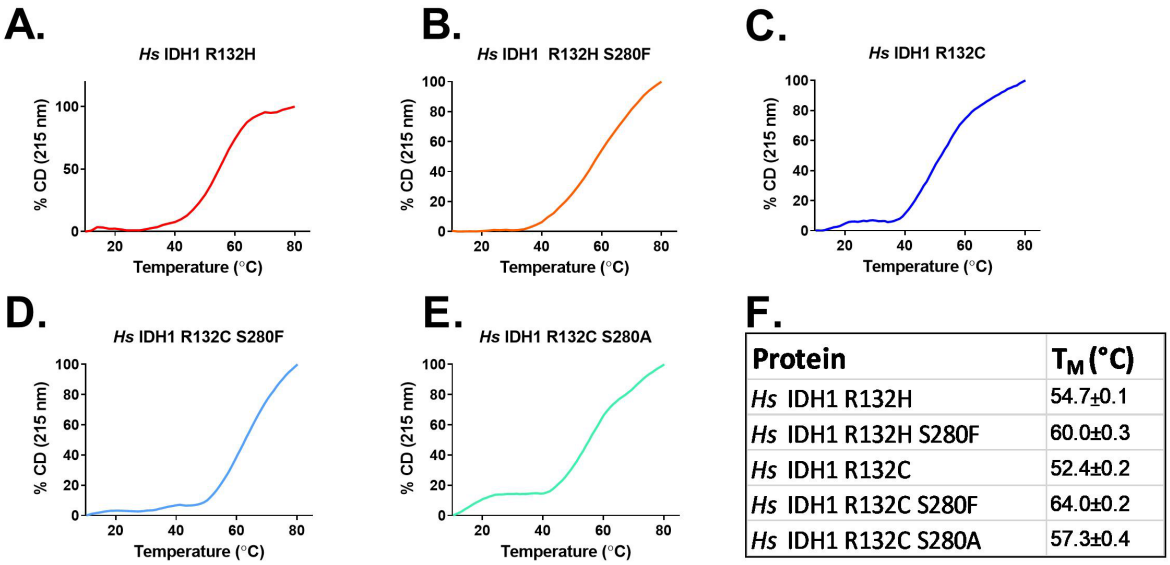

F.

Protein	T_M (°C)
Hs IDH1 R132H	54.7±0.1
Hs IDH1 R132H S280F	60.0±0.3
Hs IDH1 R132C	52.4±0.2
Hs IDH1 R132C S280F	64.0±0.2
Hs IDH1 R132C S280A	57.3±0.4

***Figure 2.30** | Analyses of thermal stability using CD. **A.-E.** Melting curve of R132C, R132C S280F, R132C S280A, R132H, and R132H S280F. **F.** Table of melting temperatures. Conditions: See Figure 2.29 legend.*

R132H exhibited a higher T_m than R132C (**Figure 2.30**). Interestingly, the S280F substitution exhibited a strong stabilising effect in R132C S280F and R132H S280F compared to R132C and R132H (**Figure 2.30**). The T_m of R132C S280A was increased compared to R132C.

2.7.2.2 Analysis by Differential Scanning Calorimetry (DSC)

The T_m of a protein can also be analysed using differential scanning calorimetry (DSC). This technique monitors the heat input which is required to heat up a sample with a constant linear rate over a defined range.[139] Direct comparison of reference measurements (buffer only) and sample enables determination of thermic events, e.g. protein unfolding.[139] In the instrument set up used, a positive peak translates to an endothermic process as heat (in mW) needs to be added into the system to keep the sample with the IDH1 variant at the same temperature as the reference cell. [139] Consequently, an endothermic protein unfolding event is observed for all IDH1 variants tested in **Figure 2.31** (A).

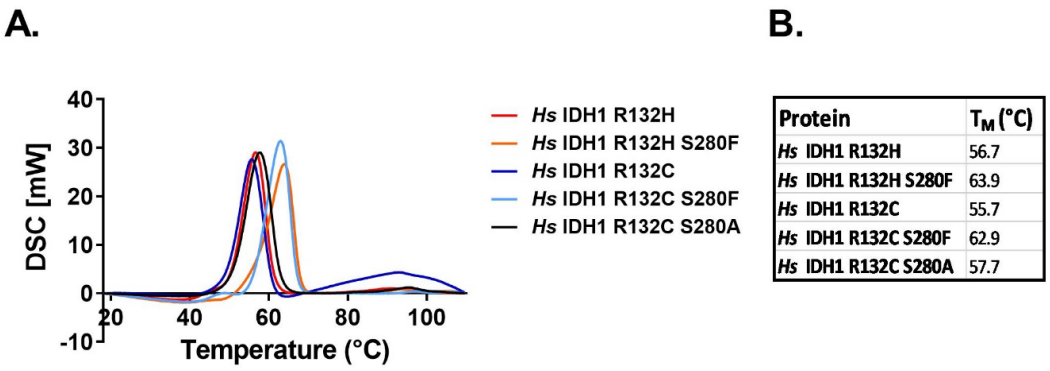

Protein	T_M (°C)
Hs IDH1 R132H	56.7
Hs IDH1 R132H S280F	63.9
Hs IDH1 R132C	55.7
Hs IDH1 R132C S280F	62.9
Hs IDH1 R132C S280A	57.7

Figure 2.31 *| Analyses of thermal stability using Differential Scanning Calorimetry (DSC).* ***A.*** *DSC curves of R132C, R132C S280F, R132C S280A, R132H, and R132H S280F.* ***B.*** *Table showing T_M for each IDH1 variant tested. Conditions: IDH1 variants (20 μM) in 20 mM Tris, 100 mM NaCl (pH 7.4). These data were acquired by Dr David Staunton.*

The maximum of the DSC curve indicates the T_ms of R132C, R132C S280F, R132C S280A, R132H, and R132H S280F (**Figure 2.31**, A) which are summarised in **Figure 2.31** (B). R132H exhibited a slightly higher T_m than R132C. R132C S280F and R132H S280F displayed a substantial increase in T_m compared to R132C and R132H. The T_m of R132C S280A was elevated compared to R132C.

2.7.2.3 Analysis by Differential Scanning Fluorimetry (DSF)

The T_ms of R132C, R132C S280F, R132C S280A, R132H, and R132H S280F were also investigated by differential scanning fluorimetry (DSF). In the DSF method, the fluorescent dye Sypro Orange is added to the aqueous protein solution. The fluorescence signal is quenched in aqueous conditions.[140] When the temperature is increased gradually, the protein denatures resulting in the exposure of lipophilic entities.[140] The dye can then bind these entities, leading to an increase in fluorescence signal indicating the denaturing of the IDH1 variants.[140]

Table 2.6 *| Comparison of Melting temperatures as measured by DSF.*

R132C	R132C S280F	R132H	R132H S280F	R132C S280A
51.3±0.3	57.2±0.0	52.1±0.1	58.9±0.1	53.8±0.0

R132H exhibited a slightly higher T_m than R132C. The T_m of R132C S280F and R132H S280F variants were substantially increased compared to R132C and R132H. T_m of R132C S280A was increased $\delta = 2.5$°C compared to R132C.

Due to differences in buffers (CD: sodium phosphate, pH 8.0; DSC: Tris 20 mM, pH 7.4; DSF: tris 20 mM, pH 7.5 + Sypro orange dye), the absolute T_m values obtained for R132C, R132C S280F, R132C S280A, R132H, and R132H S280F differ depending on the technique used. However, the trends in all the techniques employed are similar overall (**Table 2.7**). Generally,

the R132H variant seems to be a slightly more stable than the R132C variant ($\delta_{(CD)}$= 2.3°C, $\delta_{(DSC)}$ = 1.0°C, $\delta_{(DSF)}$= 0.8°C). A strong stabilising effect is observed for the IDH1 variants with the S280F substitution by all methods used: R132C S280F is more stable than R132C ($\delta_{(CD)}$= 11.6°C, $\delta_{(DSC)}$ = 7.3°C, $\delta_{(DSF)}$= 5.9°C) and R132H S280F is more stable than R132H ($\delta_{(CD)}$= 5.3°C, $\delta_{(DSC)}$ = 7.2°C, $\delta_{(DSF)}$= 6.8°C). R132C S280A is also more stable than R132C ($\delta_{(CD)}$= 4.8°C, $\delta_{(DSC)}$ = 2.1°C, $\delta_{(DSF)}$= 2.5°C).

***Table 2.7** | Comparison of T_m for R132C, R132C S280F, R132C S280A, R132H, and R132H S280F obtained by CD, DSC, and DSF.*

	$\delta_{(CD)}$°C	$\delta_{(DSC)}$°C	$\delta_{(DSF)}$°C
R132H vs R132C	2.3	1.0	0.8
R132C vs R132C S280F	11.6	7.3	5.9
R132C vs R132C S280A	4.8	2.1	2.5
R132H vs R132H S280F	5.3	7.2	6.8

In conclusion, the CD, DSC, and DSF analyses consistently show that the S280F substitution results in a substantial increase in the T_m when combined with the R132C and R132H substitutions. These results suggest that there is a new stabilising interaction potentially interfering with the binding of inhibitors at the dimer-interface. The underlying structural reasons for this proposal are investigated by X-ray crystallography studies (Section 2.10).

2.7.3 Studies on the Oligomerisation States of IDH1 Variants

IDH1 wt is reported to be dimeric in solution.[141] To investigate if R132C, R132C S280F, R132C S280A, R132H, and R132H S280F are dimeric, non-denaturing polyacrylamide gel electrophoresis (PAGE) and SEC-MALS analyses were employed to determine their oligomerisation state.

2.7.3.1 Non-Denaturing PAGE

Non-denaturing PAGE allows studies on the mass of a protein complex in solution and can thus inform on the oligomerisation state. A polyacrylamide gel was used without the addition of sodium dodecylsulfate (SDS) to maintain the protein in its native state. Care must be taken to avoid protein degradation during analysis; thus, buffers are kept at 4°C, the gel analysis is carried out in a cold room and the sample is not heated prior to analysis, as usually done for SDS-PAGE.

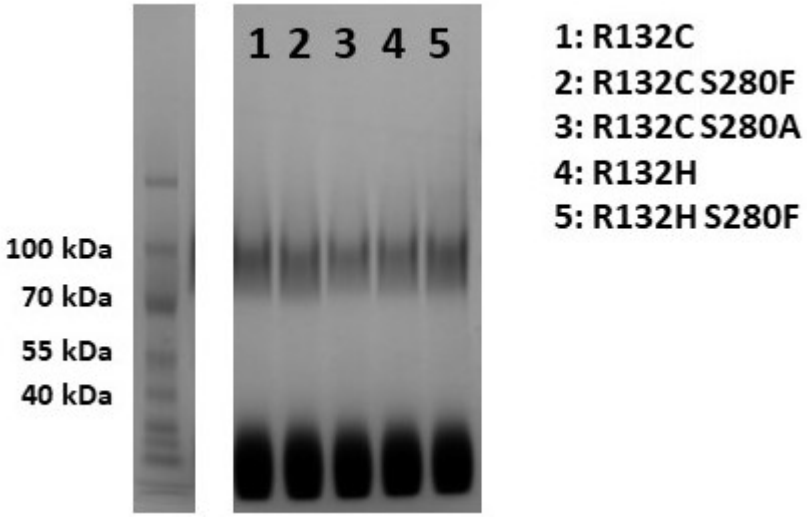

Figure 2.32 *| Non-denaturing PAGE of IDH1 variants using a Tris-Glycine gel. All variants display a single band between 70 kDa and 100 kDa corresponding to a dimer (theoretical mass ~ 95 kDa). The band at the bottom corresponds to excess G-250 sample additive, an anionic dye binding to the protein to ensure migration towards the cathode which is added for non-denaturing PAGE (Section 7.2.6).*

A 4-12 % polyacrylamide Tris-Glycine gel was used for analyses (**Figure 2.32**). R132C, R132C S280F, R132C S280A, R132H, and R132H S280F displayed a single band running just below the 100 kDa ladder control band corresponding to the IDH1 dimer (calculated mass ~95 kDa) indicating that IDH1 variants tested are predominantly dimeric in solution.

2.7.3.2 Size Exclusion Chromatography Multi Angle Light Scattering

The oligomerisation state of a protein in solution can be determined using size exclusion chromatography coupled to multi angle light scattering (SEC-MALS). [142] In SEC-MALS analyses the protein sample is first applied to size exclusion chromatography to determine if the protein sample is composed of a mixture of oligomerisation states or a single species.[142] The refractive index is monitored to observe protein species from the size exclusion chromatograms [142] and is also used to calculate the concentration of the protein corresponding to the peak observed and hence, gives the fraction of the protein sample corresponding to a specific oligomerisation state. [142] After chromatographic separation, samples are subjected to MALS. The scattering of light at a fixed wavelength is measured as a function of the angle of the light beam. The scattering is dependent on concentration and molar mass and can be used to calculate the mass (in Da) of the protein species analysed. [142] The measurements were kindly carried out by Dr David Staunton (Department of Biochemistry, University of Oxford).

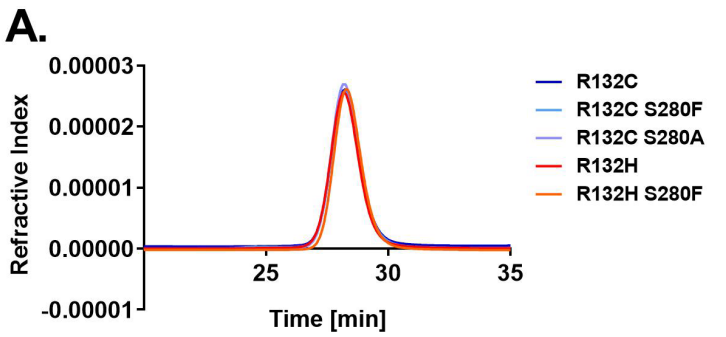

B.

Protein	Mass (measured)	Dimer Mass (Expected)
R132C	88.7	95.34
R132C S280F	91.1	95.46
R132C S280A	91.8	95.31
R132H	91.2	95.41
R132H S280F	91.2	95.53

Figure 2.33 *| SEC-MALS analysis of R132C, R132C S280F, R132C S280A, R132H, and R132H S280F. The proteins were diluted to 1 mg/L in buffer containing 20 mM Tris, 100 mM NaCl (pH 7.4) and analysed using a Superdex 200 HR10/30. The results imply the variants are predominantly dimeric in solution. The measurements were carried out by Dr David Staunton.*

R132C, R132C S280F, R132C S280A, R132H, and R132H S280F all displayed a single protein species in the chromatogram which elutes after ~28 minutes (**Figure 2.33**, A). MALS analysis showed the mass of this species to be near the expected dimer mass within error range (**Figure 2.33**, B). This supports the proposal that R132C, R132C S280F, R132C S280A, R132H, and R132H S280F are dimeric in solution. The combined results from non-denaturing PAGE and SEC-MALS analysis imply that there is no influence on the oligomerisation state of IDH1 by the S280F or S280A substitution.

The biophysical studies showed similarly folded proteins which are all dimeric in solution. Proteins with the S280F variation exhibit a major increase in T_m. This could suggest novel interactions as a result of the S280F substitution which was further studied in Section 2.10 using X-ray crystallography.

2.8 Non-Denaturing Mass Spectrometry

To confirm the dimeric state observed in previous experiments and to study copurification with the IDH1 variants from expression in *E.coli*, the IDH1 variants were analysed using non-denaturing electrospray ionisation mass spectrometry (ESI-MS). By contrast with denaturing MS, non-denaturing MS allows the observation of protein-ligand complexes in the gas phase; not only covalent protein modifiers but also non-covalently binding ligands can be observed (Section 3.3).[143] The conditions for non-denaturing mass spectrometry analyses of IDH1 variants were based on standard conditions[48] and subsequently optimised. Initial optimisation was performed with the help of Dr Victor Mikhailov who also conducted the non-denaturing MS/MS experiments described in this section.

2.8.1 Analyses of Oligomerisation state and Copurification

The IDH1 variants (20 μM) were analysed by non-denaturing MS using a cone voltage of 100 V; exemplary mass spectra for R132C are displayed in **Figure 2.34**. The non-denaturing MS spectrum of R132C displayed a narrow charge distribution typical for non-denaturing conditions ranging from z = 17-21 (**Figure 2.34**, A).[144] A dimeric structure for R132C was supported by deconvoluting the non-denaturing MS spectrum (**Figure 2.34**, B) in accord with results described in Section 2.7.3. 96.6 kDa, i.e. IDH is dimeric, and is made without the N-terminal methionine residues of each monomer consistent with the spectrum obtained by denaturing MS (see **Table 2.1**); further it copurifies with 2 molecules of $NADP^+$/NADPH (**Figure 2.34**, C).

$NADP^+$ and NADPH cannot be distinguished by non-denaturing MS due to their small mass difference; hence, ^1H NMR was employed (**Figure 2.34**, D). Firstly, a ^1H NMR spectrum of R132C was measured to show that no $NADP^+$ or NADPH can be observed in solution. When NADPH/$NADP^+$ is bound to the large protein complex, which exhibits a slower tumbling rate compared to the fast tumbling of a small molecule like NADPH/$NADP^+$ in solution, it cannot be observed by ^1H NMR: the slow tumbling results in line broadening due to the complexes` shorter transverse relaxation time T_2.[134] Subsequently, the protein was denatured by heating (100°C) and the supernatant analysed by ^1H NMR. The sample was then spiked with NADPH. The results of this treatment, in combination with results from non-denaturing MS (**Figure 2.34**, B), showed binding of 2x NADPH molecules to each IDH1 dimer. The copurification with two molecules of NADPH was consistent for all IDH1 variants in this chapter.

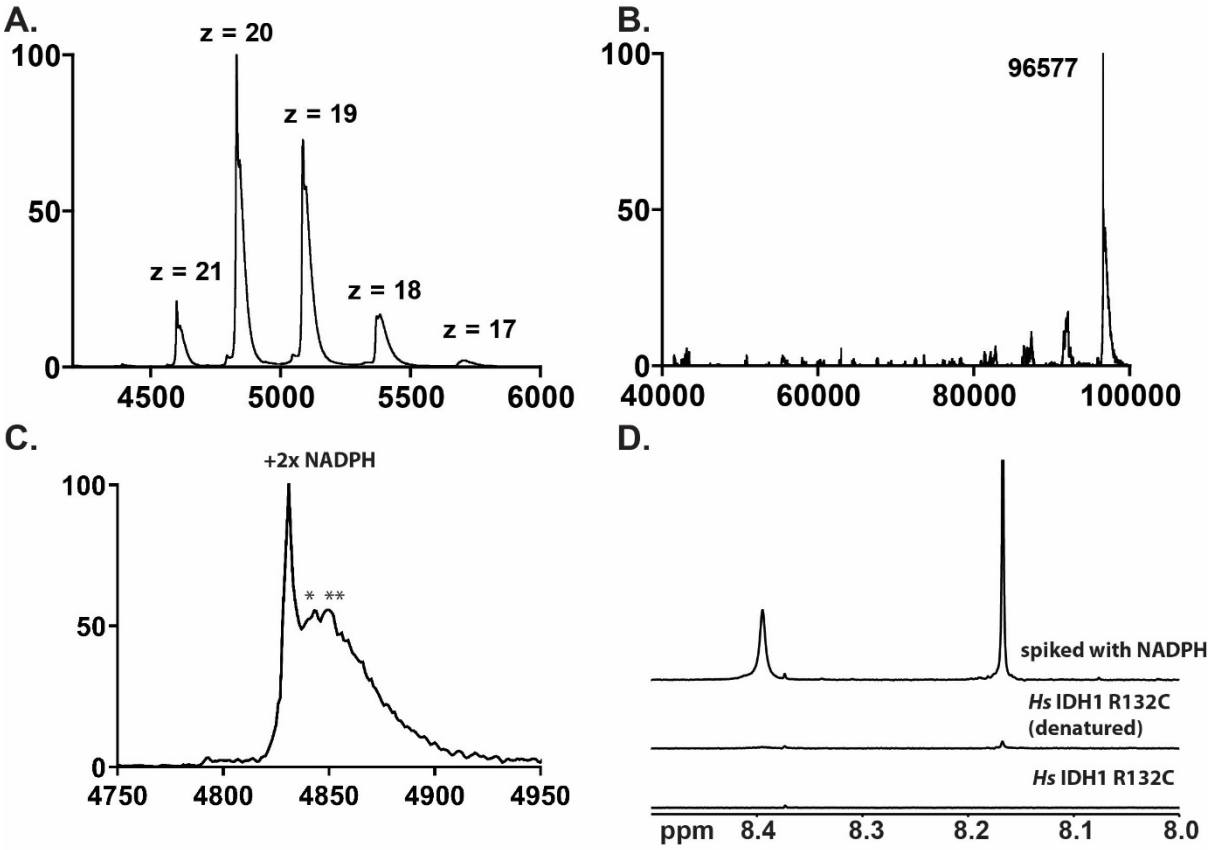

Figure 2.34| *Non-denaturing MS and NMR analyses of IDH1 R132C.* ***A.*** *Non-denaturing MS spectrum of IDH1 R132C shows a narrow charge-state distribution which is typical for this MS technique.* ***B.*** *Deconvolution of the non-denaturing MS spectrum from* ***A.*** *confirms the presence of R132C as a dimer.* ***C.*** *Magnified section of the z = 20 charge-state shows that the dimer is almost exclusively present with two NADPH molecules bound. A shoulder at around m/z 4850 is indicative of covalent modifications of R132C which is discussed in Section 2.8.2.* ***D.*** *^{1}H NMR (700 MHz) was used to distinguish between $NADP^+$ and NADPH. Spiking of denatured R132C samples confirm the binding of NADPH. Conditions: Non-denaturing MS was performed in ammonium citrate buffer (200 mM, pH 7.5); ^{1}H NMR was performed in 50 mM d_{11}-Tris (90:10 H_2O:D_2O; pH 7.5).*

2.8.2 Identification of Covalent Modifications of IDH

In addition to its copurification with NADPH, as for the other IDH1 variants studied, R132C displayed two adducts with 178 Da and 258 Da mass shifts relative to the 2x NADPH complex in the non-denaturing MS spectrum (**Figure 2.34**, C).

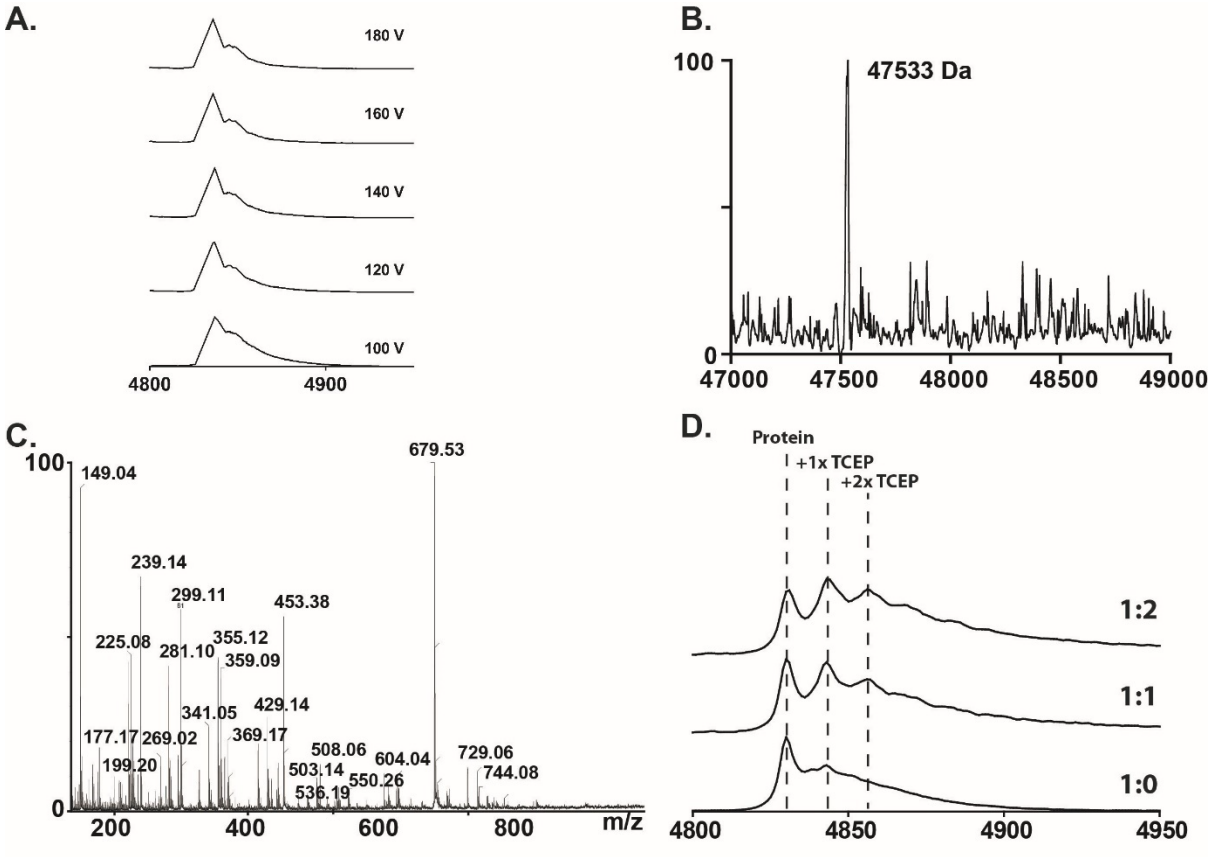

Figure 2.35 *| Analyses of the adducts bound to R132C using different MS techniques.* ***A.*** *Non-denaturing MS measurements with increasing cone voltages did not result in removal of the shoulder at m/z 4850.* ***B.*** *Denaturing MS analyses were not able to confirm a covalent binder in contradiction to* ***A.*** ***C.*** *Non-denaturing MS/MS analyses did not reveal a small molecule with a mass corresponding to the shoulder signals (178 or 258 Da).* ***D.*** *Spiking with TCEP leads to an increase of the signal at 258 Da. Additionally a signal corresponding to binding of 2 TCEP molecules rises.*

The two adducts could not be removed by increasing the cone voltage suggesting they result from covalent modifications (**Figure 2.35**, A). However, analysis by denaturing MS using a Waters LCT time-of-flight (TOF) intact protein LC-MS did not show evidence for covalent modifications (**Figure 2.35**, B) which conflicts with findings from **Figure 2.35** (A). Next, non-denaturing MS/MS analyses was conducted on R132C; no ions corresponding to the 178 or 258 Da mass adducts could be identified (**Figure 2.35**, C). Thus, samples were spiked with metabolites and components of buffers used for purification and analysed by non-denaturing MS. Spiking with Tris(2-carboxyethyl)phosphine (TCEP), used during the protein purification process (**Figure 2.35**, D), led to an increase in the adduct at 258 Da suggesting this peak might result from TCEP bound to protein (potential formation of a phosphorus-sulphur adduct). However, treatment with high concentrations of DTT did not remove the potential phosphorus-sulphur adduct.

To further investigate the initial discrepancy between observation by non-denaturing (**Figure 2.35**, A) and denaturing MS (**Figure 2.35**, B) regarding covalent vs. non-covalent binding,

R132C was subjected to intact protein analysis by denaturing MS. This time a Waters Xevo G2-XS LC-MS machine was used which exhibits greater sensitivity than the Waters LCT (TOF) LC-MS instrument. When using the Waters Xevo G2-XS LC-MS machine under denaturing conditions, additional mass signals were observed indicating covalent modification of the protein (**Figure 2.36**, A). The most abundant signal for the covalent adduct was +258 Da and the second most abundant signal was +178 Da (highlighted by red boxes). The latter 178 Da shift has been reported in the literature as being due to gluconoylation of the N-terminus during recombinant protein production in *E. coli*.[145] Additional phosphorylation of this gluconoyl residue is reported to result in a mass shift of 258 Da.[145] To confirm that these mass shifts indeed correspond to potential (phospho-)gluconoylation of the protein, R132C was treated with alkaline phosphatase overnight. After buffer exchange, the resultant R132C was analysed using a Waters Xevo G2-XS LC-MS (**Figure 2.36**, A/B). The phosphate group was cleaved off from the (phospho-)gluconoyl residue resulting in depletion of the peak at 258 Da, and an increase in abundance of the gluconoyl signal at 178 Da was observed (**Figure 2.36**, B). These observations support the proposal that the adduct observed in non-denaturing MS spectra is a result of covalent (phospho-)gluconoylation of R132C. Spiking protein samples with TCEP and analysis by denaturing MS using a Waters Xevo G2-XS LC-MS did not lead to an increase of the peak at 258 Da (**Figure 2.36**, C). The observation of potential adducts in TCEP-treated samples in non-denaturing MS analyses (**Figure 2.35**, D) is thus likely due to non-specific binding of TCEP.

Similar adducts with mass shifts of around 178 Da and 258 Da have been observed for all IDH1 variants discussed in this chapter and indicate (phospho-)gluconoylation of a subset of the respective proteins.

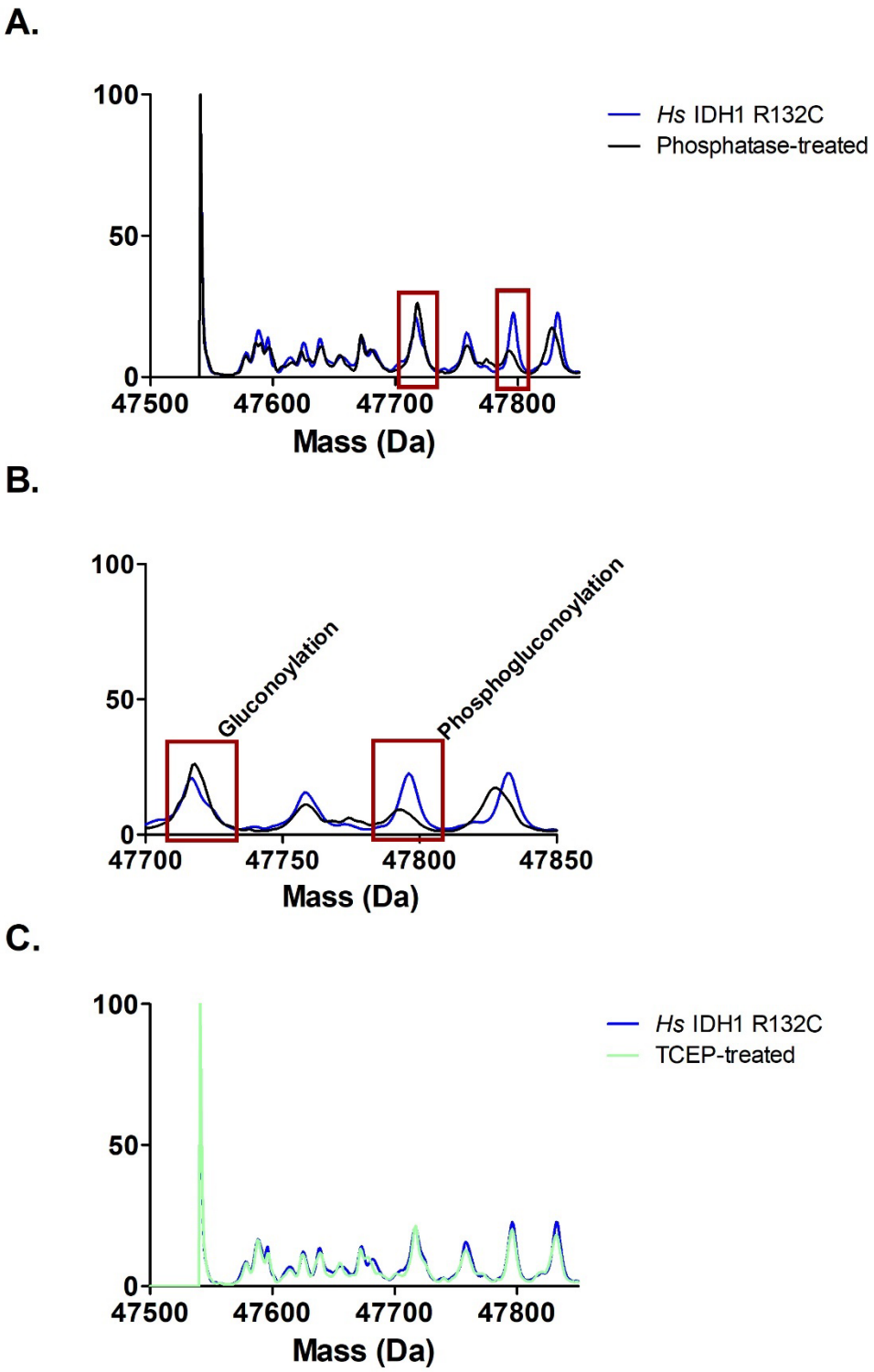

Figure 2.36 | *Analyses of R132C using a Xevo G2-XS LC-MS.* ***A.*** *Superimposed mass spectra of R132C before and after treatment with alkaline phosphatase.* ***B.*** *Magnified section of* ***A.*** *Red boxes highlight the signals corresponding to a +178 Da mass shift and a +258 Da mass shift.* ***C.*** *Overlaid spectra of R132C before and after TCEP treatment. No substantial changes can be observed.*

2.9 Substrate and Co-Factor Binding Experiments

To investigate substrate/co-factor binding, the influence of different concentrations of substrates/co-factors on the T_m of R132C, R132C S280F, R132H, and R132H S280F was investigated using DSF. The binding of a substrate/co-factor increases the stability of a protein, which is indicated by an increase in T_m.

IDH1 requires the presence of the divalent cation magnesium for turnover of isocitrate or 2-OG.[48] To measure binding of isocitrate and 2-OG to R132C, R132C S280F, R132H, and R132H S280F, the effect of the addition of isocitrate and 2-OG was investigated in the absence of magnesium ions. As all IDH1 variants tested copurify with NADPH (Section 2.8.1), the presence of which could result in turnover of 2-OG (if magnesium ions are present), the inactive close 2-OG analogue N-oxalylglycine (NOG)[51] was used for the following studies. No binding of isocitrate or NOG to any of the IDH1 variants tested was observed without magnesium ions present (**Figure 2.37**).

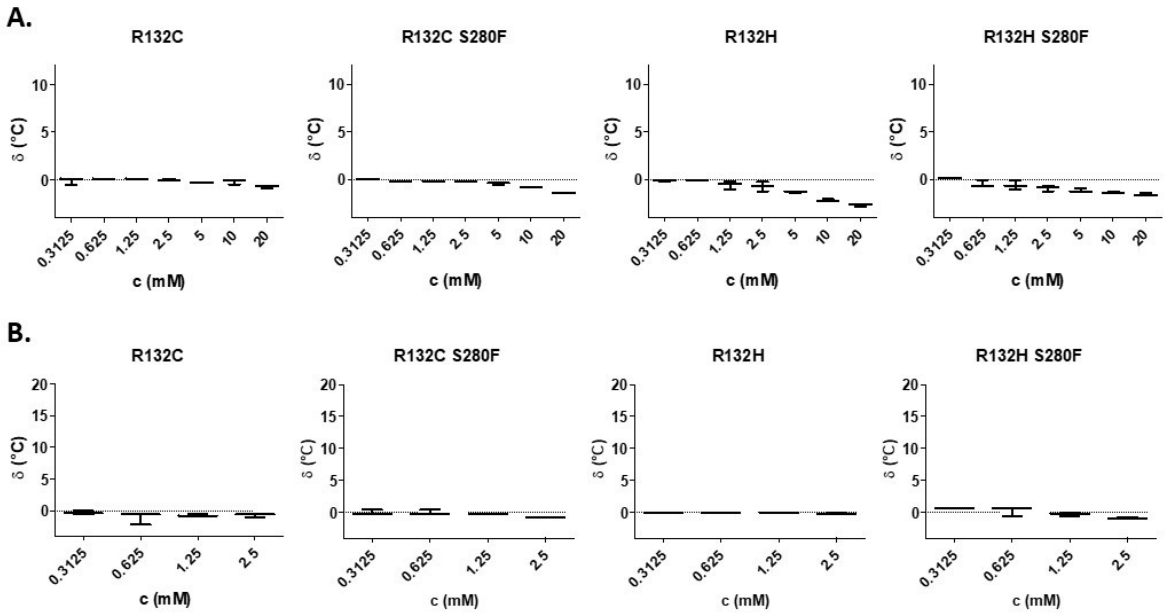

***Figure 2.37** | T_m-shift analyses of R132C, R132C S280F, R132H, and R132H S280F by DSF. The influence on thermal stability of IDH1 variants by addition of DL-isocitrate (**A.**) or NOG (**B.**) is shown with the standard error of the mean (n = 3). Conditions: 3 µM enzyme, in 50 mM Tris buffer, pH 7.5 (Dye: Sypro Orange 3x).*

To investigate if magnesium ions can stabilise R132C, R132C S280F, R132H, and R132H S280F, the effect of increasing concentrations of $MgCl_2$ was investigated (**Figure 2.38**).

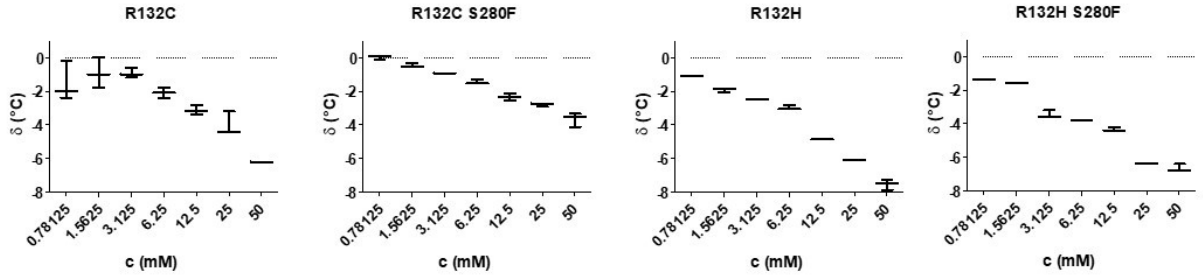

***Figure 2.38** | T_m-shift analyses of R132C, R132C S280F, R132H, and R132H S280F by DSF. The influence on thermal stability of IDH1 variants by addition of $MgCl_2$ is shown with the standard error of the mean (n = 3). Conditions: 3 µM enzyme, in 50 mM Tris buffer, pH 7.5 (Dye: Sypro Orange 3x).*

The IDH1 variants tested were apparently not stabilised by addition of magnesium ions (**Figure 2.38**) but a concentration-dependent destabilisation effect by magnesium ions was observed. Next, binding of isocitrate and NOG to IDH1 variants was investigated in the presence of 10 mM $MgCl_2$ (**Figure 2.39**).

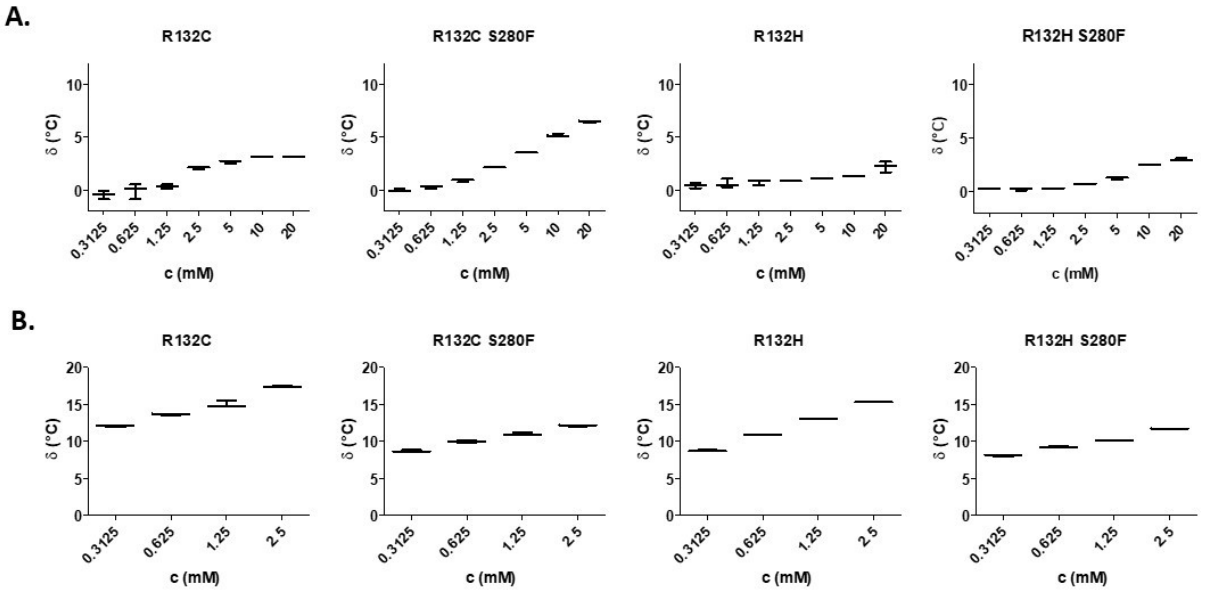

***Figure 2.39** | T_m-shift analyses of R132C, R132C S280F, R132H, and R132H S280F by DSF. The influence on thermal stability of IDH1 variants by addition of DL-isocitrate (**A.**) or NOG (**B.**) is shown with the standard error of the mean (n = 3). Conditions: 3 µM enzyme, in 50 mM tris buffer, pH 7.5 (Dye: Sypro Orange 3x) with 10 mM $MgCl_2$.*

In the presence of magnesium ions, binding of isocitrate to R132C, R132C S280F, R132H, and R132H S280F was observed. Isocitrate stabilised R132C and R132C S280F similarly but the increase in T_m was lower for R132H and R132H S280F, which were similar amongst themselves. Binding of NOG in the presence of magnesium ions (10 mM) resulted in a substantial concentration-dependent increase in T_m for all IDH1 variants tested. Binding of

NOG resulted in a larger increase in T_m for R132C and R132H compared to R132C S280F and R132H S280F.

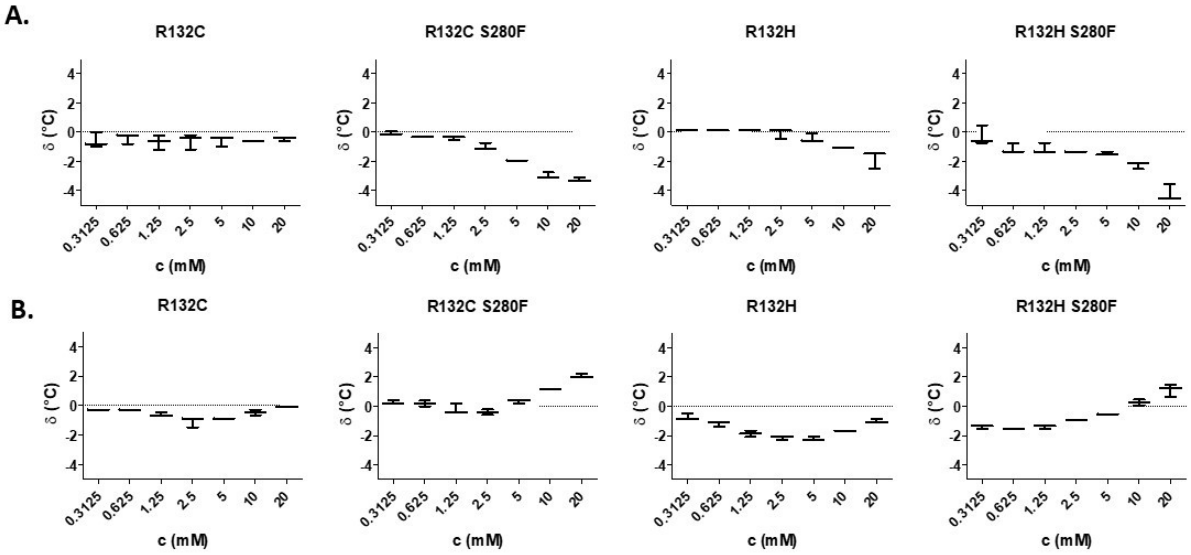

***Figure 2.40** | T_m-shift analyses of R132C, R132C S280F, R132H, and R132H S280F by DSF. The influence on thermal stability of IDH1 variants by addition of 2-HG (**A**) or 2-HG + 10 mM $MgCl_2$ (**B**) is shown with the standard error of the mean (n =3). Conditions: 3 µM enzyme, in 50 mM Tris buffer, pH 7.5 (Dye: Sypro Orange 3x).*

Because the product of turnovers from isocitrate or 2-OG catalysed by R132C, R132C S280F, R132H, and R132H S280F is 2-HG, binding of the product 2-HG to them was investigated using DSF. Binding of 2-HG was not observed in magnesium free solutions (**Figure 2.40**, A). With magnesium ions present (10 mM), R132C S280F and R132H S280F displayed a small increase in T_m at high concentrations ($\geq$ 10 mM) of 2-HG (**Figure 2.40**, B) but generally, 2-HG did not bind well to the IDH1 variants tested.

R132C, R132C S280F, R132H, and R132H S280F can utilise both NADPH and $NADP^+$ (Section 2.4): the reduction of 2-OG to 2-HG requires NADPH and turnover of isocitrate to 2-OG requires $NADP^+$. Consequently, binding of NADPH and $NADP^+$ to the aforementioned IDH1 variants was investigated.

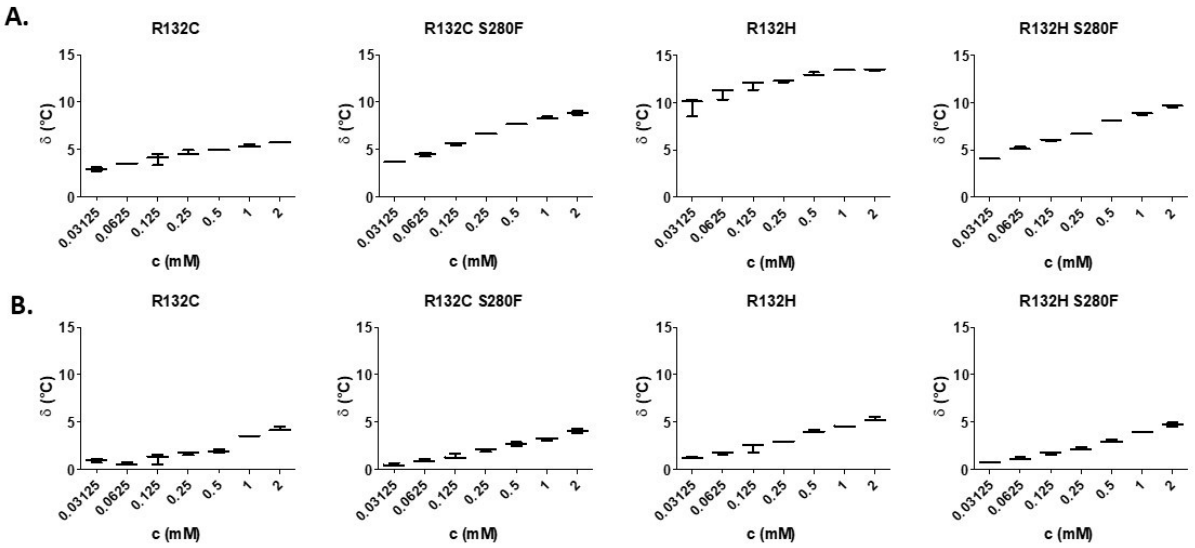

***Figure 2.41** | T_m-shift analyses of R132C, R132C S280F, R132H, and R132H S280F by DSF. The influence on thermal stability of IDH1 variants by addition of NADPH (**A**) or $NADP^+$ (**B**) is shown with the standard error of the mean (n =3). Conditions: 3 µM enzyme, in 50 mM tris buffer, pH 7.5 (Dye: Sypro Orange 3x).*

NADPH was observed to substantially stabilise all the IDH1 variants tested (**Figure 2.41**, A). Binding to R132H led to the largest increase in T_m compared to the other IDH1 variants tested. $NADP^+$ increased T_m less than NADPH for all IDH1 variants tested (**Figure 2.41**, B.). There were no substantial differences of $NADP^+$ binding between the IDH1 variants tested.

Studies by DSF revealed binding of *DL*-isocitrate and NOG only if magnesium ions are present. NOG binding leads to a larger increase in T_m than isocitrate, and similarly, NADPH leads to a greater increase in T_m than $NADP^+$ for all IDH1 variants tested. This is consistent with results from Section 2.5 showing that the predominant reaction catalysed by the IDH1 variants tested is the turnover of 2-OG to 2-HG utilising NADPH. Binding of isocitrate is stronger to R132C and R132C S280F compared to R132H and R132H S280F consistent with results from Section 2.4 and 2.5 showing a higher efficiency of R132C and R132C S280F for the turnover of isocitrate to 2-HG compared to R132H and R132H S280F.

2.10 Crystallographic Studies

X-ray diffraction studies of protein crystals are useful to obtain structural information of proteins which can elucidate biochemical questions. Typically, a highly purified recombinant protein needs to be produced ensuring homogeneity of the crystals to grow.[146] Next, protein crystals with periodically repeating arrangements need to be grown for which suitable conditions must be found. [146] This can be achieved using commercially available broad screening plates or it can be based on crystallisation conditions of similar proteins reported

previously.[146] Once conditions have been optimised, single crystals need to be fished and cryoprotected before they can be analysed using a focussed x-ray beam.[146] From the diffraction images, electron density maps can be calculated which can subsequently be used to build a model of the protein. [146] After iterative rounds of refinements to optimise the initial model, it can be deposited (with other parameters) on the protein data bank (PDB). [146]

To investigate the underlying mechanisms of the effects of the S280F dimer-interface variation observed in turnover assays (Section 2.3/2.4/2.5) and thermal stability studies (Section 2.7.3), crystallisation studies of R132C S280F in its closed-active conformation with NADPH, 2-OG and calcium bound were conducted. For structural comparison, crystallographic studies also attempted to obtain a crystal structure of R132C with NADPH, 2-OG and calcium bound.

2.10.1 Crystallographic Studies on IDH1 Variants

The first crystal structure of an IDH1 cancer-associated variant, i.e. R132H, was reported in 2009.[11] The R132H variant was crystallised in its closed active conformation complexed with NADPH, 2-OG, and calcium. Since then, 32 (as of December 2021) structures of R132H were deposited on the PDB. However, most of the structures are complexed with inhibitors and are therefore in an open inactive conformation (see Section 1.7). There is one reported crystal structure of R132C in its open-inactive conformation complexed with an analogue of the inhibitor DS-1001B.[147] R132H is the only IDH1 variant with a reported crystal structure in the closed active conformation (closed vs open conformation, Section 1.6).[51] Hence, studies to obtain a crystal structure of R132C S280F in its closed-active conformation complexed with NADPH, 2-OG, and calcium were conducted. It was envisaged that these could aid in the understanding of underlying structural effects on kinetic differences and differences in T_m between IDH1 variants and thus help to understand the mechanism of ivosidenib drug resistance. Studies to obtain a crystal structure of R132C S280F in its open inactive conformation with the inhibitor DS-1001B bound, are discussed in Chapter 3.

2.10.2 Production of R132C S280F for Crystallisation Studies

Initially, commercially available broad screens were used for crystallisation studies of R132C S280F. R132C S280F (12.81 mg/mL), containing a C-terminal hexahistidine tag, was incubated with NADPH (10 mM), $CaCl_2$ (20 mM), and 2-OG (200 mM) in buffer (Tris 20 mM, NaCl 100 mM; pH 7.4) for 1 h and used for broad screens. The broad screens included PEG-free screens like Salt-Rx, Anions and Cations as well as PEG containing screens like Crystal-Screen, PACT-Premier, Wizard Classic 1 and 2, JCSG$^+$, Index, Quiagen Classics L. All broad

screens were conducted at ambient temperature. None of the broad screens yielded suitable crystallisation conditions for R132C S280F after 4 weeks.

Subsequently, constructs were modified to cleave the hexahistidine tag from R132C S280F as it might interfere with crystallisation. [146] The cloning efforts were based on a template of a pET22b vector with an ORF encoding for R132C S280F with a C-terminal hexahistidine tag (no cleavage site), which was used for expression of R132C S280F in Section 2.2.5. Firstly, a Tobacco Etch Virus (TEV) cleavage-site was introduced to enable cleavage of the C-terminal hexahistidine tag. The DNA sequence for the cleavage-site was obtained from the commercially available vector pET15-MHL[1] (**Figure 2.42**). TEV is reported to cut the protein sequence between the Q and G residues[148].

```
E  N  L  Y  F  Q  G
gaaaacttgtatttccagggc
```

***Figure 2.42** | DNA and amino acid sequence of the Tobacco Etch Virus (TEV) cleavage-site obtained from the commercially available vector pET15-MHL[1].*

Additionally, constructs were designed to encode for R132C S280F with an N-terminal TEV-cleavable hexahistidine tag instead of the C-terminal hexahistidine tag. The new open-reading frames (ORF) were produced by PCR, digested with restriction enzymes, and reintroduced into the pET22b vector by ligation facilitated by T4 ligase.

2.10.2.1 Cloning

Primers were designed to introduce a TEV-cleavage site at the C-terminus before the hexahistidine-tag or an N-terminal TEV-cleavable his-tag (see Section 2.9.9). To enable ligation into pET22b, the primers included a C-terminal Xho1 restriction-site and an N-terminal Nde1 restriction-site. The primers also included a CCCGGG overhang to improve restriction enzyme efficiency (see Section 2.9.9).

After PCR, the PCR product and the pET22b vector were digested with the restriction enzymes Xho1 and Nde1. After agarose gel purification, the digested PCR product and the empty pET22b vector were used for ligation facilitated by T4 ligase which was allowed to proceed for 3 days. The ligation mixture was transformed into commercially sourced XL10 gold cells. Colonies were analysed by colony-PCR. The plasmid DNA of two positive colony-PCR clones was purified. Samples were sequenced; demonstrating that the new plasmids for R132C S280F contained a C-terminal TEV-Cleavage-site (**Figure 2.43**).

Additionally, an N-terminal TEV-cleavable hexahistidine tag was successfully introduced into an ORF encoding for R132C S280F according to the procedure described in the previous paragraph and the identity of the desired construct was confirmed by sequencing (**Figure 2.43**).

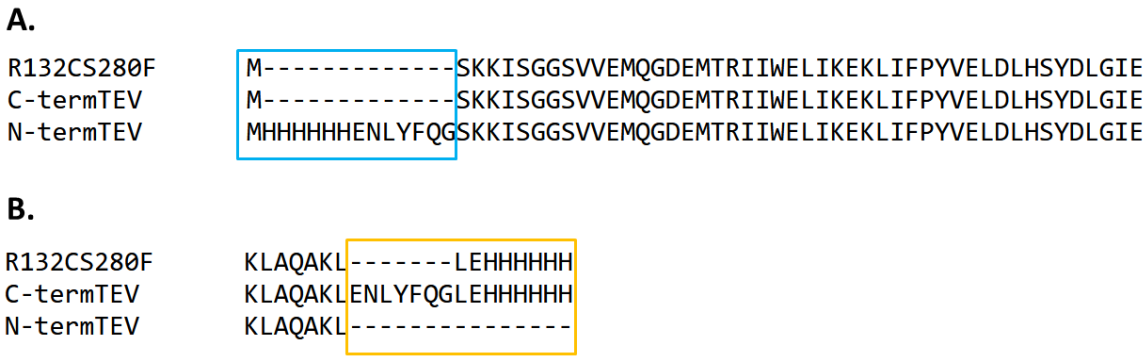

Figure 2.43 *| Protein sequence alignment of new constructs encoding for R132C S280F including a N- or C-terminal TEV-cleavage site. The blue box (**A**) highlights the N-terminal TEV-cleavable hexahistidine tag and the orange box (**B**) highlights the C-terminal TEV cleavage-site ("ENLYFQG"). The alignment was carried out using MAFFT*[128].

2.10.2.2 Production of R132C S280F with a C-Terminal Hexahistidine Tag with a TEV Cleavage Site

Due to its similarity with the original C-terminal hexahistidine tagged construct, R132C S280F with a TEV-cleavable C-terminal hexahistidine tag was produced according to standard procedures described in Section 2.2. Because of *E. coli* growth issues in the laboratory likely caused by a phage contamination, the plasmid was transformed into the phage-resistant cell line Lemo21 instead of BL21(DE3)plysS. After expression according to standard conditions (Section 2.12.10) and purification by immobilised metal affinity chromatography (IMAC), R132C S280F was buffer exchanged into imidazole free buffer (20 mM Tris, 100 mM NaCl). TEV protease was added (1:50 of protein concentration as measured by Nanodrop) and incubated overnight (4°C). Successful cleavage was shown by LC/MS. The solution was then subjected to a manual reverse IMAC column according to standard procedures (Section 7.1.12) and subjected to gel filtration, which yielded pure R132C S280F. Preliminary studies demonstrated activity of R132C S280F using an NADPH absorbance assay (data not shown).

2.10.2.3 Production of R132C S280F with a N-Terminal Hexahistidine Tag and a TEV Cleavage Site

To obtain suitable expression conditions for production of R132C S280F with an N-terminal hexahistidine tag including a TEV-cleavage site, the appropriate plasmid was transformed into the Lemo21 cell line, and an expression optimisation conducted in 100 mL 2TY (varying concentrations of IPTG: 0.1 mM, 0.5 mM, 1 mM) at a post-expression temperature of 20°C.

1 mL culture was centrifuged and lysed using BugBuster Protein Extraction Reagent and 5 µL Lysonase. Lysed cells were purified using Proafinity IMAC resin (Section 2.12.10) and analysed by SDS-PAGE gel electrophoresis.

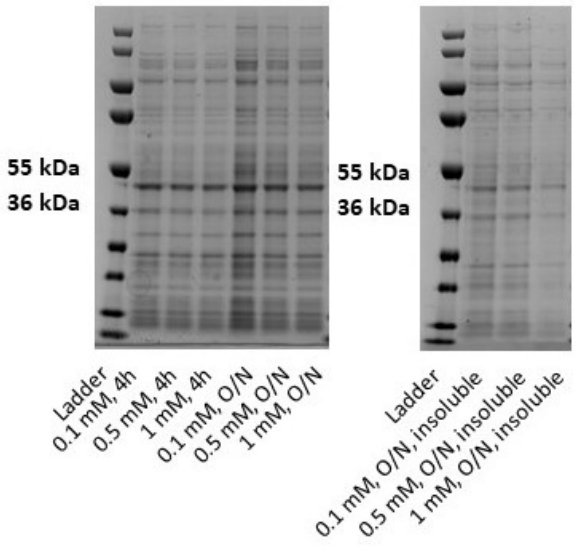

Figure 2.44 *| SDS-PAGE analysis of expression optimization of R132C S280F with an N-terminal TEV-cleavable hexahistidine tag.*

The insoluble fractions contained low amounts of protein (**Figure 2.44**). In the soluble fractions, the overnight cultures contain more protein than the cultures harvested after 4 h (**Figure 2.44**). No substantial differences in expression levels at different IPTG concentrations were observed (**Figure 2.44**). Therefore, the expression of R132C S280F with a TEV-cleavable N-terminal hexahistidine tag should be induced with 0.1-1 mM IPTG and expressed overnight at 20°C.

While cloning and expression testing of the new constructs of R132C S280F (with TEV-cleavable N- or C-terminal hexahistidine tag) were conducted, repurification of the original R132C S280F construct (no cleavage site) was conducted according to the section below.

2.10.2.3.1 Repurification of R132C S280F with a C-terminal His Tag

After initial broad screens did not yield suitable crystallisation conditions, the purity of R132C S280F with a C-terminal hexahistidine tag (without a cleavage-site) was reassessed using SilverXpress stain. This stain is more sensitive than Instant Blue (used to stain SDS PAGE gels) and can, according to the manufacturer, detect protein amounts in the nanogram-level.[149]

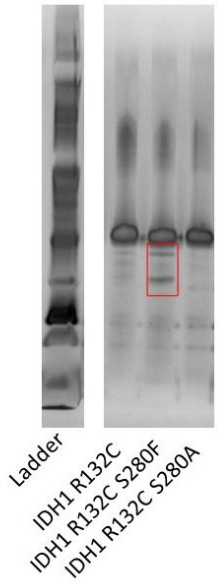

Figure 2.45 | *SilverXpress stain of SDS-PAGE gel analysis of IDH1 variants. There are two impurity bands below the band corresponding to R132C S280F.*

The Silver stain revealed two small impurity bands in the R132C S280F protein sample which are absent in R132C or R132C S280A (**Figure 2.45**). Consequently, R132C S280F was repurified employing IMAC, anion exchange (note this purification step was not conducted in the standard IDH1 purification procedures used for the original R132C S280F batch) and gel filtration. The purification strategy yielded pure R132C S280F (**Figure 2.46**).

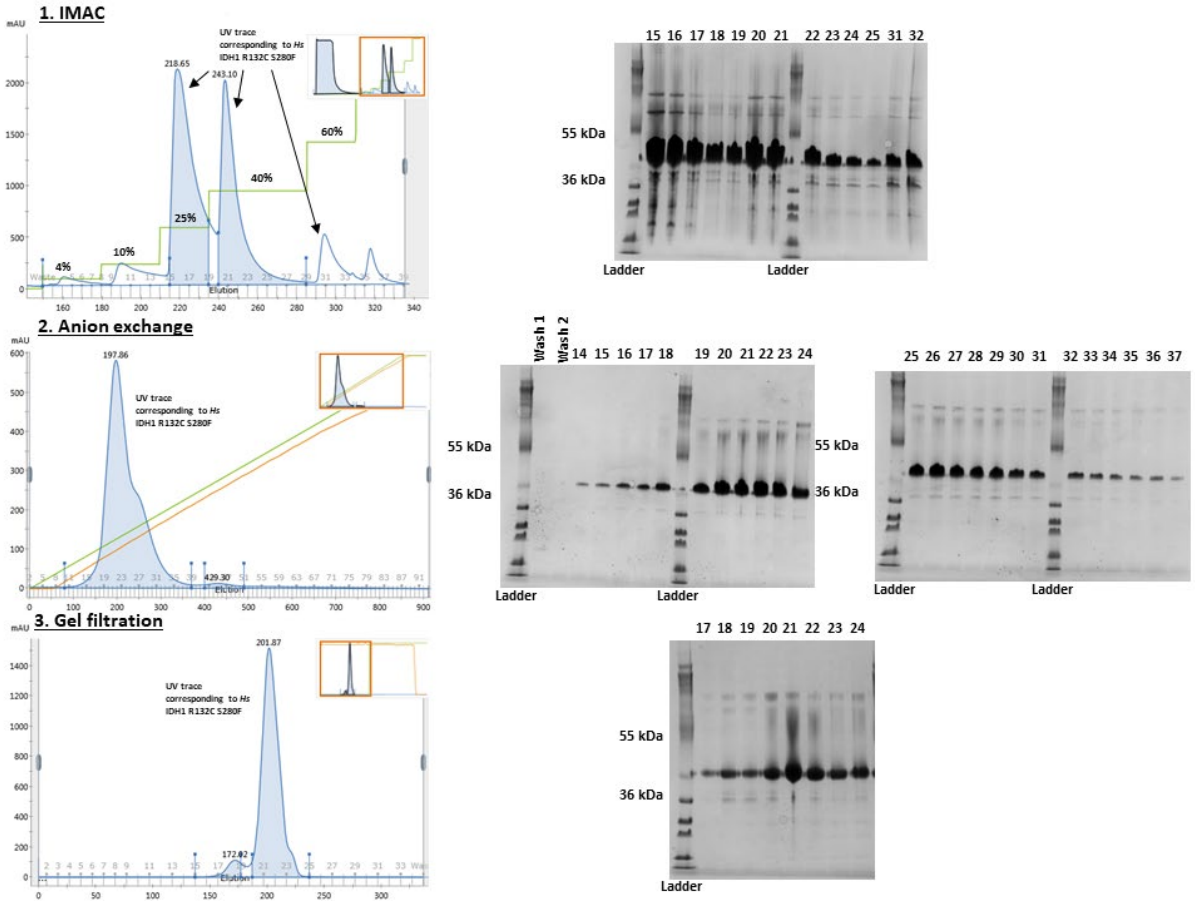

Figure 2.46 *| R132C S280F purification. The chromatograms of each purification technique are shown on the left, the SDS-PAGE gels on the right.* ***A.*** *Nickel-affinity chromatography using imidazole step gradient elution (percentages of elution buffer are shown on the chromatogram), see Section 2.12.1 for details.* ***B.*** *Anion-exchange chromatography using a linear NaCl gradient elution, see Section 2.12.1 for details.* ***C.*** *Size-exclusion chromatography using isocratic elution.*

2.10.3 Crystallisation Studies on R132C S280F

The repurified batch of R132C S280F (no cleavage-site, Section 2.10.2.2.1) was incubated with NADPH (10 mM), $CaCl_2$ (20 mM), and 2-OG (200 mM) in buffer (Tris 20 mM, NaCl 100 mM) for 1 h. The same broad crystallisation screenings as described in Section 2.10.2 were used, but these did not yield suitable crystallisation conditions after 4 weeks (all crystals obtained were analysed for diffraction at the Diamond Light Source but were salt crystals). After this, 24 well optimisation plates were set up based on literature conditions.[126, 35] Firstly, an optimisation plate (Optimisation plate 1) was prepared based of PDBID 3INM[35]: PEG6000 (6-26%, horizontal axis in steps of 4%); MES monohydrate pH 6.5 (100 - 250 mM, vertical axis in steps of 50 mM). Secondly, an optimisation plate (Optimisation plate 2) was prepared based on PDBID 4KZO[126]: ((PEG3350 12-22%, horizontal axis in steps of 2%); calcium acetate (100 or 250 mM, vertical axis in steps of 50 mM) and a constant concentration of Bis-Tris (0.1 M) at pH 7.

While the Optimisation plate 1 did not yield any suitable crystallisation conditions, nucleation was observed in some wells in Optimisation plate 2 after 5 days (**Figure 2.47**).

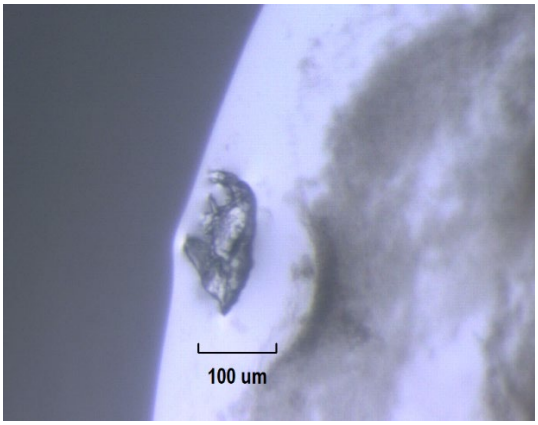

***Figure 2.47** | Photograph of nucleation observed in Optimization plate 2. These were observed in conditions including: 16 - 18 % PEG 3350 and 200 mM Ca acetate.*

The conditions of Optimisation plate 2 were subsequently optimised (Optimisation plate 2.2): The plate was set up using PEG3350 (14-24%, horizontal axis in steps of 2%), calcium acetate (175 or 250 mM, vertical axis in steps of 25 mM) and a constant concentration of Bis-Tris (0.1 M) at pH 7) which yielded several wells with microcrystals after 2 days (**Figure 2.48**) indicating that further optimisation is needed.

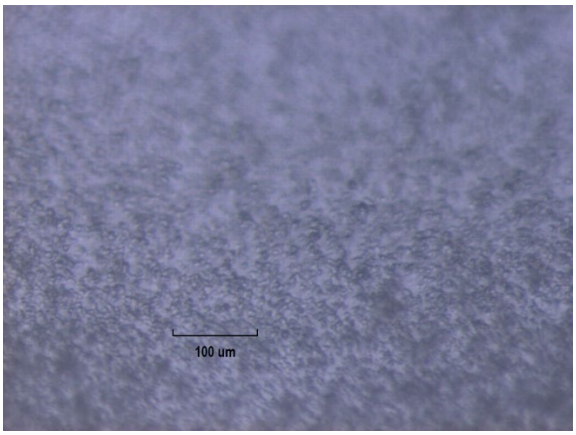

***Figure 2.48** | Photograph of microcrystals obtained in Optimisation plate 2.2. Micro crystals appeared after 2 days in multiple wells.*

All wells with microcrystals from Optimisation plate 2.2 were combined and crystal seeds were produced according to Section 2.12.10. The crystal seeds were used for the setup of Optimisation plate 2.3: PEG3350 15-20% (horizontal axis in steps of 1%), calcium acetate (200 (row A + C) or 225 mM (row B + D), vertical axis in steps of 25 mM) and a constant concentration of Bis-Tris (0.1 M) at pH 7 was used; row A + B were unseeded, row C+D were seeded). Substantial crystals (400x100 µm) manifested within 14 days (**Figure 2.49**).

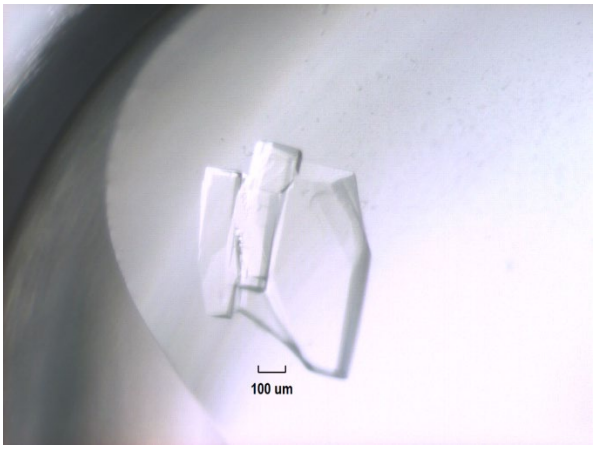

Figure 2.49 | *Photograph of crystals obtained in Optimisation plate 2.3. This crystal was broken in three pieces one of which yielded diffraction data with 2.1 Å resolution which was used to obtain the crystal structure discussed in this section.*

Crystal-containing droplets were cryo-protected by mixing them in a ratio of 1:1 with reservoir solution containing glycerol (25%), harvested with a nylon loop, and cryo-cooled in liquid N_2. Diffraction data were kindly collected by Dr Patrick Rabe using synchrotron radiation at Diamond Light Source (DLS) beamline I24. The crystals diffracted to 2.1 Å resolution. Processing was conducted using the Xia2[150] strategy of the beamline auto-processing pipeline according to Section 2.12.10.

Table 2.8 *| Data collection and refinement statistics for structures PDBID 7PJM and PDBID 7PJN.*

Datasets	***IDH1:NADPH:CA:AKG*** *(PDB ID: 7PJM)*
Data Collection (T in K)	*cryo-MX (100)*
Beamline (Wavelength, Å)	*DLS I24 (0.96863)*
Detector	*DECTRIS PILATUS 6M*
Data Processing	*Xia2*
Space group	*C 2 2 2_1*
Cell dimensions	
a,b,c (Å)	*96.58, 273.01, 117.42*
α, β, γ (°)	*90, 90, 90*
No. of molecules/ASU	*3*
No. reflections	*90634 (6591)*
Resolution (Å)	*71.950 - 2.100 (2.150 - 2.100)**
R_{meas}(I)	*0.110 (2.469)**
I/σI	*13.400 (1.1)**
CC-half	*0.999 (0.550)**
Completeness (%)	*99.96 (99.87)**
Multiplicity	*13.2 (12.7)**
Wilson B value ($Å^2$)	*47.61*
Refinement	*PHENIX*
R_{work}/R_{free+}	*0.1805/0.2098*
No. atoms	*10275*
- *Enzyme*	*9730*
- *Ligand*	*204*
- *Water*	*341*
Average B-factors	*59.91*
- *Enzyme ($Å^2$)*	*59.99*
- *Ligand ($Å^2$)*	*64.88*
- *Water ($Å^2$)*	*54.66*
R.m.s deviations	
- *Bond lengths (Å)*	*0.003*
- *Bond angles (°)*	*0.52*

**Highest resolution shell in parentheses. DLS = Diamond Light Source.*

A crystal structure of R132C S280F complexed with NADPH, 2-OG, and calcium was solved by molecular replacement using a crystal structure of R132H in the active conformation (4KZO[51]) as a model (3 chains in the asymmetric unit). The data collection and refinement statistics are shown in **Table 2.8**. R132C S280F crystallised in a $C222_1$ space group with 3 monomers (chain A-C; **Figure 2.50**) in the asymmetric unit.

As demonstrated by non-denaturing PAGE, SEC-MALS analysis, and non-denaturing MS (Section 2.7/2.8), R132C S280F is dimeric in solution. In the asymmetric unit, chains A and B form a dimer (**Figure 2.50**), while chain C likely forms a dimer with chain C from another asymmetric unit. The apparent dimer formed by chains A and B is used for subsequent

discussions on the R132C S280F crystal structure, which was deposited in the PDB with the accession code 7PJM (on hold for publication).

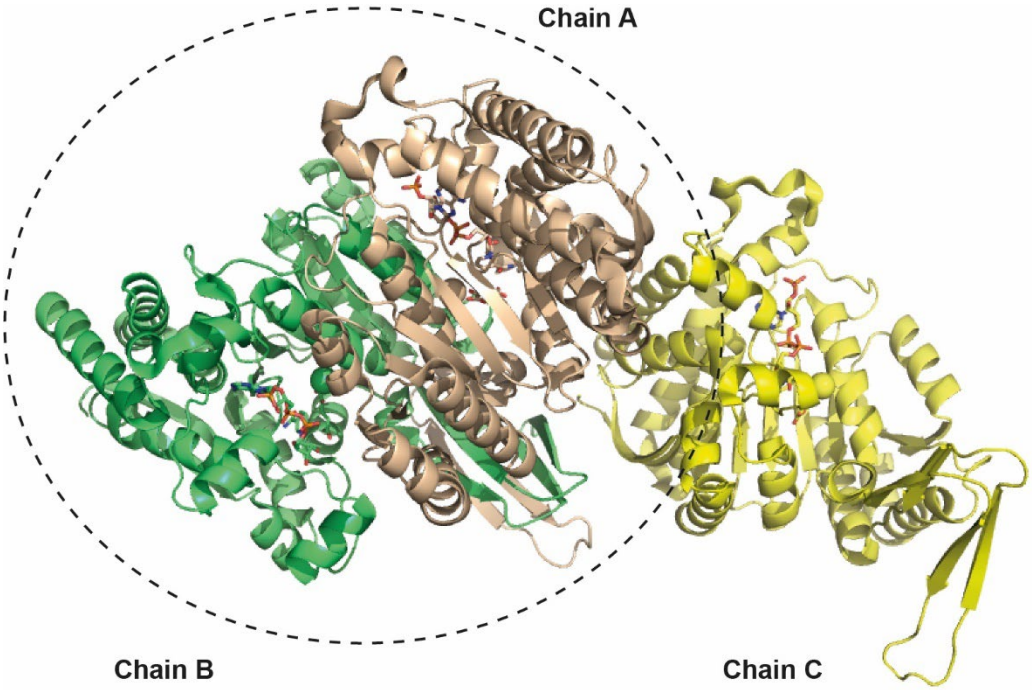

***Figure 2.50** | Ribbon view of the asymmetric unit from a crystal structure of R132C S280F (2.1 Å resolution) complexed with NADPH, 2-OG, and calcium ions likely in a closed active conformation. There are 3 monomers in the asymmetric unit (chain A (wheat), chain B (green), chain C (yellow)). Non-denaturing PAGE, SEC MALS and non-denaturing MS analyses imply that R132C S280F is predominantly dimeric in solution. Chains A and B form an apparent dimer in the asymmetric unit; chain C forms an apparent dimer with a chain C from another asymmetric unit.*

R132C S280F likely co-crystallised with NADPH (incubation with 10 mM NADPH; note: NADPH and $NADP^+$ cannot be distinguished at a resolution of 2.1 Å), 2-OG and calcium ions in the active site. The distance between the C-α carbons of I76 and L250, which are residues at the entrance of the active site[151], is used to distinguish between the closed (active) conformation and the open (inactive) conformation. [151] The distances for both active site clefts of the dimer built by chain A and B are 12.6 Å and 13.0 Å (**Figure 2.51**, A./B. respectively) indicating that the enzyme is in the closed active conformation[151] (Section 1.6.1).

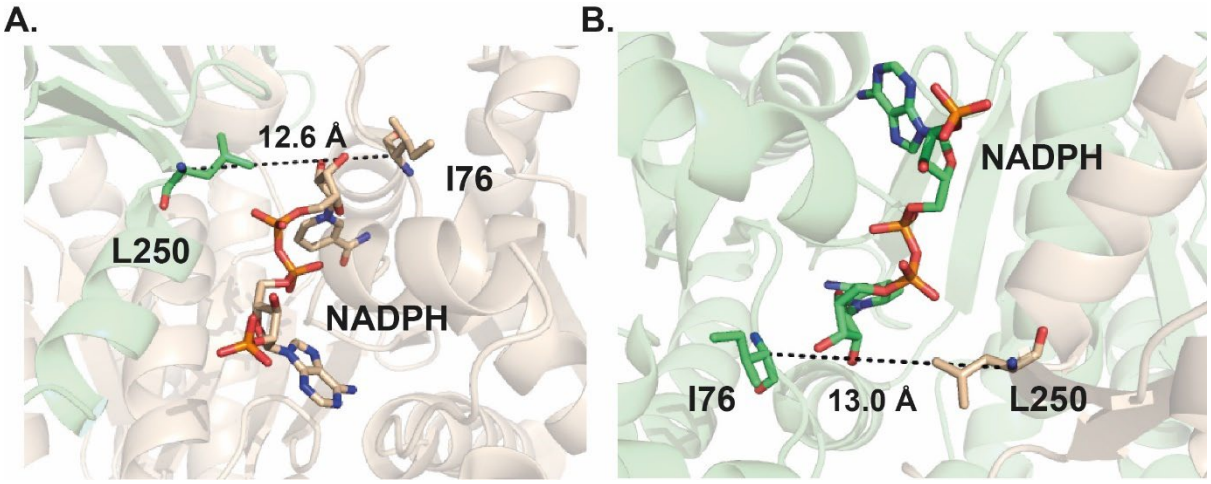

Figure 2.51 *| Ribbon view from a crystal structure of R132C S280F in the closed active conformation. Chain A: wheat, chain B: green. Each of the two active sites in the dimer is composed of residues from both chain A and chain B. The distance between I76 and L250 C-α carbons, which is used to measure the width of the active site cleft[153], is 12.6 Å (**A.**; I76 (chain A), L250 (chain B)) or 13.0 Å (**B.**; I76 (chain B), L250 (chain A)) at the active sites in the dimer.*

The R132C S280F dimer-interface is between the α9 and α10 helices from both monomers next to the active sites (**Figure 2.52**, A/B). The side chain of the F280 residue points towards the dimer-interface, which is covered by the L1 loop (**Figure 2.52**, B). There are novel hydrophobic interactions between W124 (L1), F280 (α10), and W267 (**Figure 2.52**, C). The distance of the residues *in crystallo* are between 3.4-4.6 Å which could be in range for pi-pi-stacking in solution. NADPH, 2-OG, and calcium are well resolved in the active site (**Figure 2.52**, D). The R132C variation does not directly interact with any substrate in the active site consistent with crystal structures of R132H in the active conformation.[126]

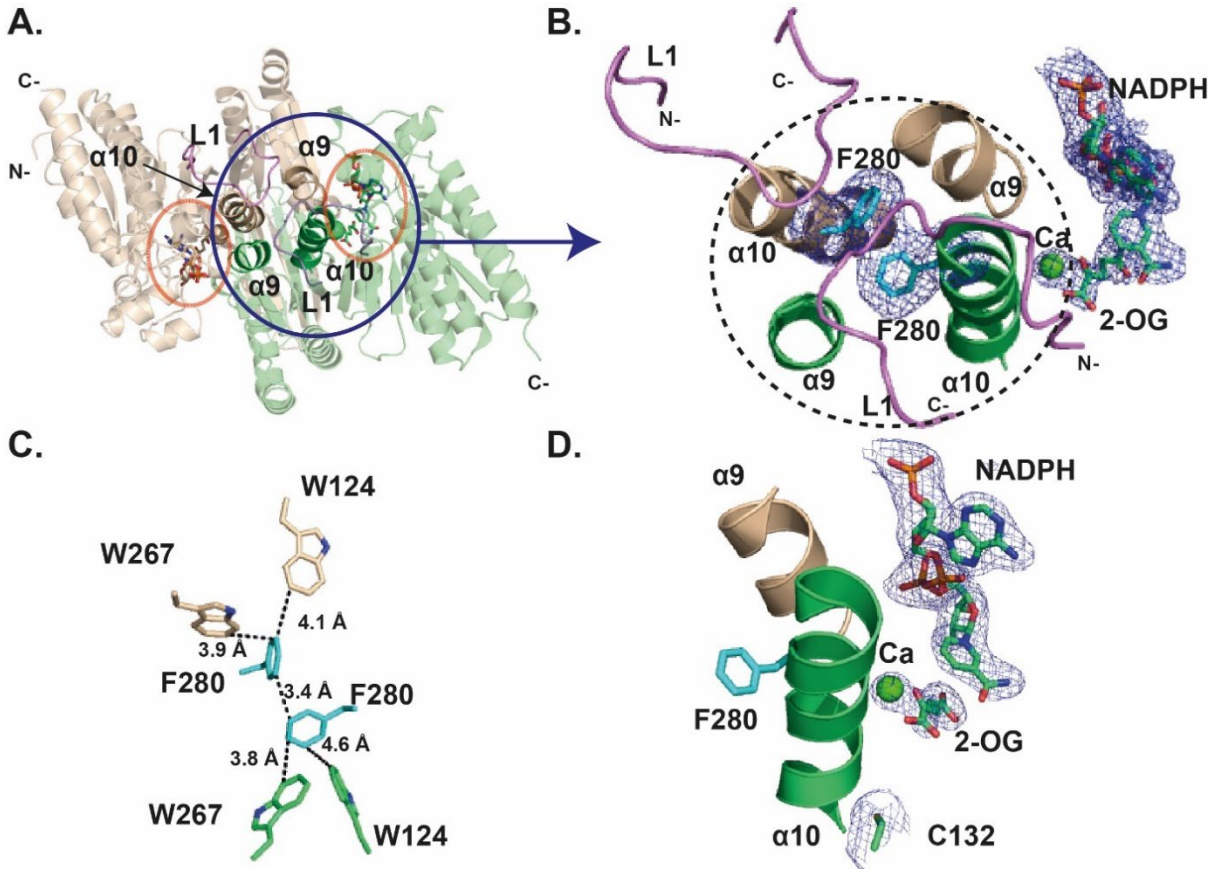

Figure 2.52 *| R132C S280F variant in its closed active conformation bound to calcium, 2-OG, and NADPH (2.1 Å).* ***A.*** *Ribbon view from a crystal structure of R132C S280F. An apparent dimer is formed by chain A (wheat) and chain B (green) as observed in the asymmetric unit. Orange circles: active sites with 2-OG, NADPH, and calcium. L1 loop: violet.* ***B.*** *Close-up view with a Polder omit map (blue mesh, contour 3.0 σ) showing 2-OG, NADPH, and calcium. The L1 loop covering the dimer-interface is in violet. Black circle: dimer-interface with a Polder omit map (blue mesh, contour 3.0 σ) showing F280 (cyan).* ***C.*** *View of the dimer-interface highlighting hydrophobic interactions between W124 (L1), F280 (cyan, α10), and W267 in both monomers.* ***D.*** *Ribbon view of the active site from a structure of R132C S280F (chain A: wheat, chain B: green) with a Polder omit map (blue mesh, contour 3.0 σ) showing C132, calcium, 2-OG and NADPH.*

The overall structure of R132C S280F aligns well (RMSD for backbone C-α: 0.486 Å) with that R132H (4KZO[51]; **Figure 2.53**, A) which is in accord with CD analyses showing a similar secondary structure fold of R132C S280F and R132H (Section 2.7).[126] The three aspartate residues D252, D275, and D279 are reported to be involved in metal binding in IDH1.[152] D252, is a residue on the α9 helix of chain A, and D275 and D279 are on the α10 helix of chain B (**Figure 2.53**, B). Compared to the structure of R132H, all 3 metal binding residues are shifted while the orientation of D252 also changes.

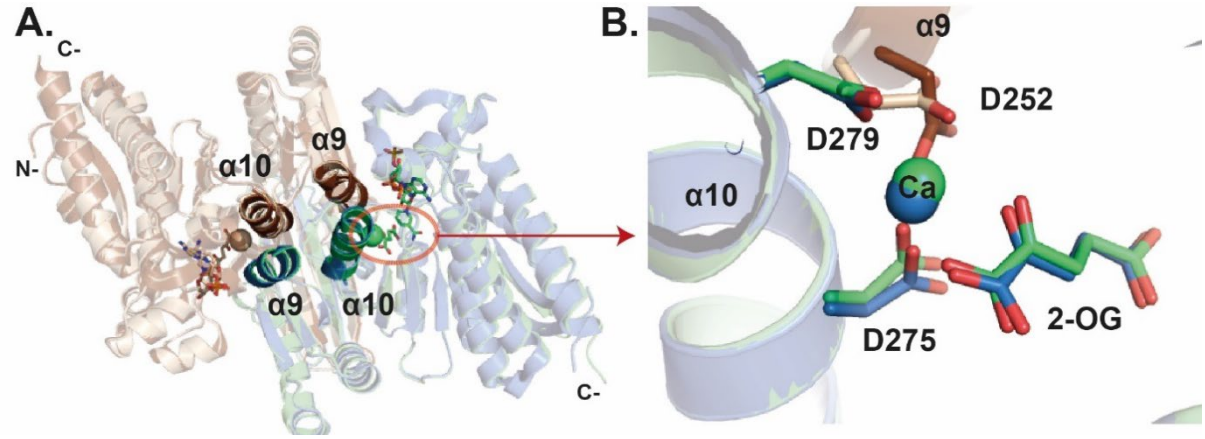

Figure 2.53 *| Views from a crystal structure of R132C S280F highlighting the metal binding site.* ***A.*** *Ribbon view from a crystal structure of R132C S280F (RMSD 0.486, 2.1 Å; chain A: wheat, chain B: green) superimposed with a view from a crystal structure of IDH1 R132H (PDB: 4KZO[51]; chain A: brown, chain B: blue). Orange circle: metal binding site.* ***B.*** *View from R132C S280F superimposed with one of IDH1 R132H (PDB: 4KZO[51]). The calcium binding residues D252 (chain A, α9, wheat), D275 and D279 (chain B, α10, green) are shown.*

As previously discussed (Section 1.7), the most potent IDH1 mutant inhibitors bind at the dimer-interface between the α9 and α10 helices. This binding pocket is partially covered by loop L1 and L1' (one from each monomer; **Figure 2.54**, A), which is located just above F280 and is shifted in the R132C S280F structure compared to R132H (1.6 Å and 1.2 Å between the Cα atoms of S122, respectively; **Figure 2.54**, B).

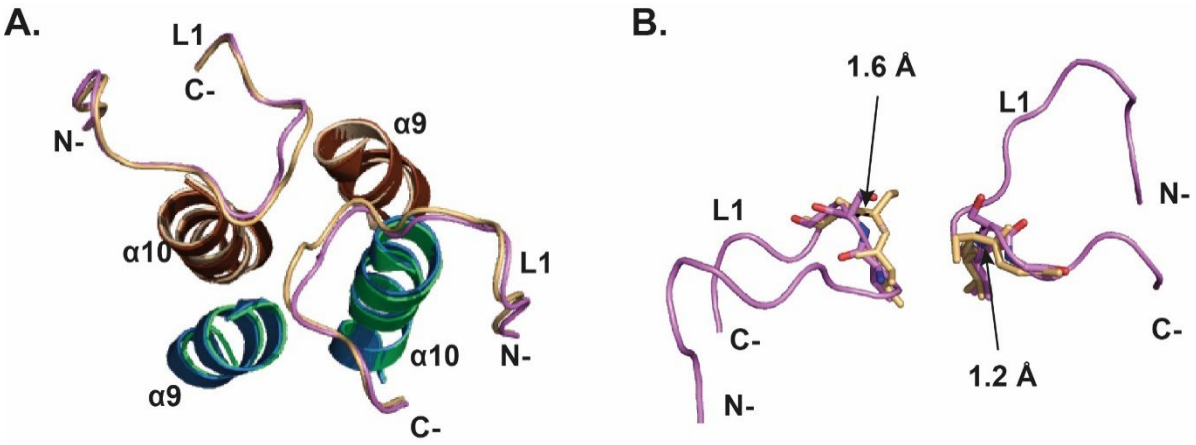

Figure 2.54 **|** Dimer-interface of the R132C S280F variant showing the L1 loop. **A.** Ribbon view of the dimer-interface and L1 loop of R132C S280F (chain A: wheat, chain B: green; L1: violet) superimposed with a view from a structure of R132H (PDB: 4KZO[51]; chain A: brown, chain B: blue; L1: beige). **B.** Close-up view showing movement of the L1 loop which partially covers the inhibitor binding pocket (violet: R132C S280F, beige: R132H) and the conformational change associated with residue S122 relative to R132H.

In summary, the crystal structure of R132C S280F superimposes well with that of R132H. The F280 residue in the R132C S280F crystal structure points towards the dimer-interface and builds a hydrophobic region with W124 and W267. The new hydrophobic interactions might be causing the observed increase of T_m of R132C S280F (Section 2.7.3). Additionally, the

movement of the L1 loop partially covering the binding pocket, the higher rigidity of the dimer-interface due to increased intramolecular hydrophobic interactions, and the steric hindrance by the phenylalanine residues themselves, could contribute to resistance to ivosidenib. Furthermore, conformational changes of the metal binding residues were observed in R132C S280F when compared to R132H. This could be the reason for alterations in kinetic parameters for metal ion and 2-OG binding (lower K_M and higher k_{cat}/K_M values for 2-OG and magnesium) in R132C S280F compared to R132C as observed in Section 2.3. As IDH1 ivosidenib is reported to compete with 2-OG and metal binding[48], the increased affinity of 2-OG and magnesium for R132C S280F (as judged by K_M) compared to R132C might play an additional role in inhibitor resistance.

2.10.4 Crystallisation Studies on R132C

Crystallisation of R132C was attempted in its closed active conformation with NADPH, 2-OG and calcium based on literature conditions used to obtain a structure of R132H (PDB:4KZO[126]). An optimisation plate was set up using PEG3350 (15-20%, horizontal axis in steps of 1%), calcium acetate (180-240 mM, vertical axis in steps of 20 mM) and a constant concentration of Bis-Tris (0.1 M) at pH 7. This optimisation plate did not yield any suitable crystallisation conditions (no crystals were observed). Subsequentially, another optimisation plate was prepared using seeds obtained from Optimisation plate 2.2 from Section 2.10.3 (cross seeding). The conditions were PEG3350 (15-20%, horizontal axis in steps of 1%), calcium acetate (220 (row A + C) and 240 mM (row B + D)) and a constant concentration of Bis-Tris (0.1 M) at pH 7. These conditions were used to prepare two unseeded rows (A+B) and two seeded rows (C+D) but did not yield any suitable crystallisation conditions after 6 weeks.

An alternative strategy to obtain suitable crystallisation conditions for R132C with a C-terminal TEV-cleavable hexahistidine tag and an N-terminal TEV-cleavable hexahistidine tag could not be fully explored due to time constraints: although the constructs were obtained, their expression conditions could not be optimised.

2.11 Summary and perspectives

Soon after the IDH1 variant inhibitor ivosidenib was introduced to clinical practice, resistances emerged linked to a second-site S280F substitution at the dimer-interface of R132C.[28] In this chapter, the recombinant production of human IDH1 R132C, R132C S280F, R132C S280A, R132H and R132H S280F has been described (Section 2.2). Using kinetic studies, it was demonstrated that the S280F substitution is not only involved in resistance to ivosidenib but

can influence kinetic parameters of the reduction of 2-OG to 2-HG by increasing the affinity for 2-OG and magnesium ions (as judged by K_M), and consequently increasing the catalytic efficiency (k_{cat}/K_M; Section 2.3). The increased affinity for 2-OG and magnesium ions in 2-OG reduction catalysed by R132C S280F compared to R132C might play a role in resistance, as ivosidenib is reported to compete with 2-OG and magnesium ion binding.[48] This is further discussed in Chapter 3. ^{1}H NMR time course analysis demonstrated that R132C S280F and R132H S280F catalyse the reduction of 2-OG to 2-HG with higher efficiency than R132C or R132H, respectively (Section 2.4.1).

Interestingly, R132C, R132C S280F, R132H, and R132H S280F can catalyse the turnover of *D*-isocitrate to 2-HG by ^{1}H NMR studies (Section 2.4.2). Using cyclic voltammetry, it was shown that the oxidation of isocitrate to 2-OG is substantially influenced by the R132 variation but that the full turnover of isocitrate to 2-HG is enhanced by the S280F variation (Section 2.5). This is an important finding in understanding the catalytic mechanism of IDH1 variants especially regarding the utilisation of isocitrate.

All IDH1 variants tested have similar secondary structures (Section 2.7.1) and are dimeric in solution (Section 2.7.3/2.8). The T_m is substantially increased as a result of the S280F dimer-interface variation (Section 2.7.2). Non-denaturing mass spectrometry and ^{1}H NMR studies revealed that all IDH1 variants tested copurify with two NADPH molecules per dimer (Section 2.8.1) and it was shown that there is a posttranslational (phospho-)gluconoylation on a subset of the variants from production in *E.coli* (Section 2.8.2).

Cofactor binding experiments by DSF showed binding of NOG (as a surrogate for 2-OG) to all proteins but only with magnesium ions present (**Figure 2.38**). Similarly, isocitrate can only bind to the IDH1 variants tested with magnesium ions present. Binding is strongest to R132C and R132C S280F which is consistent with findings that these variants catalyse the turnover of isocitrate more efficiently than R132H and R132H S280F (**Figure 2.38**). A crystal structure of R132C S280F in its closed active conformation with NADPH, 2-OG and calcium was obtained (**Figure 2.52**). The S280F substitution forms a novel hydrophobic pocket at the dimer-interface with W124 and W267 from both monomers likely resulting in the observed increase in T_m. These interactions likely increase the rigidity of the inhibitor binding site at the dimer-interface interfering with binding of ivosidenib. The phenylalanine sidechain of F280 is oriented towards the dimer-interface also imposing a direct steric hindrance to ivosidenib binding.

There are conformational changes in the metal binding residues of R132C S280F compared to R132H (D252, D275, D279). This might be linked to the differences in kinetic parameters of magnesium ions and 2-OG (note magnesium is important for 2-OG binding as shown by DSF studies, Section 2.9). Inhibitors are reported to compete with 2-OG[66] and magnesium ion[152] binding, so this finding may play an additional role in resistance to ivosidenib as a result of the S280F substitution.

In the next chapter, studies on ivosidenib inhibition of R132C, R132C S280F, R132H and R132H S280F, and investigations on how to overcome resistance are discussed. This includes further investigation of the resistance mechanism against ivosidenib using R132C S280A and characterisation of alternative inhibitors of R132C S280F and R132H S280F. In Chapter 4, studies on the differences of R132 variants and the influence of the dimer-interface on IDH1 catalysis are discussed.

2.12 Materials and methods

2.12.1.1 Primer Design

For site-directed mutagenesis, a pET22b vector containing the gene for IDH1 R132H was used.[48] Primers to introduce S280F mutations were designed to be fully complementary to each other. Primers to introduce R132C and S280A mutations were designed according to Zheng et al.[127] The mutations were introduced by SDM (Section 7.1.6). The R132H S280F encoding gene was made from that encoding for R132H. The R132C encoding gene was made from that encoding for R132H. The R132C S280F and R132C S280A encoding genes were made from that encoding for R132C.

Table 2.9 **|** *Primers used for site-directed mutagenesis.*

Protein	**Primer**
R132H S280F_forward	GGTGACGTGCAGTCGGACT**T**TGTGGCCCAA
R132H S280F_reverse	TTGGGCCACAA**A**AGTCCGACTGCACGTCACC
R132C_forward	CATAGGT**TG**TCATGCTTATGGGGATC
R132C_reverse	GCATGA**CA**ACCTATGATGATAGGTTTTACCC
R132C S280F_forward	GGTGACGTGCAGTCGGACT**T**TGTGGCCCAA
R132C S280F_reverse	TTGGGCCACAA**A**AGTCCGACTGCACGTCACC
R132C S280A_forward	GTCGGAC**G**CTGTGGCCCAAGCTATG
R132C S280A_reverse	GCCACAG**C**GTCCGACTGCACGTC

2.12.1.2 Yields of protein production

Recombinant proteins were produced according to standard procedures (Section 7.1.12).[48] The yield is presented in pellet mass divided by amount of 2TY medium. The protein yield is presented in amount of protein (mg) per litre of medium (L).

***Table 2.10** | Yields of protein production.*

Protein	Yield (g/L)	Protein Yield (mg/L)
R132H	9.83	34.7
R132H S280F	10.62	167.3
R132C	2.58	29.8
R132C S280F	5.99	42.4
R132C S280A	11.33	8.4

Proteins were produced as described in the Materials and Methods (Section 7.1.12). For nickel-affinity chromatography an imidazole step gradient was used:

***Table 2.11** | Elution of IDH1 variants from nickel-affinity column by increasing imidazole concentrations.*

Column Volumes (CV)	Percentage (V/V) of Elution Buffer
6	10
5	25
10	40
5	60
5	100

For the repurification of R132C S280F, as described in Section 2.10.2, an additional washing step with 4% (V/V) elution buffer over 6 CV was used. Subsequently, an anion-exchange purification was conducted according to standard procedures followed by size exclusion chromatography (Section 7.1.12).

2.12.2 Steady-State Kinetics

The NADPH absorbance assay was conducted using a PHERAstar FS Microplate Reader according to the Materials and Methods (Section 7.2.1). The assay buffer was prepared according to the following recipe used in a previous report[48]:

***Table 2.12** | Buffer composition for NADPH absorbance assay.*

	C (mM)	n (mol)	Mw (g/mol)	V (L)	m (g)
Assay buffer (pH 8.0)					
Tris base	100	0.025	121.14	0.25	3.0285
$MgCl_2$ ×6 H_2O	10	0.0025	203.3	0.25	0.50825
DTT	0.2	0.00005	154.253	0.25	0.007713
Tween-20 (C_V in % (V/V)	0.0050			0.25	0.0125
BSA (C_m in mg/mL)	0.1			0.25	0.025

The buffer was filtered, degassed, and used for steady-state kinetics according to the following conditions. 4x stock solutions of substrates/co-factors and the enzyme were prepared. One substrate/co-factor was varied to determine Michaelis-Menten parameters while the concentration of the other substrates/co-factors was saturating (saturating concentrations: 1.5 mM (2-OG), 0.3 mM (NADPH), 10 mM ($MgCl_2$). The final enzyme concentration was 400 nM adapted from assays previously conducted with R132H in our laboratory. Substrates/co-factors (4x), protein (4x) and assay buffer were allowed to warm up to room temperature for 10 minutes. Then 25 µL of buffer and protein were transferred into an ELISA half area Microplate (flat bottomed, medium binding). The reaction was initiated by addition of 25 µL 2-OG and NADPH (final volume: 100 µL) and the measurement was started immediately (conducted over 45 minutes). The initial rate was calculated using the specific NADPH absorption according to the Materials and Methods chapter (Section 7.2.1). The Michaelis-Menten parameters were then calculated using the GraphPad Prism software (version 5).

2.12.3 Time-Course Analyses by ^{1}H NMR (700 MHz)

Time-course analyses were conducted according to standard procedures (Section 7.2.2). To monitor the turnover of 2-OG to 2-HG, 500 nM IDH1 variant was used. 1.5 mM of 2-OG and 1.5 mM of NADPH were used (both derived from a 10 mM stock solution). The reaction was monitored for one hour (33 ^{1}H experiments, Number of scans (NS): 16).

For time-courses monitoring by ^{1}H NMR the turnover of *DL*-isocitrate, 750 nM protein was used. After addition of 1.5 mM $NADP^+$ and 3 mM *DL*-isocitrate (both from a 10 mM stock solution), the reaction was monitored for two hours (66 ^{1}H assay points, NS: 16).

To compare the reaction rate of *DL*-isocitrate and *D*-isocitrate, and to confirm which enantiomer is used by IDH, potassium *D*-threo-isocitrate monobasic was utilised (purchased

from Sigma-Aldrich). Preparation of a 10 mM stock in NMR buffer gave pH 5. Therefore, the pH was adjusted to 7.5 using NaOH. For time-course analysis the same conditions as for *DL*-isocitrate were used, but the concentration of *D*-isocitrate was decreased to 1.5 mM.

2.12.4 Circular Dichroism (CD)

CD studies were conducted according to the Materials and Methods chapter (Section 7.2.4) with a Chirascan CD spectrometer (Applied Photophysics). After averaging (n = 3) and smoothing (window size: 4), Mean Residue Ellipticity (MRE) was calculated using the molecular weight of each protein and the number of amino acids (422). Calculations were conducted with Microsoft Excel and graphs made using the GraphPad prism software (version 5).

2.12.5 Analyses of Melting Temperature (T_M)

Analyses of T_m were conducted according to the Materials and Methods (Section 7.2.5) with a Chirascan CD spectrometer (Applied Photophysics). CD, DSC and DSF analyses was used according to standard procedures.

2.12.6 Non-Denaturing PAGE

Non-denaturing PAGE was conducted according to the Materials and Methods (Section 7.2.6). To inform on an appropriate buffer pH, the isoelectric point (IEP)of the proteins was calculated using the ExPASy ProtParam tool[153]. The IEPs can be found in **Table 2.13**.

***Table 2.13** | Isoelectric points of R132H, R132H S280F, R132C, R132C S280F, and R132C S280A.*

Protein	IEP
R132H	6.47
R132H S280F	6.47
R132C	6.44
R132C S280F	6.44
R132C S280A	6.44

A pH above the isoelectric point (IEP) ensured the protein to be negatively charged and to run towards the cathode. Additionally, the G-250 sample additive was added, an anionic dye binding to the protein to ensure migration towards the cathode. The gel chamber was set up accordingly and an 4-12% polyacrylamide Tris-Glycine gel used.

2.12.7 Non-Denaturing Mass Spectrometry

Non-denaturing mass spectrometry analyses were conducted according to Section 7.2.8. The theoretical mass of the IDH dimer was calculated and demonstrated by deconvoluting the mass spectrum obtained. Z values were calculated accordingly.

2.12.8 Analysis of Protein Copurification

To confirm whether $NADP^+$ or NADPH is bound, 50 µM of protein was buffer exchanged into NMR assay buffer using Micro Bio-Spin 6 Columns (Bio-Rad) according to Bio-Rad's protocol (equilibration 4 times), denatured in an NMR tube with boiling water for 2 minutes, span down, and a ^1H spectrum (700 MHz) recorded (Section 7.2.2). The cofactor was identified by spiking with 10 µL of a 20 mM solution.

Proteins for further analysis of copurification by denaturing or non-denaturing MS techniques were prepared and measured according to the Materials and Methods (Section 7.2.8). For spiking experiments, 1-10-fold molar excess was added. For DTT treatment 20-fold excess of DTT was added and the protein incubated overnight at 4°C. The sample was buffer exchanged the next day and subjected to non-denaturing MS analysis.

Treatment with Alkaline Phosphatase

Alkaline phosphatase buffer (pH 7.5, **Table 2.14**) was prepared according to the recipe below:

Table 2.14 **|** *Buffer composition for treatment with alkaline phosphatase.*

	C (mM)	n (mol)	M_w (Da)	V (L)	m (g)
Tris	50	0.005	121.14	0.1	0.6057
$MgCl_2$ (x 6 H_2O)	5	0.0005	203.3	0.1	0.10165
DTT	1	0.0001	154.253	0.1	0.015425
Glycerol (5% V/V)					5 mL

0.5 mg/mL of protein was diluted into the buffer as well as 20 Units of alkaline phosphatase. The sample was incubated at 37°C for 1.5 h and buffer exchanged into gel filtration buffer before it was subjected to denaturing MS analysis.

2.12.9 Substrate and Co-Factor Binding by DSF

DSF was conducted according to standard procedures (Section 7.2.5). Substrate and co-factor stocks (2x) were made in DSF buffer and added to the protein solution (3 μM). Changes in T_m were calculated based on the T_m of protein without cofactors.

2.12.10 Crystallographic Studies

2.12.10.1 Introduction of TEV-Cleavage-site

A gene encoding for the Tobacco Etch virus (TEV) cleavage site was introduced into a pET22b construct encoding for R132C S280F between the ORF and a gene encoding for the C-terminal hexahistidinetag. The forward primer was designed to include an Nde1 (CA*TATG) cleavage site, the reverse primer was designed to include an Xho1 (C*TCGAG) cleavage site. Both cleavage-sites were followed by a CCCGGG sequence to enhance restriction enzyme digest efficiency.

Similarly, primers to introduce an N-terminal TEV-cleavable hexahistidine tag were designed to include an Nde1 restriction site in the forward primer, and an Xho1 cleavage-site in the reverse primer.

2.12.10.1.1 Primer Design (TEV-cleavable His-tag)

Primer Name	Sequence
C.TEV_forward	CCCGGGCATATGTCCAAAAAAATCAGTGG CGGTTCTGTGGT
C.TEV_reverse-complement	CCCGGGCTCGAGGCCCTGGAAATACAAGT TTTCAAGTTTGGCCTGAGCTAGTTT
N.TEV_forward	CCCGGGCATATGCACCACCACCACCACCA CGAAAACTTGTATTTCCAGGGCTCCAAAA AAATCAGTGGC
N.TEV_reverse-complement	CCCGGGCTCGAGTCAAAGTTTGGCCTGAG CTAGTTT

2.12.10.1.2 Polymerase Chain Reaction (PCR)

PCR was conducted from a template encoding for R132C and a template encoding for the R132C S280F protein, respectively according to Materials and Methods (Section 7.1.5). Primers were designed according to the table above. To confirm successful PCR and to purify the PCR product, agarose gel (0.8% v/v in TAE buffer) electrophoresis was conducted. Bands corresponding to the PCR product were cut out and purified using GeneJET Gel Extraction Kit - Thermo Fisher Scientific according to a modified manufacturer`s protocol.

2.12.10.1.3 Restriction Digestion

The restriction digest for the PCR products encoding for R132C and R132C S280F was set up according to Materials and Methods (Section 7.1.5) at 37°C overnight. 1µg of the PCR product was used. Additionally, 1 µg of a plasmid containing the ORF for R132C (without cleavage-site) was digested to yield the empty pET22b vector. The reaction mixture was purified using Agarose gel electrophoresis (Section 7.1.3). Bands corresponding to the PCR product and the empty vector were cut out and purified using the GeneJET Gel Extraction Kit (Thermo Fisher Scientific according to a modified manufacturer`s protocol).

2.12.10.1.4 Ligation

For ligation, 50 ng of pET22b and a 3-fold molar excess of the insert (35.45 ng) was used according to the Materials and Methods (Section 7.1.5). The ligation reaction was allowed to proceed for 5 days at room temperature. 5 µL of the ligation mixture was transformed into 35 µL commercially available XL10 gold cells (Section 7.1.9) and grown overnight on LB Agar containing ampicillin.

2.12.10.1.5 Colony PCR

Several colonies of each construct were grown overnight in 2TY medium (5 mL) containing ampicillin and used for colony PCR (10 µL cell culture used) according to Materials and Methods (Section 7.1.5). The plasmid DNA from the remaining cultures was purified using a plasmid DNA Miniprep kit (Thermo Scientific). Samples were sent for sequencing to Eurofins.

2.12.10.1.6 Protein production in Lemo21

The plasmids were transformed into Lemo21 *E. coli* cells. One colony was picked, grown into a glycerol stock and stored at -80°C. Protein production was conducted according to standard procedures (Section 7.1.12).

2.12.10.1.7 Crystallography

Crystallisation was conducted applying the sitting drop vapor diffusion method. A 24 well Cryschem Plate (Hampton Research, USA) with a reservoir solution of 250 µL was used based on previous reports[154]. The enzyme (25 µL) was incubated for 1 h on ice with 10 mM NADPH (in H_2O, 10 µL), 20 mM $CaCl_2$ (in H_2O, 5 µL) and 200 mM 2-OG (in H_2O, 10 µL) to yield a final protein concentration of 12.8 mg mL^{-1}. Crystallisation was achieved by addition of 2 µL of the protein containing solution to 2 µL precipitant solution. The plates were sealed with StarSeal Advanced Polyolefin Film (Starlab, Germany) and crystals (100 µM average size) were grown within 14 days. To obtain crystals reproducibly seeding methods were employed by crushing crystals with the SeadBeat kit according to the manufacturer's protocol (Hampton Research, USA). Crystal containing droplets were cryo-protected by mixing them in a ratio of 1:1 with reservoir solution containing glycerol (25%), harvested with a nylon loop, and cryo-cooled in liquid N_2. The crystals were stored in liquid N_2 until data collection.

2.12.10.1.8 Data processing

Data were collected at 100 K using synchrotron radiation at Diamond Light Source (DLS) beamline I24. Data were indexed, integrated, and scaled using the Xia2[150] strategy of the beamline auto-processing pipeline. The crystal structure was determined by molecular replacement (MR) using the AutoMR (PHASER[155]) subroutine in PHENIX[156]. The search model used for MR was based on IDH1 R132H (PDB: 4KZO[154]). The structural model was optimised by iterative cycles of manual re-building in COOT[157] and crystallographic refinement in phenix.refine.[158]

Chapter 3

Inhibition Studies on Ivosidenib-Resistant *Hs* IDH1 Second-Site Variants

Contents

3 Inhibition Studies on Ivosidenib-Resistant *Hs* IDH1 Dimer-Interface Second-Site Variants

3.1 Introduction

Chapter 2 described how the introduction of the S280F substitution in the IDH1 R132C and R132H variants influences their kinetics, biophysics, and the chemistry at their dimer-interface and the active site. Since the acquired resistance to ivosidenib due to the S280F substitution has emerged in the clinic[28], no experimental evidence (except modelling[103]) on the mechanism of resistance, nor investigations on methods to overcome resistance, have been reported. Hence, kinetic, biophysical, structural, and cellular studies were conducted to aid understanding of the mechanism of S280F mediated drug-resistance and to investigate alternative ways to inhibit ivosidenib-resistant IDH1 variants.

3.2 Analyses of Inhibitor Binding to IDH1 Variants Based on Published Crystal Structures

Both IDH1 variants and IDH2 variants are structurally similar (**Figure 3.1**), and hence it is perhaps not surprising that IDH1 variant specific and IDH2 variant specific inhibitors are reported to bind in the same region at the dimer-interface.[159, 160, 161, 66, 83, 82, 124] Crystal structures of the dimers of IDH1 R132H and IDH2 R140Q align well with a backbone C_α RMSD of 0.81 Å (**Figure 3.1**). Thus, relatively small differences in the structures of IDH1 R132H and IDH2 R140Q seem to account for selectivity of the inhibitors to inhibit either IDH1 or IDH2. The α9 and α10 helices at the dimer-interface (**Figure 3.1**, right panel) display a high degree of structural similarity between IDH1 R132H and IDH2 R140Q, where the allosteric inhibitors are reported to bind.[159, 160, 161, 66, 83, 82, 124]

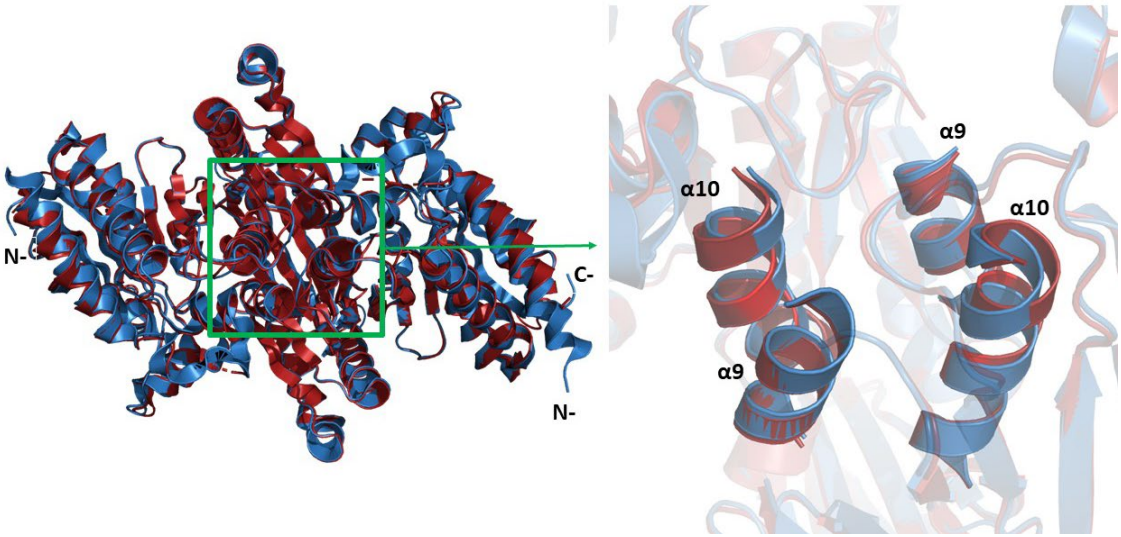

Figure 3.1 *| Views from a crystal structure of IDH1 R132H (blue, PDB ID: 4KZO[126]) superimposed with IDH2 R140Q (red, PDB ID: 5I95[162]). The dimer-interface is highlighted with a green box. A magnified section of the α9 and α10 helices at the dimer-interface is shown on the right side.*

There is no reported crystal structure and hence, no detailed binding information for the clinically approved inhibitor ivosidenib bound to an IDH1 variant. However, ivosidenib is proposed to bind between α9 and α10 based on structural studies with analogues.[102] The FDA-approved IDH2 inhibitor enasidenib has been shown to bind between α9 and α10.[124] It is therefore unsurprising that resistance acquired during treatment with these inhibitors correlates with substitutions on α10.[123] Patients bearing an IDH2 R140Q mutation treated with enasidenib, were observed to acquire either an IDH2 Q316E or an IDH2 I319M substitution (Section 1.8).[28] IDH2 I319 is homologous to IDH1 S280. Acquired resistance is reported due to a S280F substitution in patients with an IDH1 R132C variation treated with ivosidenib (**Figure 3.2**).[28]

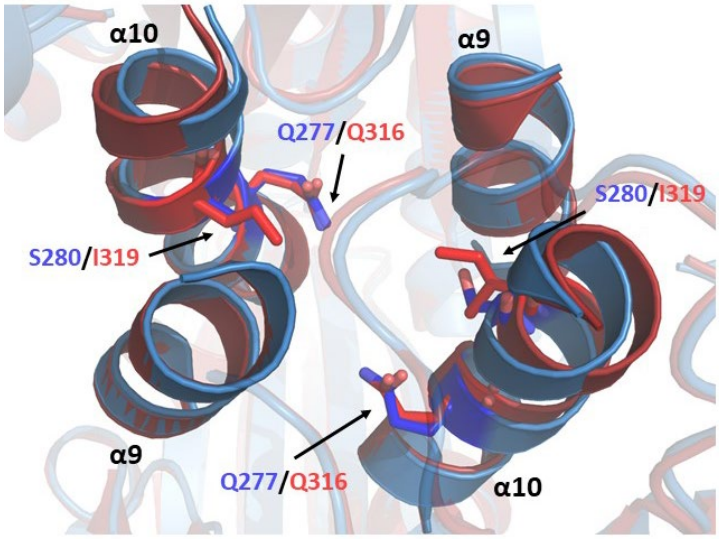

***Figure 3.2** | Views from a crystal structure of IDH1 R132H (blue, PDB ID: 4KZO[126]) superimposed with IDH2 R140Q (red, PDB ID: 5I95[162]). IDH1 residues Q277 and S280 on the α10 helix and their homologous IDH2 residues Q316 and I319 are shown as sticks.*

3.2.1 Analysis of Potential Inhibitor Resistance in S280F Variants

The S280F substitution at the IDH1 dimer-interface could interfere with inhibitor binding if it makes essential interactions with the S280 residue or if the inhibitor binds near to S280. Available crystal structures of inhibitors bound to IDH1 variants were analysed for their potential to retain activity in IDH1 variants with an S280F substitution. Several of these inhibitors are in clinical trials[163,164,92,165,166] and are potential second-line treatments for patients with IDH1 variants with an acquired S280F substitution, or part of a combination regimen. The crystal structures of inhibitors from various pharmaceutical pipelines (AG-881, GSK321, IDH305, Cmpd1, BAY-1426032, FT-2102, DS-1001B; **Figure 3.3**) bound to an IDH1 variant were investigated carefully (**Figure 3.4**, **Figure 3.5**).

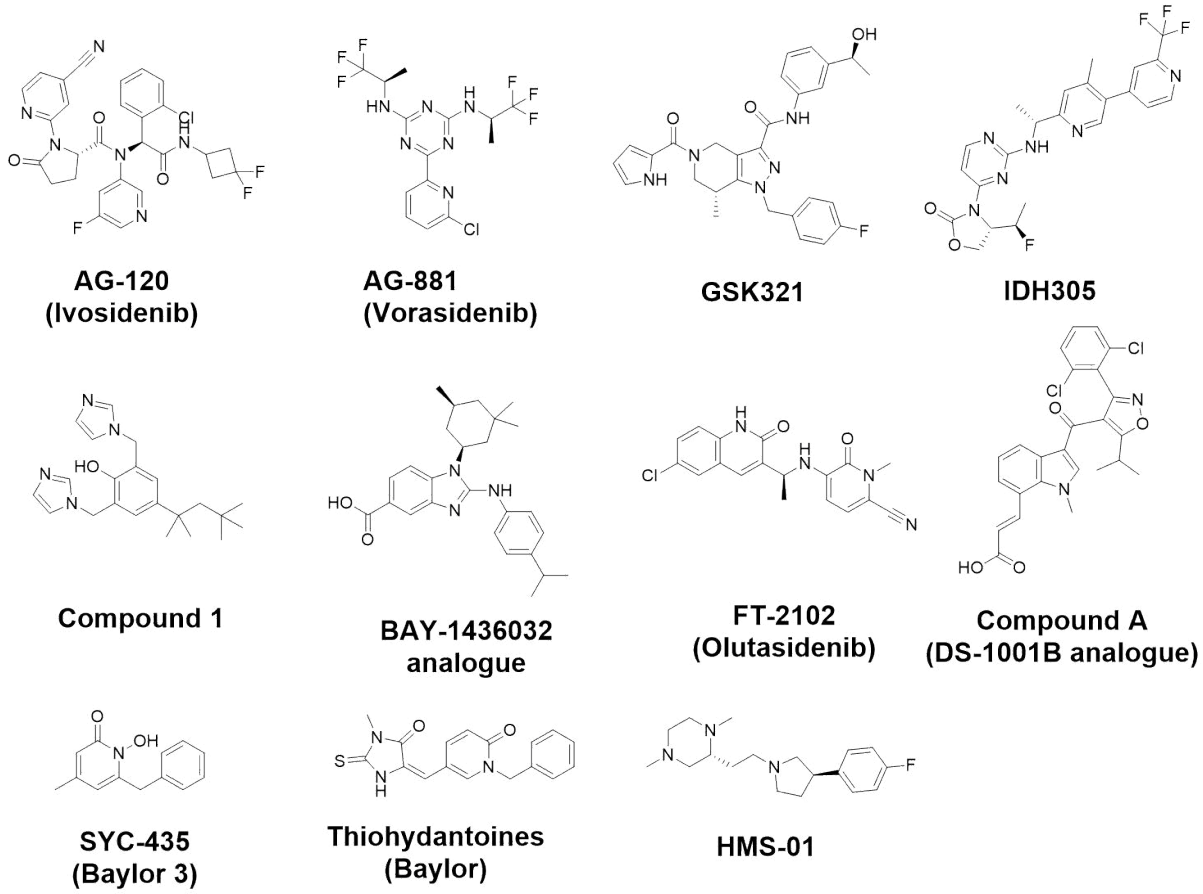

***Figure 3.3** | Structures of published IDH inhibitors[66, 58, 131, 167, 168, 79, 169, 82, 83] which were analysed for their binding to IDH1 R132H or IDH1 R132C (see **Figure 3.4**).*

As shown by crystallographic studies, AG-881[56], Cmpd1 (Sanofi)[78], and an analogue of BAY-1436032[170] bind with a stoichiometry of one inhibitor molecule per IDH1 dimer. GSK321[171], FT-2102[172], and an analogue of DS-1001B[89] bind with a ratio of two molecules to one IDH1 dimer. IDH305[73] was observed to bind with a stoichiometry of three molecules to each IDH1 dimer (**Figure 3.4**).

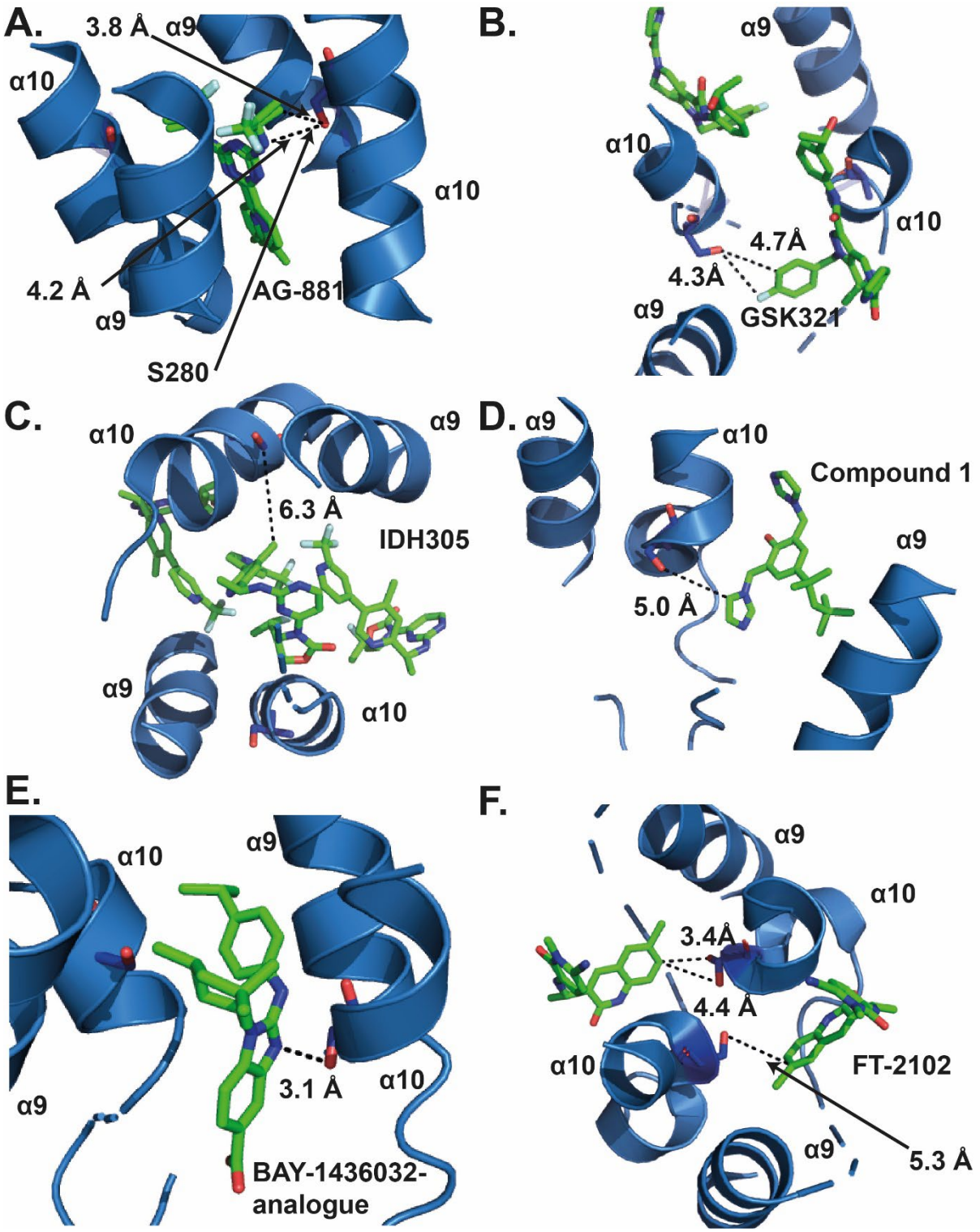

***Figure 3.4** | View from crystal structures of IDH1 R132H (blue) showing the binding mode of several IDH1 inhibitors: **A.** AG-881 (PDB: 6ADG[56]), **B.** GSK321 (PDB: 5DE1[171]), **C.** Novartis IDH305 (PDB: 6B0Z[73]), **D.** Sanofi Cmpd1 (PDB: 4UMX[78]), **E.** a BAY-1436032-analogue (PDB: 5LGE[170]), or **F.** FT-2102 (PDB: 6U4J[177]). The inhibitors are shown in green sticks.*

There is no direct binding interaction reported for the inhibitor AG-881 with residue S280 (**Figure 3.4**, A).[104] Analyses of the crystal structure of IDH1 R132H with AG-881[56] bound show that AG-881 is not in position to form a hydrogen bond with S280 *in crystallo*; however,

hydrogen bonding between the hydroxyl group of S280 and the exocyclic nitrogen of AG-881 could be possible in solution. The atoms of AG-881 (C-atom of methyl group) closest to the S280 residue (O-atom of side chain) are separated by 3.8 Å, which may result in steric interference with inhibitor binding as a result of the S280F substitution (**Figure 3.8**). According to this preliminary analysis, the S280F substitution may interfere with AG-881 binding due to the potential loss of a hydrogen bond to S280 and steric hindrance imposed by the phenylalanine side chain. Analysis of a crystal structure of GSK321 bound to IDH1 R132H (**Figure 3.4**, B)[171] shows the S280 side chain oriented away from the inhibitor with a distance of 4.3 Å between the serine O-atom and the fluor-atom of GSK321. There is the potential for resistance as a result of the S280F substitution (due to steric hindrance), however, on the basis of this preliminary analysis, this is less likely than for AG-881. IDH305 binding is analysed as an example for the IDH inhibitor series from Novartis (**Figure 3.4**, C). The S280 side chain is oriented towards IDH305 but is distant from it (6.3 Å distance between the closest C-atom of the serine side chain and the closest C-atom of IDH305). As such, IDH305 may retain activity against S280F dimer-interface variants. Sanofi-1 (**Figure 3.4**, D) is 5.0 Å from the S280 side chain (measured between the serine O-atom and a C-atom of the imidazolium ring of compound 1) which is oriented towards the inhibitor. Resistance due to an S280F substitution is unlikely due to the large distance between Sanofi-1 and S280 but remains a possibility. **Figure 3.4** (E) shows the binding of an analogue of BAY-1436032 via hydrogen bonding with S280; this interaction is reported to be important for binding of the inhibitor [170]. An S280F dimer-interface variant would result in loss of this important interaction and may consequently, lead to resistance against BAY-1436032. For the crystal structure of IDH1 R132H with the inhibitor FT-2102 (**Figure 3.4**, F), different conformations of the S280 residue were modelled. [172] The closest distance of FT-2102 to S280 is 3.4 Å (measured between the O-atom of the serine side chain and the closest C-atom of the quinoline ring of FT-2102). Resistance by the dimer-interface variant S280F against FT-2102 could hence be possible; however, in the analysed structure of IDH1 R132H, the S280 residue is oriented away from the inhibitor.

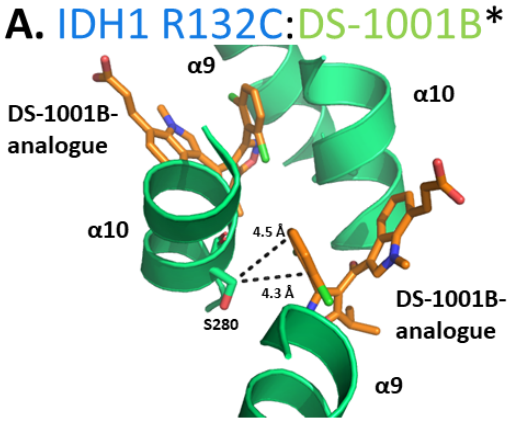

B.

Inhibitor	Shortest distance to S280
AG-881	3.8 Å
GSK321	4.3 Å
IDH305 (Novartis)	6.3 Å
Compound 1 (Sanofi)	5 Å
BAY1436032*	3.1 Å (HB)
FT-2102	3.4 Å
DS-1001B*	4.3 Å

Importance of residue highlighted in publication
Importance according to crystal structure
potential resistance
resistance unlikely

***Figure 3.5** | Inhibitor binding to IDH1 R132C and summary of inhibitor binding analyses. **A.** View from a crystal structure of IDH1 R132C complexed with an DS-1001B-analogue (PDB: 6IO0).[89] **B.** Summary table of interactions of the S280 residue in crystal structures of R132H with AG-881, GSK321, IDH305, Compound1, a BAY-1436032 analogue, and FT-2102, or R132C with a DS-1001B analogue. * Crystal structure analyses are based on inhibitor analogues as they are the only crystal structures reported. HB: Hydrogen bond.*

A crystal structure of an analogue of the inhibitor DS-1001B (Compound A, **Figure 3.5**, A) bound to IDH1 R132C[89] shows binding at the dimer-interface with a distance of 4.3 Å to S280 (closest C-atom of the serine side chain and the closest C-atom of the dichloro phenyl ring of Compound A), which is oriented away from the DS-1001B-analogue. As such, there is potential for interference of DS-1001B binding with the S280F substitution.

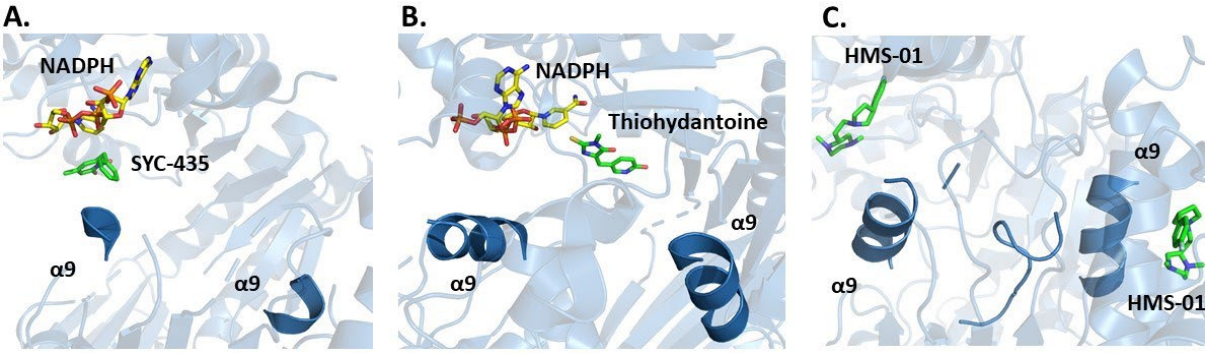

***Figure 3.6** | Inhibitor binding in the active site close to the NADPH binding site. **A.** View from a crystal structure of R132H complexed with SYC-435 (PDB: 4I3L[60]). The α10 helix is not resolved while only parts of the α9 helix are. **B.** View from a crystal structure of R132H complexed with a 2-thiohydantoin compound. (PDB: 4XRX[61]). The α9 helix is resolved but not the α10 helix. **C.** View from a crystal structure of R132H complexed with HMS-01. The α9 helix is resolved but not the α10 helix. (PDB:6Q6F[62]).*

Most IDH1 variant inhibitors bind allosterically at the dimer-interface.[159, 160, 161, 66, 83, 82] However, as highlighted in the introduction (Section 1.7.2), there are several inhibitors with a different mode-of-action, i.e. which bind in the active site close to the NADPH binding site (i.e. SYC-435[60], a thiohydantoine series[61], HMS-01[62]; **Figure 3.3**). In crystal structures of IDH1 R132H complexed with inhibitors in the active site, large regions of the α10 helices are disordered. The α10 helix is stabilised through binding of 2-OG in the active site or inhibitors

at the dimer-interface. In summary, although they are relatively weak inhibitors of IDH1 variants, SYC-435, the thiohydantoine series, and HMS-01 might not be directly affected by the S280F substitution (**Figure 3.6**).

3.2.2 Analysis of Other Potential Second-Site Variant Inhibitor Resistances

The analysis of reported IDH1-inhibitor crystal structures was then extended to investigate residues which are generally important for inhibitor binding. It was considered that such analysis may help in understanding which residues other than S280 are prone to resistance-causing substitutions. One interesting residue to investigate is IDH1 Q277, because acquired resistance of its homologous residue (IDH2 Q316) has been reported after treatment with enasidenib.[28] Similarly to S280, Q277 is located on α10 at the dimer-interface. The importance of Q277 for inhibitor binding was analysed using the same crystal structures as used in Section 3.2.1. The results are exemplified by AG-881 bound to IDH1 R132H in **Figure 3.7** (A). Q277 is important for binding of AG-881, as the amido nitrogen of the sidechain of Q277 in both monomers is positioned to form a hydrogen bond to the triazine ring of AG-881. The sidechain carbonyl groups of the Q277 residues from each monomer are also positioned to form a hydrogen bond with the exocyclic amino group of AG-881. Potential AG-881 resistance could therefore be caused by variations of the Q277 residue. As previously discussed, a IDH2 Q316E substitution, linked to acquired enasidenib resistance, is reported.[28] Hence, as described in Section 4.2, the IDH1 Q277E substitution was introduced into the IDH1 R132H variant, to test whether it causes resistance against AG-881.

The same set of inhibitors described in Section 3.2.1 was used to analyse the potential importance of Q277 for inhibitor binding in crystal structures of IDH1 R132H or IDH1 R132C (**Table 3.1**). The results indicate potential hydrogen bonds of IDH305 (Novartis) and BAY-1436032 to the amido nitrogen protons of Q277. Hence, it was proposed that treatment of patients with these inhibitors could result in the acquired second-site substitution Q277E.

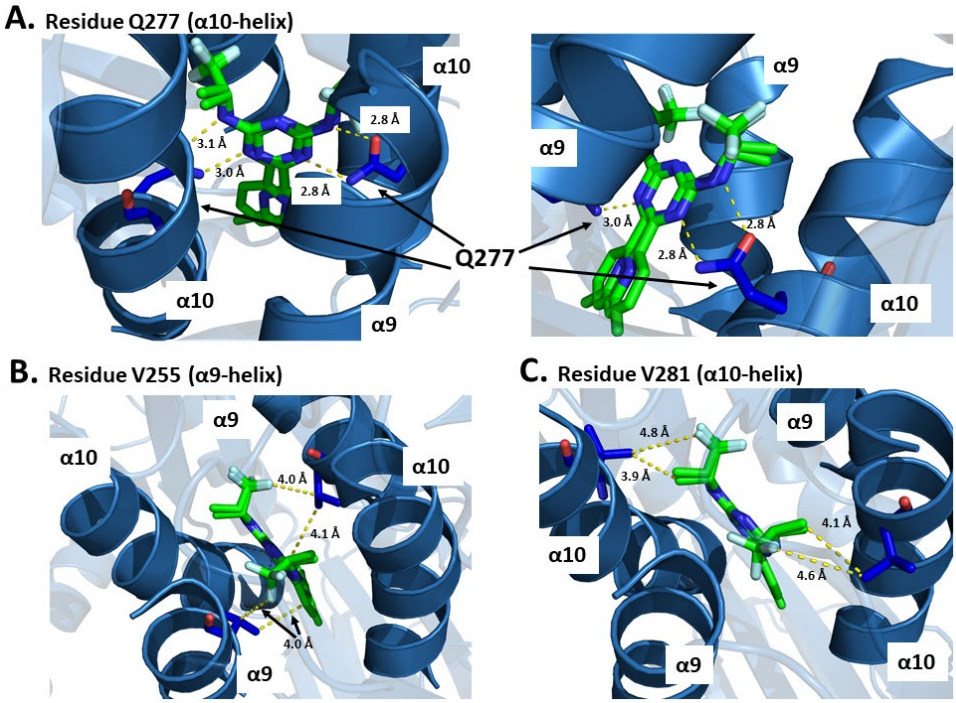

***Figure 3.7** | View from a crystal structure of IDH1 R132H bound to AG-881 (PDB: 6ADG[56]). **A.** Distances of AG-881 to Q277 in both monomers. **B.** Distances of AG-881 to V255 in both monomers. **C.** Distances of AG-881 to V281 in both monomers.*

During analyses of the inhibitor-bound crystal structures of IDH1 R132H and IDH1 R132C, two residues which are often involved in inhibitor binding, or which are in close proximity to the inhibitor became apparent, i.e. V255 on α9 and V281 on α10. IDH1 V255 and V281 are reported to play a role in the binding of AG-881 to IDH1 R132H (**Figure 3.7**, B/C).[58] The trifluoropropane moiety of AG-881 is positioned to make Van der Waals interactions with the side chains of V255 and V281 (**Figure 3.7**). Variations of V255 and V281 could therefore interfere with inhibitor binding. A potentially acquired variation during treatment with AG-881 could therefore be a V255F or V281F mutation because a substitution to phenylalanine will likely interfere with inhibitor binding due to its bulkiness (V255 and V281 are as close to AG-881 as 4.0 Å or 3.9 Å (closest C-atom of the side chains of V255 or V281 and the fluorine atom of AG-881, respectively)). Analyses of the importance of V255 and V281 for inhibitor binding (same set of inhibitors described in Section 3.2.1) in other inhibitor-bound crystal structures of IDH1 R132H and IDH1 R132C are summarised in **Table 3.1**.

Table 3.1 *| Summary table of the interactions of the residues V255, Q277, and V281 with inhibitors in crystal structures of R132H with AG-881, GSK321, IDH305, Compound 1 (a BAY-1436032 analogue), FT-2102, and R132C with a DS-1001B analogue. The likelihood of interference with inhibitor binding due to a substitution at the residues (assuming V255F, Q277E, V281F substitutions) is estimated.*

Inhibitor	IDH1 V255	IDH1 Q277	IDH1 V281
AG-881	4.0 Å	2.8 Å (HB)	3.9 Å
GSK321	4.4 A		3.1 Å
IDH305 (Novartis)	3.9 Å	3.3 Å (potential HB)	3.7 Å
Compound 1 (Sanofi)	4.3 Å		3.7 Å
BAY1436032*	4.4 Å	3.6 Å (potential HB)	3.1 Å
FT-2102	5.1 Å		3.7 Å
DS-1001B*	3.7 Å		3.7 Å
importance of residue highlighted in paper			
could be important according to crystal structure analysis			
potential resistance			
resistance unlikely			
not resolved in published crystal structure/residue not exposed to dimer-interface			

Two IDH1 residues, V255 and V281, are spatially close to where most inhibitors are proposed to bind at the dimer interface. Hence, sidechain variations occurring at these two residues (and Q277) could result in inhibitor resistance. Therefore, the genes encoding for these residues were mutated by SDM and constructs for the production of recombinant IDH1 R132H V255F, IDH1 R132H Q277E, and IDH1 R132H V281F variants were made, in addition to IDH1 R132H S280F and IDH1 R132C S280F. IDH1 R132H V255F, IDH1 R132H Q277E, and IDH1 R132H V281F will be discussed in Chapter 4. Please note that in the subsequent chapter all variants are IDH1 based, except where stated.

3.3 Loss of Inhibition by Ivosidenib

As previously discussed (see Section 1.7), the exact binding mode of ivosidenib to IDH1 variants is unknown due to the unavailability of a crystal structure. One modelling study has suggested that ivosidenib resistance due to the S280F variation is solely due to steric hindrance[102], while another modelling study concluded that the resistance is due to a mix of steric hindrance by phenylalanine and the loss of a hydrogen bond of ivosidenib to S280.[103] It was shown that ivosidenib is inactive (100 µM) against R132C S280F[102], but there are no further studies on isolated R132C S280F or R132H S280F variants.

To explore the potential steric effect of a phenylalanine substitution at position 280, a crystal structure of AG-881 bound to R132H was used to model the potential clash using the PyMOL modelling tool.

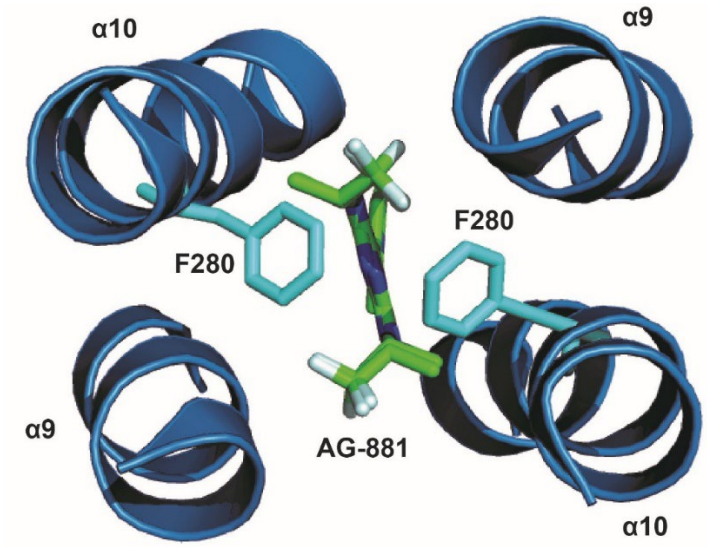

***Figure 3.8** | View from the dimer-interface of a crystal structure of R132H complexed with AG-881 (green sticks; PDB: 6ADG[56]). The PyMOL modelling tool was used to illustrate the steric effect of an S280F substitution (cyan sticks).*

While this approach does not take molecular dynamics into consideration, the model should serve as an illustration to aid initial understanding of the potential effects of the S280F substitution on inhibitor binding. Modelling of the S280F substitution shows the proximity of the bulky phenylalanine side chain to the triazine core and methyl groups of AG-881 (**Figure 3.8**). Due to the phenylalanine side chains being spatially close to AG-881, the S280F substitution likely interferes with binding of AG-881 to IDH1.

3.3.1 Inhibition Studies on Ivosidenib Including IDH1 R132C S280A

To investigate the clinical resistance to ivosidenib experimentally, an R132C S280A variant was produced. [123] Full inhibition of R132C S280A by ivosidenib would suggest that resistance by S280F is due to the steric effect of phenylalanine and the newly formed hydrophobic pocket (Section 2.10). A lack of inhibition of the R132C S280A variant would suggest that the reason for S280F mediated drug-resistance is due to the loss of the serine sidechain, e.g. the loss of a potential hydrogen bond. Kinetic studies on R132C S280A were described in Section 2.6, and showed it has a similar activity to R132C and R132C S280F.

Ivosidenib was screened (10 μM) against R132C, R132C S280F, R132H, R132H S280F, and R132C S280A using an NADPH absorbance assay as described in Section 2.3 (400 nM IDH1 variant; **Figure 3.9**, A). As anticipated, there was full inhibition of R132C and R132H, but no

inhibition of R132C S280F and R132H S280F. Enzymatic activity of R132C S280A was inhibited 60%.

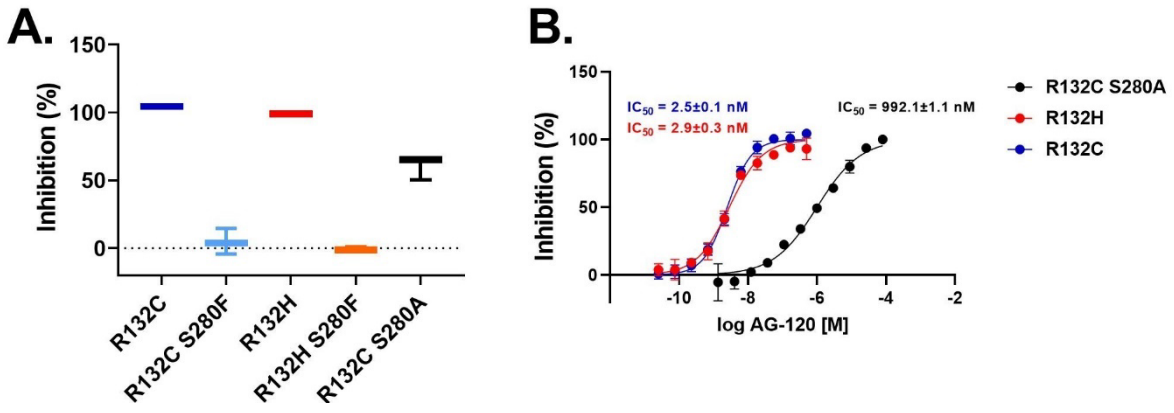

***Figure 3.9** | Inhibition Studies on R132C, R132C S280F, R132C S280A, R132H, and R132H S280F with ivosidenib. **A.** Inhibition (%) of ivosidenib (10 µM) against IDH1 variants (400 nM). Error bars: standard errors of the mean (n = 3). **B.** IC_{50} determination of ivosidenib against R132C, R132C S280A, and R132H. Dose-response graph with standard errors of the mean (n = 3). Conditions: 100 mM Tris, 10 mM $MgCl_2$, 0.2 mM DTT, 0.005 % Tween 20, 0.1 mg/mL BSA (pH 8.0). 2-OG: 1.5 mM, NADPH: 0.3 mM.*

Subsequently, the potency of ivosidenib was determined more precisely. IC_{50} determination is a useful measure to compare inhibitor potencies. The response (i.e. inhibition) of an enzyme against different doses of inhibitor is measured. The IC_{50} value is the inhibitor concentration at which the inhibition is half-maximal (i.e. 50 %). To determine the potency of ivosidenib for R132C, R132H, and R132C S280A, the NADPH absorbance assay (30 nM enzyme; see Section 3.10.1) was employed. Different concentrations of inhibitor were incubated with the enzyme and 10 mM $MgCl_2$. NADPH and 2-OG were then added to initiate the reduction of 2-OG to 2-HG, and the turnover was measured by NADPH absorbance at 340 nm. The enzymatic activity without inhibitor (i.e. 0 % inhibition) and a no enzyme control (i.e. 100 % inhibition) were used to normalise inhibitory activity. The normalised inhibition was plotted against inhibitor concentration (logarithmic) and the IC_{50} determined by non-linear regression curve-fit using the GraphPad Prism software (version 5) using the equation: y = Bottom + (Top-Bottom)/(1+10^((LogIC_{50}-x)*HillSlope)) (**Figure 3.9**, B).

Ivosidenib was observed to inhibit R132C (IC_{50} = 2.5 nM) and R132H (IC_{50} = 2.9 nM) with high potency, as expected based on previous reports (**Figure 3.9**). [63] The IC_{50} ivosidenib against R132C S280A increased ~500-fold (IC_{50} = 992.1 nM) compared to R132C suggesting that serine-280 plays a role in ivosidenib binding. However, in combination with screening data at 10 µM inhibitor (**Figure 3.9**, A), these observations are consistent with the proposal that

substantial loss of potency of ivosidenib against R132C S280F is also due to the steric hindrance of the phenylalanine side chain and the new hydrophobic pocket (see Section 2.10).

3.3.2 Binding Studies of Ivosidenib

To investigate the binding of ivosidenib to R132C, R132C S280F, R132C S280A, R132H, and R132H S280F, non-denaturing MS and CPMG-edited ^{1}H NMR were employed.

3.3.2.1 Binding studies by non-denaturing MS

Non-denaturing MS studies, which can be used to study binding of non-covalent substrates/inhibitors to proteins in the native state in the gas phase, were conducted as described in Section 2.7. Ivosidenib stock solutions were prepared in MeOH to employ a volatile solvent suitable for electrospray ionisation. Different concentrations of ivosidenib were added to the protein (20 µM) and analysed by non-denaturing MS. To illustrate observations obtained by non-denaturing MS studies, examples of binding with 5 µM (4:1 protein: inhibitor), 20 µM (1:1), and 160 µM (1:8) ivosidenib are shown in **Figure 3.10**.

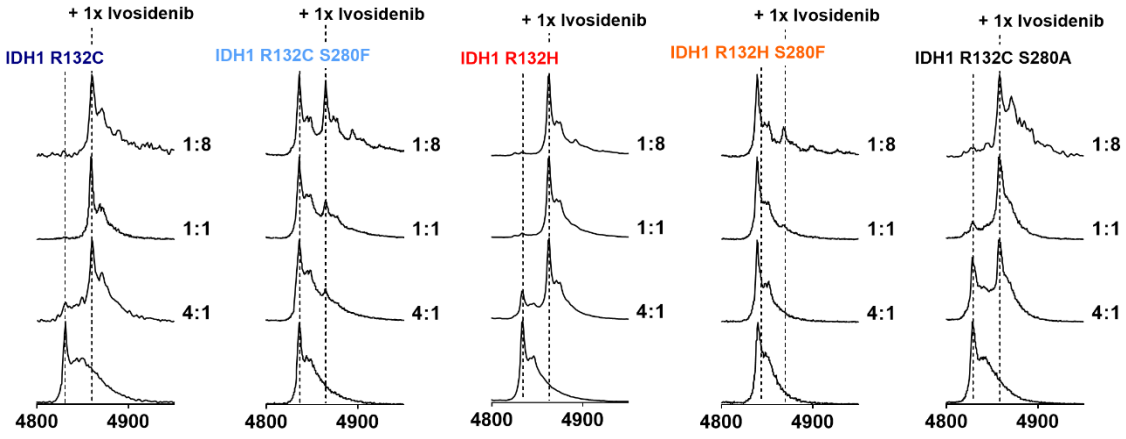

Figure 3.10 *| Non-denaturing MS spectra showing binding of ivosidenib to IDH1 variants. IDH1 variants are predominantly dimeric with 2 NADPH molecules bound - left dashed line. Ivosidenib was titrated at final concentrations of 5 µM (4:1), 20 µM (1:1), and 160 µM (1:8). Binding is indicated by a mass shift. Cone-voltage: 100 V.*

Binding of an inhibitor to a protein can be investigated by a mass shift of the signal corresponding to the IDH1 variant on incubation with an inhibitor. It can be clearly observed that ivosidenib binds with a stoichiometry of one inhibitor molecule per IDH1 dimer, consistent with previous reports.[48] While ivosidenib seemed to bind with high affinity to R132C and R132H, as indicated by the observation of binding at low ivosidenib concentrations (4:1 protein to ivosidenib ratio), clear differences were observed for the other variants. Both R132C S280F and R132H S280F appear to lose affinity for ivosidenib compared to R132C and R132H, as

indicated by the low abundance of the protein-inhibitor complex even at high ivosidenib considerations. This observation suggests that the S280F substitution interferes with ivosidenib binding. Binding to R132C S280A was weaker than to R132C, but better than to R132C S280F. This is in accord with results from inhibition assays (**Figure 3.9**) showing reduced inhibition of an R132C S280A variant, but no inhibition (at 10 µM) of an R132C S280F variant.

The non-denaturing MS approach was used to determine the dissociation constant (K_D) of the ivosidenib-IDH1 complex, which is a measure of the affinity of a substrate to a large protein. IDH1 variants were mixed with different concentrations of inhibitors and the fraction of inhibitor-protein complex was calculated using the intensity of the signal compared to the protein-only signal. Because of the shoulder of the IDH1 dimer signal (corresponding to a subset of the protein which is (phospho)-gluconoylated, Section 2.8), a baseline correction was applied. The charge states z = 19, z = 20, and z = 21 (Section 2.8.1) were used for analysis. The fraction of protein-inhibitor complex (PL/[P+PL]) was plotted against inhibitor concentration and the K_D calculated using GraphPad prism's non-linear regression curve fit with a one-site specific binding model.

The K_D values of ivosidenib as determined by non-denaturing MS for R132C and R132H were very similar, while binding to R132C S280F and R132H S280F was below 50% at 160 µM (K_D > 160 µM, **Figure 3.11**). Binding to R132H S280F seemed to be more impaired than to R132C S280F. The K_D value for R132C S280A was doubled compared to R132C.

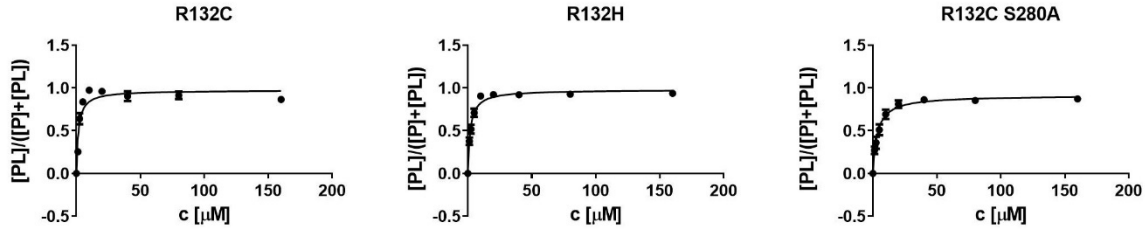

Figure 3.11 | ***Binding analyses of ivosidenib by non-denaturing MS.*** *The dissociation constant (K_D) was determined by titrating the inhibitor (in MeOH) into an IDH1 variant solution (20 µM) and analysed using non-linear regression. The bound fraction was plotted against inhibitor concentration. [PL]/([P]+[PL]) represents the fraction of the protein-inhibitor complex. Errors: standard errors of the mean (n= 3 of z= 19, 20, 21). Conditions: non-denaturing MS was carried out in ammonium citrate buffer (200 mM, pH 7.5). Cone-voltage: 100 V.*

3.3.2.2 Binding Studies by CPMG NMR

While non-denaturing MS can be used to determine the dissociation constant of a protein-inhibitor complex, it has its drawbacks, i.e. it operates in the gas-phase. Hence, Carr-Purcell-Meiboom-Gill (CPMG)-edited ^{1}H NMR was employed to measure the binding of small molecules to a large protein complex in solution. Using CPMG-edited NMR, signals corresponding to large complexes can be filtered out.[173] Commonly, a total filter time of 40 ms is used. Consequently, this technique can be used to determine the affinity of a small molecule to an enzyme by observing the concentration-dependent decrease of the signal corresponding to free inhibitor *vs* inhibitor bound to the large protein complex. [173] A spectrum of the small molecule inhibitor (10 μM) is measured initially before enzyme is titrated into the solution. The PROJECT pulse sequence is applied for CPMG-edited ^{1}H NMR measurements.[173] As the concentration of enzyme increases, more of the small molecule binds to the large enzyme complex and the signal intensity of the free inhibitor decreases (exemplified in **Figure 3.12**). This corresponds to the fraction of small molecule bound and can be plotted against the concentration of enzyme which has been added. Using GraphPad Prism curve fit with a one-site specific binding model, the dissociation constant, K_D, can be determined.

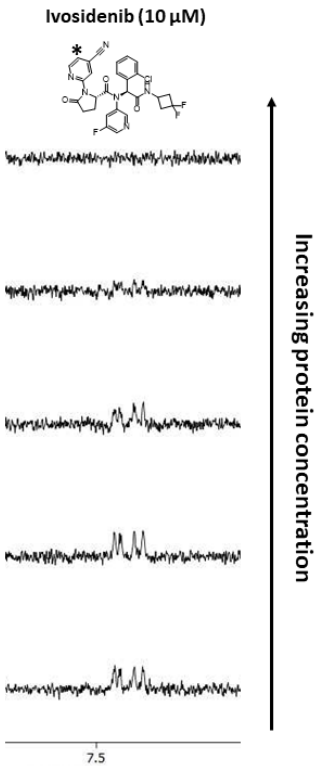

Figure 3.12 *| Spectra of ivosidenib (10 µM) with increasing concentrations of IDH1 variants as measured by CPMG-edited ^{1}H NMR (700 MHz) for the determination of ivosidenib binding affinity to IDH1 variants. Note: with increasing protein concentration, the signal corresponding to free inhibitor in solution disappears. The signal of inhibitor bound to the IDH1 variant is filtered out by the CPMG-pulse sequence. Proteins were titrated into ivosidenib (10 µM) in buffer containing 50 mM Tris-d_{11}, 100 mM NaCl (90:10 H_2O:D_2O, pH 7.5).*

A ^{1}H spectrum of ivosidenib (10 µM) was measured and increasing concentrations of IDH1 variants were titrated into the same tube (<10% volume increase). The concentration-dependent decrease of signals corresponding to ivosidenib was plotted against the concentration of protein. (**Figure 3.13**).

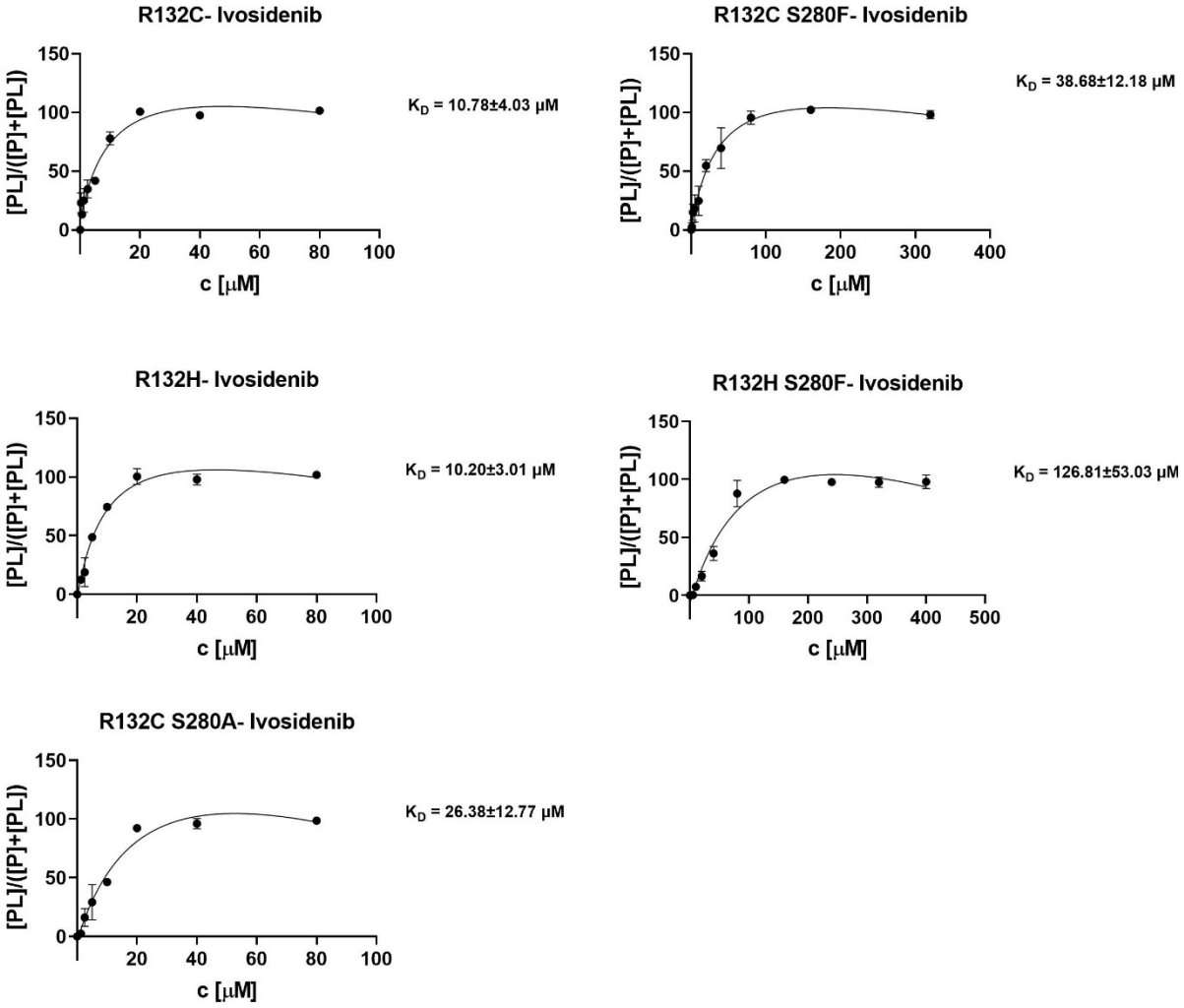

Figure 3.13 *| ^{1}H NMR binding studies using the CPMG-edited ^{1}H NMR. Proteins were titrated into 10 µM ivosidenib in buffer containing 50 mM Tris-d_{11}, 100 mM NaCl (90:10 H_2O:D_2O, pH 7.5). Errors: standard errors of the mean (n = 2).*

Consistent with data from non-denaturing MS, the K_Ds of ivosidenib for R132C and R132H were similar. The K_D of R132C S280F (K_D = 36.68 µM) was increased 4-fold relative to R132C (K_D = 10.78 µM), while the K_D for R132H S280F (K_D = 126.81 µM) was 13-fold higher than for R132H (K_D = 10.20 µM). For R132C S280A (K_D = 26.38 µM), the K_D was increased 2.5-fold compared to R132C. While the absolute K_Ds as measured by CPMG-edited ^{1}H NMR differ from K_Ds measured by non-denaturing MS, the trends between the variants are similar: the binding affinity to R132C S280F and R132H S280F is decreased substantially, while binding to R132C S280A is also decreased, but to a lesser extent.

Table 3.2 *| K_D values determined by non-denaturing MS (20 µM enzyme, n =3 (z = 19,20,21)) and using the CPMG Project pulse NMR sequence (10 µM enzyme, n =2). Errors: standard errors of the mean. Conditions: non-denaturing MS: see Figure 3.11 legend; CPMG NMR: see Figure 3.13 legend.*

	Non-denaturing MS (µM)	CPMG NMR (µM)
R132C	1.6±0.3	10.8±4.0
R132C S280F	> 160	38.7±12.2
R132H	1.9±0.2	10.2±3.0
R132H S280F	> 160	126.8±53.0
R132C S280A	3.4±0.5	26.4±12.8

In summary, the binding efficiency of ivosidenib to R132C S280F and R132H S280F is decreased substantially compared to that observed for R132C and R132H (**Table 3.2**). As determined by non-denaturing MS, binding at 160 µM ivosidenib is less than 50%. While the increase in K_D in solution as measured by CPMG-edited ^{1}H NMR is less pronounced than observed by non-denaturing MS, the binding affinity of ivosidenib is still substantially decreased (4-fold for R132C S280F and 13-fold for R132H S280F compared to R132C and R132H, respectively).

The results of non-denaturing MS and CPMG NMR studies indicate that the loss of binding efficiency of ivosidenib to R132H S280F is stronger compared to R132C S280F. The combined results of the binding assays for ivosidenib show that loss of binding affinity due to the S280F substitution is key part of inhibitor resistance. The K_D of R132C S280A is elevated 2-fold (non-denaturing MS) or 2.5-fold (CPMG-edited ^{1}H NMR) compared to R132C displaying a reduction of binding but to a lesser extent than for R132C S280F. This observation further adds to findings from ivosidenib inhibition experiments (**Figure 3.9**) against R132C S280A suggesting that the resistance is partly due to loss of a hydrogen bond to serine-280 but that the major effect is due to the steric hindrance imposed by the phenylalanine side chain and the new hydrophobic pocket.

3.3.2.3 Binding Studies by Differential Scanning Fluorimetry

To investigate binding of ivosidenib to IDH1 variants further, DSF studies were carried out as described in Section 2.9. Different concentrations of ivosidenib were added to IDH1 variants, and binding was indicated by an increase in T_m.

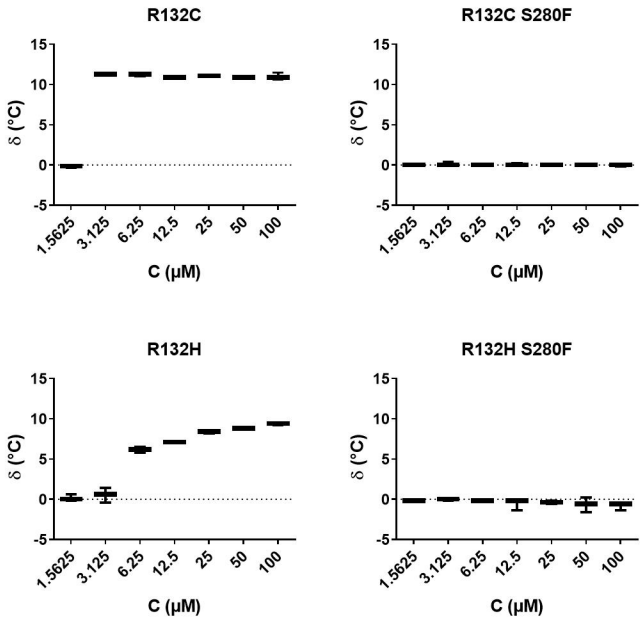

***Figure 3.14** | T_m-shift analyses of ivosidenib binding to Hs IDH1 variants by DSF. The plot shows the T_m difference compared to a sample containing protein only and the standard error of the mean (n = 3). Conditions: 3 µM enzyme in 50 mM Tris buffer, pH 7.5 (dye: Sypro Orange 3x).*

The addition of ivosidenib (AG-120) increased the thermal stabilities of R132C and R132H even at low concentrations. No increase in thermal stability was observed with of R132C S280F or R132H S280F (**Figure 3.14**). The results from the DSF analyses are consistent with the loss of binding affinity of ivosidenib as a result of the S280F substitution shown by non-denaturing MS and CPMG-edited ^{1}H NMR.

3.3.3 Inhibitor Screening

As described in Chapter 2, the IDH1 S280F substitution influences protein stability and kinetics. Importantly, crystal structure analysis (Section 2.10) shows that the sidechain of F280 is oriented towards the dimer-interface and builds a hydrophobic pocket interacting with W124 and W267. The formation of the hydrophobic pocket alters the flexibility and chemistry of the inhibitor binding site at the dimer-interface.

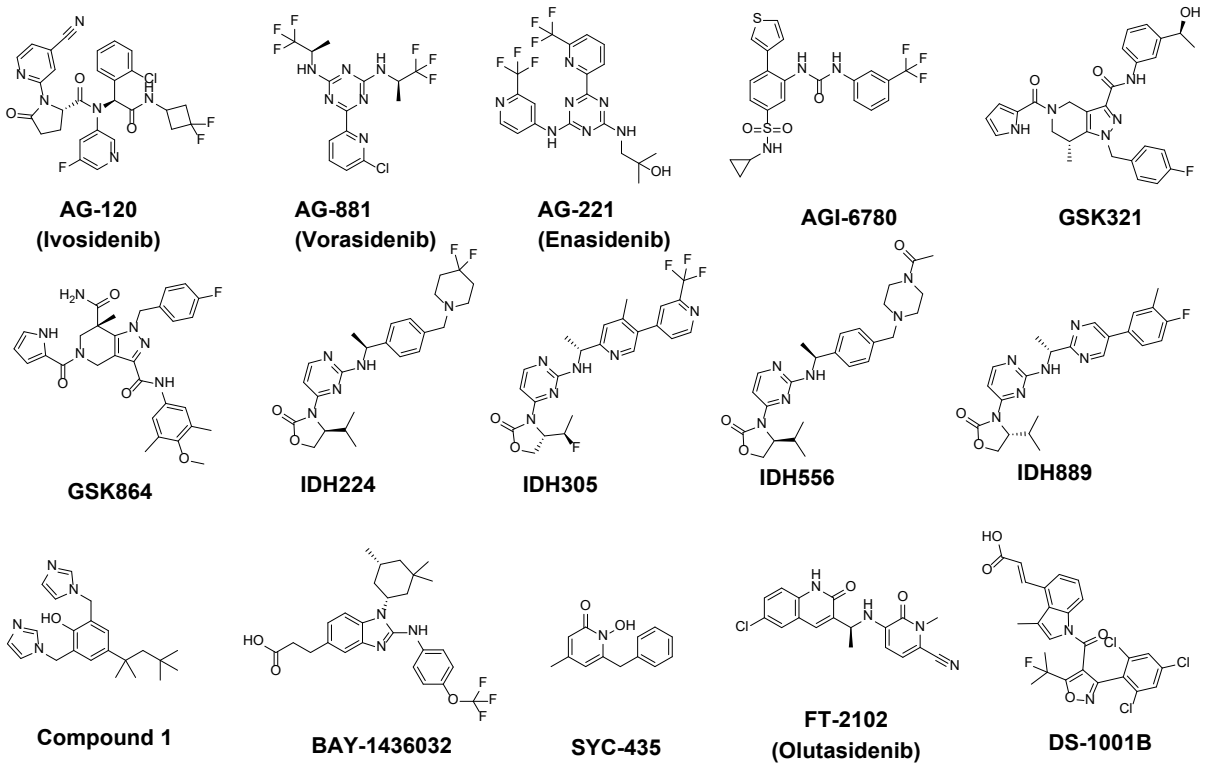

Figure 3.15 *| Known IDH1 variant inhibitors [66, 58, 131, 167, 168, 79, 169, 82, 83] used for inhibition screening against IDH1 R132C S280F and IDH1 R132H S280F.*

The inactivity of ivosidenib against R132C S280F and R132H S280F, due to the S280F substitution at the dimer-interface where allosteric inhibitors are reported to bind, highlights the need for the development of inhibitors with alternative binding/inhibition modes (e.g. potent active site inhibitors). Nevertheless, it is difficult to predict if other allosteric inhibitors could retain activity due to the complicated dynamics of the dimer-interface and the different residues involved in inhibitor binding (Section 3.2). Hence, commercially available allosteric inhibitors (**Figure 3.15**) were screened for inhibition against R132C S280F and R132H S280F (**Figure 3.16**). SYC-435 (Baylor 3) was also added to the screen, as it is the only commercially available non-allosteric IDH1 inhibitor.[60] As discussed in Section 1.7.2 it is in an early stage of development and generally less potent than allosteric inhibitors.

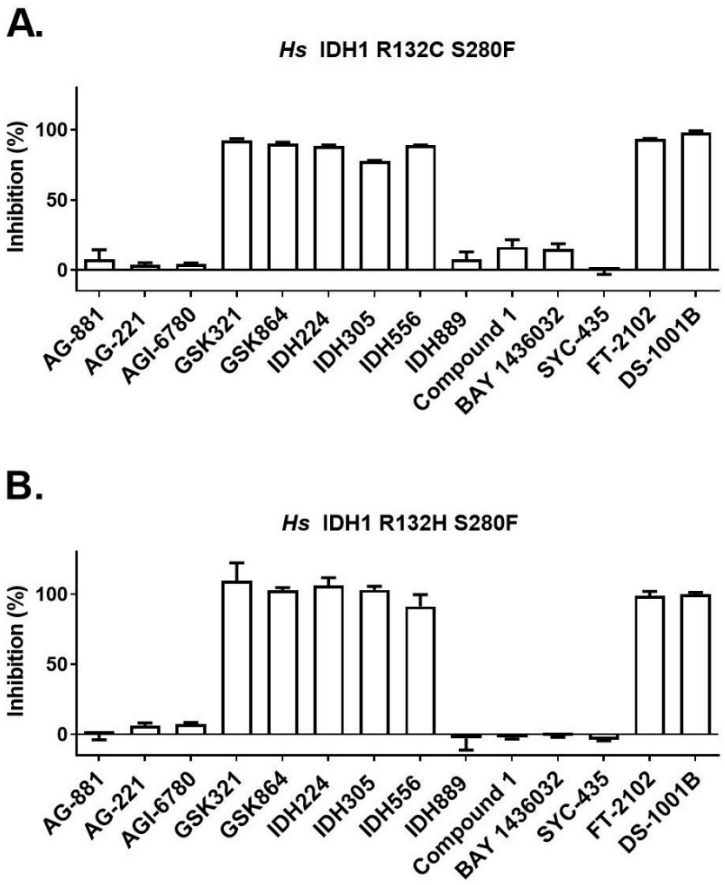

Figure 3.16 *| Inhibitor screening (%) against R132C S280F and R132H S280F (400 nM) using the NADPH absorbance assay. Error bars: standard errors of the mean (n = 3). Conditions: See Figure 3.9 legend.*

The inhibitor AG-881, which is awaiting phase 3 clinical trials (considered closest to approval in the pipeline of IDH1 inhibitors), was inactive against both R132C S280F or R132H S280F (**Figure 3.16**). IDH2 variant inhibitors (AG-221, AGI-6780), IDH889, Compound 1 (Sanofi), BAY1436032, and SYC-435 (Baylor 3) also did not exhibit inhibitory activity at 10 μM (**Figure 3.16**). However, several inhibitor series were active against R132C S280F and R132H S280F. These were a GSK series (GSK321, GSK864), a Novartis series (IDH224, IDH305, IDH556), FT-2102, and DS-1001B (**Figure 3.16**). Some of these inhibitors are in clinical trials (IDH305[165], FT-2102[164], DS-1001B[92]) and could be utilised in a clinical setting against ivosidenib-resistant S280F variants, should they prove to be potent inhibitors. Consequently, the potency of these inhibitors was determined against R132C S280F and R132H S280F and, for comparison, R132C and R132H.

3.3.4 IC_{50} Determinations

The IC_{50} determinations were conducted as described in Section 3.2.2. The dose-response curves are shown below for IDH1 R132C (**Figure 3.17**), R132C S280F (**Figure 3.18**), R132H (**Figure 3.19**), and R132H S280F (**Figure 3.20**).

3.3.4.1 Dose-Response Curves for IC_{50} Determination Against R132C

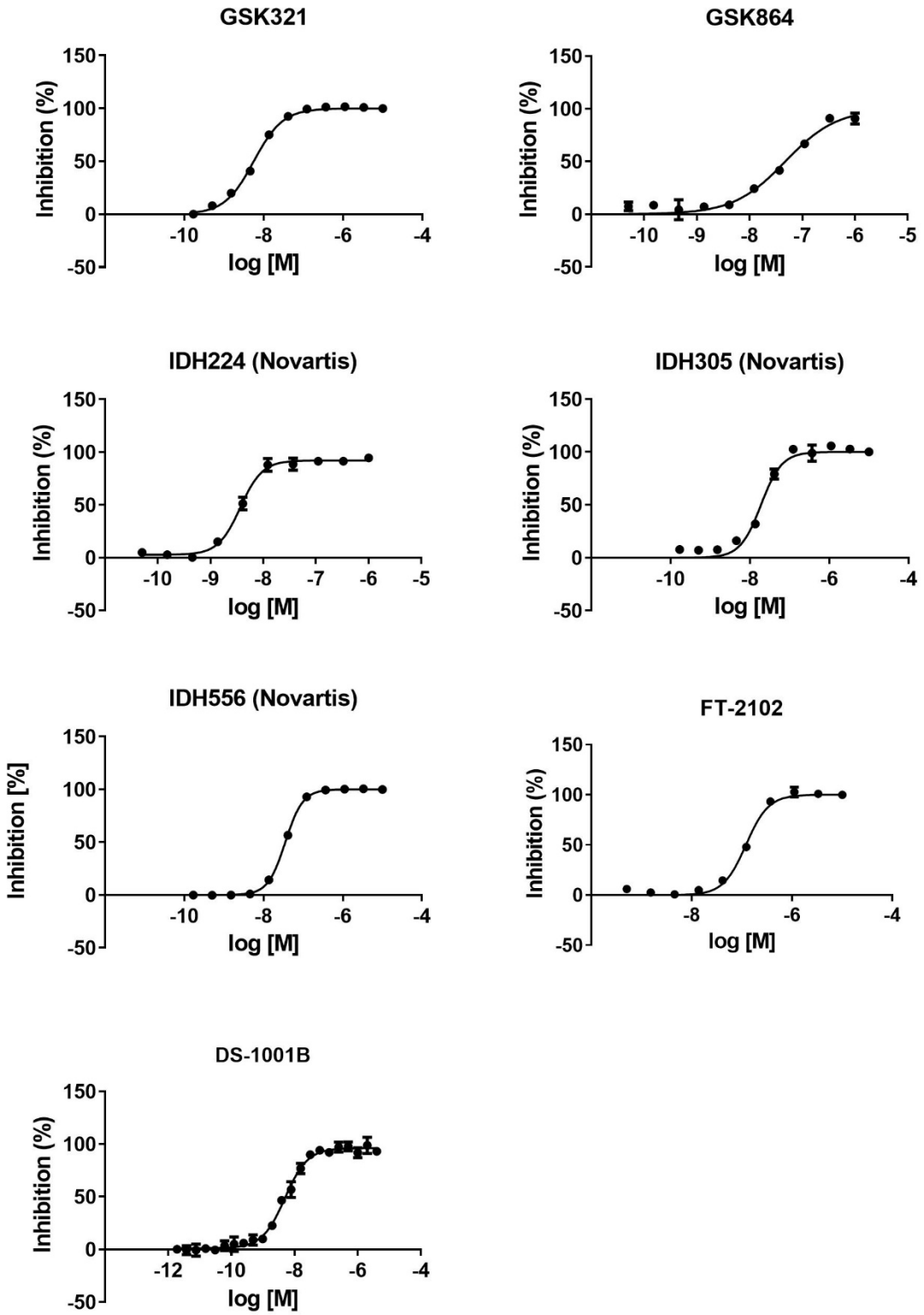

Figure 3.17| IC_{50} determination of inhibitors with IDH1 R132C. *Dose-response graphs of inhibitors with IDH1 R132C (30 nM) using an NADPH absorbance assay. Errors: standard errors of the mean (n = 3). Conditions: 100 mM Tris, 10 mM $MgCl_2$, 0.2 mM DTT, 0.005 % Tween 20, and 0.1 mg/mL BSA (pH 8.0). 2-OG: 1.5 mM, NADPH: 0.3 mM.*

3.3.4.2 Dose-Response Curves for IC_{50} Determination Against R132C S280F

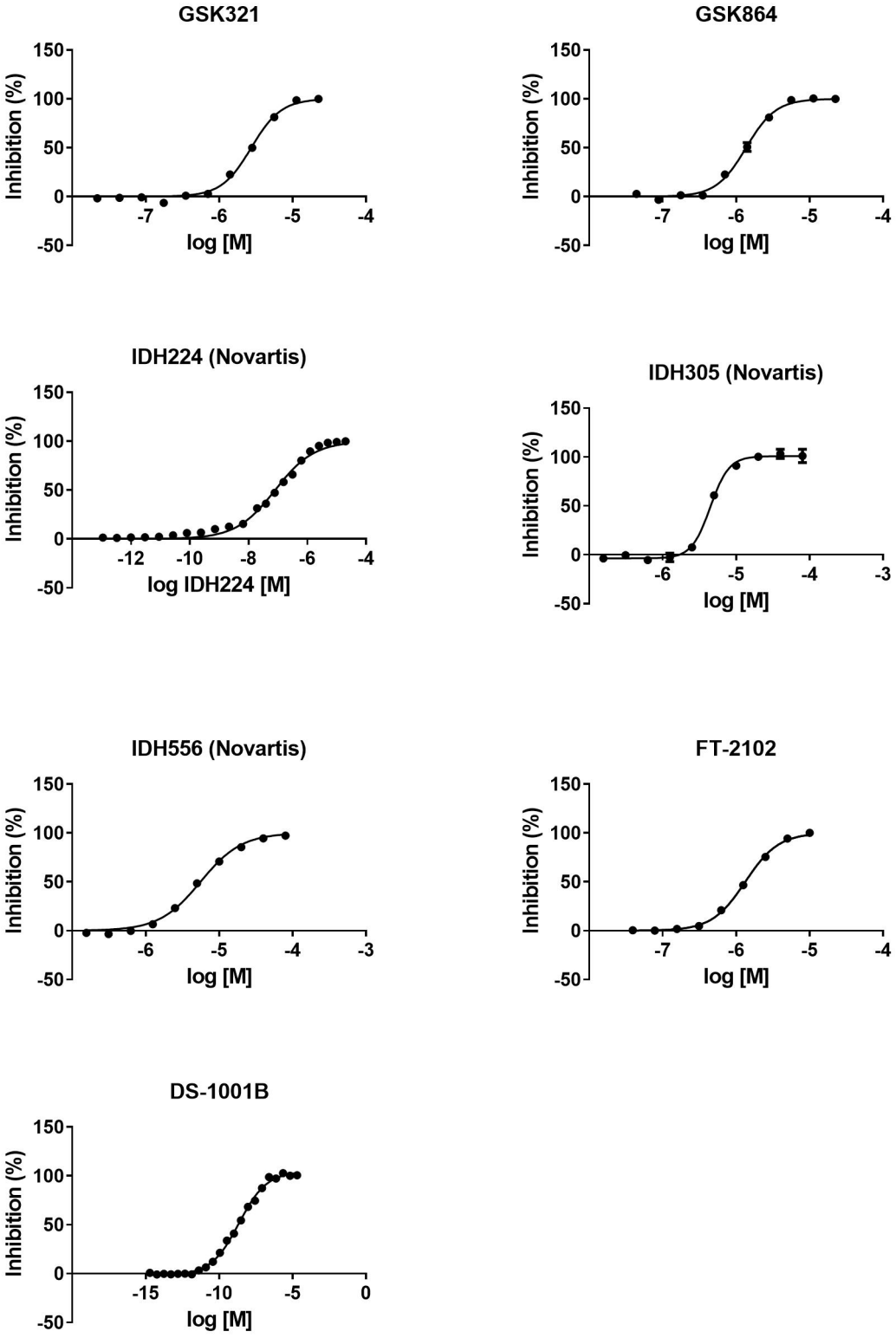

Figure 3.18 | IC_{50} determination of inhibitors with IDH1 R132C S280F. *Dose-response graphs of inhibitors with IDH1 R132C S280F (30 nM) using an NADPH absorbance assay. Errors: standard errors of the mean (n = 3). Conditions: 100 mM Tris, 10 mM $MgCl_2$, 0.2 mM DTT, 0.005 % Tween 20, and 0.1 mg/mL BSA (pH 8.0). 2-OG: 1.5 mM, NADPH: 0.3 mM.*

3.3.4.3 Dose-Response Curves for IC_{50} Determination Against R132H

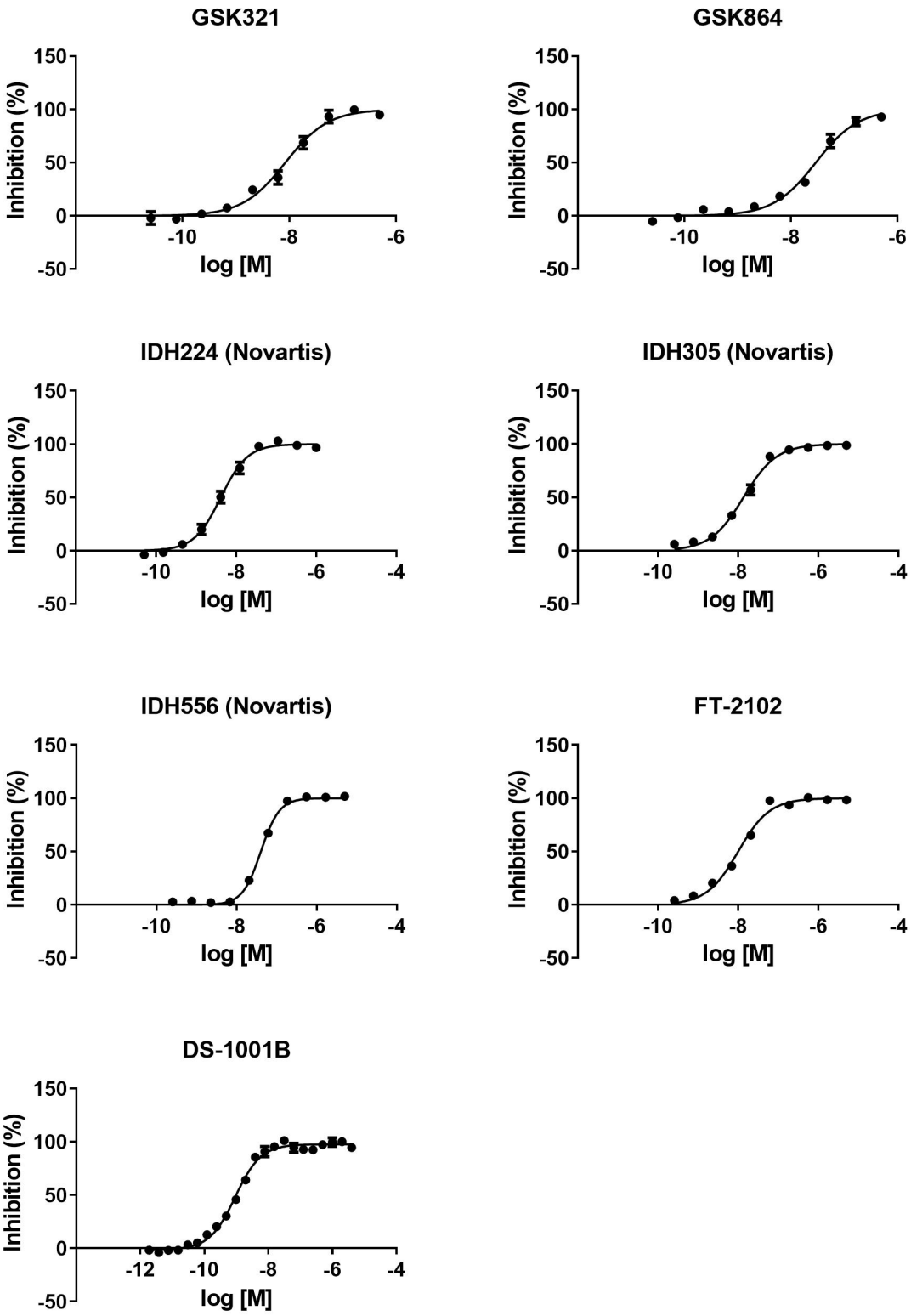

Figure 3.19 | IC_{50} determination of inhibitors with IDH1 R132H. *Dose-response graphs of inhibitors with IDH1 R132H (30 nM) using an NADPH absorbance assay. Errors: standard errors of the mean (n = 3). Conditions: 100 mM Tris, 10 mM $MgCl_2$, 0.2 mM DTT, 0.005 % Tween 20, and 0.1 mg/mL BSA (pH 8.0). 2-OG: 1.5 mM, NADPH: 0.3 mM.*

3.3.4.4 Dose-Response Curves for IC_{50} Determination Against R132H S280F

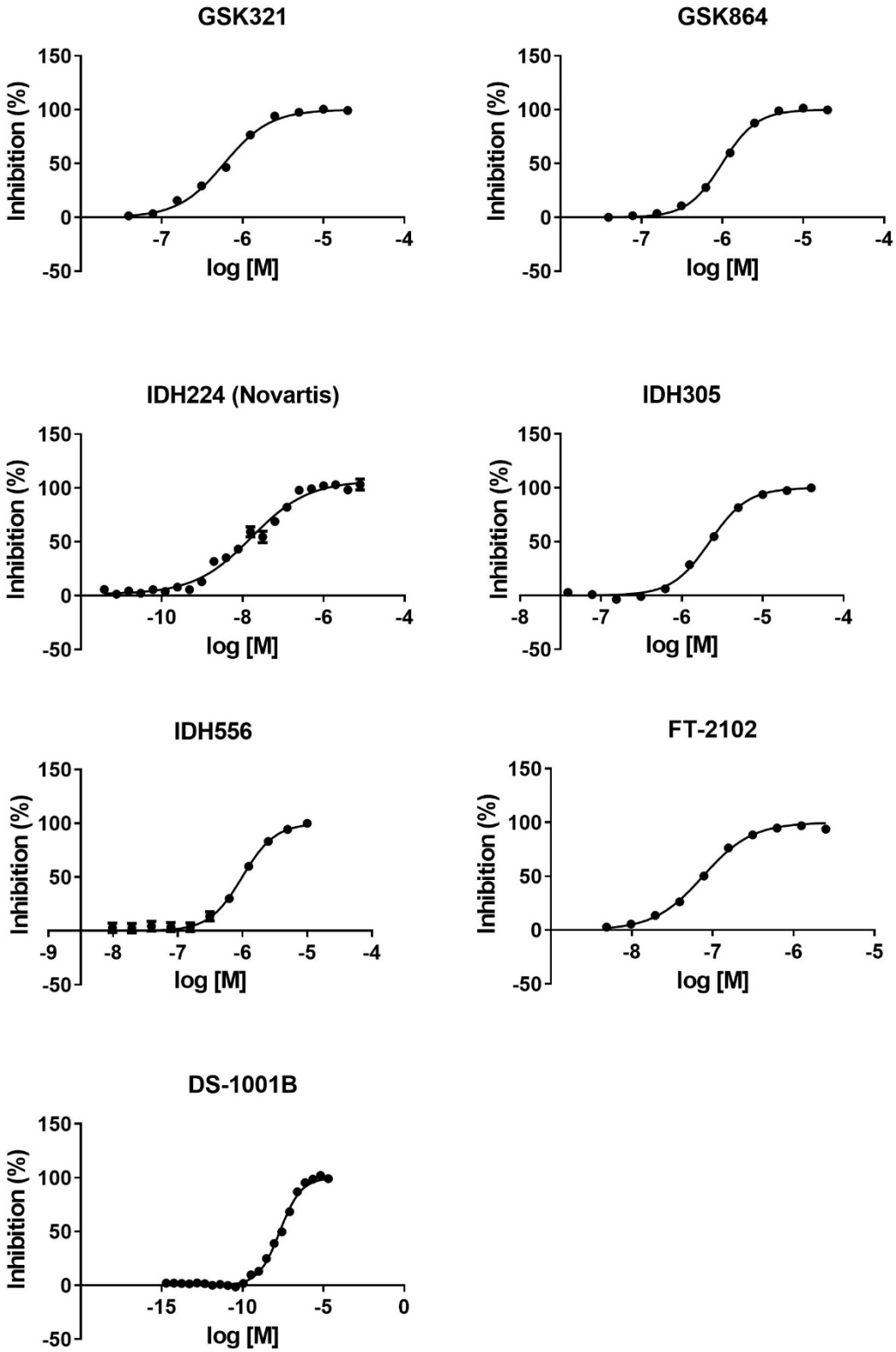

Figure 3.20 | IC_{50} determination of inhibitors with IDH1 R132H S280F. *Dose-response graphs of inhibitors with IDH1 R132H S280F (30 nM) using an NADPH absorbance assay. Errors: standard errors of the mean (n = 3). Conditions: 100 mM Tris, 10 mM $MgCl_2$, 0.2 mM DTT, 0.005 % Tween 20, and 0.1 mg/mL BSA (pH 8.0). 2-OG: 1.5 mM, NADPH: 0.3 mM.*

3.3.4.5 Comparison of Inhibitor Potency

The IC_{50} values for the IDH1 variants are summarised in **Table 3.3**. As there was no observed inhibition of R132C S280F and R132H S280F at 10 µM ivosidenib, no IC_{50} was determined. Both GSK321 and GSK864 displayed a substantial reduction in potency against R132C S280F and R132H S280F (IC_{50} >500 nM) compared to R132C and R132H (IC_{50} <50 nM). IDH305 and IDH556 also displayed a substantial decrease in potency against the R132C S280F and R132H S280F variants compared to R132C or R132H, respectively. However, IDH224 only showed a moderate decrease in IC_{50} compared to R132C and R132H, exhibiting IC_{50} values of 80.3 nM against R132C S280F and 16.5 nM against R132H S280F. FT-2102 displayed a difference in inhibition between R132C (IC_{50} = 120.2 nM) and R132H (IC_{50} = 10.0 nM) which is consistent with previous reports[172]. The difference in inhibition with respect to the R132 variation was also reflected in the low potency of FT-2102 against R132C S280F (IC_{50} = 1.3 µM) but high potency for R132H S280F (IC_{50} = 75.8 nM). The most potent inhibitor of R132C S280F was DS-1001B with an IC_{50} of 2.2 nM, exhibiting a small increase in potency compared with R132C (IC_{50} = 5.0 nM). DS-1001B was also an inhibitor of R132H S280F (IC_{50} = 20.4 nM) although with a 20-fold decrease in potency compared with R132H (IC_{50} = 0.9 nM).

***Table 3.3** | IC_{50} values (standard error of the mean, n= 3) of inhibitors against IDH1 variants (30 nM) using an NADPH absorbance assay. Conditions: See Figure 3.9 legend.*

	R132C	R132C S280F	R132H	R132H S280F
Ivosidenib	2.5±0.1 nM	0% at 10 µM	2.9±0.3 nM	0% at 10 µM
GSK321A	5.6±0.3 nM	2.7±0.2 µM	8.5±0.9 nM	594.5±23.1 nM
GSK864	47.7±5.4 nM	1.4±0.04 µM	29.4±2.4 nM	995.2±27.4 nM
Nov224	3.7±0.3 nM	80.3±4.6 nM	4.2 ±0.3 nM	16.5±2.3 nM
Nov305	4.9±0.3 nM	4.4±0.2 µM	13.6±0.9 nM	2.2±0.2 µM
Nov556	35.5±0.4 nM	5.6±0.2 µM	40.5±1.5 nM	989.7±102.6 nM
FT-2102	120.2±7.5 nM	1.3±0.03 µM	10.0±0.7 nM	75.8±1.8 nM
DS-1001B	5.0±0.5 nM	2.2±0.2 nM	0.9±0.1 nM	20.4±1.1 nM

Absolute IC_{50} values falling under the theoretical assay limit of 7.5 nM (dimer-concentration = 15 nM) must be interpreted with care. The low IC_{50} values may be the result of inaccuracies in concentrations, most likely the enzyme concentration. However, the data show that several compounds retain activity against R132C S280F and R132H S280F. Some of these compounds display high potency. Of these inhibitors, FT-2102 and DS-1001B are currently being tested in phase 2 clinical trials.[164, 92] One inhibitor from each series that retained activity against R132C S280F and R132H S280F was selected for further

investigations, including: (i) binding studies using non-denaturing MS and CPMG-edited ^{1}H NMR, (ii) competition studies with magnesium, 2-OG and NADPH using an NADPH absorbance assay, (iii) cellular studies in LN18 cell lines overproducing recombinant IDH1 variants. Furthermore, work to obtain a crystal structure of R132C S280F with DS-1001B was conducted.

3.3.5 Comparison with Crystal Structure Analysis from Section 3.2

In Section 3.2, crystal structures of known inhibitors (AG-881, GSK321, IDH305, Compound 1, BAY-1436032, FT-2102, DS-1001B) were analysed for their proximity to S280 and the importance of the S280 residue for inhibitor binding. These structural analyses (and published structural data showing a hydrogen bond between the BAY-1436032 analogue and S280[174]) suggests that BAY-1436032 may form hydrogen bonds with S280. It is hence unsurprising that BAY-1436032 is inactive against the S280F substituted IDH1 variants. AG-881 binds in close proximity to the S280 residue (3.8 Å distance *in crystallo*) and potentially forms a hydrogen bond in solution. AG-881 is inactive against R132C S280F and R132H S280F in NADPH absorbance assays. The binding of Compound 1 (Sanofi) and SYC-435 is distant from S280F. Their inactivity may be related to their general low potency against IDH1 variants (Section 1.7) and indirect effects as a result of the S280F substitution. S280 is not directly involved in binding of GSK321 and IDH305 (as shown by crystallographic studies), which both retain some activity against R132C S280F and R132H S280F; the decrease in their potency is likely a result of changes at the dimer-interface chemistry (i.e. the novel hydrophobic region) or changes in kinetic parameters (i.e. the lower K_M for 2-OG and magnesium, which could enable more efficient competition). FT-2102 and Compound A, a DS-1001B analogue, bind closely to S280, but S280 is not directly important for their binding and its side chain is oriented away from FT-2102 and Compound A, likely, at least in part, accounting for the observation that FT-2102 and DS-1001B retain activity against R132C S280F and R132H S280F.

3.4 Analysis of Inhibitor Binding by Non-Denaturing Mass Spectrometry

Next, inhibitors that retained activity against S280F substituted variants were further investigated to better understand the reasoning. One inhibitor from each series (GSK864, IDH224, FT-2102 and DS-1001B) was selected for further binding studies by non-denaturing MS. The inhibitor (20 μM) was added to the IDH1 variant (20 μM) and subjected to non-denaturing MS analyses (**Figure 3.21**).

Interestingly, binding of either one (green) or two inhibitor molecules (mint green) was observed for all the inhibitors that retained activity against R132C S280F and R132H S280F (GSK864, IDH224, FT-2102, DS-1001B; **Figure 3.21**).

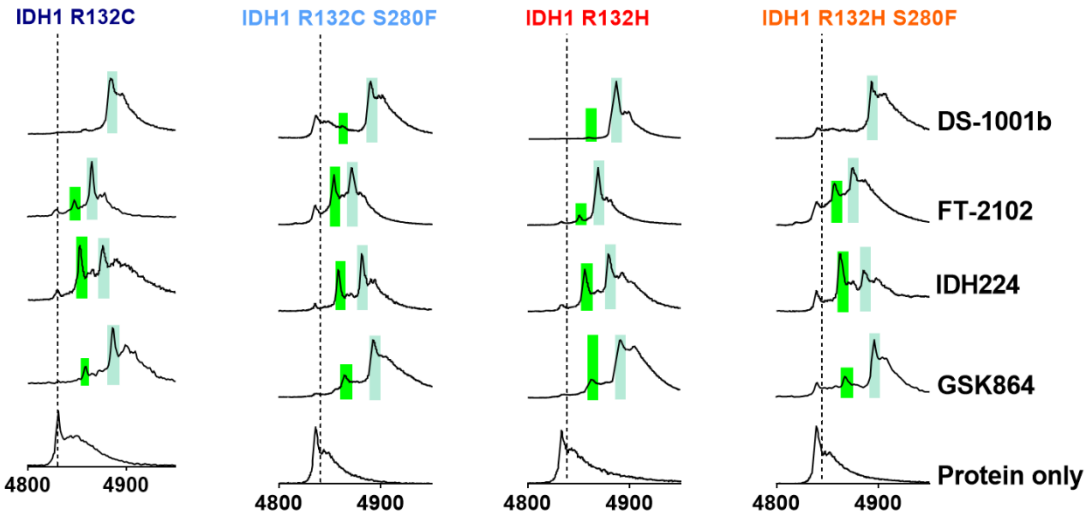

***Figure 3.21** | Binding analyses by non-denaturing mass spectrometry. Dashed line: IDH1 dimer (z = 20, with 2 NADPH molecules bound), bright green: one inhibitor bound, mint green: two inhibitors bound. Conditions: ammonium citrate buffer (200 mM, pH 7.5), 20 µM IDH1 variant, 20 µM inhibitor, cone-voltage: 100 V.*

When a higher concentration of inhibitor was added (160 µM, **Figure 3.22**) to R132C, R132C S280F, R132H, or R132H S280F, the two inhibitor-bound state was predominant for all IDH1 variants tested. Spectra of IDH224 bound to R132C and R132H displayed another signal corresponding to the binding of a third inhibitor molecule (asterisk in **Figure 3.22**) at 160 µM which is in accordance with an IDH305 crystal structure showing three inhibitor molecules bound (one in the centre of the dimer-interface, and one on each site adjacently; **Figure 3.4**, C).

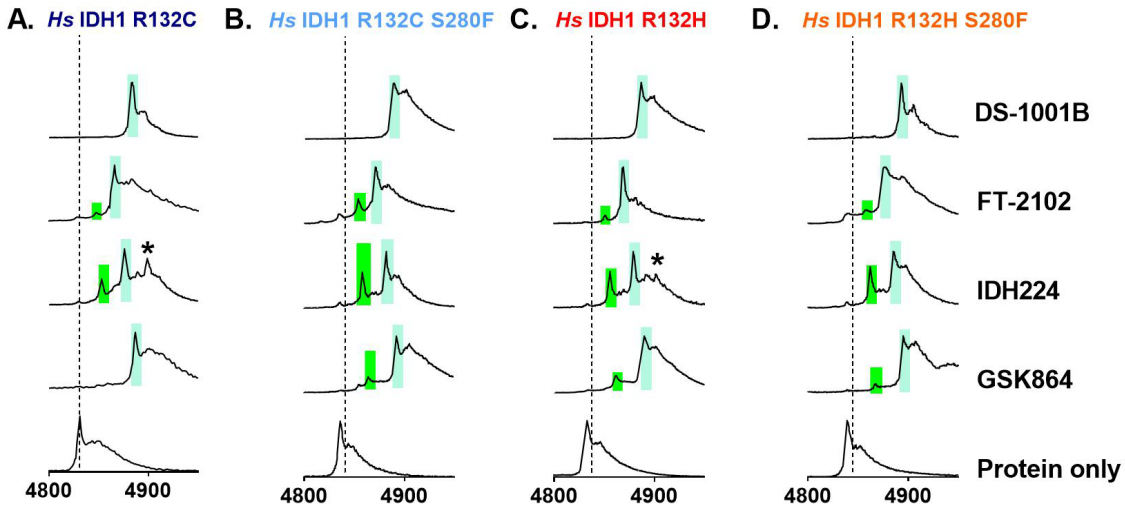

Figure 3.22 *| Binding analyses by non-denaturing mass spectrometry. Dashed line: IDH1 dimer (z = 20, with 2 NADPH molecules bound), bright green: one inhibitor bound, mint green: two inhibitors bound. The asterisk indicates binding of a third IDH224 molecule, as observed at high concentrations. Conditions: ammonium citrate buffer (200 mM, pH 7.5),20 µM IDH1 variant, 160 µM inhibitor, cone-voltage: 100 V.*

A common feature of inhibitors (GSK864, IDH224, FT-2102, DS-1001B) that retain activity against S280F substituted variants seems to be their ability to bind with a stoichiometry of two inhibitor molecules per dimer. This contrasts with the binding of ivosidenib, which binds with a stoichiometry of one inhibitor molecule per IDH1 dimer. To determine the inhibitor affinity and compare between R132C, R132C S280F, R132H, and R132H S280F, the dissociation constant K_D was measured using non-denaturing MS.

3.5 Studies on Binding Affinity

K_D-determinations were carried out using non-denaturing MS as described in Section 3.3. A one site-inhibitor binding model was used to determine K_D, though the influence of the first inhibitor binding event on the subsequent binding in the IDH1 dimer is unknown.

3.5.1 Non-denaturing Mass Spectrometry

Different concentrations of inhibitors were added to the IDH1 variants and non-denaturing MS measurements were collected. The fraction of protein-inhibitor complex was plotted against the inhibitor concentration. Analysis was conducted using non-linear regression with the GraphPad Prism software (one site-inhibitor binding model). Triplicates were from charge-states z = 19, z = 20, and z = 21 (**Figure 3.23**, **Figure 3.24**).

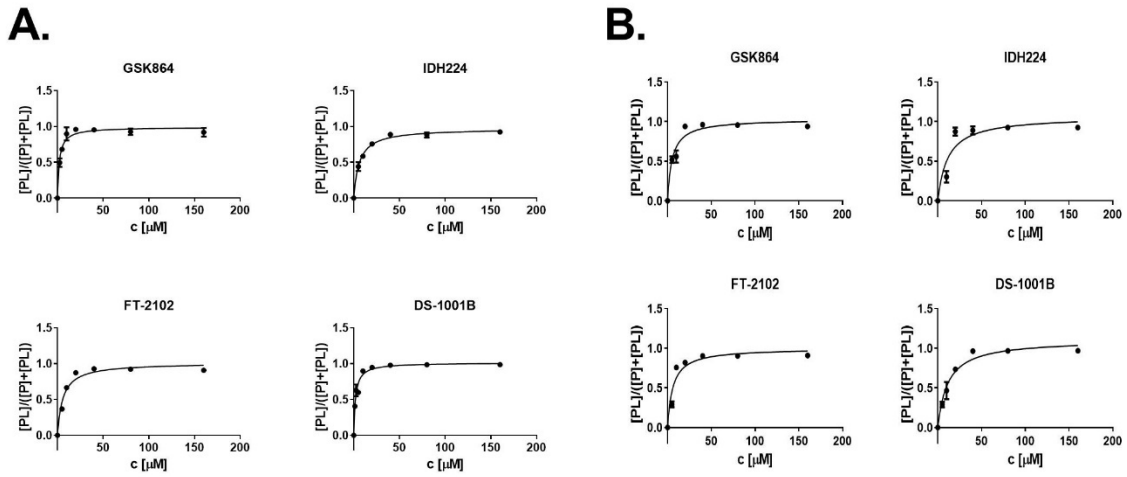

***Figure 3.23** | Binding analyses of IDH1 R132C (**A**) and R132C S280F (**B**) by non-denaturing MS. The dissociation constant (K_D) was determined by titrating the inhibitor (in MeOH) into an enzyme solution (20 µM). The bound fraction was plotted against inhibitor concentration. Errors: standard errors of the mean (n= 3 of z= 19, 20, 21). Conditions: Non-denaturing MS was in ammonium citrate buffer (200 mM, pH 7.5). Cone-voltage: 100 V.*

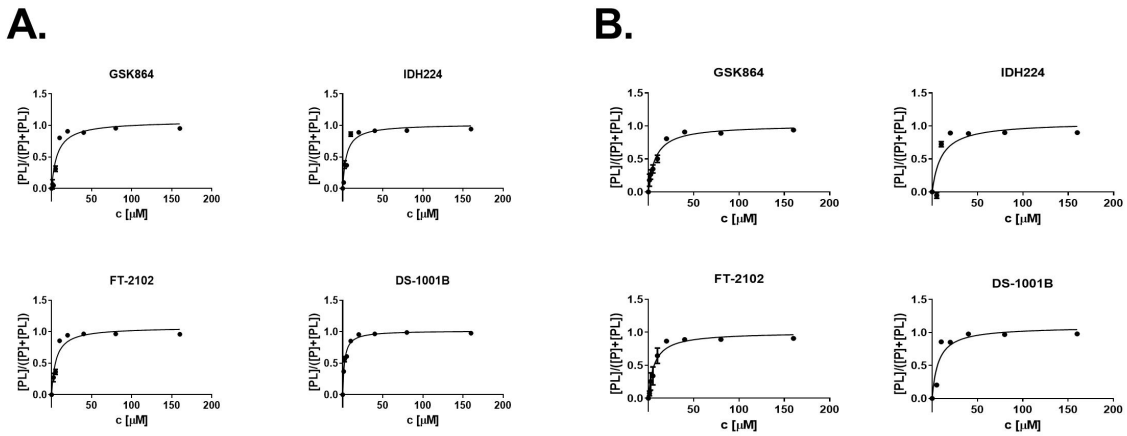

***Figure 3.24** | Binding analyses of IDH1 R132H (**A**) and R132H S280F (**B**) by non-denaturing MS. The dissociation constant (K_D) was determined by titrating the inhibitor (in MeOH) into an enzyme solution (20 µM). The bound fraction was plotted against inhibitor concentration. Errors: standard errors of the mean (n= 3 of z= 19, 20, 21). Conditions: Non-denaturing MS was in ammonium citrate buffer (200 mM, pH 7.5). Cone-voltage: 100 V.*

The binding affinity of GSK864 to R132C S280F was 2.5-fold lower than to R132C as determined by non-denaturing MS but exhibited no difference in K_D for binding to R132H and R132H S280F (**Table 3.4**). For IDH224, the K_D for both R132C S280F and R132H S280F increased 2-fold compared to R132C and R132H, respectively (**Table 3.4**). The K_D for FT-2102 was similar for all four IDH1 variants tested (**Table 3.4**). The binding affinity for DS-1001B was substantially decreased for both R132C S280F (6-fold lower than for R132C) and R132H S280F (3-fold lower than for R132H) (**Table 3.4**).

***Table 3.4** | Determination of the dissociation constant K_D by non-denaturing MS (20 µM enzyme,). Errors: standard errors of the mean (n = 3 (z = 19, 20, 21)). Conditions: see Figure legend 3.21.*

	R132C	R132C S280F	R132H	R132H S280F
GSK864	2.07±0.39 µM	5.25±1.00 µM	7.25±1.63 µM	7.85±1.23 µM
IDH224	6.04±0.68 µM	11.38±3.77 µM	4.67±0.82 µM	10.10±4.00 µM
FT-2102	5.88±0.83 µM	6.00±1.20 µM	5.46±1.00 µM	6.44±1.33 µM
DS-1001B	1.96±0.23 µM	11.39±1.98 µM	2.31±0.18 µM	6.96±1.86 µM

In general, the inhibitors bind to R132C S280F and R132H S280F with lower affinity than R132C and R132H. Exceptions are FT-2102 with both R132C S280F and R132H S280F and GSK864 with R132H S280F. The observation that binding of inhibitors to R132C S280F and R132H S280F is generally less strong suggests that the S280F substitution not only interferes with binding of ivosidenib, but, at least to some degree, with most inhibitors tested. This observation is likely a result of the new hydrophobic region at the dimer-interface (making it more rigid) and the bulkiness of the phenylalanine side chain (see section 2.10).

As non-denaturing MS is conducted in the gas phase, CPMG-edited ^{1}H NMR was additionally used to study DS-1001B binding in solution as an example of an inhibitor that retained activity against R132C S280F and R132H S280F.

3.5.2 ^{1}H CPMG NMR

CPMG-edited ^{1}H NMR was carried out as described in Section 3.3.2. The signal at 7.5 ppm corresponding to the aromatic hydrogen atom of DS-1001B (**Figure 3.25**) was used to determine free DS-1001B in solution. A decrease in signal intensity at 7.5 ppm was observed with increasing protein concentration (**Figure 3.25**).

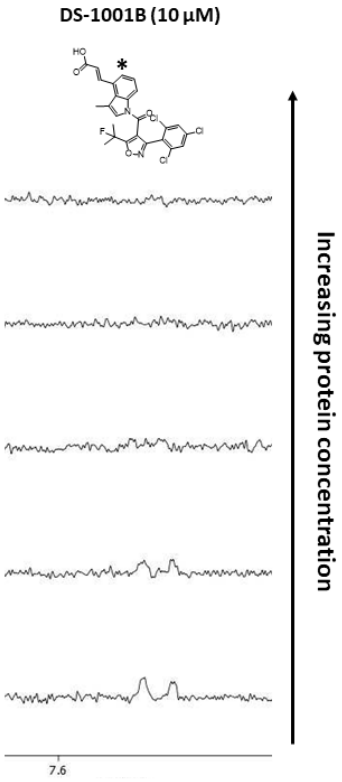

Figure 3.25 | *Spectra of DS-1001B (10 µM) with increasing concentrations of IDH1 variants as measured by CPMG-edited ^{1}H NMR (700 MHz) for the determination of DS-1001B affinity to IDH1 variants. Note: with increasing protein concentrations the signal corresponding to free inhibitor in solution decreases. The signal of inhibitor bound to the IDH1 protein is filtered out by the CPMG-edited PROJECT pulse sequence.[173] Proteins were titrated into 10 µM DS-1001B in buffer containing 50 mM Tris, 100 mM NaCl (90:10 H_2O:D_2O, pH 7.5).*

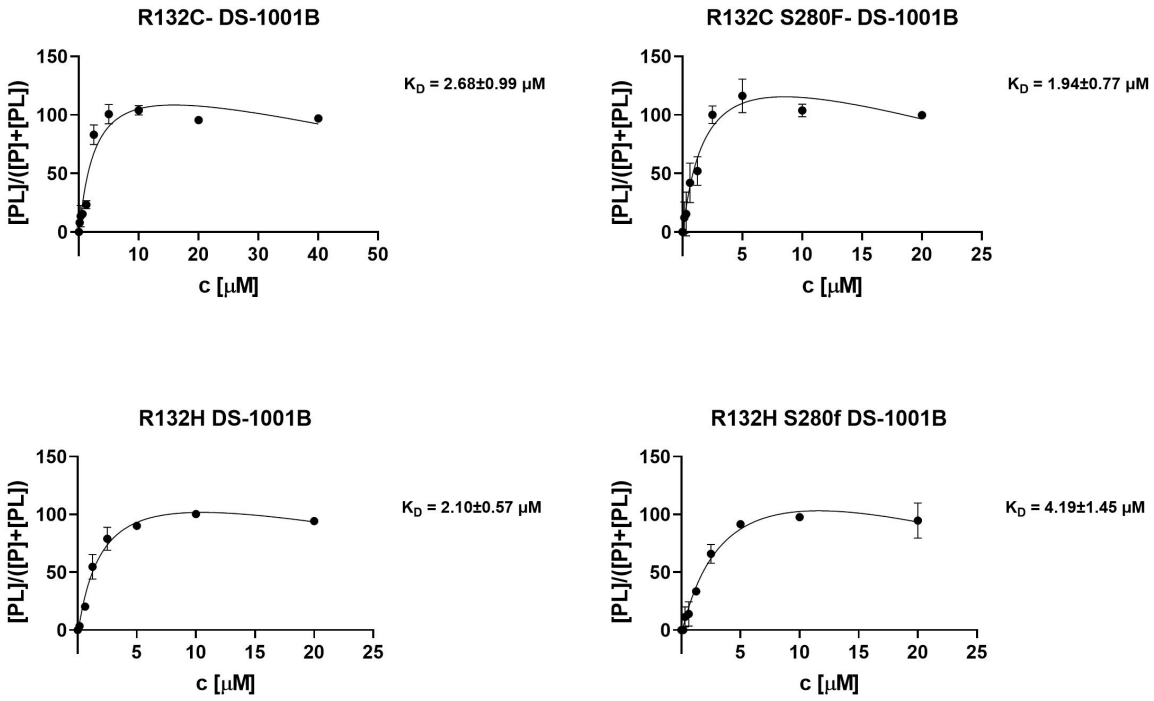

Figure 3.26 *| ^{1}H NMR binding studies using the CPMG Project pulse NMR sequence. Proteins were titrated into 10 µM DS-1001B in buffer containing 50 mM Tris, 100 mM NaCl (90:10 H_2O:D_2O, pH 7.5). Errors: Standard errors of the mean (n = 2).*

The K_D values (**Figure 3.26**) implied a similar affinity of DS-1001B to R132C and R132C S280F. The K_D value for R132H was similar to R132C and R132C S280F, but the K_D was 2-fold higher for R132H S280F.

The binding data for DS-1001B mirrors the IC_{50} data acquired for DS-1001B showing similar inhibition/binding affinity for R132C, R132C S280F, and R132H, while potency/binding affinity is lower for R132H S280F. A Spearman's rank order correlation r_2= 0.93 indicates a very strong positive correlation between the IC_{50} data and the binding affinity data as measured by CPMG-edited NMR for DS-1001B.

3.5.3 Differential Scanning Fluorimetry (DSF)

DSF analyses were carried out as described in Section 2.9. Varying concentrations of inhibitors were added, and binding was indicated by an increase in T_m of the IDH1 variant as measured by an increase in fluorescent signal.

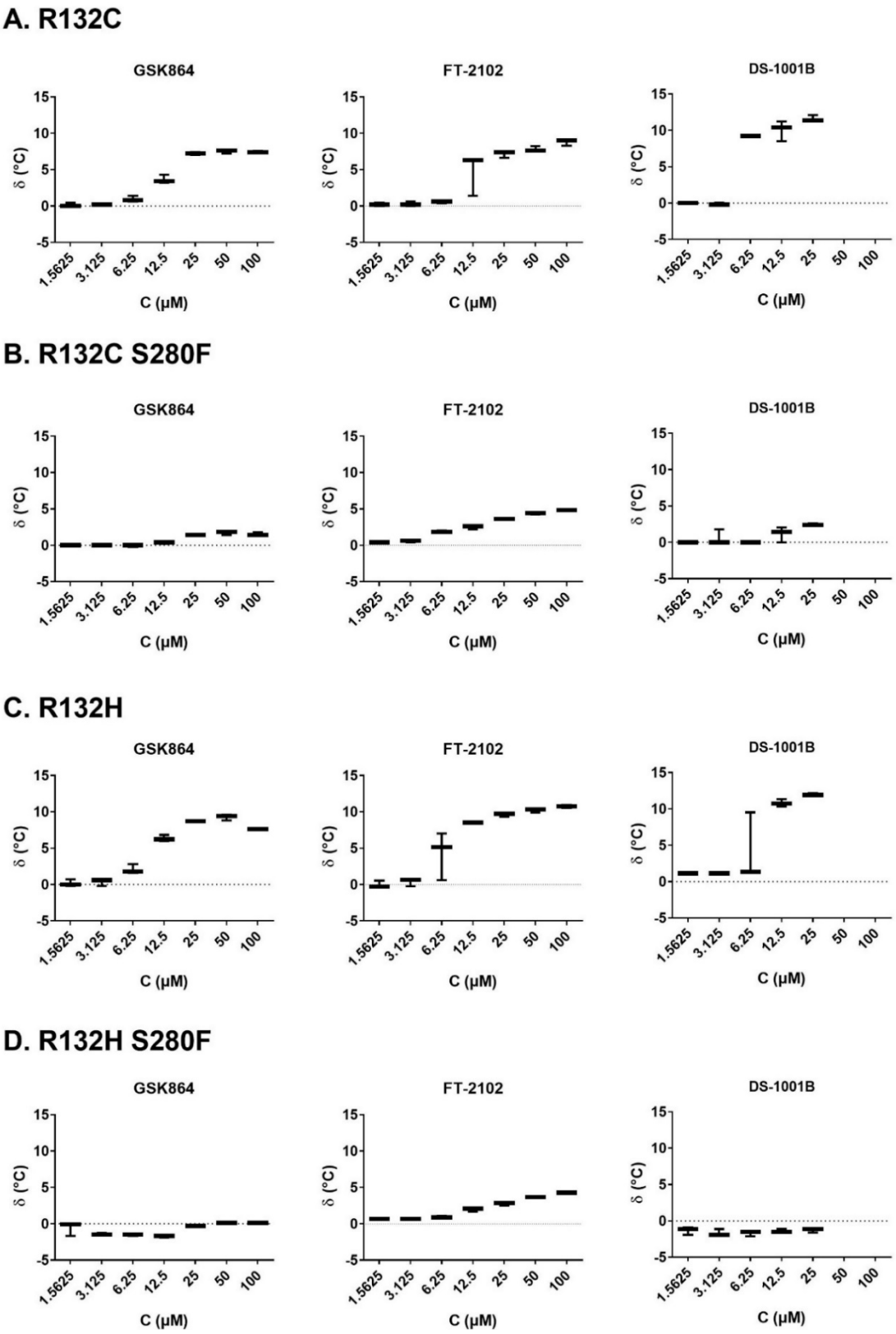

Figure 3.27 *| T_m-shift analyses of inhibitor binding to R132C (**A**), R132C S280F (**B**), R132H (**C**), or R132H S280F (**D**) by DSF. The plots show the T_m difference compared to a sample containing protein only. Errors: standard error of the mean (n = 3). IDH224 was excluded from analyses due to interference with the fluorescence signal. High concentrations of DS-1001B (50 µM, 100 µM) interfered with the fluorescence signal and were excluded. Conditions: 3 µM enzyme in 50 mM Tris buffer, pH 7.5 (Dye: Sypro Orange 3x).*

The addition of GSK864 stabilised R132C and R132H in a concentration-dependent manner, but only marginally increased the T_m of R132C S280F (**Figure 3.27**). No stabilisation was observed for R132H S280F. FT-2102 increased the stability of R132C and R132H to a maximum of δ = 10°C and resulted in an increase in thermal stability of both R132C S280F and R132H S280F to a maximum of δ = 5°C, all in a concentration-dependent manner. DS-1001B increased the T_m of R132C and R132H concentration-dependently to a maximum of around δ = 10°C. There was limited stabilisation of R132C S280F (δ = 2°C) by DS-1001B but no change was observed with R132H S280F (**Figure 3.27**).

The combined results of binding studies with inhibitors (GSK864, IDH224, FT-2102, DS-1001B) that retain activity against R132C S280F and R132H S280F generally show a decrease in binding affinity compared with R132C and R132H. Crystal structure analysis (Section 2.10) suggests that this observation might relate to new hydrophobic interactions between F280, W124 and W267 resulting in a more rigid dimer-interface, and steric hindrance imposed by F280 in the binding pocket at the dimer-interface. In assays conducted by non-denaturing MS, there was no decrease in binding affinity of FT-2102 and only a slightly lower increase in T_m as observed by DSF studies for R132C S280F and R132H S280F compared to R132C and R132H, respectively, suggesting the binding efficiency of FT-2102 is less affected by the S280F substitution compared with other inhibitors. Furthermore, the binding efficiency of DS-1001B to R132C S280F is similar to R132C in CPMG-edited ^{1}H NMR studies. This observation is consistent with DS-1001B retaining potent inhibitory activity against R132C S280F (**Table 3.3**). Conversely, the binding affinity of DS-1001B to R132C S280F was reduced compared with R132C by non-denaturing MS analysis, potentially due to operation in the gas phase.

Overall, the decrease in binding affinity of ivosidenib for R132C S280F and R132H S280F compared to R132C and R132H seems to be a key part of resistance. Even inhibitors retaining activity generally seem to have a decreased binding affinity for R132C S280F and R132H S280F compared to R132C and R132H, respectively, suggesting that steric hindrance of phenylalanine and the new hydrophobic interactions (Section 2.10) interfere with inhibitor binding at the dimer-interface. However, binding assays by non-denaturing MS, CPMG NMR or DSF were not carried out under turnover conditions, i.e. no 2-OG was present. Most inhibitors are reported to compete with 2-OG and/or magnesium binding[48]. Binding of 2-OG requires magnesium binding as shown in Section 2.9. In Section 2.3 it was shown that R132C S280F and R132H S280F may have an increased affinity for 2-OG and magnesium compared

to R132C and R132H, as judged by K_M. Consequently, inhibitors that retained activity against S280F substitutions were investigated for competition with respect to binding of 2-OG and/or magnesium. This would indicate whether alteration of kinetic parameters, as a result of the S280F substitution, plays a role in the resistance mechanism.

3.6 Competition Studies with Mg^{2+}, 2-OG and NADPH

Initially, pilot studies were conducted to determine a suitable enzyme and inhibitor concentration for subsequent competition studies using an NADPH absorbance assay. The optimised conditions employed 400 nM enzyme and 200 nM inhibitor. Magnesium concentrations were based on Michaelis-Menten parameters for R132H and were selected to be around (4 mM), below (0.8 mM, which was the lowest concentration in which R132H activity could be observed under these conditions), and above (20 mM) the K_M value. These concentrations were also used for the other IDH1 variants (R132C, R132C S280F, R132H S280F) to enable comparison.

The results showed that ivosidenib potently inhibited R132C and R132H activity and only minor effects of magnesium concentrations on inhibition were observed (**Figure 3.28**, A/C). Further, ivosidenib did not inhibit R132C S280F and R132H S280F (**Figure 3.28**, B/D) consistent with previous experiments (**Figure 3.9**). There were strong competition effects of GSK864 with respect to $MgCl_2$, especially at high concentrations (20 mM), with all IDH1 variants tested (**Figure 3.28**). For IDH224 there was a slight increase in inhibition at 4 mM $MgCl_2$ compared to 0.8 mM $MgCl_2$ in R132C and R132H, but a substantial decrease at 20 mM $MgCl_2$ (**Figure 3.28**, A/C). For R132C S280F and R132H S280F, there was a substantial decrease of inhibitory activity of IDH224 at higher magnesium concentrations (**Figure 3.28**, B/D). Inhibition of R132C, R132H, R132H S280F by FT-2102 was affected by the presence of high magnesium concentrations, however, only a small decrease of inhibition was observed for R132C S280F (**Figure 3.28**). Similarly, inhibition of R132C, R132H, and R132H S280F by DS-1001B was reduced by higher magnesium concentrations while only a small effect for R132C S280F was observed (**Figure 3.28**).

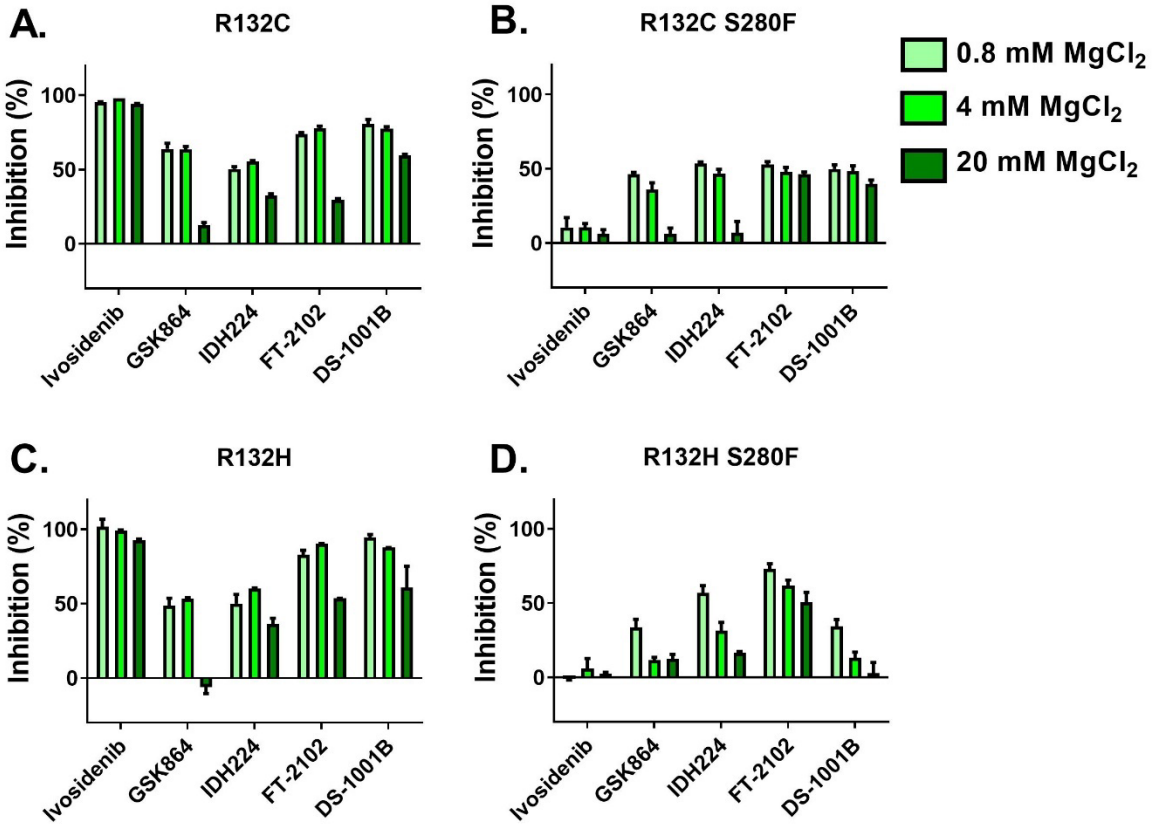

***Figure 3.28** | Determination of inhibition against the IDH1 R132C, R132C S280F, R132H, and R132H S280F variants under varying $MgCl_2$ concentrations. The inhibitory activity is influenced by the Mg^{2+} concentration. Conditions: 400 nM enzyme was pre-incubated with 200 nM inhibitor and varying concentrations of $MgCl_2$. Buffer: 100 mM Tris, 0.2 mM DTT, 0.005% Tween 20, and 0.1 mg/mL BSA (pH 8.0). 2-OG: 1.5 mM, NADPH: 0.3 mM.*

In general, there is apparent competition with magnesium ions for ivosidenib, GSK864, IDH224, FT-2102, and DS-1001B. Thus, the observed inhibition seems to be, at least in part, a result of competition between the enzyme's affinity for magnesium and the affinity for inhibitor.

Next, competition of selected inhibitors with different concentrations of 2-OG was explored. Concentrations were based on the kinetic parameters for R132H and were chosen to be around (0.5 mM), below (0.167 mM) and above (1.5 mM) the K_M value. These concentrations were also used for R132C, R132C S280F, and R132H S280F to enable comparison.

Ivosidenib inhibited the activity of R132C and R132H potently with 2-OG concentration having little effect. As previously observed, ivosidenib does not inhibit activity of R132C S280F or R132H S280F (**Figure 3.29**, **Figure 3.9**). The inhibitory activity of GSK864 and IDH224 decreased at higher 2-OG levels for all the IDH1 variants tested (**Figure 3.29**). There was also a concentration-dependent effect of 2-OG levels on FT-2102 inhibition of R132C, R132C S280F, and R132H S280F. Inhibition of R132H was unaffected by 2-OG concentration

(**Figure 3.29**), likely due to the high potency of FT-2102 for this variant (**Table 3.3**). DS-1001B inhibition was decreased at higher 2-OG concentrations for all IDH1 variants tested (**Figure 3.29**).

In addition to competition with magnesium, the inhibitors tested also competed with 2-OG. This was not unexpected as magnesium is required for 2-OG binding (see section 2.9). The low effect of the 2-OG concentration on ivosidenib inhibition of R132C and R132H, and of FT-2102 on R132H are likely related to the high potency of these inhibitors for the respective enzymes which efficiently compete with 2-OG binding even at high substrate levels.

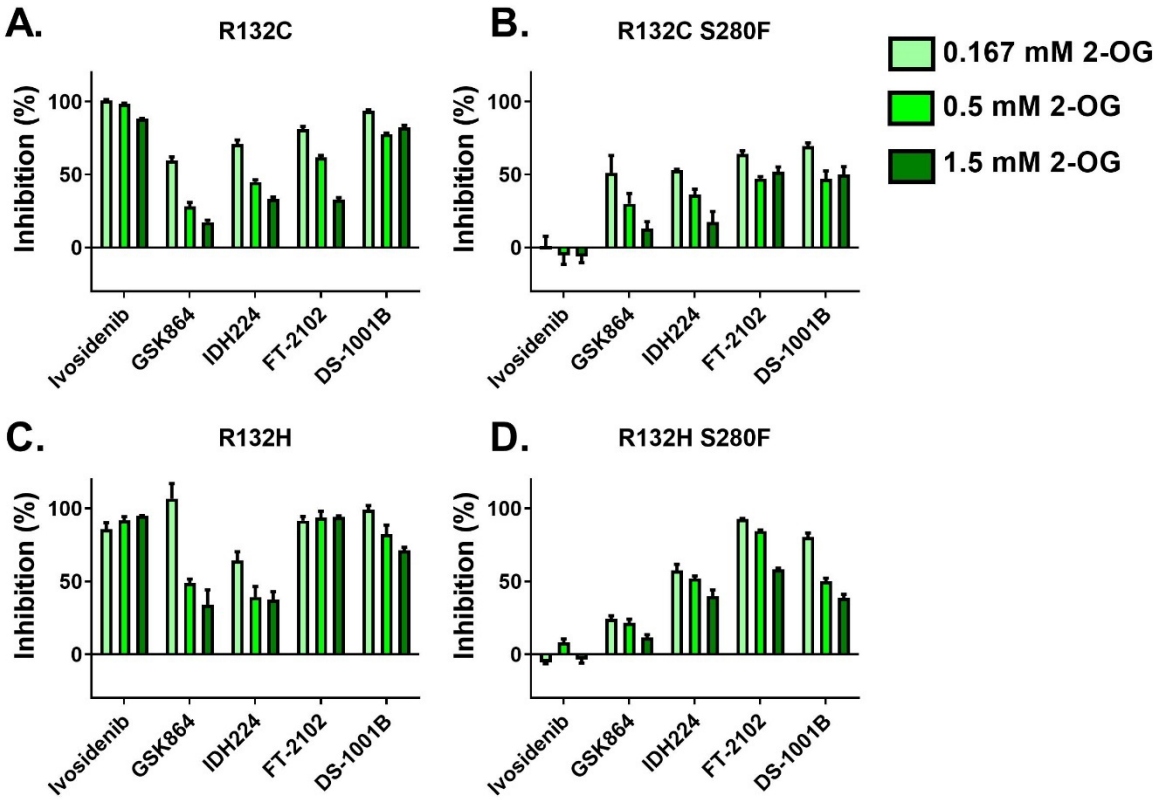

***Figure 3.29** | Determination of inhibition against the IDH1 R132C, R132C S280F, R132H, and R132H S280F variants under varying 2-OG concentrations. The inhibitory activity is influenced by the 2-OG concentrations. Conditions: 400 nM enzyme was pre-incubated with 200 nM inhibitor and 10 mM $MgCl_2$. Buffer: 100 mM Tris, 0.2 mM DTT, 0.005% Tween 20, and 0.1 mg/mL BSA (pH 8.0).* $MgCl_2$: 10 mM. NADPH: 0.3 mM.

Lastly, competition of ivosidenib, GSK864, IDH224, FT-2102, and DS-1001B with NADPH was investigated. Concentrations of NADPH were chosen to be within a 3-fold difference in a range where the initial timepoints can be observed (note: at very low NADPH concentrations (<10 µM), all NADPH is consumed, and turnover is complete before the first absorbance measurement is read) and the detector is not saturated (note: at an NADPH concentration >600 µM the detector is saturated). NADPH competition was not reported for any of the tested

inhibitors. Ivosidenib inhibited R132C and R132H potently without competing with NADPH but did not inhibit R132C S280F and R132H S280F (**Figure 3.30**) consistent with previous results (**Figure 3.9**, **Figure 3.28**, **Figure 3.29**). Inhibition of R132C, R132C S280F, and R132H S280F by GSK864 was unaffected by the NADPH concentration, although there was a slight concentration-dependent decrease in R132H inhibition (**Figure 3.30**). Similarly, there were no clear effects of NADPH on IDH224 inhibition of R132C, R132C S280F, and R132H S280F but a slight concentration-dependent decrease in R132H inhibition (**Figure 3.30**). There was a moderate decrease of FT-2102 inhibition at high NADPH concentrations for all IDH1 variants tested except R132H (**Figure 3.30**). NADPH did not affect DS-1001B inhibition except for a slight concentration-dependent decrease in inhibition for R132C S280F (**Figure 3.30**).

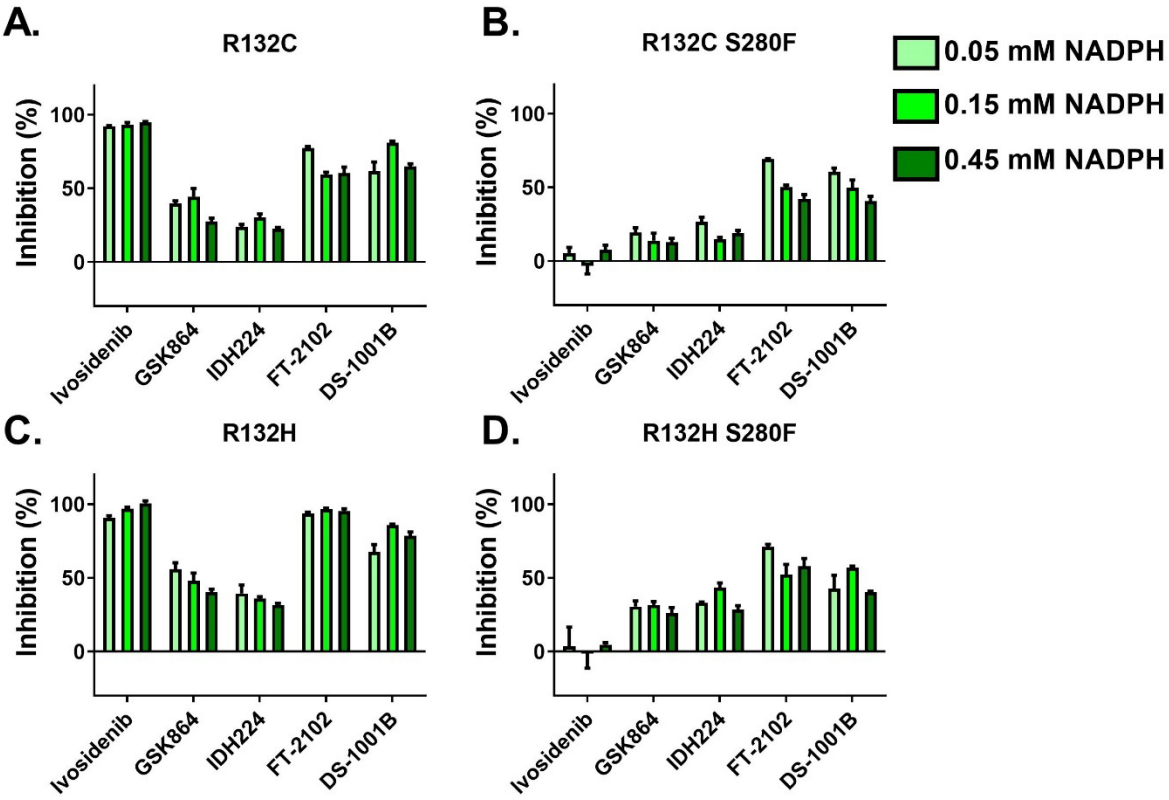

Figure 3.30 *| Determination of inhibition against the IDH1 R132C, R132C S280F, R132H, and R132H S280F variants under varying NADPH concentrations. The inhibitory activity of inhibitors is not substantially influenced by NADPH concentrations. Conditions: 400 nM enzyme was pre-incubated with 200 nM inhibitor and 10 mM* $MgCl_2$*. Buffer: 100 mM Tris, 0.2 mM DTT, 0.005% Tween 20, and 0.1 mg/mL BSA (pH 8.0).* $MgCl_2$: 10 mM. 2-OG: 1.5 mM.

In general, there seems to be no clear indication of NADPH competition although for some inhibitors there might be limited apparent competition for specific IDH1 variants. FT-2102 appears to be the only inhibitor consistently affected by higher NADPH concentrations with the exception for R132H inhibition (note: there was also no influence of higher 2-OG levels on R132H inhibition potentially related to the high potency of FT-2102 for R132H).

Inhibition of R132C, R132C S280F, R132H, and R132H S280F, as determined by an NADPH absorbance assay, is apparently competitive with magnesium and 2-OG. This observation suggests that the mechanism of resistance of R132C S280F might not solely be a result of the reduction of binding affinity of the inhibitors (likely due to the formation of a hydrophobic pocket at the dimer-interface and the steric effect of the phenylalanine sidechain, Section 2.10), but that altered kinetic parameters might also play a role. The reduction of the K_M value for magnesium and 2-OG in R132C S280F and R132H S280F likely translates to a higher affinity for them and thus more efficient competition with inhibitors which allosterically interfere with 2-OG and magnesium binding.

Potential competition with NADPH does not seem to play a general role in IDH1 variant inhibition. The exception to this might be FT-2102, which exhibits limited competition with NADPH. This might suggest a mixed mode of inhibition but needs to be followed up with further studies including the determination of IC_{50} values at different NADPH concentrations.

3.7 Crystallographic Studies of the Inhibitor DS-1001B Bound to R132C S280F

As previously discussed (Section 1.7), allosteric inhibitor binding appears to bias IDH1 towards an open inactive conformation. Structural information is available for many inhibitors bound to R132H (see Section 3.2). One crystal structure of the R132C variant with an analogue of DS-1001B is reported.[147] The inhibitor structures are usually obtained with NADPH bound (note: IDH1 copurifies with NADPH[48,44]). There is no reported inhibitor-bound crystal structure of R132C S280F and no crystal structure available for the inhibitor DS-1001B. For this reason, and because DS-1001B was the most potent inhibitor of R132C S280F, the clinically observed ivosidenib resistant IDH1 variant, work to obtain a crystal structure of R132C S280F with DS-1001B bound was conducted.

3.7.1 Crystallisation of R132C S280F with DS-1001B

Attempts were made to crystallise R132C S280F with the inhibitor DS-1001B by optimising a reported procedure for the crystallisation of R132C with an analogue of DS-1001B.[147] R132C S280F (25.62 mg×mL^{-1} in gel filtration buffer with 1 mM tris(2-carboxyethyl)phosphine (TCEP) (hereafter referred to as crystallisation buffer) with a C-terminal hexa-histidine tag purified by a 3-step purification method (see Section 2.10.2.2.1) was used for crystallisation. An optimisation screen varying the ammonium citrate concentration (pH 7.0, 0.75–2 M, horizontal axis in steps of 0.25 M) and the DTT concentration (1.5–3 mM, vertical axis in steps of 0.5 mM) was carried out based on published reports.[147] R132C S280F (12.5 µL) was

incubated on ice for 1 h with NADPH (10 mM; in crystallisation buffer), crystallisation buffer (6.8 µL), and a 10-fold excess of DS-1001B (from a 10 mM stock solution in DMSO, 0.7 µL) to a final protein concentration of 12.81 mg×mL^{-1}. 2 µL of this solution was added to 2 µL precipitant solution. Crystals manifested within 2 days in all wells containing 2 M ammonium citrate (highest ammonium citrate concentration in this screen) (**Figure 3.31**).

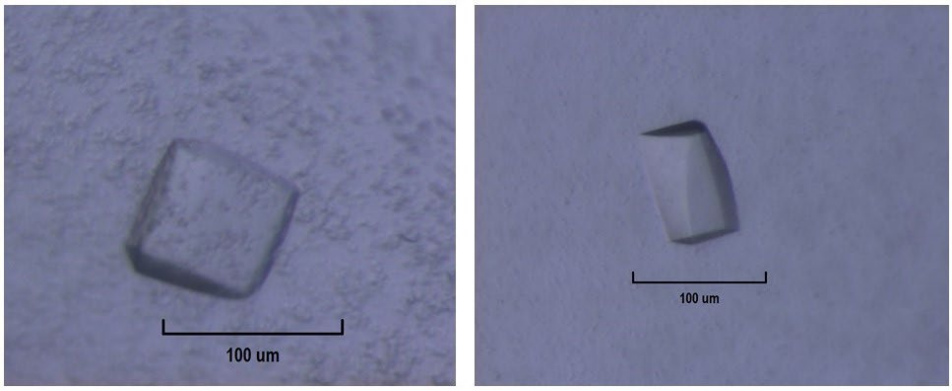

***Figure 3.31** | Photograph of crystals used to solve a structure of R132C S280F complexed with NADPH and the inhibitor DS-1001B.*

Crystal containing droplets were cryo-protected by mixing them in a ratio of 1:1 with reservoir solution containing glycerol (25%), harvested with a nylon loop, and cryo-cooled in liquid N_2. Diffraction data were collected using synchrotron radiation at the Diamond Light Source (DLS) beamline IO3. The crystals diffracted to 2.45 Å resolution. Processing was conducted using the Xia2[150] strategy of the beamline auto-processing pipeline according to Section 3.10.5.

3.7.2 Crystal Structure Analysis

An initial molecular replacement of the crystal structure of R132C S280F with DS-1001B was built using a crystal structure of R132H with IDH889 (5TQH[167]) as a model (4 monomers in the asymmetric unit). Because the fit of 2 monomers was suboptimal in this model, a starting model was re-built from this molecular replacement solution using PHENIX AutoBuild (Section 3.10.5; building of this starting model was kindly conducted by Dr Ian Clifton). The data collection and refinement statistics are shown in **Table 3.5**. R132C S280F crystallised in a $P2_12_12$ space group with 4 monomers (chain A-D; **Figure 3.32**, A) in the asymmetric unit.

Table 3.5 *| Data collection and refinement statistics for the crystal structure of R132C S280F complexed with DS-1001B.*

Datasets	***IDH1:NADPH:DS-1001B*** *(PDB ID: 7PJN)*
Data Collection (T in K)	*cryo-MX (100)*
Beamline (Wavelength, Å)	*DLS I03 (0.97933)*
Detector	*DECTRIS EIGER2 XE 16M*
Data Processing	*Xia2*
Space group	*P 2_1 2_1 2_1*
Cell dimensions	
a,b,c (Å)	*80.18, 153.05, 164.01*
α, β, γ (°)	*90, 90, 90*
No. of molecules/ASU	*4*
No. reflections	*74987 (5470)**
Resolution (Å)	*55.950- 2.450 (2.510 - 2.450)**
R_{meas}(I)	*0.096 (2.297)**
I/σI	*18.900 (1.2)**
CC-half	*1.000 (0.513)*
Completeness (%)	*99.91 (99.61)**
Multiplicity	*13.7 (13.3)**
Wilson B value ($Å^2$)	*65.35*
Refinement	*PHENIX*
R_{work}/R_{free+}	*0.1861 /0.2259*
No. atoms	*12975*
- *Enzyme*	*12432*
- *Ligand*	*433*
- *Water*	*110*
Average B-factors	*74.79*
- *Enzyme ($Å^2$)*	*74.68*
- *Ligand ($Å^2$)*	*80.48*
- *Water ($Å^2$)*	*64.20*
R.m.s deviations	
- *Bond lengths (Å)*	*0.004*
- *Bond angles (°)*	*0.68*

**Highest resolution shell in parentheses. DLS = Diamond Light Source.*

As shown by non-denaturing PAGE, SEC-MALS and non-denaturing MS (Section 2.7/2.8), R132C S280F is predominantly present as a dimer in solution. In the asymmetric unit, chains B and C build an apparent dimer (**Figure 3.32**) while chain A builds an apparent dimer with chain D from another asymmetric unit and *vice versa*. The structure was deposited on PDB with the accession code 7PJN (on hold for publication).

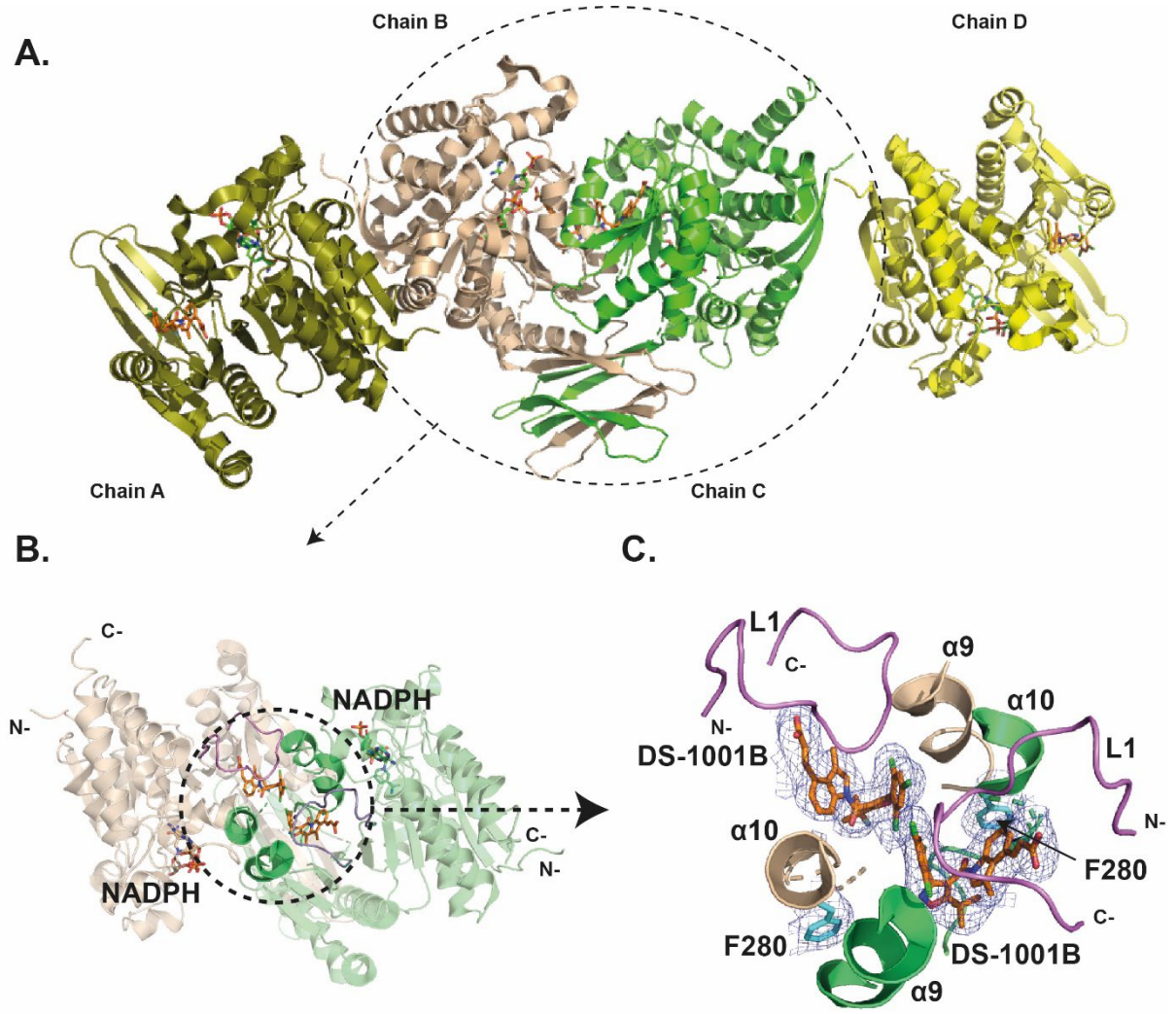

Figure 3.32 *| Ribbon view from a crystal structure of IDH1 R132C S280F (2.45 Å resolution) complexed with 4x NADPH and 4x DS-1001B (orange) likely in an open inactive conformation.* ***A.*** *There are 4 monomers in the asymmetric unit (chain A (olive), chain B (wheat), chain C (green), chain D (yellow)). Non-denaturing PAGE, SEC MALS and non-denaturing MS analyses imply that R132C S280F is predominantly dimeric in solution (Section 2.7/2.8). Chains B and C form an apparent dimer in the asymmetric unit, while chain A forms an apparent dimer with chain D from another asymmetric unit and vice versa.* ***B.*** *Ribbon view from the apparent dimer formed by chain B (wheat) and chain C (green) as observed in the asymmetric unit. DS-1001B binds at the dimer-interface (black circle).* ***C.*** *Polder omit map (blue mesh, contour 3.0 σ) showing DS-1001B and residue F280 (cyan) at the dimer-interface. The L1 loop (violet) covers the dimer-interface.*

Figure 3.32 (B) shows the apparent dimer formed by chains B and C. R132C S280F likely co-crystallised with two molecules of NADPH (note: NADPH and $NADP^+$ cannot be distinguished at a resolution of 2.45 Å) in the active site and two molecules of DS-1001B (orange) at the dimer-interface between the α9 and α10 helices. A magnified view of the dimer-interface (**Figure 3.32**, C) shows that both inhibitors are located next to each other and their trichloro phenyl rings are adjacent in the centre of the dimer-interface. The inhibitor binding site at the dimer-interface is partially covered by the L1 loop (**Figure 3.32**, C).

Allosteric IDH1 variant inhibitors are reported to lock IDH1 variants in an open-inactive conformation (Section 1.7). To distinguish between the open and closed IDH1 conformations,

the distance between the Cα carbons of the residues I76 and L250, which are located at the entrance of the active site cleft, was measured. [151] The distances for the two active sites of the dimer formed by chain B and C are 17.7 Å and 20.2 Å (**Figure 3.33**, A/B), confirming the enzyme to be in the open inactive conformation (note: the distances between I76 and L250 are 12.6 Å or 13.0 Å in the two active sites in the closed active conformation of the R132C S280F dimer (Section 2.10)).

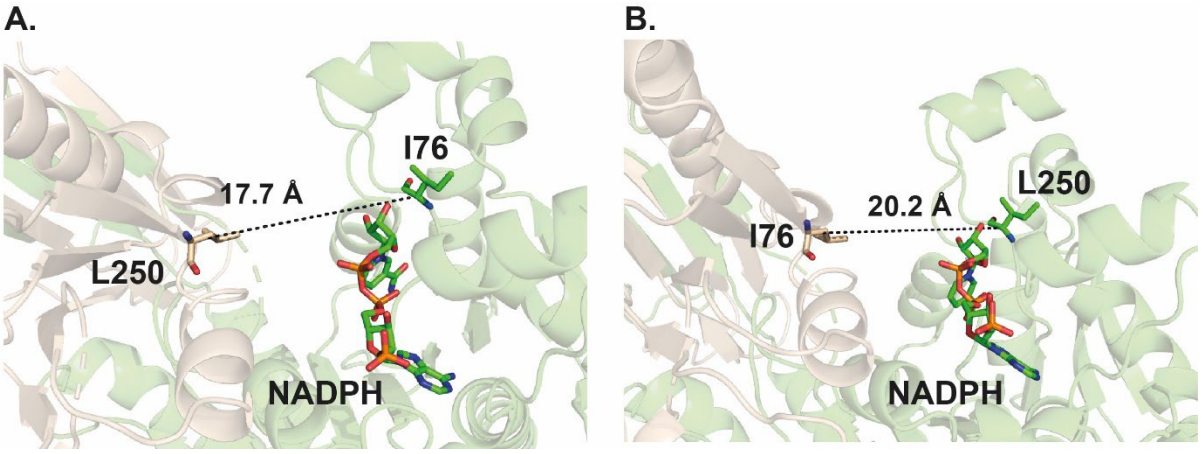

***Figure 3.33** | Ribbon view from a crystal structure of R132C S280F in the open inactive conformation. Chain B: wheat, chain C: green. Each of the two active sites in the dimer is composed of residues from both chain B and chain C. The distance between the I76 and L250 Cα carbons, which is used to measure the width of the active site cleft, is 17.7 Å **(A;** L250, chain B and I76, chain C**)** or 20.2 Å **(B;** I76, chain B and L250, chain C**)** at the active sites in the dimer.*

Neither of the F280 residues from either monomer of the inhibitor-bound crystal structure of R132C S280F are oriented towards the dimer-interface but are instead pushed to the side (**Figure 3.32**, C). This contrasts with the crystal structure of R132C S280F in the active conformation where the F280 residues from both monomers are 3.5 Å apart at the dimer-interface and likely interact with each other (Section 2.10). The closest C-atoms of the F280 residues from each monomer in the inhibitor-bound crystal structure of R132C S280F are 14.9 Å apart (**Figure 3.34**, A). Reported inhibitor-bound crystal structures of IDH1 variants were analysed to understand how inhibitor binding generally affects the S280 residue and how they compare with the DS-1001B bound structure (**Figure 3.34**). The distance between the S280 residues in IDH1 R132H structures co-crystallised with AG-881 (9.7 Å, closest C-atom from one S280 to closest O-atom of the side chain from the other S280), GSK321 (10.8 Å, closest O-atoms of the side chain of both S280), and Compound A (11.9 Å, closest C-atom from one S280 to closest C-atom of the side chain from the other S280), which is a DS-1001B analogue, are in a similar range (**Figure 3.34**, B, C, F). In the crystal structure of IDH1 R132H co-crystallised with IDH305, the S280 residues are 18.4 Å apart (closest C-atom from the side chain of one S280 to closest C-atom of the side chain from the other S280) but this is the only

R132H crystal structure with three inhibitors bound. The residues are closest in the crystal structure of R132H with FT-2102 (3.5 Å or 5.6 Å depending on the conformation of the S280 residue; distance from closest O-atoms of the side chain of both S280; **Figure 3.34**, E).

The distance between the two F280 residues at the dimer of R132C S280F (co-crystallised with DS-1001B) is larger than in all other inhibitor-bound crystal structures of IDH1 variants analysed (**Figure 3.34**), which co-crystallised with two inhibitor molecules at the dimer-interface. The large distance between both F280 residues may be related to the size of DS-1001B (note: DS-1001B was the largest inhibitor tested). This explanation is supported by a crystal structure of the smallest inhibitor from these studies, FT-2102[172], showing both S280 residues to be relatively close spatially (**Figure 3.34**, E.; distance 3.5 Å). The observation of the large distance between the F280 residues in the crystal structure of R132C S280F with DS-1001B could explain the strong binding of DS-1001B to R132C S280F, and concomitantly, its high potency by efficiently keeping the resistance causing phenylalanine residues apart from each other. Thus, DS-1001B may prevent the interaction of the F280 residues and their potential influence on the dimer-interface-chemistry and enzyme kinetics.

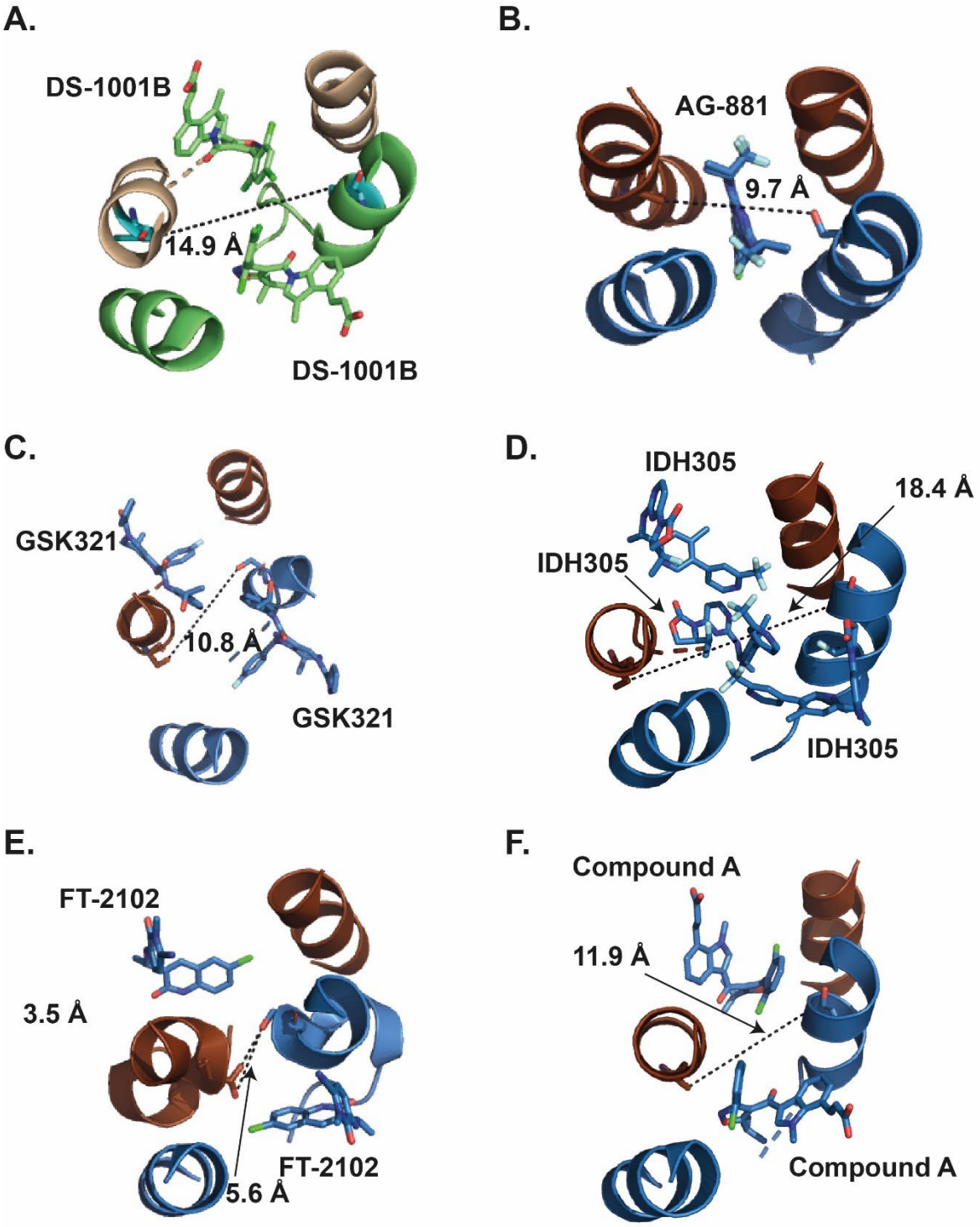

Figure 3.34 *| Ribbon views from crystal structures of IDH1 variants complexed with DS-1001B (**A**), AG-881 (**B**), GSK321 (**C**), IDH305 (**D**), FT-2102 (**E**), Compound A (**F**) measuring the distance between residue 280 in both monomers (closest carbons). **A.** One monomer of the assigned dimer is coloured in wheat, the other monomer in green. **B.-F.** One monomer is coloured in brown, the other monomer in blue. **A.** Ribbon view from a crystal structure of R132C S280F complexed with DS-1001B which manifests a distance of 14.9 Å between F280 in the two monomers. **B.** Ribbon view from a crystal structure of R132H complexed with AG-881 (6ADG[104]) which manifests a distance of 9.7 Å between S280 in the two monomers. **C.** Ribbon view from a crystal structure of R132H complexed with GSK321 (5DE1[131]) which manifests a distance of 10.8 Å between S280 in the two monomers. **D.** Ribbon view from a crystal structure of R132H complexed with IDH305 (6B0Z[168]) which manifests a distance of 18.4 Å between S280 in the two monomers. **E.** Ribbon view from a crystal structure of R132H complexed with FT-2102 (6U4J[82]) which manifests a distance of 3.5 Å or 5.6 Å (other conformer) between S280 in the two monomers. **F.** Ribbon view from a crystal structure of R132C complexed with Compound A, a DS-1001B analogue, (6IO0[83]) which manifests a distance of 11.9 Å between S280 in the two monomers.*

An interesting observation was made for the C132 residue of R132C S280F, which resides on the loop connecting the α9 and α10 helices and forms a disulphide bond with C269 (**Figure 3.35**). The formation of a disulphide bond may be a result of DS-1001B locking the enzyme in the inactive conformation, bringing the two cysteine residues spatially close to each other for a prolonged time. The proximity of the two cysteine residues results in the disulphide bond formation despite use of DTT in the precipitant solution (note: DTT is not very stable under the incubation conditions). In the only other reported structure with a cysteine at residue C132 (PDB: 6IO0[147]), both cysteine residues (C132, C269) are in close proximity, however, no disulphide bond is observed.

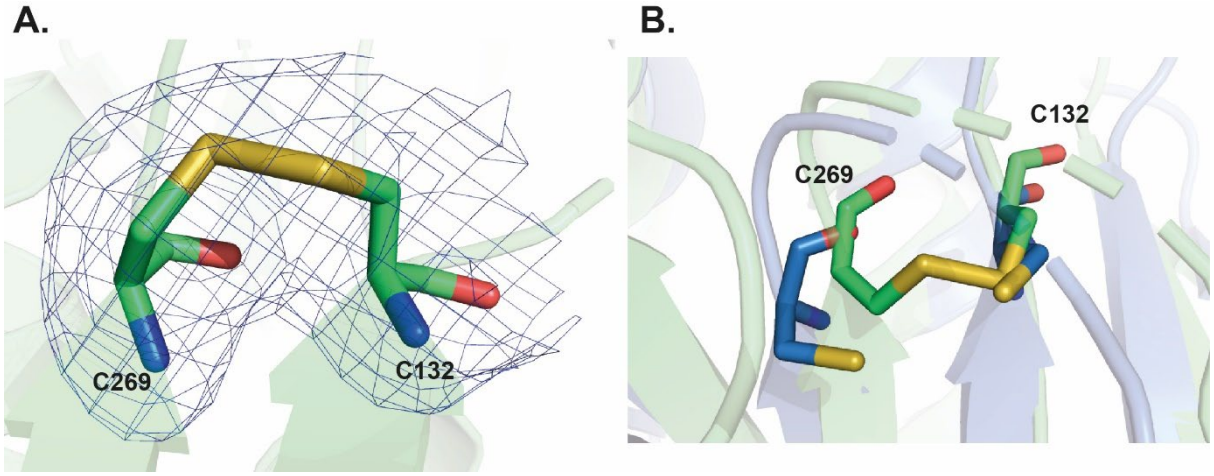

***Figure 3.35** | Ribbon view from a crystal structure of the R132C S280F variant with DS-1001B bound showing disulphide bond* formation. ***A.** Polder omit map of the R132C S280F variant showing the disulphide between C132 and C269. B. View from a crystal structure of IDH1 R132C S280F (green) superimposed with a view from one of IDH1 R132C (blue, PDB 6IO0[147]). C269 is located on the loop connecting the α9 and α10 helix. In the open conformation of IDH1, C132 and C269 are adjacent to each other and can form a disulphide bond.*

In summary, R132C S280F was co-crystallised with two molecules of DS-1001B and, likely, two molecules of NADPH. Consistent with non-denaturing MS results (**Figure 3.21**, **Figure 3.22**), two DS-1001B molecules are bound at the dimer-interface. DS-1001B appears to lock the enzyme in the open inactive conformation as reported for other inhibitors (see Section 1.7.2). Both F280 residues are oriented away from the dimer-interface and are 14.9 Å apart. The crystal structure of R132C S280F with DS-1001B bound is the first crystal structure of an S280F substituted variant with an inhibitor, and the first crystal structure of the inhibitor DS-1001B which is currently in clinical phase 2 trials. Studying the structural properties of an inhibitor-bound structure of the ivosidenib-resistant variant R132C S280F can further develop the understanding of drug resistance and can inform on future inhibitor development. One strategy could be to synthetically link both DS-1001B molecules via their trichloro phenyl

rings. However, this would result in a very large inhibitor and would likely cause pharmacokinetic issues including blood-brain barrier permeability.

3.8 Inhibitor Treatment of Cell Lines Harbouring Ivosidenib-Resistant IDH1 Variants

The LN18 cell lines used in this section were made by Dr Alina Finch and Dr Chiara Bardella at the University of Birmingham. Cell growth, cell treatment, and metabolomic analyses were conducted by Ingvild Hvinden at the University of Oxford.

Several inhibitors retained activity against R132C S280F and R132H S280F in biochemical assays (Section 3.3.3). To test whether they are active in a cellular environment, LN18 cell lines were transfected with lentiviral vectors resulting in overexpression of R132C, R132C S280F, R132H, or R132H S280F. An LN18 cell line with an empty vector was used as the control. The cell lines were then treated for 24 h with ivosidenib, GSK864, IDH224, FT-2102, or DS-1001B (5 μM final concentration, final DMSO concentration (v/v) 0.1%). The 2-HG levels were analysed by anion exchange MS as previously reported. [175]

3.8.1 Preparation and Production of LN18 Cell Lines Overproducing IDH1 Variants

The human glioblastoma cell line LN18 was used to overexpress genes encoding for IDH1 R132C, R132C S280F, R132H, and R132H S280F with a lentiviral vector transduction. Constructs were made by a PCR-based approach using lentiviral transfer vectors. The vectors were amplified and cloned into the pUltra-Chili vector (AddGene). This vector expresses the red fluorescent dTomato protein which can be used as a reporter for successful cell transduction.[176] The constructs were verified by Sanger sequencing.

Transient transfection of HEK293T cells along with 3 packaging plasmids (pVSVg, pREV, pMDL) was used to package the pUltra-Chili transfer plasmids into lentiviral vectors. The medium was harvested after 48 h, centrifuged, and filtered through 0.22 μm filters. Serial dilutions of freshly harvested conditioned medium were used to infect 1.2×10^5 LN18 cells in a six-well plate in the presence of polybrene (8 μg/ml). The control was a pUltra-Chili vector without a transfer sequence. Successful transduction was indicated by red fluorescence as a result of the expression of the dTomato gene (**Figure 3.36**).

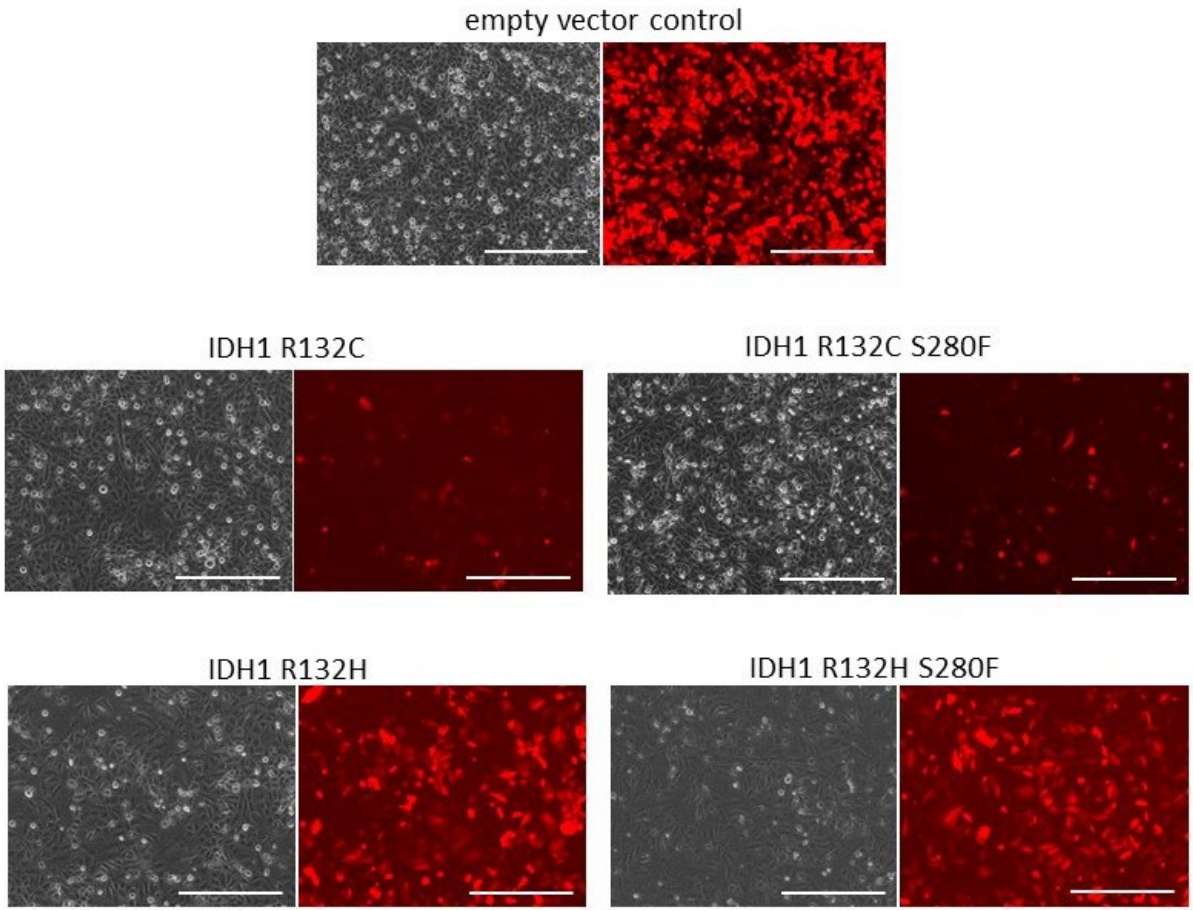

Figure 3.36 *| LN18 cell lines transfected with the pUltra Chili vector without a transfer sequence or with genes for overexpression of R132C, R132C S280F, R132H, or R132H S280F. Successful transduction was indicated by fluorescence of the dTomato reporter protein (excitation: 554 nm). Data were generated by Dr Alina Finch.*

Quantitative polymerase chain reactions (qPCR) were used to measure IDH1 mRNA expression levels in control and LV-transduced cells using an IDH1 TaqMan probe. TaqMan probes[177] are probes which consist of short DNA oligonucleotides complementary to the gene of interest. A reporter and quencher are attached to the oligonucleotide. Due to the close proximity the quencher absorbs the reporter signal and no fluorescence can be observed.[177] In the process of the PCR reaction, the TaqMan probe is annealed to the strand of interest. When the DNA polymerase reaches the probe, the DNA polymerase 5'-nuclease activity hydrolyses the TaqMan probe and separates the quencher from the reporter, and a fluorescence signal can be observed. [177] This signal is specific for the vector with the gene of interest and can be used to quantify it (**Figure 3.37**).

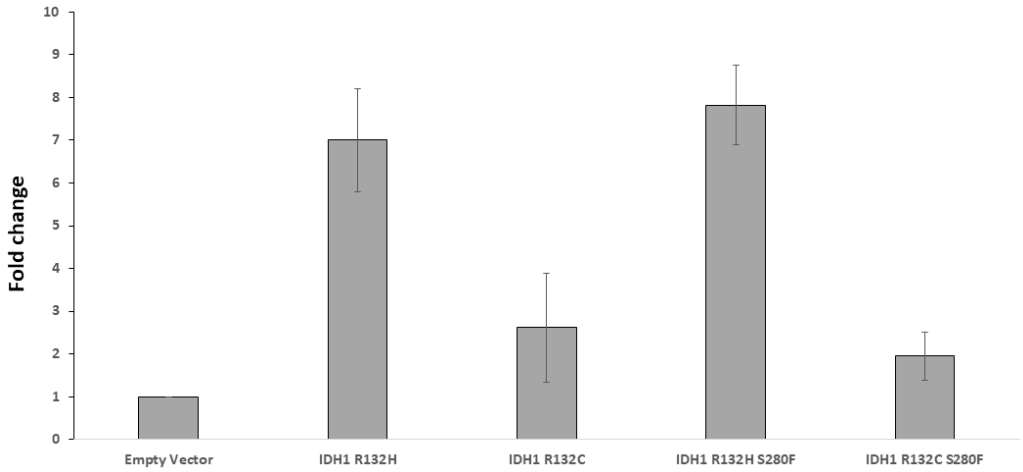

Figure 3.37 *| TaqMan plot showing levels of expression of transgenes. Data were generated by Dr Alina Finch.*

3.8.2 Cell Growth

LN18 cells containing an empty vector or producing recombinant IDH1 R132C, IDH1 R132C S280F, IDH1 R132H, or IDH1 R132H S280F were grown according to Section 7.2.10. The cell lines were treated with either 5 μM inhibitor (ivosidenib, GSK864, IDH224, FT-2102, DS-1001B prepared in DMSO) or 0.1% v/v DMSO (control samples) according to Section 7.2.10. Cells were incubated for 24 hours prior to harvest.

3.8.3 Analysis of 2-HG Levels

The DNA concentration (ng/μL) of the supernatants was measured by absorbance at 280 nm and used for the normalisation of cell numbers according to Section 7.2.10. Metabolomic analyses were carried out using anion-exchange chromatography with high-resolution orbitrap tandem MS according to published procedures.[175]

In brief, anion-exchange chromatography MS was shown to be able to provide good coverage of metabolites in central carbon metabolism.[175] The method is used for acidic molecules and the chromatographic separation is based on ionic interactions with a stationary resin. Elution is achieved by an aqueous mobile phase containing increasing concentrations of hydroxide ions. After passing through an ion suppressor, which electrochemically converts hydroxide ions to water molecules (note: this step is crucial to enable subsequent MS analysis), the sample is subjected to electrospray ionisation and orbitrap MS. The technique was shown to be useful for a complete pathway analysis of LN18 cell lines overexpressing IDH1 R132H. [175] In this

chapter, the analysis of 2-HG levels in LN18 cell lines overexpressing R132C, R132C S280F, R132H or R132H S280F is discussed.

Firstly, analysis of 2-HG levels in an LN18 cell line with an empty vector was conducted using anion-exchange chromatography MS. As anticipated, low endogenous levels of 2-HG were present. None of the inhibitors influenced the 2-HG levels within detection limits (**Figure 3.38**).

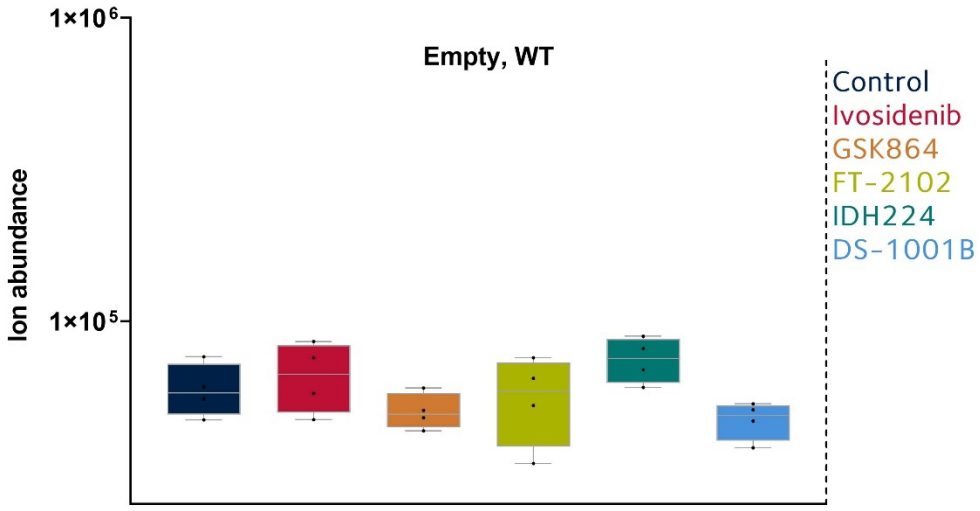

Figure 3.38 *| Studies on the influence of inhibitors on 2-HG levels produced in LN18 cell lines with an empty vector. Cells were treated with 5 μM of inhibitors ivosidenib, GSK864, FT-2102, IDH224, or DS-1001B in DMSO (error bars: standard errors of the mean, n = 4). The data were generated by Ingvild Hvinden.*

Next, analyses of 2-HG levels in LN18 cell lines overproducing R132C and R132C S280F were carried out (**Figure 3.39**). Consistent with the literature[178,172,179] and results from experiments with isolated enzymes (**Table 3.3**), all inhibitors tested potently decreased 2-HG levels from the no-inhibitor control (ion count of ~160,000) to baseline levels (ion count of ~50,000) in R132C bearing cell lines. However, the effects of the inhibitors in R132C S280F cell lines were different. The no-inhibitor control displayed an ion count for 2-HG of ~175,000. Consistent with results from biochemical assays, ivosidenib did not decrease 2-HG levels substantially (ion count of ~150,000), and GSK864 exhibited a moderate decrease (ion count of ~130,000). FT-2102, IDH224, and DS-1001B decreased 2-HG levels to baseline (ion count of ~50,000).

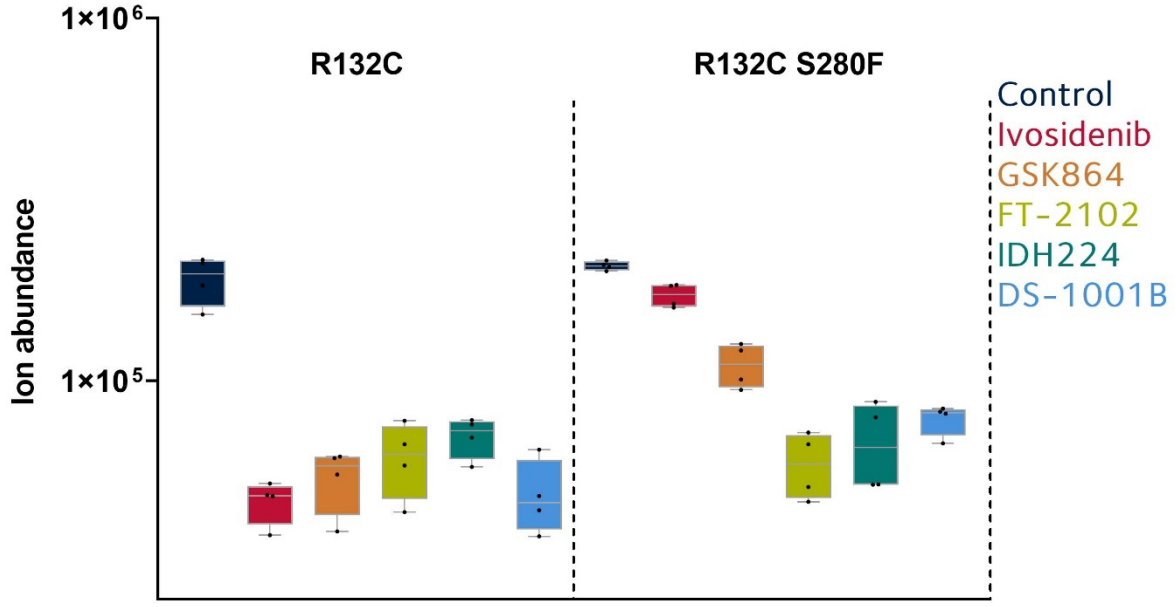

Figure 3.39 *| Studies on the influence of inhibitors on 2-HG levels produced in LN18 cell lines with recombinant R132C and R132C S280F. Cells were treated with 5 µM of inhibitors ivosidenib, GSK864, FT-2102, IDH224, and DS-1001B in DMSO (error bars: standard errors of the mean, n = 4). The data were generated by Ingvild Hvinden.*

Similar to the results for R132C, in R132H overproducing cell lines, all inhibitors tested potently decreased 2-HG levels, as evidenced by a decrease in the 2-HG ion count from 410,000 to 50,000 (**Figure 3.40**). This observation is consistent with the literature reports[172,178,179] and results from biochemical assays (**Table 3.3**). In contrast, ivosidenib exhibited little effect on 2-HG levels in R132H S280F overproducing cell lines (the no-inhibitor control displayed an ion count of ~915,000) consistent with results from biochemical assays (**Table 3.3**). A moderate decrease in 2-HG levels was observed in the presence of GSK864 (ion count of ~115,000). FT-2102 and IDH224 decreased 2-HG levels to baseline (ion count of ~50,000). Surprisingly, DS-1001B was a poor inhibitor of 2-HG production in this experiment (ion count of ~500,000).

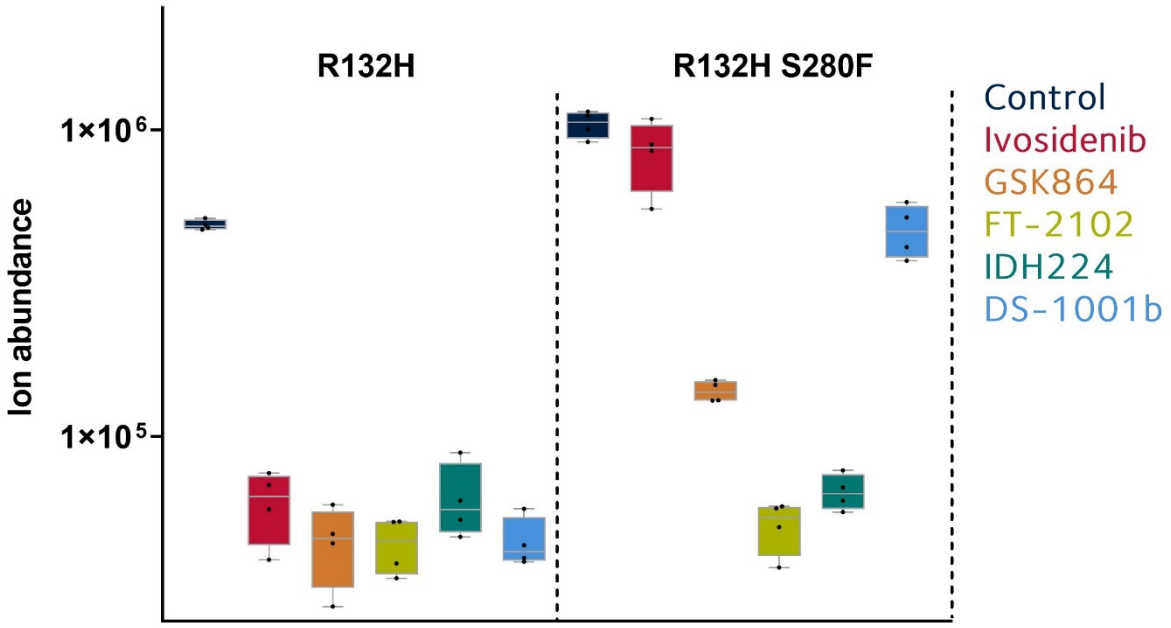

***Figure 3.40** | The influence of inhibitors on 2-HG levels produced in LN18 cell lines with recombinant R132H and R132H S280F. Cells were treated with 5 μM of inhibitors ivosidenib, GSK864, FT-2102, IDH224, or DS-1001B in DMSO (error bars: standard errors of the mean, n = 4). The data were generated by Ingvild Hvinden.*

3.8.4 Comparison with Inhibition Against Recombinant Variants

As outlined in Section 3.8.3, reduction of 2-HG levels by inhibitors tested (ivosidenib, GSK864, FT-2102, IDH224, DS-1001B) largely corresponds with the biochemical data obtained confirming ivosidenib resistance in a cellular environment. Comparison of the biochemical and cellular inhibition data using a Spearman's rank order correlation, gives r_s(R132C S280F) = 0.87 and r_s(R132H S280F) = 0.67 indicating a strong positive correlation between the two datasets.

There was no inhibition of R132C S280F and R132H S280F by ivosidenib in the biochemical assays (**Table 3.3**) and no 2-HG reduction in cell lines overproducing R132C S280F or R132H S280F (**Figure 3.39**/**3.40**). GSK864 was moderately active against isolated R132C S280F and R132H S280F (**Table 3.3**) and accordingly reduced 2-HG levels of cell lines overproducing R132C S280F and R132H S280F moderately (**Figure 3.39**/**3.40**). DS-1001B and IDH224 were potent inhibitors of isolated R132C S280F in biochemical assays (**Table 3.3**) and decreased 2-HG levels to baseline in LN18 cells overproducing R132C S280F (**Figure 3.39**). FT-2102 and IDH224 were potent inhibitors of isolated R132H S280F in biochemical assays (**Table 3.3**)

and potently decreased 2-HG levels in LN18 cell lines overproducing R132H S280F (**Figure 3.40**).

Two apparent discrepancies between inhibitor potency against recombinant enzymes and reduction of 2-HG levels in LN18 cell lines should be discussed. Firstly, FT-2102 was a poor inhibitor in biochemical assays against R132C S280F (IC_{50} = 1.3 μM; **Table 3.3**), but potently decreased 2-HG levels in LN18 cells harbouring the R132C S280F variant (**Figure 3.39**). A potential reason for this could be the low molecular weight of FT-2102 (**Figure 3.15**) resulting in disproportionately better membrane permeation and bioavailability compared to the other larger inhibitors tested. Secondly, the treatment of R132H S280F overproducing cells with DS-1001B reduced 2-HG levels poorly (**Figure 3.40**) but DS-1001B exhibits an IC_{50} of 20 nM in biochemical assays (**Table 3.3**). This likely reflects the higher IC_{50} for R132H S280F compared to all other IDH1 variants (**Table 3.3**; R132C: IC_{50} = 5 nM, R132C S280F: IC_{50} = 2 nM, R132H: IC_{50} = 1 nM) in combination with a potentially poorer bioavailability than other inhibitors (note: DS-1001B was the largest inhibitor tested and is negatively charged at physiological pH due to a carboxylic acid group, **Figure 3.15**).

3.9 Summary and perspectives

Building on the results of kinetic, structural, and substrate binding studies (Chapter 2), further studies on the ivosidenib-resistant IDH1 variants R132C S280F and R132H S280F were conducted with an emphasis on their interaction with inhibitors. Initially, published crystal structures of inhibitors bound to IDH1 R132H or R132C were analysed for their potential to retain activity in S280F substituted variants and to predict other second-site variations (based on the identification of important residues for inhibitor binding) which have the potential to cause drug resistance (Section 3.2).

Inhibition studies on isolated S280F variants were conducted using an NADPH absorbance assay. It was shown that ivosidenib loses potency against isolated R132C S280F and R132H S280F (**Figure 3.9**), which is predominantly the result of a reduction in binding efficiency as shown by non-denaturing MS, CPMG-edited ^{1}H NMR, and DSF studies (Section 3.3.2).

Using an R132C S280A variant, it was demonstrated that the loss of binding efficiency to S280F substituted variants is most likely a result of the steric effect and additional hydrophobic interactions of phenylalanine, but that loss of the serine (potential hydrogen bond to ivosidenib) may play an additional role (**Figure 3.10**-**Figure 3.13**).

An inhibitor screen (**Figure 3.16**) showed that some, but not all IDH1 inhibitors lose inhibitory activity against R132C S280F and R132H S280F. Interestingly, inhibitors retaining activity can bind with a stoichiometry of two molecules to the IDH1 dimer (as shown for GSK864, IDH224, FT-2102, DS-1001B; **Figure 3.21**/**Figure 3.22**) which is in contrast with ivosidenib which can only bind with a stoichiometry of one molecule to the IDH1 dimer (**Figure 3.10**). Some of these inhibitors retain potent inhibitory activity (IC_{50} <100 nM; **Table 3.3**, i.e. IDH224, FT-2102, DS-1001B). Non-denaturing MS, CPMG-NMR and DSF studies showed that binding of inhibitors was mostly weak (**Figure 3.23**-**Figure 3.26**, **Table 3.4**), although some inhibitors exhibited high binding affinity (**Figure 3.27**).

Using an NADPH absorbance assay to measure inhibition at different substrate concentrations, it was shown that the potent inhibitors of R132C, R132C S280F, R132H, and R132H S280F are competitive with respect to magnesium and 2-OG binding (**Figure 3.28**/**Figure 3.29**), but not with NADPH (**Figure 3.30**; although FT-2102 may be minorly influenced by NADPH concentration). A crystal structure of R132C S280F with DS-1001B in the open inactive conformation (**Figure 3.33**) showed binding of two inhibitors at the dimer-interface (**Figure 3.32**). The two trichlorophenyl rings of DS-1001B are adjacent, suggesting production of a homodimeric version of DS-1001B could result in higher potency. In the DS-1001B-bound structure the two phenylalanine residues are not interacting and are oriented to the side of the dimer-interface (**Figure 3.34**; 14.9 Å apart). Previously, the occurrence of the R132C S280F variation was correlated with a relapse in AML patients and increasing 2-HG levels in their plasma during treatment with ivosidenib.[180] In cellular studies with LN18 cell lines overexpressing IDH1 variants, ivosidenib resistance was demonstrated in R132C S280F and R132H S280F overexpressing variants. However, several inhibitors retained potency in a cellular environment including IDH224, FT-2102, and DS-1001B (**Figure 3.39**,**Figure 3.40**). FT-2102 and DS-1001B are presently in phase 2 clinical trials[181,164,92] and hence these findings could have an immediate clinical impact suggesting second-line treatments if ivosidenib resistance emerges. Furthermore, combination regimens of inhibitors could be used to avoid the emergence of resistances in the first place.

3.10 Materials and Methods

3.10.1 Inhibition Studies

The NADPH absorbance assay using a PHERAstar FS Microplate Reader according to the Materials and Methods (Section 7.2.1) was employed. Inhibitors were dissolved in DMSO to

a concentration of 10 mM. The inhibitor screening was conducted with 400 nM IDH1 variant. Enzyme and inhibitor were incubated for 12 minutes, and the reaction was initiated by addition of 2-OG and NADPH. The turnover was measured continuously and inhibition was normalised to a no-inhibitor control (0% inhibition) and a no enzyme control (100% inhibition). For the IC_{50} determination the same procedure was used, but the enzyme concentration was decreased to 30 nM. A pilot study showed no interference of 1% DMSO with enzymatic activity. Subsequently, the maximal DMSO concentration used was 0.8%. An inhibitor dilution series was prepared, and the normalised response was plotted against the inhibitor concentration on a logarithmic scale. The IC_{50} was determined using the non-linear regression curve fit tool (variable slope with 4 parameters) of the GraphPad Prism software (version 5).

Competition studies were conducted with 400 nM enzyme and 200 nM inhibitor. For 2-OG and NADPH competition studies, the same buffer as described in Section 2.12.2 was used. Inhibitor and enzyme were incubated in buffer for 12 minutes, and the reaction was initiated by the addition of 2-OG and NADPH. For competition studies with magnesium, the buffer was prepared according to the following recipe (as described in 2.12.2, but without $MgCl_2$, pH 8.0):

	C (mM)	n (mol)	Mw (g/mol)	V (L)	m (g)
Tris base	100	0.025	121.14	0.25	3.0285
DTT	0.2	0.00005	154.25	0.25	0.007713
Tween-20 (C_V in %)	0.0050			0.25	0.0125
BSA (C_m in mg/mL)	0.1			0.25	0.025

Inhibitor, enzyme, buffer and magnesium were incubated for 12 minutes, and the reaction was initiated by addition of 2-OG and NADPH. For all competition studies, the inhibition was calculated using a no inhibitor control (0% inhibition) and a no enzyme control (100% inhibition).

3.10.2 Non-Denaturing Mass Spectrometry

Non-denaturing mass spectrometry experiments analyses were conducted according to the Materials and Methods (Section 7.2.7). Inhibitors were dissolved in MeOH (10 mM). Inhibitors were added to the protein solution, the solution spun down at 13,000 rpm, and subjected to electrospray ionisation. To calculate the dissociation constant, a baseline correction was

applied. The fraction of bound inhibitor was calculated using the charge states z = 19, z = 20, and z = 21 and used for the calculation of the standard error of the mean.

3.10.3 ^{1}H CPMG-Edited NMR

^{1}H CPMG-edited NMR was conducted according to the Materials and Methods section (Section 7.2.2). Inhibitors were dissolved in d_6-DMSO (10 mM). A ^{1}H spectrum of inhibitor (10 µM) was collected and increasing concentrations of protein were titrated in (<10% volume). To make highly concentrated protein stocks, Amicon 50,000 MWCO centrifugal filter units (0.5 mL) were used. The protein was added into the NMR tube and mixed before it was spun down.

3.10.4 Differential Scanning Fluorimetry

DSF was conducted according to Materials and Methods (Section 7.2.5). An inhibitor dilution series (2x) was prepared in DSF buffer and added to the protein solution (3 µM). Changes in T_m were calculated based on the T_m of protein without inhibitors.

3.10.5 Crystallographic Studies

The crystallization buffer consisted of 25.62 mg×mL^{-1} in 20 mM Tris, 100 mM NaCl, 1 mM tris(2-carboxyethyl)phosphine (TCEP), pH 7.4. IDH1 R132C S280F (in crystallisation buffer) was used for crystallisation. For the sitting drop setup, a 24-well Cryschem Plate (Hampton Research, USA) with a reservoir solution of 250 µL was used based on previous reports.[182] A screen varying the ammonium citrate concentration (pH 7.0, 0.75-2 M, horizontal axis in steps of 0.25 M) and the DTT concentration (1.5-3 mM, vertical axis in steps of 0.5 mM) was carried out. The protein (12.5 µL) was incubated on ice for 1 h with NADPH (10 mM; in crystallisation buffer), crystallisation buffer (6.8 µL), and a 10-fold excess of DS-1001B (from a 10 mM stock in DMSO, 0.7 µL) to a final protein concentration of 12.81 mg×mL^{-1}. 2 µL of this solution was then added to 2 µL precipitant solution. The sitting drop plate was sealed with StarSeal Advanced Polyolefin Film (Starlab, Germany) and the crystals appeared after 1 day. Crystal harvesting was performed with glycerol as a cryo-protectant as described in Section 2.10.

Data were collected at 100 K using synchrotron radiation at Diamond Light Source (DLS) beamline I03. Data were indexed, integrated, and scaled using the Xia2[150] strategy of the beamline auto-processing pipeline (Supplemental Table 3). An initial MR solution was obtained with an inhibitor bound structure of IDH1 R132H (PDB: 5TQH[183]) which has a similar space group and unit cell. A starting model was re-built from this MR solution using

PHENIX AutoBuild[158 184 185 186 187] (this was conducted by Dr Ian Clifton). The structural model was optimised by iterative cycles of manual re-building in COOT[157] and crystallographic refinement in phenix.refine.[158] Due to the limited resolution (2.45 Å), NCS restraints were used throughout, as well as TLS refinement of *B* factors (16 TLS groups for the four chains).

3.10.6 Cell Studies and Metabolomic Analyses

Cell preparation and growth was conducted according to the Materials and Methods section (7.2.10). Inhibitor treatment and metabolomics analyses were conducted according to Section 7.2.10 of the Materials and Methods.

Chapter 4

Studies on the Role of Catalytic and Allosteric Variations on the Activity of Hs IDH1

Contents

4 Studies on the Role of Catalytic and Allosteric Substitutions on the Activity of *Hs* IDH1

4.1 Introduction

IDH1 catalyses the oxidative decarboxylation of isocitrate to 2-oxoglutarate (2-OG). The residue R132, situated in the active site, is involved in isocitrate binding by IDH.[50] Mis-sense mutations in the gene encoding for IDH1 R132 are frequently observed in several types of cancer resulting in a gain-of-function activity (Section 1.4).[35]

All reported clinically observed R132 substitutions promote the ability of IDH1 variants to catalyse the reduction of 2-OG to 2-hydroxyglutarate (2-HG).[35,188] The most common variants are R132H and R132C, as discussed in Chapter 2, where they were compared with the double variants R132H S280F and R132C S280F, respectively. The work described in the first part of this chapter compares the activity of R132H and R132C with the previously not studied R132S variant using kinetic, biophysical, and binding studies.

The influence of dimer-interface variations on IDH1 wt activity was investigated using the IDH1 S280F variant, in which the catalytic region remains unmodified. Additionally, several novel IDH1 R132H second-site variants were studied to investigate the role of the dimer-interface in IDH1 catalysis and inhibition, i.e. R132H V255F, R132H Q277E, and R132H V281F (as outlined in Chapter 3.2.2). The second part of this chapter describes work comparing the properties of these variants with IDH1 wt and IDH1 R132H. Investigations on the influence of dimer-interface variations on enzymatic properties using kinetic, biophysical, and binding studies were carried out. Please note that in this chapter, all variants referred to are of IDH1, unless stated otherwise.

4.1.1 R132 Cancer Variants of IDH1

Crystal structures of the active enzyme conformation of IDH1 are available for IDH1 wt, and the R132H and R132C S280F variants. An overlay of crystal structures of IDH1 wt (PDB: 1T0L[151]), R132H (PDB: 4KZO[126]) and R132C S280F (see Section 2.10) was made (**Figure 4.1**) to compare the residues at position 132 focussing on the active site.

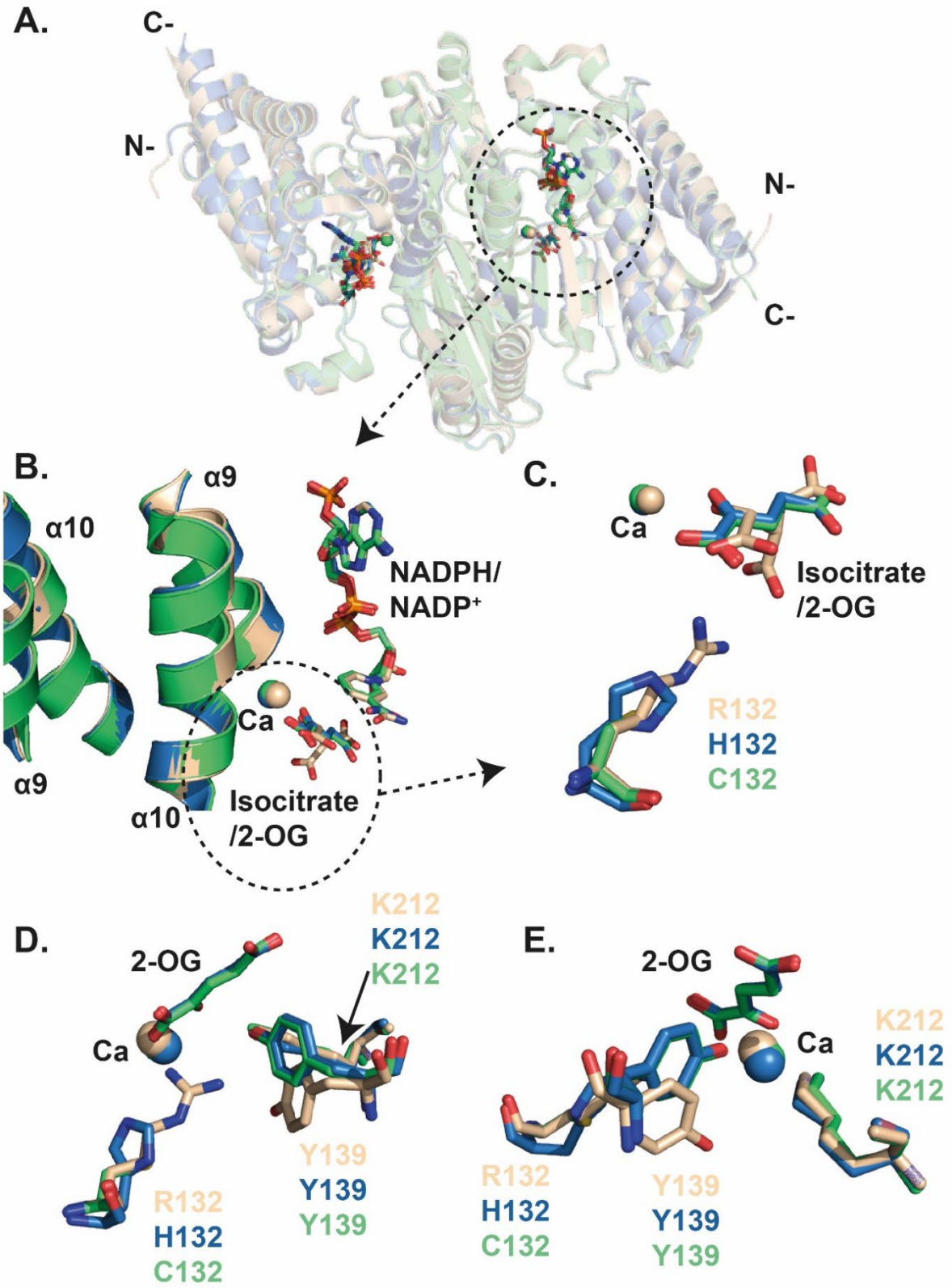

Figure 4.1 | *Overlay of crystal structures of IDH1 wt, R132H and R132C S280F.* ***A.*** *View from a crystal structure of IDH1 wt (beige, PDB ID: 1T0L[153]) superimposed with IDH1 R132H (blue, PDB ID:4KZO[126]) and R132C S280F (green). R132H and R132C S280F are co-crystallised with 2-OG, NADPH and calcium, while IDH1 wt is co-crystallized with isocitrate, $NADP^+$ and calcium.* ***B.*** *A magnified section showing the α9 and α10 helices at the dimer-interface as well as the active site with calcium, 2-OG/isocitrate and NADPH/$NADP^+$.* ***C.*** *View of the active site showing variations at residue 132 and their spatial relationship to calcium and 2-OG/isocitrate.* ***D./E.*** *Magnified sections of the active site showing variations at residue 132, as well as the binding of 2-OG by calcium, Y139 and K212.*

The overall dimeric structures of IDH1 wt, R132H, and R132C S280F exhibit high overall structural similarity (**Figure 4.1**, A; C_α RMSDs: IDH1 wt and R132H = 0.39 Å, IDH1 wt and R132C S280F = 0.42 Å, R132H and R132C S280F = 0.30 Å). The active site is located next to the α9 and α10 helices, which substantially form the dimer-interface. There are no apparent differences in NADPH or $NADP^+$ binding modes (**Figure 4.1**, B). R132, which is located on a loop at the active site, is involved in the binding of the isocitrate C3 carboxylate (Section 1.6). R132 substitutions in general reduce affinity for isocitrate,[189] and promote reduction of 2-OG to 2-HG.

Insight into reduced binding affinity of isocitrate to the IDH1 R132 variants is given by comparing the crystal structures of wt, R132H and R132C S280F. In IDH1 wt, isocitrate binds via its C3 carboxylate group to the guanidino group of R132. Introducing a histidine or cysteine at this position reduces interactions of residue 132 with the isocitrate C3 carboxylate (**Figure 4.1**, C). In the structures of IDH1 R132H and IDH1 R132C S280F, 2-OG is bound through interactions with K212 and Y139. Likely due to its involvement in 2-OG binding, Y139 is observed to move towards 2-OG in R132H and R132C S280F compared to IDH1 wt (**Figure 4.1**, D/E).

4.2 Protein Production

To investigate the effect of R132 variations and variations at the dimer-interface, recombinant proteins were produced. A pET22b plasmid containing an open reading frame (ORF) for IDH1 wt with a C-terminal His-tag was kindly provided by Dr Martine Abboud. The procedures were conducted as described in Section 4.7.1 and Section 7.1.12. Primers were designed to alter the ORF to encode for R132S, S280F, R132H V255F, R132H Q277E or R132H V281F. Forward and reverse primers were designed completely overlapping or according Zheng et al.[127](Section 4.7.1.1). Site-directed mutagenesis (SDM) was conducted, and successful mutagenesis demonstrated by Sanger Sequencing (**Figure 4.2**). The plasmids were transformed into BL21(DE3)pLysS *E. coli* cells and expressed (Section 7.1.12). The cells were harvested by centrifugation. The pellet was lysed and IDH1 variant enzymes were purified by nickel-affinity chromatography (5 mL fractions) and size-exclusion chromatography (10 mL fractions) (Section 4.7.1). Fractions containing purified protein were pooled based on SDS-page analysis, concentrated, and stored in gel filtration buffer. Observed lower molecular weight protein bands on SDS-PAGE gels possibly correspond to degradation products due to the heating process in SDS-PAGE sample preparation (95°C for 5 minutes; **Figure 4.3**-**Figure 4.8**).

LC/MS analyses was used to demonstrate the correct molecular weight of all IDH1 variants (**Table 4.1**).

Figure 4.2 *| Sequence alignment of IDH1 variants. The residue R132 is highlighted (red box), as are the variations introduced at the dimer-interface (green box). The green box on the left highlights V255, the next green box highlights Q277, and the last green box highlights the residues S280 and V281. The purple box highlights part of the L1 loop. The blue boxes highlight the α9 and α10 helix.*

4.2.1 IDH1 R132S

Following lysis of cells, purification (**Figure 4.3**) yielded 21.2 mg/L (**Table 4.12**) of IDH1 R132S, which was aliquoted at a concentration of 25.5 mg/mL (534.2 µM).

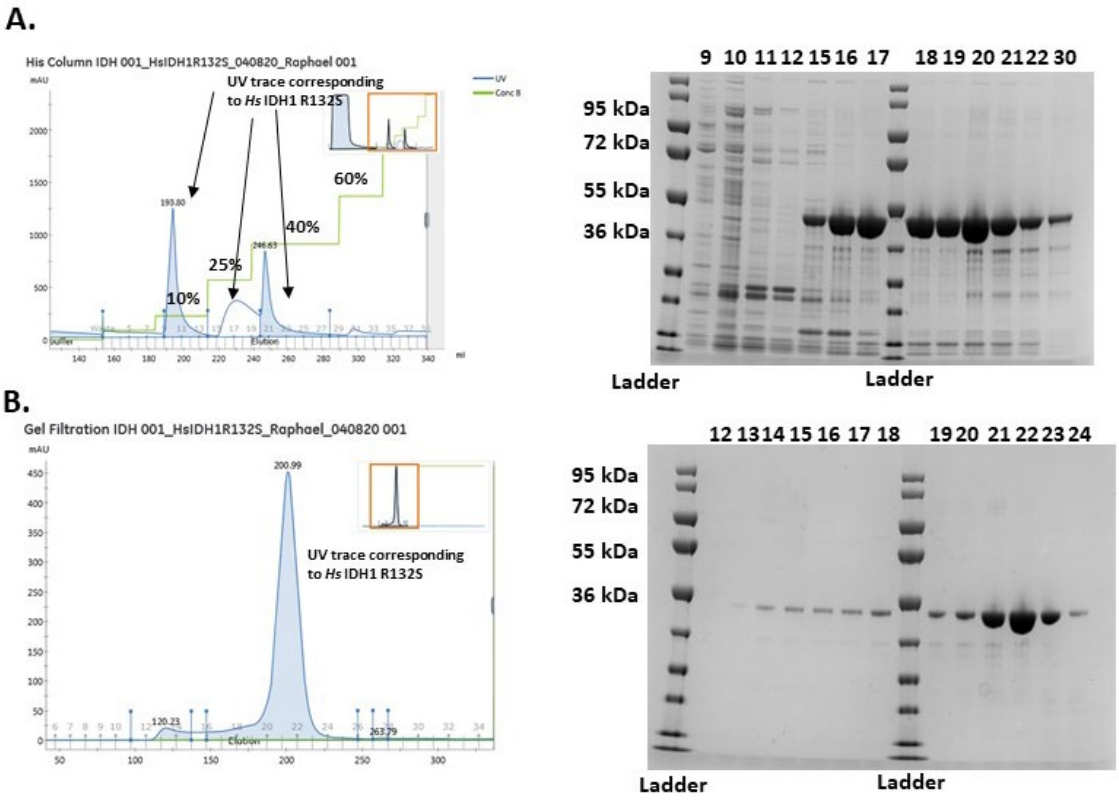

***Figure 4.3** | IDH1 R132S purification. The chromatogram of each purification technique is shown on the left, the SDS-PAGE gel on the right. **A**. Nickel-affinity chromatography using imidazole step gradient elution (percentages of elution buffer are shown on the chromatogram). **B.** Size-exclusion chromatography using an isocratic elution.*

4.2.2 IDH1 wt

Following lysis of cells, purification (**Figure 4.4**) yielded 50.0 mg/L (**Table 4.12**) of IDH1 wt, which was aliquoted at a concentration of 20.0 mg/mL (419.1 μM). The purification process was kindly conducted by Dr Martine Abboud.

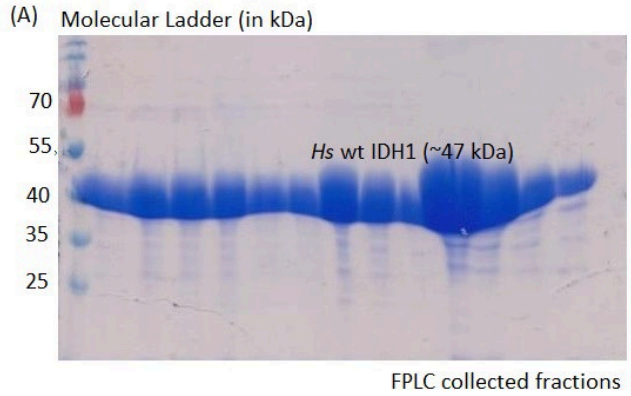

Figure 4.4 *| SDS-PAGE of IDH1 wt after the final size-exclusion purification step.*

4.2.3 IDH1 S280F

Following lysis of cells, purification (**Figure 4.5**) yielded 30.4 mg/L (**Table 4.12**) of IDH1 S280F, which was aliquoted at a concentration of 29.6 mg/mL (619.4 µM).

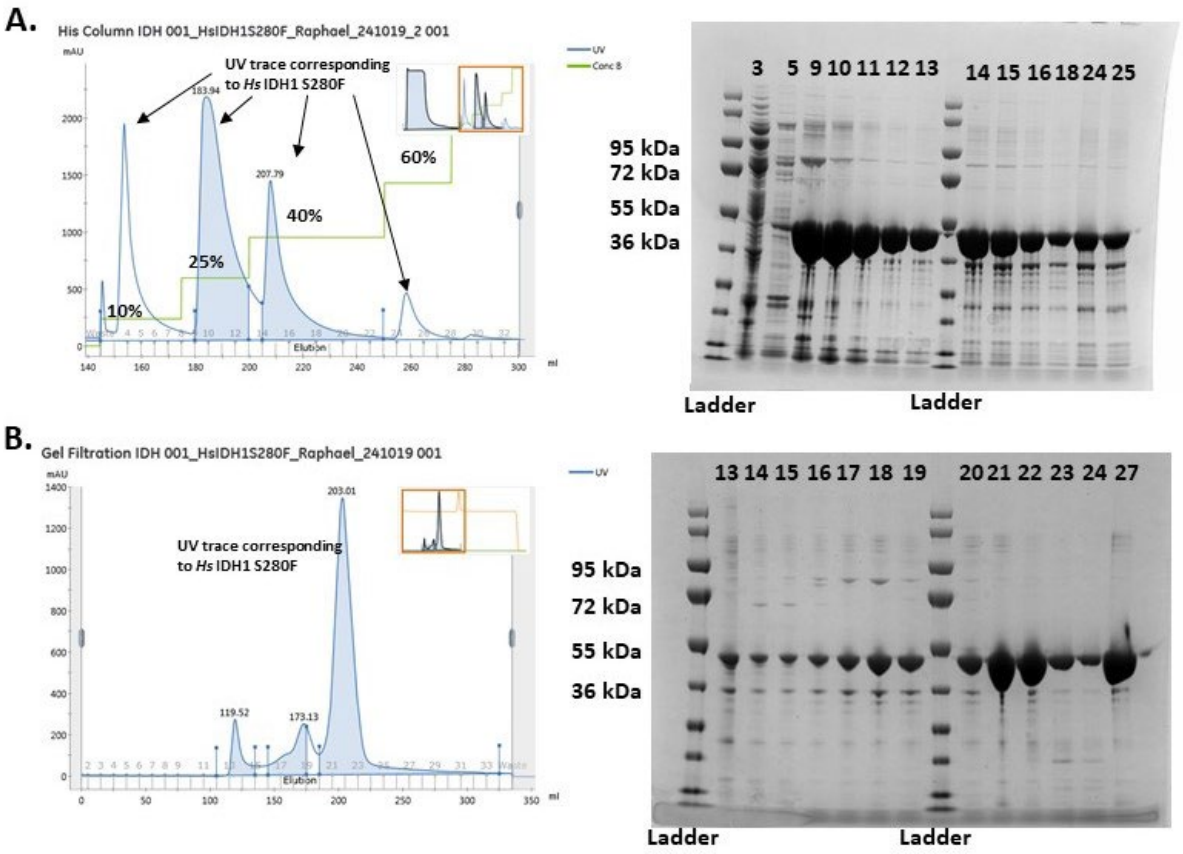

***Figure 4.5** | IDH1 S280F purification. The chromatogram of each purification step is shown on the left, the SDS-PAGE gel on the right. **A**. Nickel-affinity chromatography using imidazole step gradient elution (percentages of elution buffer are shown on the chromatogram). **B.** Size-exclusion chromatography using an isocratic elution.*

4.2.4 IDH1 R132H V255F

Following lysis of cells, purification (**Figure 4.6**) yielded 109.2 mg/L (**Table 4.12**) of IDH1 R132H V255F, which was aliquoted at a concentration of 27.9 mg/mL (584.6 µM).

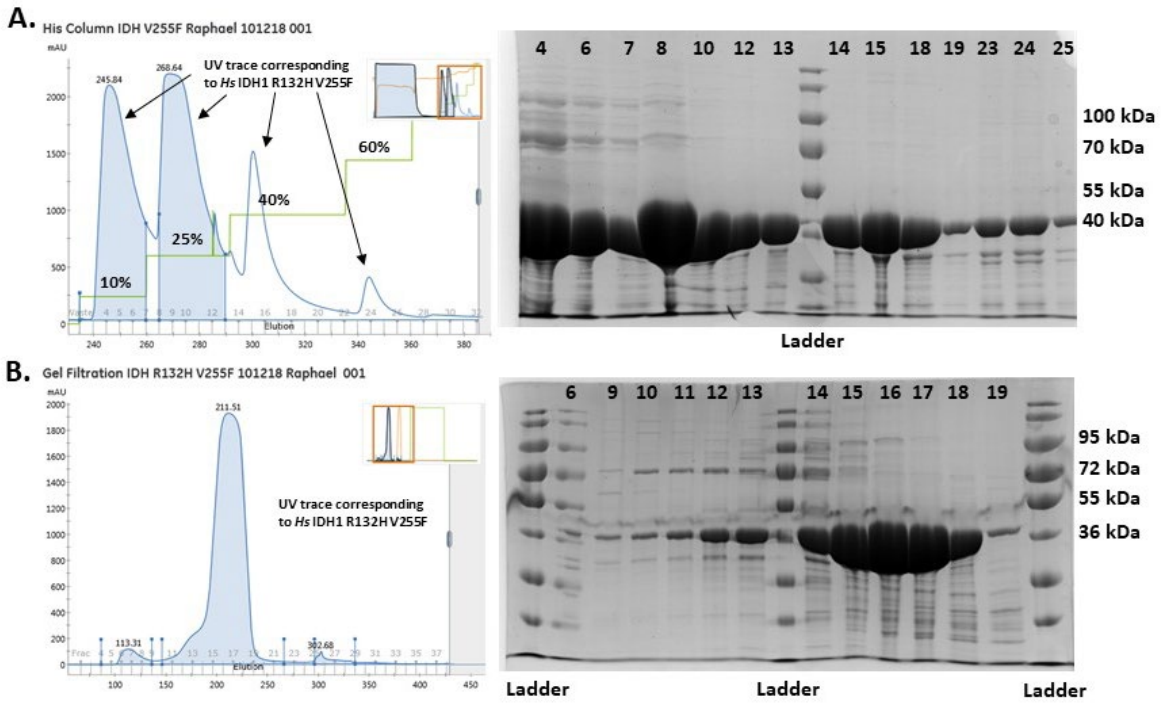

***Figure 4.6** | IDH1 R132H V255F purification. The chromatogram of each purification step is shown on the left-hand side, the SDS-PAGE gel on the right-hand side. **A.** Nickel-affinity chromatography using imidazole step gradient elution (percentages of elution buffer are shown on the chromatogram). **B.** Size-exclusion chromatography using an isocratic elution.*

4.2.5 IDH1 R132H Q277E

Following lysis of cells, purification (**Figure 4.7**) yielded 144.5 mg/L (**Table 4.12**) of IDH1 R132H Q277E, which was aliquoted at a concentration of 27.8 mg/mL (582.2 μM).

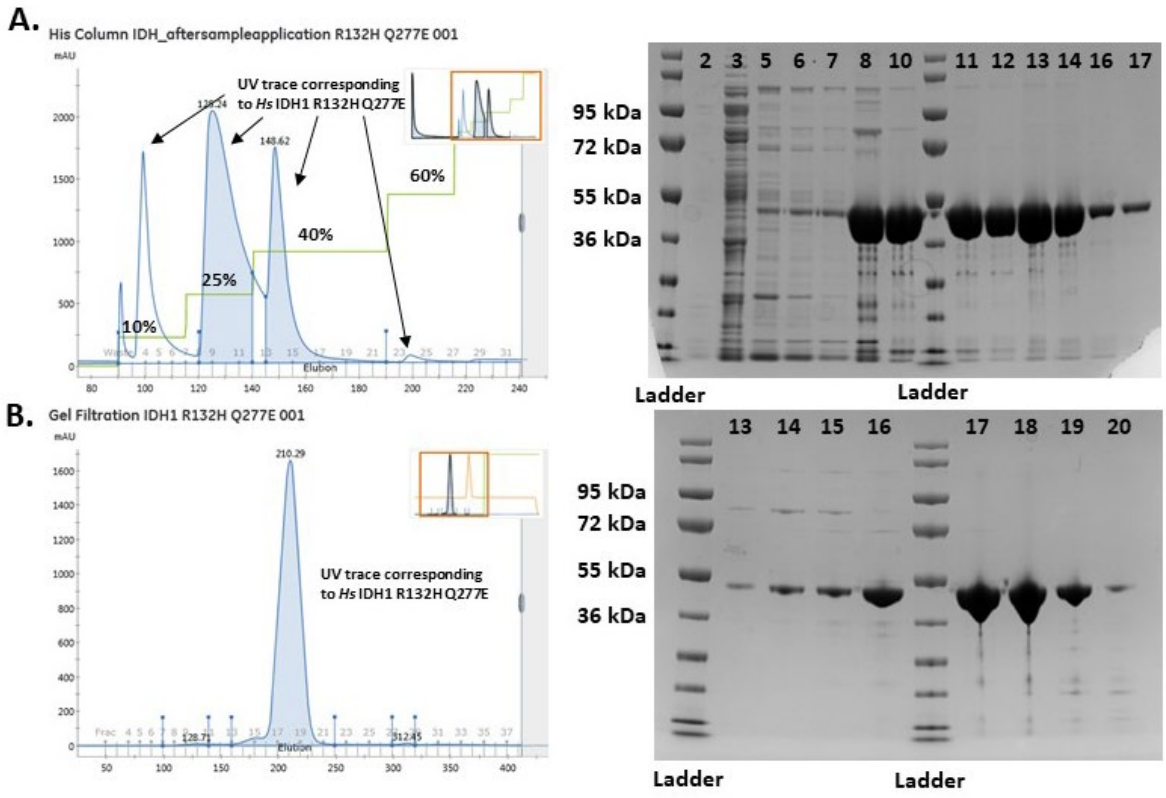

***Figure 4.7** | IDH1 R132H Q277E purification. The chromatogram of each purification technique is shown on the left-hand side, the SDS-PAGE gel on the right-hand side. **A.** Nickel-affinity chromatography using imidazole step gradient elution (percentages of elution buffer are shown on the chromatogram). **B.** Size-exclusion chromatography using an isocratic elution.*

4.2.6 IDH1 R132H V281F

Following lysis of cells, purification (**Figure 4.8**) yielded 154.6 mg/L (**Table 4.12**) of IDH1 R132H V281F, which was aliquoted at a concentration of 26.5 mg/mL (554.0 μM).

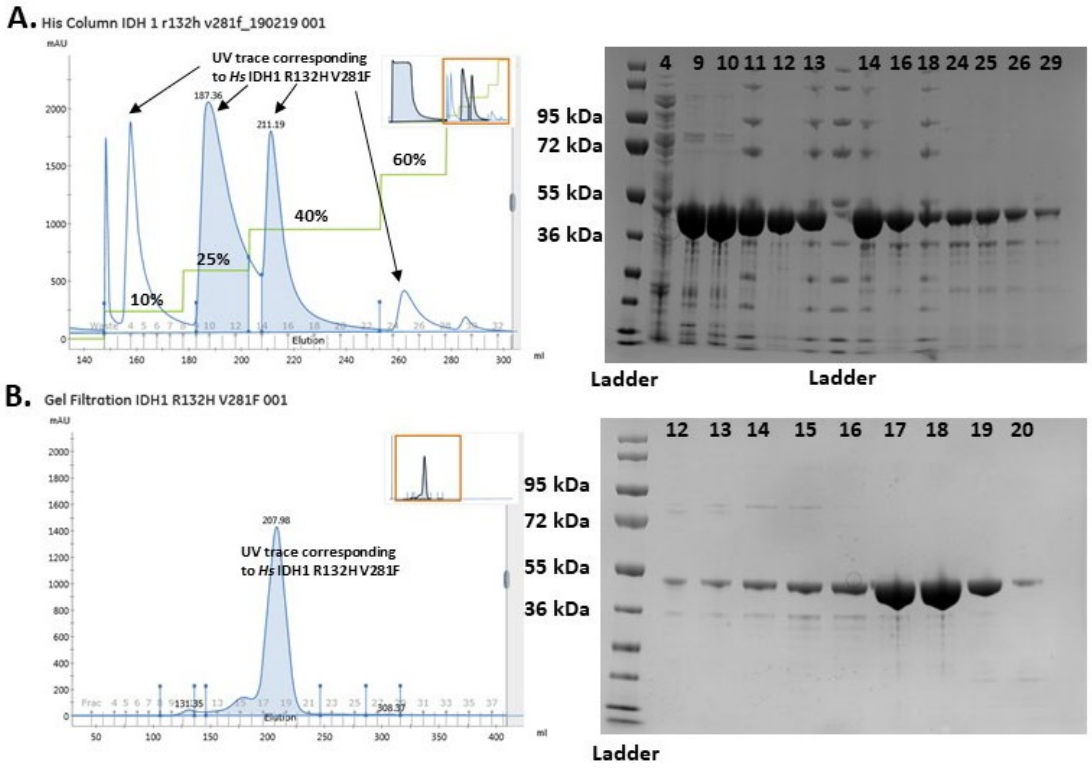

***Figure 4.8** | IDH1 R132H V281F purification. The chromatogram of each purification technique is shown on the left-hand side, the SDS-PAGE gel on the right-hand side. **A.** Nickel-affinity chromatography using imidazole step gradient elution (percentages of elution buffer are shown on the chromatogram). **B.** Size-exclusion chromatography using an isocratic elution.*

In summary, all the desired recombinant IDH1 variants were produced with high yield (**Table 4.12**) and purity (> 95% based on SDS-PAGE analysis).

4.2.7 Analysis of Protein Mass by LC/MS

The masses of IDH1 variants produced in Section 4.2 were analysed using LC/MS; all proteins were produced with the loss of the N-terminal methionine (**Table 4.1**), as is commonly observed for recombinant proteins produced in *E. coli*.[129]

***Table 4.1** | Analyses of proteins by LC/MS shows their masses with a loss of N-terminal methionine (-131 Da[130]).*

Protein	Mw (theoretical)	Mw (observed)	Difference in Mw
IDH1 wt	47724.4	47591.8	-132.6
IDH1 R132S	47655.3	47523.0	-132.3
IDH1 S280F	47784.5	47651.31	-133.2
IDH1 R132H V255F	47753.4	47622.0	-131.4
IDH1 R132H Q277E	47706.4	47575.5	-130.9
IDH1 R132H V281F	47753.4	47622.2	-131.2

4.3 Characterisation of Catalytic Variants

Studies to compare the ability of R132H, R132C, and R132S to reduce 2-OG to 2-HG utilised the NADPH absorbance and ^{1}H NMR assays (as described in Section 2.3 and 2.4). The turnover of isocitrate to 2-HG was also studied by ^{1}H NMR; the focus was to study the influence of substitutions at the R132 position.

4.3.1 Biochemical Characterisation

Steady state Michaelis-Menten kinetic analyses were performed for R132S, R132H and R132C using the NADPH absorbance assay. Initial velocities were plotted against the substrate concentration and a non-linear regression curve fit of the data using GraphPad Prism software (version 5) was used to determine the kinetic parameters (**Figure 4.9**).

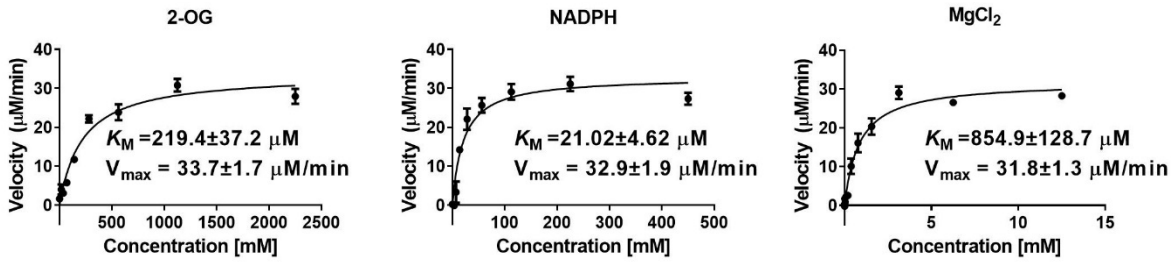

***Figure 4.9** | Kinetic analysis of R132S (400 nM). Non-linear regression curve fits are shown with the standard error of the mean (n =3). Conditions: 100 mM Tris, 0.2 mM DTT, 0.005 % Tween 20, and 0.1 mg/mL BSA (pH 8.0).*

For further analysis, k_{cat} and k_{cat}/K_M were calculated and R132S was compared with the R132H and R132C variants. The hyperbolic curves for the Michaelis-Menten parameters are shown in Chapter 2 (**Figure 2.9**).

Table 4.2 *| Kinetic parameters of IDH1 variants (400 nM) for 2-OG from non-linear regression curve fits. Errors: standard error of the mean (n =3). $MgCl_2$: 10 mM, NADPH: 0.3 mM.*

Protein	2-Oxoglutarate		
	K_M (μM)	k_{cat} (s^{-1})	k_{cat}/K_M ($s^{-1}\times\mu M^{-1}$) ($\times10^{-3}$)
R132C	216.3±27.57	1.6±0.1	7.2
R132H	403.7±10.4	0.8±0.1	1.9
R132S	219.4±37.2	1.4±0.1	6.4

R132S exhibited similar K_M and k_{cat} values for 2-OG to those of R132C for reduction of 2-OG to 2-HG resulting in similar k_{cat}/K_Ms for R132S and R132C. Interestingly, IDH1 R132H exhibited a lower catalytic efficiency compared to R132S and R132C (**Table 4.2**).

Table 4.3 *| Kinetic parameters of IDH1 variants (400 nM) for NADPH from non-linear regression curve fits. Errors: standard error of the mean (n =3). $MgCl_2$: 10 mM, 2-OG: 1.5 mM.*

Protein	NADPH		
	K_M (μM)	k_{cat} (s^{-1})	k_{cat}/K_M ($s^{-1}\times\mu M^{-1}$) ($\times10^{-3}$)
R132C	31.2±10.4	1.4±0.1	44.6
R132H	56.8±5.1	0.9±0.0	15.4
R132S	21.0±4.6	1.4±0.1	65.2

R132S exhibited the lowest K_M for NADPH from the variants tested (1.5-fold lower than R132C). The catalytic efficiency (k_{cat}/K_M) for the turnover of NADPH was 1.5-fold higher for the R132S variant than R132C. R132H showed the highest K_M for NADPH and a 3-fold lower catalytic efficiency compared to R132C (**Table 4.3**).

Table 4.4 *| Kinetic parameters of IDH1 variants (400 nM) for $MgCl_2$ from non-linear regression curve fits. Errors: standard error of the mean (n =3). 2-OG: 1.5 mM, NADPH: 0.3 mM.*

Protein	$MgCl_2$		
	K_M (μM)	k_{cat} (s^{-1})	k_{cat}/K_M ($s^{-1}\times\mu M^{-1}$) ($\times10^{-3}$)
R132C	669.1±151.1	1.4±0.1	2.1
R132H	(4.0±0.7)×10^3	0.7±0.0	0.2
R132S	854.9±128.7	1.3±0.1	1.6

The K_M values for magnesium ions were similar for R132S and R132C, while R132H exhibits a 5-fold higher K_M for magnesium ions. The catalytic efficiencies (k_{cat}/K_M) of R132S and R132C were similar whereas R132H exhibited the lowest catalytic efficiency for magnesium (**Table 4.4**).

In summary, according to these kinetic studies using the NADPH absorbance assay, R132S and R132C catalyse the reduction of 2-OG to 2-HG with similar efficiencies and have similar substrate affinities (as judged by K_M). The R132H variant catalyses the reduction of 2-OG with lower efficiency compared to R132S and R132C.

4.3.2 Time-course Studies by ^{1}H Nuclear Magnetic Resonance (NMR)

To complement the results from kinetic analysis using the NADPH absorbance assay, ^{1}H NMR was employed enabling direct observation of all metabolites (as described in Section 2.4).

4.3.2.1 Analysis of the Turnover of 2-OG to 2-HG

Firstly, the R132S catalysed reduction of 2-OG and the concomitant oxidation of NADPH was analysed. R132S catalyses the turnover of 2-OG to 2-HG as observed by ^{1}H NMR. The products, 2-HG and $NADP^+$, built up rapidly and the reaction was completed after ~3000 sec (50 min) (**Figure 4.10**).

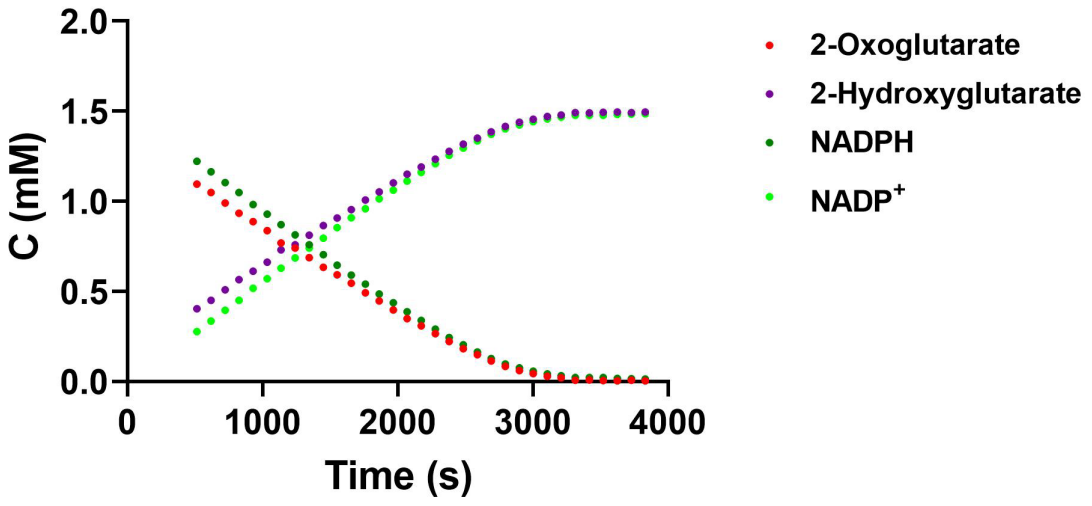

***Figure 4.10** | Turnover of 2-OG to 2-HG and concomitant reduction of NADPH to $NADP^+$ as catalysed by R132S observed by ^{1}H NMR (700 MHz). Conditions: 500 nM R132S, 10 mM $MgCl_2$, 1.5 mM 2-OG, 1.5 mM NADPH; 50 mM d_{11}-Tris buffer (90:10 H_2O:D_2O; pH 7.5).*

Levels of 2-HG produced by R132S were compared by ^{1}H NMR with those produced by R132C and R132H under the same conditions (from Section 2.3; **Figure 4.11**, A). After 9

minutes, product levels were lowest with R132H (not measurable) (**Figure 4.11**, B); the 2-HG concentration with R132S was double the concentration of R132C.

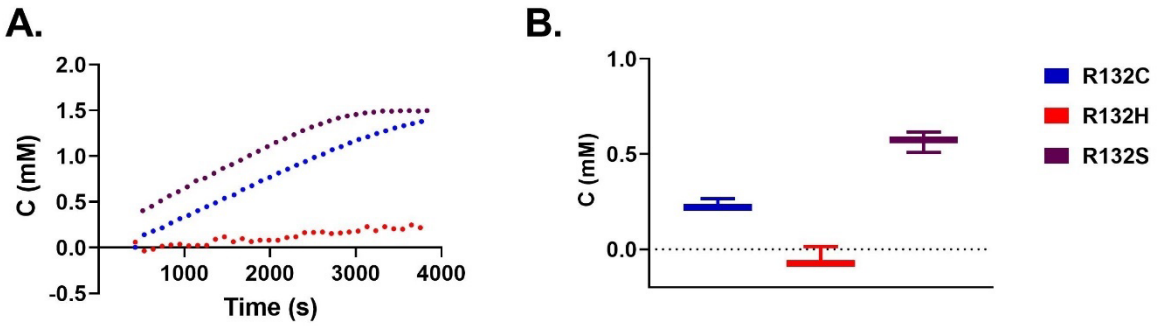

***Figure 4.11** | Reduction of 2-OG to 2-HG as catalysed by R132S, R132C, and R132H observed by ^{1}H NMR (700 MHz). **A.** 2-HG formation from 2-OG catalysed by R132S measured by ^{1}H NMR. **B.** Comparison of 2-HG levels after 9 minutes. Error bars: standard error of the mean (n =3). Conditions: See Figure 4.10 legend.*

R132S rapidly catalyses turnover of 2-OG to 2-HG. Although k_{cat} and the catalytic efficiency (as indicated by k_{cat}/K_M) in the NADPH absorbance assays are similar for the R132S and R132C variants, the ^{1}H NMR time-course analyses show the reaction rates differ substantially. This observation may relate to the different assay buffers and pHs used (pH 7.5 for NMR assays vs pH 8.0 for NADPH absorbance assays) or the addition of NaCl (100 mM) in the ^{1}H NMR assays. Furthermore, different enzyme-substrate ratios (NMR assay: 500 nM IDH1 variant, 1.5 mM 2-OG, 1.5 mM NADPH, 10 mM $MgCl_2$; NADPH absorbance assay: 400 nM IDH1 variant, 1.5 mM 2-OG, 300 µM NADPH, 10 mM $MgCl_2$) could play a role. Note that the NADPH concentration in ^{1}H NMR assays was 5-fold higher than in the NADPH absorbance assays to enable full turnover of 2-OG (1.5 mM NADPH cannot be used in the NADPH absorbance assays because the detector is saturated at ~600 µM NADPH).

4.3.2.2 Analysis of the Turnover of Isocitrate to 2-HG

The turnover of isocitrate to 2-HG was investigated using ^{1}H NMR, as described in Section 2.4. R132S was incubated with 10 mM $MgCl_2$ for 10 minutes and the reaction initiated by addition of *DL*-isocitrate (3 mM) and $NADP^+$ (1.5 mM). Note that hereafter isocitrate refers to *DL*-isocitrate, unless otherwise stated.

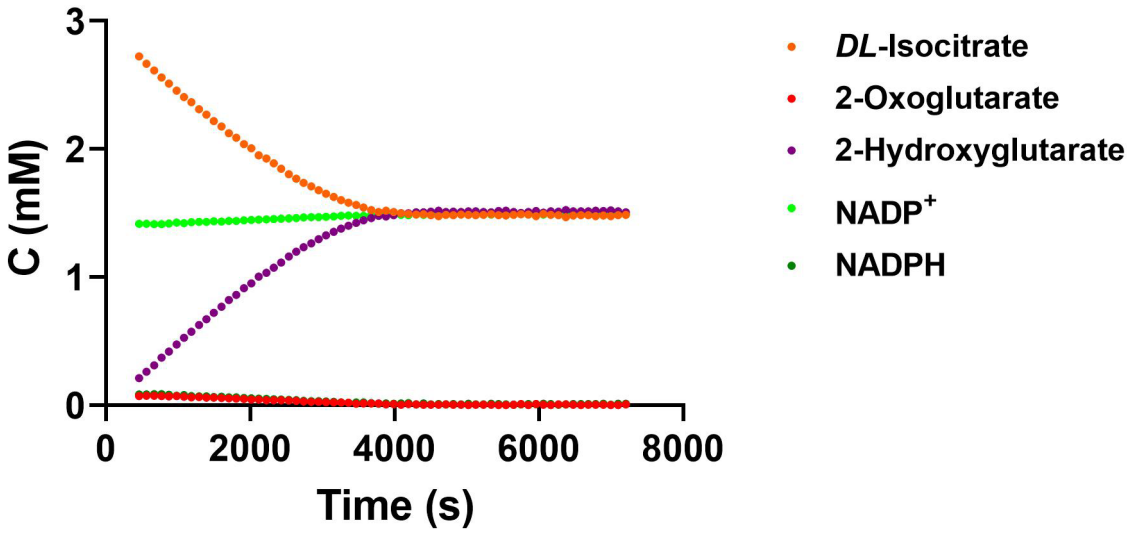

***Figure 4.12** | Conversion of isocitrate to 2-HG as catalysed by R132S monitored by ^{1}H NMR (700 MHz). No major changes in NADPH/NADP^{+} levels can be detected, while the velocity of 2-HG formation differs. Conditions: 750 nM R132S, 10 mM $MgCl_2$, 3 mM DL-isocitrate, 1.5 mM NADP^{+}; 50 mM d_{11}-Tris buffer (90:10 H_2O:D_2O; pH 7.5).*

As observed for the IDH1 variants tested in Section 2.4, R132S catalyses turnover of isocitrate to 2-HG (**Figure 4.12**). The changes in NADPH and NADP^{+} levels were marginal. There were low levels of 2-OG present at the start (formed from isocitrate while the sample was transferred into the NMR machine), but its concentration decreased rapidly as it was turned over by R132S.

2-HG formation catalysed by R132S was compared with results from ^{1}H NMR time-courses for the reaction of isocitrate to 2-HG, as catalysed by R132C and R132H (Section 2.4; **Figure 4.13**, A). The 2-HG concentration after 9 minutes in R132S assays was half that of R132C (**Figure 4.13**, B). 2-HG was not measurable after 9 minutes in the reaction catalysed by R132H using the same conditions (**Figure 4.13**, B).

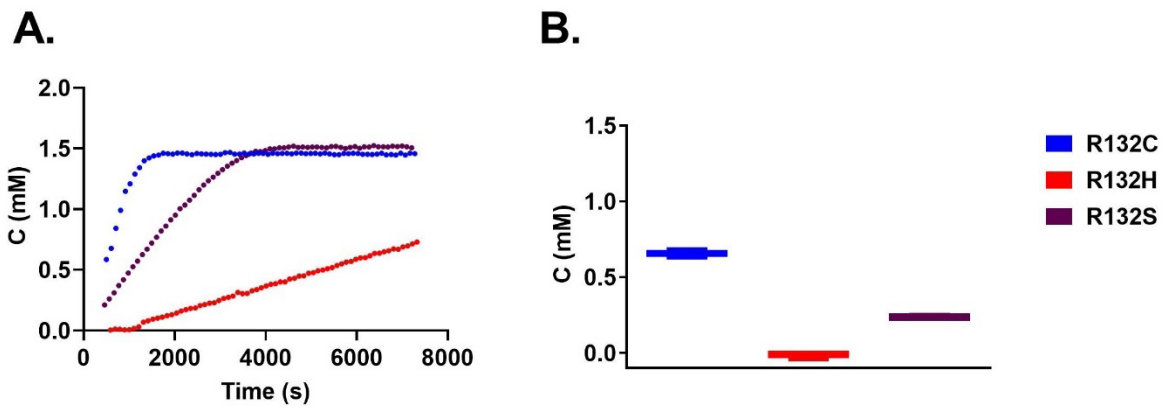

Figure 4.13 *| Turnover of isocitrate to 2-HG as catalysed by R132S, R132C, and R132H observed by ^{1}H NMR (700 MHz).* ***A.*** *2-HG formation from isocitrate catalysed by R132S measured by ^{1}H NMR (700 MHz).* ***B.*** *Comparison of 2-HG levels after 9 minutes (standard error of the mean, n =3). Conditions: 750 nM R132S, 10 mM $MgCl_2$, 3.0 mM DL-isocitrate, and 1.5 mM $NADP^+$ was used 50 mM d_{11}-Tris buffer (90:10 H_2O:D_2O; pH 7.5).*

Only half the *DL*-isocitrate was observed to be consumed (**Figure 4.12**) in the reaction catalysed by R132S. To investigate if *D*-isocitrate is the substrate of R132S (as it is for the IDH1 variants tested in Section 2.4; as opposed to *L*-isocitrate), the turnover of *D*-isocitrate (1.5 mM) and $NADP^+$ (1.5 mM) was measured by ^{1}H NMR (**Figure 4.14**).

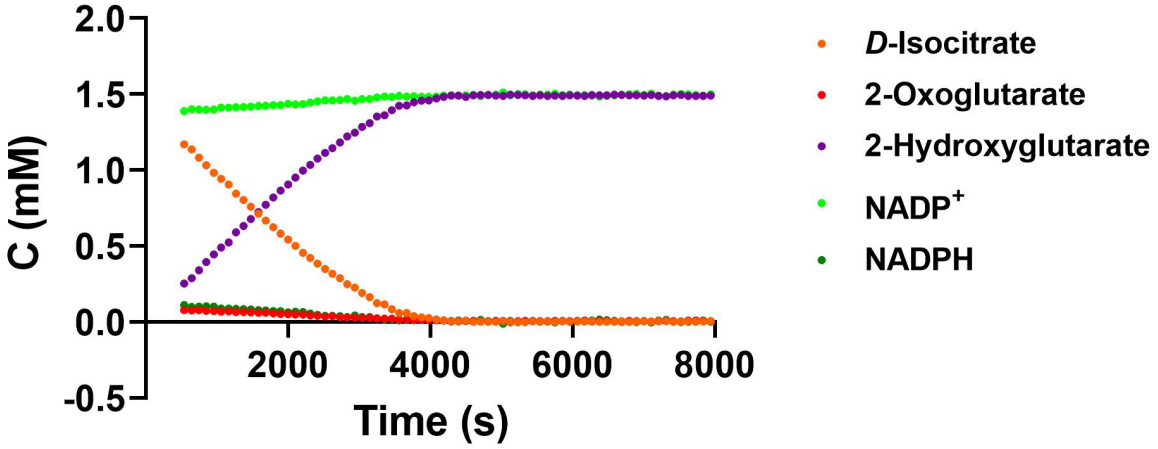

Figure 4.14 *| ^{1}H NMR (700 MHz) analyses of the turnover of D-Isocitrate to 2-HG as catalysed by R132S showing D-ICT as the substrate. Conditions: 750 nM R132S, 10 mM $MgCl_2$, 1.5 mM D-isocitrate, and 1.5 mM $NADP^+$ was used 50 mM d_{11}-Tris buffer (90:10 H_2O:D_2O; pH 7.5).*

As anticipated, R132S catalysed the turnover of *D*-isocitrate to completion after ~4000 seconds (67 min) indicating that *D*-isocitrate is the substrate for R132S catalysed conversion of isocitrate to 2-HG (**Figure 4.14**).

In summary, R132S can catalyse the turnover of 2-OG to 2-HG. While under ^{1}H NMR conditions, the reaction rate is doubled compared with that of the reduction of 2-OG catalysed

by R132C, the Michaelis-Menten parameters (e.g. k_{cat} and k_{cat}/K_M), as determined by the NADPH absorbance assay, are similar. This observation should be followed up with studies on the influence of pH and other variables on the reaction rate. Like R132C and R132H, R132S can catalyse the turnover of *D*-isocitrate to 2-HG. In ^{1}H NMR time-course assays, 2-OG is initially present at low levels and consumed rapidly. This observation suggests that, as observed for other IDH1 variants (Section 2.4), the first part of the reaction (oxidative decarboxylation of isocitrate to 2-OG) is the rate-limiting step and 2-OG is relatively rapidly reduced to 2-HG by R132S. The apparent reaction rate (as measured by the concentration of 2-HG formed after 9 minutes) of the turnover of isocitrate to 2-HG as catalysed by R132S is lower than for R132C but higher than for R132H.

4.3.3 Electrochemical experiments

The turnover of isocitrate by R132S was analysed by cyclic voltammetry according to Section 2.5. This technique allows measurement of the oxidation of isocitrate and reduction of 2-OG to be separated from one another, permitting the first part of the reaction to be analysed independently (**Figure 4.15**).

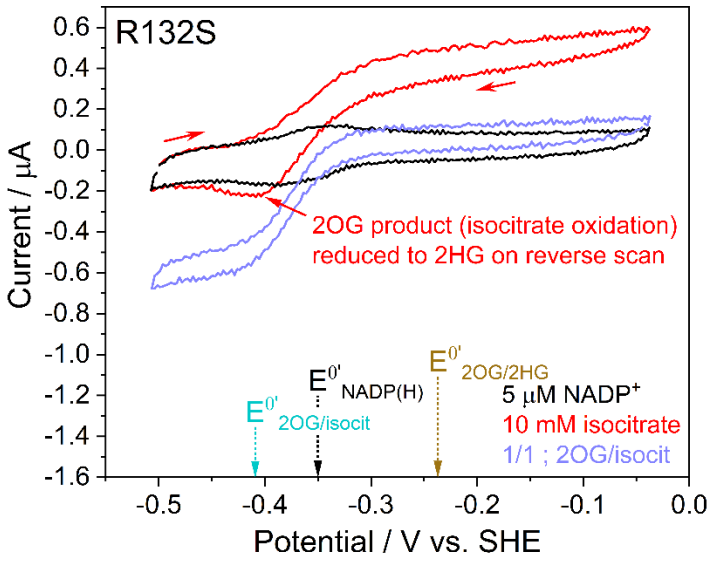

Figure 4.15 *| Stationary cyclic voltammetry measuring the ability of IDH1 R132S to catalyse the oxidation of DL-isocitrate and reduction of 2-oxoglutarate. Conditions: stationary (FNR+E2)@ITO/PGE electrode (E2 IDH1 R132S), electrode area 0.03 cm^2, scan rate 1 mV/s, temperature 25°C, volume 4 mL, pH 8 (20 mM each: MES, TAPS, CHES), 10 mM $MgCl_2$, 5 µM $NADP^+$. Purple traces (1/1; 2-OG/DL-isocitrate) contained 10 mM 2-OG + 10 mM DL-isocitrate. Enzyme molar loading ratio: FNR/IDH1; 1/2.5. E0'NADP(H), E0'2OG/DL-isocitrate and E0'2-OG/2-HG denote formal potentials for the $NADP^+$/NADPH, 2-OG/DL-isocitrate, and 2-OG/2-HG couples, respectively (see Herold et al.[135] for further information). This experiment was conducted by Ryan Herold.*

Under the cyclic voltammetry assay conditions, the current observed for the reduction of 2-OG by R132S was similar to that for R132C (Section 2.5). Interestingly, the current for oxidation of isocitrate (red trace) was higher than for all other IDH1 variants tested in Section 2.5 (i.e., R132C, R132C S280F, R132H, R132H S280F). Compared to the oxidation of isocitrate by R132S, the current for the reduction of 2-OG by R132S had a similar amplitude suggesting that R132S keeps a lot of its native capacity to catalyse the turnover of isocitrate to 2-OG. The data suggest that the oxidation of isocitrate to 2-OG and reduction of 2-OG to 2-HG, are catalysed by R132S with similar efficiencies.

4.3.4 Biophysical Characterisation

To compare the secondary structures of IDH1 variants R132S with R132C and R132H, biophysical studies were conducted using circular dichroism (CD). The thermal stabilities of the IDH1 variants were analysed by CD, Differential Scanning Calorimetry (DSC), and Differential Scanning Fluorimetry (DSF). The oligomerisation state was analysed by non-denaturing PAGE and SEC-MALS.

4.3.4.1 Circular Dichroism Experiments

The procedure was conducted as described in Section 2.7.1. CD spectra were normalised to the protein concentration and MRE plotted against wavelength (**Figure 4.16**).

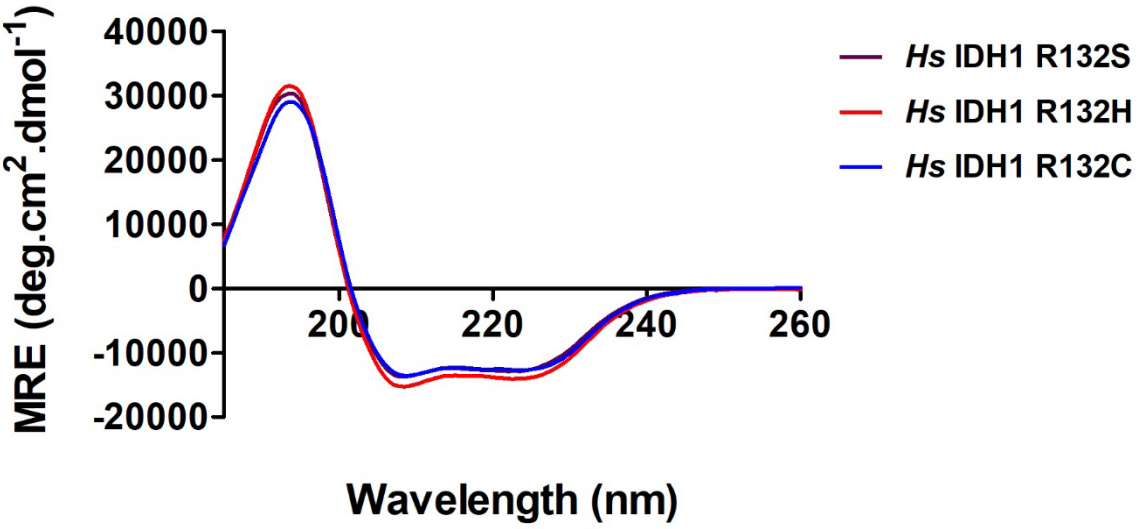

Figure 4.16 *| Circular Dichroism spectra of IDH1 variants. Conditions: protein (0.2 mg/mL in sodium phosphate (10 mM, pH 8.0)) buffer. Conditions: protein (0.2 mg/mL in sodium phosphate (10 mM, pH 8.0) buffer.*

The CD spectra of R132S, R132C, and R132H overlay well, suggesting similarly folded, well-structured proteins. As previously discussed (Section 2.7.1), the two minima at 208.5 nm and 224 nm are typical for proteins with α-helices present, and the maximum at 194 nm can be indicative of α-helices and β-sheets.[138] These results are in agreement with the reported R132H crystal structures, which exhibit both α-helices and β-sheets. Small differences in amplitudes are likely due to small inaccuracies in the protein concentration.

4.3.4.2 Analyses of the Melting Temperatures (T_m)

To investigate whether the R132S variant exhibits a different melting temperature (T_m) to R132C and R132H (which have similar T_ms; Section 2.6), the thermal stability of R132S was determined using CD, DSC, and DSF analysis (described in Section 2.7).

4.3.4.2.1 Analysis by CD

Firstly, the T_ms of R132S, R132C, and R132H were examined using CD by setting the wavelength to 215 nm and measuring the signal as a function of the temperature (**Figure 4.17**).

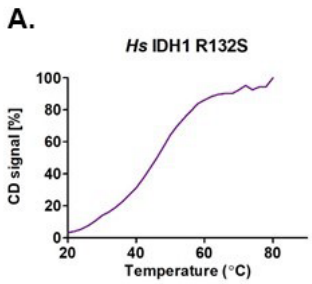

B.

Protein	T_m (°C)
Hs IDH1 R132S	45.1±0.2
Hs IDH1 R132H	54.7±0.1
Hs IDH1 R132C	52.4±0.2

***Figure 4.17** | Analyses of thermal stability using CD. **A.** Melting curve of IDH1 R132S. **B.** Table of melting temperatures (°C). Conditions: protein (0.2 mg/mL in sodium phosphate (10 mM, pH 8.0)) buffer.*

While the T_m of R132H and R132C was very similar, the T_m of R132S was substantially lower (δ = -7.3°C compared to R132C, δ= -9.6°C compared to R132H) indicating a decreased thermal stability (**Figure 4.17**).

4.3.4.2.2 Analysis by Differential Scanning Calorimetry (DSC)

To determine T_m with an alternative technique to CD, DSC was employed. The T_m of R132S was determined as described in Section 2.7.2.2 (**Figure 4.18**).

A.

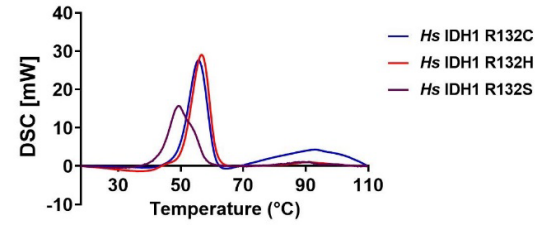

B.

Protein	T_m (°C)
***Hs* IDH1 R132C**	55.7
***Hs* IDH1 R132H**	56.7
***Hs* IDH1 R132S**	49.5 (51.4)

Figure 4.18 | *Analyses of thermal stability using Differential Scanning Calorimetry (DSC).* ***A.*** *DSC curves of the R132C, R132H, and R132S variants.* ***B.*** *Table showing the T_ms for each IDH1 variant. Conditions: IDH1 variants (20 µM) in 20 mM Tris, 100 mM NaCl (pH 7.4). These data were acquired by Dr David Staunton.*

While the melting curves of R132C and R132H exhibited a single T_m, R132S produced a melting curve with an additional shoulder (**Figure 4.18**). The maximum of the R132S melting curve and shoulder were at substantially lower temperatures than the maxima of the melting curves for R132C (δ = -6.2°C, δ = -4.3°C) and R132H (δ = -7.2°C, δ = -5.3°C).

4.3.4.2.3 Analysis by Differential Scanning Fluorimetry (DSF)

The T_m was also determined using DSF as described in Section 2.7.2.3 (**Table 4.5**).

Table 4.5 | *Comparison of the T_ms as measured by DSF.*

R132C	R132H	R132S
51.3±0.3	52.1±0.1	47.0±0.4

While the T_m values for R132C and R132H were similar, the T_m for R132S was lower (δ= -4.3°C vs R132C, δ= -5.1°C vs R132H).

The combined melting temperature results indicate that the T_m of R132S is substantially lower compared to those for R132C and R132H. This observation is in accordance with the casual observation that R132S activity decreases quickly when the enzyme sample is stored on ice, a phenomenon not observed for R132C and R132H. Furthermore, R132S precipitates when stored on ice for several hours which is not observed for R132C and R132H. These observations could suggest differences in intramolecular interactions in R132S compared with R132H and R132C, however, there is no crystal structure available for R132S. In experiments conducted by DSC, R132S showed two T_ms, which could be the result of two separate melting events, e.g. an initial dimer-melting event followed by melting of the monomer. Studies on the oligomerisation state at different temperatures could be conducted to follow this up.

4.3.4.3 Analysis of the Oligomerisation State

IDH1 variants are usually present as a dimer in solution (see Section 2.7). To investigate if different variations in the residue R132 have an influence on the oligomerisation state of IDH1, non-denaturing PAGE and SEC-MALS were conducted.

4.3.4.3.1 Analysis by Non-Denaturing PAGE

Non-denaturing PAGE was conducted according to the same procedure as described in Section 2.7.3. A 4-12 % polyacrylamide Tris-Glycine gel was used.

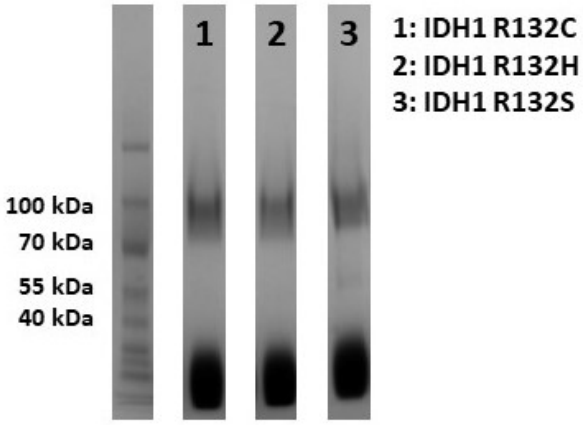

Figure 4.19 *| Non-denaturing PAGE of R132H, R132C, and R132S using a Tris-Glycine gel. All display a single band between 70 kDa and 100 kDa corresponding to a dimer (theoretical mass ~ 95 kDa, the monomer would be expected between 40-55 kDa). The band at the bottom corresponds to excess G-250 sample additive, an anionic dye binding to the protein to ensure migration towards the cathode which is added for non-denaturing PAGE (Section 7.2.6).*

As observed for R132C and R132H, R132S displayed a single band between 70 and 100 kDa, which corresponds to the mass of the IDH1 dimer.

4.3.4.3.2 Analysis by SEC-MALS

The oligomerisation state of R132S, R132C and R132H in solution was analysed using SEC-MALS, conducted according to the procedure described in Section 2.7.3.

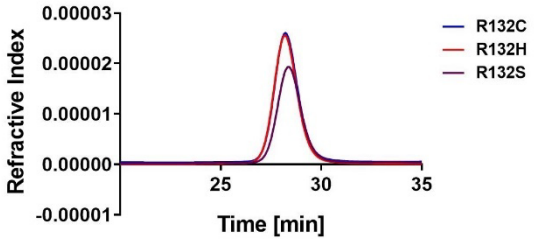

Protein	Mass (measured)	Dimer Mass (Expected)
R132C	88.7	95.34
R132H	91.2	95.41
R132S	107.4	95.31

Figure 4.20 *| SEC-MALS analysis of IDH1 variants R132H, R132C, and R132S. The proteins were diluted to 1 mg/L in buffer containing 20 mM Tris, 100 mM NaCl (pH 7.4) and analysed using a Superdex 200 HR10/30. The results imply the variants are predominantly dimeric in solution.*

Similar to R132C and R132H, SEC-MALS shows the predominant species of R132S to be dimeric (**Figure 4.20**).

R132C, R132H and R132S have a similar secondary structure content (as observed by CD) and they are all present predominantly as dimers in solution, consistent with studies on other IDH1 variants (Section 2.6). R132S is substantially less stable than R132C or R132H. The reason for this is unclear and further biophysical studies are required.

4.3.4.4 Binding Studies by Differential Scanning Fluorimetry (DSF)

To investigate the binding of substrates and co-factors to R132S, DSF was employed as described previously (Section 2.9). Varying concentrations of co-factors were titrated into a solution of the IDH1 variant, and the T_m was determined. Favourable binding typically improves protein stability at higher temperatures, which results in an increase in T_m.

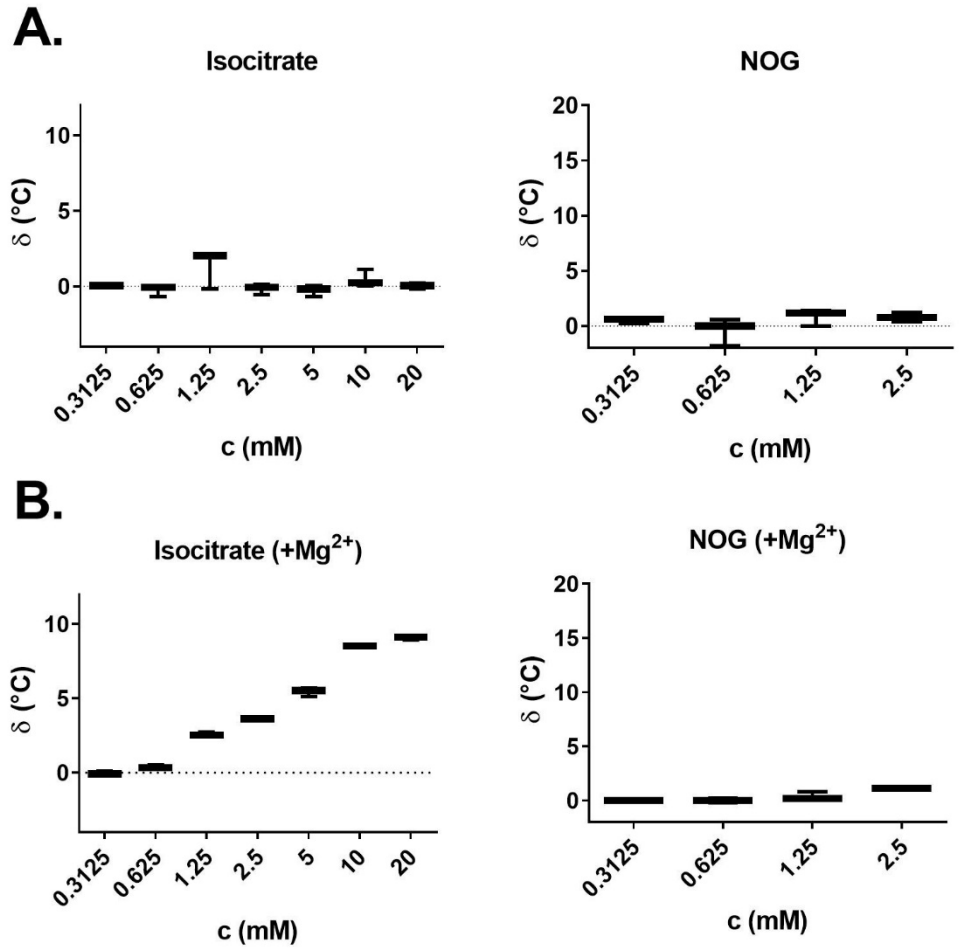

Figure 4.21 *| T_m-shift analyses of R132S by DSF. The influence on the thermal stability of IDH1 variants by addition of DL-isocitrate or NOG is shown (**A**) without and (**B**) with 10 mM $MgCl_2$ added. Errors: standard errors of the mean (n =3). Conditions: 3 µM R132S in 50 mM Tris, pH 7.5 (Dye: Sypro Orange 3x).*

Similarly to the results shown for R132C and R132H, no change in the T_m for R132S was observed in the absence of magnesium ions suggesting that isocitrate or NOG do not bind (**Figure 4.21**, A). When magnesium ions were present, isocitrate was observed to bind to R132S, increasing the T_m up to 10°C for high isocitrate concentrations (**Figure 4.21**, B). Compared to R132C and R132H (Figure 2.32), R132S was stabilised more strongly by isocitrate. Strikingly and in contrast to other IDH1 variants (e.g. R132C), NOG did not stabilise the R132S variant with magnesium ions present.

As observed for other IDH1 variants (Section 2.9), magnesium ions by themselves did not seem to bind to the IDH1 R132S variant (**Figure 4.22**) but instead resulted in destabilisation of the protein indicated by a decrease in T_m.

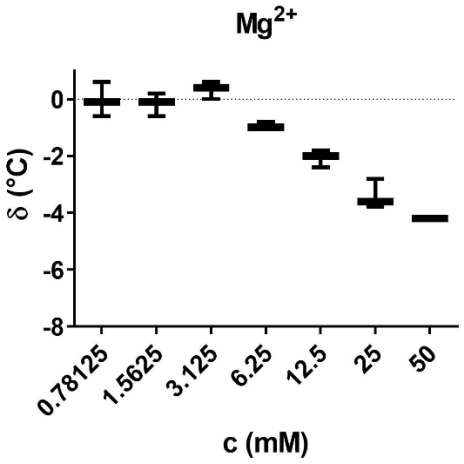

***Figure 4.22** | T_m-shift analyses of R132S by DSF. The influence on the thermal stability of IDH1 variants by addition of $MgCl_2$ is shown. Errors: standard errors of the mean (n =3). Conditions: 3 µM enzyme, in 50 mM Tris, pH 7.5 (Dye: Sypro Orange 3x).*

2-HG was not observed to bind to the R132S variant but caused destabilisation of R132S at high concentrations, in a concentration-dependent manner and in a manner independent of the presence of magnesium ions (**Figure 4.23**). This destabilisation is more prevalent compared to IDH1 R132C and IDH1 R132H (**Figure 2.33**).

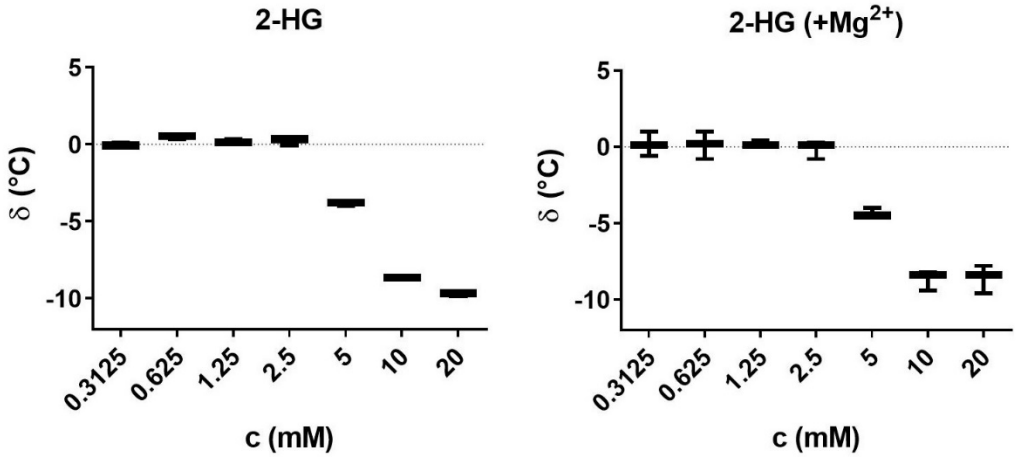

***Figure 4.23** | T_m-shift analyses of R132S by DSF. The influence on the thermal stability of IDH1 variants by addition of **(A)** 2-HG or **(B)** 2-HG in the presence of 10 mM $MgCl_2$ is shown. Errors: standard errors of the mean (n =3). Conditions: 3 µM R132S, in 50 mM Tris, pH 7.5 (Dye: Sypro Orange 3x).*

NADPH and $NADP^+$ bound to R132S similarly to R132C, causing stabilisation in a concentration-dependent manner (**Figure 4.24**); a maximum increase in T_m of 10°C was observed for NADPH (2 mM) and of 6°C for $NADP^+$ (2 mM).

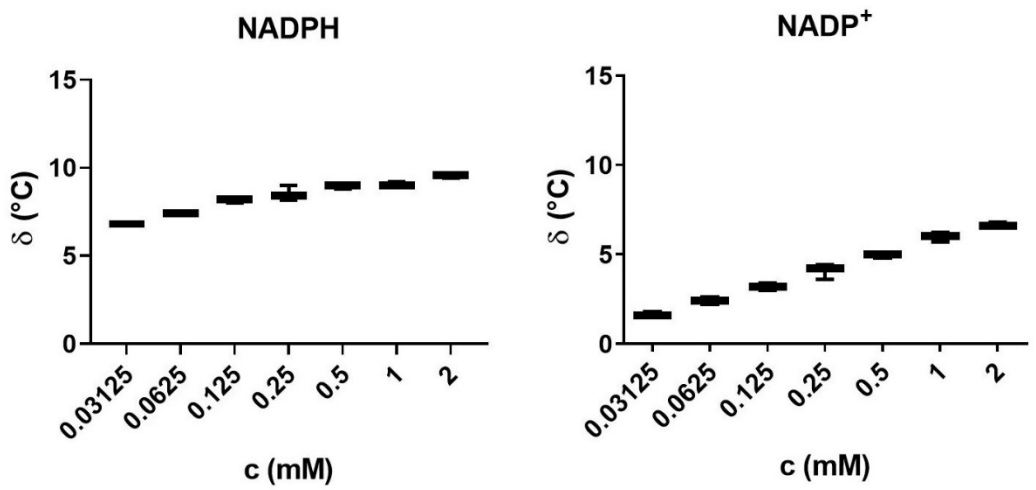

***Figure 4.24** | T_m-shift analyses of R132S by DSF. The influence on the thermal stability of IDH1 variants by addition of (**A**) NADPH or (**B**) $NADP^+$ is shown. Errors: standard errors of the mean (n =3). Conditions: 3 µM R132S, in 50 mM Tris, pH 7.5 (Dye: Sypro Orange 3x).*

These binding results as determined by DSF show substrate binding to R132S is dependent on the presence of magnesium ions, as previously observed (Section 2.9). Isocitrate was observed to bind best to IDH1 R132S compared with the other IDH1 variants tested (e.g. IDH1 R132C, Section 2.9), but shows no thermal stabilisation by NOG. This is in contrast to observations on the reaction rate of R132S when 2-OG is turned over to 2-HG (Section 4.3.1, 4.3.2), which is comparable to IDH1 R132C in kinetic assays and elevated in ^{1}H NMR assays. A potential reason for the high turnover rate despite poor NOG binding could be that NOG and 2-OG bind differently to IDH1 R132S. This proposal could be investigated by testing 2-OG in combination with the catalytically inactive metal ion calcium for binding instead of using the combination of NOG and magnesium ions. NADPH and $NADP^+$ bind well to IDH1 R132S and in a similar manner to IDH1 R132C.

4.4 Characterisation of Novel Dimer Interface Variants

To further investigate the role of the dimer-interface in catalysis and, subsequently, inhibition of IDH1, further dimer-interface variants were produced (Section 4.2). First, IDH1 wt and an IDH1 S280F variant (without an R132 variation) were analysed to investigate the oxidation of isocitrate and the reduction of 2-OG using the NADPH absorbance assay and ^{1}H NMR time-course analyses. Note that hereafter isocitrate refers to *DL*-isocitrate, unless otherwise stated.

Similarly, R132H V255F, R132H Q277E and R132H V281F were produced, and their kinetic parameters analysed using the NADPH absorbance assay and ^{1}H NMR time-course analysis. The results are compared with the R132H and R132H S280F variants (Section 2.3/2.4).

4.4.1 Biochemical Characterisation

To investigate the influence of an S280F substitution on IDH1 wt catalysis, the NADPH absorbance assay was employed, as described in Section 2.3.

4.4.1.1 Influence of the S280F Variation on IDH1 wt

IDH1 wt catalyses the oxidative decarboxylation of isocitrate to 2-OG. IDH1 wt turnover was observed to be higher than for IDH1 variants like R132H; to accurately observe the initial linear reaction rate, the enzyme concentration was decreased compared to the assays described in Section 2.3 (to 1 nM). The initial reaction rate was plotted against the substrate concentration and the Michaelis-Menten parameters were calculated using a non-linear regression curve fit using the GraphPad prism software (**Figure 4.25**; version 5).

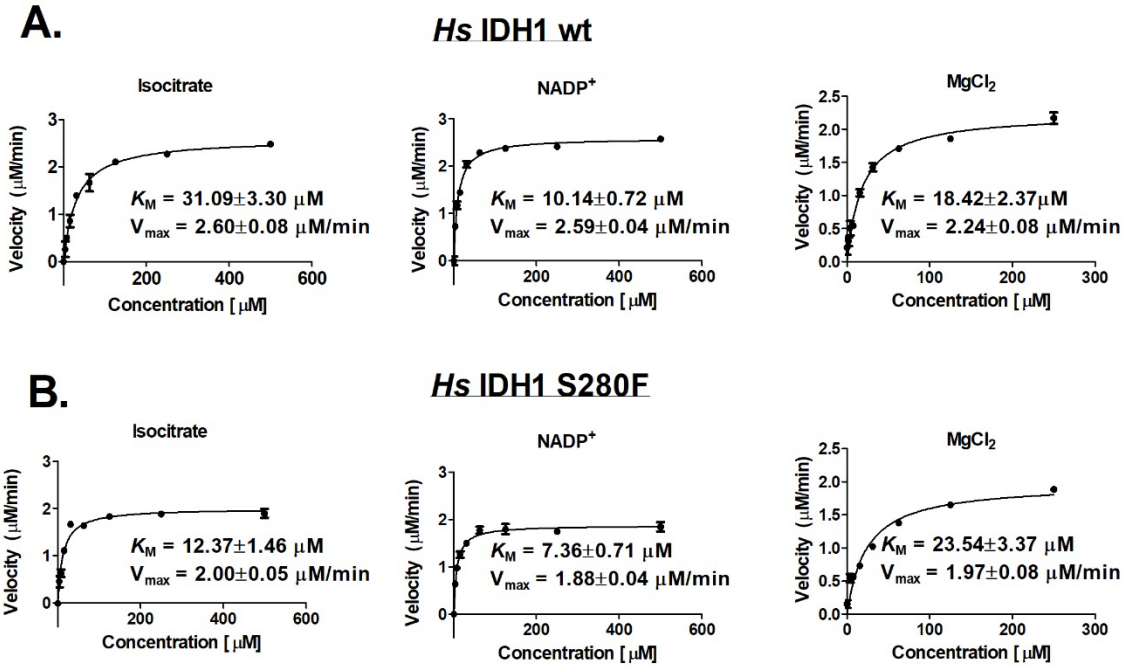

Figure 4.25 *| Kinetic studies on IDH1 wt (**A**, 1 nM enzyme) and the S280F variant (**B**, 1 nM enzyme). Nonlinear regression curve fits are shown with the standard error of the mean (n =3). Conditions: 100 mM Tris, 10 mM $MgCl_2$, 0.2 mM DTT, 0.005 % Tween 20, and 0.1 mg/mL BSA (pH 8.0).*

The substrates isocitrate, $NADP^+$ and the divalent cation magnesium were analysed. Michaelis-Menten parameters including k_{cat} and the catalytic efficiency, as indicated by k_{cat}/K_M, were calculated (**Table 4.6**).

The k_{cat} of S280F was lower compared to IDH1 wt. The K_M value for isocitrate was 3-fold lower in S280F compared to IDH1 wt and despite a decrease in the k_{cat}, a 2-fold increase in the catalytic efficiency (k_{cat}/K_M) was observed. The K_M value for magnesium was lower in IDH1

wt resulting in a 1.5-fold elevated catalytic efficiency (k_{cat}/K_M) compared with IDH1 S280F. There were no substantial changes in the K_M for $NADP^+$.

Table 4.6 *| Kinetic parameters of IDH1 wt and the S280F variant (1 nM) for DL-isocitrate, $NADP^+$ and $MgCl_2$ from non-linear regression curve fits with the standard error of the mean (n =3). Saturation concentrations: DL-isocitrate: 0.3 mM, $NADP^+$: 0.1 mM, $MgCl_2$: 10 mM.*

Enzyme	**IDH1 wt**		
	K_M **(μM)**	k_{cat} **(s^{-1})**	k_{cat}/K_M **($s^{-1}\times\mu M^{-1}$)**
***DL*-Isocitrate**	31.1±3.3	43.4±1.3	1.4
$NADP^+$	10.1±0.7	43.2±0.7	4.3
$MgCl_2$	18.4±2.4	37.3±1.4	2.0
	IDH1 S280F		
	K_M **(μM)**	k_{cat} **(s^{-1})**	k_{cat}/K_M **($s^{-1}\times\mu M^{-1}$)**
***DL*-Isocitrate**	12.4±1.5	33.4±0.9	2.7
$NADP^+$	7.4±0.7	31.3±0.6	4.3
$MgCl_2$	23.5±3.4	32.9±1.4	1.4

The overall decrease in k_{cat} in the reaction catalysed by S280F compared to IDH1 wt is likely a result of the introduction of the S280F variation. In contrast to R132C S280F, which is reported in the clinic[28], IDH1 wt has not been observed to acquire an S280F substitution, at least based on current evidence. The S280F variation decreases the K_M for isocitrate and hence, may increase the affinity for isocitrate which leads to a 2-fold increase in catalytic efficiency (k_{cat}/K_M). This further adds to the findings from Section 2.3, in which it was shown that the S280F substitution could enhance substrate binding (as judged by K_M) in the R132C S280F and R132H S280F variants.

4.4.1.2 Reduction of 2-OG to 2-HG as Catalysed by IDH1 wt

Previous studies have shown that IDH1 wt can, albeit inefficiently, catalyse the reduction of 2-OG to 2-HG.[50] However, this reaction is less favourable than the turnover of isocitrate to 2-OG, and thus, to study kinetic parameters, the enzyme concentration was optimised for sufficient turnover of 2-OG using the NADPH absorbance assay (2.5 μM).

IDH1 wt and IDH1 S280F both catalysed reduction of 2-OG under the conditions used (**Figure 4.26**). The k_{cat} of the reduction of 2-OG to 2-HG catalysed by IDH1 S280F was 10-fold lower than for IDH1 wt (**Table 4.7**). The K_M for 2-OG was substantially lower in the S280F variant

compared to IDH1 wt resulting in a similar k_{cat}/K_M for both enzymes. Strikingly, IDH1 wt and IDH1 S280F differ substantially in their K_M for magnesium. The S280F variant exhibited a 100-fold lower K_M and consequently a 10-fold higher k_{cat}/K_M.

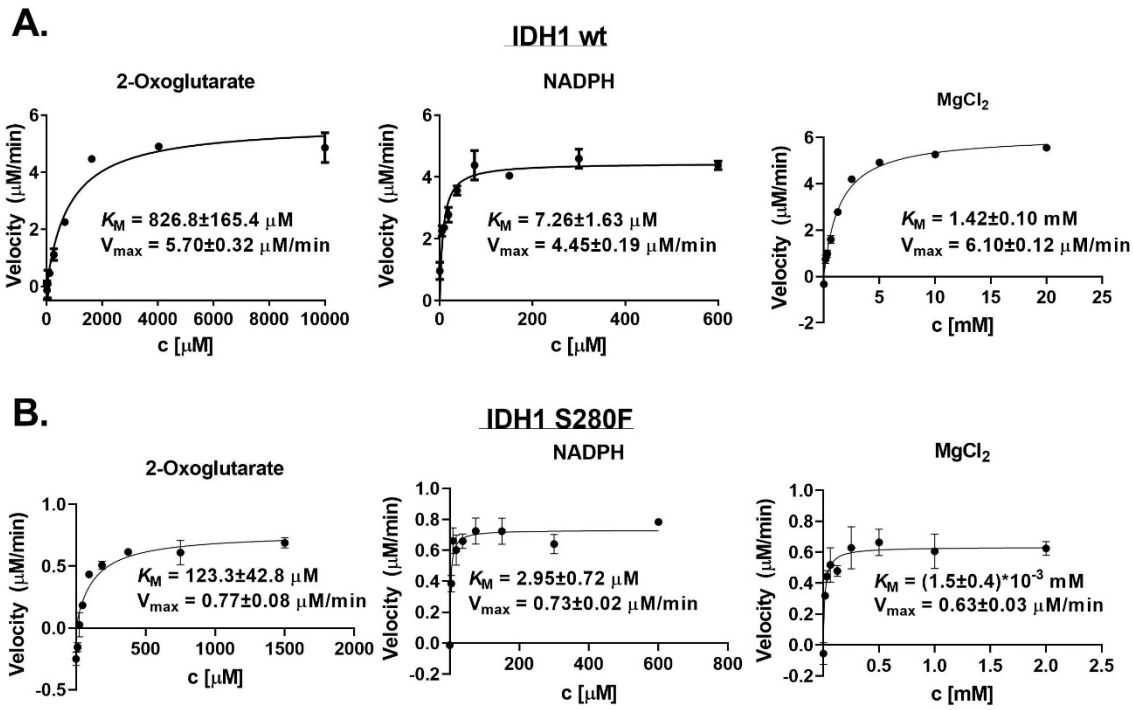

Figure 4.26 *| Kinetic studies on IDH1 wt (**A**, 2.5 µM enzyme) and the S280F variant (**B**, 2.5 µM enzyme) for the reduction of 2-OG to 2-HG. Non-linear regression curve fits are shown with the standard error of the mean (n =3). Conditions: 100 mM Tris, 10 mM $MgCl_2$, 0.2 mM DTT, 0.005 % Tween 20, and 0.1 mg/mL BSA (pH 8.0).*

Compared to the k_{cat}/K_M for the reduction of 2-OG catalysed by R132H (Section 2.3), the k_{cat}/K_M for the reaction catalysed by wt or the S280F variant was 50-fold lower; this indicates the increased ability of R132H to catalyse the reduction of 2-OG to 2-HG.

***Table 4.7** | Kinetic parameters of IDH1 wt and the S280F variant (2.5 µM enzyme) for 2-OG, NADPH and $MgCl_2$ from nonlinear regression curve fits with the standard error of the mean (n =3). Saturation concentrations: 2-OG: 10 mM, NADPH: 0.3 mM, $MgCl_2$: 10 mM.*

Enzyme	**IDH1 wt**		
	K_M **(µM)**	k_{cat} **(s^{-1})**	k_{cat}/K_M **($s^{-1}\times\mu M^{-1}$)**
2-oxoglutarate	826.8±165.4	$(3.8\pm0.2)\times10^{-2}$	4.6×10^{-5}
NADPH	7.3±1.6	$(3.0\pm0.1)\times10^{-2}$	4.1×10^{-3}
$MgCl_2$	$(1.4\pm0.1)\times10^{3}$	$(4.1\pm0.1)\times10^{-2}$	2.9×10^{-5}
	IDH1 S280F		
	K_M **(µM)**	k_{cat} **(s^{-1})**	k_{cat}/K_M **($s^{-1}\times\mu M^{-1}$)**
2-oxoglutarate	123.3±4.3	$(5.1\pm0.5)\times10^{-3}$	4.1×10^{-5}
NADPH	3.0±0.3	$(4.9\pm0.2)\times10^{-3}$	1.7×10^{-3}
$MgCl_2$	15.4±3.8	$(4.2\pm0.2)\times10^{-3}$	2.8×10^{-4}

The Michaelis-Menten parameters obtained must be interpreted with care; an assumption made in the process of determining Michaelis-Menten parameters (Section 2.3) is that a high excess of substrate over the enzyme is used (Section 2.3). This was not feasible in this case due to the low activity of IDH1 wt and S280F for the reduction of 2-OG to 2-HG.

However, notable effects of the S280F variation on the reduction of 2-OG to 2-HG were a decrease in the K_M for 2-OG and a substantial decrease in the K_M for magnesium, potentially reflecting a higher affinity for both 2-OG and magnesium.

These findings further add to results from Section 2.3 and Section 4.4.1.2, which suggest that in most cases, the S280F substitution promotes substrate and metal binding. This conclusion further highlights the importance of the α10 helix for IDH1 catalysis and the complex nature of the dynamics at the dimer-interface.

4.4.1.3 Kinetic Studies on IDH1 R132H V255F/Q277E/V281F

Several R132H second-site dimer-interface variants were made based on predictions of potential inhibitor resistance causing substitutions, using available crystal structures of inhibitors bound to R132H or R132C (Section 3.3). In Chapter 2, it was shown that substitutions at the dimer-interface can not only lead to inhibitor resistance, but also have the potential to alter kinetic properties of the enzymes (e.g. R132H vs R132H S280F). Therefore,

before inhibition studies were conducted, the kinetic properties of the novel second-site variants R132H V255F, R132H Q277E, and R132H V281F were investigated.

In pilot studies using the same conditions as in Section 2.3 (400 nM enzyme), no turnover was observed for the reduction of 2-OG to 2-HG with R132H V255F, R132H Q277E or R132H V281F. The enzyme concentration was increased to 10 µM which led to measurable turnover catalysed by R132H V255F and R132H V281F. However, no activity was observed for R132H Q277E, which was therefore assigned as an inactive variant.

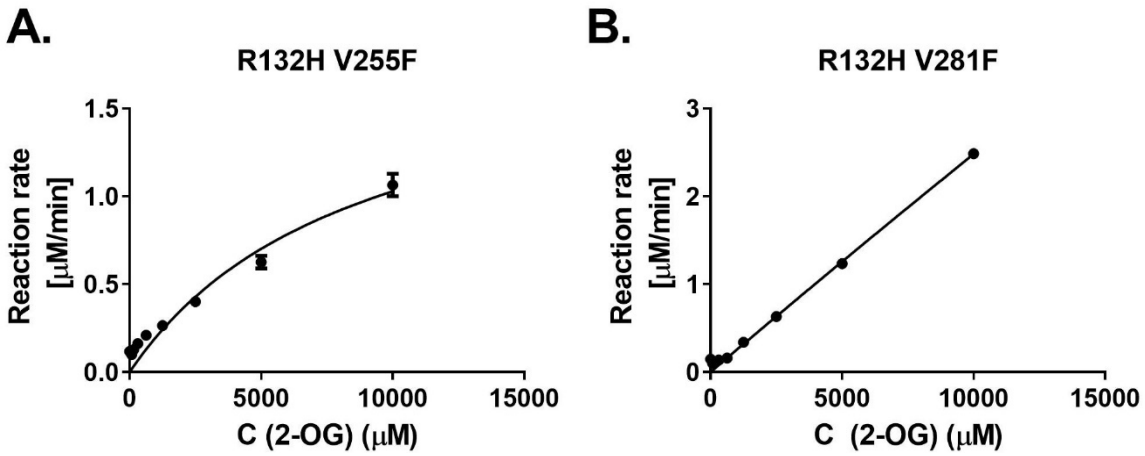

***Figure 4.27** | Kinetic studies on R132H V255F (**A**, 10 µM enzyme) and R132H V281F (**B**, 10 µM enzyme) for the reduction of 2-OG to 2-HG. Non-linear regression curve fits are shown with the standard error of the mean (n =3). Conditions: 100 mM Tris, 10 mM $MgCl_2$, 0.2 mM DTT, 0.005 % Tween 20, and 0.1 mg/mL BSA (pH 8.0). NADPH: 0.3 mM.*

To determine the Michaelis-Menten parameters, varying 2-OG and NADPH concentrations were assayed to determine their saturating concentrations. At the maximum possible NADPH contractions (600 µM; higher concentrations result in saturation of the absorbance detector), 2-OG could not be saturated at physiologically relevant concentrations (**Figure 4.27**). Therefore, no Michaelis-Menten parameters for the reduction of 2-OG to 2-HG as catalysed by R132H V255F and R132H V281F could be determined.

Next, the NADPH absorbance assay was used to investigate whether R132H V255F, R132H Q277E, and R132H V281F can utilise isocitrate as a substrate (10 µM enzyme). With the NADPH absorbance assay conditions, no activity was observed for R132H Q277E, but low apparent activity was observed for catalysis by R132H V255F and R132H V281F. The reaction rate was plotted against substrate concentration and a non-linear regression curve fit using the GraphPad prism software (version 5) was used to calculate Michaelis-Menten parameters (**Figure 4.28**).

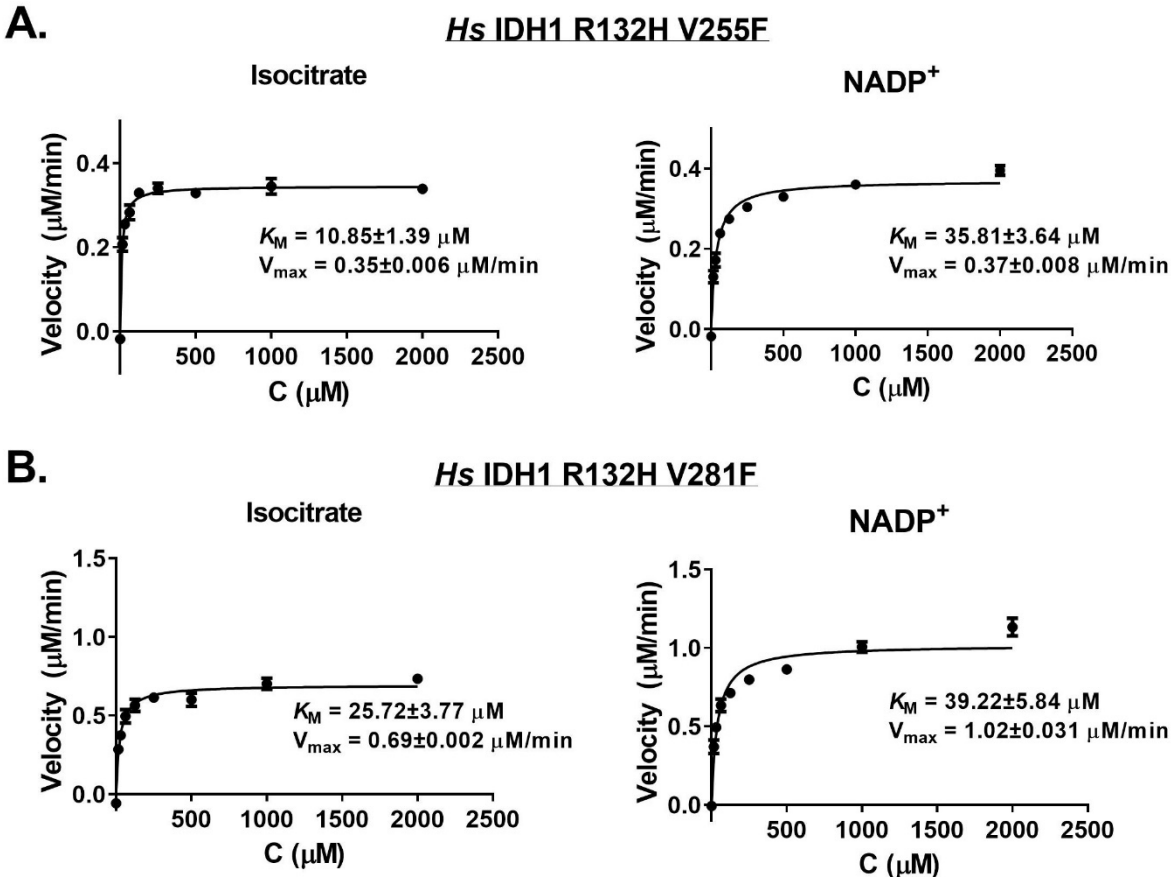

Figure 4.28 *| Kinetic studies on R132H V255F (**A**, 10 μM enzyme) and R132H V281F (**B**, 10 μM enzyme) for the oxidation of isocitrate to 2-OG using the NADPH absorbance assay. Non-linear regression curve fits are shown with the standard error of the mean (n =3). Conditions: 100 mM Tris, 10 mM $MgCl_2$, 0.2 mM DTT, 0.005 % Tween 20, and 0.1 mg/mL BSA (pH 8.0).*

Although high enzyme concentrations were used (10 μM), the reaction rate for the turnover of isocitrate to 2-OG as catalysed by R132H V255F and R132H V281F was low, as is reflected in the values for V_{max} (**Figure 4.28**). The catalytic efficiency for turnover of isocitrate was 30,000-fold lower for catalysis by R132H V255F and R132H V281F compared with IDH1 wt (**Table 4.8**). The catalytic efficiency for $NADP^+$ was 300,000-fold lower for catalysis by R132H V255F and 100,000-fold for reactions catalysed by R132H V281F compared with IDH1 wt (**Table 4.8**).

***Table 4.8** | Kinetic parameters R132H V255F (**A**, 10 µM enzyme) and R132H V281F (**B**, 10 µM enzyme) for DL-isocitrate and $NADP^+$ from non-linear regression curve fits with the standard error of the mean (n =3). Saturation concentrations: DL-isocitrate: 1 mM, $NADP^+$: 1 mM, $MgCl_2$: 10 mM.*

Enzyme	k_{cat}/K_M ($s^{-1}\times\mu M^{-1}$)	k_{cat}/K_M ($s^{-1}\times\mu M^{-1}$)
	Isocitrate	**$NADP^+$**
R132H V255F	0.000053	0.000017
R132H V281F	0.000045	0.000043
IDH1 wt	1.39	4.26

The overall results from the NADPH absorbance assay suggest a substantial interference with enzymatic activity as a result of the introduction of novel dimer-interface variations. While no activity could be observed for turnover of isocitrate or 2-OG as catalysed by IDH1 R132H Q277E, low activity could be observed for R132H V255F and R132H V281F. For the reduction of 2-OG to 2-HG as catalysed by R132H V255F and R132H V281F, no Michaelis-Menten parameters could be obtained because the 2-OG substrate could not be saturated at physiologically relevant concentrations. Michaelis-Menten parameters obtained for R132H V255F and R132H V281F for the turnover of isocitrate to 2-OG display a 50,000-300,000-fold decrease in catalytic efficiency compared to IDH1 wt.

4.4.2 Time-Course Studies by ^{1}H Nuclear Magnetic Resonance (NMR)

To further study reactions catalysed by IDH1 wt and IDH1 S280F (Section 4.4.2.1), and R132H V255F, R132H Q277E, and R132H V281F (Section 4.4.2.2) ^{1}H NMR was used. As described in Section 2.4, this method allows for the direct observation of substrates involved.

4.4.2.1 Time-Course Studies of IDH1 wt and S280F by ^{1}H NMR

Firstly, the oxidative decarboxylation of isocitrate to 2-OG, as catalysed by IDH1 wt and IDH1 S280F, was monitored. Subsequently, the reduction of 2-OG to 2-HG was investigated to complement findings from the NADPH turnover assays, suggesting IDH1 wt and IDH1 S280F can produce 2-HG from 2-OG.

4.4.2.1.1 Oxidative Decarboxylation of Isocitrate

To analyse the turnover of isocitrate to 2-OG, the enzyme concentration was optimised, and a suitable concentration of 10 nM was selected. Note that hereafter isocitrate refers to *DL*-isocitrate, unless otherwise stated. Both IDH1 wt and IDH1 S280F catalysed the conversion of *DL*-isocitrate with concomitant consumption of $NADP^+$ (**Figure 4.29**).

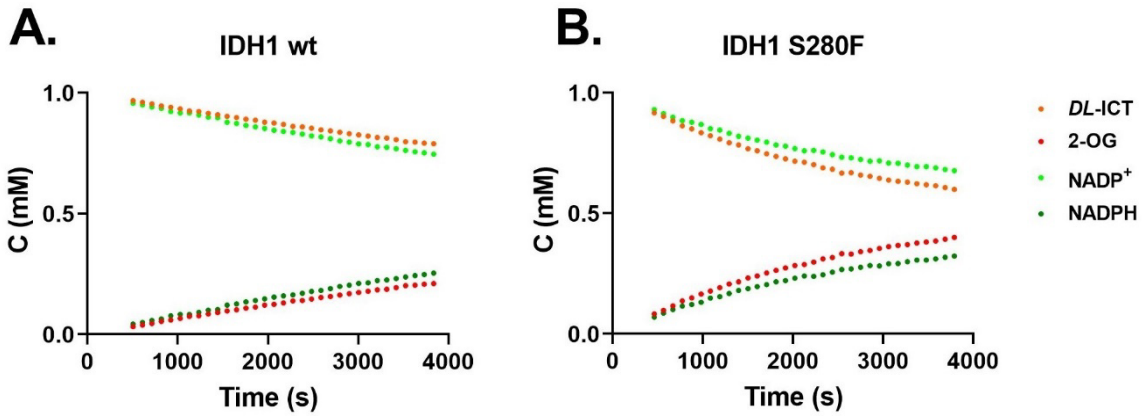

Figure 4.29 *| Turnover of DL-isocitrate to 2-OG and concomitant oxidation of $NADP^+$ to NADPH as catalysed by IDH1 wt (**A**) or IDH1 S280F (**B**) observed by ^1H NMR (700 MHz). Conditions: 10 nM enzyme, 10 mM $MgCl_2$, 1.0 mM DL-isocitrate, 1.0 mM $NADP^+$.*

There were apparent differences in the rate of 2-OG product formation as catalysed by IDH1 wt and IDH1 S280F (**Figure 4.30**).

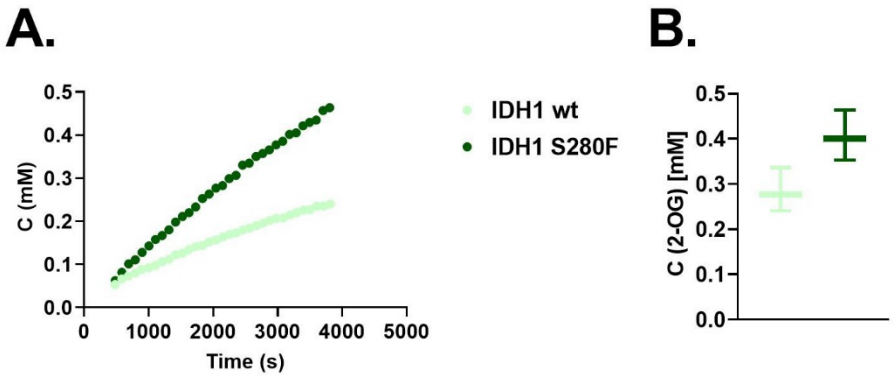

Figure 4.30 *| Oxidation of DL-isocitrate to 2-OG as catalysed by IDH1 wt and IDH1 S280F observed by ^1H NMR (700 MHz). **A.** 2-OG formation from isocitrate as catalysed by IDH1 wt (dark green) or the S280F variant (light green) measured by ^1H NMR. **B.** Comparison of 2-OG levels after 60 minutes. Errors bars: standard errors of the mean (n =3). Conditions: See Figure 4.29 legend.*

Under the experimental conditions of the ^1H NMR assay, the rate of the reaction catalysed by IDH S280F was higher than for IDH1 wt. The product concentration (2-OG) in the reaction catalysed by IDH1 wt was 75% of the 2-OG concentration in the reaction catalysed by IDH1 S280F after 1h.

The substrate for IDH1 wt is *D*-isocitrate. To investigate *D*-isocitrate as the substrate for both IDH1 wt and IDH1 S280F, its turnover to 2-OG was monitored by ^1H NMR (**Figure 4.31**). As anticipated, *D*-isocitrate was consumed, with concomitant reduction of $NADP^+$.

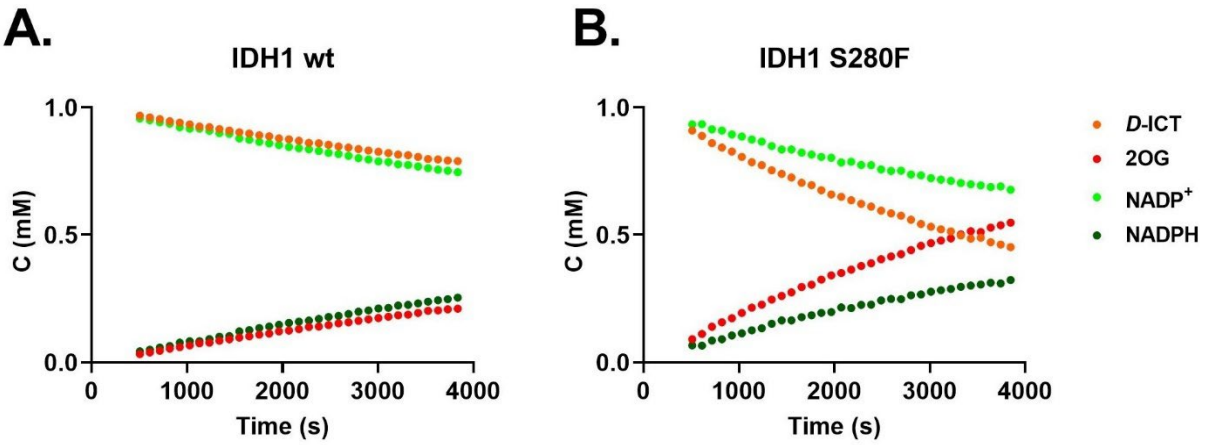

Figure 4.31 *| ^{1}H NMR (700 MHz) analyses of the turnover of D-Isocitrate to 2-OG, as catalysed by IDH1 wt (**A**), or the S280F variant (**B**) demonstrate D-isocitrate as the substrate. Conditions: 10 nM protein, 10 mM $MgCl_2$, 1.0 mM D-ICT, and 1.0 mM $NADP^+$, in 50 mM d_{11}-Tris buffer (90:10 H_2O:D_2O; pH 7.5).*

It was shown that both IDH1 wt and IDH1 S280F catalyse the oxidative decarboxylation of *D*-isocitrate to 2-OG. By contrast with the results from the NADPH absorbance assays, IDH1 S280F shows an elevated reaction rate in ^{1}H NMR time-course analysis. This difference may relate to the different pHs (7.5 vs 8.0) or the presence of NaCl (100mM) in the ^{1}H NMR assay buffer.

4.4.2.1.2 Reduction of 2-OG to 2-HG

Using the NADPH absorbance assay, it was shown that IDH1 wt and IDH1 S280F catalyse the turnover of 2-OG to 2-HG, but that the reaction rate is low (Section 4.4.1.2). To show formation of 2-HG and to complement those findings from the NADPH absorbance assay, ^{1}H NMR time-course studies were employed.

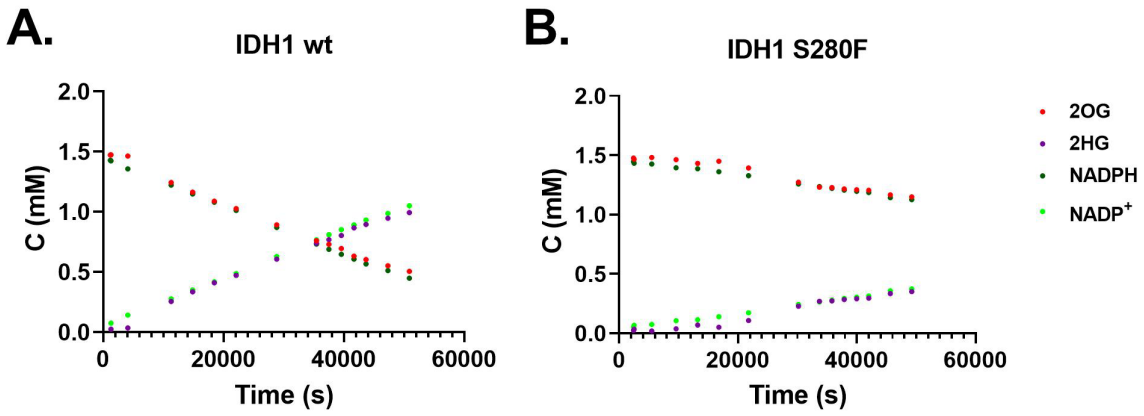

Figure 4.32 *| Turnover of 2-OG to 2-HG and concomitant oxidation of NADPH to $NADP^+$ as catalysed by IDH1 wt (**A**) or the S280F variant (**B**) monitored by ^1H NMR (700 MHz). Conditions: 1 µM enzyme, 10 mM $MgCl_2$, 1.5 mM 2-OG, 1.5 mM NADPH.*

Due to the low turnover rate of IDH1 wt and IDH1 S280F for the reduction of 2-OG to 2-HG, an enzyme concentration of 1 µM was used and the reaction was monitored overnight (~14 h). The results showed that IDH1 wt catalysed the turnover 2-OG to 2-HG, with 67% of the starting material (2-OG) consumed after the overnight reaction. The reaction catalysed by the S280F variant was slower than by IDH1 wt and only 33% of the starting material 2-OG was consumed after 14 h.

^1H NMR was also used to investigate if there are differences in the IDH1 wt and IDH1 S280F catalysed turnover of *DL*-isocitrate to 2-HG, compared to the reduction of 2-OG to 2-HG. When the first ^1H spectrum was acquired, half of the racemic *DL*-isocitrate mixture had apparently been converted to 2-OG (likely reflecting turnover of *D*-isocitrate). With overnight incubation (~14 h), the so formed 2-OG was subsequently reduced to 2-HG. The reaction catalysed by IDH1 wt showed a similar rate of 2-HG product formation such as when 2-OG was used as starting material (**Figure 4.32)** with 67% of 2-OG being turned over after ~14 h (**Figure 4.33**). In the reaction catalysed by IDH1 S280F, no substantial turnover was observed.

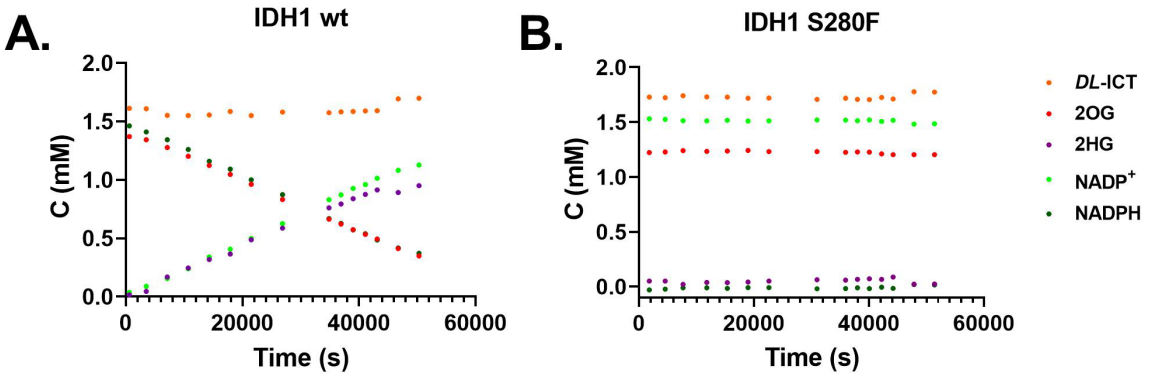

Figure 4.33 *| Turnover of DL-isocitrate to 2-HG as catalysed by IDH1 wt (**A**) or the S280F variant (**B**) monitored by ^{1}H NMR (700 MHz). Conditions: 1 µM enzyme, 10 mM $MgCl_2$, 3 mM DL-isocitrate, 1.5 mM $NADP^+$.*

The ^{1}H NMR time-course studies demonstrated the ability of IDH1 wt and IDH1 S280F to convert 2-OG to 2-HG, however, at much lower rates compared to the IDH1 variants tested (e.g. R132C, R132C S280F, R132H, R132H S280F, R132S; Section 2.4/4.3.1). The formation of 2-HG from 2-OG catalysed by IDH1 S280F was slower than IDH1 wt. This observation is consistent with a decreased k_{cat} of IDH1 S280F compared to IDH1 wt for the reduction of 2-OG to 2-HG observed by the NADPH absorbance assay (Section 4.4.1.2). When *DL*-isocitrate is used as a substrate, it appears there is no influence by *L*-isocitrate in the reaction mixture on IDH1 wt catalysis (as the 2-HG formation rate is similar to when 2-OG is used as starting material), but the reaction catalysed by S280F might be inhibited by *L*-isocitrate.

4.4.2.2 Time-Course Studies by ^{1}H Nuclear Magnetic Resonance on IDH1 R132H V255F/Q277E/V281F

To further investigate the low activity of R132H V255F and R132H V281F and the inactivity of R132H Q277E as observed by the NADPH assay, ^{1}H NMR was employed. With the same conditions as used in Section 4.4.2.1.2 (1 µM enzyme, 1.5 mM 2-OG, and 1.5 mM NADPH), no turnover was observed for R132H V255F, R132H Q277E or R132H V281F after 1 h. Therefore, samples were allowed to react overnight at ambient temperature and the first ^{1}H spectrum (t = 5 min) overlaid with a ^{1}H spectrum after 14 h. Comparison with an authentic spectrum of 2-HG was used to investigate product formation; no turnover was observed overnight under these conditions (**Figure 4.34**).

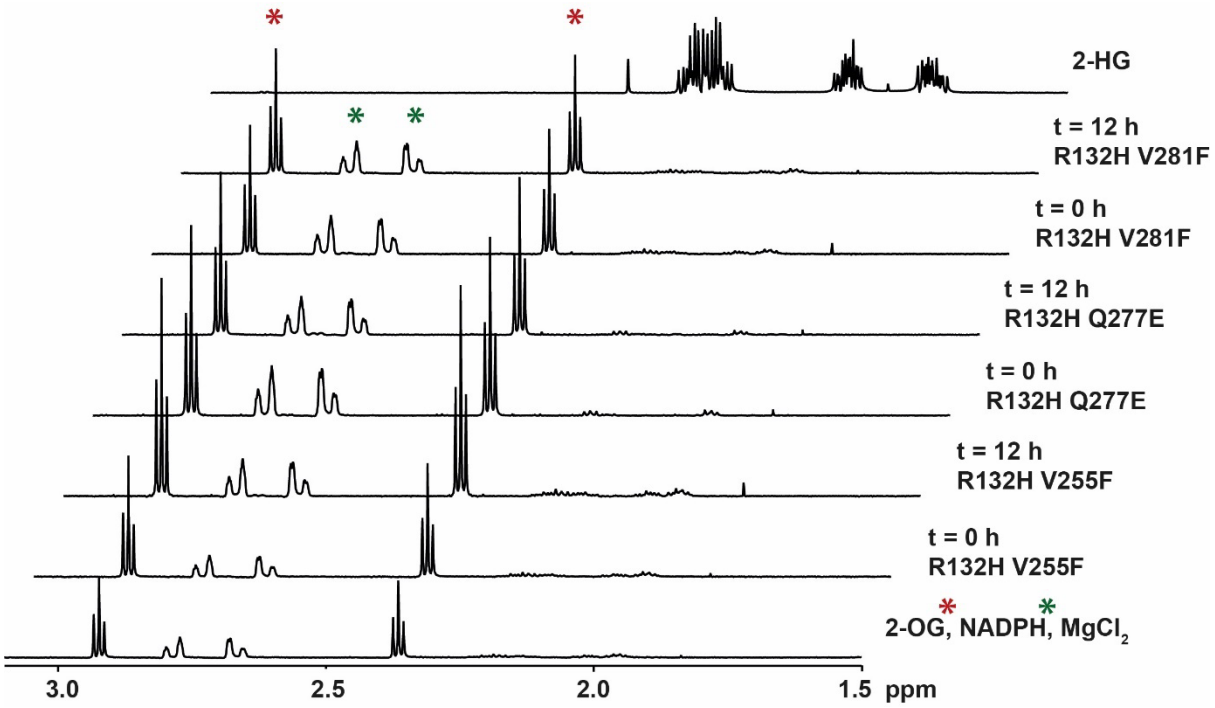

Figure 4.34 *| ^{1}H NMR (700 MHz) analyses of the turnover of 2-OG as catalysed by R132H V255F, R132H Q277E, R132H V281F. Conditions: 1 µM protein, 10 mM $MgCl_2$, 1.5 mM 2-OG, and 1.5 mM NADPH was used 50 mM d_{11}-Tris buffer (90:10 H_2O:D_2O; pH 7.5).*

Next, the turnover of isocitrate was analysed. The reaction mixtures contained 1 µM enzyme, *DL*-isocitrate (3 mM), and $NADP^+$ (1.5 mM). No turnover was observed after 1 h, so the reaction was allowed to proceed overnight (14 h). Comparison with an authentic spectrum of 2-OG and 2-HG showed that there was no product formation with the R132H V255F, R132H Q277E, and R132H V281F variants (**Figure 4.35**).

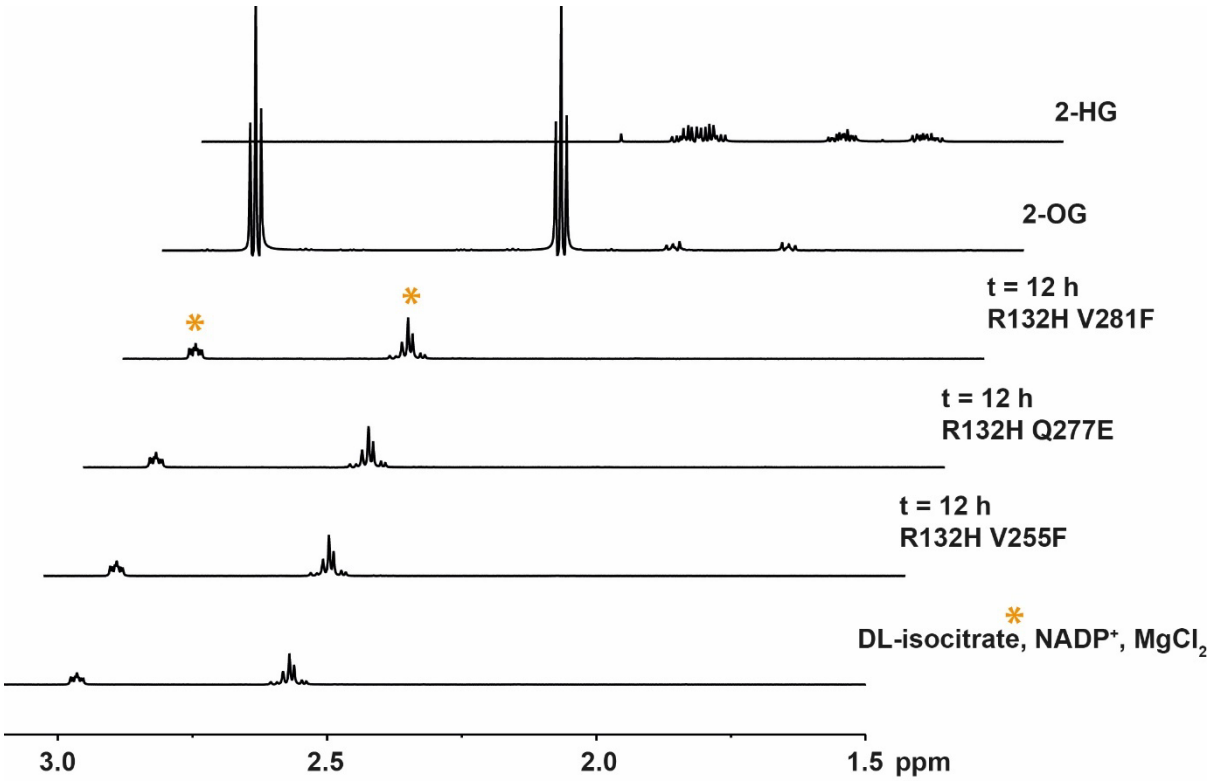

Figure 4.35 *| ^{1}H NMR (700 MHz) analyses of the turnover of 2-OG as catalysed by R132H V255F, R132H Q277E, R132H V281F. Conditions: 1 µM protein, 10 mM $MgCl_2$, 3 mM DL-ICT, and 1.5 mM $NADP^+$ was used 50 mM d_{11}-Tris buffer (90:10 H_2O:D_2O; pH 7.5).*

The overall results from the NADPH absorbance and ^{1}H NMR assays show that the dimer-interface variations V255F, Q277E, and V281F have a major impact on the activity of IDH1 R132H. No activity was observed for the R132H Q277E variant using either the NADPH absorbance or ^{1}H NMR assays. While there was no turnover of isocitrate or 2-OG by R132H V255F or R132H V281F as observed by the ^{1}H NMR assay, there was low apparent activity for both variants using isocitrate and 2-OG as substrates using the NADPH absorbance assay. The different activities observed might be a result of the different pH values (7.5 (NMR assay) vs 8.0 (NADPH absorbance assay)) or the presence of NaCl (100 mM) in the NMR assay buffer.

In summary, all three novel dimer-interface substitutions (V255F, Q277E and V281F), which were predicted to interfere with inhibitor binding (see Section 3.2), manifest a loss in activity for oxidation of isocitrate and reduction of 2-OG and are therefore, unlikely to occur in clinic under treatment with various IDH1 variant inhibitors. These results are in accord with other findings showing that changes at the dimer-interface, i.e. substitutions, can have substantial effects on IDH1 enzymatic activity (Section 2.3).

4.4.3 Biophysical Characterisation

To investigate if changes to the dimer interface alter the (structural) properties of the IDH1 variants, biophysical studies were carried out to examine variations in their secondary structures (as measured by CD), their thermal stabilities (as measured by CD, DSC, or DSF), and their oligomerisation states (as measured by non-denaturing PAGE or SEC-MALS).

4.4.3.1 Circular Dichroism Experiments

Circular dichroism (CD) was used to analyse the secondary structure content and to compare IDH1 wt, IDH1 S280F, R132H, R132H V255F, R132H Q277E, R132H V281F for differences as a result of the dimer-interface residue variations. The procedure used was conducted as described in Section 2.7.1.

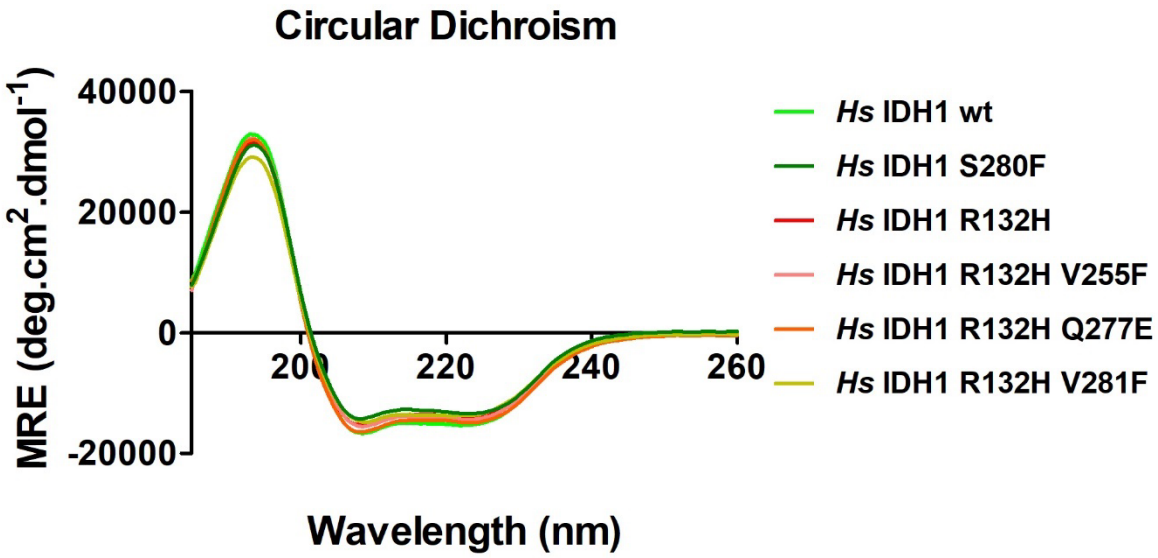

Figure 4.36 | *Circular Dichroism spectra of IDH1 variants. All variants display spectra of well-structured proteins. Conditions: protein (0.2 mg/mL in sodium phosphate (10 mM, pH 8.0) buffer.*

No substantial differences in the CD spectra of the IDH1 variants were observed (**Figure 4.36**). All the IDH1 variants tested seemed to have similar secondary structures. As discussed in Section 2.7.1, the two minima at 208.5 nm and 224 nm are typical for proteins with α-helices present and the maximum at 194 nm can be indicative of α-helices and β-sheets.[138] Minor differences in amplitude of the spectra are likely due to small differences in sample concentration.

4.4.3.2 Analyses of the Melting Temperature (T_m)

To investigate if the S280F variation increases the thermal stability independently of a variation in residue R132, T_m of IDH1 wt and IDH1 S280F was determined. Furthermore, to investigate

if the decreased activity/inactivity of R132H V255F, R132H Q277E and R132H V281F can be correlated to a change in protein stability, T_m was determined. As previously described, CD, DSC and DSF were employed to determine T_m of IDH1 wt, IDH1 S280F, R132H, R132H V255F, R132H Q277E, R132H V281F.

4.4.3.2.1 Analysis by CD

Determination of T_m values by CD was conducted using the procedure described in Section 2.7.2.1 by setting the wavelength to 215 nm and increasing the temperature gradually.

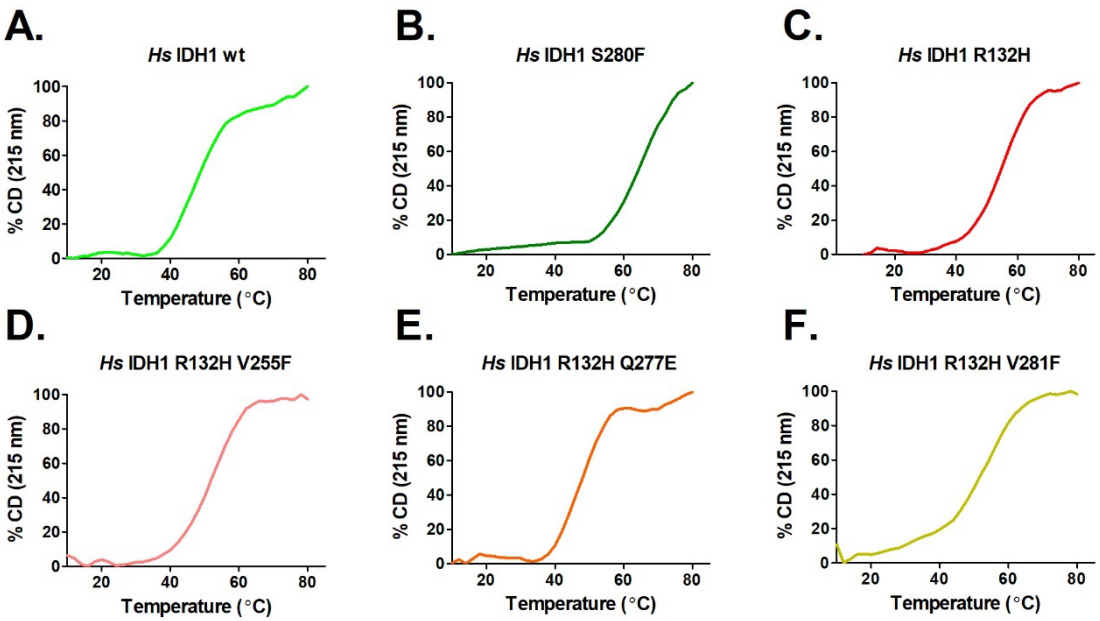

Figure 4.37 *| Analyses of thermal stability using CD.* ***A.-F.*** *Melting curves of IDH1 variants. Conditions: see Figure 4.36 legend.*

The denaturation of the IDH1 variants was indicated by the change in CD signal as a function of the temperature (**Figure 4.37**). The T_ms for the IDH1 variants tested are summarised in **Table 4.9**.

Table 4.9 | *Table of T_ms of IDH1 variants as determined by CD.*

Protein	T_m (°C)
IDH1 wt	48.3±0.3
IDH1 S280F	65.47±0.3
IDH1 R132H	54.7±0.1
IDH1 R132H V255F	51.8±0.1
IDH1 R132H Q277E	47.6±0.2
IDH1 R132H V281F	52.4±0.3

The T_m of IDH1 S280F was substantially higher (δ = 17.18°C) compared to IDH1 wt. There was a small decrease in the thermal stability of R132H V255F (δ = -2.91°C) and R132H V281F (δ = -2.34°C) compared to R132H. The decrease in thermal stability of R132H Q277E compared to R132H was more dominant (δ = -7.05°C).

4.4.3.2.2 Analysis by Differential Scanning Calorimetry (DSC)

The T_ms of IDH1 wt, IDH1 S280F, R132H V255F, R132H Q277E and R132H V281F were also analysed using DSC according to the procedure in Section 2.7.2.2.

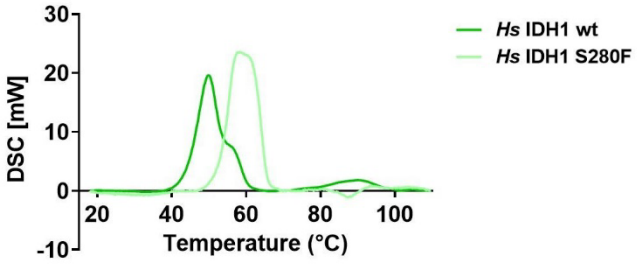

Protein	T_{m1} (°C)	T_{m2} (°C)
Hs **IDH1 wt**	49.9	55.9
Hs **IDH1 S280F**	57.3	61.2

Figure 4.38 **|** *Analyses of thermal stability using Differential Scanning Calorimetry (DSC). DSC curves of IDH1 wt and IDH1 S280F, and table showing T_m for IDH1 wt and IDH1 S280F. These data were acquired by Dr David Staunton.*

Interestingly, the DSC melting curves for IDH1 wt and IDH1 S280F showed two T_ms 6.05°C (IDH1 wt) and 3.86°C (IDH1 S280F) apart. The main melting peak of each variant was 7.42°C higher in IDH1 S280F compared with IDH1 wt.

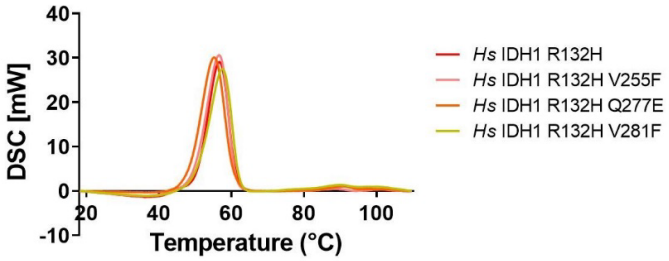

Protein	T_{m1} (°C)
***Hs* IDH1 R132H**	56.7
***Hs* IDH1 R132H V255F**	56.5
***Hs* IDH1 R132H Q277E**	55.3
***Hs* IDH1 R132H V281F**	57.5

Figure 4.39 *| Analyses of thermal stability using Differential Scanning Calorimetry (DSC). DSC curves of IDH1 R132H, IDH1 R132H V255F, IDH1 R132H Q277E, and IDH1 R132H V281F, and a table showing T_m for each variant.*

The melting curves for R132H and R132H V255F were similar. The T_m of R132H Q277E was lower (δ = -1.40°C) while the T_m of R132H V281F was slightly higher (δ = 0.85°C).

4.4.3.2.3 Analysis by Differential Scanning Fluorimetry

Following the procedure described in Section 2.7.2.3, the T_ms of IDH1 wt, IDH1 S280F, and R132H Q277E were determined using DSF (**Table 4.10**). The T_m of R132H is shown for comparison.

Table 4.10 *| Comparison of Melting temperatures as measured by DSF.*

R132H	R132H Q277E	wt	S280F
52.1±0.1°C	49.8±0.2°C	41.7±0.1°C	51.7±0.1°C

The T_m of R132H Q277E was lower compared to R132H (δ = -2.30°C). The T_m of IDH1 S280F was substantially higher (δ = 10.0°C) compared to IDH1 wt.

Because of differences in buffers (CD: sodium phosphate, pH 8.0; DSC: Tris 20 mM, pH 7.4; DSF: Tris 20 mM, pH 7.5 + Sypro orange dye), the absolute T_m values differ slightly. However, the trends in results from the T_m assays are largely the same. Similarly to the observations for R132C S280F and R132H S280F (Section 2.7.2), the S280F variation increases the T_m of IDH1 wt substantially. This may be due to a similar effect on the thermal stability as observed in the crystal structure of R132C S280F (Section 2.10.3). The F280 residues of both monomers in the R132C S280F structure interact and build a hydrophobic region at the dimer-interface together with the residues W124 and W267 of both monomers.

The influence on T_m by the second-site substitutions V255F and V281F on the R132H variant remains unclear, based on results from CD (T_m slightly decreased) and DSC (T_m slightly increased for R132H V281F and no change for R132H V255F). This is an indication that their lower activity is not a result of substantial changes in protein structure and stability but may be a result of interferences in dynamic processes at the dimer-interface during catalysis. The R132H Q277E variant shows a lower T_m compared to R132H by all the methods employed in this section. There may be a potential disruption of interactions at the dimer-interface which could explain the inactivity of this variant. This hypothesis will be further investigated by X-ray crystallographic analysis (Section 4.5).

4.4.3.3 Analysis of Oligomerisation State

IDH1 is predominantly dimeric in solution (see Section 2.7). To investigate if variations at the dimer-interface change the oligomerisation state, which might account for altered enzymatic activity, non-denaturing PAGE and SEC-MALS analyses were employed.

4.4.3.3.1 Non-Denaturing PAGE

Non-denaturing PAGE (4-12 % polyacrylamide Tris-Glycine) was conducted according to the procedure described in Section 2.7.3.

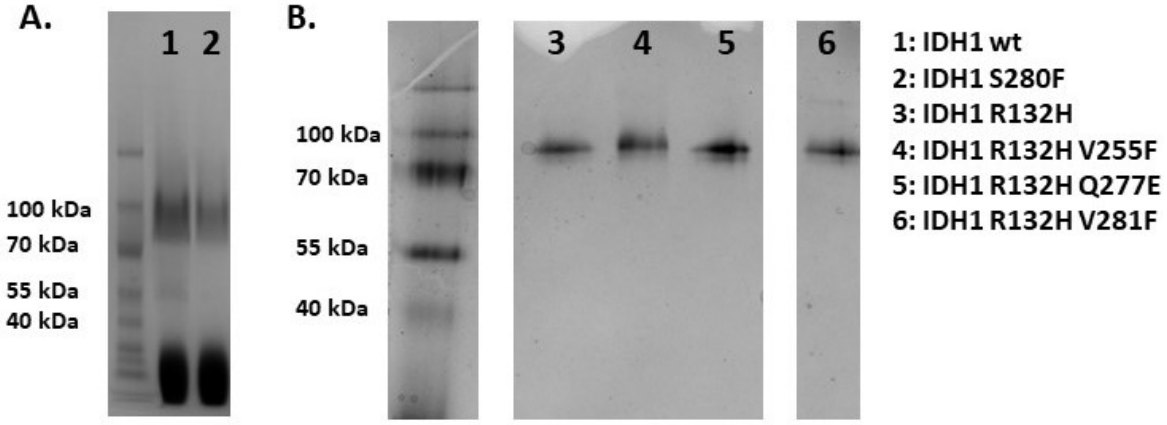

Figure 4.40 *| Non-denaturing PAGE of* ***A.*** *IDH1 wt and IDH1 S280F* ***B.*** *IDH1 R132H, IDH1 R132H V255F, IDH1 R132H Q277E, and IDH1 R132H V281F using a Tris-Glycine gel. All variants display a single band between 70 kDa and 100 kDa corresponding to a dimer (theoretical mass ~ 95 kDa). The large band at the bottom of* ***A*** *corresponds to excess G-250 sample additive, an anionic dye binding to the protein to ensure migration towards the cathode which is added for non-denaturing PAGE.*

All proteins showed a single band between 70 and 100 kDa corresponding to the IDH1 dimer (**Figure 4.40**). This was consistent with previous studies and experiments conducted in Section 2.7 and Section 4.3.4.3.1 showing IDH1 is dimeric in solution.

4.4.3.3.2 Analysis by SEC-MALS

The oligomerisation state of IDH1 wt, IDH1 S280F, R132H, R132H V255F, R132H Q277E, and R132H V281F in solution was additionally analysed by SEC-MALS, conducted according to the procedure described in Section 2.7.3.

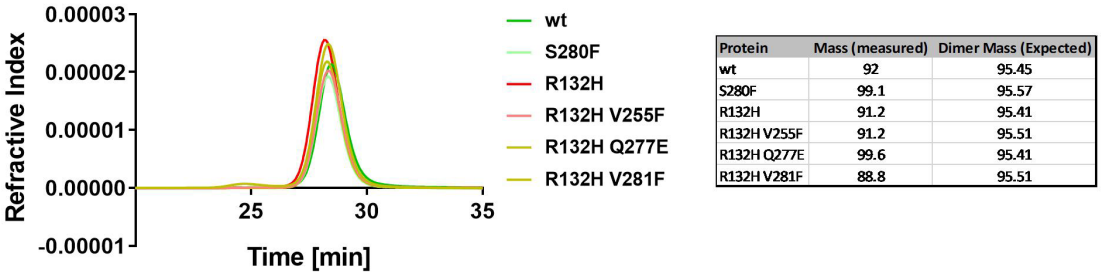

Protein	Mass (measured)	Dimer Mass (Expected)
wt	92	95.45
S280F	99.1	95.57
R132H	91.2	95.41
R132H V255F	91.2	95.51
R132H Q277E	99.6	95.41
R132H V281F	88.8	95.51

Figure 4.41 *| SEC-MALS analysis of IDH1 wt, IDH1 S280F, IDH1 R132H, IDH1 R132H V255F, IDH1 R132H Q277E, and IDH1 R132H V281F. The proteins were diluted to 1 mg/L in buffer containing 20 mM Tris, 100 mM NaCl (pH 7.4) and analysed using a Superdex 200 HR10/30 column. The results imply the proteins tested are predominantly present as a dimer in solution with masses 90-100 kDa.*

The SEC-MALS analyses showed the predominant species in solution to be dimeric for all of IDH1 wt, IDH1 S280F, R132H, R132H V255F, R132H Q277E, and R132H V281F (**Figure 4.41**).

In summary, studies on the oligomerisation state using non-denaturing PAGE or SEC-MALS show IDH1 wt and IDH1 S280F to be predominantly dimeric in solution. This is also true for R132H V255F, R132H Q277E and R132H V281F showing that none of the dimer-interface substitutions results in, at least, substantial changes in the preferred oligomerisation state. Disruption of the oligomerisation state can therefore be ruled out as the reason for the decreased catalytic activity of R132H V255F, R132H Q277E, and R132H V281F.

The novel variant R132H Q277E is the only dimer-interface variant tested that was catalytically inactive in all experiments – at least with the tested substrates. Therefore, IDH1 R132H Q277E was selected for further studies on the inactivity of the novel dimer-interface variants. This included substrate binding studies and crystallographic studies to investigate the mechanistical/structural reasons for the inactivity of R132H Q277E.

4.4.4 Substrate and Co-factor Binding Studies by DSF

According to the procedure as described in Section 2.9, cofactor binding studies using DSF were conducted.

4.4.4.1 Binding Studies on IDH1 wt and the S280F Variant

It is reported that isocitrate can bind to IDH1 wt in the absence of magnesium ions, although its binding is reduced.[48] However, at least some, IDH1 variants (e.g. R132H) only bind isocitrate in the presence of Mg^{2+} ions (Section 2.9). To investigate binding of substrate to IDH1 wt and IDH1 S280F, tertiary structure stabilisation was measured by DSF after the addition of varying concentrations of isocitrate or NOG in the absence of magnesium ions.

Addition of isocitrate led to an increase in the T_ms of both IDH1 wt and IDH1 S280F in the absence of magnesium ions in a concentration-dependent manner (**Figure 4.42**). The increase in T_m was larger for IDH1 wt than for IDH1 S280F. The addition of NOG resulted in a small increase in the T_m for both IDH1 wt and IDH1 S280F, with IDH1 wt showing a larger increase compared to IDH1 S280F (**Figure 4.42**).

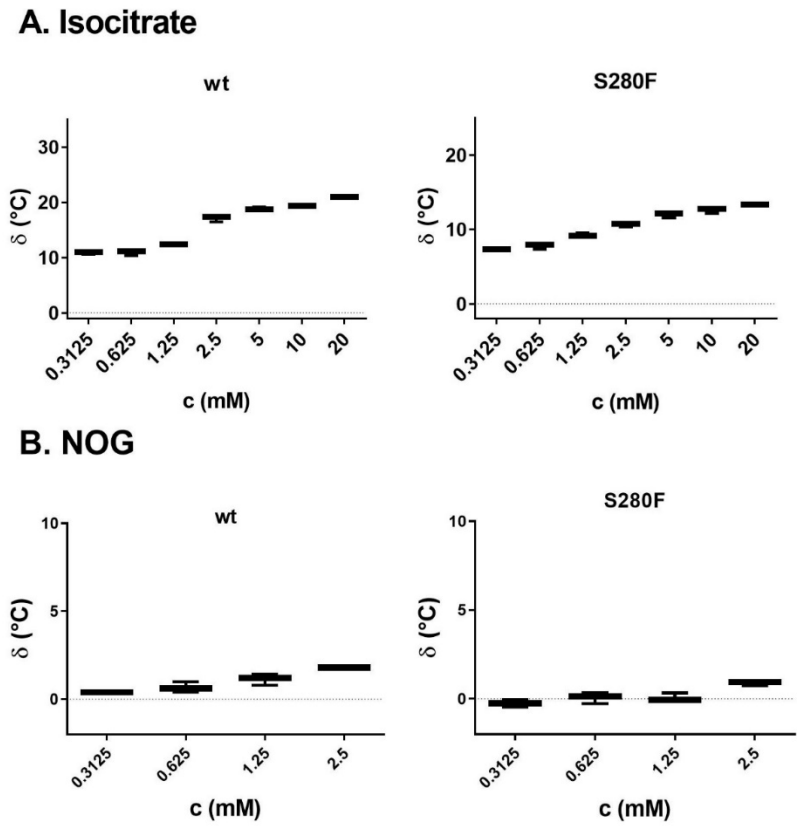

***Figure 4.42** | T_m-shift analyses of IDH1 wt and IDH1 S280F by DSF. The influence of DL-isocitrate(**A**) or NOG (**B**) on the thermal stability of IDH1 wt and IDH1 S280F is tested. Errors: standard error of the mean (n =3). Conditions: 3 µM enzyme, in 50 mM Tris, pH 7.5 (Dye: Sypro Orange 3×).*

The binding of magnesium ions to IDH1 wt and IDH1 S280F in the absence of substrate was then investigated (**Figure 4.43**). While the addition of magnesium ions showed no stabilisation of IDH1 wt at low concentrations (< 6.25 mM), at concentrations of 12.5 mM and above, there

was an increase of the T_m for IDH1 wt up to 8°C at 50 mM. The addition of magnesium ions, however, stabilised IDH1 S280F at relatively low concentrations (0.78 mM).

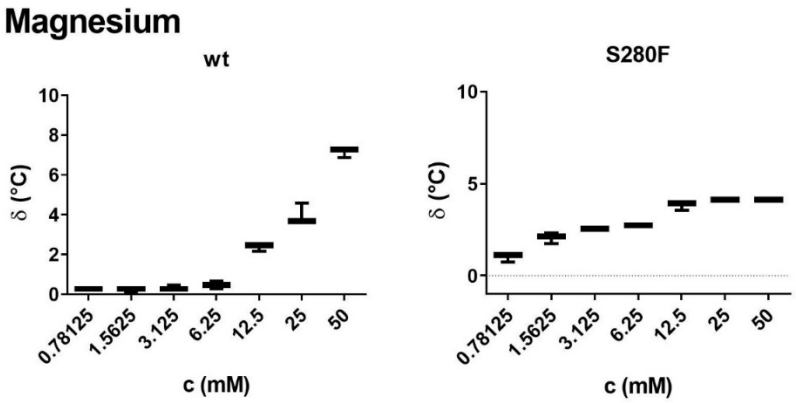

***Figure 4.43** | T_m-shift analyses of IDH1 wt and IDH1 S280F by DSF. The influence of magnesium on the thermal stability of IDH1 wt and IDH1 S280F is tested. Errors: standard error of the mean (n = 3). Conditions: 3 µM enzyme, in 50 mM Tris, pH 7.5 (Dye: Sypro Orange 3x).*

The effect of isocitrate and NOG on protein stability in the presence of magnesium was then investigated (**Figure 4.44**).

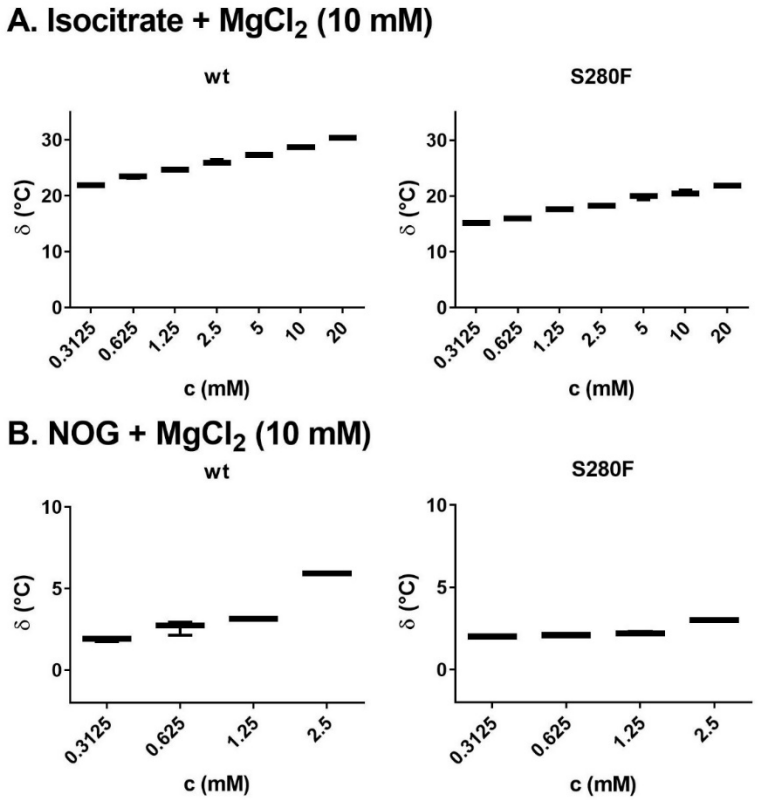

***Figure 4.44** | T_m-shift analyses of IDH1 wt and IDH1 S280F by DSF. The influence of DL-isocitrate (**A**) and NOG (**B**) on the thermal stability of IDH1 variants in the presence of magnesium is tested. Errors: standard error of the mean (n = 3). Conditions: 3 µM enzyme, 10 mM $MgCl_2$, in 50 mM Tris, pH 7.5 (Dye: Sypro Orange 3×).*

As previously reported[48], magnesium ions enhance the thermal stabilisation of IDH1 wt by isocitrate and also enhance the thermal stabilisation of IDH1 S280F by isocitrate, but the overall increase in T_m was smaller than for IDH1 wt (**Figure 4.44**). Magnesium ions also enhanced the thermal stabilisation by NOG with both IDH1 wt and IDH1 S280F, however, to a substantially lower degree than for isocitrate (**Figure 4.44**).

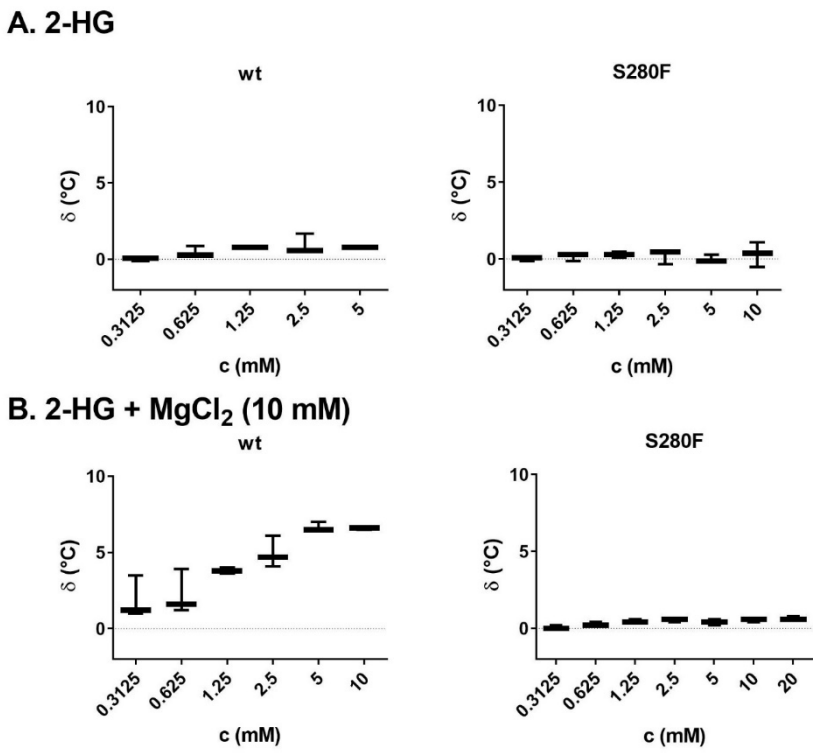

***Figure 4.45** | T_m-shift analyses of IDH1 wt and IDH1 S280F by DSF. The influence of 2-HG (**A**) and 2-HG + 10 mM $MgCl_2$ (**B**) on the thermal stability of IDH1 wt and IDH1 S280F is tested. Errors: standard error of the mean (n = 3). Conditions: 3 µM enzyme, 50 mM Tris, pH 7.5 (Dye: Sypro Orange 3x).*

In Section 4.4.2.1.2, it was shown that both IDH1 wt and IDH1 S280F can catalyse the reduction of 2-OG to 2-HG. It was observed by DSF that 2-HG did not increase the T_m of IDH1 wt or IDH1 S280F without magnesium ions present. However, in the presence of magnesium ions, 2-HG addition increased the T_m of IDH1 wt, but not of IDH1 S280F (**Figure 4.45**).

Finally, binding of NADPH and $NADP^+$ was examined. Addition of NADPH produced a large increase in T_m for both IDH1 wt and IDH1 S280F. Similarly, $NADP^+$ increased T_m for both proteins, although the effect was larger for IDH1 wt compared with IDH1 S280F (**Figure 4.46**).

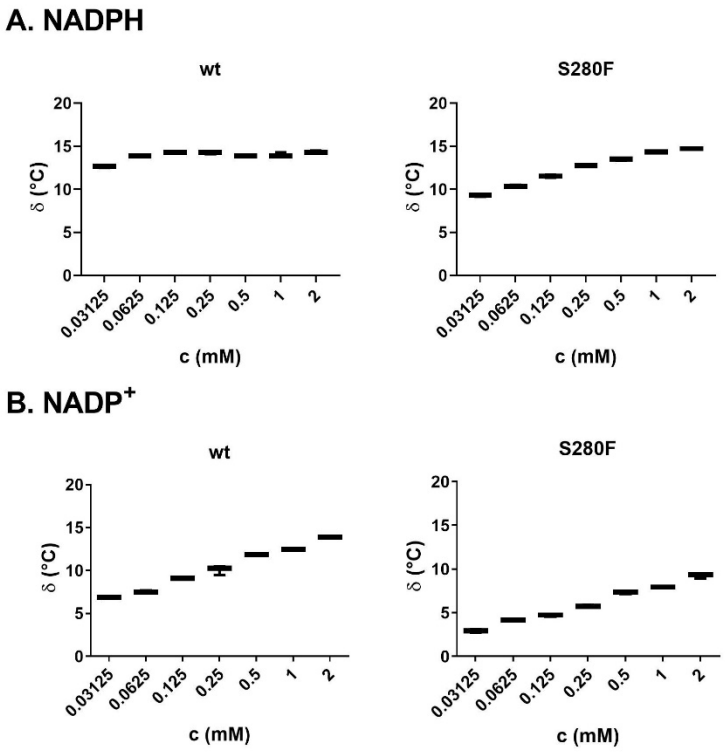

Figure 4.46 *| T_m-shift analyses of IDH1 wt and IDH1 S280F by DSF. The influence of NADPH (**A**) and $NADP^+$ (**B**) on the thermal stability of IDH1 wt and IDH1 S280F is tested. Errors: standard error of the mean (n = 3). Conditions: 3 µM enzyme, 50 mM Tris, pH 7.5 (Dye: Sypro Orange 3x).*

The overall results indicate that isocitrate binds more strongly to both IDH1 wt and IDH1 S280F than NOG. This observation is in accord with kinetic data from both the NADPH absorbance (Section 4.4.1) and ^{1}H NMR assays (Section 4.4.2), which show a preference of IDH1 wt and IDH1 S280F for the turnover of isocitrate compared to the turnover of 2-OG. Binding of isocitrate and NOG to IDH1 wt and IDH1 S280F was enhanced by the presence of magnesium ions (**Figure 4.43**), and magnesium ions alone were also shown to bind to both enzymes (**Figure 4.42**, **Figure 4.44**). While IDH1 wt is only stabilised by high magnesium ion concentrations (≥ 12.5 mM), IDH1 S280F was stabilised by magnesium ion concentrations as low as 0.78 mM. In the presence of magnesium ions, NOG bound better to IDH1 wt compared with IDH1 S280F. These observations could (in part) explain why the isocitrate K_M for IDH1 wt is higher than that for IDH1 S280F (which would suggest isocitrate binding is better to IDH1 S280F, Section 4.4.1.1) but, according to binding studies by DSF, isocitrate binding is better to IDH1 wt compared to IDH1 S280F. Under turnover conditions, 2-OG (which is formed from the turnover of isocitrate) can be released more easily by IDH1 S280F (as suggested by a smaller increase in T_m from NOG, compared with IDH1 wt). 2-HG can bind to recombinant IDH1 wt, suggesting that 2-HG could also bind to the IDH1 wt homodimer inside

the cell if 2-HG producing IDH variants are present (note that IDH1 mutations are usually heterozygous[190], i.e. an IDH1 wt and an IDH1 R132 variant can be present at the same time).

4.4.4.2 Binding Studies on R132H Q277E

While R132H V255F and IDH1 R132H V281F show decreased activity compared with R132H, R132H Q277E is completely inactive (Section 4.4.2). Therefore, R132H Q277E was selected for DSF binding studies (conducted as described in Section 2.9) to investigate the cause of its inability to turn over isocitrate or 2-OG (**Figure 4.47**).

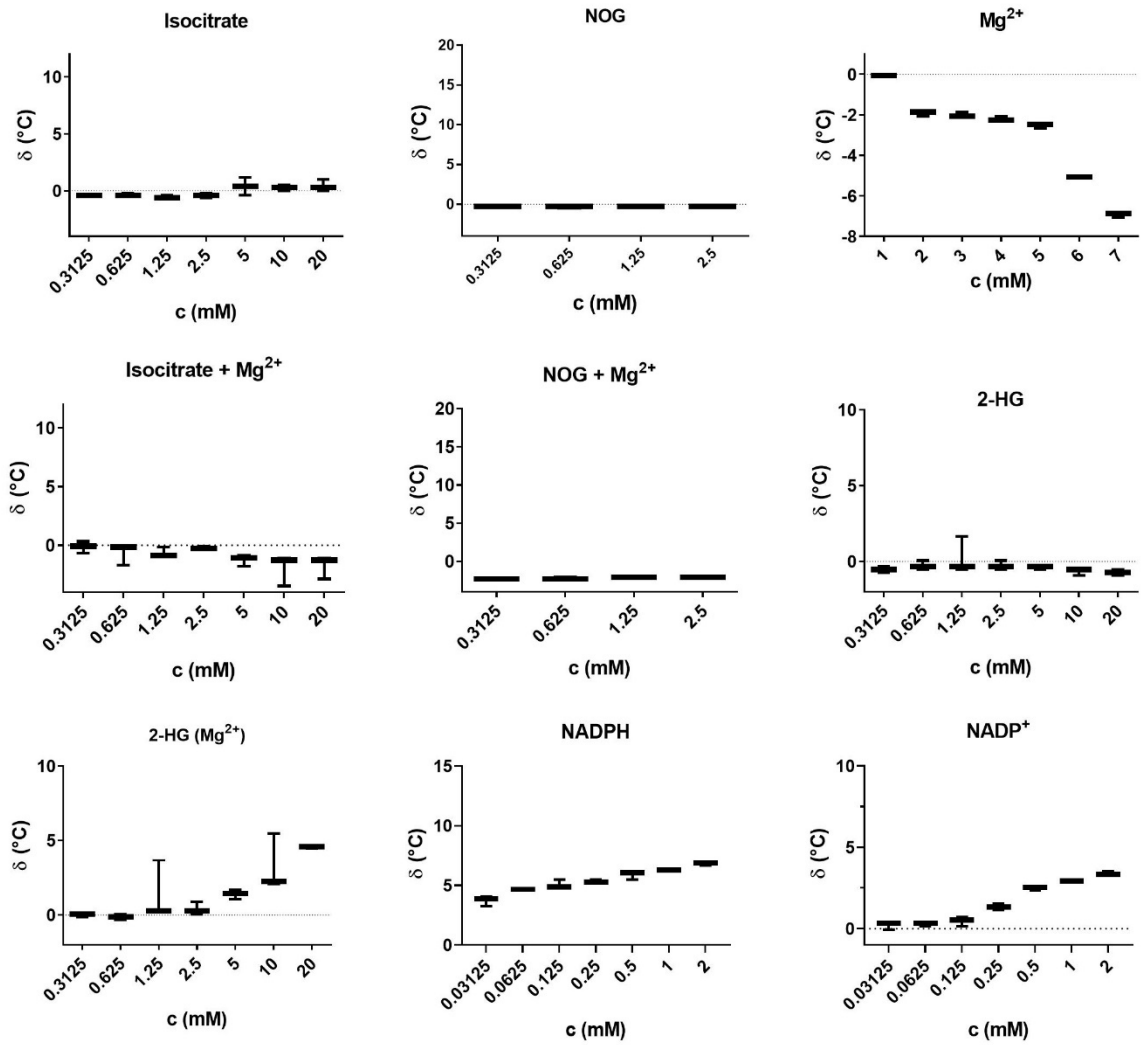

***Figure 4.47** | T_m-shift analyses of IDH1 R132H Q277E by DSF. The influence of a selection of co-factors, substrates and products on the thermal stability is tested. Errors: standard errors of the mean (n = 3). Conditions: 3 µM enzyme, in 50 mM Tris buffer, pH 7.5 (Dye: Sypro Orange 3x).*

As previously observed for other IDH1 variants (Section 2.9), the addition of isocitrate and NOG did not result in an increase in T_m of R132H Q277E in the absence of magnesium ions. Increasing concentrations of magnesium ions led to destabilisation of the R132H Q277E

variant. With magnesium ions present (10 mM), neither isocitrate nor NOG increased the thermal stability of R132H Q277E (**Figure 4.47**). In the case of 2-HG, an increase in T_m was observed only in the presence of magnesium ions. Addition of NADPH and $NADP^+$ both resulted in a concentration-dependent increase in the thermal stability of R132H Q277E.

The overall results imply that R132H Q277E inactivity is likely substantially due to its inability to bind isocitrate and NOG (and by implication 2-OG) even if magnesium ions are present. Binding of NADPH and $NADP^+$ to R132H Q277E was reduced compared with R132H (**Figure 2.41**); however, addition of NADPH and $NADP^+$ still resulted in an increase in T_m. The Q277E substitution is located on α10, which is reported to be involved in metal binding and in the binding of isocitrate and 2-OG (Section 1.6).[15] A potential effect of Q277E on the dynamics of α10 during catalysis may explain the inability of R132H Q277E to bind isocitrate and 2-OG.

These results further highlight the importance of the dimer-interface in IDH catalysis and show how changes at the dimer-interface can cause severe changes to the catalytic ability of the enzyme. Crystallographic studies on R132H Q277E were then conducted to investigate the influence of the Q277E substitution on the structure and function of the α10 helix of IDH1 R132H.

4.5 Crystallographic Studies

Whilst the R132H Q277E variant is apparently inactive, the homologous clinically observed IDH2 Q316E variation is linked to acquired enasidenib (IDH2 variant inhibitor) resistance (as indicated by increasing plasma 2-HG levels).[28] To investigate this apparent discrepancy, crystallographic studies with R132H Q277E were conducted.

Based on the crystallisation conditions used to crystallise R132C S280F in its closed active conformation (Section 2.10), 24-well optimisation plates were set up (Optimisation plate 1). The PEG3350 concentration (15-20% (v/v), horizontal axis in steps of 1% (v/v)) and the calcium acetate concentration (180-240 mM, vertical axis in steps of 20 mM) were varied, with the concentration of Bis-Tris (0.1 M, pH 7) kept constant. R132H Q277E was incubated for 1 h on ice with 10 mM NADPH, 20 mM $CaCl_2$ and 200 mM 2-OG to yield a final protein concentration of 12.81 $mg \times mL^{-1}$. Crystallisation was achieved by addition of 2 µL of the protein containing solution to 2 µL of the precipitant solution. Crystals were observed within 6 weeks (**Figure 4.48**, A-C).

Another optimisation plate was prepared with cross-seeded wells with the seeds made from crystals of R132C S280F incubated with NADPH, 2-OG, and calcium (Optimisation plate 2.2; Section 2.10.3). The PEG3350 concentration (16-21%, horizontal axis in steps of 1%) and the calcium acetate concentration (220 or 240 mM, vertical axis; seeded or unseeded, respectively) were varied with the Bis-Tris concentration (0.1 M, pH 7) kept constant. R132H Q277E was incubated for 1 h on ice with 10 mM NADPH, 20 mM $CaCl_2$ and 200 mM 2-OG to yield a final protein concentration of 12.81 $mg \times mL^{-1}$. Crystallisation was achieved by addition of 2 µL of the protein containing solution to 2 µL of the precipitant solution. Crystals were observed within 4 weeks (**Figure 4.48**, D).

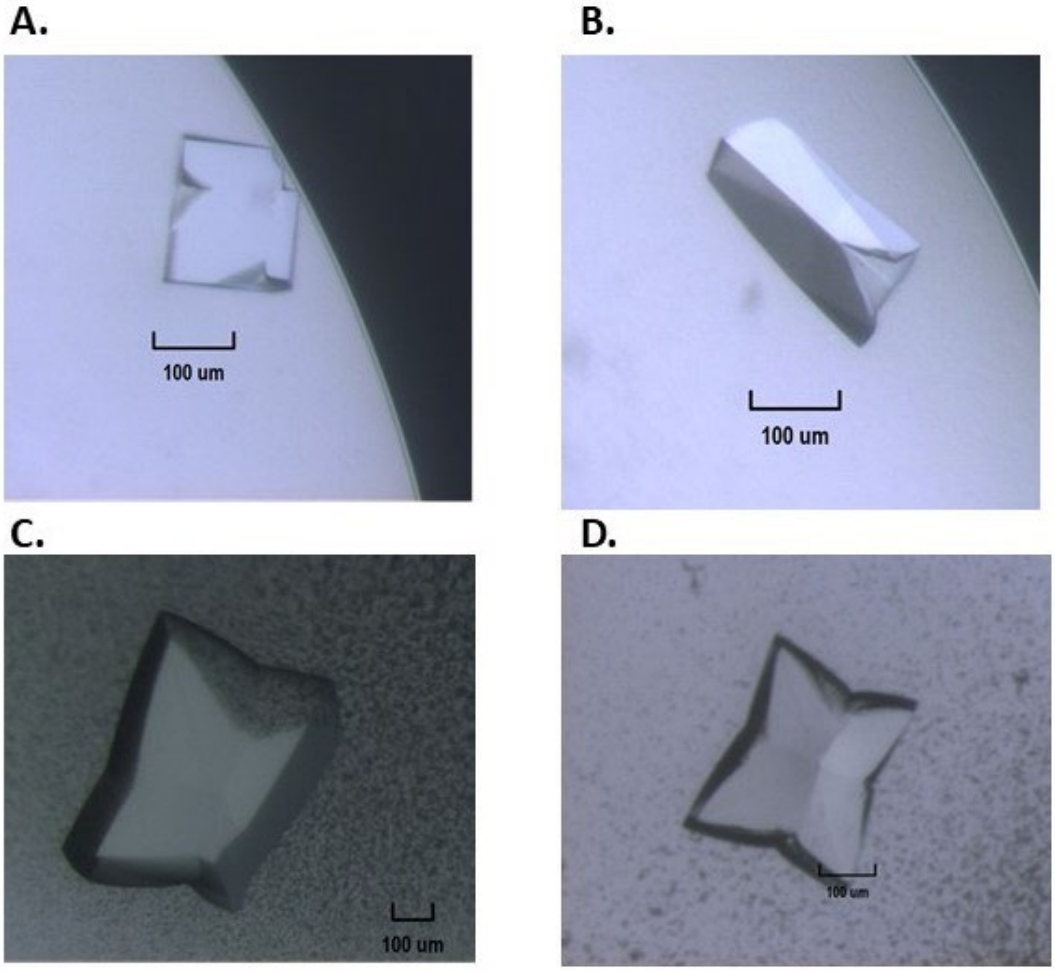

Figure 4.48 *| Photographs of crystals of R132H Q277E incubated with NADPH, 2-OG, and calcium harvested for X-ray diffraction studies.* ***A.-C.*** *Crystals appeared in Optimisation plate 1 after 6 weeks.* ***D.*** *Crystals appeared in seeded wells of Optimisation plate 2 after 4 weeks.*

Crystal containing droplets were mixed 1:1 with reservoir solution containing glycerol (25% (v/v)), harvested with a nylon loop and cryo-cooled in liquid N_2. Diffraction data were collected using synchrotron radiation at Diamond Light Source (DLS) beamline IO3.

The crystals diffracted to 1.9 Å resolution in the space group $P4_12_12$. Molecular replacement was conducted using two crystal structures with the same point group ($P4_32_12$); R132H co-crystallised with isocitrate and $NADP^+$ (PDB: 3MAP[191]) or IDH1 wt co-crystallised with $NADP^+$ (PDB: 1T09[15]). Both molecular replacements worked successfully.

In both the molecular replacement solutions of R132H Q277E, the loop with the R132 residue (132-140) and the α10 helix (271-286) were disordered. Furthermore, no evidence for calcium or 2-OG binding was observed. Because of this, and time constraints, no further refinements of these crystal structures were conducted.

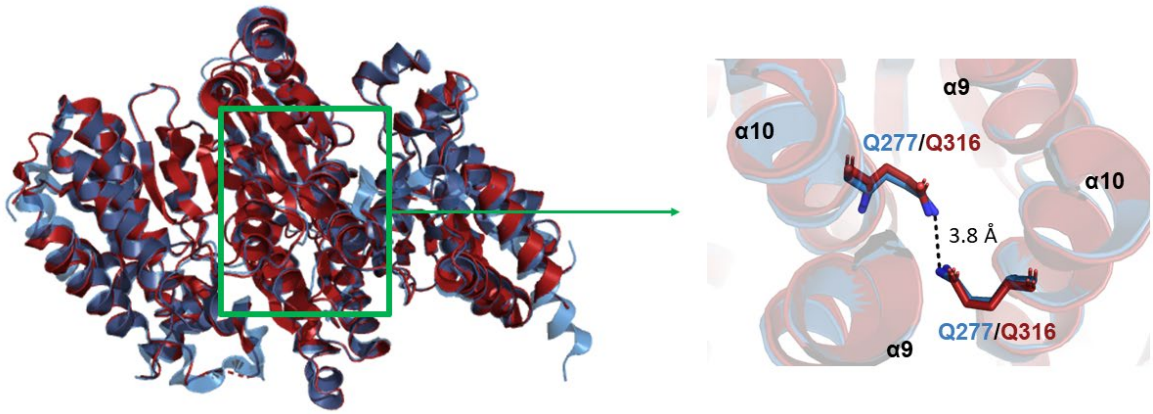

***Figure 4.49** | Views from a crystal structure of IDH1 R132H (blue, PDB ID: 4KZO[126]) superimposed with one of IDH2 R140Q (red, PDB ID: 5I95[57]). The dimer interface is highlighted in green. In the magnified view, α9 and α10 are at the centre of the dimer interface. IDH1 Q277 is homologous to IDH2 Q316. IDH1 Q277 and IDH2 Q316 have a similar distance to IDH1 Q277 or IDH2 Q316, respectively, on the other monomer.*

A potential explanation for the disordered α10 helix observed in IDH1 R132H Q277E comes from analysis of a structure of IDH1 R132H in its closed active conformation (PDB: 4KZO[126]). The Q277 residues of both monomers are ~3.8 Å apart *in crystallo* (as measured by the distance between the amido nitrogens of both residues). Substitution of glutamine to a glutamate (Q277E) could result in electrostatic repulsion at the dimer-interface. The distance between the residues Q316 (homologous to IDH1 Q277) at the dimer-interface is similar in IDH2 and IDH1. An IDH2 Q316E variant has been found in clinic and is linked to acquired enasidenib resistance and rising 2-HG levels.[28] However, this IDH2 variant is possibly heterodimeric in cells, i.e. it is composed of IDH2 R140Q and IDH2 Q316E (mutation is acquired in trans).[28] IDH1 R132H Q277E was produced as a homodimer, i.e. the glutamate residues are present in both monomers, potentially leading to electrostatic repulsion at the dimer-interface.

It has been reported for IDH1 R132H that two residues on the α10 helix (D275 and D279) are involved in magnesium ion (or calcium ion, which is used as an inactive metal in crystal

structures) binding (Section 1.6). Magnesium ions were shown to be important for 2-OG binding to IDH1 R132H by DSF studies (see Section 2.9). This observation is consistent with analyses on the crystal structure of R132C S280F (obtained in Section 2.10) showing that D275 and D279 are involved in metal binding. In accord with the results from binding assays using DSF (Section 4.4.4.2), suggesting that the R132H Q277E variant is unable to bind isocitrate or NOG; initial results from X-ray crystallography studies indicate no calcium ion or 2-OG binding. The apparent lack of binding of 2-OG and calcium ions to IDH1 R132H Q277E could result from disorder of α10. Disorder in α10 may be caused by electrostatic repulsion between the Q277E residues in separate monomers.

These observations further illustrate the dynamics at the IDH1 and IDH2 dimer-interface are complicated. Crystallographic, or other biophysical, studies, potentially in a time-resolved manner, are required to better understand the dimer-interface and its influence on active site chemistry and catalysis.

4.6 Summary and perspectives

In this Chapter, studies on the influence of catalytic (R132) and dimer-interface residue variations on IDH1 activity are described. Firstly, using an NADPH absorbance assay, it was shown that R132H generally shows lower activity for the reduction of 2-OG to 2-HG than R132C or R132S, which are similar amongst themselves (Section 4.3.1). ^{1}H NMR time-course analyses indicate that R132S catalyses the reduction of 2-OG at a higher rate than R132C (Section 4.3.2). The differences to the results from the NADPH absorbance assay are potentially related to the different buffer conditions used. The turnover of isocitrate to 2-HG, as observed by ^{1}H NMR, is catalysed more efficiently by R132C compared to R132S. Using cyclic voltammetry, it is shown that R132S catalyses the oxidation of isocitrate with similar efficiency to the subsequent reduction of 2-OG (Section 4.3.3). R132S apparently thus retains more of IDH1 wt's ability to catalyse the oxidation of isocitrate to 2-OG than R132C and R132H. This result is consistent with binding studies by DSF showing that isocitrate binds better to R132S (Section 4.3.4.4) than to R132C and R132H. The secondary structure and the oligomerisation state of R132S are similar to R132C and R132H, but the T_m of R132S is substantially decreased compared to R132C or R132H (Section 4.3.4). The decrease in T_m and findings on R132S reactivity (esp. regarding the turnover of isocitrate) should be further investigated by crystallographic analyses. It is also of interest to make an R132S S280F variant to study the influence of the S280F substitution on R132S reactivity and inhibition.

In the second part of this chapter, studies on the influence of the dimer-interface on enzymatic activity are described. IDH S280F shows increased catalytic efficiency compared with IDH1 wt for the turnover of isocitrate (determined by an NADPH absorbance assay) which is the result of a higher affinity for isocitrate, as judged by K_M (Section 4.4.1.1). It was shown that IDH1 wt can catalyse the reduction of 2-OG to 2-HG (Section 4.4.1.2/4.4.2.1.2) and that the S280F substitution (without an R132 variation) increases the extent of magnesium ion and 2-OG binding (as judged by K_M) but decreases the k_{cat}. Consistent with previous observations for R132C S280F (Section 2.6), the IDH1 S280F variation (without an R132 variation) does not change the secondary structure or oligomerisation state, but substantially increases the T_m compared to IDH1 wt (Section 4.4.3). This is likely due to interactions between the F280 residues of both monomers and the formation of a new hydrophobic pocket with W124 and W267, as observed in the crystal structure of R132C S280F (see Section 2.10.3).

Both IDH1 wt and IDH1 S280F can bind isocitrate in the absence of magnesium ions, however, binding is enhanced by magnesium ions (Section 4.4.4.1). The increase in T_m of IDH1 wt and IDH1 S280F by addition of NOG is substantially smaller than by addition of isocitrate, which is consistent with the predominant reaction of IDH1 wt and IDH1 S280F being the turnover of isocitrate (as judged by k_{cat} of the turnover of isocitrate vs k_{cat} of the turnover of 2-OG, Section 4.4.1). While magnesium ions can bind to IDH1 S280F in the absence of substrate even at relatively low concentrations (from 0.78 mM), binding of magnesium ions to IDH1 wt was observed only at concentrations above ≥ 12.5 mM (Section 4.4.4.1).

As shown by the NADPH absorbance assay (Section 4.4.1.3), the R132H V255F and R132H V281F variants exhibit a substantial decrease in activity in the turnover of isocitrate or 2-OG compared to R132H, while the R132H Q277E variant is inactive in the turnover of isocitrate or 2-OG. ^{1}H NMR time-course analyses, indicate that the R132H V255F, R132H Q277E and R132H V281F variants are inactive for turnover of isocitrate or 2-OG (Section 4.4.2.2) under the assay conditions. While the secondary structures and oligomerisation states of these variants are very similar to R132H, their T_ms are similar (R132H V255F, R132H V281F) or lower (R132H Q277E) than for R132H (Section 4.4.3). R132H Q277E, which was inactive in both the NADPH absorbance and ^{1}H NMR assays, was subsequently further analysed using binding studies by DSF and crystallography. Binding analyses by DSF suggest that R132H Q277E is unable to bind isocitrate or NOG (and by implication 2-OG; Section 4.4.4.2) even in the presence of magnesium ions, which is likely one reason for its inactivity.

A crystal structure of R132H Q277E (incubated with NADPH, calcium, 2-OG; Section 4.5), shows a disordered α10 helix. As α10 is involved in metal and substrate binding, the inability of R132H Q277E to bind isocitrate and NOG is likely linked to its inactivity. Analysis of a crystal structure of R132H in its closed active conformation (with NADPH, 2-OG, calcium) shows the side chains of the Q277 residues from both monomers to be spatially close (3.8 Å). Therefore, the Q277E variation could result in electrostatic repulsion between the carboxylate groups of the Q277E residues from both monomers leading to disruption of α10, in accord with a decreased T_m of R132H Q277E compared with R132H. The IDH2 Q316E variation was acquired in clinic in a patient bearing a IDH2 R140Q variant linked to enasidenib (IDH2 variant inhibitor) resistance; it may form an IDH2 R140Q/IDH2 Q316E heterodimer in cells.[28] This heterodimer is probably active (as indicated by rising plasma 2-HG levels), likely because only one Q316 residue in the heterodimer is substituted to Q316E, i.e. there is no electrostatic repulsion.

The results of this chapter further show that the dimer-interface is important for IDH1 variant activity and that subtle changes (i.e. substitution of residues) can substantially alter catalysis. This proposal is consistent with results from studies on R132C S280F and R132H S280F variants, which show enhanced activity compared to R132C or R132H, respectively (see Section 2.3/2.4).

4.7 Materials and Methods

4.7.1 Site-Directed Mutagenesis and Protein Production

All site-directed mutageneses (SDM) and protein productions were carried out as described in the Materials and Methods (Section 7.1.6, 7.1.12).

4.7.1.1 Primer Design

Forward and reverse primers to introduce V255F, Q277E, S280F and V281F encoding mutations were designed to be fully complementary with each other. Forward and reverse primers to introduce R132S were designed according to Zheng et al.[127]. The mutations were introduced by SDM. The plasmid encoding IDH1 R132S was made, based on a template encoding for IDH1 R132C. The plasmid encoding IDH1 S280F was made from an IDH1 wt encoding template. The plasmids encoding IDH1 R132H V255F, IDH1 R132H Q277E and IDH1 R132H V281F were made from a template encoding IDH1 R132H.

Table 4.11 | *Primers used for site-directed mutagenesis.*

Protein	Primer
IDH1 R132S_forward	CATAGGTT**C**TCATGCTTATGGGGATCAATACA G
IDH1 R132S_reverse	GCATGA**G**AACCTATGATGATAGGTTTTACCCA TCC
IDH1 S280F_forward	GGTGACGTGCAGTCGGACT**T**TGTGGCCCAA
IDH1 S280F_reverse	TTGGGCCACA**A**AGTCCGACTGCACGTCACC
IDH1 R132H V255F_forward	GGCTCATCGACGACATG**T**T**C**GCCCAAGCTATG AAATC
IDH1 R132H V255F _reverse	GATTTCATAGCTTGGGC**G**AA**C**ATGTCGTCGAT GAGCC
IDH1 R132H Q277E _forward	GACGTG**G**AGTCGGACTCTGTGGC
IDH1 R132H Q277E _reverse	CCGACT**C**CACGTCACCATCATAGTTTTTACAG G
IDH1 R132H V281F _forward	GACTCT**T**T**C**GCCCAAGGGTATGGCTCTC
IDH1 R132H V281F _reverse	CTTGGGC**G**A**A**AGAGTCCGACTGCACGTC

4.7.1.2 Yields of Protein Production

The yields are presented as pellet mass divided by the amount of 2TY medium. The protein yield is presented as amount of protein (mg) per litre of medium (L).

Table 4.12 | *Yields of protein production of IDH1 R132S, IDH1 wt, IDH1 S280F, IDH1 R132H V255F, IDH1 R132H Q277E, and IDH1 R132H V281F.*

Protein	Yield (g/L) (m(cell pellet)/ V(2TY medium)	Protein Yield (mg/L) (m(protein)/ V(2TY medium)
IDH1 R132S	9.2	21.2
IDH1 wt	9.9	50.0
IDH1 S280F	9.8	30.4
IDH1 R132H V255F	9.6	109.2
IDH1 R132H Q277E	8.8	144.5
IDH1 R132H V281F	8.9	154.6

The proteins were produced according to the procedure in the Materials and Methods (Section 7.1.12). For nickel-affinity chromatography, an imidazole step gradient was used:

***Table 4.13** | Imidazole step gradient elution of IDH1 variants from nickel-affinity column.*

Column Volumes (CV)	Percentage (v/v) of Elution Buffer
6	10
5	25
10	40
5	60
5	100

4.7.2 Steady-State Kinetics

The NADPH absorbance assays were conducted using a PHERAstar FS Microplate Reader according to the Materials and Methods chapter (Section 7.2.1). The assay buffer was prepared according to the following recipe[48]:

***Table 4.14** | Composition of buffer used for NADPH absorbance assay.*

	C (mM)	n (mol)	Mw (g/mol)	V (L)	m (g)
Assay buffer (pH 8.0)					
Tris base	100	0.025	121.14	0.25	3.0285
$MgCl_2$ x6H_2O	10	0.0025	203.3	0.25	0.50825
DTT	0.2	0.00005	154.253	0.25	0.007713
Tween-20 (C_V in %)	0.0050	-	-	0.25	0.0125
BSA (C_m in mg/mL)	0.1	-	-	0.25	0.025

The buffer was filtered, degassed and used for steady-state kinetics according to the following conditions. 4x stock solutions of substrates/co-factors and enzyme were prepared. To determine Michaelis-Menten parameters, the concentrations of one substrate/co-factor was varied whilst the other substrates/co-factors were saturated. The final protein concentration was 400 nM, adapted from assays previously conducted with IDH1 R132H in the laboratory. Substrates (4x), protein (4x) and assay buffer were allowed to warm to room temperature for 10 minutes. Then, 25 µL of buffer, protein and 2-OG were transferred into an ELISA half area Microplate (flat bottomed, medium binding). The reaction was initiated by addition of 25 µL NADPH (final volume: 100 µL) and the measurement was started immediately (conducted over 45 minutes). The initial rate was calculated using the specific NADPH absorption

according to the Materials and Methods (Section 7.2.1). The Michaelis-Menten parameters were then calculated using the GraphPad Prism software (Version 5).

4.7.3 Time-Course Analyses by NMR

^{1}H NMR time-course analyses were conducted according to the Materials and Methods (Section 7.2.2). Specific parameters and concentrations are in the respective figure legends.

4.7.4 Circular Dichroism (CD)

CD studies were conducted according to the Materials and Methods (Section 7.2.4). After averaging (n = 3) and smoothing (window size: 4), the MRE was calculated using the molecular weight of each protein and the number of amino acids (422). Calculations were conducted with Microsoft Excel and graphs made using the GraphPad prism software (version 5).

4.7.5 Analyses of Melting Temperature (T_m)

Analyses of T_m were conducted according to the Materials and Methods (Section 7.2.5). CD, DSC, and DSF analyses were used according to standard procedures.

4.7.6 Non-denaturing PAGE Analyses

Non-denaturing PAGE analyses were conducted according to the Materials and Methods (Section 7.2.6). To inform on an appropriate buffer pH, the isoelectric point of the proteins was calculated using the ExPASy ProtParam tool.[153] The IEPs can be found in the table below.

Protein	IEP
IDH1 wt	6.58
IDH1 R132S	6.47
IDH1 S280F	6.58
IDH1 R132H V255F	6.47
IDH1 R132H Q277E	6.36
IDH1 R132H V281F	6.47

A pH above the IEP ensured the protein to be negatively charged and to run towards the cathode. In addition to that, the G-250 sample additive was added, an anionic dye binding to the protein to ensure migration towards the cathode. The gel chamber was set up accordingly and an 8-12% polyacrylamide gel used.

4.7.7 Crystallographic Studies

Crystallisation was conducted by applying the sitting drop vapor diffusion method. A 24 well Cryschem Plate (Hampton Research, USA) with a reservoir solution of 250 µL was used, based on previous reports.[154] R132H Q277E (25 µL) was incubated for 1 h on ice with 10 mM NADPH (in H_2O, 10 µL), 20 mM $CaCl_2$ (in H_2O, 5 µL) and 200 mM 2-OG (in H_2O, 10 µL) to yield a final protein concentration of 13.89 mg mL^{-1}. Crystallisation was achieved by the addition of 2 µL of the protein containing solution to 2 µL of the precipitant solution. The plates were sealed with StarSeal Advanced Polyolefin Film (Starlab, Germany) and crystals (100 µM average size) were grown within 4-6 weeks. Additionally, seeding methods were employed by crushing crystals with the SeadBeat kit (Hampton Research, USA) according to the manufacturer's protocol. Crystal containing droplets were cryo-protected by mixing them in a ratio of 1:1 with reservoir solution containing glycerol (25%), harvested with a nylon loop, and cryo-cooled in liquid N_2. The crystals were stored in liquid N_2 until data collection.

Data were collected at 100 K using synchrotron radiation at the Diamond Light Source (DLS) beamline I24. Data were indexed, integrated, and scaled using the Xia2[150] strategy of the beamline auto-processing pipeline. The crystal structure was determined by molecular replacement (MR) using the AutoMR (PHASER[155]) subroutine in PHENIX[156]. The search model used for MR was based on R132H co-crystallised with isocitrate and $NADP^+$ (PDB: 3MAP[191]) or of IDH1 wt co-crystallised with $NADP^+$ (PDB: 1T09[15]).

Chapter 5

Studies on Mycobacterial Isocitrate Dehydrogenases

Contents

5 Studies on Mycobacterial Isocitrate Dehydrogenases

5.1 Introduction

A key feature to the success of *Mycobacterium tuberculosis* (*Mtb)* as a pathogen is its flexibility in central carbon metabolism allowing it to adapt to different environmental conditions.[111] An important part of this is the flexibility in isocitrate metabolism. Isocitrate can be metabolised as part of the tricarboxylic acid (TCA) cycle via isocitrate dehydrogenase (IDH) catalysed oxidative decarboxylation of isocitrate to 2-OG (**Figure 5.1**). However, an alternative pathway is the glyoxylate shunt, in which isocitrate lyase (ICL) catalyses the turnover of isocitrate to glyoxylate and succinate. In *Mtb*, there are two isoforms of ICL and two of IDH (**Figure 5.1**). Understanding metabolic flexibility in isocitrate metabolism is important because the regulation between glyoxylate shunt and TCA cycle is a crucial feature of *Mtb* metabolism and important for persistence.[114] Interference with the enzymes involved, e.g. by small molecule inhibitors, could be a promising strategy for the development of new drugs.

The subsequent studies focused on the two isoforms of IDH present in *Mtb*, *Mtb* IDH1 and *Mtb* IDH2. Furthermore, an IDH enzyme from a mycobacterial species with only one IDH isoform is discussed: *Mycobacterium smegmatis* (*Msm*). The aims of the work described in this chapter were to:

(i) establish a production strategy for the mycobacterial enzymes *Mtb* IDH1, *Mtb* IDH2, and *Msm* IDH for use in our laboratory and the Carvalho laboratory (Francis Crick Institute)

(ii) study the enzyme kinetics of *Mtb* IDH1, *Mtb* IDH2, and *Msm* IDH, and their biophysical properties

(iii) investigate divalent metal cation utilisation by *Mtb* IDH1 and *Mtb* IDH2, and their inhibition by metal cations

(iv) search for alternative substrates for *Mtb* IDH1 and investigate metabolic cross-regulation of *Mtb* IDH1, *Mtb* IDH2, and *Msm* IDH

(v) screen *Hs* IDH1 variant inhibitors against *Mtb* IDH1, *Mtb* IDH2, and *Msm* IDH

Experiments in this chapter were conducted by myself or (where indicated) by a visiting student, Maximillian Staudt, who I supervised in the laboratory (at the University of Oxford).

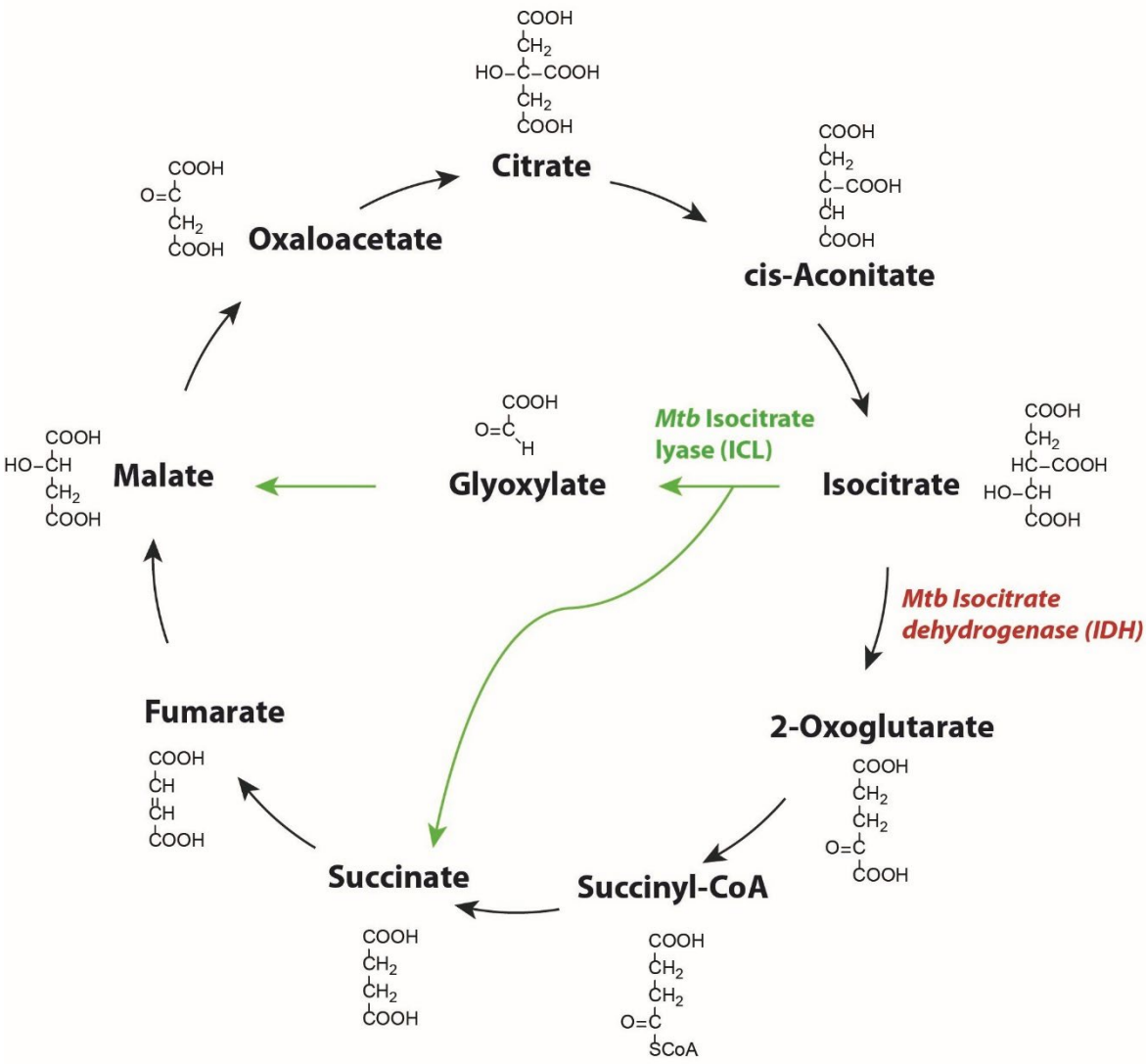

Figure 5.1 *| Tricarboxylic acid (TCA) cycle with the glyoxylate shunt in Mtb. The branch point between the two metabolic pathways is the turnover of isocitrate which is either metabolised by IDH (red, TCA cycle) or ICL (green, glyoxylate shunt).*

5.2 Expression trials

The work described in this section was conducted at the Francis Crick Institute in the laboratory of Dr Luiz de Carvalho. The recombinant expression of *Mtb* IDH1 in *E. coli* has been reported as challenging, yielding only small amounts of protein.[47] After successful cloning of the *Mtb* IDH1 open reading frame (ORF, not codon-optimised for expression in *E. coli*; with a C-terminal hexahistidine-tag and Flag-tag) into a pNIC vector, initial expression trials were carried out using BL21(DE3) cells. The majority of expressed *Mtb* IDH1 was present in the insoluble fraction (**Figure 5.2**). Recovery of the insoluble fraction, lysis in buffer containing urea, and purification of *Mtb* IDH1 by nickel-affinity chromatography yielded inactive protein. Therefore, optimisation of expression to increase the amount of soluble *Mtb* IDH1 protein was attempted. Use of a relatively low expression temperature (16°C) and a low concentration of

IPTG (0.1 mM) resulted in improved expression of *Mtb* IDH1 in the soluble fraction (**Figure 5.2**). Further optimisation trials were conducted; these included the use of autoinduction medium for expression in BL21(DE3), in which lactose was added to allow slow induction; co-expression with *Mtb* GroEL in BL21(DE3) to support correct folding of the protein (with standard IPTG induction), and the use of the Rosetta expression strain, which supplies additional tRNAs for rare codons that are absent in BL21(DE3) cells (with standard IPTG induction). None of these methods improved the soluble expression of *Mtb* IDH1 (data not shown).

Mtb IDH2 and *Msm* IDH expression was based on a previously reported method with a C-terminal His-tag.[192] Induction of expression at 16°C overnight with 0.1 mM IPTG yielded large amounts of soluble *Mtb* IDH2 and *Msm* IDH (**Figure 5.2**). These construct and expression conditions were used for large-scale expression.

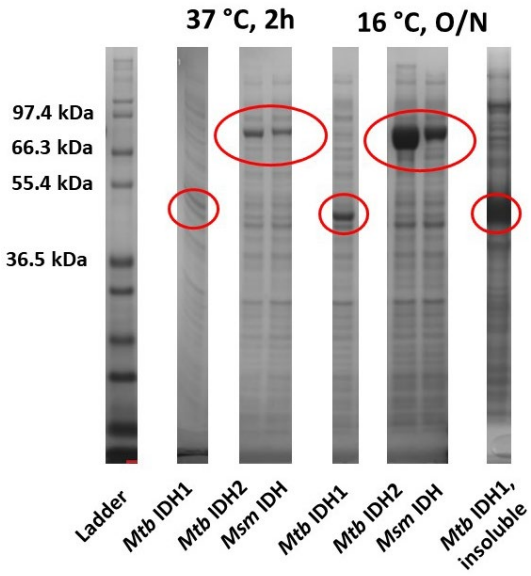

***Figure 5.2** | Expression trials of IDH1 of Mtb IDH1, Mtb IDH2 and Msm IDH at different expression conditions in BL21(DE3) cells. The red circle highlights Mtb IDH1 (~45.5 kDa), or Mtb IDH2 and Msm IDH (both ~82.6 kDa).*

Subsequently, a codon-optimised gene for the expression of *Mtb* IDH1 in *E. coli* was designed with a C-terminal His-Tag in a pNIC vector and transformed into BL21(DE3) cells. The new construct resulted in a substantially higher expression of soluble *Mtb* IDH1 and so this construct was selected for large scale expression (**Figure 5.3**).

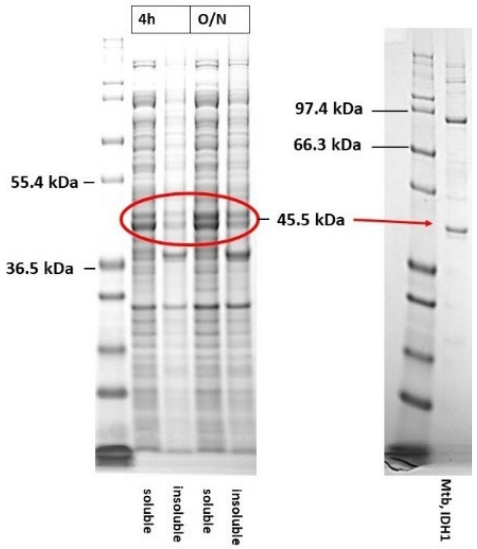

***Figure 5.3** | Left: Expression trials of a codon-optimised construct encoding for Mtb IDH1 with a C-terminal His-tag in BL21(DE3) cells at 16°C. Shown are the soluble and the insoluble fractions. The highest amount of protein was obtained in the soluble fraction of the overnight expression. Right: Mtb IDH1 after large-scale expression and purification using nickel-affinity chromatography (imidazole gradient elution), anion exchange chromatography (NaCl gradient elution) and size exclusion chromatography (isocratic elution). The additional band (~90 kDa) is likely dimeric Mtb IDH1.*

5.3 Large Scale Protein Production

A codon-optimised construct of *Mtb* IDH1 wt was expressed in BL21(DE3) after induction with 0.1 mM IPTG overnight (16°C). The cell pellet was harvested, lysed by sonication, and purified by nickel-affinity chromatography, anion-exchange chromatography and size exclusion chromatography. Purification yielded *Mtb* IDH1, which was aliquoted at a concentration of 2.9 mg/mL (**Figure 5.3**, Section 5.11.2).

Mtb IDH2 and *Msm* IDH production in BL21(DE3) cells was induced with 0.1 mM IPTG, following overnight growth (16°C). The cell pellet was harvested, lysed, and purified by nickel-affinity chromatography and size exclusion chromatography (Section 5.3.2/3).

5.3.1 *Mtb* IDH1 R135H

Mtb IDH1 R135 is homologous to *Hs* IDH1 R132, a residue for which variants in cancer are reported, i.e. *Hs* IDH1 R132H (see Chapter 2), which have an increased ability for producing the oncometabolite 2-HG from 2-OG.[11] To investigate if an *Mtb* IDH1 R135H variant can efficiently reduce 2-OG to 2-HG, the corresponding mutation was introduced into the gene encoding for *Mtb* IDH1 by site-directed mutagenesis (SDM) to yield *Mtb* IDH1 R135H. SDM was conducted according to standard procedures (Section 5.11.1) using *Mtb* IDH1 in a pNIC vector as the template. The mutation in the gene encoding for *Mtb* IDH1 R135H was demonstrated by Sanger sequencing.

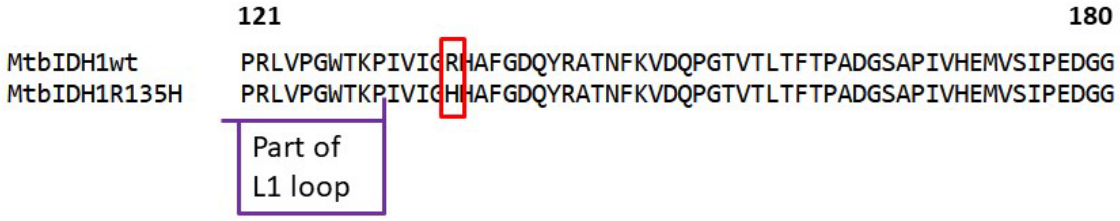

Figure 5.4 *| Protein sequence alignment of Mtb IDH1 wt with Mtb IDH1 R135H variant. The Mtb R135H substitution is in the red box. The purple box highlights a part of the L1 loop.*

Mtb IDH1 R135H was produced using a BL21(DE3)pLysS expression strain using the same conditions as for *Mtb* IDH1 wt. Following cell lysis, purification by nickel-affinity chromatography and size exclusion chromatography (**Figure 5.5**) yielded *Mtb* IDH1 R135H, which was aliquoted at a concentration of 3.8 mg/mL.

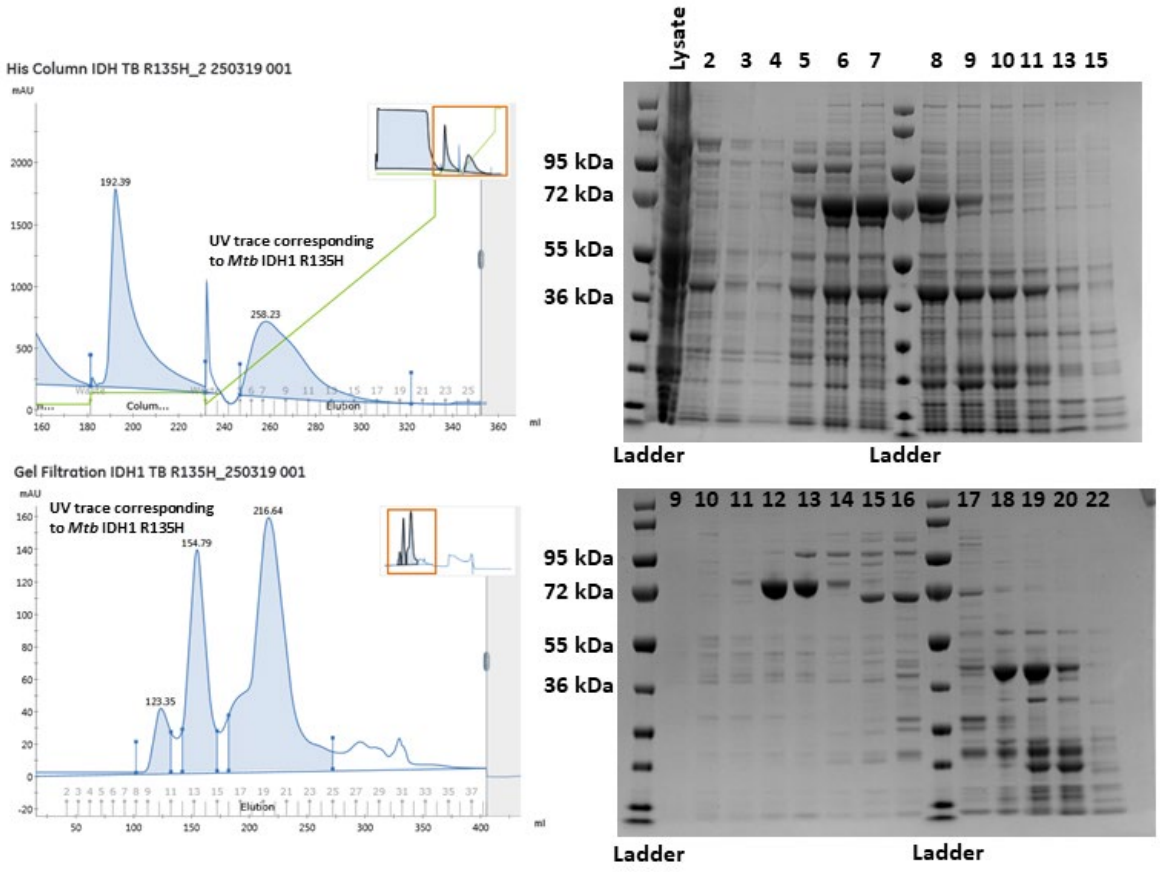

Figure 5.5 *| Mtb IDH1 R135H purification.* ***A.*** *Nickel-affinity chromatography using imidazole linear gradient elution (chromatogram on left-hand side, SDS-PAGE gel on right-hand side).* ***B.*** *Size-exclusion chromatography using isocratic elution (chromatogram left-hand side, SDS-PAGE gel on right-hand side). Fractions 18+19 were pooled and used for subsequent studies.*

5.3.2 *Mtb* IDH2

Following cell lysis, purification yielded *Mtb* IDH2, which was aliquoted at a concentration of 10.7 mg/mL.

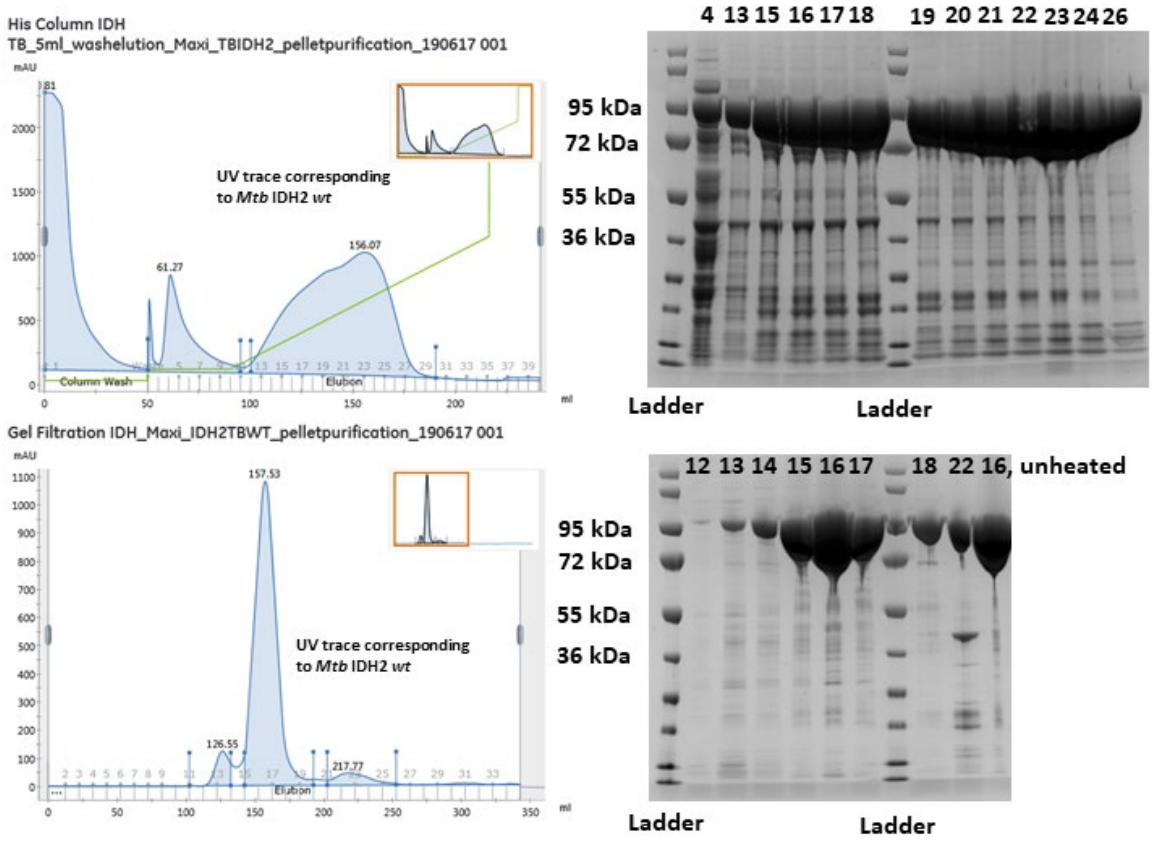

Figure 5.6 | *Mtb IDH2 wt purification.* ***A.*** *Nickel-affinity chromatography using imidazole step gradient elution (chromatogram on the left (shown are percentages of elution buffer), SDS-PAGE gel on the right).* ***B.*** *Size-exclusion chromatography using isocratic elution (chromatogram on the left, SDS-PAGE gel on the right).*

5.3.3 *Msm* IDH

Following cell lysis, the purification of *Msm* IDH was conducted by Dr Martine Abboud and yielded purified *Msm* IDH, which was aliquoted at a concentration of 9.2 mg/mL.

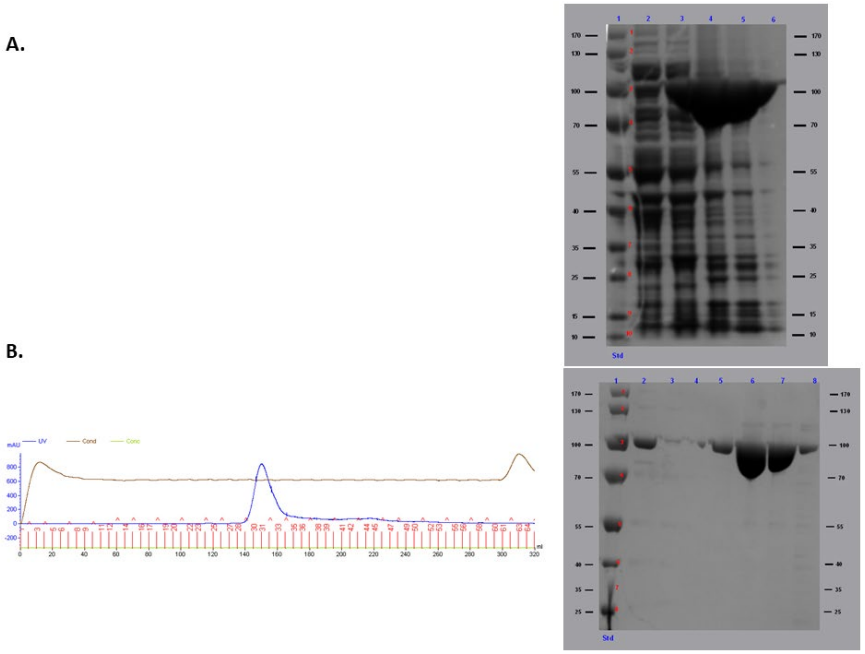

Figure 5.7 *| Msm IDH purification.* ***A.*** *Nickel-affinity chromatography using imidazole step gradient elution (chromatogram not shown, SDS-PAGE gel on the right).* ***B.*** *Size-exclusion chromatography using isocratic elution (chromatogram on the left, SDS-PAGE gel on the right). The data were acquired by Dr Martine Abboud.*

5.3.4 Analysis of Recombinant IDH1 Variants by LC/MS

To demonstrate isolation of the target proteins, their masses were investigated using LC/MS. The masses of all IDH1 variants were shown with the loss of the N-terminal methionine (**Table 5.1**) which is commonly observed in C-terminally tagged proteins expressed in *E. coli*.[129]

Table 5.1 *| Analyses of proteins by LC/MS demonstrates their masses with a loss of N-terminal methionine (-131 Da[130]).*

Protein	Mw (calculated)	Mw (observed)	Difference in Mw
***Mtb* IDH1 wt**	48284.63	48153	-131.6
***Mtb* IDH1 R135H**	48265.58	48133	-132.6
***Mtb* IDH2 wt**	85320.87	85188	-132.9
***Msm* IDH**	85375.02	85244	-131.0

5.4 Biochemical Characterisation

Mtb IDH2 is reported to be the important IDH isoform for turnover of isocitrate to 2-OG in *Mtb* metabolism as suggested by knockout studies: knockout strains of *Mtb* IDH2 are not viable.[113] To investigate if this might be reflected in Michaelis-Menten parameters for *Mtb* IDH2 compared to *Mtb* IDH1, an NADPH absorbance assay was employed to compare *Mtb* IDH1 and *Mtb* IDH2.

While there are two isoforms of IDH present in *Mtb*, there is only one present in *Msm* (closely related to *Mtb* IDH2, Section 1.10*)*.[113] To investigate if this is reflected in differences in enzyme kinetics, *Msm* IDH was analysed using the NADPH absorbance assay, and the Michaelis-Menten parameters compared to those for *Mtb* IDH1 and *Mtb* IDH2.

5.4.1 Determination of Michaelis-Menten Parameters

As described in Section 2.3, the Michaelis-Menten parameters for *Mtb* IDH1, *Mtb* IDH2, and *Msm* IDH were determined for the oxidative decarboxylation of isocitrate to 2-OG. The assay buffer was different to the one used for *Hs* IDH1 (Section 2.3). The mycobacterial assay buffer used in this section was prepared according to Quartararo et al.[47], which employs manganese as the catalytic divalent metal cation (100 mM HEPES (pH 7.5), 5 mM $MnCl_2$). The NADPH absorbance assay was employed, and the initial velocity plotted against the substrate concentration. Non-linear regression curve fit of the GraphPad Prism software (version 5) was used to determine the Michaelis-Menten parameters (**Figure 5.8**).

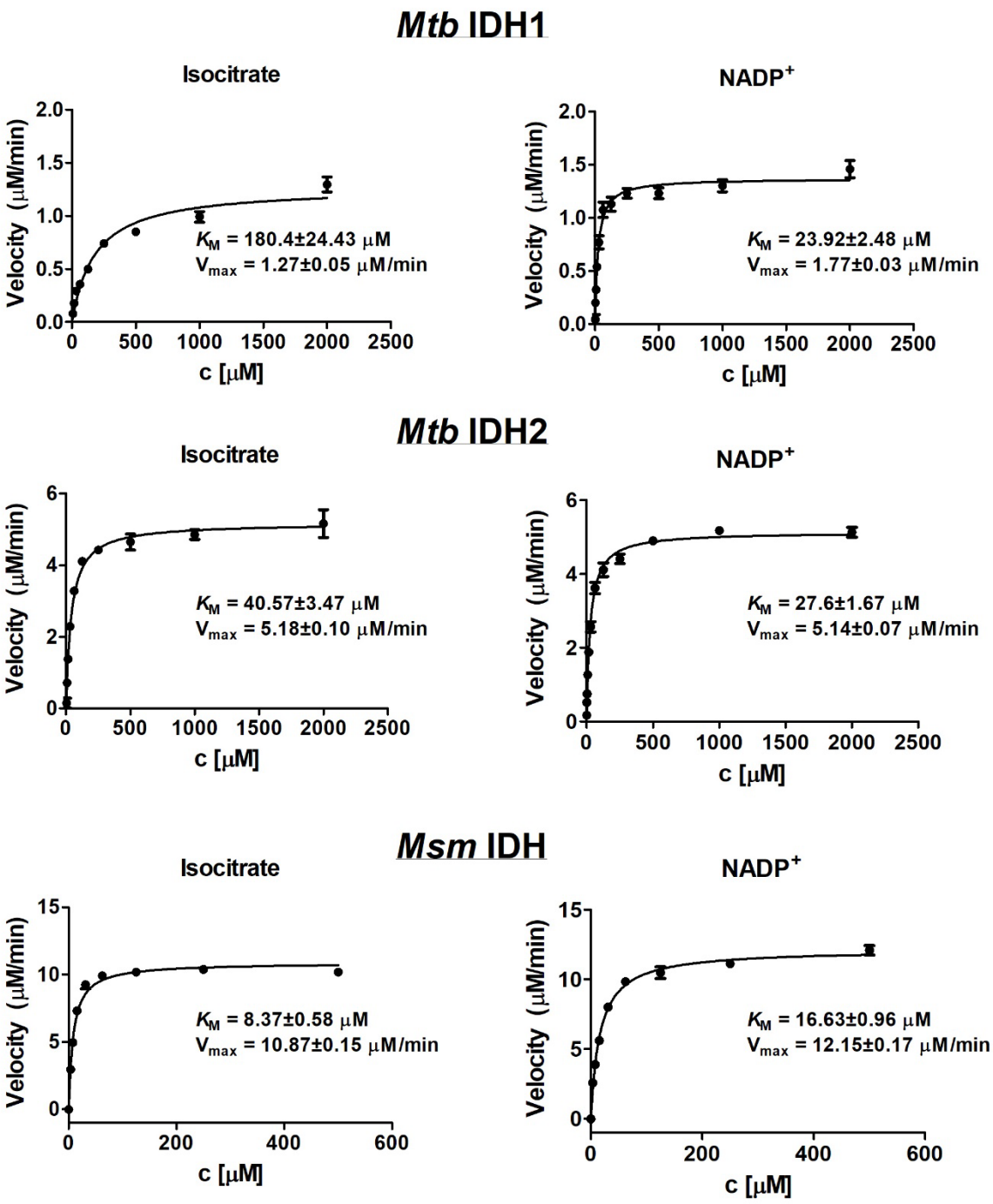

***Figure 5.8** | Kinetic studies on Mtb IDH1, Mtb IDH2, and Msm IDH catalysing the turnover of isocitrate to 2-OG. Non-linear regression curve fits are shown. Errors: standard errors of the mean (n =3). Conditions: 100 mM HEPES, 5 mM $MnCl_2$, pH 7.5. These data were acquired together with Maximillian Staudt.*

For further analysis, k_{cat} and k_{cat}/K_M were determined for *Mtb* IDH1, *Mtb* IDH2, and *Msm* IDH. The k_{cat} for *Mtb* IDH2 catalysing the turnover of isocitrate was 200-fold higher than for *Mtb* IDH1. The K_M for isocitrate was 4.5-fold higher and the k_{cat}/K_M for isocitrate 2000-fold lower for *Mtb* IDH1 compared to *Mtb* IDH2 (**Table 5.2**).

Table 5.2 *| Kinetic parameters of Mtb IDH1 (50 nM), Mtb IDH2 (1 nM), and Msm IDH (1 nM) for isocitrate from nonlinear regression curve fits. Errors: standard errors of the mean (n =3). $NADP^+$: 1 mM.*

Enzyme	**Isocitrate**		
	K_M **(µM)**	k_{cat} **(s^{-1})**	k_{cat}/K_M **($s^{-1}\times\mu M^{-1}$)**
***Mtb* IDH1**	180.4±24.4	0.4±0.0	2.3×10^{-3}
***Mtb* IDH2**	40.6±3.5	86.3±1.7	2.1
***Msm* IDH**	8.4±0.6	181.2±2.6	21.7

The K_M for $NADP^+$ was similar for *Mtb* IDH1 and *Mtb* IDH2, but the k_{cat}/K_M for $NADP^+$ was 150-fold lower for *Mtb* IDH1 than for *Mtb* IDH2 (**Table 5.3**). *Msm* IDH displayed a lower K_M for isocitrate and $NADP^+$ compared to the *Mtb* IDHs. The k_{cat} was 2-fold higher than in the reaction catalysed by *Mtb* IDH2 and the k_{cat}/K_M for isocitrate was 10-fold higher in the reaction catalysed by *Msm* IDH compared to *Mtb* IDH2 (**Table 5.2**, **Table 5.3**).

Table 5.3 *| Kinetic parameters of Mtb IDH1 (50 nM), Mtb IDH2 (1 nM), and Msm IDH (1 nM) for $NADP^+$ from nonlinear regression curve fits. Errors: standard errors of the mean (n =3). Isocitrate: 1 mM.*

Enzyme	**$NADP^+$**		
	K_M **(µM)**	k_{cat} **(s^{-1})**	k_{cat}/K_M **($s^{-1}\times\mu M^{-1}$)**
***Mtb* IDH1**	23.9±2.5	0.5±0.0	1.9×10^{-2}
***Mtb* IDH2**	27.6±1.7	85.7±1.1	3.1
Msm IDH	16.6±1.0	202.5±2.8	12.2

The k_{cat}/K_M for the turnover of isocitrate for *Mtb* IDH2 was 1000-fold higher than for *Mtb* IDH1 suggesting that *Mtb* IDH2 may be the main enzyme catalysing the turnover of isocitrate to 2-OG in *Mtb*. This proposal is in accord with reports that a knockout of *Mtb* IDH2 is lethal for *Mtb*.[113] *Mtb* IDH1 might have alternative or additional roles in *Mtb* metabolism which is discussed in the subsequent chapter. This includes studies on utilisation of catalytic metal cations and inhibition of *Mtb* IDH1 and *Mtb* IDH2 by metal cations (Section 5.6), as well as investigations on alternative substrates of *Mtb* IDH1 (Section 5.7) and metabolic cross-regulation of *Mtb* IDH1, *Mtb* IDH2, and *Msm* IDH (Section 5.8).

5.4.1.1 Production of 2-HG

It was reported by Quartararo et al. that *Mtb* IDH1, like *Hs* IDH1 R132H, can catalyse turnover of 2-OG to 2-HG. To investigate if this could be an additional function of IDH1 in *Mtb* metabolism, the NADPH absorbance assay was employed to determine the Michaelis-Menten parameters for *Mtb* IDH1 and *Mtb* IDH2 catalysing the reduction of 2-OG to 2-HG (**Figure 5.9**).

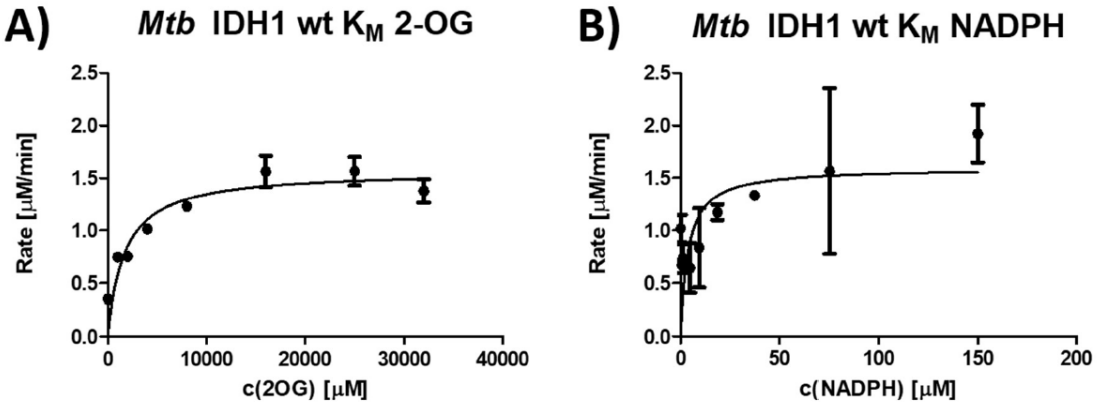

Figure 5.9 *| Kinetic studies on Mtb IDH1 (400 nM) catalysing the reduction of 2-OG to 2-HG. Nonlinear regression curve fits are shown. Errors: standard errors of the mean (n =3). Conditions: 100 mM HEPES, 5 mM $MnCl_2$, pH 7.5. NADPH: 0.3 mM.*

Mtb IDH1 was able to catalyse the turnover of 2-OG to 2-HG, however, the k_{cat} was very low (**Table 5.4**). The parameters for NADPH could not be determined accurately due to high error values (**Figure 5.9**).

Table 5.4 *| Kinetic parameters of Mtb IDH1 (400 nM) and Mtb IDH2 (1 µM) catalysing the reduction of 2-OG to 2-HG from nonlinear regression curve fits. Errors: standard errors of the mean (n =3). Conditions: 100 mM HEPES, 5 mM $MnCl_2$, pH 7.5. For the conditions for Hs IDH1 wt, see Figure 4.25.*

Enzyme	**2-Oxoglutarate**		
	K_M (µM)	**k_{cat} (s^{-1})**	**k_{cat}/K_M ($s^{-1}\times\mu M^{-1}$)**
***Mtb* IDH1**	1718±449.9	$(6.6\pm0.4)\times10^{-2}$	3.8×10^{-5}
***Mtb* IDH2**	not saturated at 150 mM		
***Hs* IDH1 wt**	826.8±165.4	$(3.8\pm0.2)\times10^{-2}$	4.6×10^{-5}

The K_M for 2-OG of *Mtb* IDH1 was 10-fold higher than for isocitrate. *Mtb* IDH2 apparently catalyses the reduction of 2-OG, but the Michaelis-Menten parameters could not be determined because the turnover rate could not be saturated at 150 mM 2-OG (which is likely not a physiologically relevant concentration). The k_{cat}/K_M for the reduction of 2-OG to 2-HG catalysed by *Mtb* IDH1 was the same as for the turnover catalysed by *Hs* IDH1 wt (Section

4.4.1.2). This suggests that, although *Mtb* IDH1 can catalyse the turnover of 2-OG to 2-HG more efficiently than *Mtb* IDH2, it is on a similar level to *Hs* IDH1 wt, and unlikely to be physiologically relevant.

5.4.1.2 Comparison of *Mtb* IDH1 R135H and *Hs* IDH1 R132H

Mtb IDH1 shares 70% sequence identity with *Hs* IDH1 and is structurally similar (Section 1.10). An *Mtb* IDH1 R135H variant was produced (Section 5.3.2) to investigate its ability to catalyse turnover of 2-OG to 2-HG more efficiently than *Mtb* IDH1 wt (similarly to a *Hs* IDH1 R132H variant). Interestingly, *Mtb* IDH1 R135H was inactive for both the oxidation of isocitrate and reduction of 2-OG as observed by the NADPH absorbance assay. Thus, despite the structural similarity to *Hs* IDH1 wt, the *Mtb* IDH1 R135H substitution renders *Mtb* IDH1 inactive. This illustrates that even though *Mtb* IDH1 and *Hs* IDH1 are structurally similar, there are likely subtle differences that can make a large difference in catalysis. As already discussed in Section 4, the roles of dynamic motions in IDH catalysis are complicated and the impact of single residue substitutions on enzymatic turnover can be profound.

5.4.1.3 Production of *Mtb* IDH1 Using the Lemo21 Cell Line

While all experiments in this chapter were conducted with the batch of *Mtb* IDH1 purified as described in Section 5.3.1, a new batch was purified in the end of my DPhil to allow follow-up studies. Due to issues with phage contamination, this batch was expressed in the phage resistant Lemo21 cell line. Purification was conducted using a 3-step protocol by nickel-affinity chromatography, anion exchange chromatography, and gel filtration (**Figure 5.10**).

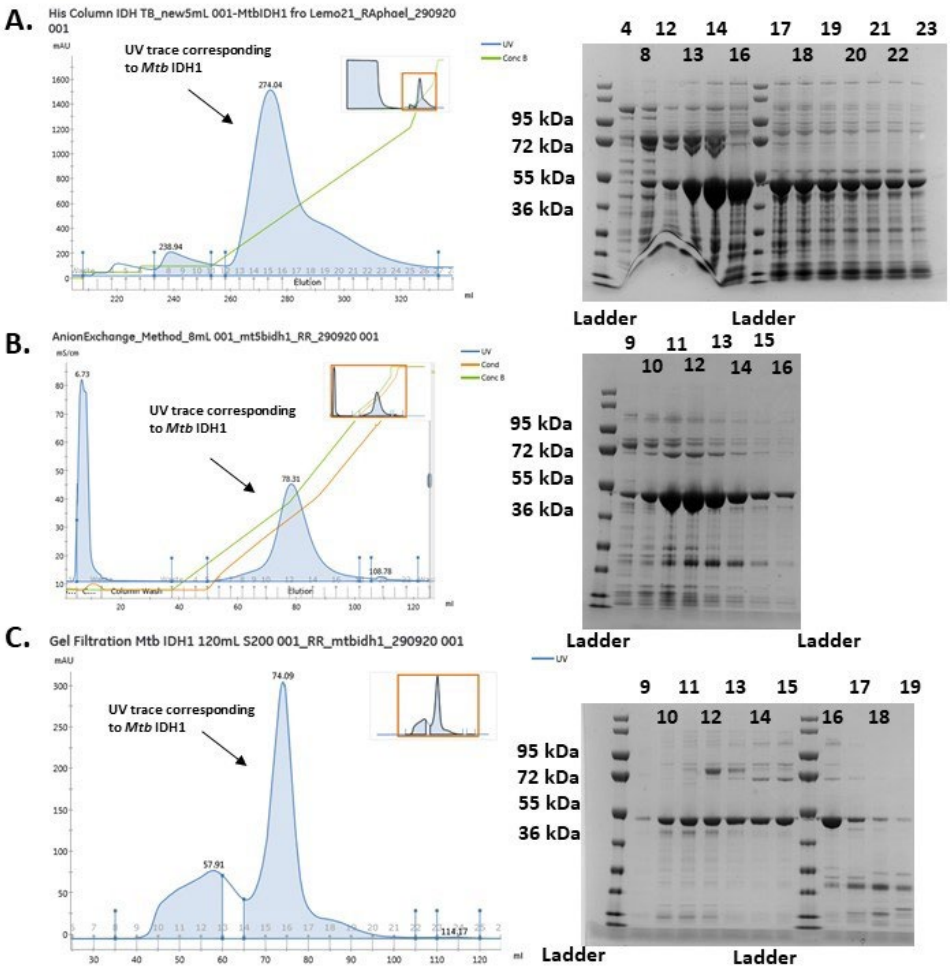

Figure 5.10 | *Mtb IDH1 wt purification.* ***A.*** *Nickel-affinity chromatography using a linear imidazole gradient elution (chromatogram on the left (shown are percentages of elution buffer), SDS-PAGE gel on the right).* ***B.*** *Anion-exchange chromatography purification using a linear NaCl gradient (chromatogram on the left, SDS-PAGE gel on the right).* ***C.*** *Size-exclusion chromatography using isocratic elution (chromatogram on the left, SDS-PAGE gel on the right).*

The process yielded purified *Mtb* IDH1. The mass of *Mtb* IDH1 was confirmed by LC/MS analysis (48,153 Da). Half of the *Mtb* IDH1 purified was treated with excess EDTA overnight to obtain *apo* enzyme. *Mtb* IDH1 was active, but, surprisingly, activity was substantially higher than compared to the previously produced batch. (**Figure 5.11**).

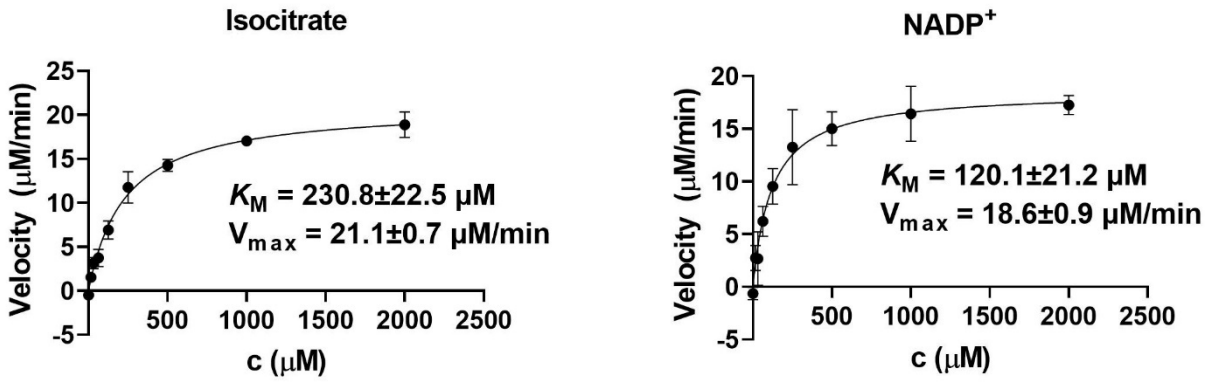

Figure 5.11 *| Kinetic studies on a new batch of Mtb IDH1 catalysing the turnover of isocitrate to 2-OG. Nonlinear regression curve fits are shown. Errors: standard errors of the mean (n =3). Conditions: 100 mM HEPES, 5 mM $MnCl_2$, pH 7.5.*

For comparison, k_{cat} and k_{cat}/K_M for *Mtb* IDH1 were calculated (**Table 5.5**). The Michaelis-Menten parameters were similar between the *apo* and non-*apo* enzymes (only the data obtained with *apo Mtb* IDH1 is shown). The catalytic efficiency of the new *Mtb* IDH1 batch, as indicated by k_{cat}/K_M, was substantially elevated compared to the other batch of *Mtb* IDH1. The k_{cat}/K_M for isocitrate catalysed by the new batch of *Mtb* IDH1 (0.15 $s^{-1}\times\mu M^{-1}$) was only 15-fold lower than for *Mtb* IDH2 (2.13 $s^{-1}\times\mu M^{-1}$) whereas it was 1000-fold lower for the previously produced batch of *Mtb* IDH1 ((2.33×10^{-3}) $s^{-1}\times\mu M^{-1}$).

Table 5.5 *| Kinetic parameters of Mtb IDH1 for isocitrate and $NADP^+$ from nonlinear regression curve fits. Errors: standard errors of the mean (n =3).*

	K_M (μM)	k_{cat} (s^{-1})	k_{cat}/K_M ($s^{-1}\times\mu M^{-1}$)
Isocitrate	230.8±22.5	35.1±1.1	0.15
$NADP^+$	120.1±21.2	30.9±1.5	0.26

The observation of increased activity of the new batch of *Mtb* IDH1 was surprising. It could potentially be related to use of a different expression strain, Lemo21. This would, however, mean that comparison of kinetic differences as conducted in Section 5.3.1, could be flawed due to substantial differences in activity of batches of isolated enzymes. Findings on the importance of *Mtb* IDH1 vs *Mtb* IDH2 in isocitrate metabolism from kinetic studies (Section 5.4.1) are in accordance with knockout studies showing *Mtb* IDH2 is the important IDH isoform in *Mtb.*[113] Thus follows that further studies on an alternative or additional role of *Mtb* IDH1, which are pursued in the subsequent sections, are valid.

5.4.2 Time Course Studies using ^{1}H NMR

To complement the kinetic analysis on the turnover of *DL*-isocitrate (hereafter referred to as isocitrate) to 2-OG by the NADPH absorbance assay as catalysed by *Mtb* IDH1 and *Mtb* IDH2,

^{1}H NMR was employed to enable direct observation of substrates and products. Isocitrate, 2-OG, $NADP^{+}$, and NADPH were identified, and their levels analysed as described in Section 2.4. The standard NMR assay buffer was used, i.e. 50 mM d_{11}-Tris buffer (90:10 H_2O:D_2O; pH 7.5). As Mn^{2+} is paramagnetic and would interfere with ^{1}H NMR measurements[193], Mg^{2+} was used as the catalytic metal cation (10 mM). Both *Mtb* IDH1 and *Mtb* IDH2 are reported to be able to utilise magnesium[118], which is also discussed in Section 5.6.1.

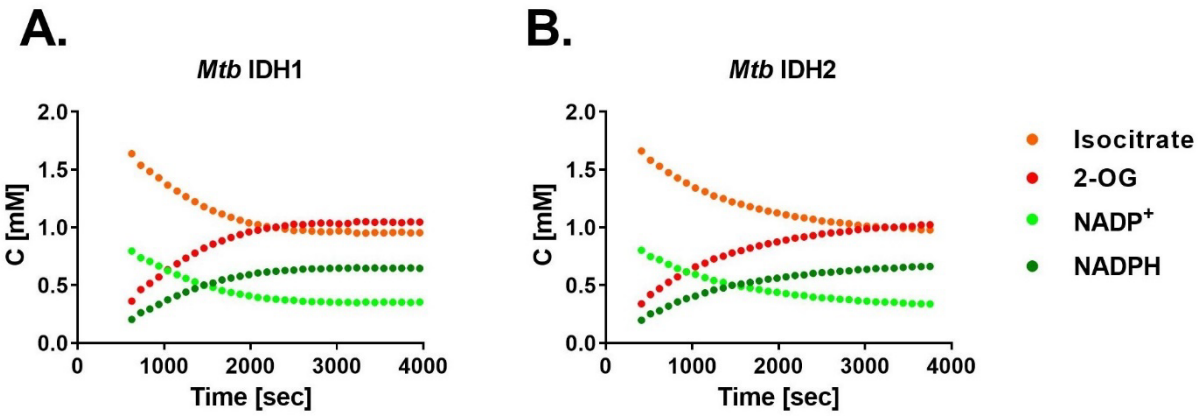

***Figure 5.12** | Turnover of isocitrate to 2-OG and concomitant oxidation of $NADP^{+}$ to NADPH catalysed by Mtb IDH1 (**A**, 50 nM enzyme) or Mtb IDH2 (**B**, 40 nM enzyme) as observed by ^{1}H NMR (700 MHz). Conditions: 10 mM $MgCl_2$, 2 mM DL-isocitrate, 1.0 mM $NADP^{+}$; 50 mM d_{11}-Tris buffer (90:10 H_2O:D_2O; pH 7.5).*

Both *Mtb* IDH1 and *Mtb* IDH2 catalysed turnover of isocitrate to 2-OG with concomitant reduction of $NADP^{+}$ as observed by ^{1}H NMR (**Figure 5.12**). Only half the *DL*-isocitrate was consumed suggesting that, like *Hs* IDH1 wt (Section 4.4.2), *Mtb* IDH1 and *Mtb* IDH2 utilise *D*-isocitrate as substrate. To investigate this, a follow-up study on the turnover of *D*-isocitrate and $NADP^{+}$ as observed by ^{1}H NMR should be carried out.

Studies on the reduction of 2-OG to 2-HG were conducted, but no activity was observed with *Mtb* IDH1 or *Mtb* IDH2 over 12 h. This observation contrasts results from NADPH absorbance assays in Section 5.4.1, in which both enzymes were apparently able to catalyse the reduction of 2-OG. The inactivity under NMR conditions could be linked to use of magnesium ions in the ^{1}H NMR assay whereas NADPH absorbance assays utilised manganese ions. Another explanation could be the use of Tris-d_{11} in ^{1}H NMR assays while HEPES buffer was used in NADPH absorbance assays. Furthermore, conditions like enzyme concentration could be optimised (note that *Hs* IDH1 wt catalysis for the turnover of 2-OG to 2-HG under ^{1}H NMR conditions was slow, Section 4.4).

5.5 Biophysical Characterisation

Biophysical studies were conducted to compare *Mtb* IDH1, *Mtb* IDH2, *Msm* IDH, and *Mtb* IDH1 R135H investigating their secondary structure using circular dichroism (CD). Additionally, the T_ms of *Mtb* IDH1, *Mtb* IDH2, *Msm* IDH, and *Mtb* IDH1 R135H were analysed by CD and by Differential Scanning Calorimetry (DSC). The oligomerisation state was analysed by non-denaturing PAGE and SEC-MALS.

5.5.1 Circular Dichroism (CD) Experiments

The procedure for CD studies was as described in Section 2.7.1. CD spectra were normalised to the protein concentration and the mean residue ellipticity (MRE) was plotted against the wavelength (**Figure 5.13**).

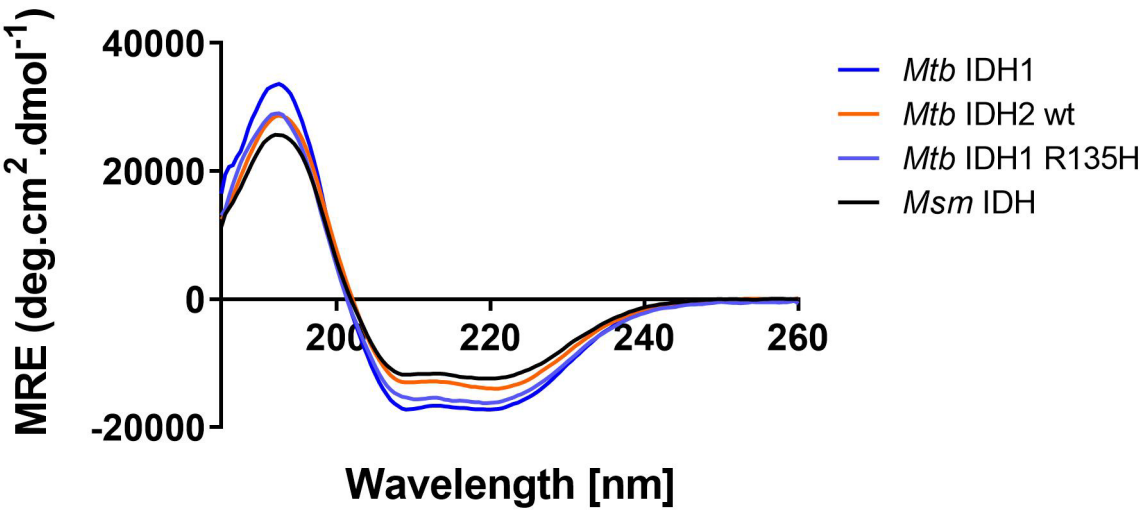

Figure 5.13 *| Circular Dichroism spectra of Mtb IDH1, Mtb IDH2, Msm IDH, and Mtb IDH1 R135H. All variants display spectra of well-structured proteins. Conditions: protein (0.2 mg/mL in sodium phosphate (10 mM, pH 8.0) buffer.*

The CD spectra of the proteins tested indicated well-structured proteins. As previously discussed (Section 2.7.1), the two minima at 208.5 nm and 224 nm are typical for proteins with α-helices, and the maximum at 194 nm can be indicative of α-helices and β-sheets.[138] The CD spectra of *Mtb* IDH1 and *Mtb* IDH1 R135H were similar, while *Mtb* IDH2 and *Msm* IDH showed similar secondary structure features (α-helices, ß-sheets) but differences in the amplitude of the peaks, suggesting that the proportions of the secondary structure features could be different.

5.5.2 Analyses of the Melting Temperature (T_m)

To investigate if the inactivity of *Mtb* IDH1 R135H is linked to changes in thermal stability, and to compare *Mtb* IDH1, *Mtb* IDH2 and *Msm* IDH, T_m values were determined using the previously described procedures (Section 2.7), CD and differential scanning calorimetry (DSC) analysis.

5.5.2.1 Analysis by CD

For CD studies, the wavelength was set to 215 nm and the T_m determined as described in Section 2.7.2 using the change in CD signal as a function of the temperature (**Figure 5.14**).

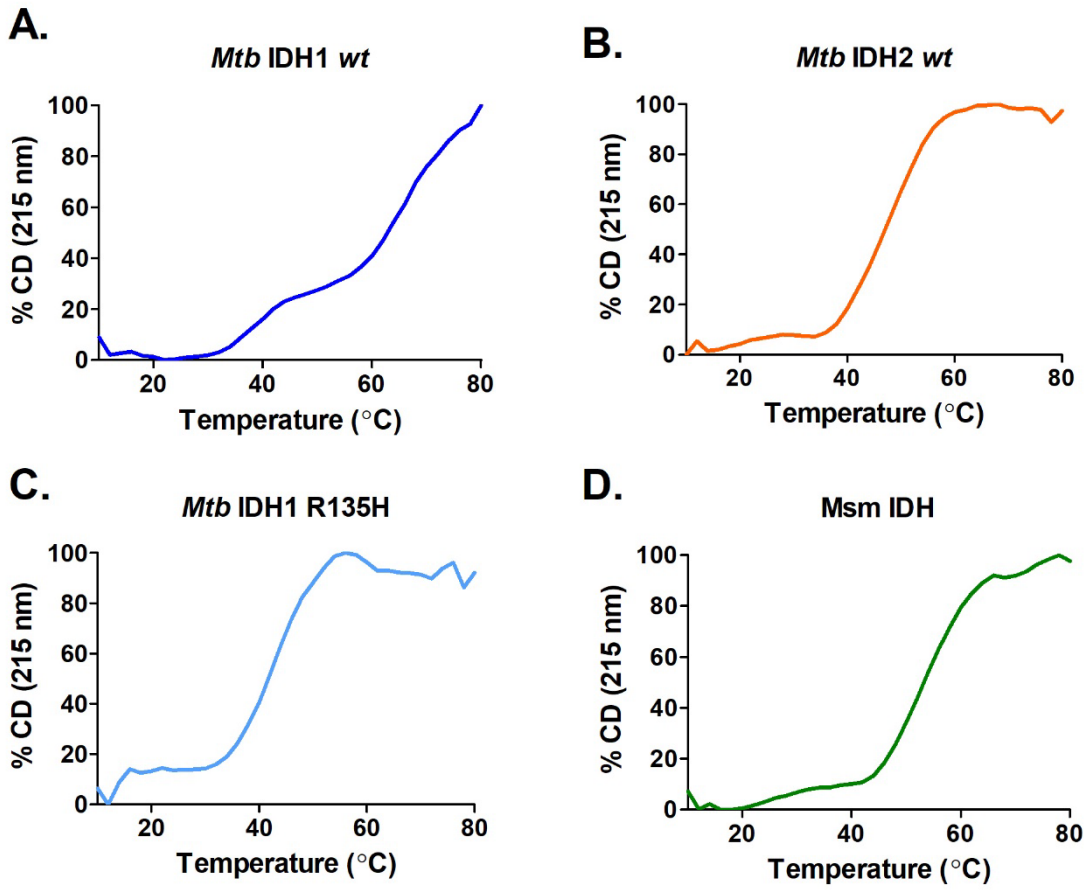

***Figure 5.14** | Analyses of thermal stability using CD. Melting curves of Mtb IDH1 (**A**) Mtb IDH2 (**B**), Mtb IDH1 R135H (**C**), and Msm IDH (**D**). Conditions: protein (0.2 mg/mL in sodium phosphate (10 mM, pH 8.0) buffer. These data were acquired by Maximillian Staudt.*

Interestingly, like *Hs* IDH1 wt, *Mtb* IDH1 displayed two T_ms while only one T_m could be observed for *Mtb* IDH1 R135H (**Figure 5.14**). *Mtb* IDH2 and *Msm* IDH displayed a single T_m and the T_m for *Msm* IDH was higher than for *Mtb* IDH2 (**Table 5.6**). At least the first T_m of *Mtb* IDH1 and the T_m of *Mtb* IDH1 R135H were lower than the T_m of *Mtb* IDH2 (**Table 5.6**).

Table 5.6 *| Comparison of Melting temperatures as measured by CD. These data were acquired by Maximillian Staudt.*

Protein	T_m1 (°C)	T_m2 (°C)
***Mtb* IDH1 wt**	39.6	72.0
***Mtb* IDH2 wt**	47.2	
***Mtb* IDH1 R135H**	42.0	
***Msm* IDH**	53.4	

5.5.2.2 Analysis by Differential Scanning Calorimetry (DSC)

The T_ms of *Mtb* IDH1, *Mtb* IDH1 R135H, *Mtb* IDH2, and *Msm* IDH were investigated using the DSC procedure, as described in Section 2.7.2.2 (**Figure 5.15**).

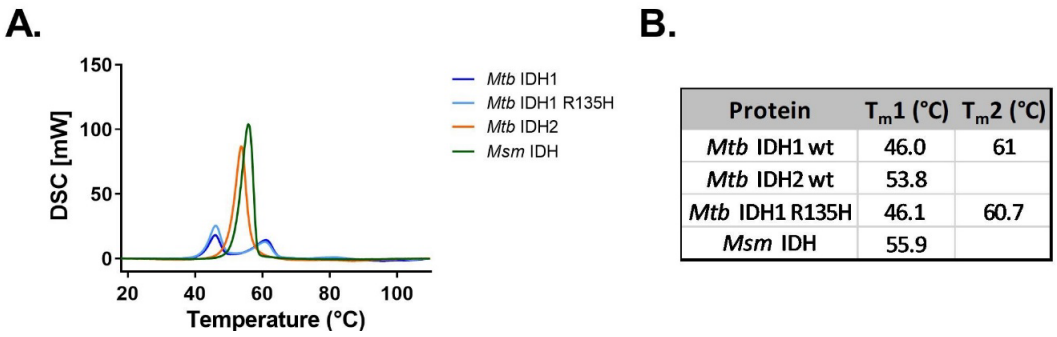

Protein	T_m1 (°C)	T_m2 (°C)
Mtb IDH1 wt	46.0	61
Mtb IDH2 wt	53.8	
Mtb IDH1 R135H	46.1	60.7
Msm IDH	55.9	

Figure 5.15 *| Analyses of the thermal stability using differential scanning calorimetry (DSC).* ***A.*** *DSC curves of Mtb IDH1 wt, Mtb IDH1 R135H, Mtb IDH2, Msm IDH.* ***B.*** *Summary table showing the T_m for each protein. Conditions: Enzyme (20 µM) in 50 mM Tris, 150 mM NaCl, 5 % glycerol (pH 8.0). These data were acquired by Dr David Staunton.*

Mtb IDH1 and *Mtb* IDH1 R135H displayed two T_ms which were identical (**Figure 5.15**). The single T_m of *Mtb* IDH2 and *Msm* IDH was in between the two T_ms of *Mtb* IDH1 and *Mtb* IDH1 R135H. *Msm* IDH exhibited a higher T_m than *Mtb* IDH2 (**Figure 5.15**).

Interestingly, *Mtb* IDH1 wt displayed two T_ms like observed for *Hs* IDH1 wt (**Figure 4.38**). This can be indicative of a two-stage melting, e.g. caused by dimer-denaturation and subsequent denaturation of the monomer. A two-step T_m was observed for *Mtb* IDH1 R135H by DSC (**Figure 5.15**) but not by CD (**Figure 5.14**). *Mtb* IDH2 and *Msm* IDH display a single T_m with a higher thermal stability for *Msm* IDH compared to *Mtb* IDH2.

The combined results imply that *Mtb* IDH1 melts in two stages which might also be the case for *Mtb* IDH1 R135H (at least as determined by DSC). This might be caused by an initial stage in which the higher-state oligomer denatures and an additional stage for denaturing of a lower-state oligomer. The T_ms of *Mtb* IDH2 and *Msm* IDH apparently manifest a single step, and

Msm IDH exhibits a higher T_m than *Mtb* IDH2. The substantial difference in thermal denaturing behaviour between *Mtb* IDH1 compared to *Mtb* IDH2 and *Msm* IDH, suggests there are differences in intramolecular interactions in the quaternary structures of these enzymes.

5.5.3 Analysis of Oligomerisation State

Mtb IDH1 and *Mtb* IDH2 are reported to be active as dimers in solution.[118] However, it is also reported that there are tetrameric species present of *Mtb* IDH1.[118] Tetrameric species of *Mtb* IDH2 were reported to be present at low salt concentrations (100 mM NaCl) which dissociated to exclusively the dimer at high salt concentrations (1 M NaCl).[118] To investigate if *Mtb* IDH1, *Mtb* IDH2 and *Msm* IDH used in our experiments are dimeric in solution, non-denaturing PAGE and SEC-MALS were conducted.

5.5.3.1 Non-Denaturing PAGE

Non-denaturing PAGE was conducted according to the procedure described in Section 2.7.3 using a 4-12 % polyacrylamide Tris-Glycine gel.

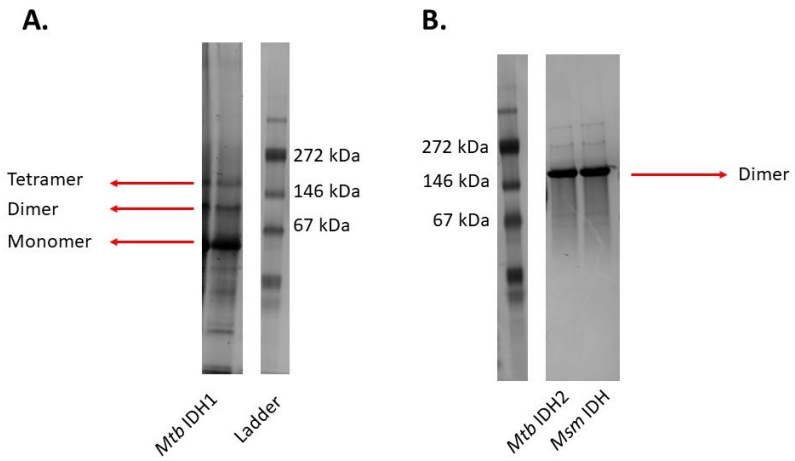

***Figure 5.16** | Non-denaturing PAGE using a Tris-Glycine gel. **A.** Analysis of Mtb IDH1. **B.** Analysis of Mtb IDH2 and Msm IDH. Ladder: Serva Native Marker.*

The analyses of *Mtb* IDH1 showed impurities potentially corresponding to degradation products. The main species seemed to be the monomer, but evidence for dimeric and tetrameric species was also accrued (**Figure 5.16**, A). *Mtb* IDH2 and *Msm* IDH were predominantly dimeric as indicated by non-denaturing PAGE analysis. There were traces of masses which could correspond to a monomer, tetramer, and hexamer (**Figure 5.16**, B).

5.5.3.2 SEC-MALS

The oligomerisation states of *Mtb* IDH1, *Mtb* IDH2, and *Msm* IDH in solution were investigated using size exclusion chromatography multi angle light scattering (SEC-MALS) analysis, conducted according to the procedure described in Section 2.7.3.

SEC-MALS analysis of *Mtb* IDH1 revealed predominantly a dimeric species, but also evidence for a monomeric species, and the presence of higher-level aggregates. There was a single species present in *Mtb* IDH2 samples around 300 kDa which could correspond to a trimer or tetramer. The predominant species in the sample with *Msm* IDH had a mass of around 200 kDa which likely corresponds to a dimer.

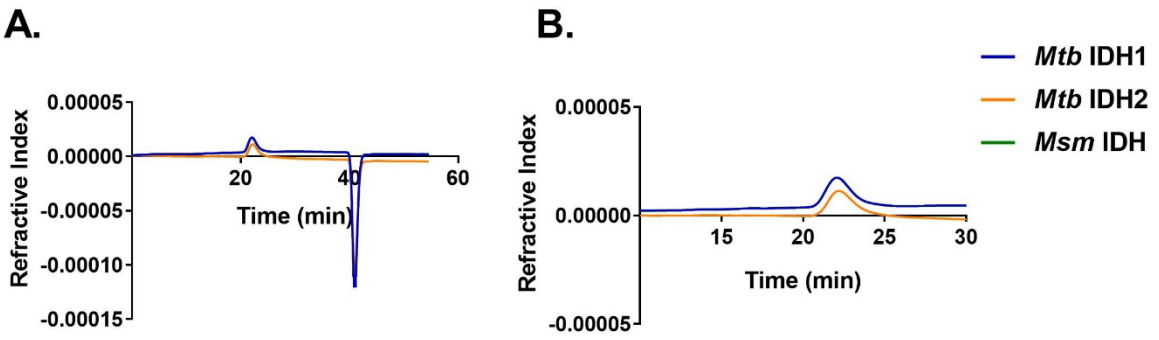

Figure 5.17 *| Size exclusion chromatograms (**A**) before MALS analysis of Mtb IDH1, Mtb IDH2, and Msm IDH. **B.** Extract of **A**. The proteins were diluted to 1 mg/L in buffer containing 50 mM Tris, 150 mM NaCl, 5% glycerol (pH 8.0) and analysed using a Superdex 200 HR10/30.*

The combined results of oligomerisation state analyses by non-denaturing PAGE and SEC-MALS suggest that the predominant species of *Mtb* IDH1 is either a monomer (as indicated by non-denaturing PAGE) or a dimer (as indicated by SEC-MALS). However, there are apparent impurities present, which may correspond to degradation products as indicated by additional bands in non-denaturing gel analyses or aggregates as indicated by SEC-MALS. There is a single oligomerisation state in *Mtb* IDH2, which is suggested to be dimeric by non-denaturing PAGE analysis or tri- or tetrameric by SEC-MALS. Further studies on the oligomerisation state of *Mtb* IDH2 are of interest. The results on the oligomerisation states of *Mtb* IDH1 and *Mtb* IDH2 are not consistent with findings from Banerjee et al. who found dimeric and tetrameric species for both *Mtb* IDH1 and *Mtb* IDH2 in gel filtration experiments.[118] *Msm* IDH is predominantly present as a dimer as shown by non-denaturing PAGE and SEC-MALS.

5.6 Studies with Divalent Metal Cations

The activities of *Mtb* IDH1 and *Mtb* IDH2 with various divalent metal cations were tested. *Mtb* IDH1 and *Mtb* IDH2 were treated with a 2000-fold excess of EDTA overnight and buffer exchanged into HEPES buffer (100 mM). The *apo* enzymes were used for studies of metal utilisation by the NADPH absorbance assay.

5.6.1 Activity with Divalent Cations

Stock solutions (10 mM) of salts of divalent metal cations were prepared in MQ water: $MnCl_2$, $MgCl_2$, $ZnSO_4$, $CaCl_2$, $NiCl_2$, $CoCl_2$, and $CuCl_2$. Then *Mtb* IDH1 and *Mtb* IDH2 were incubated with metal ions for 10 minutes, and the reaction initiated by addition of isocitrate and $NADP^+$. The turnover was monitored by NADPH absorbance and the initial rate determined. The initial reaction rates were normalised to the reaction rate with $MnCl_2$ (100%), which is the metal ion used in the standard mycobacterial IDH assay buffer.

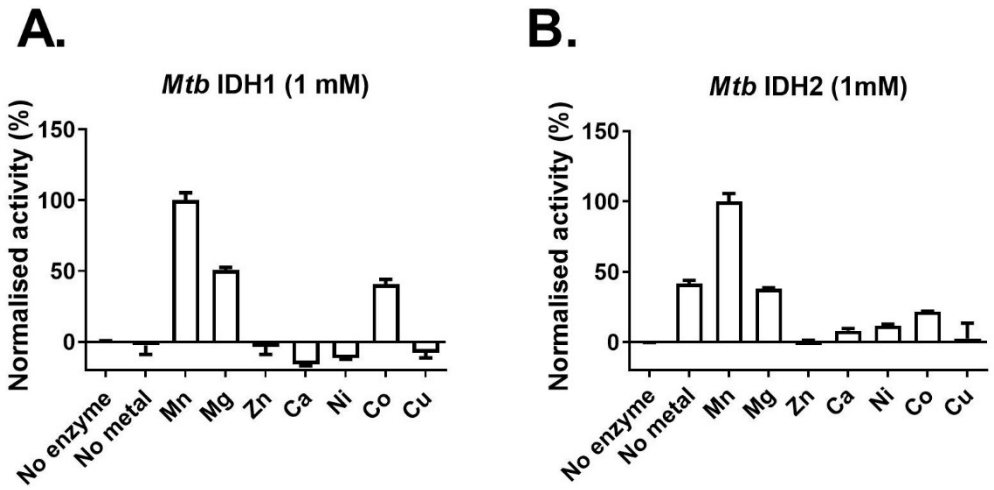

***Figure 5.18** | Kinetic analysis on the utilisation of divalent metal cations by Mtb IDH1 (**A**, 50 nM enzyme) and Mtb IDH2 (**B**, 1 nM enzyme). Conditions: 100 mM HEPES, pH 7.5. These data were acquired together with Maximillian Staudt. Isocitrate: 1 mM, $NADP^+$: 1 mM.*

Mtb IDH1 displayed the highest activity with Mn^{2+} (**Figure 5.18**). *Mtb* IDH1 was also active with Mg^{2+} but 2-fold lower, and there was some activity with Co^{2+}. There was no activity with Zn^{2+}, Ca^{2+}, Ni^{2+}, and Cu^{2+}. *Mtb* IDH2 displayed activity without metal present (**Figure 5.18**). There was an increase in activity with Mn^{2+}, whereas with Mg^{2+} the activity was the same as without metal ions added. There was a decrease in activity with Ca^{2+}, Ni^{2+}, Co^{2+}. No activity could be observed with Zn^{2+} and Cu^{2+}.

The activity of *Mtb* IDH2 observed without the addition of metal ions is likely because copurified metal ions were not completely removed by EDTA treatment. This observation suggests a high affinity of the copurified metal to *Mtb* IDH2. Therefore, the observed activities for divalent metal with *Mtb* IDH2 must be interpreted with care. While *Mtb* IDH2 is active with Mn^{2+} (increase in activity compared to control) and likely Mg^{2+} (same activity as control), Ca^{2+}, Ni^{2+}, and Co^{2+} might inhibit activity. It could also be the case that Ca^{2+}, Ni^{2+}, and Co^{2+} bind to the protein with higher affinity than the copurified metal but exhibit lower activity. However, this is unlikely as the copurified metal seems to bind with high affinity, i.e. cannot be removed by treatment with a large excess of EDTA. There is clear inhibition of enzymatic activity by Zn^{2+} and Cu^{2+}.

Mtb IDH1 and *Mtb* IDH2 are most active with Mn^{2+} but can also utilise Mg^{2+} (**Figure 5.18**). *Mtb* IDH1 can additionally utilise Co^{2+}, but not Ca^{2+}, Ni^{2+}, Cu^{2+}. In these experiments *Mtb* IDH1 also could not utilise Zn^{2+} which is in contrast with results from Banerjee et al.[118] showing low turnover with Zn^{2+}. Furthermore, findings on utilisation of Mn^{2+} are not consistent with Banerjee et al., who reported no activity of *Mtb* IDH1 and IDH2 with Mn^{2+}. However, Quartararo et al. found that *Mtb* IDH1 exhibits the highest activity with Mn^{2+} compared to other divalent metal ions, consistent with the results in this section.

5.6.2 Inhibition by Divalent Metal Ions

Varying concentrations of metal ions in physiological settings can influence enzymatic activity. Hence, *Mtb* IDH1 and *Mtb* IDH2 were tested for inhibition by divalent metal cations using the NADPH absorbance assay with the mycobacterial IDH assay buffer (HEPES 100 mM, $MnCl_2$ 5 mM). Inhibition was calculated using a no-enzyme control (100% inhibition) and a control without additional metal ions (0% inhibition).

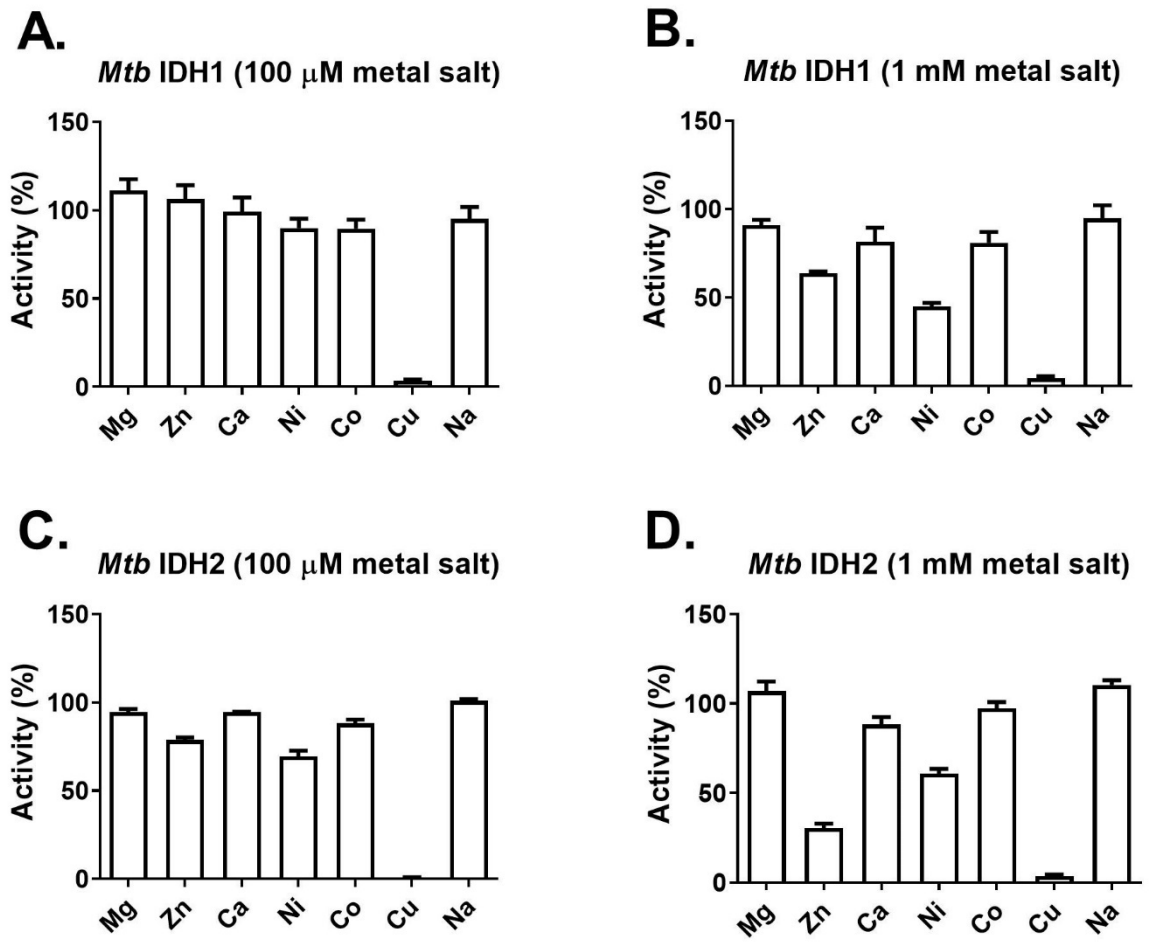

***Figure 5.19** | Inhibition analysis of Mtb IDH1 (50 nM) and Mtb IDH2 (1 nM) by metal ions. **A.** Mtb IDH1 inhibition by 100 μM metal ions. **B.** Mtb IDH2 inhibition by 1 mM metal ions. **C.** Mtb IDH2 inhibition by 100 μM metal ions. **D.** Mtb IDH2 inhibition by 1 mM metal ions. Errors: Standard errors of the mean (n = 3). Conditions: 100 mM HEPES, 5 mM $MnCl_2$, pH 7.5. Isocitrate: 1 mM, $NADP^+$: 1 mM.*

Mtb IDH1 and *Mtb* IDH2 were fully inhibited by the addition of Cu^{2+} at 100 μM, while there were no substantial effects by other metal ions at 100 μM. At 1 mM metal ion, *Mtb* IDH1 was, additionally to Cu^{2+}, inhibited by Ni^{2+} (50%) and Zn^{2+} (40%). *Mtb* IDH2 activity was inhibited by Ni^{2+} (40%) and Zn^{2+} (70%) at 1 mM, as well as Cu^{2+} (100%) at 1 mM and 100 μM (**Figure 5.19**). The most potent inhibition of *Mtb* IDH1 and *Mtb* IDH2 by a metal ion was observed for Cu^{2+}. Hence, the IC_{50} of $CuCl_2$ was determined for *Mtb* IDH1 and *Mtb* IDH2 using the NADPH absorbance assay (buffer: HEPES 100 mM, $MnCl_2$ 5 mM). The IC_{50} for $CuCl_2$ (**Figure 5.20**) against *Mtb* IDH1 was 1.18 μM while $CuCl_2$ inhibited *Mtb* IDH2 with 6-fold higher potency (IC_{50} = 0.18 μM).

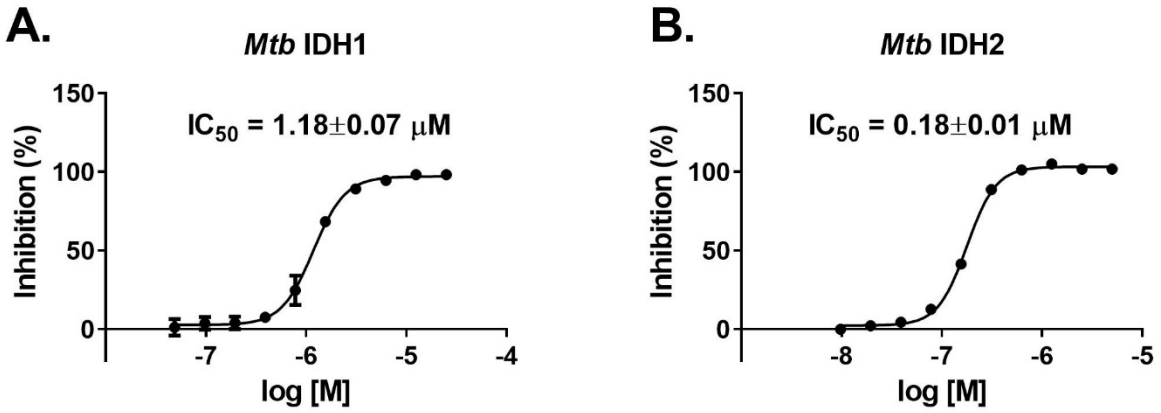

Figure 5.20 *| Determination of potency of inhibition by $CuCl_2$ with Mtb IDH1 (**A**) and Mtb IDH2 (**B**). Errors: Standard errors of the mean (n = 3). Conditions: 100 mM HEPES, 5 mM $MnCl_2$, pH 7.5. Isocitrate: 1 mM, $NADP^+$: 1 mM.*

Cu^{2+} levels in macrophages are high as part of the bodies defence mechanism against pathogens, and Cu^{2+} levels increase substantially in macrophages in response to mycobacterial infection.[194, 195, 196] Furthermore, zinc plays a role in the host-defence mechanism of macrophages and zinc levels increase in macrophages in the presence of *Mtb*.[194,196] *Mtb* IDH1 shows a higher tolerance to zinc than *Mtb* IDH2 (**Figure 5.19**). The combined results suggest that a higher resistance to elevated Cu^{2+} levels, indicated by a less potent Cu^{2+} inhibition (**Figure 5.20**) of *Mtb* IDH1, and a better tolerance to high levels of Zn^{2+} (**Figure 5.19**) compared to *Mtb* IDH2 could contribute to the role of *Mtb* IDH1 in *Mtb* metabolism and adaptation of *Mtb* to conditions in macrophages.

5.7 Alternative Substrate of *Mtb* IDH1

Mtb IDH2 is likely the important IDH isoform in *Mtb* for the oxidative decarboxylation of isocitrate (Section 5.3.1). It was investigated if an additional/alternative role of *Mtb* IDH1 could be the catalysis of the turnover of an alternative substrate. A library of metabolites was screened for turnover catalysed by *Mtb* IDH1. *Mtb* IDH1 and $MnCl_2$ were incubated, and oxidative turnover investigated by addition of substrate and $NADP^+$.

The turnover was normalised to the turnover rate with isocitrate (100%) and a no-enzyme control (0%). Oxaloacetate showed around 60% of the activity of isocitrate. None of the other metabolites displayed turnover (**Figure 5.21**, A).

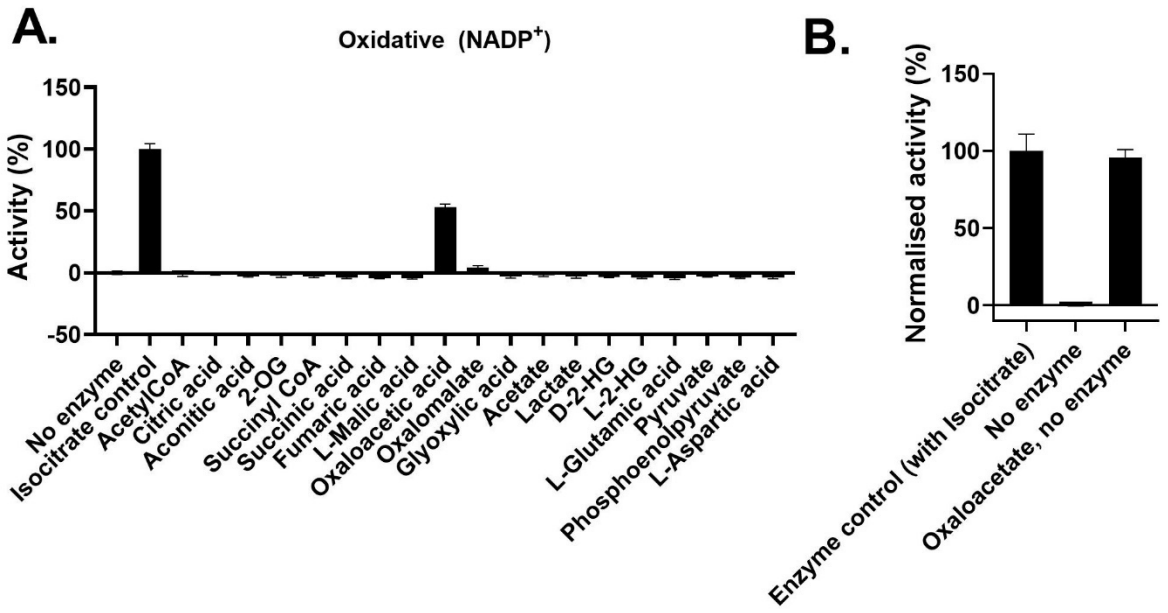

Figure 5.21 | A. *Kinetic analysis of oxidative turnover of metabolites (1 mM) as catalysed by Mtb IDH1 with the co-substrate NADP+.* ***B.*** *Kinetic analysis of oxidative turnover of oxaloacetate (1 mM) without Mtb IDH1 but with NADP+ (1 mM). Errors: Standard errors of the mean (n = 3). Conditions: 100 mM HEPES, 5 mM $MnCl_2$, pH 7.5. These data were acquired by Maximillian Staudt.*

To investigate whether oxaloacetate was turned over enzymatically, oxaloacetate was incubated with $NADP^+$ in assay buffer (without *Mtb* IDH1). This time course also showed turnover which suggests oxaloacetate and $NADP^+$ react non-enzymatically under these conditions (**Figure 5.21**, B).

The same selection of metabolites, that was used for the screening of the oxidative turnover, was also screened for reductive turnover using the co-substrate NADPH. *Mtb* IDH1 was incubated with $MnCl_2$ for 10 minutes and the reaction initiated by the addition of substrate and NADPH, and the reaction monitored by NADPH absorbance. The turnover was normalised to the turnover of 2-OG (100 %) and a no-enzyme control (0%) (**Figure 5.22**).

The reaction rate of the turnover of 2-OG and NADPH catalysed by *Mtb* IDH1 is low, consistent with previous experiments (Section 5.3.1). Because of the low-level turnover, the margin between the positive result and the negative control is not large and hence, the relative error is high resulting in some minor apparent activity of all metabolites apart from succinyl-CoA and glyoxylate (**Figure 5.22**, A). Consequently, metabolites displaying an apparent activity of 20 % were not treated as hits. However, two substrates displayed substantial turnover: succinyl-CoA showed 100% activity while glyoxylate displayed 200% activity. Subsequently, the metabolite selection was tested for non-enzymatic turnover with NADPH (**Figure 5.22**, B) but without *Mtb* IDH1. Turnover was observed with succinyl-CoA

(100%) and glyoxylate (200%), suggesting non-enzymatic reactions with NADPH. No other metabolite showed non-enzymatic turnover. Note that it is possible that the non-enzymatic turnover with succinyl-CoA and glyoxylate is due to impurities in the starting material.

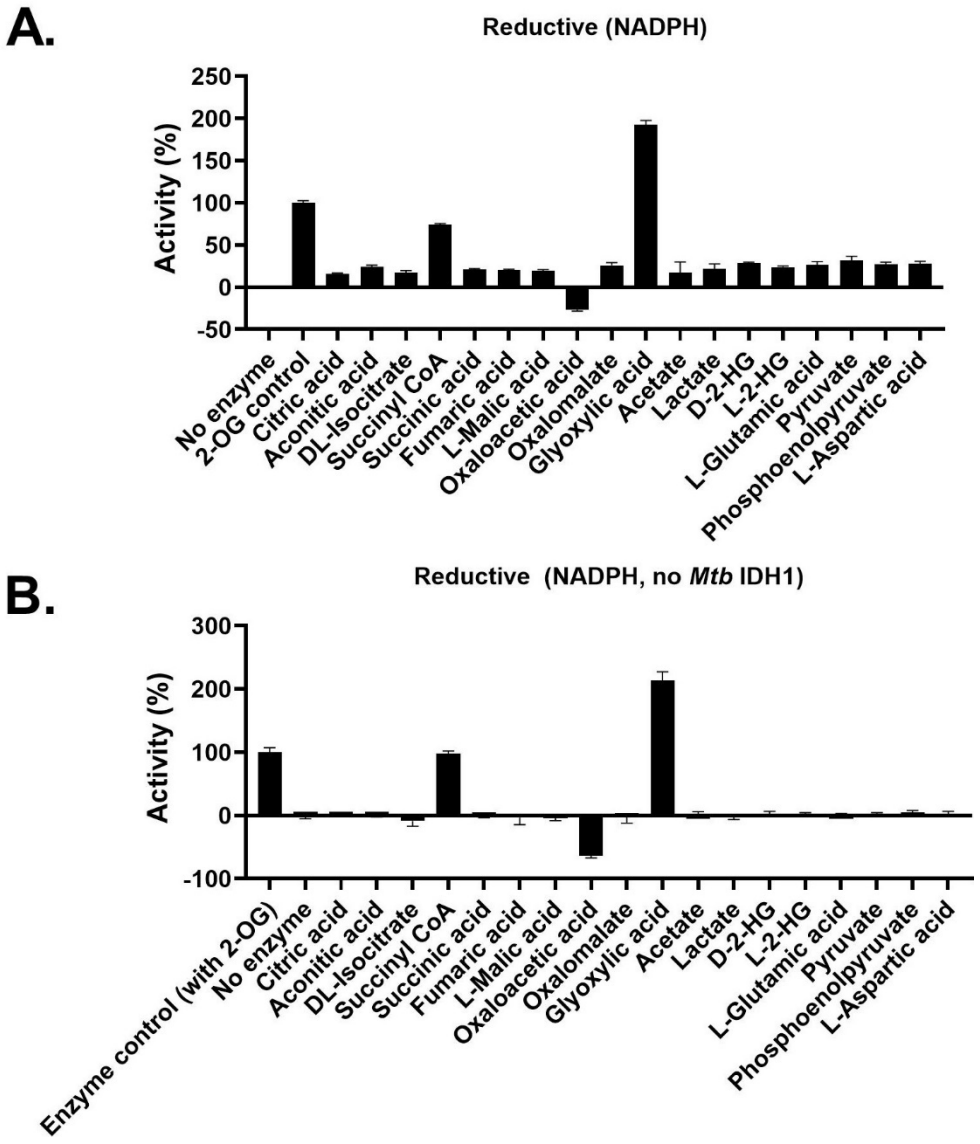

Figure 5.22 *| Kinetic analysis of reductive turnover of metabolites (1 mM) as catalysed by Mtb IDH1 with the co-substrate NADPH (**A**) and control assay of metabolites and NADPH without Mtb IDH1 (**B**). Errors: Standard errors of the mean (n = 3). Conditions: 100 mM HEPES, 5 mM $MnCl_2$, pH 7.5. These data were acquired by Maximillian Staudt.*

The combined results of experiments on turnover of metabolites catalysed by *Mtb* IDH1 oxidatively or reductively using $NADP^+$ or NADPH, respectively, imply that none of the metabolites are turned over, at least substantially, by *Mtb* IDH1.

In summary, no alternative turnover catalysed by *Mtb* IDH1 can be attributed to *Mtb* IDH1 function in *Mtb* metabolism, at least with the selection of metabolites tested. However, a

follow-up screen should investigate turnover of metabolites using the cofactors NAD^+ and NADH.

5.8 Metabolic Cross-Regulation of Mycobacterial IDHs

As discussed in Section 1.11, metabolic cross-enhancement of *Msm* IDH is reported for glyoxylate.[113] Another example of metabolic cross-enhancement in mycobacteria is reported for *Mtb* ICL2 which only exhibits substantial activity following binding of acetyl-CoA to it, leading to conformational changes.[116] Furthermore, metabolic enhancement of *Pseudomonas aeruginosa* IDH by oxaloacetate, glyoxylate, and pyruvate has been reported[122], as is enhancement of *Mtb* IDH2 by glyoxylate.[113] To test whether activity of *Mtb* IDH1, *Mtb* IDH2, and *Msm* IDH can be modulated, the influence of metabolites on the turnover of isocitrate to 2-OG was tested using the NADPH absorbance assay.

5.8.1 Screening of the Set of Metabolites against *Mtb* IDHs and *Msm* IDH

A set of metabolites from the TCA cycle and other metabolites found in glycolysis and energy metabolism surrounding ATP was composed (**Table 5.7**).

Mtb IDH1, *Mtb* IDH2, and *Msm* IDH were incubated with 100 μM of the metabolite in buffer containing $MnCl_2$ (5 mM) for 10 minutes. The reaction was initiated by the addition of isocitrate and $NADP^+$ and monitored using the NADPH absorbance assay. The activity was normalised to a no-enzyme control (0% activity) and a no-metabolite control (100 % activity).

***Table 5.7** | Library of metabolites used for screening for modulation of activity of Mtb IDH2.*

Number	Metabolite/Analogue	Number	Metabolite/Analogue
1	Acetyl CoA (Na-salt)	18	Pyruvate (Na-salt)
2	Citric acid	19	Phosphoenolpyruvate (Tricyclohexylammonium-salt)
3	Aconitic acid	20	*L*-Aspartic acid
4	*DL*-Isocitrate (Tri-Na-salt)	21	*L*-Kynurenine
5	2-OG (Di-Na-salt)	22	Sodium bicarbonate
6	Succinyl CoA (Na-salt)	23	AMP (Na-salt)
7	Succinic acid	24	ADP (Na-salt)
8	Fumaric acid	25	ATP (Mg-salt)
9	*L*-Malic acid	26	cAMP (Na-salt)
10	Oxaloacetic acid	27	2-Oxoadipic acid
11	Oxalomalic acid sodium salt	28	3-Hydroxyglutarate
12	Glyoxylic acid	29	Malonic acid
13	Acetate (Na-salt)	30	Itaconic acid
14	Lactate (Li-salt)	31	Glutaconic acid
15	*D*-2-Hydroxyglutarate (Di-Na-salt)	32	Citraconic acid
16	*L*-2-Hydroxyglutarate (Di-Na-salt)	33	Mesaconic acid
17	*L*-Glutamic acid		

The screening results showed that there is no influence on *Mtb* IDH1 activity by any of the metabolites tested (**Figure 5.23**, A). By contrast, screening with *Mtb* IDH2 displayed a large increase in activity in the presence of oxaloacetate (250%), oxalomalate (150%), glyoxylate (300%), and pyruvate (330%) (**Figure 5.23**, B). The activity of *Msm* IDH was inhibited by oxaloacetate (70% activity) and oxalomalate (50% activity), but enhanced by glyoxylate (130% activity), pyruvate (150% activity) (**Figure 5.23**, C). The results with *L*-kynurenine must be interpreted with care for all three enzymes as *L*-kynurenine interferes with the NADPH absorbance signal. The largest increase in activity was observed for modulators of *Mtb* IDH2. Subsequently, they were investigated in more depth.

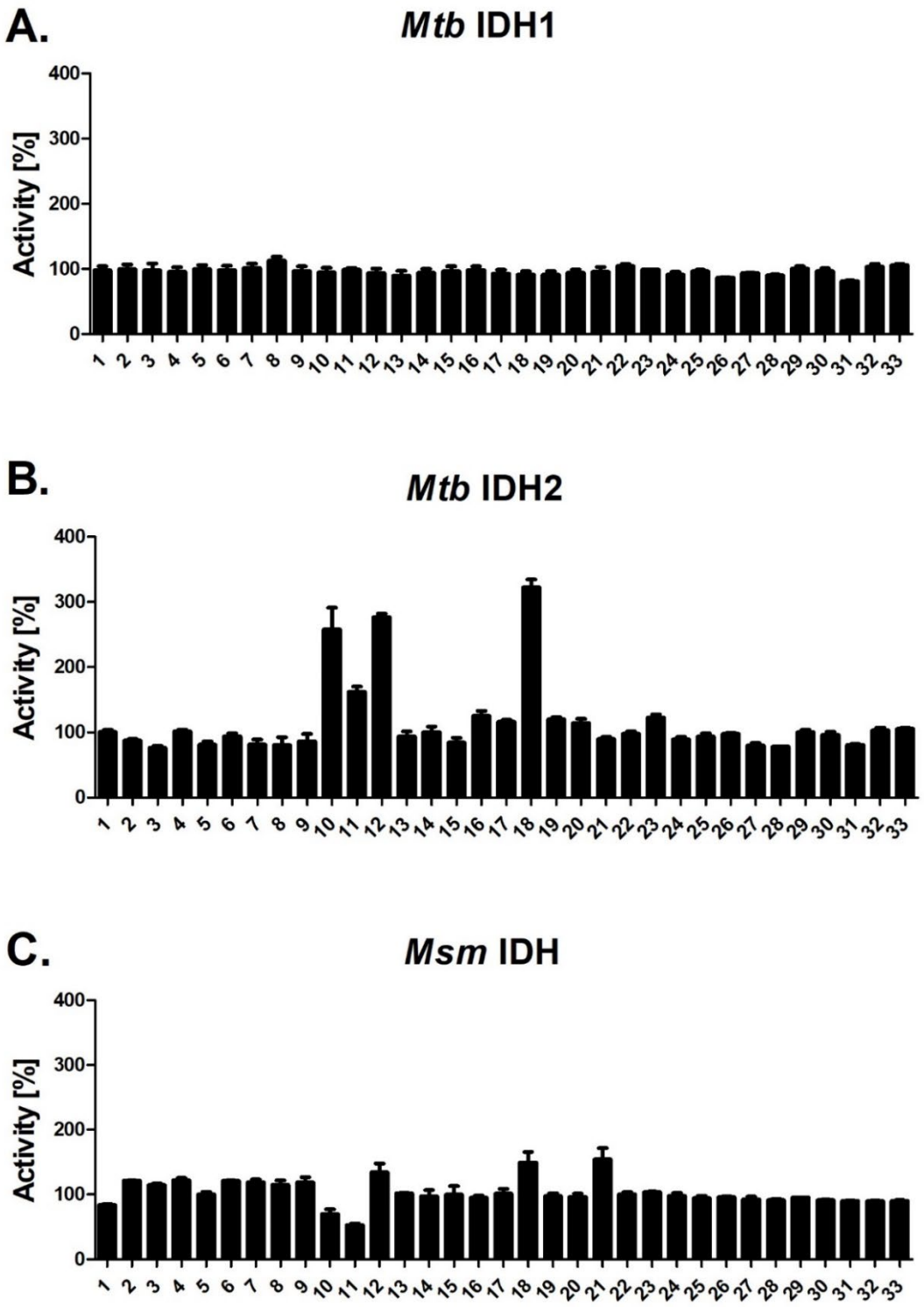

***Figure 5.23** | Screening of a set of metabolites (100 µM) for metabolic cross-regulation of the turnover of isocitrate to 2-OG as catalysed by Mtb IDH1 (**A**, 50 nM), Mtb IDH2 (**B**, 1 nM) or Msm IDH (**C**, 1 nM) observed by the NADPH absorbance assay. Conditions: 100 mM HEPES, 5 mM $MnCl_2$, pH 7.5. Errors: Standard error of the mean (n = 3). These data were acquired by Maximillian Staudt. Isocitrate: 1 mM, $NADP^+$: 1 mM.*

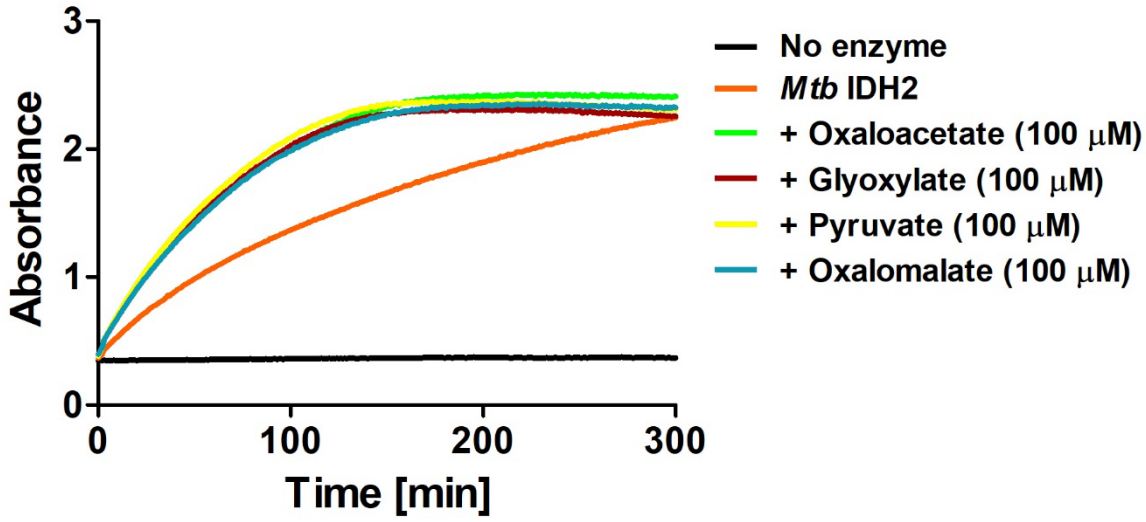

Figure 5.24 *| Time course analysis of the turnover of isocitrate to 2-OG as catalysed by Mtb IDH2 (1 nM) in the presence of oxaloacetate, glyoxylate, pyruvate, or oxalomalate, observed by the NADPH absorbance assay. Conditions: 1 mM DL-isocitrate, 1 mM $NADP^+$ in 100 mM HEPES, 5 mM $MnCl_2$, pH 7.5. These data were acquired by Maximillian Staudt.*

To investigate the enhancement of *Mtb* IDH2 activity, time-course analyses measured by NADPH absorbance were conducted (**Figure 5.24**). The initial rate of the turnover of isocitrate to 2-OG was elevated when oxaloacetate, glyoxylate, pyruvate, or oxalomalate were present. The turnover of isocitrate to 2-OG was complete after ~150 minutes in the presence of oxaloacetate, glyoxylate, pyruvate, or oxalomalate while, without modulating compounds present, the turnover of isocitrate to 2-OG was complete after ~300 minutes.

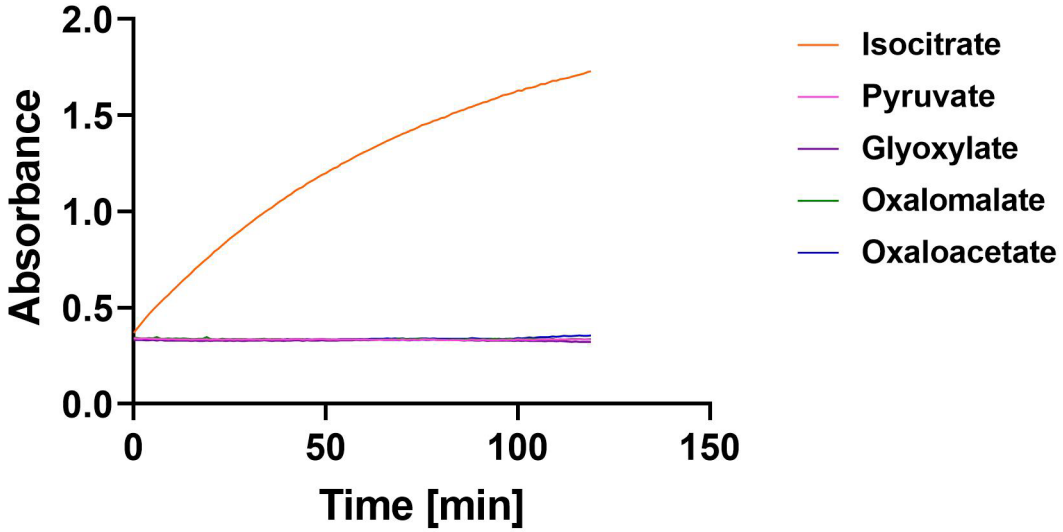

Figure 5.25 *| Turnover analysis of metabolic cross-enhancers with Mtb IDH2 (1 nM). Mtb IDH2 does not turn over oxaloacetate, oxalomalate, glyoxylate, and pruvate with $NADP^+$ present as observed by an NADPH absorbance assay. Conditions: 100 mM HEPES, 5 mM $MnCl_2$, pH 7.5. These data were acquired by Maximillian Staudt.*

To investigate whether the observation on increased activity is due to an increase in turnover of isocitrate on 2-OG, and not *Mtb* IDH2 catalysed turnover of oxaloacetate, glyoxylate, pyruvate, or oxalomalate, control assays were conducted with *Mtb* IDH2 and different modulators with addition of the co-factor $NADP^+$ (**Figure 5.25**). No turnover was observed for any metabolite demonstrating enhancement of the *Mtb* IDH2 catalysed turnover of isocitrate to 2-OG by oxaloacetate, glyoxylate, pyruvate, or oxalomalate as observed in **Figure 5.24**.

5.8.2 Influence of Metabolites on the Michaelis-Menten Parameters of *Mtb* IDH2

To investigate the mode of enhancement of *Mtb* IDH2 activity, the Michaelis-Menten parameters for isocitrate and $NADP^+$ were determined in the presence of oxaloacetate, pyruvate, glyoxylate, or oxalomalate. Two different concentrations of metabolites were added to test concentration dependency. The metabolites were incubated with *Mtb* IDH2 for 10 minutes, and the reaction initiated by addition of isocitrate and $NADP^+$. The Michaelis-Menten parameters were determined using non-linear regression curve fit of the GraphPad Prism software (version 5). The Michaelis-Menten parameters for *Mtb* IDH2 without modulator were determined again because there was a decrease in *Mtb* IDH2 activity (indicated by a decrease in k_{cat}) since the initial Michaelis-Menten analysis was conducted (Section 5.3.1, ~2 years apart from this study).

Table 5.8 *| Kinetic parameters for isocitrate oxidation to 2-OG in the presence of oxaloacetate, pyruvate, glyoxylate, or oxalomalate catalysed by Mtb IDH2 as measured by the NADPH absorbance assay. Errors: standard errors of the mean (n =3). Conditions: 100 mM HEPES, 5 mM $MnCl_2$, pH 7.5. $NADP^+$: 1 mM.*

Enzyme	**Isocitrate**		
	K_M **(µM)**	k_{cat} **(s^{-1})**	k_{cat}/K_M **($s^{-1}\times\mu M^{-1}$)**
***Mtb* IDH2 wt**	42.4±10.9	48.6±3.1	1.1
+ Oxaloacetate (100 µM)	66.3±8.9	79.3±2.9	1.2
+ Oxaloacetate (400 µM)	255.1±40.8	99.3±6.2	0.4
+ Pyruvate (100 µM)	41.1±6.3	56.5±2.1	1.4
+ Pyruvate (400 µM)	12.4±1.2	99.5±1.8	8.0
+ Glyoxylate (100 µM)	18.4±3.0	102.9±3.5	5.6
+ Glyoxylate (400 µM)	26.7±2.2	117.0±2.2	4.4
+ Oxalomalate (100 µM)	110.9±21.4	68.4±4.1	0.6
+ Oxalomalate (400 µM)	202.1±71.8	54.2±6.8	0.27

Both oxaloacetate and oxalomalate addition led to a concentration-dependent increase in K_M values for the *Mtb* IDH2 catalysed turnover of isocitrate to 2-OG (**Table 5.8**). The k_{cat} in the presence of oxaloacetate was increased in a concentration-dependent manner up to 2-fold in reactions with 400 µM oxaloacetate. The catalytic efficiency (as indicated by k_{cat}/K_M) in reactions with 100 µM oxaloacetate was the same as without oxaloacetate present but was decreased 3-fold in reactions with 400 µM oxaloacetate. In reactions with oxalomalate, the k_{cat} was increased with 100 µM and also, but less, with 400 µM oxalomalate. The k_{cat}/K_M with 100 µM oxalomalate present was decreased 2-fold and 4-fold with 400 µM oxalomalate present. The presence of 100 µM pyruvate (**Table 5.8**) did not result in a change of K_M but marginally increased k_{cat} which resulted in a small increase in k_{cat}/K_M. At a concentration of 400 µM, the presence of pyruvate resulted in a 3-fold lower K_M and increased the k_{cat} 2-fold resulting in an 8-fold increase in k_{cat}/K_M, which was the biggest increase observed for the catalytic efficiency of isocitrate turnover in these experiments. The presence of 100 µM glyoxylate (**Table 5.8**) led to a 2-fold decrease in K_M and a 2-fold increase in k_{cat} consequently increasing k_{cat}/K_M 5-fold. There was also a decrease in K_M when 400 µM glyoxylate was present and an increase in k_{cat} leading to a 4-fold increase in k_{cat}/K_M.

Table 5.9 *| Kinetic parameters for $NADP^+$ in the presence of oxaloacetate, pyruvate, glyoxylate, or oxalomalate as catalysed by Mtb IDH2 and measured by the NADPH absorbance assay. Errors: standard errors of the mean (n =3). Conditions: 100 mM HEPES, 5 mM $MnCl_2$, pH 7.5. Isocitrate: 1 mM.*

Enzyme	**$NADP^+$**		
	K_M (µM)	**k_{cat} (s^{-1})**	**k_{cat}/K_M ($s^{-1}\times\mu M^{-1}$)**
***Mtb* IDH2 wt**	32.3±3.7	41.9±1.1	1.3
+ Oxaloacetate (100 µM)	19.5±1.7	75.5±1.4	3.9
+ Oxaloacetate (400 µM)	14.0±1.2	89.8±1.5	6.4
+ Pyruvate (100 µM)	25.0±3.8	57.7±2.0	2.3
+ Pyruvate (400 µM)	9.2±1.0	100.8±1.8	11.0
+ Glyoxylate (100 µM)	22.8±2.1	96.3±1.9	4.2
+ Glyoxylate (400 µM)	16.5±1.3	102.8±1.6	6.2
+ Oxalomalate (100 µM)	10.6±1.6	76.6±2.1	7.2
+ Oxalomalate (400 µM)	16.7±3.4	56.1±2.3	3.4

The trends of the changes observed for the Michaelis-Menten parameters of $NADP^+$ in the presence of oxaloacetate, pyruvate, glyoxylate, or oxalomalate were more consistent than for isocitrate (**Table 5.9**). All the modulators tested decreased the K_M for $NADP^+$ and increased

the k_{cat} for turnover of isocitrate to 2-OG. For oxaloacetate, pyruvate, and glyoxylate this led to a concentration-dependent increase in k_{cat}/K_M with a maximal 9-fold increase in the presence of pyruvate (400 μM) compared to the no-modulator control (**Table 5.9**). When oxalomalate was present, the decrease of K_M and the increase in k_{cat} were lower in the reaction with 400 μM compared to the reaction with 100 μM (**Table 5.9**).

There are two broad proposed types of enhancement of Michaelis-Menten enzymes.[197] In a K-type activation, the maximum rate (k_{cat}) does not change but the K_M, while in a V-type activation both K_M and the maximum turnover change.[197] Hence, the activation of *Mtb* IDH2 by oxaloacetate, pyruvate, glyoxylate, and oxalomalate is of the V-type assuming Michaelis Menten type kinetics (an assumption which might not be valid). While the maximum rate (k_{cat}) is consistently increased for all four metabolites, the influence on K_M differs. All the metabolites tested decrease the K_M value for $NADP^+$, but the trend in K_M is less clear for isocitrate. There is a concentration-dependent increase in K_M for isocitrate caused by oxaloacetate and oxalomalate, but a decrease by glyoxylate and, at least at 400 μM, by pyruvate. Glyoxylate increases the k_{cat} for the turnover of isocitrate to 2-OG most compared to oxaloacetate, pyruvate, and oxalomalate. This is consistent with proposed metabolic cross-enhancement of IDH when glyoxylate is produced in the glyoxylate shunt.[113] The biggest increase in k_{cat}/K_M for both isocitrate and $NADP^+$ is observed in the presence of pyruvate (400 μM). Pyruvate enters the TCA cycle after conversion to acetyl-CoA. Enhancement of *Mtb* IDH2 is likely with the purpose to increase the turnover of the TCA cycle as more starting material in the form of pyruvate and subsequently Acetyl-CoA is available. Similarly, high levels of oxaloacetate activate *Mtb* IDH2 to enable more efficient flux through the TCA cycle. Oxalomalate is formed by reaction of oxaloacetate and glyoxylate[198], and hence, enhancement of *Mtb* IDH2 is likely a result of the decomposition of oxalomalate to glyoxylate and oxaloacetate in solution.

5.8.3 ^{1}H NMR Time Course Studies on Modulation by Metabolites

The influence of metabolites on *Mtb* IDH2 activity (for turnover of isocitrate to 2-OG) from NADPH absorbance assays shows evidence for enhancement by oxaloacetate, glyoxylate, pyruvate, and oxalomalate. NADPH absorbance assays indicated that none of these four metabolites are turned over by *Mtb* IDH2. To investigate if there is no turnover of oxaloacetate, glyoxylate, pyruvate, and oxalomalate using a different method, and to show the metabolic

cross-enhancement of *Mtb* IDH2, ^{1}H NMR time-course analyses were employed according to the conditions described in Section 5.3.2.

The enzyme concentration was optimised so that full turnover of *D*-isocitrate (in the racemic mixture of *DL*-isocitrate) by *Mtb* IDH2 could be observed in 1 h but that the turnover in reactions with enhancing metabolites present is not already completed when the first ^{1}H NMR measurement is conducted (~ 5 min). Comparing the first and last ^{1}H NMR measurement of the time-course, it can be observed that none of the metabolic modulators are turned over, i.e. none of the integrals of the signals corresponding to the metabolites tested changed and no new signals could be observed, which were not 2-OG or NADPH.

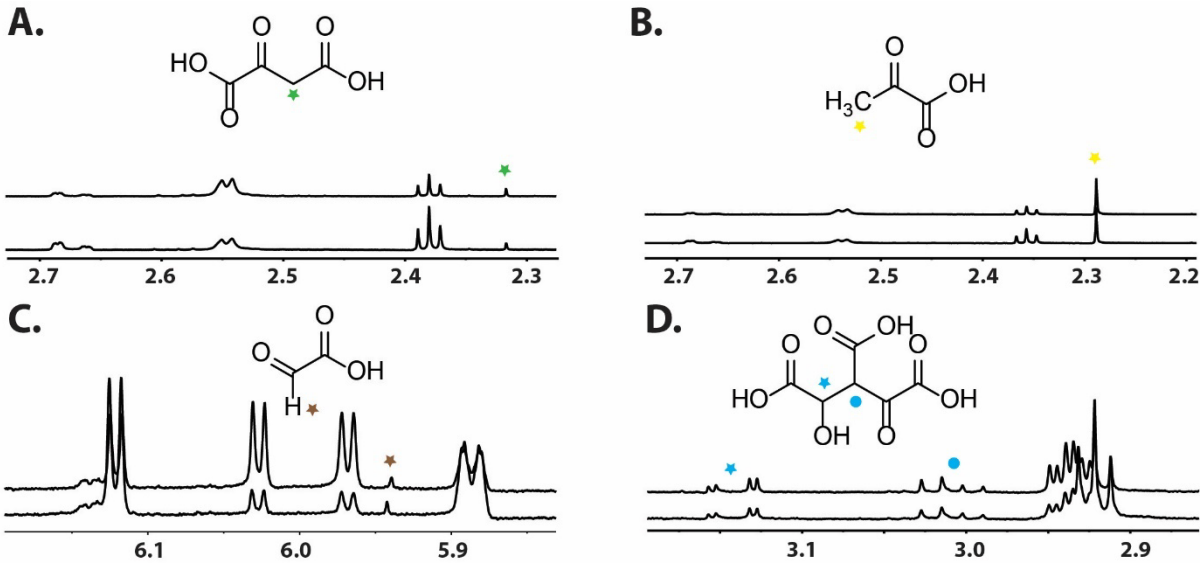

Figure 5.26 *| Extract of a ^{1}H NMR (700 MHz) spectrum of the Mtb IDH2 catalysed oxidation of isocitrate to 2-OG in the presence of oxaloacetate (**A**), pyruvate (**B**), glyoxylate (**C**), and oxalomalate (**D**). Overlays of spectra after t = 5 min and t = 60 min demonstrate that the metabolites are not turned over by Mtb IDH2. Conditions: 40 nM Mtb IDH2, 10 mM $MgCl_2$, 2.0 mM DL-isocitrate, 1.0 mM $NADP^+$; in 50 mM d_{11}-Tris (90:10 H_2O:D_2O; pH 7.5).*

^{1}H NMR time-course analyses showed that in the presence of oxaloacetate, pyruvate, glyoxylate or oxalomalate, the rate of the *Mtb* IDH2 catalysed turnover of isocitrate to 2-OG is apparently enhanced, in accordance with results from NADPH absorbance assays (**Figure 5.27**).

L-Kynurenine could not be analysed in NADPH absorbance assays due to its interference with the absorbance readout. Hence, its influence on *Mtb* IDH2 catalysed turnover of isocitrate to 2-OG was analysed by ^{1}H NMR time-course analysis. The presence of *L*-kynurenine (500 µM) apparently inhibited *Mtb* IDH2 activity (**Figure 5.27**). The 2-OG concentration after 1000 seconds was 50% of the 2-OG concentration in the reaction without *L*-kynurenine added.

The combined results of ^{1}H NMR time-course analyses demonstrate enhancement of *Mtb* IDH2 catalysed isocitrate turnover to 2-OG by oxaloacetate, pyruvate, glyoxylate, and oxalomalate. Furthermore, *Mtb* IDH2 activity was apparently inhibited by *L*-kynurenine.

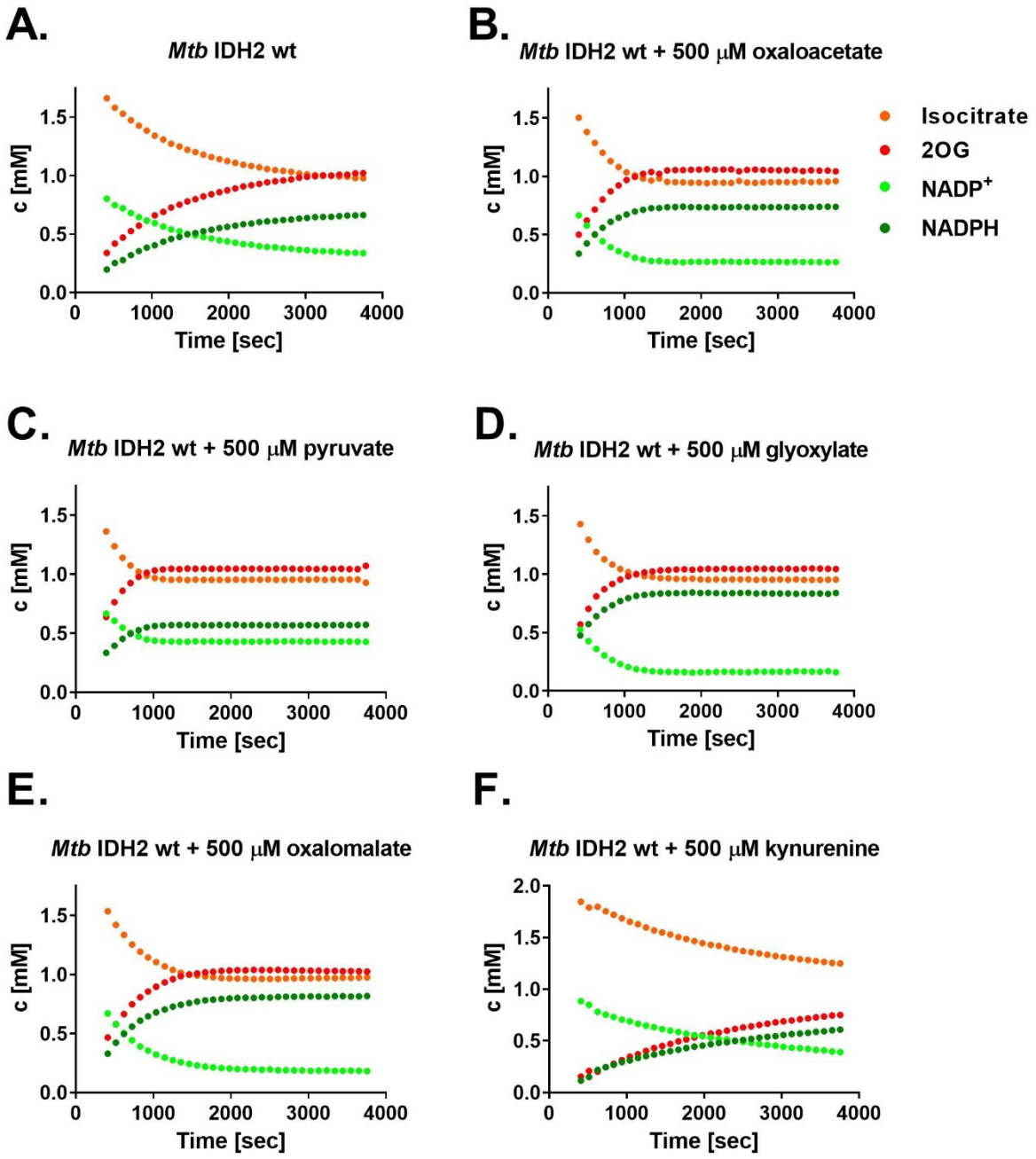

***Figure 5.27** | Time-course analyses of the Mtb IDH2 catalysed oxidation of isocitrate to 2-OG (**A**), and oxidation of isocitrate to 2-OG in the presence of oxaloacetate (**B**), pyruvate (**C**), glyoxylate (**D**), oxalomalate (**E**), and kynurenine (**F**). Conditions: 40 nM Mtb IDH2, 10 mM $MgCl_2$, 2.0 mM DL-isocitrate, 1.0 mM $NADP^+$; in 50 mM d_{11}-Tris (90:10 H_2O:D_2O; pH 7.5).*

5.8.4 Influence of Metabolites on *Mtb* IDH2 Secondary Structure and Stability

As discussed previously (Section 1.11), for ICL2 it is reported that high acetyl-CoA levels lead to a substantial conformational change in the enzyme structure linked to an increase in activity.[116] To investigate if similar effects can be observed on *Mtb* IDH2 by the modulators oxaloacetate, pyruvate, glyoxylate and oxalomalate, CD analyses were employed as described in Section 5.4.1.

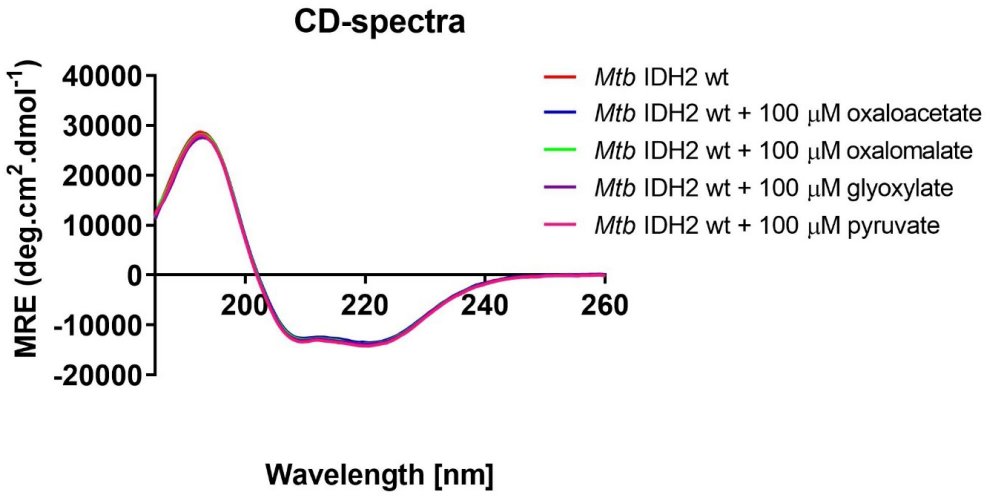

Figure 5.28 *| Circular Dichroism spectra of Mtb IDH2 with oxaloacetate (100 µM), oxalomalate (100 µM), glyoxylate (100 µM), or pyruvate (100 µM). All spectra overlay well. Conditions: Mtb IDH2 (0.2 mg/mL in sodium phosphate (10 mM, pH 8.0) buffer. These data were acquired by Maximillian Staudt.*

There was no influence of oxaloacetate, pyruvate, glyoxylate and oxalomalate on the CD spectrum of *Mtb* IDH2 (**Figure 5.28**). This implies that there are no substantial structural changes associated with the enhancement of *Mtb* IDH2 activity. To investigate if binding of the metabolic modulators can increase the T_m, the T_m was determined by CD as described in Section 5.4.2.

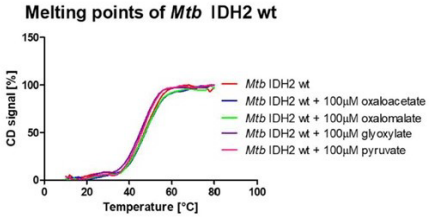

Sample	T_m (°C)	δ (°C)
***Mtb* IDH2**	47.2	0
with oxaloacetate	47.6	0.4
with oxalomalate	46.2	-1
with glyoxylate	45.1	-2.1
with pyruvate	45.9	-1.3

Figure 5.29 *| Analyses of the thermal stability using CD.* ***A.*** *Melting curves of Mtb IDH2 with oxaloacetate (100 µM), oxalomalate (100 µM), glyoxylate (100 µM), or pyruvate (100 µM). Conditions: Mtb IDH2 (0.2 mg/mL in sodium phosphate (10 mM, pH 8.0) buffer.* ***B.*** *Summary Table of T_ms. These data were acquired by Maximillian Staudt.*

There was no substantial influence on T_m by addition of oxaloacetate or oxalomalate (**Figure 5.29**). There was a small decrease in T_m by the addition of glyoxylate and pyruvate (**Figure 5.29**).

The combined results of CD analyses show that there are no changes in secondary structure of *Mtb* IDH2 and only minor changes on T_m in the presence of oxaloacetate, glyoxylate, pyruvate and oxalomalate implying that these metabolites have no influence on protein structure and no substantial influence on protein stability. Consequently, metabolic enhancement is likely a result of influences on dynamic processes in *Mtb* IDH2 catalysis.

5.9 Inhibition Studies with *Hs* IDH Cancer Variant Inhibitors

Isocitrate metabolism and the metabolic flexibility associated with it, are important features in host-adaptation of *Mtb* and, eventually, for its success as a pathogen.[111] Inhibition of enzymes associated with isocitrate metabolism could be a promising strategy for treatment of *Mtb*. There are no inhibitors reported for *Mtb* IDH1 or *Mtb* IDH2. However, there has been substantial interest in developing inhibitors against *Hs* IDH1 variants found in cancer (Chapter 3). Such inhibitors mostly bind in an allosteric manner at the dimer-interface. As discussed in Section 1.7, *Mtb* IDH1 and *Hs* IDH1 share 70% of their sequence and crystal structures of *Mtb* IDH1 and *Hs* IDH1 overlay well (Section 1.10). However, inhibitor selectivity to *Hs* IDH1 variants over *Hs* IDH1 wt is likely achieved as a result of subtle enzymatic differences.[48] Presently, it is not possible to predict whether *Hs* IDH1 variant inhibitors could potentially be active against *Mtb* IDH1 or other more structurally dissimilar IDHs, like *Mtb* IDH2. Consequently, screening of the set of *Hs* IDH1 variant inhibitors (Section 3.4) against *Mtb* IDH1 and *Mtb* IDH2 was conducted.

Treatment strategies for infections with *Msm* are needed urgently due to its role in opportunistic infections and its resistance to most first line drugs used for *Mtb* treatment.[110] As *Msm* IDH is the only isocitrate dehydrogenase in *Msm*[113], inhibition of it would be impactful. Consequently, the *Hs* IDH1 variant inhibitor selection was also screened against *Msm* IDH.

5.9.1 Inhibitor Screening

Inhibition assays were conducted as described in Section 3.3, but with the mycobacterial IDH assay buffer described in Section 5.4.1 (100 mM HEPES, 5 mM $MnCl_2$). Inhibitors were incubated with enzyme and Mn^{2+} for 12 minutes, before the reaction was initiated by addition

of isocitrate and $NADP^+$. Inhibition was normalised to a no-enzyme control (100% inhibition) and a no-inhibitor control (0 % inhibition).

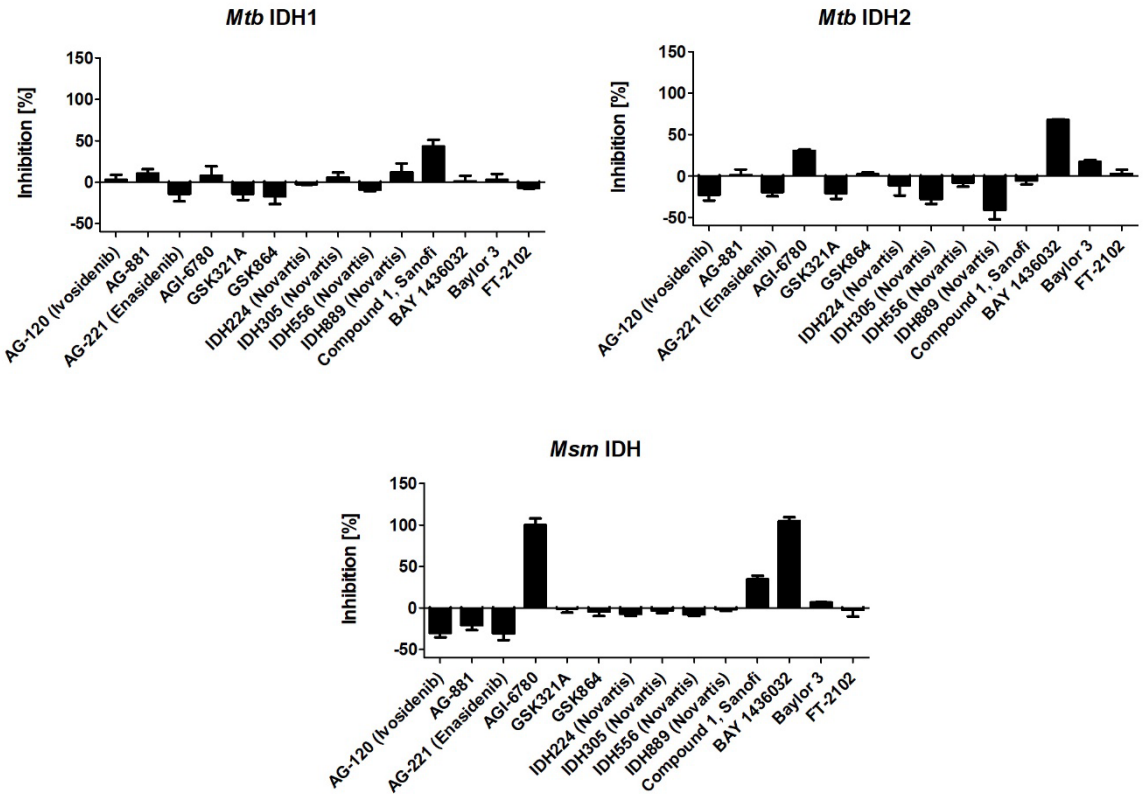

***Figure 5.30** | Inhibitor screening (10 μM) against Mtb IDH1, Mtb IDH2 and Msm IDH using the NADPH absorbance assay. Error bars: standard errors of the mean (n =3). Conditions: 100 mM HEPES, 5 mM $MnCl_2$, pH 7.5. These data were acquired together with Maximillian Staudt. Isocitrate: 1 mM, $NADP^+$: 1 mM.*

There were no potent inhibitors of *Mtb* IDH1 activity when tested at 10 μM. The highest inhibitory activity was observed for Compound 1 (Sanofi)[78], which inhibited 50 % of *Mtb* IDH1 activity (**Figure 5.30**). The most potent inhibitor of *Mtb* IDH2 was BAY-1436032[170], which inhibited 70% of its activity at 10 μM (**Figure 5.30**). BAY-1436032 was active against *Msm* IDH inhibiting 100% of its activity, and AGI-6780[199] also inhibited 100% *Msm* IDH activity at 10 μM (**Figure 5.30**).

5.9.2 Preliminary IC_{50} Determination for *Mtb* IDH1, *Mtb* IDH2, and *Msm* IDH

Subsequently, preliminary IC_{50} data were obtained according to the procedure described in Section 3.3.

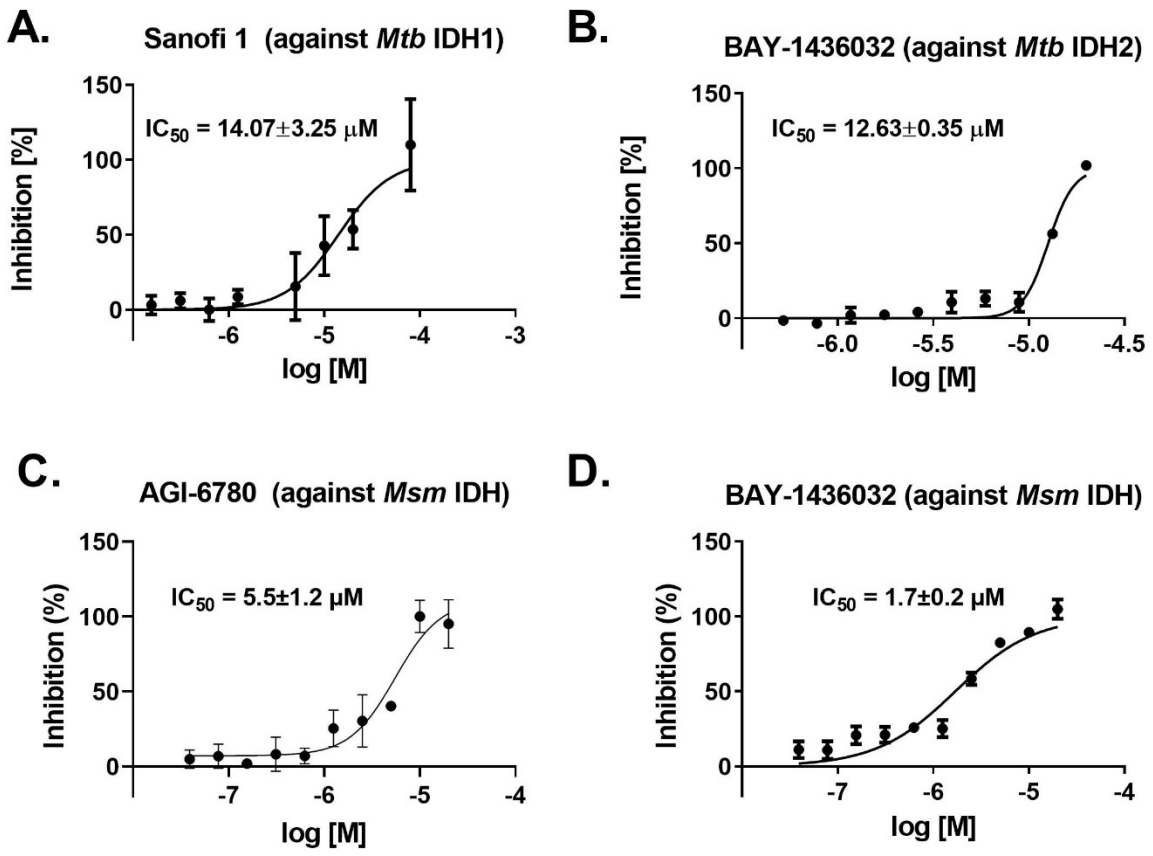

Figure 5.31 *| IC_{50} determination of Sanofi 1 with Mtb IDH1 (**A**) and BAY-1436032 (**B**) with Mtb IDH2, as well as AGI-6780 (**C**) and BAY-1436032 (**D**) with Msm IDH. Dose-response curves of inhibitors are shown using the NADPH absorbance assay. Error: standard error of the mean (n = 3). Conditions: 100 mM HEPES, 5 mM $MnCl_2$, pH 7.5. Isocitrate: 1 mM, $NADP^+$: 1 mM.*

In preliminary data, compound 1 (Sanofi) inhibited *Mtb* IDH1 with an IC_{50} = 14.1 µM (**Figure 5.31**, A) and BAY-1436032 inhibited *Mtb* IDH2 with an IC_{50} = 12.6 µM (**Figure 5.31**, B). AGI-6780 inhibited *Msm* IDH with an IC_{50} = 5.5 µM and BAY-143032 inhibited *Mtb* IDH2 with an IC_{50} = 1.7 µM (**Figure 5.31**, C/D). However, the dose-response assays only yielded preliminary IC_{50} values as the full range of the inhibition was not covered (no full sigmoidal curve). The assays need to be repeated to cover a more relevant inhibitor concentration range.

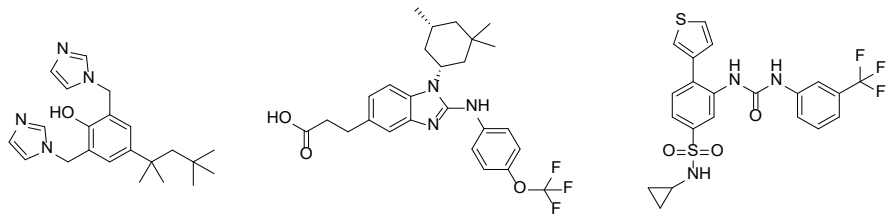

Figure 5.32 *| Structures of inhibitors with activity against Mtb IDH1, Mtb IDH2, and Msm IDH. Sanofi 1 and BAY-1436032 have been developed for Hs IDH1 variants (blue) whereas AGI-6780 has been developed for Hs IDH2 variants (red).*

It was shown that some *Hs* IDH1 variant inhibitors exhibit low activity against *Mtb* IDH1 and *Mtb* IDH2 (**Figure 5.32**). However, the most potent inhibitors arising from this screen are for *Msm* IDH (BAY-1436032 and AGI-6780, **Figure 5.32**). The findings on inhibition of *Mtb* IDH1, *Mtb* IDH2, and *Msm* IDH need to be followed-up to obtain more accurate IC_{50}s. Additionally, investigations on substrate competition, binding mode, and crystallographic studies to obtain structural information should be conducted. This could serve as a starting point for the optimisation of small molecule inhibitors for *Mtb* IDH1, *Mtb* IDH2, and *Msm* IDH.

5.10 Summary and Perspectives

Work on IDH enzymes from mycobacteria has been conducted for the first time in Oxford. Protocols for the recombinant expression of several IDHs from different species were established. Initially, constructs to express *Mtb* IDH1 and *Mtb* IDH2, and, as an example for a mycobacterial species with only one IDH isoform[113], *Msm* IDH were cloned into pNIC expression vectors (Section 5.2). Expression optimisation (Section 5.2) yielded suitable conditions to produce all three IDH enzymes on a relatively large scale (Section 5.3). Additionally, with the objective of making an efficient mycobacterial 2-HG producer, *Mtb* IDH1 R135H was produced, but this enzyme is not able to catalyse the oxidation of isocitrate or reduction of 2-OG (Section 5.3).

Biochemical characterisation using an NADPH absorbance assay (Section 5.4.1) shows that the catalytic efficiency (k_{cat}/K_M) for turnover of isocitrate is 1000-fold lower for *Mtb* IDH1 than for *Mtb* IDH2. This suggests, in accordance with knockout studies reported[113], that *Mtb* IDH2 is the essential enzyme for turnover of isocitrate to 2-OG, and that *Mtb* IDH1 may have other roles in *Mtb* metabolism. The catalytic efficiency of *Msm* IDH is 10-fold higher than *Mtb* IDH2, likely because it is the only IDH isoform in *Msm*. *Mtb* IDH1 catalyses the turnover of 2-OG to 2-HG with a similar catalytic efficiency to *Hs* IDH1 wt, which is unlikely to be physiologically relevant. ^{1}H NMR studies demonstrate that *Mtb* IDH1 and *Mtb* IDH2 catalyse the turnover of isocitrate to 2-OG with concomitant reduction of $NADP^+$ to NADPH (Section 5.4.2).

Mtb IDH1, *Mtb* IDH2 and *Msm* IDH display similar secondary structure features although there are small differences (Section 5.5.1). While *Mtb* IDH1 displays a two-step T_m, *Mtb* IDH2 and *Msm* IDH display a single T_m (Section 5.5.2). *Msm* IDH is dimeric in solution while *Mtb* IDH2 might be dimeric (as per non-denaturing PAGE) or trimeric (as per SEC-MALS). *Mtb* IDH1 is present as a mix of monomeric and dimeric species (Section 5.5.3).

Studies on the utilisation of divalent metal cations of recombinantly produced *Mtb* IDH1 and *Mtb* IDH2 (Section 5.6.1) show that both can likely utilise Mg^{2+}, but that both are more active with Mn^{2+}. There are no reported studies on metal utilisation of *Mtb* IDH1 and *Mtb* IDH2 *in vivo* (as is the case for *Hs* IDH1). *Mtb* IDH1 can utilise Co^{2+} but, in contrast to a previous report[118], does not utilise Zn^{2+}, at least under the tested conditions. Subsequent studies on inhibition by metals (Section 5.6.2, using Mn^{2+} as the catalytically active metal), show potent inhibition of *Mtb* IDH1 and *Mtb* IDH2 by Cu^{2+}. The potency of Cu^{2+} against *Mtb* IDH2 is 10-fold higher than for *Mtb* IDH1. Similarly, Zn^{2+} inhibits *Mtb* IDH2 more potently than *Mtb* IDH1. High levels of Cu^{2+} and $Zn^{2+}$are reported in the phagosome in macrophages and are involved in the response to pathogens. [194] A higher tolerance of *Mtb* IDH1 to Cu^{2+} and Zn^{2+} could be an alternative role of *Mtb* IDH1 in *Mtb* metabolism.

Studies on alternative substrates of *Mtb* IDH1 (Section 5.7) did not reveal any oxidative (with $NADP^+$) or reductive (with NADPH) turnover. Investigations of potential metabolic cross-regulation (Section 5.8) show that oxaloacetate, pyruvate, glyoxylate and oxalomalate enhance *Mtb* IDH2 activity. The mode of enhancement is of the V-type[197] which means an increase in the maximum turnover rate (k_{cat}) and changes in K_M (whereas for K-type activation, the maximum rate (k_{cat}) would not change but the K_M).

The evidence for potential metabolic cross-enhancement may relate to increased flux in the TCA cycle. Pyruvate and oxaloacetate may increase flux through the TCA cycle to signal their availability as substrates. The increase in activity observed for glyoxylate may reflect a positive feedback mechanism when the glyoxylate shunt is turned on and high levels of glyoxylate are produced. Oxalomalate potentially decomposes to oxaloacetate and glyoxylate, which then leads to an increase in turnover of isocitrate by *Mtb* [200]. Neither of the potential metabolic cross-enhancers oxaloacetate, pyruvate, glyoxylate and oxalomalate lead to conformational changes (as judged by CD spectra) of recombinantly produced *Mtb* IDH2 or a substantial change in T_m.

Screening of a selection of *Hs* IDH1 variant inhibitors (Section 5.9) revealed two inhibitors for *Msm* IDH, and two weak inhibitors of *Mtb* IDH1 and *Mtb* IDH2. These inhibitors need to be characterised for their mode-of-inhibition; X-ray crystallography studies could be conducted to obtain a starting point for structural optimisation. Subsequently, further IDH inhibitors, including inhibitors originally developed for *Hs* IDH1 wt, will be screened against *Mtb* IDH1, *Mtb* IDH2, and *Msm* IDH.

5.11 Materials and Methods

5.11.1 Site-directed mutagenesis

Site-directed mutagenesis (SDM) to obtain the gene encoding *Mtb* IDH1 R135H was conducted as described in Section 7.1.6.

***Table 5.10** | Forward and reverse primers for SDM. Codon CGT was mutated to CAT.*

Primer Name	Primer Sequence (5' to 3')
	5'- GGCATGA**T**GACCGATGACAATCGG-3'
g512a_	5'-CATCGGTCATC**A**TGCCTTCGGTG-3'

5.11.2 Protein Production

The proteins were produced according to Section 7.1.12. The yields are presented as pellet mass divided by the amount of 2TY medium. The protein yield is presented as amount of protein (mg) per litre of medium (L).

***Table 5.11** | Yields of protein production of Mtb IDH1, Mtb IDH1 R135H, Mtb IDH2, and Msm IDH,*

Protein	Yield (g/L)	Protein Yield (mg/L)
***Mtb* IDH1 wt**	6.9	2.2
***Mtb* IDH1 R135H**	11.9	2.0
***Mtb* IDH2 wt**	12.7	120.2
***Msm* IDH**	12.5	65.7

5.11.3 NADPH-absorbance Assay

NADPH absorbance assays were conducted using a PHERAstar FS Microplate Reader according to the Materials and Methods (Section 7.2.1). The buffer used was HEPES (100 mM) and $MnCl_2$ (5 mM) at pH 7.5.

For activity studies with various metal cations, HEPES buffer (100 mM, pH 7.5) was prepared. *Mtb* IDH1 and *Mtb* IDH2 were treated with EDTA overnight (2000-fold excess) to remove copurifying metal. The proteins were buffer exchanged into HEPES buffer (100 mM, pH 7.5) using Micro Bio-Spin 6 Columns (Bio-Rad). The enzyme solution was incubated with metal ions for 10 minutes before the reaction was initiated by the addition of isocitrate and $NADP^+$.

For inhibition studies with metal salts and *Hs* IDH1 variant inhibitors, standard mycobacterial assay conditions (HEPES 100 mM, $MnCl_2$ 5 mM, pH 7.5) were used. *Mtb* IDH1, *Mtb* IDH2, or *Msm* IDH were incubated with metal salt or inhibitor for 12 minutes, and the reaction initiated by the addition of isocitrate and $NADP^+$. The activity was normalised to a no-enzyme control (100% inhibition) and a no-inhibitor control (0% inhibition). Other parameters and analyses were as described in Section 3.10.1.

To investigate the influence of metabolic modulators on Michaelis-Menten parameters, the standard mycobacterial IDH assay buffer (HEPES 100 mM, $MnCl_2$ 5 mM, pH 7.5) was used. *Mtb* IDH2 was incubated for 10 minutes with 100 μM or 400 μM of the metabolite, and the reaction initiated by addition of isocitrate and $NADP^+$.

5.11.4 Time Course Analyses by NMR

^1H NMR time courses were conducted according to Section 7.2.2. For analyses of metabolic modulators, 500 μM of the metabolite was added to *Mtb* IDH2 and $MgCl_2$. After a 10-minute incubation, the reaction was initiated by addition of isocitrate and $NADP^+$.

5.11.5 Non-denaturing PAGE

Non-denaturing PAGE was conducted according to the Materials and Methods chapter (7.2.6). To inform on an appropriate buffer pH, the isoelectric point (IEP) of the proteins was calculated using the ExPASy ProtParam tool. [153] The IEPs are in **Table 5.12**.

Table 5.12 **|** *Isoelectric points (IEPs) of Mtb IDH1, Mtb IDH2, and Msm IDH.*

Protein	IEP
Mtb IDH1	5.13
Mtb IDH2	5.24
Msm IDH	5.58

A pH above the IEP ensured the protein to be negatively charged and to run towards the cathode. The gel chamber was set up accordingly and an 8-12% Tris-glycine gel used.

6 Summary and Conclusions

6.1 Overview of the Work Described in This Thesis

The work described in this thesis primarily focused on studies of *Hs* IDH1 cancer variants, which enable resistance to the FDA-approved inhibitor ivosidenib by acquiring a second-site dimer-interface substitution (S280F).[28] The overall aim of the work was to investigate the emerging IDH1 variants, the mechanism of their resistance against ivosidenib, and to find ways to overcome S280F mediated drug resistance (**Chapter 2/3**). The initial findings triggered further detailed mechanistic studies on the influence of catalytic R132 variations and the influence of the dimer-interface on IDH1 catalysis (**Chapter 4**). Lastly, the role of mycobacterial isocitrate metabolism was explored, with the aim of evaluating mycobacterial IDHs as potential drug targets. Production and assay procedures for mycobacterial IDHs were established and initial biochemical and biophysical results were obtained for them (**Chapter 5**).

6.2 Studies of Resistance to *Hs* IDH1 Variant Inhibition

Distinctive changes in metabolism have emerged to be of central importance to cancer.[1] The best-studied mutations in metabolic enzymes are those in the genes encoding for IDH1 and IDH2, which confer a gain-of-function mutation leading to variant enzymes that reduce the normal 2-OG product of IDH catalysis to the oncometabolite 2-HG.[35] The major physiological role of IDH1 and IDH2 is reported to be the production of NADPH.[17] As a result of the gain-of-function mutation, cellular NADPH levels are reduced, rendering the cell more vulnerable to reactive oxygen species.[12] Elevated cellular 2-HG levels, enabled by IDH1 variants, can inhibit the KDMs, TETs, or other 2-OG using enzymes, in a manner proposed to help promote tumorigenesis, likely via chromatin destabilisation (in combination with other mutations).[201] IDH1 variant inhibitors have been disclosed and ivosidenib has recently been FDA-approved for AML.[64] Resistance to ivosidenib has emerged, which is linked to second-site mutations in IDH1.[28]

In **Chapter 2**, biochemical, biophysical, and structural studies on R132C S280F and R132H S280F are described, and the results compared with studies on R132C and R132H. The results suggested that the S280F substitution not only directly leads to ivosidenib resistance but also increases the affinity of IDH1 R132C and R132H for 2-OG and Mg^{2+} (as judged by K_M comparisons), and consequently, increases catalytic efficiency (k_{cat}/K_M; **Table 2.2/2.4**) for

reduction of 2-OG to 2-HG. It is notable that ivosidenib has been reported to compete with 2-OG and Mg^{2+} binding, suggesting that the increase in 2-OG and Mg^{2+} affinity likely plays a role in S280F-mediated inhibitor resistance. [48]

All IDH1 variants tested can utilise *D*-isocitrate as a substrate and catalyse the turnover of *D*-isocitrate to give 2-HG (^{1}H NMR time course studies, **Figure 2.17**). This observation is in accord with recent studies by Liu et al. on the IDH1 R132H homodimer showing catalysis of the turnover of isocitrate to 2-HG for the first time (by ^{1}H NMR).[48] Contrary to this observation, most reports in the literature until then had not observed turnover of isocitrate catalysed by IDH1 homodimer variants (note that Pietrak et al. reported turnover of isocitrate to 2-HG catalysed by an IDH1 wt/IDH1 R132H heterodimer[50]). The overall turnover of isocitrate to 2-HG is redox neutral, i.e. the $NADP^+$ levels do not change, which means the turnover cannot be readily monitored by NADPH-based assays, likely contributing to the lack of reports on this reaction in the literature. The results show that the isocitrate oxidation step is rate-limiting and NADPH formed in this step is readily turned over (**Figure 2.20**). The oxidation of isocitrate to 2-OG is substantially influenced by the R132 variation (R132C is more efficient than R132H), while the full turnover of isocitrate to 2-HG is enhanced by the S280F variation (**Figure 2.23**). This observation is consistent with results showing isocitrate binding is more efficient for the R132C variants than the R132H variants (**Figure 2.39**). All the tested IDH1 variants were only observed to bind isocitrate and NOG (a close analogue of 2-OG) when magnesium ions were present; with NOG binding being similar across all the IDH1 variants.

In its closed active conformation, the crystal structure of R132C S280F (**Figure 2.52**) shows that the sidechains of F280 from both monomers point towards the dimer-interface and help to build a hydrophobic region along with W124 and W267 (this is reflected in a substantial increase in T_m of S280F substituted variants; **Table 2.6**), increasing the rigidity of the dimer-interface. Together with the bulkiness of the phenylalanine side chain, this interferes with ivosidenib binding.

Chapter 3 describes studies on the understanding of S280F-mediated ivosidenib resistance and the goal of identifying potential alternative inhibitors. These data showed that ivosidenib binding to R132C S280F and R132H S280F is inefficient (**Table 3.2**) and as a result, ivosidenib is inactive (**Figure 3.9**). The loss of binding efficiency to S280F variants is mostly due to the bulkiness of the phenylalanine side chain and the addition of a new hydrophobic region at the

dimer-interface. The loss of a potential hydrogen bond of S280 to ivosidenib may play an additional role in hindering binding of ivosidenib (**Figure 3.9**, **Table 3.2**).

Some, but not all, IDH1 variant inhibitors lose activity against R132C S280F and R132H S280F (**Figure 3.16**). Inhibitors retaining activity can bind with a stoichiometry of two molecules to the IDH1 dimer (as shown for GSK864, IDH224, FT-2102, DS-1001B; **Figure 3.21**). This stoichiometry contrasts with that for ivosidenib, which can only bind with a stoichiometry of one inhibitor molecule to the IDH1 dimer (**Figure 3.10**). Some of the inhibitors retain potent inhibitory activity against R132C S280F and R132H S280F (IC_{50} <100 nM; **Table 3.3**, i.e. IDH224, FT-2102, DS-1001B), suggesting that S280F mediated resistance can be overcome.

Potent inhibitors of R132C, R132C S280F, R132H, and R132H S280F are apparently competitive with respect to Mg^{2+} and 2-OG binding (**Figure 3.28/3.29**) but are not competitive with respect to NADPH (**Figure 3.30**). This observation is consistent with the proposal that a higher affinity of S280F variants for 2-OG and Mg^{2+} plays a role in inhibitor resistance (Section 2.3). The crystal structure of R132C S280F complexed with DS-1001B shows that inhibitor binding results in the two F280 residues being pushed to the side of the dimer-interface, which hinders their interaction (**Figure 3.32**; 14.9 Å apart).

Ivosidenib is inefficient in reducing 2-HG levels in LN18 cell lines overexpressing R132C S280F and R132H S280F. By contrast, IDH224, FT-2102, and DS-1001B retain activity in a cellular environment (**Figure 3.39/3.40**). FT-2102 and DS-1001B are presently in phase 2 clinical trials.[181,164,92] There is thus the possibility of developing efficient treatment regimens involving the substitution of one IDH variant inhibitor for another as resistance emerges. There is also the possibility of using combinations of inhibitors, especially when the types of resistance that will likely emerge can be predicted prior to initial treatment.

In the first part of **Chapter 4**, studies on the influence of various catalytic R132 variations on IDH1 activity are described. R132H is less efficient in the reduction of 2-OG to 2-HG than R132C or R132S, which are similar amongst themselves (**Table 4.3**) consistent with previous reports.[52] The turnover of isocitrate to 2-HG is catalysed more efficiently by R132C compared to R132S (**Figure 4.13**). However, R132S retains more of the IDH1 wt ability to catalyse the oxidation of isocitrate to 2-OG than R132C and R132H (**Figure 4.15**), consistent with DSF data showing a stronger isocitrate binding to R132S compared to R132C and R132H (**Figure 4.21**).

In the second part of **Chapter 4**, studies on the influence of the dimer-interface on enzymatic activity are described. IDH S280F increases the catalytic efficiency for the turnover of isocitrate compared to IDH1 wt. IDH1 wt can catalyse the reduction of 2-OG to 2-HG (**Figure 4.32**), but IDH1 S280F is less efficient in catalysis. However, binding of a magnesium ion and 2-OG is enhanced by the S280F substitution (as judged by K_M), similarly as described in Chapter 2 for R132C S280F and R132H S280F. Both IDH1 wt and IDH1 S280F can bind isocitrate and NOG in the absence of magnesium ions, but binding is more efficient in the presence of magnesium ions (**Figure 4.42/4.44**).

Several dimer-interface variations were introduced into R132H to study potential inhibitor resistance and the influence of the dimer-interface on IDH1 catalysis. While V255F and V281F decrease the activity of the R132H variant substantially, the R132H Q277E variant is inactive. R132H Q277E is unable to bind isocitrate or NOG (and by implication 2-OG; **Figure 4.47**), which is likely the reason for its inactivity (DSF). The α10 helix of a crystal structure of R132H Q277E (incubated with NADPH, calcium, and 2-OG) is disordered; this may be linked to its inability to bind isocitrate and NOG as the α10 helix is involved in metal and substrate binding. A potential reason for this observation may be electrostatic repulsion between Q277E residues in separate monomers in the R132H Q277E homodimer. These observations demonstrate the importance of the dimer-interface for IDH1 R132H catalysis and how subtle changes (i.e. a substitution) can substantially impact on activity.

The work on *Hs* IDH1 cancer variants has shown that S280F-mediated resistance can be overcome by the use of alternative inhibitors, which are active in cells; some of which are presently in clinical phase 2 trials (DS-1001B, FT-2102). DS-1001B and FT-2102 could be evaluated in a clinical setting in patients harbouring the R132C S280F variant or evaluated as a combination regimen with ivosidenib in a clinical study.

All the clinically observed IDH1 variants tested in this thesis catalyse the turnover of isocitrate to 2-HG and thus, inhibition studies on this turnover must be conducted using ^{1}H NMR. Cyclic voltammetry is a new technique in the cancer metabolism field and can be used to study the influence of inhibitors on the isocitrate oxidation and the 2-OG reduction separately with the aim of identifying inhibitors, which could inhibit the IDH1 variant catalysed reduction of 2-OG to 2-HG, but not the oxidation of isocitrate to 2-OG. To investigate structural features underlying varying kinetic properties, further IDH1 variants could be crystallised in their closed active conformation, based on the crystallisation conditions obtained for R132C S280F.

This may help in understanding the underlying dynamic processes of IDH1 catalysis caused by the gain-of-function mutations; further, studies can potentially be extended to time-resolved crystallography. Based on the conditions for co-crystallisation of DS-1001B with R132C S280F, additional inhibitors like FT-2102 should be crystallised with R132C S280F to obtain preliminary insights into how inhibitors can generally retain activity against S280F substituted variants as this may inform future drug design.

6.3 Studies on Mycobacterial IDHs

Isocitrate is an important branch point metabolite in mycobacteria and can be metabolised via IDHs[118] for which there is limited understanding on their biochemistry and regulation, and at present, no inhibitors are available. In **Chapter 5**, work on mycobacterial IDHs was initiated by establishing protein production and assay protocols. The catalytic efficiency (k_{cat}/K_M) for the turnover of isocitrate is 1000-fold lower for *Mtb* IDH1 than for *Mtb* IDH2 (**Table 5.2**), suggesting that *Mtb* IDH2 is the important isoform for turnover of isocitrate to 2-OG in *Mtb* metabolism, and that *Mtb* IDH1 may have other roles. *Mtb* IDH1 and *Mtb* IDH2 can utilise Mg^{2+} but both exhibit higher activity with Mn^{2+}. *Mtb* IDH1 and *Mtb* IDH2 are potently inhibited by Cu^{2+} and Zn^{2+} but the potency for *Mtb* IDH2 is higher than for *Mtb* IDH1 (**Figure 5.21/5.22**). It has been observed that in response to an *Mtb* infection, Cu^{2+} and Zn^{2+} levels in macrophages are elevated. [194] *Mtb* IDH1 has a better tolerance to Cu^{2+} and Zn^{2+} than *Mtb* IDH2, suggesting a potential alternative role of *Mtb* IDH1 in *Mtb* metabolism.

Mtb IDH2 activity is enhanced by the presence of oxaloacetate, pyruvate, and glyoxylate (**Figure 5.25**). The enhancement could potentially signal high substrate availability in the TCA cycle (oxaloacetate, pyruvate) or could provide a feedback mechanism for increased flux through the glyoxylate shunt (glyoxylate). Two *Hs* IDH1 variant inhibitors were found to be moderately active against *Msm* IDH, and two inhibitors exhibit weak activity for *Mtb* IDH1 or *Mtb* IDH2 (**Figure 5.33**) yielding a potential starting point for inhibitor optimisation.

The work on mycobacterial IDHs provides recombinant protein production and assay procedures. Assay optimisation should be conducted to enable screening procedures with different manganese and magnesium concentrations. With the optimised assay, further inhibitor screens should be conducted, and suitable crystallisation conditions (based on literature reports) could be obtained to enable inhibitor co-crystallisation and inform structure optimisation.

Chapter 7

Materials and Methods

Contents

7 Materials and Methods

7.1 Molecular Biology Methods

7.1.1 Preparation of LB Agar Plates

LB agar was prepared according to the following recipe:

Component	Amount
Agar	20 g
NaCl	10 g
Tryptone	10 g
Yeast extract	5 g

Ingredients were dissolved in MQ water (purified using a Millipore Milli-Q system) (1 L) and autoclaved (TouchClaveR II autoclave; LTE Scientific Ltd). The LB agar was allowed to cool down to ~50°C and selection markers (antibiotics, from 1000x concentrated stock solutions) were added. LB agar (20 mL) was poured into Petri Dishes in a sterile laminar flow hood and left to set. The Petri Dishes were closed and stored at 4°C.

7.1.2 Preparation of TRIS-Acetate-EDTA (TAE) Buffer

Tris-Acetate-EDTA (TAE) buffer (10x) was prepared according to the following recipe.

Component	Amount
Tris base	48.4 g
Glacial acetic acid (17.4 M)	11.4 mL
EDTA	3.7 g

The components were dissolved in MQ water (1 L), and the resultant buffered solution was diluted 10-fold before usage.

7.1.3 Agarose Gel Electrophoresis

Agarose (0.8%) was added to the TAE buffer; the solution was heated to dissolve the agarose using a microwave (800 W, 3 min). The agarose solution was allowed to cool and SYBR Safe-DNA gel stain solution (Invitrogen; 10000x concentrated stock solution in DMSO) was added. The gel was poured into a gel tray (Alpha Laboratories) with a comb and allowed to set. After removal of the comb, the gel was transferred to a running chamber (Alpha Laboratories) and

submerged with TAE buffer. DNA samples were mixed with 6x loading buffer and loaded onto the gel. The gel was run at 85 V for 30 minutes and imaged using a Universal Hood III (Bio-Rad).

7.1.4 Primer Preparation

Primers were purchased from Sigma Aldrich or Life Sciences. They were dissolved in autoclaved MQ water to a concentration of 100 μM and diluted 10-fold for further usage.

7.1.5 Cloning

7.1.5.1 Cloning Mycobacterial IDH Genes into a pNIC Vector

The cloning process was conducted with Dr Acely Garza-Garcia at the Francis Crick Institute. According to previously reported *Mtb* IDH1 expression protocols[120,202,192], primers for the gene encoding for *Mtb* IDH1 were designed to produce *Mtb* IDH1. After initial expression trials were not successful in producing *Mtb* IDH1 in sufficient quantities, a codon-optimised gene was used. Primers for the gene encoding for *Mtb* IDH2 and *Msm* IDH were designed according to reported procedures.[202, 192]

7.1.5.1.1 Polymerase Chain Reaction (PCR)

Genomic DNA was purified from single colonies of each mycobacterial species using the QIAprep 2.0 DNA purification Kit (Qiagen) according to the manufacturer's protocol (for *Mtb* this was conducted by Dr Hua Wang at the Francis Crick Institute). The DNA templates were amplified using the polymerase chain reaction (PCR) with 10 μM primer and polymerases listed below with a 96 Well Thermal Cycler (Veriti) using a 3-step protocol. The yields and purities of the PCR products were optimised with varying temperature protocols, the addition of DMSO, varying concentrations of templates/primers and varying polymerases (Taq, KOD; both from Thermo Scientific). The PCR products were purified with a QIAquick PCR purification Kit (Qiagen) according to the manufacturer's protocol. For the expression of *Mtb* IDH1, additionally, a codon-optimised gene for the expression of *Mtb* IDH1 in *E. coli* was purchased (Invitrogen) and amplified according to the procedure above.

7.1.5.1.2 Restriction Digestions

The restriction digestion for the PCR products (1 μg) encoding for *Mtb* IDH1, *Mtb* IDH2, and *Msm* IDH were set up at 37°C overnight using BfuAI (New England Biolabs; 10 min) in NEBuffer (New England Biolabs). The reaction mixture was purified using agarose gel electrophoresis (Section 7.1.3). Bands corresponding to the PCR product and the empty vector

were cut out and purified using the GeneJET Gel Extraction Kit (Thermo Fisher Scientific) according to a modified manufacturer`s protocol.

7.1.5.1.3 Ligation

The ligation into the pNIC-CTHF vector was conducted using isothermal assembly with the NEBuilder (New England Biolabs) with a molar ratio of vector to insert of 1 to 2. The assembly was conducted at 50°C for 15 min. The plasmid was then transformed into NEB5α cells and grown at 37°C overnight.

7.1.5.1.4 Colony PCR

Three colonies were picked, and a colony PCR performed. 2TY medium (5 mL) containing ampicillin (100µg/mL) was inoculated with a single colony and grown at 37 °C in an incubator shaker (New Brunswick Scientific; 200 rpm). On the next day, the cell suspension (10 µL) was mixed with MQ water (10 µL) and boiled for 10 min at 100 °C. Samples were span down (13,000 rpm, 20 s) and the supernatant was used for the colony PCR according to the following protocol.

Component	Volume
Supernatant	5 µL
2x BioMix Red (BioLine)	10 µL
Autoclaved MQ water	3 µL
Primer TEV.1 (10 µM)	1 µL
Primer TEV.3 (10 µM)	1 µL

The colony PCR reaction was conducted according to the following temperature protocol.

Step	Temperature (°C)	Time (min)
Initial denaturation	95	5:00
2 steps- 20 cycles	95	0:30
2 steps- 20 cycles	72	3:00
Final Extension	72	2:30
Hold	4	-

Due to the high melting temperature of the primers, a 2-step method was adopted: the annealing time (10 s at 72°C) and extension time (20-30 s/kBp) were combined.

The samples were then loaded onto an Agarose gel (0.8% in TAE buffer) and imaged using a Universal Hood III (Bio-Rad). The plasmid DNA from positive clones (5 mL of cell suspension) was purified with a GeneJET Plasmid Miniprep Kit (Thermo Scientific) or QIAprep 2.0 DNA purification Kit (Qiagen) according to the manufacturer`s protocol and eluted in autoclaved MQ water (40 µL). The DNA concentration was determined using a NanoDrop One (absorbance at λ = 260 nm; Thermo Scientific). The samples were sent for sequencing to Eurofins Genomics or GATC and the plasmids were stored at -20°C. Sequences were translated using the ExPASy Translate tool[153] and aligned using MAFFT version 7[128].

7.1.5.2 Cloning *Hs* IDH1 Genes into a pET22b Vector

Cloning into pET22b vector was conducted at the University of Oxford.

7.1.5.2.1 PCR

The primer stock solutions were diluted to 10 µM and used for PCR. Other components were added in a PCR tube (200 µL) according to the table below to give a final volume of 50 µL.

Component	Amount
5x Q5 Reaction Buffer	10 µL
10 mM dNTP mix	1 µL
10 µM forward primer	2.5 µL
10 µM reverse primer	2.5 µL
Template DNA	~10 ng
Q5 DNA Polymerase	0.5 µL
Autoclaved MQ water	to 50 µL

The PCR was conducted using a GeneAmp PCR System 9700 (Applied Biosystems) or a Prime Thermal Cycler (Applied Biosystems) according to the conditions below.

Step	Temperature (°C)	Time (min)
Initial denaturation	98	1:00
2 steps- 30 cycles	98	0:10
2 steps- 30 cycles	72	0:50
Final Extension	72	2:00
Hold	4	-

Due to the high melting temperature of the primers, a 2-step method was adopted: the annealing time (10 s at 72°C) and extension time (20-30 s/kBp) were combined. The extension time was calculated according to the size of the construct (6.7 kBp).

The agarose gel (0.8 % in TAE buffer) electrophoresis (Section 7.1.3) was conducted with the products of the PCR in a gel tank (Alpha Laboratories). The bands corresponding to the PCR product were cut out from the gel and purified using the GeneJET Gel Extraction Kit (Thermo Fisher Scientific) according to a modification of the manufacturer`s protocol. While the manufacturer`s protocol only uses one washing step, the column was washed three times with wash buffer based on previous experience. The product was eluted in autoclaved MQ water and used for restriction. This protocol was used for all subsequent purifications with a GeneJET Gel Extraction Kit (Thermo Fisher Scientific).

7.1.5.2.2 Restriction Digestion

The restriction digestion was set up according to the following protocol.

Component	Amount
Purified PCR Product	1 µg
10x CutSmart Buffer	5 µL
Nde1	2 µL (40 units)
Xho1	2 µL (40 units)
Autoclaved MQ water	to 50 µL

The reaction was allowed to proceed at 37°C overnight. Additionally, 1 µg of a plasmid containing the ORF for R132C (without cleavage-site) was digested to yield the empty pET22b vector (Novagen). The reaction mixtures were purified using agarose gel electrophoresis (Section 7.1.3.).

7.1.5.2.3 Ligation

The purified pET22b (Novagen) vector (50 ng) was used for the ligation. The molar ratio of vector to insert was 1 to 3. T4 ligase was used to facilitate ligation according to the following protocol.

Component	Amount
T4 DNA Ligase Buffer (10x)	2 µL
Vector DNA	50 ng
Insert DNA	35.45 ng
Autoclaved MQ water	to 20 µL
T4 ligase	1 µL

The reaction was allowed to proceed for 2 days at ambient temperature. The ligation mixture (5 µL) was then transformed into commercially available XL10-gold *E.coli* cells (35 µL) and a colony PCR conducted (see Section 7.1.5.1.4).

7.1.6 Site-Directed Mutagenesis

Primer stock solutions (10 µM) were used for site-directed mutagenesis (SDM). [127] Other components were added in a PCR tube (200 µL) according to the table below to a final volume of 50 µL.

Component	Amount
5x Q5 Reaction Buffer	10 µL
10 mM dNTP mix	1 µL
10 µM forward primer	2.5 µL
10 µM reverse primer	2.5 µL
Template DNA	~60 ng
Q5 DNA Polymerase	0.5 µL
5x Q5 High GC enhancer (when GC content >60 %)	10 µL
Autoclaved MQ water	to 50 µL

The mixture was subjected to thermocycling in a GeneAmp PCR System 9700 (Applied Biosystems) or a Prime Thermal Cycler (Applied Biosystems) according to the conditions below.

Step	Temperature (°C)	Time (min)
Initial denaturation	98	3:00
2 steps- 30 cycles	98	0:10
2 steps- 30 cycles	72	3:00
Final Extension	72	2:00
Hold	4	-

Due to the high melting temperature of the primers, a 2-step method was adopted. The annealing time (10 s at 72°C) and extension time (20-30 s/kBp) were added. The extension time was calculated according to the size of the construct (6.7 kBp). Subsequently, the mixture was purified by GeneJET PCR Purification Kit (Thermo Scientific) according to the manufacturer`s protocol. The sample was eluted with autoclaved MQ water (45 µL) and 10x CutSmart buffer (5 µL; New England Biolabs) was added.

7.1.7 Dpn1 Digestion

To digest the methylated parent DNA, Dpn1 (1 µL of 20,000 units/ml; New England Biolabs) was added and the mixture incubated for 3 h.

7.1.8 Preparation of Chemically Competent *E. coli* Cells

A solution (500 mL) containing $CaCl_2$ (100 mM) and glycerol (20 %, *v/v*) was prepared and autoclaved. XL10-Gold and BL21(DE3)pLysS *E. coli* cells were streaked out on two separate LB agar plates containing chloramphenicol and grown overnight at 37°C in a Heraeus® TypB 6030 incubator (Thermo Fisher Scientific). On the next day, one colony was used to inoculate sterile 2TY medium (100 mL) and grown in a shaker incubator (New Brunswick Scientific) overnight. This starting culture (200 µL) was used to inoculate sterile 2TY medium (100 mL) and grown at 37°C in a shaker incubator (New Brunswick Scientific) until OD_{600}= 0.6-0.8 was reached. The cells were harvested by centrifugation (750xg, 4°C, 5 minutes) and gently resuspended in the sterile solution (25 mL) containing $CaCl_2$ (100 mM) and glycerol (20 %, *v/v*). The cells were incubated on ice for 20 min, centrifuged and resuspended in the sterile solution (25 mL) containing $CaCl_2$ (100 mM) and glycerol (20 %, *v/v*). The cells were aliquoted (100 µL and 200 µL) and stored at -80°C.

7.1.9 Transformation

The plasmid stock solution (< 1 µL), the product of PCR-ligation (5 µL) or the product of the SDM (12 µL) was added to XL10-Gold *E. coli* cells (35 µL) in sterile conditions and mixed by

flicking. The mixture was placed on ice for 30 min. The transformation was heat shocked by placing the tube into a 42°C water bath for 45 sec. Subsequently, the tube was kept on ice for 2 min before SOC medium (250 µL) was added. The cells were grown for 45 min at 37°C in a shaker incubator (New Brunswick Scientific) and then transferred onto an LB plate containing selection marker. The LB plate was incubated overnight at 37°C in a Heraeus® TypB 6030 incubator (Thermo Fisher Scientific). For the transformation into BL21DE3 plysS *E. coli* cells, plasmid stock solution (<1 µL) was added to BL21DE3 plysS *E. coli* cells (35 µL) and the transformation conducted according to the procedure above.

7.1.10 Small Scale Growth and Purification of Plasmid DNA

Colonies were picked the next day with a sterile loop and grown in 2TY medium (100 mL) overnight containing the appropriate antibiotic. The plasmid was purified with a GeneJET Plasmid Miniprep Kit (Thermo Scientific) according to the manufacturer`s protocol and eluted in autoclaved MQ water (40 µL). The DNA concentration was determined by a NanoDrop One (Thermo Scientific) using the absorbance at $\lambda = 260$ nm. The samples were sent for sequencing to Eurofins Genomics and the plasmids were stored at -20°C. The DNA sequences were translated using the ExPASy Translate tool[153] and aligned using MAFFT (version 7)[128].

7.1.11 Preparation of a Glycerol Stock of BL21(DE3)pLysS

2TY medium (2 mL) was mixed with the appropriate antibiotic in a falcon tube (50 mL). One colony was transferred into the medium using a sterile loop and grown for 3-4 h until $OD_{600} \sim 0.4$ was reached. The suspension (700 µL) was mixed with glycerol in MQ water (300 µL, 50 % *(v/v)*, autoclaved) and stored at -80°C.

7.1.12 Protein Production

7.1.12.1 Preparation of 2TY Medium and LB Medium for Large-Scale Growth

2TY medium was prepared according to the following recipe or provided by Mr Manso Jubier:

Component	Mass (g)
Tryptone	115.2
Yeast Extract	72
NaCl	36

LB medium was prepared according to following recipe:

Component	Mass (g)
Tryptone	72
Yeast Extract	36
NaCl	72

The components were dissolved in 7.2 L MQ water, transferred into flasks (600 mL each), and closed with a foam stopper and tin foil. They were autoclaved at 121°C for 20 min (TouchClaveR II; LTE Scientific Ltd.).

7.1.12.2 Large-Scale Cell growth

Antibiotic/IPTG stock solutions (1000x stock concentration) were prepared according to the following recipe and were sterile filtrated (Minisart® High Flow, 0.22 µM; Sartorius) in a laminar flow hood.

Antibiotic	Solid	Solvent
Chloramphenicol	300 mg	10 mL EtOH
Ampicillin	1 g	10 mL MQ water (autoclaved)
Kanamycin	500 mg	10 mL MQ water (autoclaved)
IPTG	2.38 g (*Hs*)/238 mg (*Mtb*)	10 mL MQ water (autoclaved)

2TY medium (100 mL) with the appropriate antibiotic selection marker was inoculated with the glycerol stock and a seed culture grown overnight at 37°C in an incubator shaker (New Brunswick Scientific). Each flask containing 2TY medium (600 mL) and the appropriate antibiotic (600 µL) was inoculated with seed culture (6 mL) and grown at 37°C in a shaker. Flasks were shaken at 200 rpm; when baffled flasks were used, they were shaken at 150 rpm. When the cultures reached OD_{600} = 0.6-0.8 the temperature was decreased (to 20°C for *Hs* IDH1, to 16°C for mycobacterial IDHs) and IPTG was added to each flask. The protein was produced overnight and harvested by centrifugation on an Avanti J-25 centrifuge (Beckman Coulter, Inc.) using a JA-10 rotor at 8000 rpm for 10 min. The pellets were frozen at -80°C prior to cell lysis.

7.1.12.3 Buffer Preparation for Protein Purification

The buffers for the purification of *Hs* IDHs were adapted from previous procedures in our laboratory[135, 48] according to the table below. Buffers for stripping and recharging of the Nickel-affinity column (Cytiva) were based on the manufacturer's protocol.

	C (mM)	n (mol)	M_w (Da)	V (L)	m (g)
1. Nickel-affinity Chromatography					
Stripping Buffer (pH 7.4)					
Sodium phosphate (Na_2HPO_4 * $7H_2O$)	0.02	0.01	177.99	0.5	1.78
NaCl	0.5	0.25	58.44	0.5	14.61
EDTA disodium dihydrate	0.05	0.025	372.24	0.5	9.31
Recharging Solution					
$NiSO_4$ * $7H_2O$	0.1	0.05	280.86	0.5	14.04
Binding Buffer (pH 7.4)					
Tris base	0.02	0.04	121.14	2	4.85
Imidazole	0.005	0.01	68.077	2	0.68
NaCl	0.5	1	58.44	2	58.44
Elution Buffer (pH 7.4)					
Tris base	0.02	0.02	121.14	1	2.42
Imidazole	0.5	0.5	68.077	1	34.04
NaCl	0.1	0.1	58.44	1	5.84
2. Gel Filtration					
Gel filtration Buffer (pH 7.4)					
Tris base	0.02	0.04	121.14	2	4.85
NaCl	0.1	0.2	58.44	2	11.69
3. Anion Exchange					
Ion Exchange Binding Buffer (pH 7.4)					
Tris base	0.05	0.1	121.14	2	12.11
Ion Exchange Elution buffer (pH 7.4)					
Tris base	0.05	0.05	121.14	1	6.06
NaCl	0.5	0.5	58.44	1	29.22

Buffers for the purification of mycobacterial IDHs were adapted from previous procedures in our laboratory and reports by Quartararo et al.[120] according to the table below.

	C (mM)	n (mol)	M_w (Da)	V (L)	m (g)
1. Nickel-affinity Chromatography					
Binding Buffer (pH 8.0)					
Tris base	0.05	0.1	121.14	2	12.11
Imidazole	0.01	0.02	68.077	2	1.36
NaCl	0.3	0.6	58.44	2	35.06
Elution Buffer (pH 8.0)					
Tris base	0.05	0.05	121.14	1	6.06
Imidazole	0.3	0.3	68.077	1	20.42
NaCl	0.1	0.1	58.44	1	5.84
2. Gel filtration					
Gel filtration buffer (pH 8.0)					
Tris base	0.05	0.1	121.14	2	12.11
NaCl	0.15	0.3	58.44	2	17.53
Glycerol (5%) (in mL)					100
3. Anion Exchange					
Ion Exchange Binding Buffer (pH 8.0)					
Tris base	0.05	0.1	121.14	2	12.11
Ion Exchange Elution buffer (pH 8.0)					
Tris base	0.05	0.05	121.14	1	6.06
NaCl	0.5	0.5	58.44	1	29.22

The buffer components were dissolved in MQ water, and the pH adjusted accordingly using HCl or NaOH. The buffers were then filtered through a 0.22 μM filter (Millipore) and degassed for 30 minutes.

7.1.12.4 Bacterial Cell Lysis

A portion of the pellet was crushed up and weighed out in a beaker. Binding buffer (25 mL per 5 g of cell pellet) was poured into the beaker and the following ingredients added: 1% Triton X-100 (Thermo Scientific), a spatula of each: EDTA free DNAse 1 (Roche), phenylmethylsulfonyl fluoride (PMSF; Sigma Aldrich), lysozyme (from chicken egg white, Sigma Aldrich), and 12.5 mg/100 mL tris(2-carboxyethyl)phosphine (TCEP; Sigma Aldrich).

The slurry was stirred until homogeneity and lysed by sonication (9.9 s on, 9.9 s off, 7 min (total on time), 60% amplitude; MSE Soniprep 150 sonicator (Sanyo)) on ice. The lysed cells were centrifuged in an Avanti J-25 centrifuge (Beckman Coulter, Inc.; JA-25.50 rotor, 24000 rpm, 30 min, 4°C).

7.1.12.5 Sodium Dodecylsulfate Polyacrylamide Gel Electrophoresis (SDS-PAGE)

7.1.12.5.1 Preparation of Loading Buffer (6x)

Component	Final concentration
Tris base	375 mM
SDS	9%
Glycerol	50%
Bromophenolblue	0.03%
β-Mercaptoethanol	~10%

Tris base was added to SDS solution (22.5 mL, 20 % (*v/v)*) and the pH adjusted to 6.8 with HCl. Subsequently, glycerol, bromophenolblue and β-mercaptoethanol were added.

7.1.12.5.2 SDS-PAGE Gels

Gels were prepared according to the following recipes.

Stacking Gel (6 gels)

Component	Amount
0.5 M Tris HCl, pH 6.8 (mL)	1.875
MQ water (mL)	4.71
30% Bis-Acrylamide (mL)	0.75
10 % SDS (µL)	75
10% APS (µL)	75
TEMED (µL)	7.5

Running Gel (6 gels)

Component	Amount
1.5 M Tris HCl, pH 8.8 (mL)	6
MQ water (mL)	9.53
30% Bis-Acrylamide (mL)	8.06
10 % SDS (µL)	240
10% APS (µL)	399.9
TEMED (µL)	19.95

The polymerisation process was initiated by addition of ammonium persulfate (APS) and tetramethylethylenediamine (TEMED). The running gel was then poured and submerged with isopropyl alcohol (IPA). After 20 min, IPA was removed and the stacking gel (after the polymerisation initiated by addition of APS and TEMED) poured on top of the running gel before addition of a comb. After 20 min, the comb was removed, each gel wrapped into a wet paper towel and stored in a bag at 4°C.

Running buffer (10x)

Component	Amount
Tris-HCl	30 g
Glycine	144 g
SDS	10 g

The running buffer was diluted 1:10 with MQ water. Protein samples (10 µL) were mixed with loading buffer (2 µL), and heated for 2-5 min at 98°C. The gel was fixed in a running chamber (Invitrogen) and submerged with running buffer. Samples (5-10 µL) were loaded onto the gel. PAGE Ruler prestained protein ladder (5 µL, Thermo Fisher) was added in lane one. Gel electrophoresis was conducted at 180 V for 45 min. The gels were stained using Coomassie Blue (15 min). The staining solution was removed, and the gel washed with water. The gel was subsequently boiled with water using a microwave, the water was removed, and new water was added. This process was repeated three times before the destaining was completed by addition of destaining buffer (Acetic acid (10 % (*v/v)*), Methanol (30 % (*v/v)*); in Water) overnight. Gels were imaged using a Universal Hood III (Bio-Rad).

7.1.12.5.3 Precasted SDS-PAGE Gels

NuPAGE Novex 4-12% Bis-Tris Protein Gels (1mm) and NuPAGE MES SDS Running Buffer (20X) were used (Thermo Fisher). Protein samples (10 µL) were mixed with loading buffer (2 µL), and heated for 2-5 min at 98°C. The gel was fixed in a running chamber (Invitrogen) and submerged with NuPAGE MES SDS Running Buffer. Samples (5-10 µL) were loaded onto the gel. PAGE Ruler prestained protein ladder (5 µL, Thermo Fisher) was added in lane one. Gel electrophoresis was conducted at 200 V for 35 min. The gels were stained using InstantBlue Coomassie stain (1 h; Expedeon).

7.1.12.6 Fast Protein Liquid Chromatography (FPLC)

The purification was conducted using an Äkta pure System. The lysate was filtered through a 0.22 µM filter (Minisart® High Flow; Sartorius) and loaded on a preequilibrated nickel-affinity column (Cytiva). The column was washed with binding buffer and the proteins of interest were eluted with an imidazole step or linear gradient. The fractions containing protein of interest were identified by SDS PAGE gel electrophoresis, pooled, and concentrated by spin-concentration (Amicon Ultra Centrifugal filter, 50 kDa, 15 mL). If anion exchange chromatography was used, the protein of interest was desalted using a PD-10 column (Merck) according to the manufacturer`s protocol and loaded on a Q Sepharose Fast Flow column (Cytiva). The column was washed with ion exchange binding buffer and the protein eluted using a linear NaCl gradient (up to 1000 mM NaCl). The fractions containing protein of interest were identified by SDS PAGE gel electrophoresis, pooled, and concentrated by spin-concentration (Amicon Ultra Centrifugal filter, 50 kDa, 15 mL). The concentrated fractions of nickel-affinity purification or the anion exchange purification were loaded on a preequilibrated gel filtration column (GE Healthcare, S200, 330 mL). Isocratic elution (gel filtration buffer) was conducted overnight, and the protein fractions were identified by SDS PAGE gel electrophoresis. The fractions containing protein were concentrated to the desired concentration by spin-concentration (Amicon Ultra Centrifugal filter, 50 kDa, 15 mL) and aliquoted. The SDS PAGE gels were imaged using a Universal Hood III (Bio-Rad).

7.1.12.7 Determination of Protein Concentration

The protein concentration was determined with a NanoDrop One (Thermo Scientific) using the absorbance at λ = 280 nm and the molar absorption coefficient. The molar absorption coefficient was calculated using the ExPASy ProtParam online tool.[153]

7.2 Biochemical and Biophysical Techniques

7.2.1 Steady-State Kinetics

The spectrophotometric assay for IDH catalysis was based on changes in concentration of NADPH and measured by changes of its absorption at 340 nm (ε = 6,220 $M^{-1}.cm^{-1}$).[203] Analyses were conducted in a 96 well format using a PHERAstar FS Microplate Reader (BMG Labtech) at 25°C. The reaction mixture for each substrate or inhibitor concentration was prepared in triplicate and each replicate measured simultaneously in the same 96 well plate. This assay was used to analyse kinetics and inhibition studies on IDH. The specific parameters are described in each chapter. The approximate standard error of the mean (n = 3) of the non-linear regression curve fit was calculated by GraphPad Prism. For IC_{50} determination, the error was calculated for logarithmical concentration values and then converted into the error of the IC_{50} value.

DL-Isocitric acid trisodium salt was from ChemCruz, 2-oxoglutarate disodium salt was from Sigma-Aldrich. NADPH tetrasodium salt (approximately 98% pure, 100 mg) and $NADP^+$ disodium salt (approximately 98% pure, 100 mg) were from Sigma-Aldrich. 4x stock solutions of all components were prepared, allowed to warm up to room temperature. The change of absorption over time was used to calculate the change in concentration over time according to the Beer-Lambert law:

$$A = \varepsilon * c * d$$

Microsoft Excel (Office 16) was used to execute this calculation to obtain the reaction rates. The reaction rates were used for further analysis by GraphPad Prism (Version 5 or Version 9). For inhibition assays, inhibitors were purchased from MedChemexpress LLC (Ivosidenib (AG-120), enasidenib (AG-221), AGI-6780, IDH224, IDH556, FT-2102, DS-1001B), Enzo Life Sciences (AG-881), Cambridge Bioscience (IDH305), DC Chemicals (IDH889), Sigma-Aldrich (Compound 1, Sanofi), Biovision (BAY-1436032), or kindly provided by GSK (GSK321, GSK864).

7.2.2 Nuclear Magnetic Resonance Spectroscopic Studies

7.2.2.1 ^{1}H NMR Time-Course Studies

The NMR assay buffer was prepared according to the following recipe:

	C (mM)	n (mol)	M_w (Da)	V (L)	m (g)
Tris-d_{11}	0.05	0.0025	121.14	0.05	0.30
NaCl	0.1	0.005	58.44	0.05	0.29

The components were dissolved in MQ water, and pH 7.5 adjusted using HCl and NaOH. The enzymes were buffer exchanged into NMR assay buffer using Micro Bio-Spin 6 Columns (Bio-Rad) according to the manufacturer's protocol (four repeats of the equilibration step). $MgCl_2$ and D_2O were from Sigma-Aldrich. Potassium *D*-isocitrate monobasic was from Sigma-Aldrich. The other components were the same as used for spectrophotometric assays (Section 7.2.1).

The NMR assay buffer was mixed with the enzyme stock solution, $MgCl_2$ stock solution (10 mM final) and D_2O (16 µL, 10% of total volume) in an Eppendorf tube. The mixture was allowed to settle at room temperature for 10 minutes. The reaction was initiated by addition of 2-OG/isocitrate and NADPH/$NADP^+$, and then transferred to a 3 mm NMR tube. Nuclear Magnetic Resonance (NMR) spectra were obtained using a Bruker AVIII 700 MHz NMR spectrometer equipped with an inverse 5mm TCI $^1H/^{13}C/^{15}N$ cryoprobe. The samples were measured using ^1H NMR (700 MHz) (NS: 16, Relaxation delay: 2 s). The water signal was suppressed by excitation sculpting.

7.2.2.2 ^1H CPMG NMR

Carr-Purcell-Meiboom-Gill (CPMG) NMR spectroscopy was carried out according to following parameters: total echo time, 40 ms; relaxation delay, 2 s; number of scans: 600. Water suppression was achieved by pre-saturation. 10 µM inhibitor was used in 50 mM Tris-d_{11} (pH 7.5) and 10 % D_2O.

7.2.3 Electrochemical Experiments

Electrochemical experiments were performed by Ryan Herold (DPhil student, University of Oxford) in an anaerobic glovebox (Glove Box Technology) containing a nitrogen atmosphere (O_2 < 1 ppm). The electrochemical apparatus (an in-house glass electrochemical cell and in-house rotating pyrolytic graphite edge (PGE) electrodes) were as previously described.[204] An Autolab PGSTAT 10 potentiostat using Nova software was used to carry out electrochemical experiments. Electrode potentials (*E*) were measured against a saturated calomel electrode (SCE) and converted to the standard hydrogen electrode (SHE) using a temperature-dependent potential conversion equation that has been previously described[204] (at 25°C the conversion is:

E_{SHE} = E_{SCE} + 0.2412 V). Nanoporous indium tin oxide (ITO) electrodes were made by electrophoretically depositing ITO nanoparticles (< 50 nm, Sigma-Aldrich) onto pyrolytic graphite edge electrodes (ITO/PGE) as previously described.[204] Enzymes were loaded onto the electrode by dropcasting a 4–6 μL mixed enzyme solution onto the ITO electrode and allowing it to incubate at room temperature for at least 30 minutes while making sure that the solution did not evaporate. In all cases, 0.85 nmol (homodimer basis) of IDH1 was used. All tested IDH1 variants (R132C, R132C S280F, R132H, R132H S280F, R132S) were loaded at a 2.5 to 1 molar ratio with FNR (i.e. 2.5-fold more (homodimer molar equivalent) of each IDH1 variant was loaded relative to FNR for each experiment). IDH1 enzyme concentrations were calculated based on their respective homodimers. Electrodes were thoroughly rinsed using buffer solution before submerging them in the reaction buffer for each experiment to ensure that there was no free enzyme in solution.

7.2.4 Circular Dichroism Studies

Sodium phosphate buffer (10 mM, pH 8.0) was prepared, and proteins were buffer exchanged using Micro Bio-Spin 6 Columns (Bio-Rad) according to the manufacturer`s protocol (four repeats of the equilibration step). The protein concentration was adjusted to 0.2 mg/mL using a Nanodrop One (Thermo Scientific). The measurements were carried out using a Chirascan CD spectrometer (Applied Photophysics) equipped with a Peltier temperature-controlled cell holder. The spectra were recorded in a range from 260-185 nm (0.5 nm intervals). Measurements were conducted in triplicate at 23 °C and the background was subtracted from that of the buffer. The spectra were averaged and smoothed using the Savitzky–Golay filter (Window size 4). Data were normalised to the protein concentration (measured by NanoDrop One, Thermo Scientific) and the mean residue ellipticity (MRE) was calculated according to the formula:

$$MRE = [deg.cm^2.dmol^{-1}]$$

θ: Degree of ellipticity

N: Number of amino acids

C: Concentration (mol/L)

l: Path length (0.1 cm)

7.2.5 Melting Temperature Studies

7.2.5.1 Circular Dichroism

The same solutions and instrument as described in Section 7.2.4 were used. The wavelength was fixed at 215 nm and the temperature gradually increased from 10-80°C to measure the melting temperature (T_m). The heating rate was 1°C/min and the CD signal measured every 2°C (tolerance 0.4°C). The spectra were smoothed using the Savitzky–Golay filter (4th order polynomial, 12 neighbours) of the GraphPad Prism software (version 5). T_m was calculated using a Boltzmann sigmoidal model with the Graph Pad Prism software (version 5).

7.2.5.2 Differential Scanning Calorimetry

Protein samples were diluted in the gel filtration buffer to a concentration of 20 μM. Samples were submitted to the DSC Service in the Department of Biochemistry (University of Oxford) and the measurements kindly carried out by Dr David Staunton. The measurements were performed on a Malvern VP Capillary DSC instrument. Gel filtration buffer was used as blank. The measurements were carried out using a thermal ramp of 200 °C h^{-1} between 10 °C and 110 °C at a pressure of 55 psi. Graphs were made using Graph Pad Prism (version 5).

7.2.5.3 Differential Scanning Fluorimetry

Measurements were conducted in Tris buffer (50 mM, pH 7.4) with 3 μM protein and 3x Sypro Orange (Invitrogen) on a Thermal Cycler CFX96 machine (Bio-Rad). The heat rate was +0.2°C s^{-1} in a range of 20-95°C. The data were analysed using the CFX Manager 3.1 (Bio-Rad).

7.2.6 Non-denaturing PAGE

Non-denaturing PAGE was conducted using precast gels. Novex™ WedgeWell™ 4-12% Tris-glycine gels (Invitrogen) were used. The G-250 sample additive was added, an anionic dye binding to the protein to ensure migration towards the cathode. The gel chamber (Invitrogen) was cooled in an ice bath and the gel electrophoresis conducted in the cold room (4°C) using NativePAGE running buffer (Invitrogen). The gel electrophoresis was carried out for 1.5 h at 160 V and the gel was stained using InstantBlue Coomassie (Expedeon).

7.2.7 Size Exclusion Chromatography-Multi Angle Light Scattering (SEC-MALS)

SEC-MALS was kindly conducted by Dr David Staunton in the Department of Biochemistry, University of Oxford. The measurements were carried out using a Wyatt Dawn HELEOS-II 8-angle light scattering detector and Wyatt Optilab rEX refractive index monitor linked to a

Shimadzu HPLC system comprising LC-20AD pump, SIL-20A Autosampler and SPD20A UV/Vis detector. Samples were analysed with a Superdex 200 HR10/30 column (Cytiva) with a flowrate of 0.5 ml×min^{-1}. The sample concentration was 1 mg×mL^{-1} in a buffer containing Tris (20 mM, pH 7.4) and NaCl (100 mM) for *Hs* IDH1 or Tris (50 mM, pH 8.0) and NaCl (150 mM) for mycobacterial IDHs.

7.2.8 Mass Spectrometry

7.2.8.1 Non-denaturing Mass Spectrometry

To prepare buffer for non-denaturing mass spectrometry, ammonium acetate (1 M, 5x) was dissolved in MQ water, and the pH adjusted to 7.5 with acetic acid. The solution was filtered (Minisart® High Flow, 0.22 µM; Sartorius) and stored at 4°C. This stock solution was diluted 5-fold with MQ water to give the final non-denaturing MS buffer (200 mM). The proteins were buffer exchanged into ammonium acetate buffer using Micro Bio-Spin 6 Columns (Bio-Rad) according to the manufacturer`s protocol (the equilibration step was conducted 7 times). The protein concentration was adjusted and measured using a Nanodrop One (Thermo Scientific). After sample preparation, the tubes were spun down at 13,000 rpm for 5 minutes and the supernatant used for analysis. Non-denaturing mass spectrometry experiments were carried out using a quadrupole-TOF (Waters Synapt G2Si) instrument connected to an Advion Nanomate system. The mass spectrum was analysed using MassLynx v4.1 (Waters).

7.2.8.2 Denaturing Mass Spectrometry

Denaturing mass spectrometry was used for the analysis of intact protein mass and analysis of covalent binding to the protein. Samples were diluted in gel filtration buffer to the appropriate concentration, spun down at 13,000 rpm for 5 minutes and the supernatant used for analysis.

7.2.8.2.1 LCT (TOF) LC-MS

The protein sample was diluted to 0.03 mg/mL and analysed on a Waters LCT (TOF) LC-MS (LCT Premier mass spectrometer interfaced with a AcQuity™ Ultra Performance liquid chromatography (UPLC) system using a AcQuity™ UPLCR BEH300 C-18 column (Waters Corporation)) with electrospray ionisation (positive mode). The column was washed with IPA before each run. The mass spectrum was analysed using MassLynx v4.1 (Waters) and deconvoluted using the maximal entropy method (MaxEnt1).

7.2.8.2.2 Xevo G2-XS LC-MS

The protein sample was diluted to 1 μM in gel filtration buffer and analysed on a Waters XEVO G2-XS system coupled to Acquity UHPLC systems using a C-4 column. The column was washed with IPA before each run. The mass spectrum was analysed using MassLynx v4.1 and deconvoluted using the Maximum Entropy Method (MaxEnt1).

7.2.9 Crystallographic Studies

Protein crystals were obtained using the sitting-drop vapor diffusion method. A 24 well Cryschem Plate (Hampton Research, USA) with a reservoir solution of 250 μL was used. Specific parameters are described in each chapter.

7.2.10 Cellular Studies and Metabolomics

The preparation of the cell lines was conducted by Dr Chiara Bardella and Dr Alina Finch at the University of Birmingham. The inhibitor treatment and metabolomic analyses was conducted by Ingvild Hvinden (DPhil student) at the University of Oxford.

7.2.10.1 Lentiviral Expression of IDH1 Variants in LN18 Cell Lines

7.2.10.1.1 Molecular Cloning and Cell Transduction with Lentiviral Vectors

Human glioblastoma LN18 cells were obtained from the ATCC (CRL-2610) and cultured according to the supplier's instructions. LN18 cells were genetically modified to overexpress genes encoding IDH1 R132H, IDH1 R132C, IDH1 R132H S280F or IDH1 R132C S280F of the human IDH1 gene by lentiviral vector transduction. First, the IDH1 S280F mutant sequence of IDH1 was generated by a recombinant PCR-based approach, using the lentiviral transfer vectors pCC.sin.36.IDH1R132H.PPTWpre.CMV.tTA-S2tet and the pCC.sin.36.IDH1R132C.PPTWpre.CMV.tTA-S2tet (see Bardella et al.[205]), as templates in a PCR reaction. In this reaction the following primers were used:

Primer	Sequence (5' to 3')
Forward	GGTGACGTGCAGTCGGACTTTGTGGCCCAA
Reverse	TCTTTCCCCTGCACTGTACC

The IDH1 S280F mutant amplicon was subsequently subcloned into the pCC.sin.36.IDH1R132H.PPTWpre.CMV.tTA-S2tet and the

pCC.sin.36.IDH1R132C.PPTWpre.CMV.tTA-S2tet transfer vectors, which encode for the IDH1 R132H and R132C mutant sequences of IDH. This was done using BamH1-HF (New England Biolabs) and Nhe1-HF (New England Biolabs) restriction enzymes and cloning in the gene fragment encoding for S280F. DNA encoding sequences for IDH1 R132H, R132C, IDH1 R132H S280F or IDH1 R132C S280F were amplified in PCR reactions by using the following primers:

Primer	Sequence (5' to 3')
Forward	TATACCCGGGCCTATGTCCAAAAAAATCAGTGGCGG
Reverse	TCCACATAGCGTAAAAGGAGCA

The genes were cloned into to the pUltra-Chili vector (AddGene) using Xma1 and NheI-HF restriction enzymes (New England Biolabs). All bacterial transformations were performed using XL10-Gold ultracompetent cells (Agilent) according to the manufacturer's instructions. All constructs were verified by Sanger sequencing using the following primers:

Primer	Sequence (5' to 3')
Forward	GACCAAGTCACCAAGGATGC
Reverse	GCTTTGCTCTGTGGGCTAA

7.2.10.1.2 Generation of lentiviral vectors and cell transduction

All the IDH1 mutant pUltra-Chili transfer plasmids were packaged into lentiviral vectors (LVs) by transient transfection of HEK293T cells along with the 3 packaging plasmids pVSVg, pREV and pMDL (Addgene). 48h after transfection HEK293T conditioned medium was harvested, centrifuged, and filtered using 0.22 µm filters (Minisart® High Flow; Sartorius). The viral p24 antigen concentration was measured by using an HIV-1 p24 core profile enzyme-linked immunosorbent assay ELISA assay Lenti-X p24 Rapid Titer kit (Takara) according to the manufacturer's instructions. Serial dilutions of freshly harvested conditioned medium were used to infect $1.2x10^5$ LN18 cells in a six-well plate, in the presence of polybrene (8 µg/ml). As a control, cells were transduced with pUltra-Chili lentiviral vector, which do not contain any transfer sequence.

7.2.10.1.3 RNA extraction and RT-PCR and qPCR Reactions

RNA was extracted using the RNeasy microkit (Qiagen) according to the manufacturer's instructions. When required, complementary DNA was reverse transcribed using the High-Capacity cDNA Reverse Transcription Kit (Applied Biosystems). qPCR was used to measure IDH1 expression in control and LV-transduced cells by using an IDH1 TaqMan probe (Life Technologies) and the TaqMan Fast Universal PCR Master-Mix (Applied Biosystems). The reaction was performed using the QuantStudio™ 5 Dx Real-Time PCR System (Applied Biosystems) with GAPDH serving as an endogenous control (Life Technologies). Each target gene's expression was evaluated using a relative quantification approach ($2-\Delta\Delta CT$ method).

7.2.10.2 Inhibitor Treatment of LN18 cell lines

Liquid and sterile filtered Dulbecco's phosphate buffered saline (PBS), foetal bovine serum (FBS) of non-US origin, and Dulbecco's Modified Eagle's Medium (DMEM) with 4500 mg/L glucose and sodium bicarbonate, without L-glutamine, were all from Merck Life Sciences. GlutaMAX™ supplement was from Thermo Fisher Scientific. Dimethyl sulfoxide (DMSO) for molecular biology was from Merck. Sterile syringe filters (15 mm diameter, 0.2 µM pore, RC membrane) were from Corning. Inhibitors for cell culture were dissolved in DMSO to 5 mM concentration and filtered prior to use with Corning® syringe filters (regenerated cellulose, 18 mm diameter, 0.2 µm pores).

LN18 cells containing an empty vector or producing recombinant IDH1 R132C, IDH1 R132C S280F, IDH1 R132H, or IDH1 R132H S280F were incubated at 37 °C and 5% CO_2 and grown in DMEM (4500 mg/L glucose) supplemented with 10% (v/v) FBS and 1% (v/v) GlutaMAX™. Cells were seeded into 12-well plates, 0.700 mL per well at 200,000 cells/mL. After 24 hours of incubation, the original medium was replaced with fresh 0.700 mL medium (DMEM (4500 mg/L glucose), 10% FBS and 1% GlutaMAX™) with either 5 µM inhibitor (ivosidenib, GSK864, IDH224, FT-2102, DS-1001B) or 0.1% DMSO (control samples). Cells were incubated for a further 24 hours prior to harvesting. During harvest, the medium was removed by aspiration before the wells were gently washed twice with 0.700 mL PBS per well. 75 µL of 80% (v/v) aqueous methanol was added to each well and the plate was placed on dry ice. The cells were scraped, and the content of each well was transferred to separate microtubes.

7.2.10.3 Sample Preparation and MS Studies

Cell extracts were spun down at 14,000 *g* for 25 minutes. The DNA concentration (ng/µL) of the supernatants were measured using a ClarioStar Plus (BMG Labtech) with an LVis plate.

2.5 µL of the supernatant was added to each well. The plate was blanked with 2.5 µL 80% (v/v) aqueous methanol per well prior to measurement of DNA concentration. The remaining cell sample supernatant was transferred to Total Recovery vials (Waters) and diluted relative to DNA concentration. Anion-exchange chromatography MS was carried out as previously described.[206]

References

1. Hanahan, D. & Weinberg, R. A. Hallmarks of cancer: the next generation. *Cell* **144**, 646–674 (2011).
2. Warburg, O. On the Origin of Cancer Cells. *Science* **123**, 309–314 (1956).
3. Warburg, O. On Respiratory Impairment in Cancer Cells. *Science* **124**, 269–270 (1956).
4. Alauddin, M. M. Positron emission tomography (PET) imaging with 18F-based radiotracers. *Am J Nucl Med Mol Imaging* **2**, 55–76 (2011).
5. Hanahan, D. & Weinberg, R. A. The hallmarks of cancer. *Cell* **100**, 57–70 (2000).
6. Schmidt, C., Sciacovelli, M. & Frezza, C. Fumarate hydratase in cancer: A multifaceted tumour suppressor. *Semin Cell Dev Biol* **98**, 15–25 (2020).
7. Sciacovelli, M. & Frezza, C. Oncometabolites: Unconventional triggers of oncogenic signalling cascades. *Free Radic Biol Med* **100**, 175–181 (2016).
8. Cascón, A. *et al.* Whole-exome sequencing identifies MDH2 as a new familial paraganglioma gene. *J Natl Cancer Inst* **107**, djv053 (2015).
9. Tommasini-Ghelfi, S. *et al.* Cancer-associated mutation and beyond: The emerging biology of isocitrate dehydrogenases in human disease. *Science Advances* **5**, eaaw4543.
10. Golub, D. *et al.* Mutant Isocitrate Dehydrogenase Inhibitors as Targeted Cancer Therapeutics. *Front Oncol* **9**, (2019).
11. Dang, L. *et al.* Cancer-associated IDH1 mutations produce 2-hydroxyglutarate. *Nature* **462**, 739–744 (2009).
12. Liu, S., Cadoux-Hudson, T. & Schofield, C. J. Isocitrate dehydrogenase variants in cancer — Cellular consequences and therapeutic opportunities. *Current Opinion in Chemical Biology* **57**, 122–134 (2020).
13. Al-Khallaf, H. Isocitrate dehydrogenases in physiology and cancer: biochemical and molecular insight. *Cell Biosci* **7**, 37 (2017).

14. Sun, P., Liu, Y., Ma, T. & Ding, J. Structure and allosteric regulation of human NAD-dependent isocitrate dehydrogenase. *Cell Discov* **6**, 94 (2020).
15. Xu, X. *et al.* Structures of human cytosolic NADP-dependent isocitrate dehydrogenase reveal a novel self-regulatory mechanism of activity. *J Biol Chem* **279**, 33946–33957 (2004).
16. Xie, X. *et al.* Allosteric Mutant IDH1 Inhibitors Reveal Mechanisms for IDH1 Mutant and Isoform Selectivity. *Structure* **25**, 506–513 (2017).
17. Al-Khallaf, H. Isocitrate dehydrogenases in physiology and cancer: biochemical and molecular insight. *Cell Biosci* **7**, 37 (2017).
18. Hvinden, I. C., Cadoux-Hudson, T., Schofield, C. J. & McCullagh, J. S. O. Metabolic adaptations in cancers expressing isocitrate dehydrogenase mutations. *CR Med* **2**, (2021).
19. Sellés Vidal, L., Kelly, C. L., Mordaka, P. M. & Heap, J. T. Review of NAD(P)H-dependent oxidoreductases: Properties, engineering and application. *Biochimica et Biophysica Acta (BBA) - Proteins and Proteomics* **1866**, 327–347 (2018).
20. Parsons, D. W. *et al.* An integrated genomic analysis of human glioblastoma multiforme. *Science* **321**, 1807–1812 (2008).
21. Mardis, E. R. *et al.* Recurring mutations found by sequencing an acute myeloid leukemia genome. *N Engl J Med* **361**, 1058–1066 (2009).
22. Losman, J.-A. & Kaelin, W. G. What a difference a hydroxyl makes: mutant IDH, (R)-2-hydroxyglutarate, and cancer. *Genes Dev.* **27**, 836–852 (2013).
23. Nakagawa, M. *et al.* Selective inhibition of mutant IDH1 by DS-1001b ameliorates aberrant histone modifications and impairs tumor activity in chondrosarcoma. *Oncogene* **38**, 6835–6849 (2019).

24. Cadoux-Hudson, T., Schofield, C. J. & McCullagh, J. S. O. Isocitrate dehydrogenase gene variants in cancer and their clinical significance. *Biochemical Society Transactions* BST20210277 (2021) doi:10.1042/BST20210277.

25. Matteo, D. A. *et al.* Molecular mechanisms of isocitrate dehydrogenase 1 (IDH1) mutations identified in tumors: The role of size and hydrophobicity at residue 132 on catalytic efficiency. *The Journal of Biological Chemistry* **292**, 7971 (2017).

26. Amary, M. F. *et al.* IDH1 and IDH2 mutations are frequent events in central chondrosarcoma and central and periosteal chondromas but not in other mesenchymal tumours. *J Pathol* **224**, 334–343 (2011).

27. The oncometabolite 2-hydroxyglutarate inhibits histone lysine demethylases. *EMBO reports* **12**, 463–469 (2011).

28. Intlekofer, A. M. *et al.* Acquired resistance to IDH inhibition through trans or cis dimer-interface mutations. *Nature* **559**, 125–129 (2018).

29. Livermore, L. J. *et al.* Rapid intraoperative molecular genetic classification of gliomas using Raman spectroscopy. *Neuro-Oncology Advances* **1**, vdz008 (2019).

30. Ohka, F. *et al.* Quantitative metabolome analysis profiles activation of glutaminolysis in glioma with IDH1 mutation. *Tumour Biol* **35**, 5911–5920 (2014).

31. Heil, C. S., Wehrheim, S. S., Paithankar, K. S. & Grininger, M. Fatty Acid Biosynthesis: Chain-Length Regulation and Control. *ChemBioChem* **20**, 2298–2321 (2019).

32. Cytosolic NADP+-dependent isocitrate dehydrogenase status modulates oxidative damage to cells. *Free Radical Biology and Medicine* **32**, 1185–1196 (2002).

33. Control of Mitochondrial Redox Balance and Cellular Defense against Oxidative Damage by Mitochondrial NADP+-dependent Isocitrate Dehydrogenase. *Journal of Biological Chemistry* **276**, 16168–16176 (2001).

34. Bleeker, F. E. *et al.* The prognostic IDH1R132 mutation is associated with reduced NADP+-dependent IDH activity in glioblastoma. *Acta Neuropathol* **119**, 487–494 (2010).
35. Dang, L. *et al.* Cancer-associated IDH1 mutations produce 2-hydroxyglutarate. *Nature* **462**, 739–744 (2009).
36. Selak, M. A. *et al.* Succinate links TCA cycle dysfunction to oncogenesis by inhibiting HIF-alpha prolyl hydroxylase. *Cancer Cell* **7**, 77–85 (2005).
37. Semenza, G. L. HIF-1: upstream and downstream of cancer metabolism. *Current Opinion in Genetics & Development* **20**, 51–56 (2010).
38. Koivunen, P. *et al.* Transformation by the (R)-enantiomer of 2-hydroxyglutarate linked to EGLN activation. *Nature* **483**, 484–488 (2012).
39. Tarhonskaya, H. *et al.* Non-enzymatic chemistry enables 2-hydroxyglutarate-mediated activation of 2-oxoglutarate oxygenases. *Nat Commun* **5**, 3423 (2014).
40. Avellaneda Matteo, D. *et al.* Molecular mechanisms of isocitrate dehydrogenase 1 (IDH1) mutations identified in tumors: The role of size and hydrophobicity at residue 132 on catalytic efficiency. *J Biol Chem* **292**, 7971–7983 (2017).
41. Acker, T. *et al.* Genetic evidence for a tumor suppressor role of HIF-2α. *Cancer Cell* **8**, 131–141 (2005).
42. Song, L.-P. *et al.* Hypoxia-inducible factor-1alpha-induced differentiation of myeloid leukemic cells is its transcriptional activity independent. *Oncogene* **27**, 519–527 (2008).
43. Sudhamalla, B., Dey, D., Breski, M. & Islam, K. A rapid mass spectrometric method for the measurement of catalytic activity of ten-eleven translocation enzymes. *Analytical Biochemistry* **534**, 28–35 (2017).
44. Roman, J. V., Melkonian, T. R., Silvaggi, N. R. & Moran, G. R. Transient-State Analysis of Human Isocitrate Dehydrogenase I: Accounting for the Interconversion of Active and Non-Active Conformational States. *Biochemistry* **58**, 5366–5380 (2019).

45. Xu, W. *et al.* Oncometabolite 2-Hydroxyglutarate Is a Competitive Inhibitor of α-Ketoglutarate-Dependent Dioxygenases. *Cancer Cell* **19**, 17–30 (2011).

46. Aktas, D. F. & Cook, P. F. A Lysine-Tyrosine Pair Carries Out Acid−Base Chemistry in the Metal Ion-Dependent Pyridine Dinucleotide-Linked β-Hydroxyacid Oxidative Decarboxylases. *Biochemistry* **48**, 3565–3577 (2009).

47. Quartararo, C. E., Hazra, S., Hadi, T. & Blanchard, J. S. Structural, Kinetic and Chemical Mechanism of Isocitrate Dehydrogenase-1 from Mycobacterium tuberculosis. *Biochemistry* **52**, 1765–1775 (2013).

48. Liu, S. *et al.* Roles of metal ions in the selective inhibition of oncogenic variants of isocitrate dehydrogenase 1. *Commun Biol* **4**, 1–16 (2021).

49. Glioma-Derived Mutations in IDH1 Dominantly Inhibit IDH1 Catalytic Activity and Induce HIF-1α. https://www.science.org/doi/abs/10.1126/science.1170944.

50. Pietrak, B. *et al.* A Tale of Two Subunits: How the Neomorphic R132H IDH1 Mutation Enhances Production of αHG. *Biochemistry* **50**, 4804–4812 (2011).

51. Rendina, A. R. *et al.* Mutant IDH1 enhances the production of 2-hydroxyglutarate due to its kinetic mechanism. *Biochemistry* **52**, 4563–4577 (2013).

52. Pusch, S. *et al.* D-2-Hydroxyglutarate producing neo-enzymatic activity inversely correlates with frequency of the type of isocitrate dehydrogenase 1 mutations found in glioma. *Acta Neuropathologica Communications* **2**, 19 (2014).

53. Bunse, L. *et al.* Proximity ligation assay evaluates $IDH1^{R132H}$ presentation in gliomas. *J Clin Invest* **125**, 593–606 (2015).

54. Schumacher, T. *et al.* A vaccine targeting mutant IDH1 induces antitumour immunity. *Nature* **512**, 324–327 (2014).

55. Platten, M. *et al.* A vaccine targeting mutant IDH1 in newly diagnosed glioma. *Nature* **592**, 463–468 (2021).

56. Ma, R. & Yun, C.-H. Crystal structures of pan-IDH inhibitor AG-881 in complex with mutant human IDH1 and IDH2. *Biochem. Biophys. Res. Commun.* **503**, 2912–2917 (2018).
57. Yen, K. *et al.* AG-221, a First-in-Class Therapy Targeting Acute Myeloid Leukemia Harboring Oncogenic IDH2 Mutations. *Cancer Discov* **7**, 478–493 (2017).
58. Ma, R. & Yun, C.-H. Crystal structures of pan-IDH inhibitor AG-881 in complex with mutant human IDH1 and IDH2. *Biochemical and Biophysical Research Communications* **503**, 2912–2917 (2018).
59. Lin, J. *et al.* Discovery and Optimization of Quinolinone Derivatives as Potent, Selective, and Orally Bioavailable Mutant Isocitrate Dehydrogenase 1 (mIDH1) Inhibitors. *J. Med. Chem.* **62**, 6575–6596 (2019).
60. Zheng, B. *et al.* Crystallographic Investigation and Selective Inhibition of Mutant Isocitrate Dehydrogenase. *ACS Med Chem Lett* **4**, 542–546 (2013).
61. Wu, F. *et al.* Inhibition of Cancer-Associated Mutant Isocitrate Dehydrogenases by 2-Thiohydantoin Compounds. *J. Med. Chem.* **58**, 6899–6908 (2015).
62. Chaturvedi, A. *et al.* In vivo efficacy of mutant IDH1 inhibitor HMS-101 and structural resolution of distinct binding site. *Leukemia* **34**, 416–426 (2020).
63. Popovici-Muller, J. *et al.* Discovery of AG-120 (Ivosidenib): A First-in-Class Mutant IDH1 Inhibitor for the Treatment of IDH1 Mutant Cancers. *ACS Med. Chem. Lett.* **9**, 300–305 (2018).
64. Research, C. for D. E. and. Approved Drugs - FDA approves ivosidenib for relapsed or refractory acute myeloid leukemia (2018). https://www.fda.gov/Drugs/InformationOnDrugs/ApprovedDrugs/ucm614128.htm.
65. MD, J. J. L. *Phase II Study of IDH1 Inhibitor Ivosidenib and Nivolumab in IDH1 Mutant Gliomas and Advanced Solid Tumors*. https://clinicaltrials.gov/ct2/show/NCT04056910 (2021).

66. Urban, D. J. *et al.* Assessing inhibitors of mutant isocitrate dehydrogenase using a suite of pre-clinical discovery assays. *Sci Rep* **7**, 12758 (2017).

67. Agios Pharmaceuticals, Inc. *A Phase I, Multicenter, Open-Label, Dose-Escalation and Expansion, Safety, Pharmacokinetic, Pharmacodynamic, and Clinical Activity Study of Orally Administered AG-881 in Patients With Advanced Hematologic Malignancies With an IDH1 and/or IDH2 Mutation*. https://clinicaltrials.gov/ct2/show/NCT02492737 (2019).

68. Agios Pharmaceuticals, Inc. *A Phase 3, Multicenter, Randomized, Double-blind, Placebo-Controlled Study of AG-881 in Subjects With Residual or Recurrent Grade 2 Glioma With an IDH1 or IDH2 Mutation*. https://clinicaltrials.gov/ct2/show/NCT04164901 (2020).

69. Okoye-Okafor, U. C. *et al.* New IDH1 mutant inhibitors for treatment of acute myeloid leukemia. *Nat Chem Biol* **11**, 878–886 (2015).

70. Cho, Y. S. *et al.* Discovery and Evaluation of Clinical Candidate IDH305, a Brain Penetrant Mutant IDH1 Inhibitor. *ACS Med Chem Lett* **8**, 1116–1121 (2017).

71. Deng, G. *et al.* Selective Inhibition of Mutant Isocitrate Dehydrogenase 1 (IDH1) via Disruption of a Metal Binding Network by an Allosteric Small Molecule. *Journal of Biological Chemistry* **290**, 762–774 (2015).

72. Optimization of 3-Pyrimidin-4-yl-oxazolidin-2-ones as Allosteric and Mutant Specific Inhibitors of IDH1 | ACS Medicinal Chemistry Letters. https://pubs.acs.org/doi/10.1021/acsmedchemlett.6b00334.

73. Cho, Y. S. *et al.* Discovery and Evaluation of Clinical Candidate IDH305, a Brain Penetrant Mutant IDH1 Inhibitor. *ACS Med Chem Lett* **8**, 1116–1121 (2017).

74. Trial of IDH305 in IDH1 Mutant Grade II or III Glioma - Full Text View - ClinicalTrials.gov. https://clinicaltrials.gov/ct2/show/NCT02977689.

75. Novartis Pharmaceuticals. *A Phase I Study of IDH305 in Patients With Advanced Malignancies That Harbor IDH1R132 Mutations*. https://clinicaltrials.gov/ct2/show/NCT02381886 (2019).
76. Cho, Y. S. *et al.* 3-pyrimidin-4-yl-oxazolidin-2-ones as inhibitors of mutant idh. (2013).
77. Urban, D. J. *et al.* Assessing inhibitors of mutant isocitrate dehydrogenase using a suite of pre-clinical discovery assays. *Sci Rep* **7**, 12758 (2017).
78. Deng, G. *et al.* Selective inhibition of mutant isocitrate dehydrogenase 1 (IDH1) via disruption of a metal binding network by an allosteric small molecule. *J. Biol. Chem.* **290**, 762–774 (2015).
79. Pusch, S. *et al.* Pan-mutant IDH1 inhibitor BAY 1436032 for effective treatment of IDH1 mutant astrocytoma in vivo. *Acta Neuropathol* **133**, 629–644 (2017).
80. Bayer. *An Open-label, Non-randomized, Multicenter Phase I Study to Determine the Maximum Tolerated and / or Recommended Phase II Dose of Oral Mutant IDH1 (mIDH1) Inhibitor BAY1436032 and to Characterize Its Safety, Tolerability, Pharmacokinetics, Pharmacodynamics, and Preliminary Clinical Efficacy in Patients With mIDH1-R132X Advanced Acute Myeloid Leukemia (AML)*. https://clinicaltrials.gov/ct2/show/NCT03127735 (2019).
81. Bayer. *An Open-label, Non-randomized, Multicenter Phase I Study to Determine the Maximum Tolerated or Recommended Phase II Dose of Oral Mutant IDH1 Inhibitor BAY1436032 and to Characterize Its Safety, Tolerability, Pharmacokinetics and Preliminary Pharmacodynamic and Anti-tumor Activity in Patients With IDH1-R132X-mutant Advanced Solid Tumors*. https://clinicaltrials.gov/ct2/show/NCT02746081 (2020).
82. Caravella, J. A. *et al.* Structure-Based Design and Identification of FT-2102 (Olutasidenib), a Potent Mutant-Selective IDH1 Inhibitor. *J Med Chem* **63**, 1612–1623 (2020).

83. A Potent Blood-Brain Barrier-Permeable Mutant IDH1 Inhibitor Suppresses the Growth of Glioblastoma with IDH1 Mutation in a Patient-Derived Orthotopic Xenograft Model - PubMed. https://pubmed.ncbi.nlm.nih.gov/31727689/.

84. Lin, J. *et al.* Discovery and Optimization of Quinolinone Derivatives as Potent, Selective, and Orally Bioavailable Mutant Isocitrate Dehydrogenase 1 (mIDH1) Inhibitors. *J. Med. Chem.* **62**, 6575–6596 (2019).

85. Forma Therapeutics, Inc. *A Phase 1b/2 Study of FT 2102 in Participants With Advanced Solid Tumors and Gliomas With an IDH1 Mutation*. https://clinicaltrials.gov/ct2/show/NCT03684811 (2020).

86. ASTX727 and FT-2102 in Treating IDH1-Mutated Recurrent/Refractory Myelodysplastic Syndrome or Acute Myeloid Leukemia - Full Text View - ClinicalTrials.gov. https://clinicaltrials.gov/ct2/show/NCT04013880.

87. Forma Therapeutics, Inc. *A Phase 1/2, Multicenter, Open-label Study of FT-2102 as a Single Agent and in Combination With Azacitidine or Cytarabine in Patients With Acute Myeloid Leukemia or Myelodysplastic Syndrome With an IDH1 Mutation*. https://clinicaltrials.gov/ct2/show/NCT02719574 (2019).

88. Nakagawa, M. *et al.* Selective inhibition of mutant IDH1 by DS-1001b ameliorates aberrant histone modifications and impairs tumor activity in chondrosarcoma. *Oncogene* **38**, 6835–6849 (2019).

89. Machida, Y. *et al.* A Potent Blood–Brain Barrier-Permeable Mutant IDH1 Inhibitor Suppresses the Growth of Glioblastoma with IDH1 Mutation in a Patient-Derived Orthotopic Xenograft Model. *Mol Cancer Ther* **19**, 375–383 (2020).

90. Natsume, A. *et al.* Phase I study of a brain penetrant mutant IDH1 inhibitor DS-1001b in patients with recurrent or progressive IDH1 mutant gliomas. *JCO* **37**, 2004–2004 (2019).

91. Study of DS-1001b in Patients With Gene IDH1-Mutated Gliomas - Full Text View - ClinicalTrials.gov. https://clinicaltrials.gov/ct2/show/NCT03030066.
92. Daiichi Sankyo Co., Ltd. *A Phase II Study of DS-1001b in Patients With Chemotherapy- and Radiotherapy-naive IDH1 Mutated WHO Grade II Glioma*. https://clinicaltrials.gov/ct2/show/NCT04458272 (2020).
93. Brooks, N. *et al.* Abstract LB-274: Identification and characterization of LY3410738, a novel covalent inhibitor of cancer-associated mutant Isocitrate Dehydrogenase 1 (IDH1). *Cancer Res* **79**, LB-274 (2019).
94. Pauff, J. M. *et al.* A phase I study of LY3410738, a first-in-class covalent inhibitor of mutant IDH1 in cholangiocarcinoma and other advanced solid tumors. *JCO* **39**, TPS350–TPS350 (2021).
95. Eli Lilly and Company. *A Phase 1 Study of LY3410738 Administered to Patients With Advanced Solid Tumors With IDH1 or IDH2 Mutations*. https://clinicaltrials.gov/ct2/show/NCT04521686 (2021).
96. Eli Lilly and Company. *A Phase 1 Study of Oral LY3410738 in Patients With Advanced Hematologic Malignancies With IDH1 or IDH2 Mutations*. https://clinicaltrials.gov/ct2/show/NCT04603001 (2021).
97. Zheng, B. *et al.* Crystallographic Investigation and Selective Inhibition of Mutant Isocitrate Dehydrogenase. *ACS Med. Chem. Lett.* **4**, 542–546 (2013).
98. Liu, Z. *et al.* Inhibition of cancer-associated mutant isocitrate dehydrogenases: synthesis, structure-activity relationship, and selective antitumor activity. *J. Med. Chem.* **57**, 8307–8318 (2014).
99. Wu, F. *et al.* Inhibition of Cancer-Associated Mutant Isocitrate Dehydrogenases by 2-Thiohydantoin Compounds. *J Med Chem* **58**, 6899–6908 (2015).

100. Chaturvedi, A. *et al.* A Novel Inhibitor of Mutant IDH1 Induces Differentiation in Vivo and Prolongs Survival in a Mouse Model of Leukemia. *Blood* **124**, 3598–3598 (2014).

101. Harding, J. J. *et al.* Isoform Switching as a Mechanism of Acquired Resistance to Mutant Isocitrate Dehydrogenase Inhibition. *Cancer Discov* **8**, 1540–1547 (2018).

102. Choe, S. *et al.* Molecular mechanisms mediating relapse following ivosidenib monotherapy in IDH1-mutant relapsed or refractory AML. *Blood Advances* **4**, 1894–1905 (2020).

103. Oltvai, Z. N. *et al.* Assessing acquired resistance to IDH1 inhibitor therapy by full-exon IDH1 sequencing and structural modeling. *Cold Spring Harb Mol Case Stud* **7**, a006007 (2021).

104. Ma, R. & Yun, C.-H. Crystal structures of pan-IDH inhibitor AG-881 in complex with mutant human IDH1 and IDH2. *Biochem Biophys Res Commun* **503**, 2912–2917 (2018).

105. Jones, S. *et al.* Discovery and Optimization of Allosteric Inhibitors of Mutant Isocitrate Dehydrogenase 1 (R132H IDH1) Displaying Activity in Human Acute Myeloid Leukemia Cells. *J Med Chem* **59**, 11120–11137 (2016).

106. Li, J. *et al.* Targeting Metabolism in Cancer Cells and the Tumour Microenvironment for Cancer Therapy. *Molecules* **25**, E4831 (2020).

107. Global tuberculosis report 2021. Geneva: World Health Organization; 2021. Licence: CC BY-NC-SA 3.0 IGO.

108. Queval, C. J., Brosch, R. & Simeone, R. The Macrophage: A Disputed Fortress in the Battle against Mycobacterium tuberculosis. *Frontiers in Microbiology* **8**, 2284 (2017).

109. Decroo, T., Jong, B. C. de, Piubello, A., Lynen, L. & Deun, A. V. Tuberculosis treatment: one-shot approach or cascade of regimens? *The Lancet Respiratory Medicine* **8**, e4–e5 (2020).

110. Best, C. A. & Best, T. J. Mycobacterium smegmatis Infection of the Hand. *Hand (N Y)* **4**, 165–166 (2009).

111. Dolan, S. K. & Welch, M. The Glyoxylate Shunt, 60 Years On. *Annu. Rev. Microbiol.* **72**, 309–330 (2018).

112. Kondrashov, F. A., Koonin, E. V., Morgunov, I. G., Finogenova, T. V. & Kondrashova, M. N. Evolution of glyoxylate cycle enzymes in Metazoa: evidence of multiple horizontal transfer events and pseudogene formation. *Biol Direct* **1**, 31 (2006).

113. Murima, P. *et al.* A rheostat mechanism governs the bifurcation of carbon flux in mycobacteria. *Nat Commun* **7**, 12527 (2016).

114. McKinney, J. D. *et al.* Persistence of Mycobacterium tuberculosis in macrophages and mice requires the glyoxylate shunt enzyme isocitrate lyase. *Nature* **406**, 735–738 (2000).

115. McKinney, J. D. *et al.* Persistence of Mycobacterium tuberculosis in macrophages and mice requires the glyoxylate shunt enzyme isocitrate lyase. *Nature* **406**, 735–738 (2000).

116. Bhusal, R. P. *et al.* Acetyl-CoA-mediated activation of Mycobacterium tuberculosis isocitrate lyase 2. *Nat Commun* **10**, 4639 (2019).

117. Ko, E.-M. *et al.* Regulation of the icl1 Gene Encoding the Major Isocitrate Lyase in Mycobacterium smegmatis. *Journal of Bacteriology* **203**, e00402-21.

118. Banerjee, S., Nandyala, A., Podili, R., Katoch, V. M. & Hasnain, S. E. Comparison of Mycobacterium tuberculosis isocitrate dehydrogenases (ICD-1 and ICD-2) reveals differences in coenzyme affinity, oligomeric state, pH tolerance and phylogenetic affiliation. *BMC Biochem* **6**, 20 (2005).

119. Banerjee, S. *et al.* Mycobacterium tuberculosis (Mtb) isocitrate dehydrogenases show strong B cell response and distinguish vaccinated controls from TB patients. *Proc Natl Acad Sci U S A* **101**, 12652–12657 (2004).

120. Quartararo, C. E., Hazra, S., Hadi, T. & Blanchard, J. S. Structural, Kinetic and Chemical Mechanism of Isocitrate Dehydrogenase-1 from Mycobacterium tuberculosis. *Biochemistry* **52**, 1765–1775 (2013).

121. LaPorte, D. C. & Koshland, D. E. A protein with kinase and phosphatase activities involved in regulation of tricarboxylic acid cycle. *Nature* **300**, 458–460 (1982).

122. Crousilles, A., Dolan, S. K., Brear, P., Chirgadze, D. Y. & Welch, M. Gluconeogenic precursor availability regulates flux through the glyoxylate shunt in Pseudomonas aeruginosa. *J Biol Chem* **293**, 14260–14269 (2018).

123. Intlekofer, A. M. *et al.* Acquired resistance to IDH inhibition through trans or cis dimer-interface mutations. *Nature* **559**, 125–129 (2018).

124. AG-221, a First-in-Class Therapy Targeting Acute Myeloid Leukemia Harboring Oncogenic IDH2 Mutations | Cancer Discovery. https://cancerdiscovery.aacrjournals.org/content/7/5/478.

125. Research, C. for D. E. and. Approved Drugs - FDA granted regular approval to enasidenib for the treatment of relapsed or refractory AML (2017). https://www.fda.gov/drugs/informationondrugs/approveddrugs/ucm569482.htm.

126. Rendina, A. R. *et al.* Mutant IDH1 Enhances the Production of 2-Hydroxyglutarate Due to Its Kinetic Mechanism. *Biochemistry* **52**, 4563–4577 (2013).

127. Zheng, L., Baumann, U. & Reymond, J.-L. An efficient one-step site-directed and site-saturation mutagenesis protocol. *Nucleic Acids Res.* **32**, e115 (2004).

128. Katoh, K., Misawa, K., Kuma, K. & Miyata, T. MAFFT: a novel method for rapid multiple sequence alignment based on fast Fourier transform. *Nucleic Acids Research* **30**, 3059–3066 (2002).

129. Hirel, P. H., Schmitter, M. J., Dessen, P., Fayat, G. & Blanquet, S. Extent of N-terminal methionine excision from Escherichia coli proteins is governed by the side-chain length of the penultimate amino acid. *PNAS* **86**, 8247–8251 (1989).

130. Bonissone, S., Gupta, N., Romine, M., Bradshaw, R. A. & Pevzner, P. A. N-terminal Protein Processing: A Comparative Proteogenomic Analysis. *Mol Cell Proteomics* **12**, 14–28 (2013).

131. Okoye-Okafor, U. C. *et al.* New IDH1 mutant inhibitors for treatment of acute myeloid leukemia. *Nat Chem Biol* **11**, 878–886 (2015).

132. Johnson, K. A. & Goody, R. S. The Original Michaelis Constant: Translation of the 1913 Michaelis–Menten Paper. *Biochemistry* **50**, 8264–8269 (2011).

133. Matteo, D. A. *et al.* Molecular Mechanisms of Isocitrate Dehydrogenase 1 (IDH1) Mutations Identified in Tumors: The Role of Size and Hydrophobicity at Residue 132 on Catalytic Efficiency. *J. Biol. Chem.* jbc.M117.776179 (2017) doi:10.1074/jbc.M117.776179.

134. Fielding, L. NMR methods for the determination of protein-ligand dissociation constants. *Curr Top Med Chem* **3**, 39–53 (2003).

135. Herold, R. A. *et al.* Exploiting Electrode Nanoconfinement to Investigate the Catalytic Properties of Isocitrate Dehydrogenase (IDH1) and a Cancer-Associated Variant. *J. Phys. Chem. Lett.* **12**, 6095–6101 (2021).

136. Choe, S. *et al.* Molecular mechanisms mediating relapse following ivosidenib monotherapy in IDH1-mutant relapsed or refractory AML. *Blood Advances* **4**, 1894–1905 (2020).

137. Oltvai, Z. N. *et al.* Assessing acquired resistance to IDH1 inhibitor therapy by full-exon IDH1 sequencing and structural modeling. *Cold Spring Harb Mol Case Stud* **7**, a006007 (2021).

138. Greenfield, N. J. Using circular dichroism spectra to estimate protein secondary structure. *Nat Protoc* **1**, 2876–2890 (2006).

139. Johnson, C. M. Differential scanning calorimetry as a tool for protein folding and stability. *Archives of Biochemistry and Biophysics* **531**, 100–109 (2013).

140. Niesen, F. H., Berglund, H. & Vedadi, M. The use of differential scanning fluorimetry to detect ligand interactions that promote protein stability. *Nat Protoc* **2**, 2212–2221 (2007).

141. Henderson, N. S. Isozymes of isocitrate dehydrogenase: Subunit structure and intracellular location. *Journal of Experimental Zoology* **158**, 263–273 (1965).

142. Some, D., Amartely, H., Tsadok, A. & Lebendiker, M. Characterization of Proteins by Size-Exclusion Chromatography Coupled to Multi-Angle Light Scattering (SEC-MALS). *J Vis Exp* (2019) doi:10.3791/59615.

143. Hernández, H. & Robinson, C. V. Determining the stoichiometry and interactions of macromolecular assemblies from mass spectrometry. *Nat Protoc* **2**, 715–726 (2007).

144. Chalk, R. *et al. Electrospray Surface Charge Describes Protein Molecular Motion*. http://biorxiv.org/lookup/doi/10.1101/571091 (2019) doi:10.1101/571091.

145. Geoghegan, K. F. *et al.* Spontaneous alpha-N-6-phosphogluconoylation of a 'His tag' in Escherichia coli: the cause of extra mass of 258 or 178 Da in fusion proteins. *Anal. Biochem.* **267**, 169–184 (1999).

146. Rupp, B. *Biomolecular Crystallography: Principles, Practice, and Application to Structural Biology*. (Garland Science, 2009).

147. Machida, Y. *et al.* A Potent Blood-Brain Barrier-Permeable Mutant IDH1 Inhibitor Suppresses the Growth of Glioblastoma with IDH1 Mutation in a Patient-Derived Orthotopic Xenograft Model. *Mol Cancer Ther* **19**, 375–383 (2020).

148. Carrington, J. C. & Dougherty, W. G. A viral cleavage site cassette: identification of amino acid sequences required for tobacco etch virus polyprotein processing. *PNAS* **85**, 3391–3395 (1988).

149. Chevallet, M., Luche, S. & Rabilloud, T. Silver staining of proteins in polyacrylamide gels. *Nat Protoc* **1**, 1852–1858 (2006).

150. Winter, G., Lobley, C. M. C. & Prince, S. M. Decision making in xia2. *Acta Crystallogr D Biol Crystallogr* **69**, 1260–1273 (2013).

151. Xu, X. *et al.* Structures of human cytosolic NADP-dependent isocitrate dehydrogenase reveal a novel self-regulatory mechanism of activity. *J Biol Chem* **279**, 33946–33957 (2004).

152. Deng, G. *et al.* Selective Inhibition of Mutant Isocitrate Dehydrogenase 1 (IDH1) via Disruption of a Metal Binding Network by an Allosteric Small Molecule. *Journal of Biological Chemistry* **290**, 762–774 (2015).

153. The Proteomics Protocols Handbook | SpringerLink (Accessed 23/12/2021). https://link.springer.com/book/10.1385/1592598900.

154. Rendina, A. R. *et al.* Mutant IDH1 enhances the production of 2-hydroxyglutarate due to its kinetic mechanism. *Biochemistry* **52**, 4563–4577 (2013).

155. McCoy, A. J. *et al.* Phaser crystallographic software. *J Appl Crystallogr* **40**, 658–674 (2007).

156. Adams, P. D. *et al.* PHENIX: building new software for automated crystallographic structure determination. *Acta Crystallogr D Biol Crystallogr* **58**, 1948–1954 (2002).

157. Emsley, P., Lohkamp, B., Scott, W. G. & Cowtan, K. Features and development of Coot. *Acta Crystallogr D Biol Crystallogr* **66**, 486–501 (2010).

158. Liebschner, D. *et al.* Macromolecular structure determination using X-rays, neutrons and electrons: recent developments in Phenix. *Acta Crystallogr D Struct Biol* **75**, 861–877 (2019).

159. Xie, X. *et al.* Allosteric Mutant IDH1 Inhibitors Reveal Mechanisms for IDH1 Mutant and Isoform Selectivity. *Structure* **25**, 506–513 (2017).

160. Merk, A. *et al.* Breaking Cryo-EM Resolution Barriers to Facilitate Drug Discovery. *Cell* **165**, 1698–1707 (2016).

161. Okoye-Okafor, U. C. *et al.* New IDH1 mutant inhibitors for treatment of acute myeloid leukemia. *Nat Chem Biol* **11**, 878–886 (2015).

162. Yen, K. *et al.* AG-221, a First-in-Class Therapy Targeting Acute Myeloid Leukemia Harboring Oncogenic IDH2 Mutations. *Cancer Discov* **7**, 478–493 (2017).

163. Agios Pharmaceuticals, Inc. *A Phase 3, Multicenter, Randomized, Double-blind, Placebo-Controlled Study of AG-881 in Subjects With Residual or Recurrent Grade 2 Glioma With an IDH1 or IDH2 Mutation*. https://clinicaltrials.gov/ct2/show/NCT04164901 (2021).

164. Forma Therapeutics, Inc. *A Phase 1b/2 Study of FT 2102 in Participants With Advanced Solid Tumors and Gliomas With an IDH1 Mutation*. https://clinicaltrials.gov/ct2/show/NCT03684811 (2020).

165. Novartis Pharmaceuticals. *A Phase I Study of IDH305 in Patients With Advanced Malignancies That Harbor IDH1R132 Mutations*. https://clinicaltrials.gov/ct2/show/NCT02381886 (2021).

166. Bayer. *An Open-label, Non-randomized, Multicenter Phase I Study to Determine the Maximum Tolerated or Recommended Phase II Dose of Oral Mutant IDH1 Inhibitor BAY1436032 and to Characterize Its Safety, Tolerability, Pharmacokinetics and*

Preliminary Pharmacodynamic and Anti-tumor Activity in Patients With IDH1-R132X-mutant Advanced Solid Tumors. https://clinicaltrials.gov/ct2/show/NCT02746081 (2021).

167. Levell, J. R. *et al.* Optimization of 3-Pyrimidin-4-yl-oxazolidin-2-ones as Allosteric and Mutant Specific Inhibitors of IDH1. *ACS Med Chem Lett* **8**, 151–156 (2017).

168. Cho, Y. S. *et al.* Discovery and Evaluation of Clinical Candidate IDH305, a Brain Penetrant Mutant IDH1 Inhibitor. *ACS Med Chem Lett* **8**, 1116–1121 (2017).

169. Liu, Z. *et al.* Inhibition of Cancer-Associated Mutant Isocitrate Dehydrogenases: Synthesis, Structure–Activity Relationship, and Selective Antitumor Activity. *J. Med. Chem.* **57**, 8307–8318 (2014).

170. Pusch, S. *et al.* Pan-mutant IDH1 inhibitor BAY 1436032 for effective treatment of IDH1 mutant astrocytoma in vivo. *Acta Neuropathol* **133**, 629–644 (2017).

171. Okoye-Okafor, U. C. *et al.* New IDH1 mutant inhibitors for treatment of acute myeloid leukemia. *Nat. Chem. Biol.* **11**, 878–886 (2015).

172. Caravella, J. A. *et al.* Structure-Based Design and Identification of FT-2102 (Olutasidenib), a Potent Mutant-Selective IDH1 Inhibitor. *J. Med. Chem.* **63**, 1612–1623 (2020).

173. Aguilar, J. A., Nilsson, M., Bodenhausen, G. & Morris, G. A. Spin echo NMR spectra without J modulation. *Chem. Commun.* **48**, 811–813 (2011).

174. Pusch, S. *et al.* Pan-mutant IDH1 inhibitor BAY 1436032 for effective treatment of IDH1 mutant astrocytoma in vivo. *Acta Neuropathol* **133**, 629–644 (2017).

175. Walsby-Tickle, J. *et al.* Anion-exchange chromatography mass spectrometry provides extensive coverage of primary metabolic pathways revealing altered metabolism in IDH1 mutant cells. *Commun Biol* **3**, 1–12 (2020).

176. Yeom, C. J. *et al.* A novel hNIS/tdTomato fusion reporter for visualizing the relationship between the cellular localization of sodium iodide symporter and its iodine uptake function under heat shock treatment. *Mol Imaging* **14**, (2015).

177. Tajadini, M., Panjehpour, M. & Javanmard, S. Comparison of SYBR Green and TaqMan methods in quantitative real-time polymerase chain reaction analysis of four adenosine receptor subtypes. *Adv Biomed Res* **3**, 85 (2014).

178. Urban, D. J. *et al.* Assessing inhibitors of mutant isocitrate dehydrogenase using a suite of pre-clinical discovery assays. *Sci Rep* **7**, 12758 (2017).

179. Nakagawa, M. *et al.* Selective inhibition of mutant IDH1 by DS-1001b ameliorates aberrant histone modifications and impairs tumor activity in chondrosarcoma. *Oncogene* **38**, 6835–6849 (2019).

180. Intlekofer, A. M. *et al.* Acquired resistance to IDH inhibition through trans or cis dimer-interface mutations. *Nature* **559**, 125–129 (2018).

181. Forma Therapeutics, Inc. *A Phase 1/2, Multicenter, Open-label Study of FT-2102 as a Single Agent and in Combination With Azacitidine or Cytarabine in Patients With Acute Myeloid Leukemia or Myelodysplastic Syndrome With an IDH1 Mutation*. https://clinicaltrials.gov/ct2/show/NCT02719574 (2019).

182. Machida, Y. *et al.* A Potent Blood-Brain Barrier-Permeable Mutant IDH1 Inhibitor Suppresses the Growth of Glioblastoma with IDH1 Mutation in a Patient-Derived Orthotopic Xenograft Model. *Mol Cancer Ther* **19**, 375–383 (2020).

183. Levell, J. R. *et al.* Optimization of 3-Pyrimidin-4-yl-oxazolidin-2-ones as Allosteric and Mutant Specific Inhibitors of IDH1. *ACS Med Chem Lett* **8**, 151–156 (2017).

184. Afonine, P. V. *et al.* Towards automated crystallographic structure refinement with phenix.refine. *Acta Crystallogr D Biol Crystallogr* **68**, 352–367 (2012).

185. Terwilliger, T. SOLVE and RESOLVE: automated structure solution, density modification and model building. *J Synchrotron Radiat* **11**, 49–52 (2004).

186. Terwilliger, T. C. *et al.* Iterative model building, structure refinement and density modification with the PHENIX AutoBuild wizard. *Acta Crystallogr D Biol Crystallogr* **64**, 61–69 (2008).

187. Zwart, P. H., Grosse-Kunstleve, R. W. & Adams, P. D. Xtriage and Fest: automatic assessment of X-ray data and substructure structure factor estimation. 9.

188. Matteo, D. A. *et al.* Molecular mechanisms of isocitrate dehydrogenase 1 (IDH1) mutations identified in tumors: The role of size and hydrophobicity at residue 132 on catalytic efficiency. *Journal of Biological Chemistry* **292**, 7971–7983 (2017).

189. Pietrak, B. *et al.* A Tale of Two Subunits: How the Neomorphic R132H IDH1 Mutation Enhances Production of αHG. *Biochemistry* **50**, 4804–4812 (2011).

190. Yang, H., Ye, D., Guan, K.-L. & Xiong, Y. IDH1 and IDH2 mutations in tumorigenesis: mechanistic insights and clinical perspectives. *Clin Cancer Res* **18**, 5562–5571 (2012).

191. Yang, B., Zhong, C., Peng, Y., Lai, Z. & Ding, J. Molecular mechanisms of "off-on switch" of activities of human IDH1 by tumor-associated mutation R132H. *Cell Research* **20**, 1188–1200 (2010).

192. Banerjee, S., Nandyala, A., Podili, R., Katoch, V. M. & Hasnain, S. E. Comparison of Mycobacterium tuberculosis isocitrate dehydrogenases (ICD-1 and ICD-2) reveals differences in coenzyme affinity, oligomeric state, pH tolerance and phylogenetic affiliation. *BMC Biochemistry* **6**, 20 (2005).

193. Kang, Y. S. & Gore, J. C. Studies of tissue NMR relaxation enhancement by manganese. Dose and time dependences. *Invest Radiol* **19**, 399–407 (1984).

194. Stafford, S. L. *et al.* Metal ions in macrophage antimicrobial pathways: emerging roles for zinc and copper. *Biosci Rep* **33**, e00049 (2013).

195. Samanovic, M. I., Ding, C., Thiele, D. J. & Darwin, K. H. Copper in Microbial Pathogenesis: Meddling with the Metal. *Cell Host & Microbe* **11**, 106–115 (2012).

196. Wagner, D. *et al.* Elemental analysis of Mycobacterium avium-, Mycobacterium tuberculosis-, and Mycobacterium smegmatis-containing phagosomes indicates pathogen-induced microenvironments within the host cell's endosomal system. *J Immunol* **174**, 1491–1500 (2005).

197. Traut, T. *Allosteric regulatory enzymes*. (Springer, 2008).

198. Nimmo, H. G. Kinetic mechanism of *Escherichia coli* isocitrate dehydrogenase and its inhibition by glyoxylate and oxaloacetate. *Biochemical Journal* **234**, 317–323 (1986).

199. Wang, F. *et al.* Targeted inhibition of mutant IDH2 in leukemia cells induces cellular differentiation. *Science* **340**, 622–626 (2013).

200. Festa, M., Colonna, A., Pietropaolo, C. & Ruffo, A. Oxalomalate, a competitive inhibitor of aconitase, modulates the RNA-binding activity of iron-regulatory proteins. 6 (2000).

201. Raineri, S. & Mellor, J. IDH1: Linking Metabolism and Epigenetics. *Front Genet* **9**, 493 (2018).

202. Banerjee, S. *et al.* Mycobacterium tuberculosis (Mtb) isocitrate dehydrogenases show strong B cell response and distinguish vaccinated controls from TB patients. *Proc. Natl. Acad. Sci. U.S.A.* **101**, 12652–12657 (2004).

203. Veskoukis, A. S., Margaritelis, N. V., Kyparos, A., Paschalis, V. & Nikolaidis, M. G. Spectrophotometric assays for measuring redox biomarkers in blood and tissues: the NADPH network. *Redox Report* **23**, 47–56 (2018).

204. Herold, R. A. *et al.* Exploiting Electrode Nanoconfinement to Investigate the Catalytic Properties of Isocitrate Dehydrogenase (IDH1) and a Cancer-Associated Variant. *The Journal of Physical Chemistry Letters* **12**, 6095–6101 (2021).

205. Bardella, C. *et al.* Expression of Idh1R132H in the Murine Subventricular Zone Stem Cell Niche Recapitulates Features of Early Gliomagenesis. *Cancer Cell* **30**, 578–594 (2016).

206. Walsby-Tickle, J. *et al.* Anion-exchange chromatography mass spectrometry provides extensive coverage of primary metabolic pathways revealing altered metabolism in IDH1 mutant cells. *Commun Biol* **3**, 1–12 (2020).